

**4**

# **Springer Series on Fluorescence**

**Methods and Applications**

**Series Editor: O. S. Wolfbeis**

# **Springer Series on Fluorescence**

**Series Editor: O. S. Wolfbeis**

Recently Published and Forthcoming Volumes

**Standardization and Quality Assurance  
in Fluorescence Measurements**

State of the Art and Future Challenges

Volume Editor: Resch-Genger, U.

Vol. 5, 2008

**Fluorescence of Supermolecules,  
Polymers, and Nanosystems**

Volume Editor: Berberan-Santos, M. N.

Vol. 4, 2007

**Fluorescence Spectroscopy in Biology**

Volume Editor: Hof, M.

Vol. 3, 2004

**Fluorescence Spectroscopy, Imaging and Probes**

Volume Editor: Kraayenhof, R.

Vol. 2, 2002

**New Trends in Fluorescence Spectroscopy**

Volume Editor: Valeur, B.

Vol. 1, 2001

# Fluorescence of Supermolecules, Polymers, and Nanosystems

Volume Editor: M. N. Berberan-Santos

With contributions by

A. U. Acuña · N. Adjimatera · F. Amat-Guerri · D. L. Andrews  
C. Baleizão · A. Benda · M. N. Berberan-Santos · E. J. Bieske  
D. K. Bird · I. S. Blagbrough · E. N. Bodunov · S. M. Borisov  
P. Chojnacki · R. G. Crisp · A. Deres · J. Enderlein · Y. Engelborghs  
J. P. S. Farinha · B. A. Harruff · A. Hennig · M. Hof · J. Hofkens  
O. Inganäs · K. G. Jespersen · N. Kahya · A. A. Karasyov · I. Klimant  
A. S. Kocincova · A. L. Koner · T. Kral · M. Langner · J. C. Lima  
Y. Lin · C. Lodeiro · L. M. S. Loura · G. Maertens · J. M. G. Martinho  
T. Mayr · L. J. McKimmie · S. Melnikov · D. Merkle · C. Moser  
B. Muls · S. Nagl · S. Nascimento · W. M. Nau · M. Orrit · A. J. Parola  
F. Pina · M. Prieto · T. Pullerits · M. Schaeferling · P. Schwill  
T. A. Smith · M. I. Stich · Y.-P. Sun · V. Sundström · H. Uji-i  
B. Valeur · J. Vercammen · P. J. Wearne · S. Westenhoff · O. S. Wolfbeis  
A. Yartsev · Y. Zaushitsyn · B. Zhou

Fluorescence spectroscopy, fluorescence imaging and fluorescent probes are indispensable tools in numerous fields of modern medicine and science, including molecular biology, biophysics, biochemistry, clinical diagnosis and analytical and environmental chemistry. Applications stretch from spectroscopy and sensor technology to microscopy and imaging, to single molecule detection, to the development of novel fluorescent probes, and to proteomics and genomics. The Springer Series on Fluorescence aims at publishing state-of-the-art articles that can serve as invaluable tools for both practitioners and researchers being active in this highly interdisciplinary field. The carefully edited collection of papers in each volume will give continuous inspiration for new research and will point to exciting new trends.

Library of Congress Control Number: 2007931851

ISSN 1617-1306

ISBN 978-3-540-73927-2 Springer Berlin Heidelberg New York

DOI 10.1007/978-3-540-73928-9

This work is subject to copyright. All rights are reserved, whether the whole or part of the material is concerned, specifically the rights of translation, reprinting, reuse of illustrations, recitation, broadcasting, reproduction on microfilm or in any other way, and storage in data banks. Duplication of this publication or parts thereof is permitted only under the provisions of the German Copyright Law of September 9, 1965, in its current version, and permission for use must always be obtained from Springer. Violations are liable for prosecution under the German Copyright Law.

**Springer is a part of Springer Science+Business Media**

springer.com

© Springer-Verlag Berlin Heidelberg 2008

The use of registered names, trademarks, etc. in this publication does not imply, even in the absence of a specific statement, that such names are exempt from the relevant protective laws and regulations and therefore free for general use.

Cover design: WMXDesign GmbH, Heidelberg

Typesetting and Production: LE-TeX Jelonek, Schmidt & Vöckler GbR, Leipzig

Printed on acid-free paper 02/3180 YL - 5 4 3 2 1 0

---

## **Series Editor**

Prof. Dr. Otto S. Wolfbeis

Institute of Analytical Chemistry,  
Chemo- and Biosensors  
University of Regensburg  
93040 Regensburg, Germany  
*otto.wolfbeis@chemie.uni-regensburg.de*

## **Volume Editor**

Prof. Dr. Mário N. Berberan-Santos

Centro de Química-Física Molecular  
Instituto Superior Técnico  
1049-001 Lisboa  
Portugal  
*mbs@ist.utl.pt*

---

## Preface

The field of fluorescence continues to grow steadily, both in fundamental aspects and in applications. For instance, the number of scientific articles published every year that contain the word 'fluorescence' in the title has increased approximately linearly in the last 50 years (ISI data), from 150 in 1960 to 3,200 in 2005. These articles are only a small fraction of the total number of publications. A search with the same keyword 'fluorescence' anywhere in the article yielded nearly 16,000 articles for the year 2005, a high number indeed, and that exceeds the corresponding figure for 'NMR,' another powerful spectroscopy.

The present book, which is the fourth in the Springer Series on Fluorescence, collects articles written by speakers of the *9th International Conference on Methods and Applications of Fluorescence: Spectroscopy, Imaging and Probes* (MAF 9), held in Lisbon, Portugal, in September 2005, along with a few invited articles. The meeting, with more than 300 participants from 33 countries, included 18 plenary and invited lectures.

Current issues related to fluorescence are discussed in the present book, including recent advances in fluorescence methods and techniques, and the development and application of fluorescent probes. Historical aspects and an overview of fluorescence applications are also covered. Special emphasis is placed on the fluorescence of artificial and biological nanosystems, single-molecule fluorescence, luminescence of polymers, microparticles, nanotubes and nanoparticles, and on fluorescence microscopy and fluorescence correlation spectroscopy.

Lisboa, October 2007

Mário N. Berberan-Santos

---

# Contents

## History and Fundamental Aspects

<b>Early History of Solution Fluorescence: The <i>Lignum nephriticum</i> of Nicolás Monardes</b> A. U. Acuña · F. Amat-Guerri . . . . .	3
<b>From Well-Known to Underrated Applications of Fluorescence</b> B. Valeur . . . . .	21
<b>Principles of Directed Electronic Energy Transfer</b> D. L. Andrews · R. G. Crisp . . . . .	45
<b>Luminescence Decays with Underlying Distributions of Rate Constants: General Properties and Selected Cases</b> M. N. Berberan-Santos · E. N. Bodunov · B. Valeur . . . . .	67
<b>Fluorescence as the Choice Method for Single-Molecule Detection</b> M. Orrit . . . . .	105

## Molecular and Supramolecular Systems

<b>Water-soluble Fluorescent Chemosensors: in Tune with Protons</b> A. J. Parola · J. C. Lima · C. Lodeiro · F. Pina . . . . .	117
<b>Fluorescence of Fullerenes</b> S. Nascimento · C. Baleizão · M. N. Berberan-Santos . . . . .	151
<b>Squeezing Fluorescent Dyes into Nanoscale Containers— The Supramolecular Approach to Radiative Decay Engineering</b> W. M. Nau · A. Hennig · A. L. Koner . . . . .	185

**Polymers, Semiconductors, Model Membranes and Cells****Resonance Energy Transfer in Polymer Interfaces**

J. P. S. Farinha · J. M. G. Martinho . . . . . 215

**Defocused Imaging in Wide-field Fluorescence Microscopy**

H. Uji-i · A. Deres · B. Muls · S. Melnikov · J. Enderlein · J. Hofkens . . . . . 257

**Dynamics of Excited States and Charge Photogeneration  
in Organic Semiconductor Materials**K. G. Jespersen · Y. Zaushitsyn · S. Westenhoff · T. Pullerits  
A. Yartsev · O. Inganäs · V. Sundström . . . . . 285**Resonance Energy Transfer in Biophysics:  
Formalisms and Application to Membrane Model Systems**

L. M. S. Loura · M. Prieto . . . . . 299

**Measuring Diffusion in a Living Cell****Using Fluorescence Correlation Spectroscopy.****A Closer Look at Anomalous Diffusion****Using HIV-1 Integrase and its Interactions as a Probe**

J. Vercammen · G. Maertens · Y. Engelborghs . . . . . 323

**Pushing the Complexity of Model Bilayers:****Novel Prospects for Membrane Biophysics**

N. Kahya · D. Merkle · P. Schwille . . . . . 339

**Nanotubes, Microparticles and Nanoparticles****Photoluminescence Properties of Carbon Nanotubes**

B. Zhou · Y. Lin · B. A. Harruff · Y.-P. Sun . . . . . 363

**Fluorescence Correlation Spectroscopic Studies  
of a Single Lipopolyamine–DNA Nanoparticle**N. Adjimatera · A. Benda · I. S. Blagbrough · M. Langner  
M. Hof · T. Kral . . . . . 381**Morphology-Dependent Resonance Emission  
from Individual Micron-Sized Particles**T. A. Smith · A. J. Trevitt · P. J. Wearne · E. J. Bieske  
L. J. McKimmie · D. K. Bird . . . . . 415



---

**New Plastic Microparticles and Nanoparticles  
for Fluorescent Sensing and Encoding**

S. M. Borisov · T. Mayr · A. A. Karasyov · I. Klimant · P. Chojnacki

C. Moser · S. Nagl · M. Schaeferling · M. I. Stich · A. S. Kocincova

O. S. Wolfbeis . . . . . 431

**Subject Index** . . . . . 465

---

## Contributors

ACUÑA, A. U.

Instituto de Química-Física  
"Rocasolano" (CSIC),  
Serrano 119,  
28006 Madrid, Spain

ADJIMATERA, NOPPADON

Department of Pharmacy  
and Pharmacology,  
University of Bath,  
BA2 7AY Bath, UK

AMAT-GUERRI, F.

Instituto de Química Orgánica (CSIC),  
Juan de la Cierva 3,  
28006 Madrid, Spain

ANDREWS, DAVID L.

Nanostructures and Photomolecular  
Systems,  
School of Chemical Sciences,  
University of East Anglia,  
NR4 7TJ Norwich, UK

BALEIZÃO, CARLOS

Centro de Química-Física Molecular,  
Instituto Superior Técnico,  
1049-001 Lisboa, Portugal

BENDA, ALEŠ

J. Heyrovský Institute of Physical  
Chemistry,  
Academy of Sciences of the Czech Republic,  
Dolejškova 3,  
182 23 Prague 8, Czech Republic

BERBERAN-SANTOS, MÁRIO N.

Centro de Química-Física Molecular,  
Instituto Superior Técnico,  
1049-001 Lisboa, Portugal

BIESKE, EVAN J.

School of Chemistry,  
The University of Melbourne,  
3010 Victoria, Australia

BIRD, DAMIAN K.

School of Chemistry,  
The University of Melbourne,  
3010 Victoria, Australia

BLAGBROUGH, IAN S.

Department of Pharmacy and  
Pharmacology,  
University of Bath,  
BA2 7AY Bath, UK

BODUNOV, EVGENY N.

Physical Department,  
Petersburg State Transport University,  
190031 St. Petersburg, Russia

BORISOV, SERGEY M.

Institute of Analytical Chemistry,  
Chemo- and Biosensors,  
University of Regensburg,  
POB 100102,  
93040 Regensburg, Germany

CHOJNACKI, PAWEL  
Institute of Analytical Chemistry,  
Chemo- and Biosensors,  
University of Regensburg,  
POB 100102,  
93040 Regensburg, Germany

CRISP, RICHARD G.  
Nanostructures and Photomolecular  
Systems,  
School of Chemical Sciences,  
University of East Anglia,  
NR4 7TJ Norwich, UK

DERES, ANIA  
Department of Chemistry,  
Katholieke Universiteit Leuven,  
Celestijnenlaan 200F,  
3001 Heverlee, Belgium

ENDERLEIN, JÖRG  
Institute for Biological  
Information Processing I,  
Forschungszentrum Jülich,  
D-52425 Jülich, Germany

ENGELBORGHES, YVES  
Laboratory of Biomolecular Dynamics,  
University of Leuven,  
Celestijnenlaan 200G,  
3001 Leuven, Belgium

FARINHA, J. P. S.  
Centro de Química-Física Molecular,  
Instituto Superior Técnico,  
1049-001 Lisboa, Portugal

HARRUFF, BARBARA A.  
Department of Chemistry and Laboratory  
for Emerging Materials and Technology,  
Clemson University,  
P.O. Box 340973,  
29634-0973 Clemson, SC, USA

HENNIG, ANDREAS  
School of Engineering and Science,  
Jacobs University Bremen,  
Campus Ring 1,  
28759 Bremen, Germany

HOF, MARTIN  
J. Heyrovský Institute  
of Physical Chemistry,  
Academy of Sciences of the Czech Republic,  
Dolejškova 3,  
182 23 Prague 8, Czech Republic

HOFKENS, JOHAN  
Department of Chemistry,  
Katholieke Universiteit Leuven,  
Celestijnenlaan 200F,  
3001 Heverlee, Belgium

INGANÄS, OLLE  
Biomolecular and Organic Electronics,  
Linköping University,  
58183 Linköping, Sweden

JESPERSEN, KIM G.  
Department of Chemical Physics,  
Lund University,  
Box 124,  
22100 Lund, Sweden

KAHYA, NICOLETTA  
Institute of Biophysics,  
Biotechnology Center,  
Dresden University of Technology,  
Tatzberg 47-49,  
01307 Dresden, Germany  
Philips Research Eindhoven,  
High Tech Campus II,  
5656 AE Eindhoven, The Netherlands

KARASYOV, ALEXANDER A.  
Institute of Analytical Chemistry,  
Chemo- and Biosensors,  
University of Regensburg,  
POB 100102,  
93040 Regensburg, Germany

KLIMANT, INGO  
Institute of Analytical Chemistry,  
Graz University of Technology,  
Technikerstrasse 4,  
8010 Graz, Austria

KOCINCOVA, ANNA S.

Institute of Analytical Chemistry,  
Chemo- and Biosensors,  
University of Regensburg,  
POB 100102,  
93040 Regensburg, Germany

KONER, APURBA L.

School of Engineering and Science,  
Jacobs University Bremen,  
Campus Ring 1,  
28759 Bremen, Germany

KRAL, TERESA

J. Heyrovský Institute of Physical  
Chemistry,  
Academy of Sciences of the Czech Republic,  
Dolejškova 3,  
182 23 Prague 8, Czech Republic  
Department of Physics and Biophysics,  
Wrocław University of Environmental  
and Life Sciences,  
Norwida 25,  
50-375 Wrocław, Poland

LANGNER, MAREK

Institute of Physics,  
Wrocław University of Technology,  
Wybrzeże Wyspiańskiego 27,  
50-370 Wrocław, Poland

LIMA, JOÃO C.

Departamento de Química,  
REQUIMTE-CQFB,  
Faculdade de Ciências e Tecnologia,  
Universidade Nova de Lisboa,  
2829-516 Portugal

LIN, YI

Department of Chemistry and Laboratory  
for Emerging Materials and Technology,  
Clemson University,  
P.O. Box 340973,  
29634-0973 Clemson, SC, USA

LODEIRO, CARLOS

Departamento de Química,  
REQUIMTE-CQFB,  
Faculdade de Ciências e Tecnologia,  
Universidade Nova de Lisboa,  
2829-516 Portugal

LOURA, LUÍS M.S.

Faculdade de Farmácia,  
Universidade de Coimbra,  
Rua do Norte,  
3000-295 Coimbra, Portugal  
Centro de Química de Évora,  
Rua Romão Ramalho 59,  
7000-671 Évora, Portugal

MAERTENS, GOEDELE

Laboratory of Biomolecular Dynamics,  
University of Leuven,  
Celestijnenlaan 200G,  
3001 Leuven, Belgium

MARTINHO, J. M. G.

Centro de Química-Física Molecular,  
Instituto Superior Técnico,  
1049-001 Lisboa, Portugal

MAYR, TORSTEN

Institute of Analytical Chemistry,  
Graz University of Technology,  
Technikerstrasse 4,  
8010 Graz, Austria

McKIMMIE, LACHLAN J.

School of Chemistry,  
The University of Melbourne,  
3010 Victoria, Australia

MELNIKOV, SERGEY

Department of Chemistry,  
Katholieke Universiteit Leuven,  
Celestijnenlaan 200F,  
3001 Heverlee, Belgium

MERKLE, DENNIS  
Institute of Biophysics,  
Biotechnology Center,  
Dresden University of Technology,  
Tatzberg 47-49,  
01307 Dresden, Germany

MOSER, CHRISTOPH  
Institute of Analytical Chemistry,  
Graz University of Technology,  
Technikerstrasse 4,  
8010 Graz, Austria

MULS, BENOIT  
Unité CMAT, Université Catholique de  
Louvain,  
Bâtiment Lavoisier Place L. Pasteur 1,  
1348 Louvain-la-Neuve, Belgium

NAGL, STEFAN  
Institute of Analytical Chemistry,  
Chemo- and Biosensors,  
University of Regensburg,  
POB 100102,  
93040 Regensburg, Germany

NASCIMENTO, SUSANA  
Centro de Química-Física Molecular,  
Instituto Superior Técnico,  
1049-001 Lisboa, Portugal

NAU, WERNER M.  
School of Engineering and Science,  
Jacobs University Bremen,  
Campus Ring 1,  
28759 Bremen, Germany

ORRIT, MICHEL  
MoNOS, Huygens Laboratory,  
Leiden University,  
Postbus 9504,  
2300 RA Leiden, The Netherlands

PAROLA, A. JORGE  
Departamento de Química,  
REQUIMTE-CQFB,  
Faculdade de Ciências e Tecnologia,  
Universidade Nova de Lisboa,  
2829-516 Portugal

PINA, FERNANDO  
Departamento de Química,  
REQUIMTE-CQFB,  
Faculdade de Ciências e Tecnologia,  
Universidade Nova de Lisboa,  
2829-516 Portugal

PRIETO, MANUEL  
Centro de Química-Física Molecular,  
Instituto Superior Técnico,  
Av. Rovisco Pais,  
1049-001 Lisboa, Portugal

PULLERITS, T.  
Department of Chemical Physics,  
Lund University,  
Box 124,  
22100 Lund, Sweden

SCHAEFERLING, MICHAEL  
Institute of Analytical Chemistry,  
Chemo- and Biosensors,  
University of Regensburg,  
POB 100102,  
93040 Regensburg, Germany

SCHWILLE, PETRA  
Institute of Biophysics,  
Biotechnology Center,  
Dresden University of Technology,  
Tatzberg 47-49,  
01307 Dresden, Germany

SMITH, TREVOR A.  
School of Chemistry,  
The University of Melbourne,  
3010 Victoria, Australia

STICH, MATTHIAS I.  
Institute of Analytical Chemistry,  
Chemo- and Biosensors,  
University of Regensburg,  
POB 100102,  
93040 Regensburg, Germany

SUN, YA-PING

Department of Chemistry and Laboratory  
for Emerging Materials and Technology,  
Clemson University,  
P.O. Box 340973,  
29634-0973 Clemson, SC, USA

SUNDSTRÖM, VILLY

Department of Chemical Physics,  
Lund University,  
Box 124,  
22100 Lund, Sweden

TREVITT, ADAM J.

School of Chemistry,  
The University of Melbourne,  
3010 Victoria, Australia

UJI-I, HIROSHI

Department of Chemistry,  
Katholieke Universiteit Leuven,  
Celestijnenlaan 200F,  
3001 Heverlee, Belgium

VALEUR, BERNARD

CNRS UMR 8531,  
Laboratoire de Chimie Générale,  
CNAM, 292 rue Saint-Martin,  
75141 Paris cedex 03, France  
Laboratoire PPSM, ENS-Cachan,  
61 avenue du Président Wilson,  
94235 Cachan cedex, France

VERCAMMEN, JO

Laboratory of Biomolecular Dynamics,  
University of Leuven,  
Celestijnenlaan 200G,  
3001 Leuven, Belgium

WEARNE, PHILIP J.

School of Chemistry,  
The University of Melbourne,  
3010 Victoria, Australia

WESTENHOFF, SEBASTIAN

Cavendish Laboratory,  
University of Cambridge,  
Madingley Road,  
CH3 0HE Cambridge, UK

WOLFBEIS, OTTO S.

Institute of Analytical Chemistry,  
Chemo- and Biosensors,  
University of Regensburg,  
POB 100102,  
93040 Regensburg, Germany

YARTSEV, ARKADY

Department of Chemical Physics,  
Lund University,  
Box 124,  
22100 Lund, Sweden

ZAUSHITSYN, YURI

Department of Chemical Physics,  
Lund University,  
Box 124,  
22100 Lund, Sweden

ZHOU, BING

Department of Chemistry and Laboratory  
for Emerging Materials and Technology,  
Clemson University,  
P.O. Box 340973,  
29634-0973 Clemson, SC, USA

**Part A**  
**History and Fundamental Aspects**

## Early History of Solution Fluorescence: The *Lignum nephriticum* of Nicolás Monardes

A. U. Acuña<sup>1</sup> (✉) · F. Amat-Guerri<sup>2</sup>

<sup>1</sup>Instituto de Química-Física “Rocasolano” (CSIC), Serrano 119, 28006 Madrid, Spain  
roculises@iqfr.csic.es

<sup>2</sup>Instituto de Química Orgánica (CSIC), Juan de la Cierva 3, 28006 Madrid, Spain

“y pediles, me diesen personas habiles,  
y experimentadas con quien pudiese platicar:  
... señalaronme, hasta diez, o doze principales ancianos:  
y dixeronme, que con aquellos, podia comunicar”

(I requested able and experimented persons to whom I could enquire:  
they presented me up to ten or twelve old learned men:  
I was told that I could communicate with all of them.)

Fr. Bernardino de Sahagún.

Historia General de las Cosas de Nueva España (ca. 1575–1577).

1	Introduction . . . . .	4
2	Medicinal Botany in Nueva España (Mexico) in the Sixteenth Century: Monardes, Sahagún and Hernández . . . . .	5
3	Changing Perspectives: Kircher, Boyle and Newton . . . . .	11
4	The Search for the Botanic Source of <i>Lignum nephriticum</i> . . . . .	13
5	The Fluorescent Components of <i>Lignum nephriticum</i> . . . . .	16
6	Conclusions . . . . .	18
	References . . . . .	19

**Abstract** The history of molecular fluorescence is closely associated with the emission from plant extracts. N. Monardes, in his *Historia Medicinal* (Seville, 1565), was the first to describe the blue opalescence of the water infusion of the wood of a Mexican tree used to treat kidney ailments. The strange optical properties of the wood, known as *Lignum nephriticum* (kidney wood), were later investigated by Kircher, Grimaldi, Boyle, Newton and many other scientists and naturalists in the ensuing centuries. However, when G.G. Stokes published in 1852 the first correct relationship between light absorption and fluorescence, his observations were based on the emission of quinine sulphate solution, because in Europe the wood of *Lignum nephriticum* was no longer available and its botanic origin was unknown. An inspection of the works of sixteenth century Spanish missionaries and scholars who compiled information on the Aztec culture, such as Fr. Bernardino de Sahagún and Francisco Hernandez, indicates that pre-Hispanic Indian



doctors had already noticed the blue color (fluorescence) of the infusion of *coatli*, a wood used to treat urinary diseases. Coatli wood was obtained from *Eyserhardtia*, a tree of the family of *Leguminosae*, and is the most likely source of the exotic *Lignum nephriticum*. The wood of *Eysenhardtia polystachya* contains large quantities of Coatline B, a rare C-glucosyl- $\alpha$ -hydroxydihydrochalcone. This compound gives rise to a fluorescent reaction product, in slightly alkaline water at room temperature, which is responsible for the blue emission of *Lignum nephriticum* infusion.

## 1

### Introduction

For nineteenth century investigators of optical properties, what we now call fluorescent emission of some plant extracts was a well-known, yet unexplained, phenomenon [1, 2]. The enigmatic color of these solutions and of a few mineral samples (as fluorospar) was sometimes envisaged as *internal dispersion*, because it was considered a peculiar instance of light reflection or scattering. It was G. G. Stokes who in 1852 first introduced the term “fluorescence” in his study of the *internal dispersion* from quinine sulfate solution [3]. This work marked a turning point on luminescence research, because Stokes correctly identified fluorescence as an emission process, due to light *absorption*, and taking place at a frequency lower than the exciting one [4, 5]. In the first lines of this long paper (100 pages plus figures), the reader learns that his research was motivated by previous reports on the quinine emission (a *beautiful celestial blue colour*) from Herschel [6, 7]<sup>1</sup> and Brewster [8]. Stokes also checked for fluorescence a large variety of plant extracts, inorganic salts and minerals, his own skin, feathers of several birds, Port and Sherry wines, etc. Surprisingly, an exotic wood used to treat kidney and bladder disorders (*Lignum nephriticum*), which had been for centuries the best-known source of fluorescent solutions, is not even mentioned in this long list of emitting materials. Herschel, on the other hand, included only a brief statement about the different colors from this wood infusion, as observed by transmitted and reflected light, noting that “*I write from recollection of an experiment made nearly 20 years ago, and which I cannot repeat for want of a specimen of the wood*” [6, 7]. The intriguing optical properties of *Lignum nephriticum*, which gave rise to the first published observation of fluorescence (v. infra), were afterwards investigated by Boyle, Newton, Priestley and many other naturalists and philosophers. Nevertheless, they could not be analyzed under the new spectroscopic methods and concepts of the nineteenth century; the wood had vanished from the inventories of British apothecaries and druggists.

---

<sup>1</sup> Sir John Frederick William Herschel (1792–1871) was the son of William Herschel, the noted astronomer and telescope builder who discovered Uranus. John Herschel, a leading scientist of his day, made important advances in mathematics and astronomy. He was also a pioneer researcher on the chemical processes of photography, discovering the hyposulfite fixing reaction.

Here we wanted to summarize the intricate history of this plant extract, which was to play an important part in the development of fluorescence, delving into the early observations of sixteenth century Spanish scholars that compiled ancient Aztec traditions on medicinal herbs. We also present a preliminary notice of the spectral properties of a water-soluble, strongly emitting compound isolated from the Mexican tree *Eysenhardtia polystachya*, the most likely source of *Lignum nephriticum*. The interested reader is referred to previous reports on many historic aspects related with this plant, and the long search to get its botanical source identified [1, 2, 9–12].

## 2

### **Medicinal Botany at Nueva España (Mexico) in the Sixteenth Century: Monardes, Sahagún and Hernández**

In 1521 Hernán Cortés finally established Spanish control over the Mexico Valley, the home of the Mexica Indians that later became known as Aztecs. The Mexica civilization had a rich history of using plant medicines for treating all sorts of diseases, and this vast new medicinal knowledge very soon aroused the interest of the Spanish colonizers. Dr. Nicolás Bautista Monardes (1508–1588) was at that time a highly respected medical practitioner in Seville [13], who was also engaged in commercial operations with the New World (Fig. 1). Although he never crossed the Atlantic, he profited from his position at the sole Spanish trade port with America to collect samples of the new plant species, that were used with medicinal purposes in the newly discovered territories, from ship officials, travelers and correspondents. Monardes developed over the years a strong appreciation and first-hand knowledge of the therapeutic applications of many exotic plants, some of them cultivated in his own botanic garden. As a result, he published a book with the first description of the medicinal uses of more than 80 American plant species [14]. In this book, which went through several additions and editions [12, 13], Monardes included a section on a tree of Nueva España used to treat kidney and urinary diseases: *Del palo para los males de los riñones, y de vrina*. In the description of the way the wood infusion should be prepared, Monardes wrote: “*They take the wood and make slices of it as thin as possible, and not very large, and place them in clear spring water, that must be very good and transparent, and they leave them all the time the water lasts for drinking. Half an hour after the wood was put in, the water begins to take a very pale blue colour, and it becomes bluer the longer it stays, though the wood is of white colour*”. A second description of this blue coloring property is also provided in another part of the book, as a test to distinguish genuine from fake wood samples.

Monardes’ *Historia Medicinal* was a great success and was translated very soon to other languages. An early Latin translation (1574) by the influential Flemish botanist Charles de L’Écluse (1526–1609), in which the wood’s name



ELOGIO HECHO POR EL  
ILLVST. S. GONCALO CATI.

eco de Molina, al Retrato del Autor que  
se vee, en su Museo.

A 3

**Fig. 1** Nicolás B. Monardes (1508–1588), from a wood engraving in his *Historia Medicinal* (1565–1574)

is given as *Lignum nephriticum* [12], helped to extend awareness of its strange optical properties in Europe. Monardes' brief statement is considered the first published record of a fluorescent emission, but there also exists a much lesser known parallel history that took place on the other side of the Atlantic, in the country of origin of the *Lignum nephriticum*.



**Fig. 2** Fr. Bernardino de Sahagún (ca. 1500–1590)

Bernardino de Sahagún (ca. 1500–1590) was a Franciscan missionary that obtained a scholarly education at Salamanca University before departing for Mexico in 1529 (Fig. 2). Sahagún quickly became fluent in Nahuatl, the Mexica language, and was associated through his long life with the Colegio Trilingüe of Santa Cruz de Santiago de Tlatelolco, the first college of higher education of America, established in 1535 by the Viceroy Antonio de Mendoza. The pupils, sons of Indian nobility, in addition to reading and writing in Spanish and Nahuatl, were taught in Latin, logic, arithmetic, music and native medicine. One of the college's Indian teachers of Aztec traditional medicine was Martinus de la Cruz, who authored the earliest American medical herbal book (*Libellus de medicinalibus Indorum herbis ...*, 1552). The manuscript is

illustrated with beautiful color drawings of vernacular plants and was written in Latin by Juannes Badianus, reader in the same college and also “*by race an Indian*”<sup>2</sup>. This fascinating Mexica pharmacopoeia remained unknown until its discovery at the Vatican Library by Dr. Charles U. Clerk in 1929, and is an indication of the interest of the Spanish colonizers in native medicine. One of the recipes briefly records the name of a plant (*cohuatli*) which might be related with that yielding *Lignum nephriticum*, as shown below. Fr. Bernardino, on the other hand, carried out a life-long ambitious ethnologic research, by compiling the description of Mexica history, religion, agriculture, technology and medical practices with the assistance of selected groups of his former native trilingual students. With that purpose, he interrogated, with the help of a carefully designed questionnaire (in Nahuatl), a large number of “informants”, old Indians with expertise on each area of knowledge [15].

Sahagún, after many vicissitudes [15], managed to complete (ca. 1575–1577) his great ethnologic work in the form of a richly illustrated bilingual Spanish-Nahuatl manuscript, which he entitled *Historia General de las Cosas de Nueva España*. Unfortunately, the manuscript, known today as the *Florentine Codex*, was never published; in fact, the first facsimile reproduction had to wait three centuries before it was published [16]<sup>3</sup>. Those parts of the *Historia General* concerned with native medicine are to be found in Books X and XI of this impressive compilation. Fr. Bernardino was also careful enough to record the names of his sources, old Mexica doctors, who transmitted and revised the original descriptions<sup>4</sup>. One of the plants described by Fr. Bernardino is the *coatli*, which was used to treat kidney diseases and appears two times in the Nahuatl compilation<sup>5</sup>. The first text, which is the most interesting for our purposes here, is shown in Fig. 3, taken from the corresponding page on the *Florentine Codex*, which also contains in a parallel column a curious (non-literal) Spanish translation. In the Nahuatl text, we

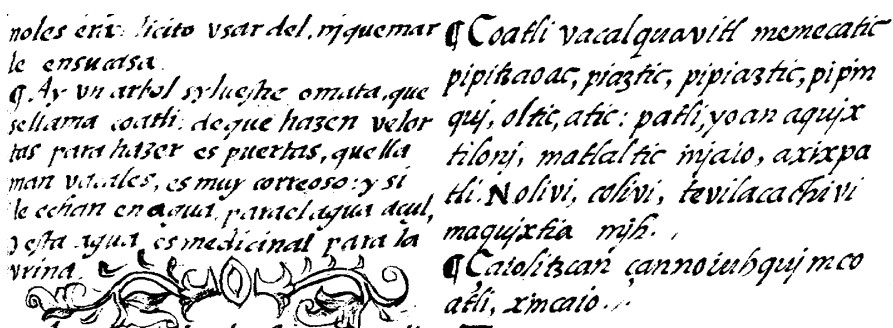
<sup>2</sup> This unique manuscript was first printed in facsimile form and supplemented with outstanding studies of its contents and historical background by Emmart EW (1940) *The Badianus manuscript. An Aztec herbal of 1522*. J. Hopkins Press.

<sup>3</sup> An additional manuscript, known as *Codex Matritense* (CM) and containing the materials compiled by Fr. Bernardino up to 1558–1559, was discovered in Madrid split between the libraries of the Royal Palace and the Royal Academy of History (RAH).

<sup>4</sup> “This relationship as placed above of the medicinal herbs, and of the other medicinal things contained above, were given by the old doctors of Tlatelolco Santiago, with a large expertise on medicinal things and all of them public healers. Their names and that of the scribe who wrote this follow. And since they don’t know how to write, they asked the scribe to place their names here: Gaspar Mathias, vecino de la Concepción; Pedro de Santiago, vecino de Santa Inés; Francisco Symón, vecino de Santo Toribio; Miguel Damián, vecino de Santo Toribio; Felipe Hernández, vecino de Santa Ana; Pedro de Requena, vecino de la Concepción; Miguel García, vecino de Santo Toribio; Miguel Motolinia, vecino de Santa Inés”. *Florentine Codex* (1575–1577) vol III, f 332v–333.

<sup>5</sup> The first description follows: “Coatli, vacalquavitl, memecatic, pipitzavac, piaztic, pipiaztic, pipinqui oltic atic. patli, yoan aqujxtloni, matlaltic iniayo axixpatli. Noliui, colivi, tevilacachivi, maquixtia mih”. CM–RAH, fol 203v and *Florentine Codex* (1575–1577) vol III, f 266. The second description follows: “Coatli: is a big tree, is broken in pieces and is put into water to be soaked: its juice must be drunken by who has fever or urine retention, because it liquifies the urine”. *Florentine Codex* (1575–1577) vol III, f 291v–333. Translated by Dr. Bustamante J.

are told that “*coatli ... patli, yoan aqujxtiloni, matlaltic iniayo axixpatli ...*”, that is, “*coatli ... is a medicine, and makes the water of blue colour, its juice is medicinal for the urine*”, showing that the native healers already noticed the unusual optical properties of the *coatli* infusion<sup>6</sup>.



noles eni: licito vsar del miquemar **C**Coatli vacalquaviti memecatic  
 le ensuatsa.  
 q. Ay un arbol syluestre ornata, que pipitaoac, piastic, pipiastic, pipim  
 sellama coatli. de que hazen velor quj, oltic, atic: patli, yoan aqujx  
 las para hazer es puectas, que lla tiloni, matlaltic iniayo, axixpa  
 man vitales, es muy corteoso: y si tli. Noliui, colivi, tevilaca (huvi  
 le echan en agua, para el agua azul, maquixtia nish.  
 y esta agua es medicinal para la **C**Catalitcani cannoieuhquj meco  
 vrina. atli, xmeaio.

**Fig. 3** The Nahuatl text describing *coatli* in Sahagún’s *Historia General de las Cosas de Nueva España*, compiled ca. 1558; Florentine Codex, V. III, f. 266

A more elaborated description of *coatli* is provided by Dr. Francisco Hernández (ca. 1515–1587), a learned naturalist and court physician to Philip II [17–19]. The Spanish king commissioned Hernández in 1570 to carry out a 5-year exploration of the natural history and native traditions of New Spain, Peru and Philippines. This was the first scientific expedition in a modern sense, carefully planned and with well-defined tasks as e.g., to undertake “a survey of herbs, trees and medicinal plants ..., consulting doctors, medicine men, herbalists, Indians and other persons with knowledge in such matters ...” [19]. An accompanying geographer was expected to map the lands being explored, and local native painters were in charge of drawing plants, animals, minerals, countryside scenes, etc. Hernández spent seven years solely in New Spain and, on his return in 1577, he presented to King Philip six large volumes of Latin text and 10 of paintings, describing more than 3000 plants, 400 animals and 35 minerals, together with collections of living plants and animals, seeds, herbaria, maps, etc. This *Natural History of New Spain* was never published; the manuscripts were reduced to ashes in the great fire of El Escorial in 1671. Fortunately, parts of the work of Hernández were finally printed in Rome and Mexico City in the 17th century (for a detailed account, see [17, 18, 20]<sup>7</sup>). In addition, several of Hernández’s manuscripts, including his personal fair copy of the *Natural History*, have been preserved [20]; in this

<sup>6</sup> The number of colors which can be identified in the visible spectrum is, of course, different in every culture. Fr. Bernardino included in his encyclopedic work a description of the pigments and dyes used by the Mexicas. According to his Nahuatl text, the *matlaltic* color would be similar to our turquoise blue and was made from the flowers of a plant (*matlalin*) whose taxonomy is unclear (translated by Dr. Bustamante J).

<sup>7</sup> Copies of the Hernández manuscripts were kindly made available to us by Dr. J. Bustamante.

last manuscript, the author refers to three *coatli* plants, but only in one of them the blue color property is mentioned (Fig. 4). This specific plant is described as *coatli* or *water snake*<sup>8</sup> and, after a brief botanical characterization, Hernández goes on to say: “The water in which chips of this wood have been soaked for some time takes a blue colour and on drinking refreshes and washes the kidneys and bladder”, and later on: “This wood is being taken to the Spaniards for quite a long time, to whom it produced great admiration to see how the water is instantly tinged of a blue colour”. The author also adds that the infusion has been tried upon himself in various occasions.

Liber 4.

795. *coatli*, quam alij *Herpa les patli*, seu medicina *Sanguis*  
*coccineam* vocant, frutex est magne, folijs cicerib,  
 minoribus tamen, rutila cerasua sed longem auribus.  
 flore luteo & elongue centi, paruo et longius Culou  
 Compositi in Spicab. frigida est atque humentis nature.  
 Saporeque in Signi Casens. Aqua <sup>ubi</sup> sti pi hum eius, <sup>que</sup> dam  
 assula aliquandiu maduerint, <sup>caeruleum</sup> <sup>contrahit</sup> <sup>color</sup>  
 lozem, renes et vesicam <sup>potu</sup> extergit, <sup>refrigeratq.</sup> <sup>†</sup>  
 Urina a Crimonia am temporet, et Colicis medetur. ]

**Fig. 4** Handwriting of Dr. Francisco Hernández, ca. 1574, describing *coatli* and remarking the blue colour (*caeruleum*) of its infusion. *De Historia Plantarum Novae Hispania, Liber Quartus*, Ms. 22436, Biblioteca Nacional, Madrid, Spain

Hernández was very likely aware of Monardes small but successful treatise, and it is known that he had access to Fr. Bernardinos manuscripts during his stay in Mexico City. Both, the learned naturalist and the Franciscan anthropology pioneer knew that *coatli* was the source of *Lignum nephriticum*. However, the unfortunate fate of their corresponding great compilations on the New Spain Natural History, which never went to print, contributed to the struggle in tracing the botanic source of the wood by later European botanists.

<sup>8</sup> Hernández was fluent in Nahuatl to such an extent that he left in Mexico a copy (now lost) of part of his manuscripts in this language. For unknown reasons he translated *coatli* as *water snake*; the correct translation is “vara medicinal” (*medicinal stick*). Bustamante J, personal communication.

### 3

#### Changing Perspectives: Kircher, Boyle and Newton

With the advent of the work of Galileo and Newton in the seventeenth century, science in the world was completely transformed. The foundation of scientific societies, such as the Royal Society of London, established in 1660, and the regular publication of research journals, such as the *Philosophical Transactions* of the Royal Society, heralded the dawn of modern science. From the many studies of the fascinating colors of *Lignum nephriticum* in this epoch [1, 9–12], we have selected those of Kircher, Boyle and Newton, which illustrate well the profound changes in the progress of science. At the beginning of the century, the learned Jesuit Athanasius Kircher (1601–1680) published a vivid description of the many colors of the wood's infusion in his *Ars Magna Lucis et Umbrae* [21]<sup>9</sup>. Kircher obtained the emitting solution pouring clear water on a cup made of the wood, which was a gift from the procurator of the Jesuits in Mexico. On his account, which was more detailed than those of the early Renaissance observers, Kircher reproduced parts of the *coatli* brief botanic description of Hernández. Later on, in the same optics treatise, he advanced the first explanation of the wood's fantastic colors (*collores illo phantasticos*). Interestingly, Kircher realized ([21], p 176) that the infusion colors became more intense in basic solution (*Cum enim dictum lignum sale ammoniaco* [ammonium chloride] *turgeat*), and from this he concluded that the seeds of all colors were present in the ammonium salt. In fact, Kircher was not very convinced with this involved explanation because he declared his willingness to subscribe a better interpretation, if ever found.

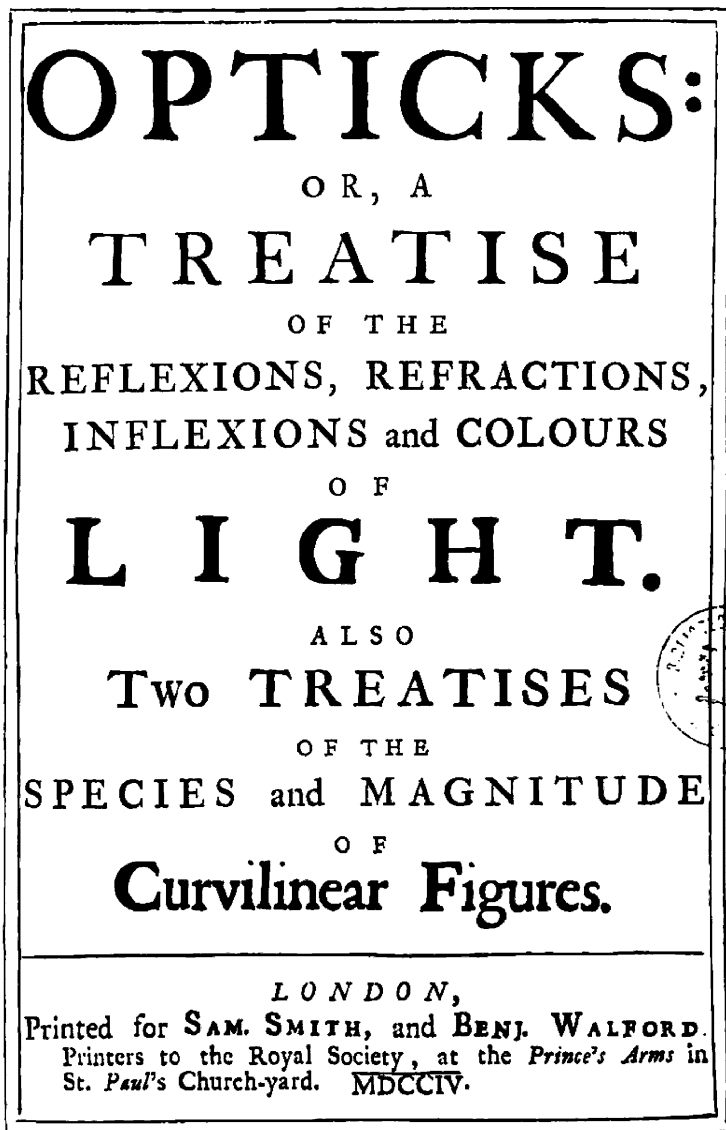
The approach of Boyle (1627–1691) to the same problem was completely different, and we concur with Stapf [9] in considering his account in *Experiments and Considerations touching Colours* [22] as the first scientific description of fluorescence. In this detailed analysis of the infusion colors, Boyle revised previous observations from Monardes and Kircher, reproducing the critical parts of their texts. In addition, he provided a discussion on the origin and morphology of the samples of *Lignum nephriticum*, and stated the descriptive character of his observations<sup>10</sup>. Still, he did not claim to have found a physical explanation of the “*deep and lovely ceruleous colour*” of the infusion. An important contribution from Boyle's experiments is the study of the sensitivity of the infusion fluorescence to the solution pH, noting that the intensity of the blue color can be completely quenched in acidic solutions. After checking that the fluorescence can be restored by adding alkalis, he writes: “*I have hinted to you a New and Easie way of Dis-*

<sup>9</sup> There is an earlier edition, published in Rome in 1646. See ref [9] and [12].

<sup>10</sup> “And I confess that the unusualness of the Phaenomena made me very sollicitous to find out the Cause of this Experiment, and though I am far from pretending to have found it, yet my enquires have, I suppose, enabled me to give such hints ...”. See ref [22], p 203.



covering in many Liquors (for I dare not say in all) wether it be an Acid or a Sulphureous [alkaline] Salt” ([22], p 213). This is, probably, the first description of the analytical application of a fluorescent indicator. Boyle



R. 120.811

Fig. 5 Title page of Newton's treatise *Opticks*, London 1704

himself used the infusion emission as a test of solution acidity in later experiments [23].

Newton (1643–1727) was also well familiarized with *Lignum nephriticum*'s unusual color play, which is referred to in some of his published work. In the first exposition of his color theory [24], Newton was already convinced that he understood the physical basis of the strange optical effects of the wood's infusion, and said: “those are substances apt to reflect one sort of light and transmit another” ([24], p 3084). In his influential treatise on optics (Fig. 5), Newton described an experiment in which the infusion was sequentially illuminated with light from which either the red or the blue parts of the spectrum were suppressed [24, 25], to conclude in classifying the blue emission as a kind of reflection. It has been pointed out [12] that this “explanation” was not different from that previously proposed by another Jesuit father, F.M. Grimaldi (1618–1663), professor of mathematics at Bologna, in the same book where he announced his discovery of light diffraction. Newton's misinterpretation of the phenomenon was reproduced without being questioned by later investigators, and the scarcity of the wood samples probably put an end to further experimental quest on the source of its luminescence.

## 4

### The Search for the Botanic Source of *Lignum nephriticum*

*Lignum nephriticum* is not, obviously, a proper botanical term, but only denotes a plant remedy. When the wood ceased to be used as a drug, that name could no longer be associated with any known botanical species, at least in Europe. The source of the wood became a mystery among European botanists of the 17th–19th centuries, until it was identified after years of research at the beginning of the past century by Stapf [9] and, later, by Safford [11] as the wood of the Mexican tree *Eysenhardtia polystachya* (Ortega) Sarg. Silva:3:29 (1982) (Figs. 6 and 7).

The actual situation in Mexico must have been quite different. A large part of current Mexican folk medicine incorporates the Aztec heritage [26]<sup>11</sup>, and Mexican popular medicine men (*curanderos*) and peasants have been using *coatli* for centuries for the same therapeutic applications as those indicated by Sahagún, Hernández and Monardes<sup>12</sup>. Thus, Mexican professional natural-

<sup>11</sup> There is an abundant bibliography dealing with Aztec medicine, which dates back to the second half of the sixteenth century. See e.g., the detailed account of Emmart EW in footnote 2.

<sup>12</sup> Several references to the wood as *palo dulce* (sweet wood) or *taray* appear e.g., in the recipes of the self-care manual of Esteyneffer J (1712) *Florilegio Medicinal*, Edition of Anzures MC, 2 Vols. Acad Nac Medicina, Mexico, 1978. The ancient name of the plant (*coatli*) is still used as *cuate* or *cuatle* in several Mexican regions, see Carmona ML, Estudio anatómico, morfológico y etnobotánico de algunas maderas de importancia medicinal en Mexico. Professional Thesis, UNAM, México, 1992. Wood samples can be obtained today from Mexico City plant vendors, who recommend it for bladder diseases and refer to it sometimes as *blue wood* (!)



**Fig. 6** *Eysenhardtia polystachya* (Ortega) Sarg. Silva:3:29 (1982), the source of *Lignum nephriticum*

ists and botanists never lost sight of the plant source of *Lignum nephriticum*. For example, Oliva, a Mexican Professor of Pharmacology, noted in 1854 that the “*cuate* (also *Palo Dulce*, *Taray*, *Leño Nefrítico*)” corresponds to *Viborquia polystachya*, an old name of *Eysenhardtia* [27].



**Fig. 7** Leaves and flowers of *Eysenhardtia polystachya*

The genus *Eysenhardtia* (*Leguminosae*) comprises at least 12–15 species, from shrubs to large trees of 20 m in height<sup>13</sup>, although only few of them have been tested for fluorescence. It is very common in several parts of Central America and the SW of the United States, even forming forests in some places<sup>14</sup>. The fortuitous duplication of its botanic description with different names<sup>15</sup> and the noted large variability among species [11] may have rendered it more difficult to identify the true source of *Lignum nephriticum*<sup>16</sup>.

---

<sup>13</sup> Sousa M, Cruz R (2005) Institute of Biology and Botanic Garden, UNAM, Mexico, personal communication.

<sup>14</sup> Cruz R, UNAM, Mexico, personal communication.

<sup>15</sup> *Eysenhardtia polysachya* was first described in 1798 by the Spanish naturalist Gómez Ortega C as *Viborquia polystachya*, from a tree grown in the Madrid Royal Botanic Garden from seeds taken from Mexico. Ortega's name was replaced by the present one, proposed much later (1823) by Humboldt, Bonpland and Kunth in their description of the species (see [11] for details). None of these naturalists noted the wood's fluorescent property nor its relationship with *Lignum nephriticum*.

<sup>16</sup> In fact, Safford suggested that Monardes' fluorescent wood sample was from a large Philippine tree (a *Pterocarpus*) and that a Mexican *Pterocarpus* was also used as a source for *Lignum nephriticum*. The Philippine origin is very unlikely, because regular traffic between New Spain and these islands (the "Manila galleon") started after 1565.

## 5 The Fluorescent Components of *Lignum nephriticum*

Fluorescent pigments are, of course, ubiquitous components of the vegetal world. In the case of *Lignum nephriticum*, its notoriety was due to the large concentration and easy water solubility of the wood's blue fluorescent dyes. The tree water extract also contains dyes emitting in the yellow spectral range that would not be discussed here. As far as we are aware, the first fluorescent compound isolated from *Eysenhardtia polystachya* was reported in 1978 as a water-soluble glucoside of unknown structure [28]. The tree wood water extract was later investigated by Beltrami and coworkers [29], who isolated two major components (ca. 0.5% dry weight), Coatline A and Coatline B (Fig. 8), with a *C*- $\beta$ -glucopyranosyl- $\alpha$ -hydroxydihydrochalcone structure. In this work, the fluorescent properties of these compounds were not discussed, although the authors referenced Boyle's work and Safford's paper [11]. Shortly after that, it was claimed [30]<sup>17</sup> that Boyle's fluorescent indicator had been finally identified from *Eysenhardtia*, in the form of the compound 7-hydroxy-2',4',5'-trimethoxyisoflavone. Apparently, this compound was isolated from a fraction of plant products first solubilized in petrol and, therefore, it is very unlikely that it could be the highly water-soluble dye from *Lignum nephriticum*. Later work on *Eysenhardtia* wood and bark components was motivated by its presumed medicinal applications [31, 32], and no attention was given to fluorescent compounds.

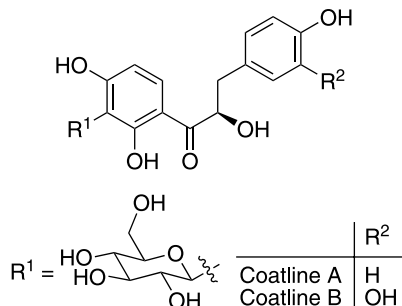


**Fig. 8** Molecular structure of the non-emitting *C*- $\beta$ -glucopyranosyl- $\alpha$ -hydroxydihydrochalcones Coatline A and B, first isolated from *Eysenhardtia polystachya* by Beltrami and coworkers [29]. In a mild alkaline solution, Coatline B yields a strongly blue-fluorescent reaction product, L

We report here the results of a preliminary study of the complex spectral properties in water solution of Coatlines A and B, isolated from *Eysenhardtia polystachya*; a more extended account will soon be published elsewhere<sup>18</sup>.

<sup>17</sup> The way the isoflavone was isolated from the wood is far from clear.

<sup>18</sup> Acuña AU, Amat-Guerri F, in preparation.

Since these experiments were prompted by the historical relevance of these compounds, special attention is given only to spectral features that appear in the visible spectrum. Coatline A absorption spectrum in water solution changes in a reversible way from slightly acidic ( $\lambda_{\max}$  282 and 320 nm, pH 6) to basic solution ( $\lambda_{\max}$  258 and 338 nm, pH 10). Both forms are essentially transparent and non-fluorescent in the visible range.

Coatline B is also non-fluorescent in acidic water solution, and its absorption spectrum is similar to that of the A analog. However, on mild alkalization, a series of slow spectral changes take place, which finally result in the irreversible formation of a strongly blue-emitting species, L. The new compound L presents an intense absorption at 429 nm (pH 8–10), with an absorption coefficient much larger than that of the original Coatline B. As a result of that, the water solution takes a golden yellow color. This new species L shows (Fig. 9) the characteristic intense pale-blue fluorescence ( $\lambda_{\max}$  466 nm) of the wood's infusion, with an emission quantum yield

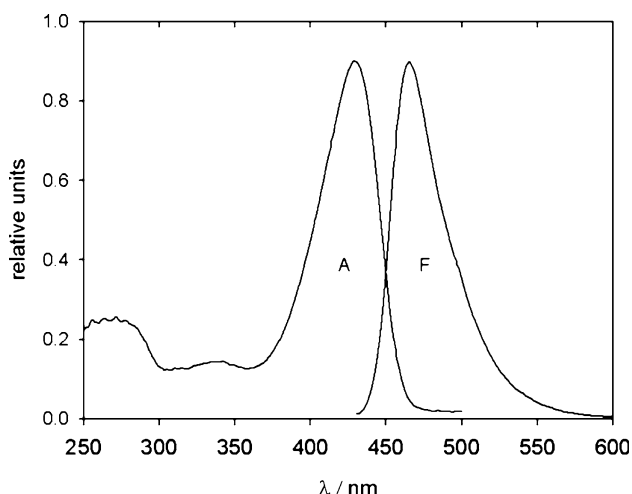


**Fig. 9** Absorption and corrected emission spectra (water, pH 10) of Coatline B reaction product L, that yields the blue fluorescence of *Lignum nephriticum*

in the 0.8–1.0 range. The fluorescence is completely quenched on acidification. Obviously, the full identification of the molecular structure of L would require much more detailed studies. Nevertheless, it is clear that the blue fluorescence of *coatli-Lignum nephriticum* infusion is due to its large contents of the water-soluble C-glucosyl hydroxydihydrochalcone Coatline B, and the later conversion of this glucoside to the strongly emitting compound L<sup>19</sup>. The

<sup>19</sup> The wood of *Eysenhardtia polystachya* contains additional glycosides with the same hydroxydihydrochalcone group as Coatline B, see [32]. It seems very likely that these compounds also contribute to the formation of blue-fluorescing products.

fact that the blue emission is largely enhanced in alkaline water was also an additional complicating factor in the search for the true source of *Lignum nephriticum*. The C-glucose group of Coatline B explains its large water solubility, as well as one of the wood's contemporary popular names (*sweet wood*).

## 6 Conclusions

The ancient pre-Hispanic Aztec doctors first noticed the bluish color (fluorescence) of the infusion of the *coatli* wood, meaning *medicinal stick*, which was used to treat kidney and bladder disorders. This early description has been preserved by Fr. Bernardino de Sahagún in his monumental *Historia General de las Cosas de Nueva España*. In 1565 Nicolás B. Monardes first published in Europe the medicinal usage and the unusual optical properties of this wood, that was known since then in the Old World as *Lignum nephriticum*.

The original source of *coatli-Lignum nephriticum* is, most likely, a tree of the genus *Eysenhardtia*, which is well distributed in Mexico and other regions of Mesoamerica. The infusion of the wood of *Eysenhardtia polystachya* contains a large amount of water-soluble fluorescent compounds. The intense blue fluorescence observed in water extracts of *E. polystachya* is due to the presence of the C-glucosyl hydroxydihydrochalcone Coatline B, first isolated from this tree by Beltrami and coworkers [29]. The glucoside is converted to a strongly blue-emitting compound in slightly alkaline water solution<sup>19</sup>. The multiple color effects that attracted the attention of many investigators over centuries result from the combination of an intense absorption in the visible range (429 nm) and a very large emission yield in the blue spectral range (466 nm) of the Coatline B reaction product.

**Acknowledgements** We wish to thank Mário Nuno Berberán for the invitation to present this work at the 9th International MAFS Conference. In the course of this long research, we received the invaluable assistance and support from many individuals from widely diverse disciplines. We express our deep gratitude to Santiago Castroviejo (Spanish Royal Botanic Garden, CSIC) for his help in many botanic and historical aspects, as well as in procuring samples of *Eysenhardtia*. We are much indebted to Jesús Bustamante (Institute of History, CSIC) for his indefatigable effort and interest in searching for references to coatli in the great works of Fr. B. de Sahagún and Dr. Francisco Hernández, as well as for translating and interpreting ancient Nahuatl and Latin texts. We also thank Nuria Valverde (Institute of History, CSIC) and Juan José Carracedo for the aid with 18th century references and texts. AUA wishes to acknowledge his indebtedness to Manuel Prieto and Mário Nuno Berberán (I.S.T., Technical University, Lisbon), who along many years gifted him with several important books and hard-to-find publications concerning the history of luminescence and *Lignum nephriticum*. In Mexico we were very fortunate to get the assistance of Robert Bye, Miguel Ángel Martínez Alfaro, Mario Sousa, Josefina Barajas and Ramiro Cruz (Botanic Garden and Institute of Biology, Universidad Nacional

Autónoma, Mexico) in our botanic pursuit. Ramiro Cruz guided one of us (AUA) to collect *Eysenhardtia* branches and provided the tree images shown in this work (Figs. 6 and 7), and Silvia Salas (SERBO, Oaxaca) even set up an expedition to procure for us the wood of *Pterocarpus acapulcensis*. We are also indebted to Benjamín Rodríguez (Institute of Organic Chemistry, CSIC) for isolating pure samples of Coatline A and B from *Eysenhardtias* wood, and to Marisela Vélez for procuring “sweet wood” from Mexico City herb markets. We also thank Puri Morcillo (Institute of Organic Chemistry, CSIC) for laboratory assistance, Guillermo Bernabeu (Institute of Physical Chemistry, CSIC) for skilful help in the spectroscopic experiments, and, last but not least, to Don Carlos López-Bustos for his valuable suggestions at the early stages of this research. Figure 3 was taken from the facsimile edition of the Florentine Codex [16], ms. Laur. Med. Palat. 220, Biblioteca Medicea Laurenziana, Firenze, and is reproduced with permission from the Ministero per il Beni e le Attività Culturali (Italy). Permission to reproduce Fig. 4, from ms. 22436, was granted by the Biblioteca Nacional, Madrid (Spain). Work financed, in part, by Project BQU 2003/4413, from the Spanish Ministry of Education and Science.

## References

1. Harvey EN (1957) A history of luminescence. From early times until 1900. The American Philosophical Society, JH Furst Co., Baltimore, USA
2. Valeur B (2002) Molecular Fluorescence. Principles and Applications. Wiley-VCH, Weinheim, pp 5–11
3. Stokes GG (1852) On the change of refrangibility of light. *Phil Trans* 142:463–562
4. Becquerel E (1854) *Cosmos* 4:509–510
5. Angström AJ (1855) *Opt Res Phil Mag* S4 9:327–342
6. Herschel JFW (1845) On a case of superficial colour presented by a homogeneous liquid internally colourless. *Phil Trans* 135:143–145
7. Herschel JFW (1845) On the epipolic dispersion of light. *Phil Trans* 135:147–153
8. Brewster D (1846) On the Decomposition and Dispersion of Light within Solid and Fluid Bodies. *Trans Roy Soc Edinburg* 16(II):111–121
9. Stapf O (1909) *Lignum nephriticum*. *Bull Miscell Inform, Kew Gardens*, pp 293–302
10. Möller HJ (1913) *Lignum nephriticum*. *Ber Deut Pharm Ges* 23:88–154
11. Safford WE (1915) *Lignum nephriticum* – Its history and an account of the remarkable fluorescence of its infusion. *Ann Rep Smithsonian Inst*, pp 271–298
12. Partington JR (1955) *Lignum nephriticum*. *Ann Sci* 11:1–26
13. López Piñero JM (1989) Critical study in the facsimile edition of Primera, Segunda y Tercera Partes de la Historia Medicinal de las Cosas que traen de nuestras Indias Occidentales, Monardes N, 1580 edition. Ministerio de Sanidad y Consumo, Madrid, Spain, pp 9–74
14. Monardes NB (1565) *Dos Libros/El vno que trata de todas las cosas que traen de nuestras Indias Occidentales que siruen al vso de Medicina y como se ha de vsar de la rayz de Mechoacan, purga excelentissima. El otro libro trata de dos medicinas marauillosas ...*, en casa de Sebastian Trugillo, Sevilla
15. Bustamante J (1990) Fr. Bernardino de Sahagún. Una versión crítica de los manuscritos y de su proceso de composición. Universidad Nacional Autónoma de México (UNAM), Mexico
16. Sahagún B (1970) *Códice Florentino. Historia General de las Cosas de Nueva España. Manuscrito 218–220, Colección Palatina de la Biblioteca Medicea-Laurenziana (edic. facsimilar) C. Edit. Giunti Barbera/Archivo General de la Nación, Florencia/México*



17. López Piñero JM, Pardo Tomás J (1996) La influencia de Francisco Hernández (1515–1587) en la constitución de la botánica y la materia médica moderna. Inst Est Docum Hist sobre la Ciencia (CSIC), Valencia, Spain
18. López Piñero JM, Pardo Tomás J (2000) The contribution of Hernández to European Botany and Materia Medica, in Searching for the secrets of Nature. In: Varey S, Chabrán R, Weiner DB (eds) The life and works of Dr. Francisco Hernández. Stanford Univ Press, Stanford, pp 122–137
19. Bustamante J (1997) Francisco Hernández, Plinio del Nuevo Mundo. Tradición clásica, teoría nominal y sistema terminológico indígena en una obra renacentista. In: Ares B, Gruzinski S (eds) Entre dos Mundos: fronteras culturales y agentes mediadores. Escuela de Estudios Hispanoamericanos, Sevilla, pp 243–268
20. Bustamante J (2000) The Natural History of New Spain. In: Varey S (ed) The Mexican Treasury: The writings of Dr. Francisco Hernández. Stanford Univ Press, Stanford, pp 26–39
21. Kircher A (1671) *Ars Magna Lucis et Umbrae*. Amsterdam, p 77
22. Boyle R (1664) Experiments and Considerations touching Colours. London, pp 199–216
23. Boyle R (1684) Short Memoirs for the Natural History of Mineral Waters. London, pp 85–86
24. Newton I (1671) New Theory about Light and Colors. *Phil Trans* 6:3075–3087
25. Newton I (1704) Optics or a Treatise of the Reflexions, Refractions, Inflexions and Colours of Light. London, p 140
26. Ortiz B (1986) Aztec sources of some Mexican folk medicine. In: Steiner RP (ed) Folk Medicine. Am Chem Soc, Washington, pp 1–22
27. Oliva L (1854) Lecciones de Farmacología, Vol 2. Universidad de Guadalajara, Guadalajara, Mexico, pp 429–430
28. Domínguez XA, Franco R, Díaz Viveros Y (1978) Mexican medicinal plants XXXIV. Rotenoids and a fluorescent compound from *Eysenhardtia polystachya*. *Rev Latinoamer Quím* 9:209–211
29. Beltrami E, de Bernardi M, Fronza G, Mellerio G, Vidari G, Vita-Finzi P (1982) Coatline A and B. Two C-glucosyl- $\alpha$ -hydroxydihydrochalcones from *Eysenhardtia polystachya*. *Phytochemistry* 21:2931–2933
30. Burns DT, Dalgarno BG, Gargan PE, Grimshaw J (1984) An isoflavone and a coumestatan from *Eysenhardtia polystachya* – Robert Boyle's fluorescent acid-base indicator. *Phytochemistry* 23:167–169
31. Álvarez L, Ríos MY, Esquivel C, Chávez MI, Delgado G, Aguilar MI, Villareal ML, Navarro V (1998) Cytotoxic isoflavans from *Eysenhardtia polystachya*. *J Nat Prod* 61:767–770
32. Álvarez L, Delgado G (1999) C- and O-glycosyl- $\alpha$ -hydroxydihydrochalcones from *Eysenhardtia polystachya*. *Phytochemistry* 50:681–687

# From Well-Known to Underrated Applications of Fluorescence

Bernard Valeur<sup>1,2</sup>

<sup>1</sup>CNRS UMR 8531, Laboratoire de Chimie Générale, CNAM,  
292 rue Saint-Martin, 75141 Paris cedex 03, France  
[valeur@cnam.fr](mailto:valeur@cnam.fr)

<sup>2</sup>Laboratoire PPSM, ENS-Cachan, 61 avenue du Président Wilson, 94235 Cachan cedex,  
France

1	Early Applications of Fluorescence . . . . .	22
2	Monitoring of Excited-State Processes . . . . .	25
3	Fluorescence Sensing . . . . .	25
3.1	Fluorescent Molecular Sensors . . . . .	25
3.2	Microfabricated Analysis Systems . . . . .	27
3.3	Fluorescence Imager for Sensing . . . . .	28
3.4	Fluorescence LIDAR . . . . .	28
4	Clinical Diagnostics . . . . .	30
4.1	Critical Care Analysis . . . . .	30
4.2	Angiography . . . . .	31
4.3	Bladder Tumor Detection . . . . .	32
4.4	Human Skin . . . . .	33
5	Imaging and Tracing . . . . .	33
5.1	Semiconductor Nanocrystals . . . . .	33
5.2	Fluorescent Proteins . . . . .	35
5.3	Surface Pressure Mapping . . . . .	37
5.4	Criminology . . . . .	39
5.5	Counterfeit Detection . . . . .	40
6	Fluorescence in Art . . . . .	40
6.1	Paintings . . . . .	40
6.2	Sculptures . . . . .	41
7	Conclusion . . . . .	42
	References . . . . .	42

**Abstract** Molecular fluorescence is extensively used in physical, chemical, material, biological, and medical sciences as a tool for detection/analysis, visualization, investigation of local properties, diagnosis, etc. In fact, fluorescent compounds can be used not only for mere visualization, but also as probes, indicators, sensors, and tracers for providing

information on local concentrations of ionic or neutral species, and on the structure and dynamics of matter or living systems (see B Valeur, *Molecular Fluorescence: Principles and Applications*, Wiley-VCH, 2002). New compounds with improved characteristics in terms of sensitivity, selectivity, and photochemical stability appear almost daily.

The present review does not intend to be exhaustive: some applications of fluorescence relevant to fundamental and applied research will be illustrated with pertinent examples. In addition, technological or industrial applications will be exemplified.

## 1

### Early Applications of Fluorescence

In 1565, Nicolas Monardes reported the first observation of fluorescence<sup>1</sup>: he described the bluish color of an infusion of wood *Lignum nephriticum* under certain conditions of observation (see the article by U. Acuna in this book). He wrote: “Make sure that the wood renders water bluish, otherwise it is a falsification. Indeed, they now bring another kind of wood that renders the water yellow, but it is not good, only the kind that renders the water bluish is genuine.” Therefore, such a method for the detection of a counterfeited object can be considered as the very first application of fluorescence.

Another old application is the fluorescent tube. In 1857, Edmond Becquerel<sup>2</sup> was the first to conceive the idea of coating the inner surface of an electric discharge tube with luminescent materials. Such tubes are similar to the fluorescent tubes that are made today. In fact, the inner coating is nowadays made of  $\text{Eu}^{\text{II}}$ ,  $\text{Eu}^{\text{III}}$ , and  $\text{Tb}^{\text{III}}$ , so that addition of blue, red, and green light yields white light.

Fluorescence has long been used as an analytical tool for the determination of the concentrations of various species, either neutral or ionic. What are the early applications of fluorescence with this aim? The answer can be found in the famous book *History of Luminescence* by E. N. Harvey [1]: the first paper was published by Victor Pierre [2] who was a professor in Prague, and later in Vienna. In a series of papers, he studied solutions of single fluorescent compounds and mixtures. He noticed that bands of fluorescent spectra were characteristic of a particular substance. He noted also the effect of solvent and acidity or alkalinity.

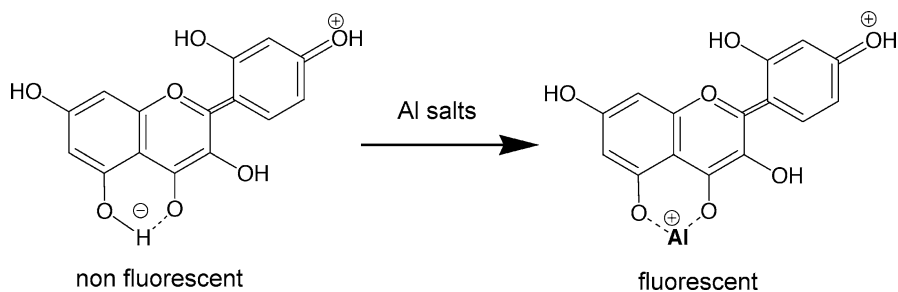
G. G. Stokes certainly had the same idea in mind. In fact, he lectured “On the application of the optical properties to detection and discrimination of organic substances” before the Chemical Society and the Royal Institution in 1864. The content of this lecture is likely to have been quite general and not

<sup>1</sup> The term fluorescence was not known at that time. It was introduced by G. G. Stokes in 1851 in the seminal paper “On the refrangibility of light”.

<sup>2</sup> Edmond Becquerel is the father of Henri Becquerel who discovered radioactivity. Edmond Becquerel invented the famous phosphoroscope that bears his name. He was professor at the Museum National d’Histoire Naturelle and at the Conservatoire Impérial des Arts et Métiers in Paris.

restricted to fluorescence. In 1883, 1884, and 1885, Stokes gave his famous Burnett lectures “On light” [3], and one of the topics of Lecture I in the second course entitled “On light as a means of investigation” is “Fluorescence—its use as a means of discrimination”. One can read on page 154: “... the observation of fluorescent substances in a pure spectrum exhibits features by which they may be followed and detected in spite of other substances even in large quantity”. However, no specific example was given in the text.

A well-known application of fluorescence to analysis was reported by Göppelsröder in 1868 [4, 5]: the complexation of morin (a hydroxyflavone derivative) with aluminum is accompanied by a dramatic enhancement of fluorescence intensity (Scheme 1), thus offering a straightforward way to detect this metal. It was the first time that the term *fluorescence analysis* was employed.



**Scheme 1**

Among the old applications of fluorescence, it is worth mentioning that uranin (the disodium salt of fluorescein) was used for the first time in 1877 as a tracer for monitoring the flow of the Danube. On all maps, it is shown that the Danube springs in the Black Forest and, after many hundreds of kilometers, flows into the Black Sea. But there are several sinks (swallow holes) in the bed of the Danube. The biggest one is near Immedingen. Ten liters of a concentrated solution of uranin were poured by Knop into the bed of the upper current of the Danube, and 50 hours later, the fluorescence could be observed in the water of the river Aache 12 km to the south. This river flows into Lake Constanz that feeds the Rhine. Therefore, only a small part of the water from the Danube spring arrives at the Black Sea. Most of it flows into the North Sea! Nowadays, fluorescence tracing is currently used in hydrology, especially to simulate pollution.

At the beginning of the twentieth century, numerous applications of fluorescence were developed and reported in several books. For instance, in the second part of the book by Radley and Grant [6], the list of applications using fluorescence analysis is impressive (Fig. 1). Dake and De Ment also described interesting applications [7]. Dake was so fond of fluorescence that he faced

## FLUORESCENT LIGHT and Its Applications

INCLUDING LOCATION AND PROPERTIES OF FLUORESCENT MATERIALS . . . A THEORETICAL AND PRACTICAL EXPOSITION OF FLUORESCENCE AND SIMILAR PHENOMENA.

By

H. C. Dake

Editor, *The Mineralogist Magazine*

Co-Author, *Quartz Family Minerals*

Honorary President, *Northwest Federation of Mineral Societies*

and

Jack De Ment

Associate Editor *The Mineralogist Magazine*

Research Chemist, *The Mineralogist Laboratories*



1941

CHEMICAL PUBLISHING CO., INC.  
BROOKLYN, N. Y.

## CONTENTS

CHAPTER	PAGE
PREFACE	i
1. HISTORICAL ASPECTS OF LUMINESCENCE . . . . .	1
2. RADIATION—COLOR—PERCEPTION . . . . . The Eye	8
3. TYPES OF LUMINESCENCE . . . . . Thermoluminescence; Cathodoluminescence; Triboluminescence; X-Ray Luminescence; Electroluminescence; Crystallolumines- cence; Pyroluminescence; Chemiluminescence; Biolumines- cence; Other Forms of Luminescence	22
4. THEORY OF LUMINESCENCE . . . . . Phosphors; Mechanism of Luminescence; Decay of Phospho- rescence; Concentration Effects; Polarized Fluorescence; Other Influences on Luminescence; Mineral Activators	47
5. METHODS OF EXAMINATION AND TECHNIC . . . . . General Considerations; Exposure of the Specimen; Color; Intensity; Duration of Phosphorescence	70
6. SOURCES OF ULTRAVIOLET RADIATIONS . . . . . Construction of an Iron Arc; Portable Units; Protection against Radiations; Filters for Fluorescence; Chemical Filters; Glass Filters; Heat Resisting Glass Filters; Non-Heat Resisting Glass Filter; Observing Fluorescence—Glasses; Tests of Wave- lengths; Test Glasses; Test Minerals	91
7. THE FLUORESCENT MINERALS . . . . . Some Noted Localities; Fluorescent Minerals; Luminescence of Meteorites	119

**Fig. 1** Contents of the book by Radley and Grant published in 1933

his fireplace with fluorescent minerals that were illuminated by a UV lamp attached to the ceiling. In their famous book, Pringsheim and Vogel [8] gave various examples of application, including fluorescent carpets and ceilings in theaters, or fluorescent ballets (Fig. 2).



**Fig. 49.**—Fluorescent carpet and ceiling. (Courtesy of Continental Lithograph Corporation, Cleveland, Ohio.)

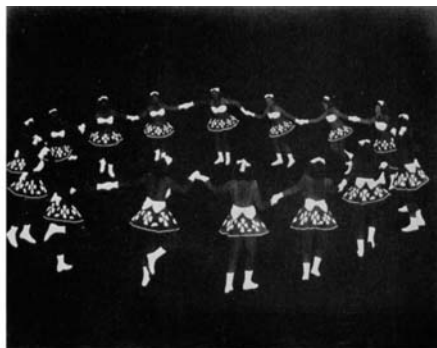


**Fig. 50.**—Fluorescent ballet. (Courtesy of Continental Lithograph Corporation, Cleveland, Ohio.)

**Fig. 2** Photographs published in the book by Pringsheim and Vogel published in 1943

After these historical aspects, let us give some examples of well-known and underrated applications of fluorescence that are currently used today.

## 2

### Monitoring of Excited-State Processes

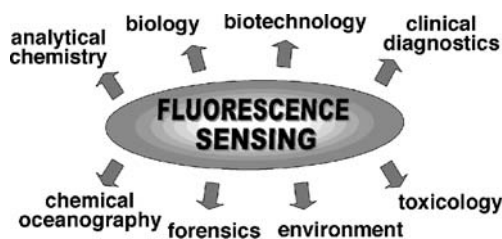
Steady-state and time-resolved fluorometries are widely used to determine the rates of photoinduced electron transfer, proton transfer, and energy transfer in artificial or living systems. In fact, the time constants of these processes fall into the experimental time window around the excited-state lifetime, so that analysis of the fluorescence decays allows one to calculate the rate constants [9]. This well-known use of fluorescence will not be further discussed.

## 3

### Fluorescence Sensing

Sensing is one of the most important applications of fluorescence, as confirmed by the recent special issue of the *Journal of Materials Chemistry* devoted to fluorescent sensors [10], and the book *Optical sensors* [11] in which fluorescence appears to play a great role.

The extensive use of fluorescence sensing in many fields (Scheme 2) can be explained by the distinct advantages of this technique in terms of sensitivity, selectivity, response time, local observation under the microscope, and remote detection by means of optical fibers.



Scheme 2

### 3.1

#### Fluorescent Molecular Sensors

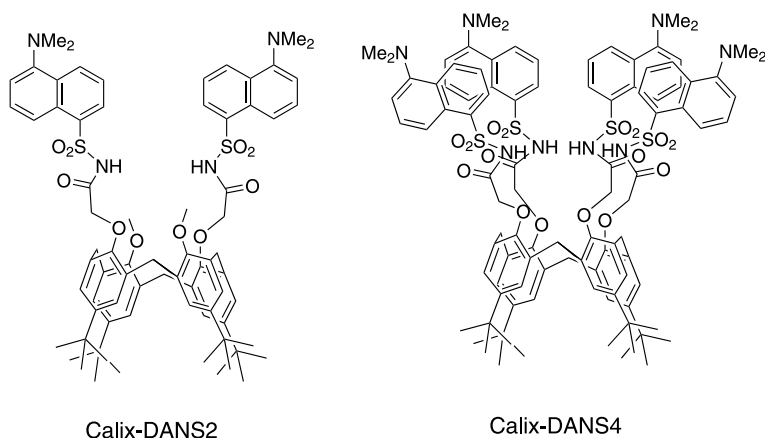
The design of a fluorescent molecular sensor that is selective of a given analyte is actually a work of molecular engineering that involves many disciplinary fields: photophysics, photochemistry, analytical chemistry, physical chemistry, coordination chemistry, and supramolecular chemistry [9, 12–14].

Numerous fluorophores have been used for fluorescence sensing: naphthalene, anthracene, pyrene, aminonaphthalimide, diamionaphthylsulfonyl, coumarins, fluorescein, eosin, rhodamines, benzidine, alizarin, seminaph-

thofluorescein, oligo- and polyphenylenes, porphyrins, ruthenium complexes, etc. The number of analyte targets is still increasing with much progress in sensitivity and selectivity:

- Cations:  $\text{H}_3\text{O}^+$  (pH), alkali, alkaline earth, transition, and post-transition
- Anions: fluoride, chloride, carboxylates, phosphates, ATP, nitrates, etc.
- Molecules: hydrocarbons, amino acids, sugars, urea, ammonia, amines, alcohols,  $\text{O}_2$ ,  $\text{CO}_2$ ,  $\text{H}_2\text{O}_2$ , etc.

As an illustration of selectivity in fluorescence sensing, the detection of toxic metal ions in the environment will now be briefly presented. Calix[4]arenes bearing two or four dansyl fluorophores, called Calix-DANS2 and Calix-DANS4, respectively (Scheme 3), exhibit outstanding complexing abilities [15]. Calix-DANS2 shows a high selectivity toward  $\text{Hg}^{2+}$  over interfering cations ( $\text{Na}^+$ ,  $\text{K}^+$ ,  $\text{Ca}^{2+}$ ,  $\text{Cu}^{2+}$ ,  $\text{Zn}^{2+}$ ,  $\text{Cd}^{2+}$ , and  $\text{Pb}^{2+}$ ) and a sensitivity in the  $10^{-7}$  mol  $\text{L}^{-1}$  concentration range. The complexation of  $\text{Hg}^{2+}$  induces a strong fluorescence quenching due to a photoinduced electron transfer process from the fluorophore to the metal center. Calix-DANS4 exhibits an extremely high affinity for  $\text{Pb}^{2+}$  with a high selectivity over various competing ions ( $\text{Na}^+$ ,  $\text{K}^+$ ,  $\text{Ca}^{2+}$ ,  $\text{Cu}^{2+}$ ,  $\text{Zn}^{2+}$ ,  $\text{Cd}^{2+}$ , and  $\text{Hg}^{2+}$ ). The unprecedented detection limit (4 mg  $\text{L}^{-1}$ ) is fully compatible with the level defined by the World Health Organization. The affinity of Calix-DANS4 for  $\text{Pb}^{2+}$  can be rationalized by the activation of the inert pair of electrons on  $\text{Pb}^{2+}$ .



**Scheme 3**

Calix-DANS2 can be chosen to illustrate the importance of immobilization of the molecular sensor when designing a sensing device. Calix-DANS2 was grafted on a large-pore mesoporous silica material (via two long alkyl chains containing triethoxysilane groups). Addition of mercury ions to water results in fluorescence quenching, and the good selectivity is maintained, as shown by the relative variation in fluorescence intensity that starts at higher

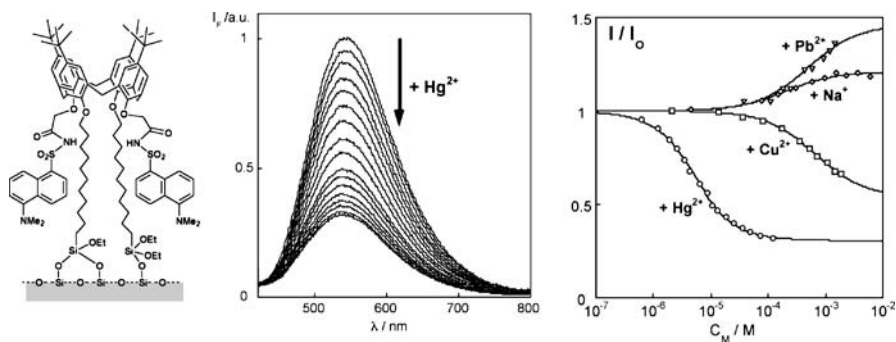


**Fig. 3** Immobilization of Calix-DANS2 on a mesoporous silica surface via two arms (*left*). Effect of addition of mercury ions on the fluorescence spectra (*middle*). The effects of other cations appear at much higher concentrations (*right*) (adapted from [16])

mercury concentrations for other possible interfering ions (Fig. 3) [16]. The response time is a few seconds and the detection limit is  $3.3 \times 10^{-7} \text{ mol L}^{-1}$  in water.

### 3.2

#### Microfabricated Analysis Systems

Considerable effort is made toward miniaturization of sensing devices with the following advantages: high speed, online monitoring, and low consumption of samples and reagents, which is a distinct advantage especially in the case of biological samples. The development of lab-on-chips, in particular the DNA gene chips, is impressive. Microfabricated analysis systems, called  $\mu$ -TAS (micro total analysis systems), are based on microfluidic technology using microchip channels, microreactors, valves, and pumps [17, 18]. Fluorescence is one of the optical detection methods employed in these systems.<sup>3</sup> Many applications, especially in the life sciences, are being developed: clinical diagnostics, immunoassays, DNA separation and analysis, sequencing, etc.

A very sophisticated microfluidic device developed by Richard Mathies and coworkers at the University of California in Berkeley aims at detecting amino acids in future missions on Mars [19] (Fig. 4). It is based on capillary electrophoresis, and fluorescamine is used as a fluorescence marker for amino acids. The first step of the analysis is sublimation of amines and amino acids onto an aluminum disk spin-coated with fluorescamine. This device was successfully tested in Atacama Desert in Chile, one of the most arid regions in the world: it is 50 times more arid than Death Valley in

<sup>3</sup> The other detection methods are electrochemical or based on chemiluminescence, electrochemiluminescence, or mass spectrometry.



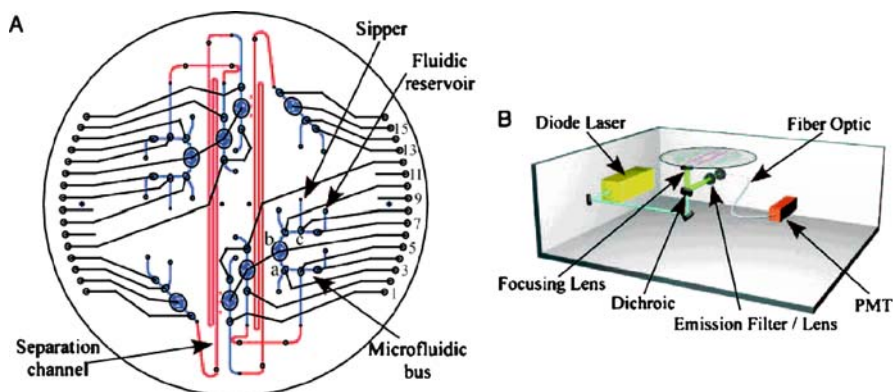


**Fig. 4** Microdevice for amino acid biomarker detection and analysis on Mars. **a** Top view of the microdevice showing registration of the capillary electrophoresis channel (red), pneumatic manifold (black), and fluidic bus wafers (blue). **b** Schematic of the instrument showing confocal excitation and detection optics [19]

California, and it can thus be considered as the best Mars analog site. Sensitivity ranges from micromolar to 0.1 nM, corresponding to parts-per-trillion sensitivity.

### 3.3

#### Fluorescence Imager for Sensing

Still with the aim of detecting life, but not based on a microfabricated system, a robot called Zoe (in Greek, Zoe ( $\zeta\omega\eta$ ) means life) has been developed by Alan Waggoner and coworkers at NASA Ames Research Center in collaboration with the Carnegie Mellon Institute. This is one of the most beautiful applications in the field of fluorescence sensing. The robot has under its carriage an outstanding fluorescence imager for the detection of chlorophyll-based life (e.g., cyanobacteria in lichens), as well as proteins, nucleic acids, lipids, and carbohydrates, using four fluorescent dyes with different ranges of excitation and emission. The optical system consists of a flash lamp, a selection of filters for excitation and emission, and a camera. Successful tests have been carried out in Chile's Atacama Desert.

### 3.4

#### Fluorescence LIDAR

LIDAR is the acronym of Light Detection And Ranging (which is a transposition of RADAR for Radiowave Detection And Ranging). LIDAR has long been used for atmospheric monitoring, and in particular for the detection of  $\text{SO}_2$  and  $\text{NO}_2$  in the atmosphere. The technique is based on

back-scattering and absorption of these species. Extension to fluorescence detection is possible by using appropriate emission filters. The applications concern:

- Status of vegetation
- Probing of plankton in seawater
- Imaging of the façades of historical monuments

In all these applications, a Nd:YAG laser is used for providing excitation pulses of about 10 ns duration at 532 and 355 nm thanks to frequency doubling and tripling, respectively.

### **Vegetation**

The aim is the remote detection of chlorophyll fluorescence upon excitation at 532 nm, which is of interest for monitoring and measuring the chemical activities and the status of trees and forests. Early detection and mapping of damaged vegetation as a consequence of pollution can also be made. Remote estimation of chlorophyll concentration as a function of time is possible by taking the ratio of the intensity of the images at 740 and 685 nm [20]. The test is validated by the comparison of the average intensity ratio and the amount of chlorophyll determined by chromatography. The average intensity ratio follows the chlorophyll concentration that increases in summer and decreases in autumn.

### **Seawater**

From aircrafts or ships, the detection of fluorescence from chlorophyll in phytoplankton and from phycoerythrin-containing plankton (e.g., cyanobacteria) (both excited at 532 nm) permits evaluation of the biomass. In addition, the fluorescence of dissolved organic substances can be detected upon excitation at 355 nm. NASA has developed an airborne oceanographic LIDAR and a shipboard laser fluorometer to achieve such evaluations.

### **Façades of Historical Monuments**

The mobile system is placed in a truck at a distance of about 60 m from the façade. A 355-nm pulsed laser beam is swept over the façade row by row. The spectrally resolved fluorescence signals are recorded on each point and allow [21]:

- Visualization of areas of biodeterogen (lichens, green algae)
- Identification of different stone types with natural surface aging or crust and pollution deposited layers

Façade status assessment is thus obtained in view of restoration planning.

## 4 Clinical Diagnostics

Clinical diagnostics is also relevant to sensing, but this topic deserves a separate section with a distinction between *in vitro* and *in vivo* methods.

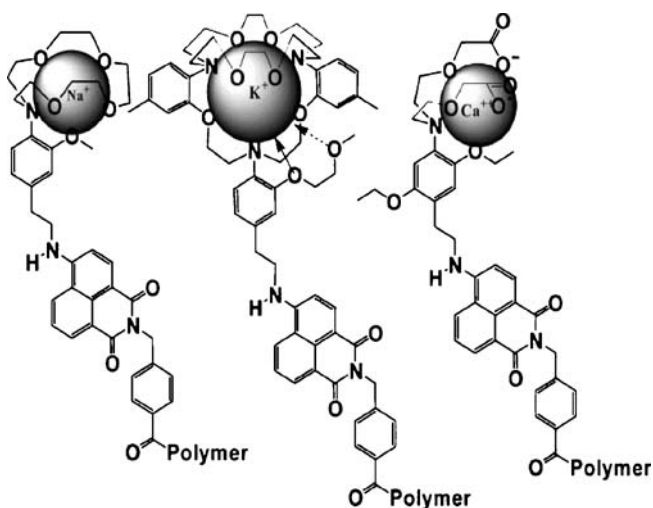
### 4.1 Critical Care Analysis

A nice example of *in vitro* analysis is the Osmetech/Roche OSPI critical care analyzer that can measure up to eight critical care analytes in whole blood [22]: pH, CO<sub>2</sub>/Hb, O<sub>2</sub>, Na<sup>+</sup>, K<sup>+</sup>, Ca<sup>2+</sup>, or Cl<sup>-</sup>. A disposable cartridge possesses six disks containing the appropriate fluorescent molecular sensors. Using 120 μL

**Table 1** Fluorescent sensors for critical care analytes (from [22])

	Normal range	Pathological range	Fluorescent sensor
pH	7.35–7.45	6.7–7.7	HPTS (pyranine)
P(CO <sub>2</sub> )/Torr	30–45	10–200	HPTS (pyranine)
P(O <sub>2</sub> )/Torr	70–100	20–600	Oxygen-sensitive dye
Na <sup>+</sup> /mM	135–145	100–180	Naphthalimide dye–aza crown <sup>a</sup>
K <sup>+</sup> /mM	3–5	1–10	Naphthalimide dye–cryptand <sup>a</sup>
Ca <sup>2+</sup> /mM	1.0–1.4	0.3–2.5	Naphthalimide dye–chelator <sup>a</sup>

<sup>a</sup> See Scheme 4



**Scheme 4**

of whole blood, it takes no more than 2 min to get the result. Table 1 shows a list of the analytes, the normal range, the pathological range, and the relevant molecular sensors. Pyranine is used as a fluorescent pH indicator.

For CO<sub>2</sub>, a membrane blocks the passage of H<sub>3</sub>O<sup>+</sup> and other ions into the sensor but allows CO<sub>2</sub> through, where it forms carbonic acid, increasing the local concentration of H<sub>3</sub>O<sup>+</sup>. For cation recognition, the naphthalimide fluorophore is linked to an aza crown for Na<sup>+</sup>, a cryptand for K<sup>+</sup>, and a chelating moiety for Ca<sup>2+</sup> (Scheme 4). The dissociation constants are consistent with the pathological ranges.

## 4.2

### Angiography

Angiography is a good example of in vivo diagnostics that permits visualization of the blood vessels of the retina in order to detect anomalies: lesions, aneurisms, or occlusions resulting from specific eye diseases. After taking a normal photograph of the retina, a fluorescent dye (fluorescein or indocyanine green) is injected into a vein in the arm of the patient. The dye is conveyed by the circulatory system and reaches the retina vessels. The photograph shown in Fig. 5 is an angiogram observed after injection of fluorescein: the existence of bright points leads to the diagnosis of an early diabetic retinopathy showing microaneurisms.

More recently, indocyanine green has been used as a tracer. It absorbs near 800 nm and emits in the near infrared, so that it can reveal deeper vessels called *choroidal vessels*. In the case of age-related macular degeneration,

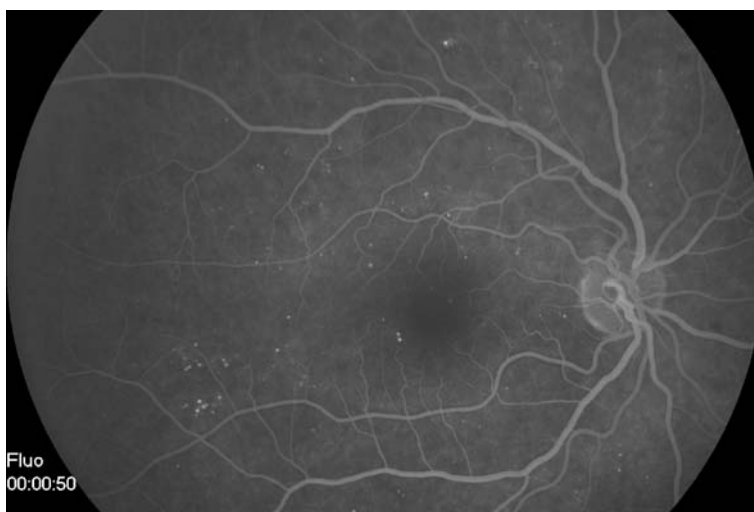


**Fig. 5** Angiogram showing microaneurisms (*bright points*) (Courtesy of Dr. J. C. Hache, Lille Hospital, France)

leaky vessels, i.e., choroidal neovascularization, can be visualized, while the angiogram with fluorescein also shows fluid leakage for the same patient.

### 4.3

#### Bladder Tumor Detection

Early detection of bladder tumors in situ is possible by looking at the relative fluorescence intensities of tryptophan and NADH by endoscopy. A catheter contains optical fibers to convey light pulses from an excimer laser (308 nm), and other fibers collect the fluorescence which is analyzed by a monochromator and a photomultiplier (Fig. 6) [23].

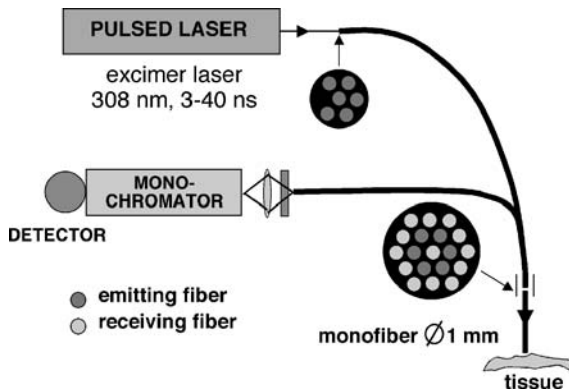


**Fig. 6** Experimental setup for the detection of bladder tumors

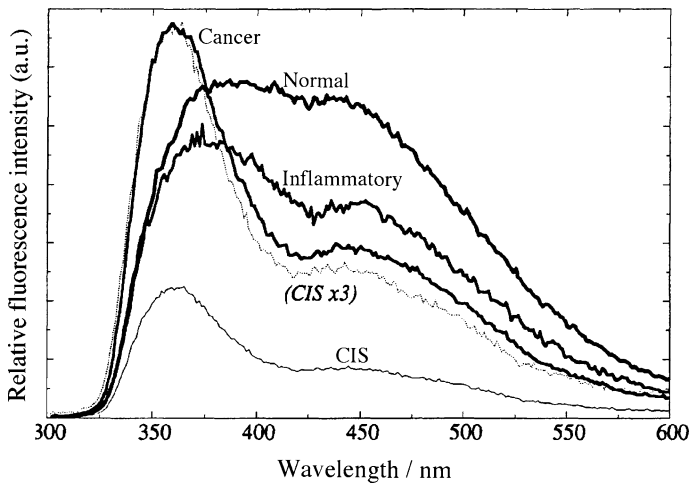


**Fig. 7** Fluorescence spectra of normal, inflammatory, and cancerous tissues upon excitation at 308 nm (CIS: carcinoma in situ)

The fluorescence spectra are different according to the state of the tissue (Fig. 7). For tumors and carcinomas in situ, the ratio of the fluorescence intensities at 360 and 440 nm is statistically greater than 2. This test is reliable and can be run during a routine visit.

#### 4.4

##### Human Skin

Measurements on human skin can be performed with a fiber-optic spectrofluorometer.<sup>4</sup> Double monochromators are necessary to isolate the fluorescence signal from strong scattering samples such as human skin.

Measurements of the fluorescence from tryptophan in epidermis and collagen in dermis provide a tool for:

- Evaluation of skin aging and photoaging
- Detection of skin disease
- Determination of epidermal proliferation (tryptophan)
- Control of drug delivery in photodynamic therapy

## 5

### Imaging and Tracing

Imaging and tracing is a most important application of fluorescence not only in biology, but also in many other fields. In biology, organic fluorophores or fluorescent antibodies have long been used as tracers; they will not be described here, whereas new methodologies using semiconductor nanocrystals and fluorescent proteins deserve particular attention.

#### 5.1

##### Semiconductor Nanocrystals

Semiconductor nanocrystals, also called quantum dots, were first studied in the 1970s, but applications emerged in the 1990s. Their photoluminescence properties are due to quantum confinement; the emission wavelength ranges from the ultraviolet to the infrared depending on the nature of the semiconductor and the size of the nanocrystal. For quantum dots made of cadmium selenide with a protective coating of zinc sulfide, the emission wavelength ranges from the blue (diameter of 2 nm) to the red (diameter of 7 nm).

Quantum dots offer distinct advantages for imaging, as a result of the following characteristics:

- Broad absorption spectrum allowing a common excitation wavelength for nanocrystals having different emission wavelengths

<sup>4</sup> SPEX SkinScan manufactured by HORIBA Jobin-Yvon.

- Narrow emission spectrum (Gaussian): 12–15 nm
- Fluorescence quantum yield greater than 50%
- Excellent photostability
- Can be coated for water solubility and biocompatibility

It should be emphasized that the photostability of quantum dots is much better than that of organic dyes, and they are much brighter in tissue.

A nice example of application in biology is the study of the diffusion dynamics of glycine receptors in the membrane of living neurons [24]. Quantum dots are linked to glycine receptors and make it possible to track them individually and thus to analyze their lateral dynamics in the neuronal membrane (Fig. 8). Thanks to the excellent photostability, it is possible to monitor the trajectories of the nanocrystals for 20 min, instead of 5 s with an antibody coupled to an organic fluorophore like Cy3. Changes in the number of receptors and synapses during synaptic plasticity and synaptogenesis can thus be investigated.

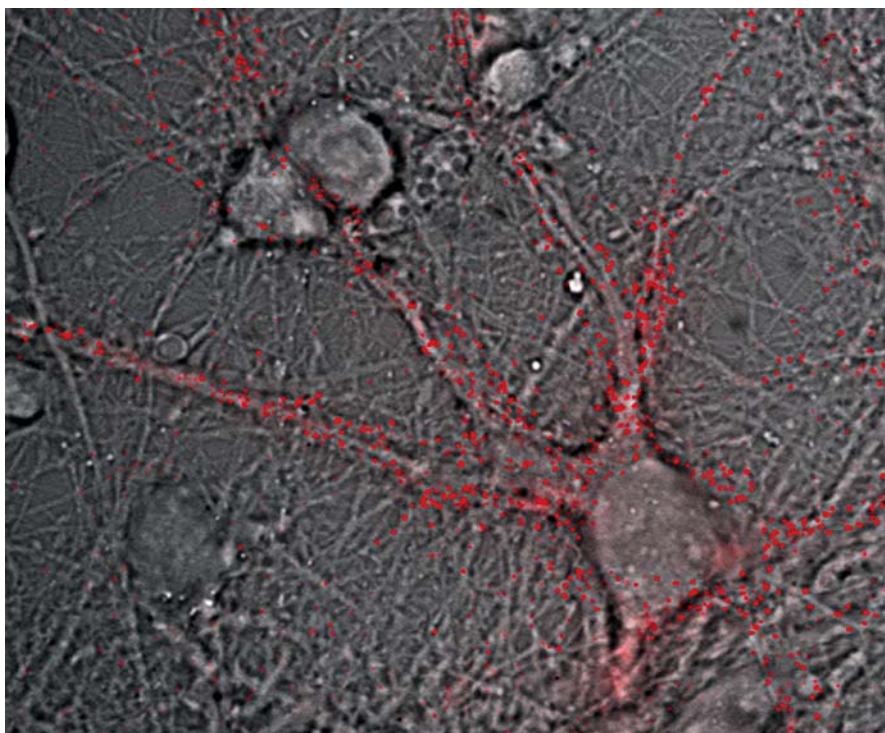


**Fig. 8** Glycine receptors located in the neuronal membrane and visualized by the red fluorescence from semiconductor nanocrystals attached to them. (Courtesy of M. Dahan and A Triller, Ecole normale supérieure, Paris)

Quantum dots have also been successfully used for in vivo cancer targeting and imaging [25]. Applications to encoding are also of great interest. For this purpose, nanocrystals are embedded in various proportions into polymer microspheres with millions of possible combinations. These microspheres can then be attached to DNA sequences, peptides, etc., and are thus useful for high-throughput screening (genomics, proteomics, drug screening).

Applications of encoding to counterfeit detection are to be expected in the near future (bank notes, ID cards, badges, etc.).

## 5.2

### Fluorescent Proteins

The use of fluorescent proteins is actually a revolution in the field of tracers in biology [26, 27]. The most popular one is GFP (green fluorescent protein) from *Aequora victoria*, a bioluminescent jellyfish. A fusion between a cloned gene and GFP can be created using standard techniques, which leads to a chimera that can be expressed in a cell. GFP thus acts as a fluorescent label for a protein of interest whose localization or activity is not affected. It is thus possible to visualize dynamic cellular events and to monitor protein localization.

Spectral variants of GFP emitting in the blue-cyan and yellowish green emission regions have been generated, but the wavelength of the emission maximum is not greater than ca. 530 nm. But corals (Anthozoa) can provide fluorescent proteins emitting in the red, like DsRed.

The simultaneous use of several colors is thus possible. A beautiful example of multicolor imaging is shown in Fig. 9. This image taken by confocal microscopy shows mossy fibers in one folium of a young adult transgenic mouse. Spectral variants of GFP are expressed in a combinatorial way following genetic recombination mediated by Cre recombinase. The various colors are produced by the particular subset of fluorescent proteins expressed in each axon and their individual concentrations. In this animal, at least 12 distinct spectral fingerprints in different cells can be discerned (J Lichtman, personal communication).

On a larger scale, fluorescent proteins also offer an outstanding tool for imaging muscle fibers in vivo, so that one can see the effect of new therapies for muscle diseases.

At an even larger scale, a whole animal can be rendered fluorescent if all cells express the gene of GFP. This has been applied to rabbits, mice, rats, pigs, and silkworms. The interest is that GFP makes it possible to follow the fate of cells in embryos, normal organs, and tumors, without requiring destruction of the cells. Figure 10 shows a transgenic fluorescent rabbit generated in the French Institut National de la Recherche Agronomique (INRA). A bioartist, Eduardo Kac from Chicago University, wished to breed these rabbits to be used as exotic pets, but this proposition was rejected by the French researchers.



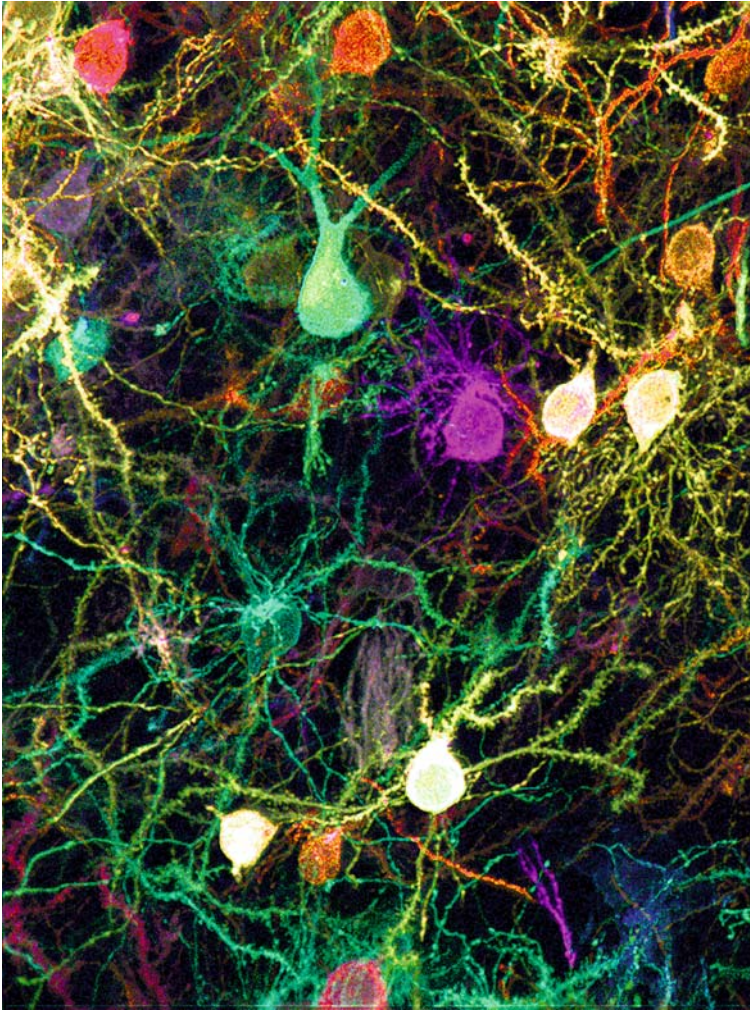


**Fig. 9** Multicolor imaging of mossy fibers in the cerebellum of a transgenic mouse (confocal microscopy). (Courtesy of J. Lichtman, Harvard University)

In 2003, a company located in Texas put on the market genetically modified aquarium fish having the capacity to be red fluorescent under UV illumination. This announcement was followed by protests from both activists and the scientific community. Indeed, this event raises several unanswered questions. Are these fish a threat to environment? Are they suffering from their transgene and from UV illumination? Is it ethical to use genetic engineering to generate this particular kind of pet [28]?

After these examples of imaging and tracing in biology, let us see examples in other fields.

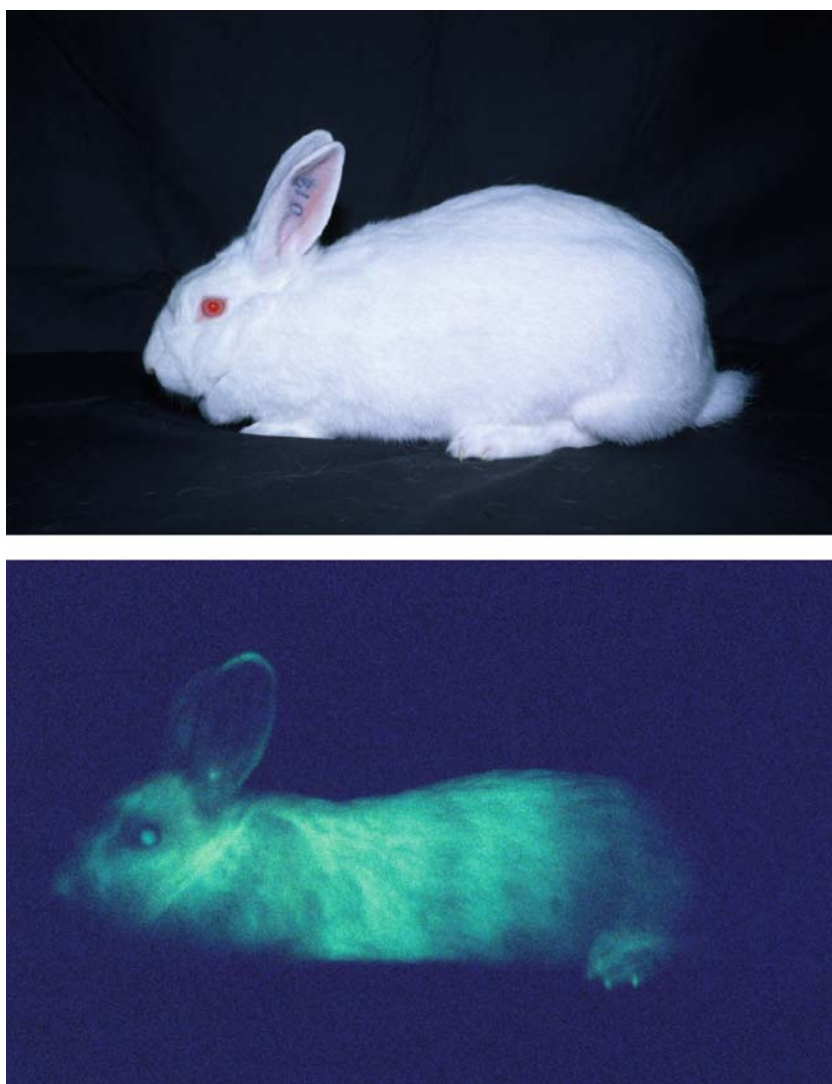


**Fig. 10** Transgenic rabbit shown under white light and under a UV lamp. Note in particular the eyes that appear green under UV illumination. (Courtesy of L.-M. Houdebine and B. Nicolas, INRA, France)

### 5.3

#### Surface Pressure Mapping

Surface pressure mapping is of major interest to study the aerodynamics of aircraft and cars. Instead of pressure sensors, a pressure-sensitive paint (PSP) is sprayed on the model, thus providing the possibility of determining instan-

taneous two-dimensional pressure distributions on the surface of the model in wind tunnels.

Instead of “pressure-sensitive”, we should say “oxygen-sensitive”. The paint contains fluorophores whose fluorescence is quenched by oxygen. Therefore, the larger the pressure, the larger the partial pressure of oxygen and the higher the efficiency of quenching of the fluorophores that are embedded in a transparent polymer. Fluorophores with a long excited-state lifetime must of course be chosen, such as pyrene derivatives, ruthenium complexes, etc.

The results are interpreted using an alternative form of the Stern–Volmer equation that holds for collisional quenching of fluorescence:

$$\frac{I_0}{I} = A + B \frac{P}{P_0} = \frac{\tau_0}{\tau},$$

where  $I$ ,  $\tau$ , and  $P$  are the fluorescence intensity, the excited-state lifetime, and the pressure, respectively. The subscript 0 refers to atmospheric pressure. Excited-state lifetimes are sometimes measured instead of fluorescence intensities.

Since the 1980s the PSP technique has been mainly applied to transonic and supersonic flow studies, and it is now commonly used in industrial wind tunnels. The problem is more difficult at low speed because of the smaller variations in pressure. Figure 11 shows an investigation carried out at ONERA [29]. The PSP is made of pyrene with gadolinium oxysulfide as reference dye (insensitive to oxygen), which permits correction for the nonhomogeneous distribution of illumination. The pressure map accurately reveals the variations in pressure at the roof/rear window junction.

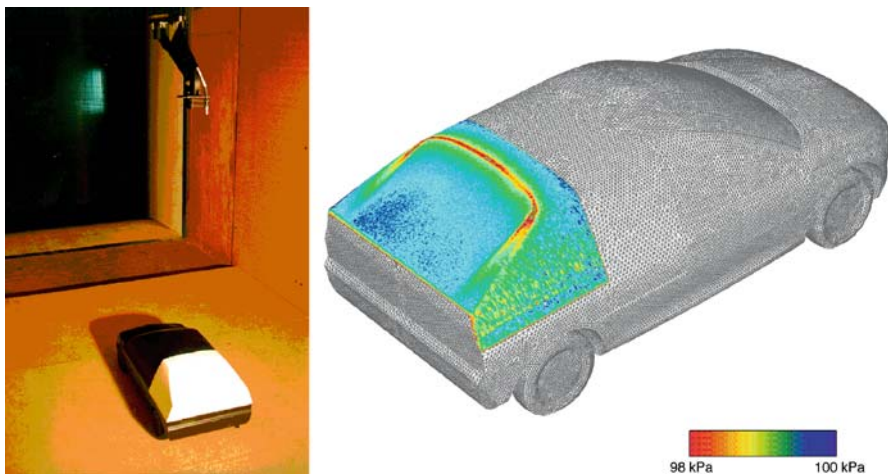


**Fig. 11** Model of a Peugeot 206 car in a wind tunnel (*left*) and pressure map (*right*). (Courtesy of M. C. Merienne, ONERA, France)

## 5.4 Criminology

In criminology, the visualization of fingerprints by means of powders is well known. The fluorescence powders are the most efficient. A difficult case is the detection of fingerprints on papers, especially when they are old. In this case,

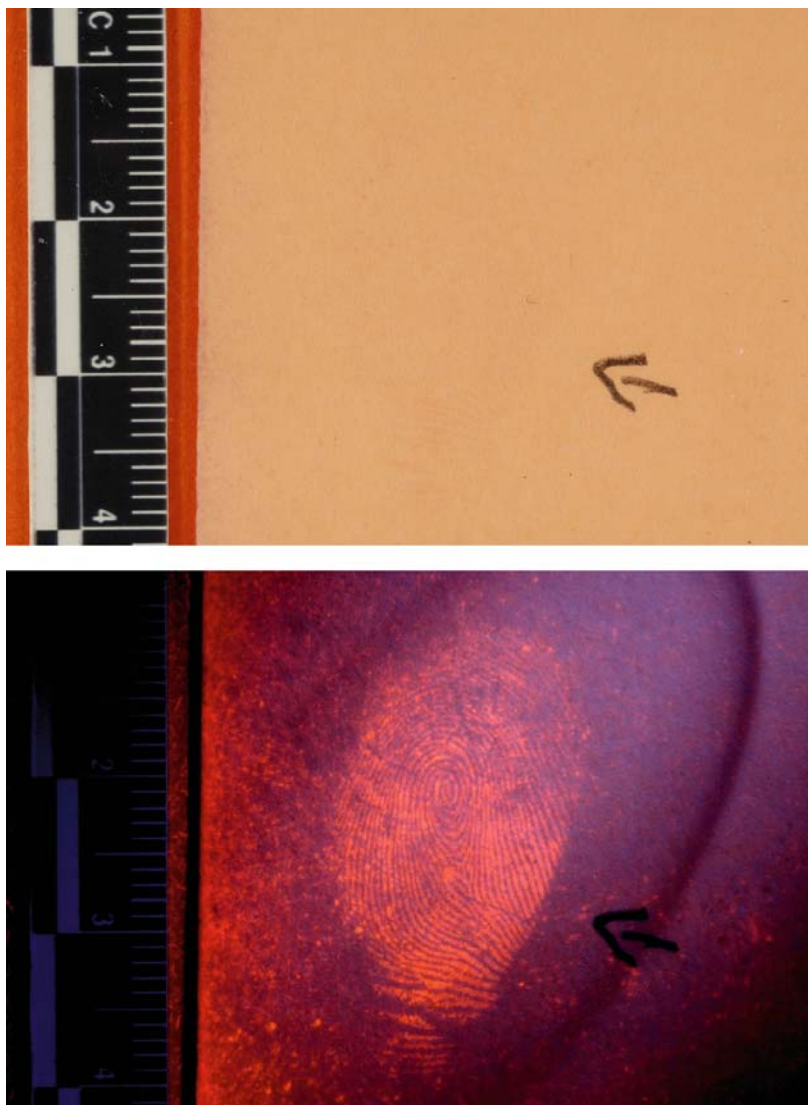


**Fig. 12** Fingerprint on a piece of paper revealed by fluorescence after treatment with diaza-9-fluorenone. (Courtesy of the Identité judiciaire de la Préfecture de police de Paris)

one answer is to soak the paper in a solution of diaza-9-fluorenone, and to dry it. Observation with appropriate filters (in order to get rid of the blue fluorescence of whitening agents) reveals the fluorescent fingerprints (Fig. 12).

## 5.5 Counterfeit Detection

It is well known that the luminescent pattern serves as a security check for documents, especially for bills. Various luminescent compounds, either organic or inorganic, are employed. For example, the Euro bills show different fluorescent colors (e.g., stars, Europe map) under UV illumination. Small fluorescent fibers can also be seen.

## 6 Fluorescence in Art

Paintings, ceramics, glassware, sculptures, ivories, old marble, and many other works of art often show fluorescence that depends on aging. Traces of restoration can thus be easily detected. Fluorescence is also a means to detect counterfeited objects.

### 6.1 Paintings

Illumination of a painting by a UV lamp permits visualization of restoration, repairs, hairline cracks, overpainting, falsified signatures, etc. An example is given in Fig. 13.

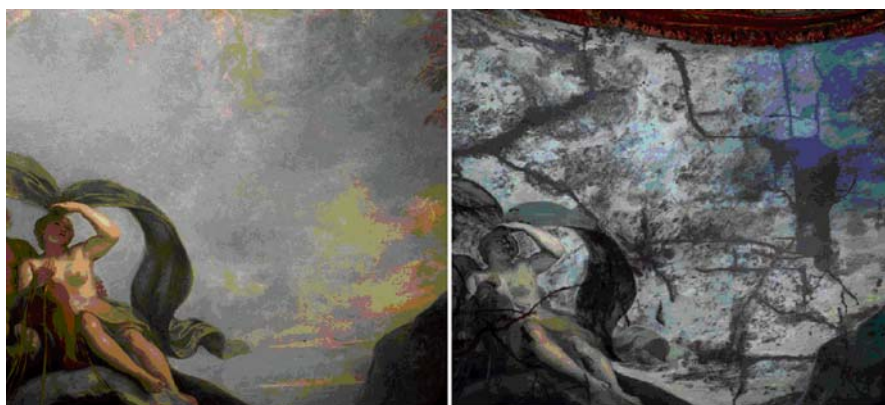


**Fig. 13** Painting in the Apollon Gallery of the Louvre museum (Courtesy of Daniel Vigears, Centre de Recherche et de Restauration des Musées de France)

**Table 2** Luminescence characteristics of some natural and synthetic pigments (from [30])

Pigments	Natural color	Color of luminescence	Emission wavelength at maximum/nm	Lifetime
Zinc white	White	Violet	385	0.3 ns
Titanium white	White	Turquoise-green	473	0.2 ns
Lead white	White	Yellow	547	100 $\mu$ s
Cadmium yellow	Yellow	Blue	483	50 ps
Naples yellow	Light yellow	Green	538	100 $\mu$ s
Cadmium red	Red	Yellow-green	568	40 ps
Red lead	Orange-red	Brown	586–600	3.7 $\mu$ s

Another important aspect is the identification of painting materials: pigments and resins [30]. The system using a pulsed laser and an intensified CCD camera is quite similar to the fluorescence LIDAR described above. The color of the luminescence of pigments is quite different from the natural color (Table 2). In addition to the luminescence spectra, it is of interest to measure the excited-state lifetimes: these are indeed very different according to the nature of the pigment (Table 2). In contrast, the fluorescence of the various resins is not very different: the wavelength of the emission maximum is located around 450 nm.

## 6.2 Sculptures

Old marble shows a mottled white or yellowish-white fluorescence, whereas recently cut marble fluoresces uniformly purple. Such a distinction in fluorescence was used by G. A. Richter in 1929 when he examined the statue of Diogenes in the Metropolitan Museum of New York. From the mottled appearance of the base and the lower portions, he concluded that only these are of ancient origin while the upper portion is of more recent date [6].

Another illustrative example is the gladiator Borghese, one of the masterpieces in Greek sculpture. It was discovered in the seventeenth century and restored in 1611. A UV lamp reveals the restored parts of the statue. The white fluorescence is due to a material used for restoration in the seventeenth century: a mixture of marble powder and beeswax. The brown color is due to the natural patina, whereas the black parts reveal an artificial patina [31].

The Ancestors statues made by the Fang nation in Gabon are surprisingly strongly fluorescent. The material itself is not fluorescent because the back of the statue is not fluorescent. It is likely that a fluorescent liquid was poured on the statue, perhaps during rites, but the nature of this liquid is not yet known

(Pascale Richardin, Centre de Recherche et de Restauration des Musées de France, personal communication).

## 7

### Conclusion

In the present review, only a selection of well-known and underrated applications of fluorescence have been presented. Other practical applications, such as whitening agents and fluorescent lighting, would have deserved attention. New applications will certainly emerge in the future.

The following citation from a paper by Queisser [32] written 25 years ago is still perfectly valid: "Luminescence research has a long history, full of splendor and surprise, and a bright future, promising variegated applications ..."

### References

1. Harvey EN (1957) A history of luminescence. The American Philosophical Society, Philadelphia
2. Pierre V (1862) Über die Anwendung der Fluorescenz zur Erkennung von fluorescirenden Stoffe [On the use of fluorescence for the detection of fluorescent compounds]. Sitzber Böhm Ges Wiss, Prague 2:66–85
3. Stokes GG (1887) Burnett Lectures *On light* in three courses delivered in Aberdeen in November 1883, December 1884, November 1885. Macmillan, London
4. Göppelsröder F (1867) Über eine fluorescirende Substanz aus dem Kuba-holze and über Fluorescenzanalyse. J Prakt Chem 101:408
5. Göppelsröder F (1868) Über eine fluorescirende Substanz aus dem Kuba-holze (Fortsetzung) and über Fluorescenzanalyse. J Prakt Chem 104:10
6. Radley JA, Grant J (1933) Fluorescence analysis in ultraviolet light. Van Nostrand, New York
7. Dake HC, De Ment J (1941) Fluorescent light and its applications. Chemical Publishing, Brooklyn
8. Pringsheim P, Vogel M (1943) Luminescence of liquids and solids and its practical applications. Interscience, New York
9. Valeur B (2002) Molecular fluorescence: principles and applications. Wiley-VCH, Weinheim
10. de Silva AP, Tecilla P (eds) (2005) Fluorescent sensors. Special issue, J Mater Chem 15:2617
11. Narayanaswamy R, Wolfbeis OS (eds) (2004) Optical sensors: industrial, environmental and diagnostic applications. Springer, Berlin
12. de Silva AP, Gunaratne HQN, Gunnlaugsson T, Huxley AJM, McCoy CP, Rademacher JT, Rice TE (1997) Chem Rev 97:1515
13. Desvergne JP, Czarnik AW (eds) (1997) Chemosensors of ion and molecule recognition. Kluwer, Dordrecht
14. Valeur B, Leray I (2000) Coord Chem Rev 205:3
15. Métivier R, Leray I, Valeur B (2004) Chem Eur J 10:4480

16. Métivier R, Leray I, Lebeau B, Valeur B (2005) *J Mater Chem* 15:2965
17. Reyes D, Iossifidis D, Auroux PA, Manz A (2002) *Anal Chem* 74:2623
18. Auroux PA, Iossifidis D, Reyes D, Manz A (2002) *Anal Chem* 74:2637
19. Skelley AM, Cherer JR, Aubrey AD, Grover WH, Ivester RHC, Ehrenfreund P, Grunthaner FJ, Bada JL, Mathies RA (2005) *Proc Natl Acad Sci USA* 102:1041
20. Saito Y, Saito R, KawaHara TD, Nomura A, Takeda S (2000) *For Ecol Manage* 128:129
21. Weibring P, Johansson T, Edner H, Svanberg S, Sundner S, Raimondi V, Cecchi G, Pantani L (2001) *Appl Opt* 40:6111
22. Tusa JK, He H (2005) *J Mater Chem* 15:2640
23. Avriillier S, Tinet E, Etti D, Anidjar M (1997) *Phys Scripta* 72:87
24. Dahan M, Lévi S, Luccardini C, Rostaing P, Riveau B, Triller A (2003) *Science* 302:442
25. Gao X, Cui Y, Levenson RM, Chung LWK, Nie S (2004) *Nat Biotechnol* 22:969
26. Zimmer M (2002) *Chem Rev* 102:759
27. Lippincott-Schwartz J, Patterson GH (2003) *Science* 300:87
28. Knight J (2003) *Nature* 426:372
29. Engler RH, Mérienne MC, Klein C, Le Sant Y (2002) *Aerospace Sci Technol* 6:313
30. Borgia I, Fantoni R, Flamini C, Di Palma TM, Giardini Guidoni A, Mele A (1998) *Appl Surf Sci* 127–129:95
31. Bagault D, Bourgeois B (1998) *Techne* 7:57
32. Queisser HJ (1981) *J Lumin* 25:3



# Principles of Directed Electronic Energy Transfer

David L. Andrews (✉) · Richard G. Crisp

Nanostructures and Photomolecular Systems, School of Chemical Sciences,  
University of East Anglia, Norwich NR4 7TJ, UK  
*d.l.andrews@uea.ac.uk*

1	Introduction . . . . .	46
2	Energy Transfer Between Isolated Chromophore Pairs . . . . .	48
2.1	Fundamental Theory for Energy Transfer in a Donor–Acceptor Pair . . . . .	48
2.2	Influence of a Static Electric Field . . . . .	50
2.3	Influence of Throughput Radiation . . . . .	52
3	Energy Transfer in Multichromophore Environments . . . . .	54
4	Directed Energy Transfer Systems . . . . .	58
4.1	Light-Harvesting Complexes . . . . .	58
4.2	Dendrimers . . . . .	59
4.3	Energy Transfer Between Dipole Arrays . . . . .	61
5	Future Applications . . . . .	63
	References . . . . .	64

**Abstract** On the optical irradiation of a complex absorptive medium, an ultrafast transfer of electronic energy between chromophores or sites generally takes place, preceding any ensuing fluorescence. Such transfer processes represent a redistribution of optically acquired energy and commonly lead to the indirect excitation of other chromophore units. Consequently, electronic energy transfer is a major determinant of detail in the fluorescence spectrum of the system. Where a sequence of energy transfer steps can be identified, the overall directionality of each sequence is important in determining any localization of the electronic energy. It is therefore highly significant that it is possible to exercise directional control over energy transfer, not only through the operation of an intrinsic spectroscopic gradient, but also by a variety of less well-known methods involving applied electrical or optical fields. Exploitation of the latter methods holds promise for advances in a wide range of technologies including optical switching and the production of energy harvesting materials.

## Abbreviations

$\alpha^M(\omega)$	Dynamic polarizability (at frequency $\omega$ ) of $M$
$A$	Acceptor
$D$	Donor
$d^\xi$	Absolute difference between the magnitudes of the excited and ground state dipole-transition moments of the chromophore $\xi$
$E$	Electric displacement vector of a static electric field

$\mathbf{e}$	Polarization vector of applied throughput radiation
$F_D(\omega)$	Donor emission spectrum
$I(\omega')$	Intensity of applied throughput radiation
IVR	Intramolecular vibrational relaxation
$\kappa_3^{\xi\xi'}$ and $\kappa_1^{\xi\xi'}$	Orientation factors for energy transfer between $\xi$ and $\xi'$
LARET	Laser-assisted resonance energy transfer
$\mu^A$	Dipole moment of the transition from the ground to excited state in $A$
$\mu^D$	Dipole moment of the transition from the excited to ground state in $D$
$\mu^M$	Static dipole-moment of $M$
$M$	Auxiliary chromophore
$\omega'$	Frequency of applied throughput radiation
QED	Quantum electrodynamics
$R_{\xi\xi'}$	Separation of the chromophores $\xi$ and $\xi'$
RET	Resonance energy transfer
$\sigma_A(\omega)$	Acceptor absorption cross-section
$\tau_D$	Donor radiative lifetime
$W$	Rate of energy transfer
$\xi$	Chromophore index
$\hbar\omega$	Energy transferred via RET

## 1

### Introduction

In non-homogeneous absorptive materials, the primary result of UV/visible absorption is the population of short-lived electronic excited states in individual molecules or chromophore sites. One or more transfers of electronic excitation energy may occur between the initial absorption and eventual fluorescence emission events, commonly on an ultrafast timescale and with some associated losses such as vibrational dissipation. The routing of energy flow is determined by a sequence of transfer steps, beginning and ending at chromophores that differ either chemically or, if the chromophores are chemically equivalent, through local modifications in energy level structure arising from differences in electronic environment (e.g. bathochromic shifts). At the molecular scale, each elementary transfer step is a radiationless pairwise interaction, generally between an electronically excited donor and an electronically distinct acceptor, which initially resides in its ground state. Förster [1] first demonstrated the Coulombic origin of this interaction, now known as resonance energy transfer (RET), also deriving its inverse sixth power dependence on the donor–acceptor separation.

It is now known [2–7] that the Förster interaction is the short-range limit of a more general result given by a unified transfer theory – a theory that is valid over any distance, and which includes additional terms with inverse fourth power and inverse square dependencies on separation. At large donor–acceptor separations, it emerges that the energy transfer is a radiative process involving the distinct emission and subsequent absorption of a photon. At

shorter separations the radiationless process is exhibited. In each case, the efficiency of transfer depends on the extent of overlap between the emission spectrum of the donor and the absorption spectrum of the acceptor. If, however, chromophores are closer still – close enough for their wavefunctions to overlap (generally a separation of less than 0.4 nm) – then a Dexter exchange mechanism comes into play [8]. This form of energy transfer involves a donor exchanging its excited electron with an unexcited one from an acceptor. Even if the donor and acceptor are separated beyond wavefunction overlap, electron exchange may still occur via a super-exchange mechanism [9–12], in which the coupling of the pair operates through a delocalization or mixing of the chromophore wavefunctions with those of bridging species (*relay chromophores*), connecting bonds, or the local solvent cage. Energy transfer may thus be further directed between chromophores linked by suitable intermediaries.

On the optical irradiation of an optically dense system comprising a large number of chromophores, a number of pairwise interactions typically occur before the system enters in a stable state. The energy transfer path accordingly comprises a series of short hops rather than one long one, largely as a result of the inverse sixth power distance dependence. Such multistep RET might be expected to have the character of a random walk, as indeed occurs in homogeneous single-component systems. However, with suitable chromophore differentiation, functionally unidirectional transfer is exhibited in multichromophore systems, assisted by suitable chromophore disposition, and often the operation of a *spectroscopic gradient*. Through experimental studies involving photobleaching spectroscopy, it has recently been shown possible to trace the intricate form of such multistep RET [13], allowing sequential mechanisms to be established in kinetically and spectroscopically complex systems. Whilst the principles that govern the directionality of energy flow in multichromophore systems are largely understood, other recent developments have identified new possibilities for effecting externally determined directional control. In particular it transpires that, by a variety of means, optical and electronic perturbations of light-harvesting systems can exert significant additional directing influences on the energy transit. The delineation and analysis of these novel mechanisms is the main subject of this chapter.

We begin in Sect. 2 by reviewing the theory underlying the fundamental mechanism for pairwise energy transfer, including modifications that result from the effects of applied electrical and optical fields. In Sect. 3 the general implications for multichromophore systems are explored, the principles then being illustrated by reference to biological and dendrimeric systems in Sect. 4. Also in Sect. 4, a model system utilizing these principles is developed, and it is shown how RET can be tailored, through the involvement of ancillary chromophores or non-resonant throughput radiation, to more efficiently direct energy flow. The chapter concludes in Sect. 5 with a discussion of the future prospects.

## 2

**Energy Transfer Between Isolated Chromophore Pairs**

To understand the multistep energy transfer that typifies the operation of many complexes, it is appropriate to begin with the theory for the prototypical case of energy transfer between one specific excited chromophore and another in its ground state. This is discussed in the first subsection. Following subsections deal with modifications to the basic process, including the influences of applied static and non-resonant radiation fields. A depiction of the three processes to be covered in this section is given in Fig. 1.

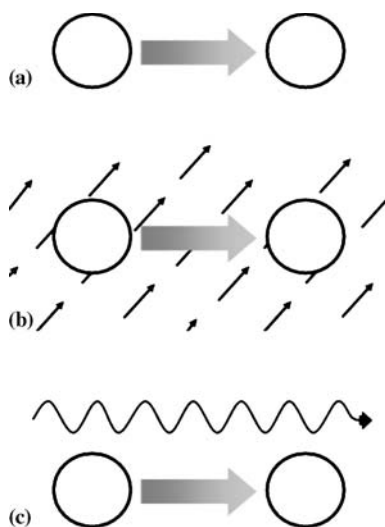


**Fig. 1** Depictions of: **a** resonance energy transfer; **b** electric field induced energy transfer; **c** laser-assisted resonance energy transfer. In each case, energy transfers from the donor on the *left* to the acceptor on the *right*; in the latter two cases an auxiliary influence affects the rate of transfer

## 2.1

**Fundamental Theory for Energy Transfer in a Donor–Acceptor Pair**

The pairwise transfer of energy between two chromophores  $D$  and  $A$  can be described by the equation:



where  $\xi^*$  denotes an excited state for chromophore  $\xi$ . Chromophore  $D$  is designated the *donor* and  $A$  the *acceptor*, though it should be emphasized that  $D$  and  $A$  may each adopt the alternative role in another part of a multistep sequential transfer process. For the description of the primary event (Eq. 1),

neither the mechanism for the excitation of  $D$  nor the subsequent decay of  $A$  comes into play; these are kinetically separable events. Using the Fermi Rule, the rate of energy transfer is determined from the square of a quantum amplitude given by the unified theory [14], and emerges as follows (based on the premise of electric dipole–electric dipole coupling):

$$W_{DA} = \frac{9}{8\pi c^2 \tau_D} \int F_D(\omega) \sigma_A(\omega) \omega^2 \eta^{DA}(\omega, \mathbf{R}_{DA}) d\omega. \quad (2)$$

Here  $\sigma_A(\omega)$  is the absorption cross-section of the acceptor,  $F_D(\omega)$  is the donor emission spectrum normalized to unity, and  $\omega$  is the circular frequency associated with the transferred energy; the latter thus designated as  $\hbar\omega$ . The spectral overlap integral given by Eq. 2 is calculated by integration over a frequency range that completely encompasses the salient features of the donor emission and acceptor absorption spectra. Also in Eq. 2,  $\tau_D$  is the donor radiative lifetime (a product of the measured fluorescence lifetime and the fluorescence quantum yield),  $\mathbf{R}_{DA} = \mathbf{R}_D - \mathbf{R}_A$  is the vector separation of the chromophores, and  $\eta^{DA}(\omega, \mathbf{R}_{DA})$  is given by:

$$\eta^{DA}(\omega, \mathbf{R}_{DA}) = \frac{c^6}{\omega^6 R_{DA}^6} (\kappa_3^{DA})^2 + \frac{c^4}{\omega^4 R_{DA}^4} \left[ (\kappa_3^{DA})^2 - 2\kappa_3^{DA} \kappa_1^{DA} \right] + \frac{c^2}{\omega^2 R_{DA}^2} (\kappa_1^{DA})^2. \quad (3)$$

The quantity given by Eq. 3 represents the overall spatial dependence for the transfer mechanism, and as such comprises both translational and orientational elements. It is interesting how the distance dependence is tempered by the transfer energy. Note that  $c/\omega R_{DA} = \lambda/2\pi R_{DA}$ , where the  $\lambda$  is the *wavelength* corresponding to the transfer energy. Furthermore, the orientation factors  $\kappa_3^{DA}$  and  $\kappa_1^{DA}$  in Eq. 3 are defined as:

$$\kappa_q^{DA} = (\hat{\boldsymbol{\mu}}^D \cdot \hat{\boldsymbol{\mu}}^A) - q (\hat{\boldsymbol{\mu}}^D \cdot \hat{\mathbf{R}}_{DA}) (\hat{\boldsymbol{\mu}}^A \cdot \hat{\mathbf{R}}_{DA}), \quad (4)$$

with  $\hat{\boldsymbol{\mu}}^D$ ,  $\hat{\boldsymbol{\mu}}^A$ ,  $\hat{\mathbf{R}}_{DA}$  being unit vectors in the direction of the dipole transition moments and the donor–acceptor separation vector. The  $\kappa$  factors thus signify an orientational dependence determined by the detailed chromophore architecture. For certain angular dispositions of the displacement vector and dipole transition moments (for example if all are mutually orthogonal) the  $\kappa$  factors vanish, obviating energy transfer by this mechanism. At the other extreme, optimization of the energy transfer is achieved when both transition moments are parallel or antiparallel to the separation vector [15]. Analysis of Eq. 2 indicates that the transfer rate is also strongly influenced by the separation and spectral features of the two chromophores, in addition to the relative orientation of the transition dipoles.

It may be observed that the detailed form delivered by the unified theory incorporates terms associated with both the commonly termed “radia-

tive” and “radiationless” processes, through  $\eta^{DA}(\omega, R_{DA})$ . In optically dilute systems with chromophore spacings of about a hundred or a few hundred nanometers, all three terms in Eq. 3 are comparable in magnitude. However, for transfer over longer distances (the *far-zone*,  $R \gg \lambda/2\pi$ , corresponding to distances well in excess of the wavelength for the transfer energy) the third term in Eq. 3 dominates and “inverse square” radiative behavior ( $W_{DA} \propto \kappa_1^2/R^2$ ) is observed. Conversely, in the *near-zone* ( $R \ll \lambda/2\pi$ , as is usual for energy transfer in optically dense condensed phase systems) Eq. 2 produces the familiar Förster rate:

$$W_{DA}^{\text{RET}} = \frac{9c^4\kappa_3^2}{8\pi\tau_D R_{DA}^6} \int F_D(\omega)\sigma_A(\omega)\omega^{-4} d\omega, \quad (5)$$

with a direct dependence on  $R^{-6}$  and  $\kappa_3^2$ . The latter near-zone behavior, usually termed “radiationless”, is by far the most significant for the near-neighbor transfers that occur in light-harvesting and allied materials.

## 2.2

### Influence of a Static Electric Field

The rate of energy transfer between a donor and acceptor pair can be significantly modified by interaction with a static electric field [16]. The effect is a direct consequence of associated shifts in the electron distributions of the interacting chromophores. In detail, it transpires that the mechanism for delivery of energy to the acceptor comprises four quantum pathways. The quantum amplitude for the overall transfer process is dominated by a term that exactly corresponds to the usual field-independent result, but it also comprises correction terms. The most significant of these entail linear coupling of the static field with either  $D$  or  $A$ , and one other involves coupling of the static field at both  $D$  and  $A$ . Moreover, when the static field engages with a transition, it is associated with different selection rules that can be formally identified with those of a *two-quantum* transition.

To elicit most clearly the principles that operate, it is expedient to apply a two-level approximation to the chromophores. This assumption is fully justified if the donor and acceptor excited states are the lowest electronically excited levels of each chromophore, and other energy levels are of significantly higher energy. The rate of energy transfer between the two chromophores in a static electric field is again determined from the Fermi Rule. Here we define  $\hat{\mathbf{E}}$  as the electric displacement unit vector of the static field (whose magnitude is  $E$ ), and  $d^\xi = \mu^{ee(\xi)} - \mu^{00(\xi)}$  as the absolute difference between the magnitudes of the excited state ( $e$ ) and ground state static dipole-moments of chromophore  $\xi$ . For simplicity it is to be assumed that all static and transition dipole moments associated with a particular chromophore are parallel, although those associated with  $D$  can have arbitrary orientation with

respect to those associated with  $A$ . Introducing the shorthand  $\mathbf{R}$  for  $\mathbf{R}_{DA}$ , the result for the rate is then cast as follows [16]:

$$\begin{aligned}
W_{DA} = & \frac{9}{8\pi c^2 \tau_D} \times \left[ S_2(\omega, \mathbf{R}) \right. \\
& + \frac{E}{\hbar} \left\{ |d^D| \left( \hat{\mathbf{E}} \cdot \hat{\boldsymbol{\mu}}^D \right) + |d^A| \left( \hat{\mathbf{E}} \cdot \hat{\boldsymbol{\mu}}^A \right) \right\} S_1(\omega, \mathbf{R}) \\
& + \frac{E^2}{\hbar^2} \left\{ \left[ |d^D| \left( \hat{\mathbf{E}} \cdot \hat{\boldsymbol{\mu}}^D \right) + |d^A| \left( \hat{\mathbf{E}} \cdot \hat{\boldsymbol{\mu}}^A \right) \right]^2 + 2 |d^A| |d^D| \left( \hat{\mathbf{E}} \cdot \hat{\boldsymbol{\mu}}^D \right) \left( \hat{\mathbf{E}} \cdot \hat{\boldsymbol{\mu}}^A \right) \right\} \\
& \times S_0(\omega, \mathbf{R}) \\
& - \frac{E^3}{\hbar^3} \left\{ |d^D| |d^A| \left( \hat{\mathbf{E}} \cdot \hat{\boldsymbol{\mu}}^D \right) \left( \hat{\mathbf{E}} \cdot \hat{\boldsymbol{\mu}}^A \right) \left[ |d^D| \left( \hat{\mathbf{E}} \cdot \hat{\boldsymbol{\mu}}^D \right) + |d^A| \left( \hat{\mathbf{E}} \cdot \hat{\boldsymbol{\mu}}^A \right) \right] \right\} \\
& \times S_{-1}(\omega, \mathbf{R}) \\
& + \left. \frac{E^4}{\hbar^4} |d^D|^2 |d^A|^2 \left( \hat{\mathbf{E}} \cdot \hat{\boldsymbol{\mu}}^D \right)^2 \left( \hat{\mathbf{E}} \cdot \hat{\boldsymbol{\mu}}^A \right)^2 S_{-2}(\omega, \mathbf{R}) \right]. \tag{6}
\end{aligned}$$

Here the set of functions  $S_n(\omega, \mathbf{R})$ , defined by:

$$S_n(\omega, \mathbf{R}) = \int F_D(\omega) \sigma_A(\omega) \omega^n \eta^{DA}(\omega, \mathbf{R}) d\omega, \tag{7}$$

denote  $\mathbf{R}$ -dependent forms of frequency-weighted overlap integral. It is important to note that, in successive terms of Eq. 6, the powers of  $\omega$  in the spectral overlap integral decrease. This indicates an increasing weighting towards the long-wavelength end of the overlap between the donor emission and acceptor absorption curves, correlating with the order of nonlinearity in the dependence on  $E$ . Figure 2 exhibits graphs derived from calculations of the transfer rate, using Eq. 6, based on typical values for the static field strength and transition dipole moments.

Equation 6 can be understood as a Taylor series expansion in powers of  $E$ , with the first term representing the normal rate of energy transfer (i.e., excluding static-field coupling), and with following terms signifying corrections of successively diminishing importance. The term describing energy transfer with one static interaction is the third term, and the last term describes energy transfer involving a coupling of both chromophores with the static field. The other terms represent quantum interference between the various pathways, of which the second term in Eq. 6 is linear in  $E$ , and generally the most significant correction. However, if either the donor or acceptor transition is electric dipole-forbidden, the first and second terms of Eq. 6 vanish and the third term provides the leading rate contribution. If both the donor *and* acceptor transitions are electric dipole-forbidden, only the final term can provide any meaningful contribution to the rate. The physical significance is that energy may not transfer to or from such species without the presence of a static field (except, conceivably, through the involvement of a much

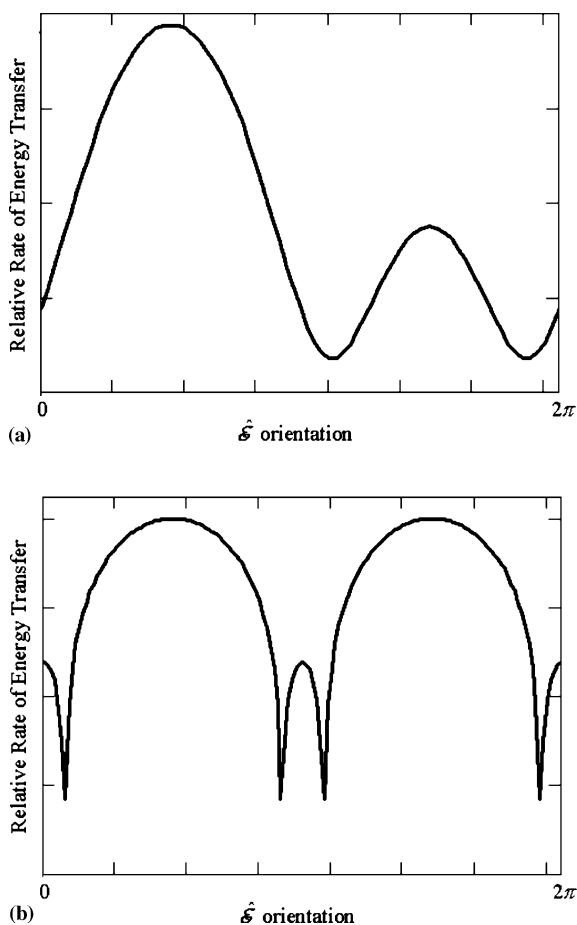


**Fig. 2** Influence of a static field on energy transfer as the polarization vector of the static field is rotated relative to the transfer pair. **a** The donor and acceptor transition moments are parallel, and the static field strength is  $10^{10} \text{ V m}^{-1}$ . **b** The donor and acceptor transition moments are anti-parallel to each other and the static field strength is  $10^{11} \text{ V m}^{-1}$

weaker, higher order multipole moment). This emphasizes the potential significance of the static field-induced mechanism; within a suitably designed system it allows a switchable electric field to control the delivery of energy to the acceptor.

### 2.3

#### Influence of Throughput Radiation

Pairwise energy transfer is influenced not only by the presence of static fields; it can also be modified by intense throughput laser radiation [17]. In this



mechanism the radiation undergoes cooperative forward Rayleigh scattering by the donor–acceptor pair, effectively leaving the radiation unchanged but either enhancing or diminishing the efficiency of energy transfer between the two chromophores. In the former, more interesting case the process is known as laser-assisted resonance energy transfer (LARET).

For simplicity, we restrict the following consideration to a system of non-polar (or only weakly polar) chromophores, again applying a two-level approximation. The laser-modified mechanism for energy transfer bears a degree of similarity to the static field-induced case described in Sect. 2.2, except that here a dynamic optical field is applied. Surprisingly, static dipoles of the donor and acceptor can still play a role, despite the oscillatory character of the field – but those which enter the rate expression now relate to electronically excited states. In other words, this mechanism again operates through shifts in the electron distributions, here associated with the donor decay and the acceptor excitation transitions. The total rate of energy transfer, in the presence of off-resonant laser light with a frequency  $\omega'$ , is expressible as [17]:

$$\begin{aligned}
W_{DA} = & \frac{9}{8\pi c^2 \tau_D} \int F_D(\omega) \sigma_A(\omega) \omega^2 \eta^{DA}(\omega, \mathbf{R}) d\omega + \frac{9 |\mu^{ee(D)}| |\mu^{ee(A)}| I(\omega')}{32\pi \hbar^2 c^3 \varepsilon_0 \omega'^2 \tau_D} \\
& \times \left\{ \frac{|\mu^{ee(D)}| |\mu^{ee(A)}| I(\omega')}{\hbar^2 c \omega'^2 \varepsilon_0} \left[ (\mathbf{e} \cdot \hat{\boldsymbol{\mu}}^D)^2 (\bar{\mathbf{e}} \cdot \hat{\boldsymbol{\mu}}^A)^2 \int F_D(\omega) \sigma_A(\omega) \right. \right. \\
& \times \eta^{DA}(\omega_+, \mathbf{R}) \omega_+^2 d\omega \\
& + (\bar{\mathbf{e}} \cdot \hat{\boldsymbol{\mu}}^D)^2 (\mathbf{e} \cdot \hat{\boldsymbol{\mu}}^A)^2 \int F_D(\omega) \sigma_A(\omega) \eta^{DA}(\omega_-, \mathbf{R}) \omega_-^2 d\omega \\
& + 2 \left[ e^{\frac{2i\omega'R}{c}} + e^{-\frac{2i\omega'R}{c}} \right] (\mathbf{e} \cdot \hat{\boldsymbol{\mu}}^D)^2 (\bar{\mathbf{e}} \cdot \hat{\boldsymbol{\mu}}^A)^2 \int F_D(\omega) \sigma_A(\omega) \eta^{DA}(\omega_+, \omega_-, \mathbf{R}) \\
& \times (\omega^2 - \omega'^2) d\omega \left. \right] \\
& - 4 \left[ (\mathbf{e} \cdot \hat{\boldsymbol{\mu}}^D) (\bar{\mathbf{e}} \cdot \hat{\boldsymbol{\mu}}^A) + (\bar{\mathbf{e}} \cdot \hat{\boldsymbol{\mu}}^D) (\mathbf{e} \cdot \hat{\boldsymbol{\mu}}^A) \right] \left[ e^{-\frac{i\omega'R}{c}} \int F_D(\omega) \sigma_A(\omega) \right. \\
& \times \eta^{DA}(\omega, \omega_+, \mathbf{R}) \omega \omega_+ d\omega + e^{\frac{i\omega'R}{c}} \\
& \left. \times \int F_D(\omega) \sigma_A(\omega) \eta^{DA}(\omega, \omega_-, \mathbf{R}) \omega \omega_- d\omega \right] \left. \right\} \quad (8)
\end{aligned}$$

In the above,  $\omega_{\pm}$  represents  $\omega \pm \omega'$ ;  $I(\omega')$  is the irradiance of the laser radiation and  $\mathbf{e}$  is the corresponding polarization vector ( $\bar{\mathbf{e}}$  being its complex conjugate, the distinction allowing for circular or elliptical polarizations). The first three  $\eta$  factors are as described previously, with  $\omega \pm \omega'$  substituted for  $\omega$  where appropriate. The other  $\eta$  factors arise from interference terms

and have a slightly more complicated form:

$$\eta^{DA}(\omega_1, \omega_2, \mathbf{R}) = \frac{c^6}{\omega_1^3 \omega_2^3 R^6} \kappa_3^2 + \frac{c^4}{\omega_1^2 \omega_2^2 R^4} \kappa_3^2 - \left[ \frac{c^4}{\omega_1^3 \omega_2 R^4} + \frac{c^4}{\omega_1 \omega_2^3 R^4} \right] \kappa_3 \kappa_1 + \frac{c^2}{\omega_1 \omega_2 R^2} \kappa_1^2 \quad (9)$$

where  $\omega_1$  and  $\omega_2$  stand for  $\omega$ ,  $\omega_+$  or  $\omega_-$  as required by Eq. 8.

The conventional (field-free) mechanism for RET is dominant at incident intensities below about  $10^{13} \text{ W m}^{-2}$ . At intensities of around  $10^{16} \text{ W m}^{-2}$  (relatively high, but easily produced using pulsed lasers) a rate enhancement of 10% or more can be introduced by the LARET mechanism, even for non-polar systems, and using significantly off-resonant frequencies. However, for chromophores that are both polar and chiral, additional terms arise [17], and these can lead to rate enhancements as high as 30% or more. Moreover, by judiciously tuning the laser in regions close to optical absorption bands, the detailed frequency dependence of the spectral overlap integrals in Eq. 8, and the distance-dependent factors of Eq. 9, can be exploited to effect even greater levels of enhancement. Finally, due to the linear and quadratic dependencies on irradiance for the LARET rate contributions, any further increase in the intensity of the throughput laser light can also be employed to generate a favorably disproportionate increase in the energy transfer rate. We believe that the use of off-resonant laser light to augment energy transfer should find many applications in artificial systems, since it provides an easily controlled, switchable process.

### 3

#### Energy Transfer in Multichromophore Environments

The previous section has described energy transfer at the fundamental level in terms of a coupling between two electronically isolated chromophores. In reality, however, most systems comprise numerous chromophores, and the vast majority of these systems are specifically non-homogeneous, or else comprise chemically similar chromophores distributed in non-homogeneous electronic environments. In the overall migration of energy, from the site of its initial deposition to the site of its chemical action, the spectroscopic gradient is one of the key directional principles obviating random diffusion. Despite each RET step occurring without energy loss, a small amount of energy is lost after each transfer step in the form of vibrational relaxation (ultimately manifest as heat). Consequently, each species when acting as acceptor receives energy associated with a longer optical wavelength than its donor initially acquired. This causes back-transfer to be very inefficient, due to the poorer overlap of the acceptor emission and donor absorption spec-

tra, enhancing a flow of energy towards acceptors with increasingly longer wavelength absorption profiles. The operation of the spectroscopic gradient on RET is shown in Fig. 3.

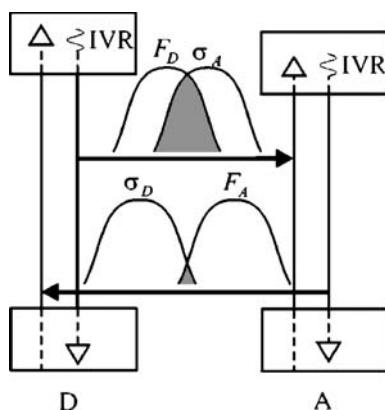


**Fig. 3** Energy level depiction illustrating the directing influence of the spectroscopic gradient on resonance energy transfer. Boxes indicate ground and excited electronic manifolds. Following excitation of donor *D*, energy transfers to the acceptor *A*. The dotted lines represent a range of vibrational energy levels within each electronic manifold, encompassed in the emission and absorption profiles of the chromophores. The strong overlap of the donor emission and acceptor absorption spectra, as denoted by the shaded area in the upper graph (wavelength increasing to the right), indicates that energy transfer is favorable in this instance. After the transfer, intramolecular vibrational relaxation (IVR) occurs in the acceptor, shifting its emission spectrum to a slightly longer wavelength than its absorption counterpart. Since the donor absorption profile is associated with a slightly higher frequency than its emission spectrum (again due to IVR), back-transfer from *A* to *D* is prohibited by the much weaker overlap of their respective emission and absorption profiles, as shown in the lower graph against wavelength. Both graphs are drawn on the same scale

Since each transfer event may take place in an electronic environment modified by one or more other chromophores in proximity to the interaction pair, it is necessary to entertain the possible role of a “third body” *M* in effecting other changes to the character of pairwise energy transfer. For example, in a dendrimeric system the third body might be another chromophore of the same type as either donor or acceptor, in the same general vicinity. In a photosynthetic complex the third body could be an ancillary pigment, or even one residue of a support protein unit. The involvement of such species as an influence on the rate of donor–acceptor transfer has received surprisingly little attention, yet it transpires that surrounding chromophores, especially any that are strongly polar, can substantially affect the rate of energy transfer without themselves changing state. This mechanism can be represented in

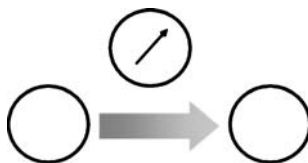
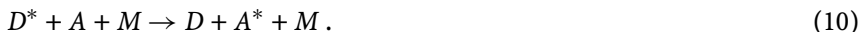


**Fig. 4** Depiction of third-body assisted energy transfer. Energy transfers from the donor on the *left* to the acceptor on the *right*, with the supporting chromophore exerting either a static or dynamic influence on the transfer pair

general terms as follows:



Associated with this mechanism, depicted in Fig. 4 (and in addition to the quantum amplitude for direct transfer not involving  $M$ , as described in the initial section), three distinct contributions to the amplitude can be identified: a static dipole of  $M$  interacts with either  $D$  or  $A$ , or a dynamic dipole of  $M$  acts as an intermediary for the energy transfer. In a sense the static interaction is comparable to that described in the last subsection, except that here the field is produced in situ rather than being externally delivered. The total rate of energy transfer between two chromophores in the presence of a third body, in the simplest case where the three involved chromophores are all non-polar, is as follows from the general result given in [18]:

$$\begin{aligned}
 W_{DA} = & \frac{9}{8\pi c^2 \tau_D} \int F_D(\omega) \sigma_A(\omega) \omega^2 \eta^{DA}(\omega, \mathbf{R}_{DA}) d\omega + \frac{9}{128\pi^3 c^2 \varepsilon_0^2 \tau_D} \\
 & \times \left\{ \int F_D(\omega) \sigma_A(\omega) |\alpha^M(\omega)|^2 \omega^2 \eta^{DM}(\omega, \mathbf{R}_{DM}) \eta^{AM}(\omega, \mathbf{R}_{AM}) d\omega \right. \\
 & + \frac{4\pi \varepsilon_0 c^6}{R_{DA}^3 R_{DM}^3 R_{AM}^3} \int F_D(\omega) \sigma_A(\omega) |\alpha^M(\omega)| \omega^{-4} \\
 & \left. \times \chi(\omega, \mathbf{R}_{DA}, \mathbf{R}_{DM}, \mathbf{R}_{AM}) d\omega \right\} \quad (11)
 \end{aligned}$$

where  $\alpha^M$  is the dynamic polarizability (at frequency  $\omega$ ) of  $M$ . Additionally,  $\chi(\omega, \mathbf{R}_{DA}, \mathbf{R}_{DM}, \mathbf{R}_{AM})$  is given by:

$$\begin{aligned}
 \Re \left\{ \left[ \left( 1 - \frac{i\omega R_{DA}}{c} \right) \kappa_3^{DA} - \frac{\omega^2 R_{DA}^2}{c^2} \kappa_1^{DA} \right] \right. \\
 \left[ \left( 1 + \frac{i\omega R_{DM}}{c} \right) \kappa_3^{DM} - \frac{\omega^2 R_{DM}^2}{c^2} \kappa_1^{DM} \right] \\
 \left. \left[ \left( 1 + \frac{i\omega R_{AM}}{c} \right) \kappa_3^{AM} - \frac{\omega^2 R_{AM}^2}{c^2} \kappa_1^{AM} \right] \right\} \quad (12)
 \end{aligned}$$

The largest influence of  $M$  occurs when it is polar, consistent with the interpretation that it thereby effects a distortion in the donor and/or acceptor electron distributions. Equally (as opposed to the case of LARET), even if the donor and acceptor are non-polar, they may acquire induced moments through the influence of  $M$ .

Previous research into the influence on energy transfer [18] has shown that the third body chromophore has a significant effect on the rate of energy transfer only when that chromophore is very close to either one of the donor-acceptor pair, typically at distances less than 1.5 nm. In this region, the third-body influence typically ranges from a 50% enhancement of the rate to a 40% reduction, depending on the arrangement of the chromophores involved. The exact rate distribution with respect to position depends on the relative dipole moment orientation of the three chromophores, but in general the influence of  $M$  is greatest when the dipole is positioned just outside wavefunction overlap of  $D$  or  $A$ . An example of this is given in Fig. 5. Considering the potential magnitude of the rate modification cited above, it is clearly imperative to take this mechanism into account when analyzing systems comprising a large number of closely spaced chromophores, such as most light-harvesting materials.

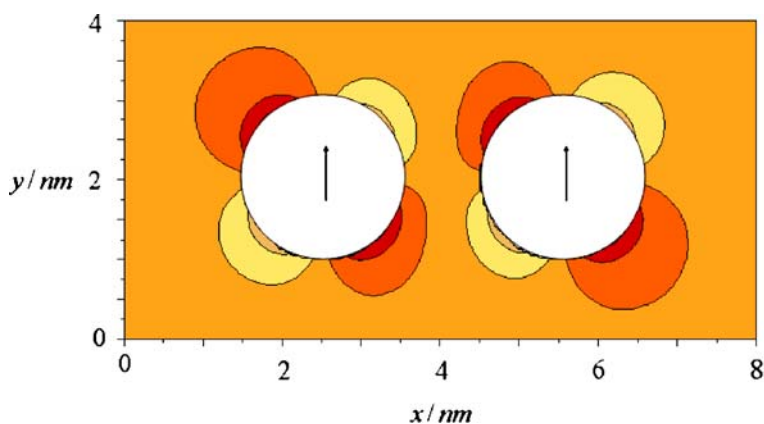


**Fig. 5** Influence of a neighboring dipole  $M$  on the rate of energy transfer between two chromophores, here located at coordinates  $(2.5, 2.0)$  and  $(5.5, 2.0)$  (positions measured in nm). Both chromophore transition moments are aligned parallel to the  $y$ -axis, the ancillary dipole is oriented at an angle of  $\pi/2$  to the  $y$ -axis. The influence of  $M$  increases as the color darkens from orange to red, with the darkest shade of red indicating a 200% increase of the rate compared to the lightest areas. White denotes positions of significant wavefunction overlap, where a different (exchange) mechanism would come into play

## 4 Directed Energy Transfer Systems

### 4.1 Light-Harvesting Complexes

In the realm of plant science, directional RET is well known to be an extremely significant process in the operation of photosynthetic units. In order to most effectively utilize the sunlight that falls on them, all photosynthetic organisms have a system of antenna complexes surrounding the reaction centers where photosynthesis takes place. The photosystems of purple bacteria, such as *Rhodospseudomonas acidophila* and *Rhodobacter sphaeroides* [19], have been most extensively studied [20–22] by means of ultrashort pulsed laser spectroscopy [23], X-ray protein crystallography [24], as well as hole-burning and absorption studies [25]. In such systems bacteriochlorophyll is the key light-harvesting pigment. Two complexes, LH1 and LH2, form coplanar ring structures in which the bacteriochlorophyll pigments are present as dimers, their local protein environment determining their precise wavelength of maximum absorption. The complex LH1, which surrounds the reaction center (RC), is composed of B880, a bacteriochlorophyll dimer with an absorption maximum at 880 nm. These structures ostensibly exhibit formation as a ring when studied independently, though some studies have suggested that the ring is not closed when the RC is present [21, 26]. The LH1 complex is in turn surrounded by a number of LH2 complexes, comprising both B850 rings above and B800 rings below.

The antenna complexes absorb sunlight and the acquired energy migrates towards the reaction center by a series of short-range, radiationless energy transfer steps. Although the energy initially absorbed by most chlorophylls is associated with shorter wavelength photons than is eventually received by the reaction center, some “red chlorophylls” absorb at longer wavelength than the RC, broadening the absorption profile of the complex [27]. Energy absorbed by outlying complexes is quickly and efficiently directed towards the reaction center (a process often referred to as *channeling* or *funneling*) due to the operation of a spectroscopic gradient between the antenna complexes and the reaction center. Not only does this allow an organism to harvest light incident on a large surface area but, by pooling energy from a large number of antenna chromophores, energy of a higher equivalent frequency can be produced. This is essential, since the majority of the incident light from the sun has too low a frequency for its individual photons to effect chemical photosynthesis.

It is not only spectroscopic properties of the chromophores that determine the direction of energy flow; the chromophore positioning and orientation are also important. Two-dimensional optical spectroscopy can unveil the intricate interplay between spectral and spatial overlap features in light-

harvesting complexes, as has been beautifully exhibited in recent studies on the Fenna–Olsen–Matthews bacteriochlorophyll *a* protein of green sulfur bacteria [28]. Interrogating the system with a sequence of ultrashort laser pulses, the optical response of the sample can be interpreted to reveal linear absorption processes as well as couplings between chromophores, and dynamical aspects of the energy transfer. The results show that excitation relocation does not simply proceed by stepwise transfer from one energy state to another of nearest energy; it depends on strong coupling between chromophores, determined by the extent of their spatial overlap. Thus, excitation relocation may involve fewer intermediary chromophores than might otherwise be expected.

## 4.2

### Dendrimers

The efficiency of photosynthetic units, especially the photobacterial systems optimized for operation at very low levels of intensity, has encouraged the design of a variety of synthetic light-harvesting systems that mimic their efficient energy funneling properties. The materials that have received most attention are dendrimers, which are macromolecules consisting of molecular units repeatedly branching out from a central core designed to act as an excitation trap [29, 30]. The branching functionalization of terminal groups leads to successive generations of structures, each with an increased number of peripheral antenna chromophores. In ideal cases, the requisite spectroscopic gradient is established through chemically similar chromophores situated in generationally different locations, and having different electronic properties due to subtly differing chemical environments. This arrangement expedites an emulation of the energy funneling observed in natural light-harvesting systems. In both cases, peripheral chromophores absorb incident photons and the excitation energy relocates across the structure [31–33], ultimately being funneled into the core [34]. Striking examples of this principle can be seen in classic work on perylene-functionalized phenylacetylene dendrimers [35, 36]. An example of a organosilicon cationic dendrimer is given in Fig. 6.

More recent work on dendrimers has seen a number of variations on the basic structural theme. As an example, dendrimers with dye molecules embedded in their internal cavities have proven to have very high energy harvesting efficiencies (approximately 80% in one case, where eosin is embedded in a dendrimer with 65 chromophore groups of four different types [38]). Other dendrimeric structures include: a molecular square, 20-chromophore unit, which exhibits biomimetic energy transfer from outer to inner (pyrene to perylene) chromophores [39]; and multiporphyrin systems [40] in which energy transfer from a zinc porphyrin to its free base counterpart is enhanced by the presence of suitable bridging chromophores [41]. Other work has focused on the synthesis and characterization of multiporphyrin arrays based on a phenylethynyl proto-dendrimeric framework [42], and den-

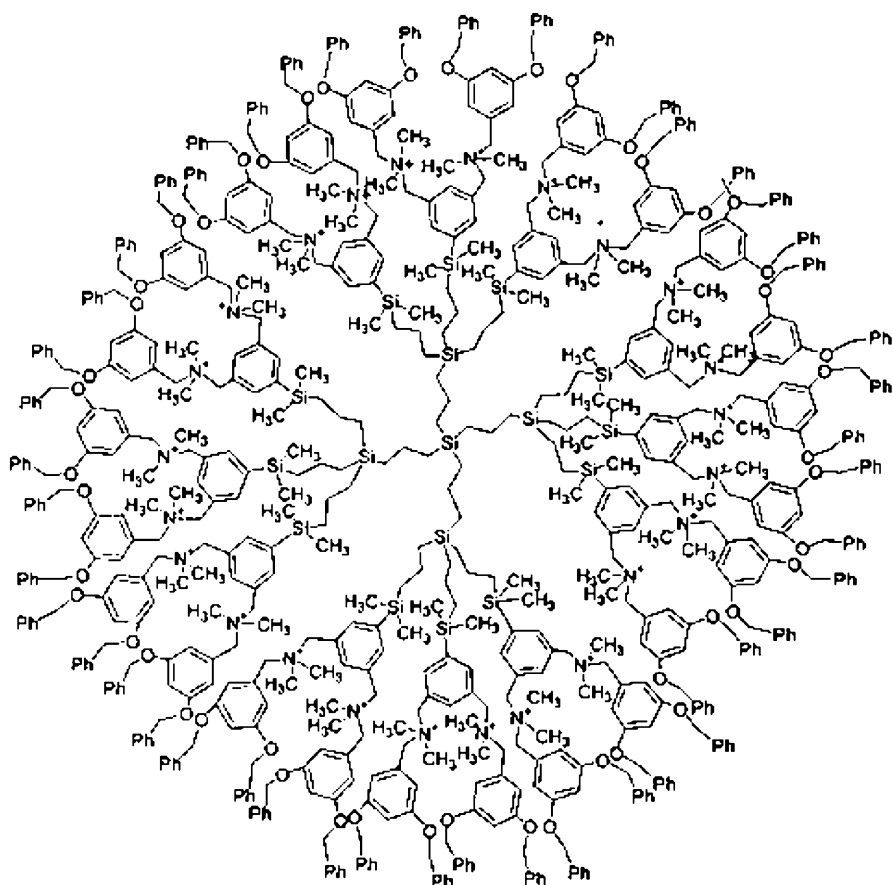


**Fig. 6** Example of a polycationic dendrimer. The core is surrounded by a repeatedly branching structure terminating in peripheral antenna groups. Reprinted with permission from [37]

dritic chains [43, 44] expediting directional energy transfer along their length (a concept holding promise for the design of nanoelectronic devices).

A particularly striking success is an artificial photosynthetic antenna-reaction center complex comprising four zinc tetraarylporphyrins covalently linked, through phenylethynyl dendrites, to a free base porphyrin-fullerene acting as a “reaction center”. Following photoexcitation of the peripheral zinc porphyrin (*antenna*), energy migrates to the central zinc porphyrin (*donor*) from which it transfers to free base porphyrin (*acceptor*), initiating electron transfer to the fullerene (*reaction center*). In this system, the charge-separated excited state is generated with an impressively high quantum yield of 0.90, based on the light absorbed by the zinc porphyrin antenna [45, 46]. Energy harvesting dendrimers are increasingly being developed for use as or-



ganic light-emitting diode materials [47–50]. Furthermore, energy pooling porphyrin dendrimers have begun to find an application in photodynamic therapy (PDT) as photosensitizers [51–53]. Energy harvesting here leads to the targeted photochemical destruction of cancer cells via the generation of singlet oxygen.

### 4.3

#### Energy Transfer Between Dipole Arrays

One of the operational principles under consideration for new optical switching devices is to configure a resonant coupling of throughput optical radiation to matter with a suitable absorption profile. Here the key requirement is to enable optically generated excitation to propagate between particles with a suitably matching frequency response. Many of the proposed systems involve internal transfers of electronic excitation, for example, electron transfer activated by an applied electric field [54–56] or laser-induced RET [57–61]. Such devices hold significant promise for the furtherance of ultrafast communication and signal processing systems. Within this context, and as one example of directed energy transfer, we now explore a nanoscale optical switching concept based on LARET.

We consider a scheme for the use of pulsed laser light to selectively channel energy between corresponding pixels in two parallel planar arrays. The concept is based on a configuration in which the transfer of energy from any excited donor to a counterpart acceptor in the opposing plane would be forbidden by conventional RET, but for which a quantum channel is opened by throughput laser radiation. For its physical implementation, a pair of two-dimensional arrays can be envisaged, each consisting of equally spaced, identical chromophores arranged on a square lattice.

The dipole transition moment of any given chromophore is parallel to all other transition moments within the same plane; each donor in one layer has a counterpart acceptor, with an orthogonal transition moment, in the other layer. For any single excited donor pixel, resonance energy transfer to its counterpart pixel is forbidden since the  $\kappa$  factor for that transfer is equal to zero. However, the application to the system of laser radiation, with an appropriate intensity, frequency, and polarization, allows energy to transfer between the two pixels, via a LARET pathway as described previously. A diagram of this system is given in Fig. 7. By engineering the separation of the layers, it can be ensured that energy transfer is always directed from any specific donor to its corresponding acceptor. In passing we note that, although electrical field influences are also capable of activating forbidden energy transfer, affording another possible basis for such an application, LARET proves to be the most amenable to controlled nanoscale implementation.

To produce a meaningful system, energy transfer from a given donor to its counterpart acceptor must be greatly favorable compared to any involving

another acceptor or even another donor; in other words, cross-talk has to be minimized. A detailed analysis of the geometric and orientational features of the system and associated constraints has been given elsewhere [62]. The analysis reveals that the probability of transfer to the intended acceptor strongly

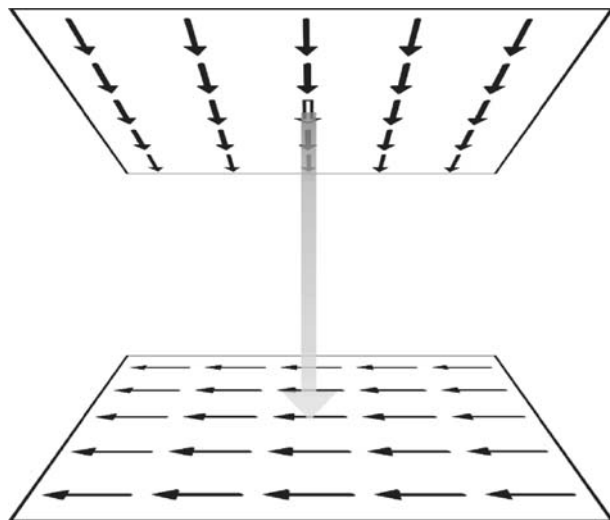


**Fig. 7** Arrays of donors (*upper array*) and acceptors (*lower array*) aligned with orthogonal dipole transition moments. Throughput laser radiation enables energy transfer from the excited donor (shown in *white* in the diagram) to its counterpart acceptor. The separation between the arrays is exaggerated for clarity. Reprinted with permission from [62]

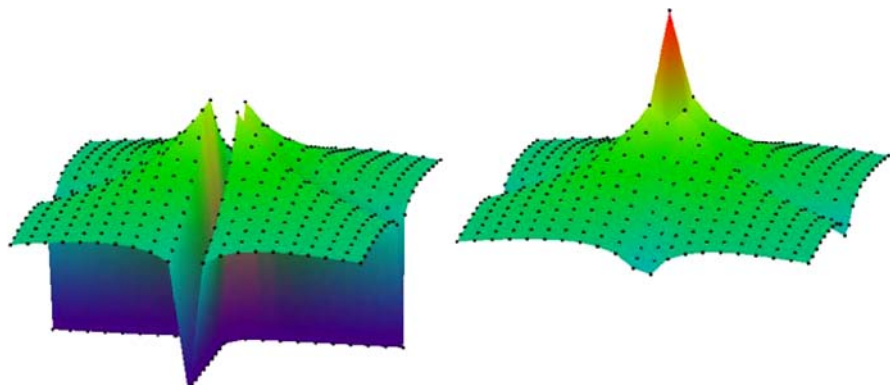


**Fig. 8** Energy transfer from a single excited donor to an array of acceptors in the absence (*left*) and presence (*right*) of throughput laser radiation. The separation between the donor and acceptor arrays is one-tenth that of the lattice spacing of each array, and an irradiance of  $10^{16} \text{ W m}^{-2}$  is sufficient to direct energy transfer. The *vertical scale* logarithmically represents the efficiency of energy transfer to the chromophore at that position in the array, *black dots* representing the position of each acceptor

depends on the aspect ratio (the relative magnitude of the lattice spacing and the spatial separation of the arrays) as well as on the intensity of the applied laser radiation. Figure 8 illustrates this with a particularly suitable relative positioning, where the spatial separation is one-tenth that of the lattice spacing. Energy can be directed to the intended acceptor on application of laser light with an irradiance in the region of  $10^{16} \text{ W m}^{-2}$ , for example. The favorability of this configuration is illustrated by the fact that a larger aspect ratio of 1 : 2 would result in a vast increase in the energy transfer probability to unintended acceptors, compromising the fidelity of the system. The appraisal of other methods for directing energy transfer in this and related systems, and potential device applications, are the subjects of ongoing research in the quantum electrodynamics group at UEA.

## 5

### Future Applications

In this chapter a variety of means for effecting directed energy transfer have been discussed and key results from the quantum theory have been presented. It has also been illustrated, by reference to several very different systems, how the principles can be implemented. Each mechanism offers distinct opportunities for future applications, which are being brought closer to fruition as new photonic technology is developed. The principle of directed electronic energy transfer is especially amenable to nanophotonic device implementation, since it enables the propagation of electronic energy to be specifically directed over subwavelength dimensions.

The best known mechanism for introducing a vector character to the flow of energy in a complex medium is a spectroscopic gradient. As has been shown, this requires a serendipitous correlation between the progression of quantum energy levels and the geometric layout of successive chromophore types in a multichromophore system. The exploitation of this principle, which operates extremely effectively in natural light-harvesting complexes, requires extraordinary skills in the design and synthesis of man-made biomimetic analogs, the best current examples of which are found in dendrimeric polymers. It now appears that the application of an electric field offers opportunities to effect further control over the flow of energy in such structures.

In device applications, the static field mechanism appears to require levels of field that would be most easily sustained in microscopic or submicroscopic domains (obviating the extremely high voltages that would otherwise be required), and these may perhaps be best achieved through surface field effects. Rapidly switching a directing field offers further intriguing possibilities. To achieve such control at the molecular level, utilizing local fields generated by neighboring dipoles, allows the necessary fields to be produced more readily; however, such a system is less amenable to real-time experimental control.

Here, one can envisage composite materials with a molecular architecture designed to deliver optically acquired energy from antenna chromophores to suitable traps, expedited by the incorporation of strongly polar groups.

It appears to be for the case of optically induced RET switching that the most promising opportunities for device implementation may arise. It is highly significant that the laser systems capable of delivering the necessary levels of irradiance are precisely those that also offer directly controllable, ultrafast speeds of switching. The parallel processing possibilities that arise with array implementation suggest a variety of optical interconnect applications, including flat panel displays and optical communications routing technology. The realization of such applications should be viewed in the context of ongoing advances in nanolithographic fabrication, which are driving optical technology to ever greater levels of speed and miniaturization. The mechanisms for controlling energy flow are only just beginning to receive attention, and it will be fascinating to observe how materials science and nanotechnology will rise to the challenge of exploiting the new opportunities that they open up.

**Acknowledgements** Research in the quantum electrodynamics group at UEA is funded by the UK Engineering and Physical Sciences Research Council (EPSRC). We gladly acknowledge the award of an EPSRC studentship to RGC.

## References

1. Förster T (1948) *Ann Phys-Berlin* 2:55
2. Craig DP, Thirunamachandran T (1986) *Accounts Chem Res* 19:10
3. Andrews DL, Sherborne BS (1987) *J Chem Phys* 86:4011
4. Juzeliunas G, Andrews DL (2000) *Adv Chem Phys* 112:357
5. Daniels GJ, Jenkins RD, Bradshaw DS, Andrews DL (2003) *J Chem Phys* 119:2264
6. Salam A (2005) *J Chem Phys* 122:044112
7. Salam A (2005) *J Chem Phys* 122:044113
8. Dexter DL (1953) *J Chem Phys* 21:836
9. Scholes GD, Ghiggino KP, Oliver AM, Paddon-Row MN (1993) *J Am Chem Soc* 115:4345
10. Yeow EKL, Haines DJ, Ghiggino KP, Paddon-Row MN (1999) *J Phys Chem A* 103:6517
11. Yeow EKL, Ghiggino KP (2000) *J Phys Chem A* 104:5825
12. Smith TA, Lokan N, Cabral N, Davies SR, Paddon-Row MN, Ghiggino KP (2002) *J Photochem Photobiol A* 149:55
13. Forde TS, Hanley QS (2005) *Photochem Photobiol Sci* 4:609
14. Juzeliunas G, Andrews DL (1999) In: Andrews DL, Demidov AA (eds) *Resonance energy transfer*. Wiley, Chichester, p 65
15. Wieb van der Meer B (1999) In: Andrews DL, Demidov AA (eds) *Resonance energy transfer*. Wiley, Chichester, p 151
16. Andrews DL, Bittner AM (1993) *J Lumin* 55:231
17. Allcock P, Jenkins RD, Andrews DL (2000) *Phys Rev A* 6102:023812
18. Daniels GJ, Andrews DL (2002) *J Chem Phys* 117(E):6882

19. Hu X, Schulten K (1998) *Biophys J* 75:683
20. Sundström V, Pullerits T, van Grondelle R (1999) *J Phys Chem B* 103:2327
21. Roszak AW, Howard TD, Southall J, Gardiner AT, Law CJ, Isaacs NW, Cogdell RJ (2003) *Science* 302:1969
22. Krueger BP, Scholes GD, Gould IR, Fleming GR (1999) *Phys Chem Commun* 8:1089
23. Katiliene Z, Katilius E, Uyeda GH, Williams JC, Woodbury NW (2004) *J Phys Chem B* 108:3863
24. Hu X, Damjanovik A, Ritz T, Schulten K (1998) *Proc Natl Acad Sci USA* 95:5935
25. Wu H-M, Rätsep M, Jankowiak R, Cogdell RJ, Small GJ (1998) *J Phys Chem B* 102:4023
26. Jungas C, Ranck JL, Rigaud JL, Joliot P, Vermeglio A (1999) *EMBO J* 18:534
27. Sener MK, Schulten K (2005) In: Andrews DL (ed) *Energy harvesting materials*. World Scientific, Singapore, p 1
28. Brixner T, Stenger J, Vaswani HM, Cho M, Blankenship RE, Fleming GR (2005) *Nature* 434:625
29. Bar-Haim A, Klafter J (1998) *J Lumin* 76–77:197
30. Bar-Haim A, Klafter J (1998) *J Phys Chem B* 102:1662
31. Tretiak S, Chernyak V, Mukamel S (1998) *J Phys Chem B* 102:3310
32. Swallen SF, Shi ZY, Tan WH, Xu ZF, Moore JS, Kopelman R (1998) *J Lumin* 76–77:193
33. Yeow EKL, Ghiggino KP, Reek JNH, Crossley MJ, Bosman AW, Schenning A, Meijer EW (2000) *J Phys Chem B* 104:2596
34. Adronov A, Frechet JMJ (2000) *Chem Commun*, p 1701
35. Devadoss C, Bharathi P, Moore JS (1996) *J Am Chem Soc* 118:9635
36. Shortreed MR, Swallen SF, Shi ZY, Tan WH, Xu ZF, Devadoss C, Moore JS, Kopelman R (1997) *J Phys Chem B* 101:6318
37. Aulenta F, Hayes W, Rannard S (2003) *Eur Polym J* 39:1741
38. Hahn U, Gorka M, Vögtle F, Vicinelli V, Ceroni P, Maestri M, Balzani V (2002) *Angew Chem Int Edit* 41:3595
39. Würthner F, Sautter A (2003) *Org Biomol Chem* 1:240
40. Van Patten PG, Shreve AP, Lindsey JS, Donohoe RJ (1998) *J Phys Chem B* 102:4209
41. Kilså K, Kajanus J, Mårtensson J, Albinsson B (1999) *J Phys Chem B* 103:7329
42. Brodard P, Matzinger S, Vauthey E, Mongin O, Papamicaël C, Gossauer A (1999) *J Phys Chem A* 103:5858
43. Cho HS, Song NW, Kim YH, Jeoung SC, Hahn S, Kim D, Kim SK, Yoshida N, Osuka A (2000) *J Phys Chem A* 104:3287
44. Tamura M, Gao D, Ueno A (2001) *Chem Eur J* 7:1390
45. Kuciauskas D, Liddell PA, Lin S, Johnson TE, Weghorn SJ, Lindsey JS, Moore AL, Moore TA, Gust D (1999) *J Am Chem Soc* 121:8604
46. Kodis G, Liddell PA, de la Garza L, Clausen PC, Lindsey JS, Moore AL, Moore TA, Gust D (2002) *J Phys Chem A* 106:2036
47. Halim M, Samuel IDW, Pillow JNG, Burn PL (1999) *Synthetic Met* 102:1113
48. Freeman AW, Koene SC, Malenfant PRL, Thompson ME, Frechet JMJ (2000) *J Am Chem Soc* 122:12385
49. Anthopoulos TD, Markham JPJ, Namdas EB, Lawrence JR, Samuel IDW, Lo SC, Burn PL (2003) *Org Electron* 4:71
50. Furuta P, Brooks J, Thompson ME, Frechet JMJ (2003) *J Am Chem Soc* 125:13165
51. Stapert HR, Nishiyama N, Jiang DL, Aida T, Kataoka K (2000) *Langmuir* 16:8182
52. Nishiyama N, Stapert HR, Zhang GD, Takasu D, Jiang DL, Nagano T, Aida T, Kataoka K (2003) *Bioconjugate Chem* 14:58
53. Zhang GD, Harada A, Nishiyama N, Jiang DL, Koyama H, Aida T, Kataoka K (2003) *J Control Release* 93:141

54. Aviram A (1988) *J Am Chem Soc* 110:5687
55. Chen J, Reed MA, Rawlett AM, Tour JM (1999) *Science* 286:1550
56. Yang ZQ, Lang ND, Di Ventra M (2003) *Appl Phys Lett* 82:1938
57. Alvaro M, Chretien MN, Ferrer B, Fornes V, Garcia H, Scaiano JC (2001) *Chem Commun*, p 2106
58. Just EM, Wasielewski MR (2000) *Superlattices Microstruct* 28:317
59. Sangu S, Kobayashi K, Shojiguchi A, Kawazoe T, Ohtsu M (2003) *J Appl Phys* 93:2937
60. Wada O (2004) *New J Phys* 6:183
61. Ham BS (2001) *ETRI J* 23:106
62. Andrews DL, Crisp RG (2006) *J Fluoresc* 16:191
63. Andrews DL, Crisp RG (2006) *J Opt A Pure Appl Opt* 8:S106

# Luminescence Decays with Underlying Distributions of Rate Constants: General Properties and Selected Cases

Mário N. Berberan-Santos<sup>1</sup> (✉) · Evgeny N. Bodunov<sup>2</sup> · Bernard Valeur<sup>3,4</sup>

<sup>1</sup>Centro de Química-Física Molecular, Instituto Superior Técnico, 1049-001 Lisboa, Portugal  
*mbs@ist.utl.pt*

<sup>2</sup>Physical Department, Petersburg State Transport University, 190031 St. Petersburg, Russia

<sup>3</sup>CNRS UMR 8531, Laboratoire de Chimie Générale, CNAM, 292 rue Saint-Martin, 75141 Paris cedex 03, France

<sup>4</sup>Laboratoire PPSM, ENS-Cachan, 61 avenue du Président Wilson, 94235 Cachan cedex, France

<b>1</b>	<b>Introduction</b> . . . . .	<b>68</b>
<b>2</b>	<b>Nature and Limitations of the Luminescence Decay Law and of the Distribution of Rate Constants</b> . . . . .	<b>70</b>
2.1	Luminescence Decay Law . . . . .	70
2.2	Distribution of Rate Constants . . . . .	71
<b>3</b>	<b>General Considerations Regarding Distributions of Rate Constants</b> . . . . .	<b>72</b>
3.1	Characteristic Parameters . . . . .	72
3.2	Influence of the Intrinsic Decay . . . . .	74
3.3	The Transform Ladder . . . . .	74
<b>4</b>	<b>Conditions that a Decay Function must Satisfy in Order to have a Distribution of Rate Constants</b> . . . . .	<b>76</b>
4.1	Sufficient Condition for $I(t)$ . . . . .	76
4.2	Necessary Conditions for $w(t)$ . . . . .	76
4.2.1	First Derivative of $w(t)$ . . . . .	77
4.2.2	Higher Derivatives of $w(t)$ . . . . .	78
<b>5</b>	<b>Construction of the Decay from Cumulant and Moment Expansions</b> . . . . .	<b>79</b>
<b>6</b>	<b>Calculation of <math>H(k)</math> from the Cumulants</b> . . . . .	<b>79</b>
<b>7</b>	<b>Decay Function Asymptotics</b> . . . . .	<b>81</b>
7.1	$H(0^+) > 0$ . . . . .	82
7.1.1	$H(k)$ Admits a Maclaurin Series Expansion . . . . .	82
7.1.2	$H(k)$ is not Analytic at the Origin . . . . .	82
7.2	$H(0^+) = 0$ . . . . .	83
7.3	$H(k)$ Contains $\delta(k)$ . . . . .	84
7.4	Cases Left Out . . . . .	84

<b>8</b>	<b>Selected Decay Functions</b> . . . . .	84
8.1	Stretched Exponential (or Kohlrausch) Function . . . . .	86
8.2	Compressed Hyperbola (or Becquerel) Function . . . . .	90
8.3	Mittag-Leffler and Heaviside Functions . . . . .	94
8.4	Weibull Probability Density Function . . . . .	96
8.5	Truncated Gaussian Probability Density Function . . . . .	98
<b>9</b>	<b>Concluding Remarks</b> . . . . .	99
	<b>References</b> . . . . .	99

**Abstract** The mathematical properties of the general luminescence decay law are described. Special attention is paid to cases represented by continuous distributions of decay rate constants. Six important decay functions are described in detail: stretched exponential (Kohlrausch), compressed hyperbola (Becquerel), Mittag-Leffler, Heaviside, Weibull, and truncated Gaussian.

**Keywords** Distribution of rate constants · Luminescence decay · Laplace transform · Stretched exponential · Becquerel decay function · Weibull distribution · Truncated Gaussian distribution

### Abbreviations

PDF	Probability density function
FRET	Förster resonance energy transfer
RET	Resonance energy transfer
$I(t)$	Luminescence decay function
$H(k)$	Distribution (PDF) of rate constants
$w(t)$	Time-dependent rate coefficient
$J(k, t)$	Renormalized distribution of rate constants
$\langle k \rangle$	Ensemble averaged rate constant ( $w(0)$ )
$\langle \tau \rangle$	Ensemble averaged lifetime (average time constant)
$\bar{k}$	Time averaged rate constant (average rate constant)
$\bar{\tau}$	Time averaged lifetime (average decay time)

## 1 Introduction

Time-resolved luminescence techniques are widely used in various fields for time scales ranging from picoseconds to hours, i.e., spanning 15 orders of magnitude. The data are usually analyzed with a sum of discrete exponentials, but there are many cases where a continuous distribution of decay times best describes the observed phenomena: Luminophores incorporated in micelles, cyclodextrins, rigid solutions, inorganic solids, sol-gel matrices, proteins, vesicles or membranes, biological tissues, luminophores adsorbed on surfaces, or linked to surfaces, quenching of luminophores in micellar solutions, energy transfer in assemblies of like or unlike fluorophores, etc.



In the most general case, a luminescence decay can be written in the following form:

$$I(t) = \mathcal{L}[H(k)] = \int_0^{\infty} H(k)e^{-kt} dk, \quad (1)$$

with  $I(0) = 1$ . This relation is always valid because  $H(k)$  is the inverse Laplace transform of  $I(t)$ . The function  $H(k)$ , also called the eigenvalue spectrum (of a suitable kinetic matrix), is normalized, as  $I(0) = 1$  implies that  $\int_0^{\infty} H(k)dk=1$ .

In many cases (e.g., in the absence of a rise-time), the function  $H(k)$  is non-negative for all  $k > 0$ , and  $H(k)$  can be understood as a *distribution of rate constants* (strictly, a *probability density function*, PDF). This is the situation addressed in this work.

Recovery of the distribution  $H(k)$  from experimental data is very difficult because this is an ill-conditioned problem [1–3]. In other words, a small change in  $I(t)$  can cause an arbitrarily large change in  $H(k)$ . The quality of the experimental data is of course of major importance. Depending on the level of precision, a decay can be fitted with a sum of two or three exponentials with satisfactory chi-squared values and weighted residuals in spite of the existence of an underlying distribution.

$H(k)$  can in principle be recovered from the experimental luminescence decay by three approaches: (i) Data analysis with a theoretical model for  $H(k)$  that may be supported by Monte Carlo simulations; (ii) Data analysis by methods that do not require an a priori form for the PDF of rate constants; (iii) Data analysis with a definite mathematical function corresponding to the PDF that contains adjustable parameters. The present work is devoted to the third approach, but it is worth to briefly recall the main features of the other two.

Examples of the first approach can be found in theoretical and experimental investigations of electronic excitation energy hopping (FRET mechanism) in heptachromophoric cyclodextrins, where the eigenvalue spectrum was obtained by Monte Carlo averaging over configurations [4, 5]. A wide range of systems was also considered theoretically in [6]. In favorable situations, the PDF  $H(k)$  can be obtained analytically, and there is no need for Monte Carlo simulations. This is, for instance, the case for donor-acceptor FRET in three-dimensions [7, 8].

In the absence of a physical model, the best way to recover the eigenvalue spectrum appears to be, at first sight, the second approach, i.e., the use of methods without assumption of the distribution shape such as the maximum entropy method or other numerical approaches [9, 10]. However, in these calculations the obtained eigenvalue spectrum can be extremely sensitive to data quality and truncation effects [1–3]. Because of the ill-conditioned nature of the lifetime distribution analysis, instability of the recovered distribution can

be observed from repeated experiments under exactly the same conditions, even when data are of excellent quality [1, 3]. A set of physically plausible results can in principle be obtained after a regularization technique is employed in the data reduction [1–3].

In the third approach, a mathematical function with adjustable parameters that is expected to best describe the distribution is used. The choice is very wide, but some specific empirical functions with a continuous distribution of rate constants enjoy special popularity, such as the stretched-exponential decay function, or decay functions resulting from the Lorentzian and Gaussian PDFs.

In addition to these well-known functions, further generalizations of the exponential decay function deserve attention and will be discussed in detail.

## 2

### Nature and Limitations of the Luminescence Decay Law and of the Distribution of Rate Constants

#### 2.1

##### Luminescence Decay Law

What is named a decay law  $I(t)$  can be, in some circumstances, related to a probability of emission between  $t$  and  $t + dt$ ,  $P(t)$ , which is a more fundamental quantity [11],

$$P(t) = - \frac{dI(t)}{dt} . \quad (2)$$

In this case it is assumed that  $I(t)$  corresponds to an experiment where all photons emitted by the system under study (or a fixed fraction of these) are collected.  $P(t)$  is the probability of emission of the photon between  $t$  and  $t + dt$ , given that it was emitted (hence no quantum yield correction is necessary). With this generality,  $P(t)$  implies an integration over emission wavelengths, and information concerning internal dynamics in the system may be lost.

It follows from Eq. 2 that the probability of emission  $P(t)$  is

$$P(t) = \int_0^{\infty} H(k) k e^{-kt} dk , \quad (3)$$

i.e., it is a weighted distribution of emission probabilities for exponential decays. A rate distribution  $f(k)$  for  $P(t)$  can obviously be defined by

$$f(k) = kH(k) . \quad (4)$$

More frequently, the emission is recorded for a narrow wavelength range, and results from a sum of weighted contributions of several emitting species. The luminescence decay law is then a *technical quantity*, whose normalization at  $t = 0$  is performed for convenience. The decay law can in principle be related to a detailed model describing the luminescence mechanism and respective dynamics, but remains a valuable formal description of the time evolution of the luminescence even in the absence of such a model.

Another important aspect relates to the preparation of the emissive state. It is assumed here that this state is instantaneously generated, e.g., by light absorption (photoluminescence). In fact, a transition to an upper vibrational or electronic excited state is followed by electronic and/or vibrational relaxation, processes that may take up to a few picoseconds. For these short time scales, not considered here, the inclusion of a rise-time in the decay law is clearly essential.

## 2.2

### Distribution of Rate Constants

Turning now our attention to  $H(k)$ , the integration limits in Eq. 1 deserve consideration. It has been argued that a positive cut-off value  $k_{\min}$  must be imposed, in order to avoid a finite number of molecules with a physically unacceptable decay rate equal to zero [12]. The argument is, however, incorrect, as this happens only if  $H(k)$  contains  $\delta(k)$ ; otherwise  $H(k)$  can tend to infinity when  $k \rightarrow 0$ , while still having  $I(t) \rightarrow 0$  when  $t \rightarrow \infty$ , as will be discussed in Sect. 7. It may, nevertheless, be objected that in certain cases the decay rate cannot be lower than a certain radiative decay rate. For well-defined molecular species this is in principle correct, but even in this case the effect of such a cut-off can be statistically and/or experimentally negligible, given a certain time window. Furthermore, a distribution of rate constants  $H(k)$  is in most cases introduced to take into account additional decay processes, and the intrinsic unimolecular decay (that includes the radiative decay) appears as a multiplicative exponential [13].

An upper integration limit  $k_{\max}$  is in general physically justified (there are no infinitely fast relaxation processes), but again it can be statistically irrelevant and mathematically inconvenient: For instance, in a study of fluorescence anisotropy decays in heptachromophoric systems undergoing excitation energy hopping [4, 5] a distribution of rate constants with a hyperbolic decay towards infinity was successfully used, while a maximum rate constant had been identified and computed [5]. Nevertheless this upper limit was located well into the tail of the distribution, whose contribution to the overall decay was negligible.

### 3 General Considerations Regarding Distributions of Rate Constants

#### 3.1 Characteristic Parameters

Let us consider the following phenomenological equation restricted to the first order

$$\frac{dN}{dt} = -w(t)N, \quad (5)$$

where  $N$  is the number of luminophores (in a given volume) after delta excitation, and  $w$  is the rate constant with a possible time dependence. That being the case, it will be called a rate coefficient.

The luminescence intensity is assumed to be proportional to  $N$ , the proportionality constant including the radiative rate constant. The normalized decay law  $I(t)$  is then simply

$$I(t) = \frac{N(t)}{N_0}, \quad (6)$$

$w(t)$  is thus given by

$$w(t) = -\frac{d \ln I(t)}{dt}, \quad (7)$$

and the decay can be written as

$$I(t) = \exp \left( -\int_0^t w(u) du \right). \quad (8)$$

Using Eq. 1, which expresses a luminescence decay with an underlying distribution  $H(k)$ , we find that the time-dependent rate coefficient becomes

$$w(t) = \frac{\int_0^{\infty} kH(k)e^{-kt} dk}{\int_0^{\infty} H(k)e^{-kt} dk}. \quad (9)$$

This time-dependent rate coefficient can in principle exhibit a complex time dependence, but for monotonic decays there are only three important cases: exponential decay, when  $w(t)$  is constant; super-exponential decay, when  $w(t)$  increases with time; and sub-exponential decay, when  $w(t)$  decreases with time.

Several average quantities that can be obtained from the decay law need to be carefully specified at the outset [13]. The most direct one, the average

decay time, is defined by

$$\bar{\tau} = \frac{\int_0^{\infty} tI(t)dt}{\int_0^{\infty} I(t)dt} . \quad (10)$$

Similarly, the time-averaged rate constant is

$$\bar{k} = \frac{\int_0^{\infty} w(t)I(t)dt}{\int_0^{\infty} I(t)dt} = \frac{1}{\int_0^{\infty} I(t)dt} . \quad (11)$$

The convention of using a bar (e.g.,  $\bar{k}$ ) for the time average, and of using brackets (e.g.,  $\langle k \rangle$ ) for the distribution (“ensemble”) average will be followed throughout.

Instead of a distribution of rate constants, a distribution of time constants is also sometimes defined, such that, instead of Eq. 1, the decay is written as

$$I(t) = \int_0^{\infty} f(\tau)e^{-\frac{t}{\tau}}d\tau , \quad (12)$$

the relation between  $f(\tau)$  and  $H(k)$  being

$$f(\tau) = \frac{1}{\tau^2}H\left(\frac{1}{\tau}\right) . \quad (13)$$

An average time constant can now be defined:

$$\langle \tau \rangle = \int_0^{\infty} \tau f(\tau)d\tau = \int_0^{\infty} I(t)dt , \quad (14)$$

hence

$$\langle \tau \rangle = \frac{1}{\bar{k}} = \left\langle \frac{1}{k} \right\rangle . \quad (15)$$

The average time constant  $\langle \tau \rangle$  and the average decay time  $\bar{\tau}$  are in general not identical and are related by

$$\bar{\tau} = \frac{\langle \tau^2 \rangle}{\langle \tau \rangle} . \quad (16)$$

On the other hand, the average rate constant is

$$\langle k \rangle = \int_0^{\infty} kH(k)dk = -I'(0) = w(0) , \quad (17)$$

and therefore

$$\langle k \rangle = \left\langle \frac{1}{\tau} \right\rangle, \quad (18)$$

while

$$\bar{\tau} = \frac{\left\langle \frac{1}{k^2} \right\rangle}{\left\langle \frac{1}{k} \right\rangle}. \quad (19)$$

### 3.2

#### Influence of the Intrinsic Decay

In many cases (e.g., energy transfer), the full decay expression contains as a multiplicative factor the intrinsic exponential decay,

$$I(t) = \exp\left(-\frac{t}{\tau_0}\right) \left( \int_0^{\infty} \exp(-kt) H(k) dk \right). \quad (20)$$

In such a situation, the full rate constant distribution is simply the shifted  $H(k)$  [13],

$$H_t(k) = H(k) \otimes \delta\left(k - \frac{1}{\tau_0}\right) = \begin{cases} 0 & \text{if } k < \frac{1}{\tau_0} \\ H(k - \frac{1}{\tau_0}) & \text{otherwise} \end{cases}, \quad (21)$$

where  $\otimes$  stands for the convolution between two functions.

Also, in this case the condition that the integral of the decay  $\int_0^{\infty} I(t) dt$  must be finite applies to the decay as a whole, but not to the reduced decay where the “natural” decay has been removed. One thus encounters decay laws where the integral diverges ( $\langle \tau \rangle$  is infinite), because they must always be multiplied by the natural decay to give the total decay, and represent in fact only additional decay pathways. The same applies to anisotropy decays,  $r(t)$ , since there is no need for normalization (in the sense of  $\int_0^{\infty} r(t) dt = 1$ ) in this case.

### 3.3

#### The Transform Ladder

The distribution of rate constants  $H(k)$  is not the only relevant transform for the study of luminescence decays. One can in fact consider the following sequence of functions (*transform ladder*), connected by successive Laplace and inverse Laplace transforms [13]:

$$G(s) \underset{\mathcal{L}^{-1}}{\overset{\mathcal{L}}{\rightleftharpoons}} H(k) \underset{\mathcal{L}^{-1}}{\overset{\mathcal{L}}{\rightleftharpoons}} I(t) \underset{\mathcal{L}^{-1}}{\overset{\mathcal{L}}{\rightleftharpoons}} J(\omega).$$

The functions  $H(k)$  and  $I(t)$  have already been discussed. The function  $J(\omega)$ , which occurs in the response to a harmonic excitation, is central in the luminescence technique of phase-modulation [15, 16], and also in dielectric relaxation theory [17], but will not be further developed here.

The function  $G(s)$  was introduced in [4] for the analysis of anisotropy decays with long tails. It is not a density function, because it is not usually normalized ( $\int_0^{\infty} G(s) ds = H(0)$ ) and because it can take negative values, e.g., when  $H(0) = 0$ . In some cases, like that of an exponential decay, it cannot even be defined (it would be the inverse Laplace transform of the delta function). Since  $H(k)$  is normalized, one has when  $G(s)$  exists

$$\int_0^{\infty} \frac{G(s)}{s} ds = 1. \quad (22)$$

Also

$$\langle k \rangle = \int_0^{\infty} \frac{G(s)}{s^2} ds. \quad (23)$$

The maximum in the  $H(k)$  distribution (if it exists) is sometimes easier to obtain numerically from  $G(s)$ ,

$$\frac{dH}{dk} = 0 \Rightarrow \int_0^{\infty} e^{-ks} s G(s) ds = 0. \quad (24)$$

This also shows that in such a case,  $G(s)$  takes necessarily both positive and negative values. The main interest of  $G(s)$  is, nevertheless, that  $I(t)$  can be written as a double Laplace transform [4], formerly called by some authors the Stieltjes transform [18],

$$I(t) = \int_0^{\infty} \frac{G(s)}{t+s} ds, \quad (25)$$

whenever  $G(s)$  exists. This representation of the decay, alternative to Eq. 1, suggests that in some cases the decay is well represented by a few terms of the discretization of Eq. 25, in an analogous way to what happens with Eq. 1 (sum of exponentials), i.e., when instead of Eq. 25 the decay is approximated by

$$I(t) = \sum_i \frac{a_i}{t + \tau_i}. \quad (26)$$

This representation is advantageous whenever the distribution of rate constants is broad and cannot be emulated by a few exponentials, while a few hyperbolae suffice to construct a broad distribution of rate constants [4], as

each hyperbola corresponds by itself to an exponential distribution, and it is, therefore, the distribution  $H(k)$  that is reconstructed with a sum of exponentials,

$$H(k) = \sum_i a_i \exp(-k\tau_i), \quad (27)$$

while  $G(s)$  is approximated by

$$G(s) = \sum_i a_i \delta(s - \tau_i). \quad (28)$$

## 4

### Conditions that a Decay Function must Satisfy in Order to have a Distribution of Rate Constants

#### 4.1

##### Sufficient Condition for $I(t)$

If  $H(k)$  is a PDF, then

$$(-1)^n I^{(n)}(t) > 0 \quad (n = 0, 1, 2, \dots). \quad (29)$$

i.e.,  $I(t)$  is a *completely monotonic function* [18, 19]. This follows directly from Eq. 1, as

$$I^{(n)}(t) = (-1)^n \int_0^{\infty} k^n H(k) e^{-kt} dk; \quad (30)$$

since  $H(k) \geq 0$ , the integral is positive for all  $t$ . The condition that all moments  $\langle k^n \rangle = (-1)^n I^{(n)}(0)$  must be positive is a special case of Eq. 29 for  $t = 0$ .

#### 4.2

##### Necessary Conditions for $w(t)$

The time-dependent rate coefficient, see Eqs. 7 and 8, can be written as [11]

$$w(t) = \frac{\int_0^{\infty} k H(k) e^{-kt} dk}{\int_0^{\infty} H(k) e^{-kt} dk} = \int_0^{\infty} k J(k, t) dk, \quad (31)$$



where

$$J(k, t) = \frac{H(k)e^{-kt}}{\int_0^{\infty} H(k)e^{-kt} dk}, \quad (32)$$

is a “renormalized” distribution of rate constants (valid for all times). This time-dependent PDF will play a central role in the remaining development. Note that Eq. 31 allows the calculation of  $w(t)$  from  $H(k)$ .

One has from Eq. 31 that

$$\frac{d^n w}{dt^n} = \int_0^{\infty} k \frac{\partial^n J(k, t)}{\partial t^n} dk. \quad (33)$$

We now proceed to obtain the form of  $w^{(n)}(t)$  explicitly.

#### 4.2.1

##### First Derivative of $w(t)$

It follows from Eq. 32 that

$$\frac{\partial J(k, t)}{\partial t} = [w(t) - k] J(k, t), \quad (34)$$

hence, using Eqs. 33 and 34

$$\frac{dw}{dt} = \left[ \left( \int_0^{\infty} kJ(k, t) dk \right)^2 - \int_0^{\infty} k^2 J(k, t) dk \right], \quad (35)$$

or

$$\frac{dw}{dt} = M_1(t)^2 - M_2(t) = -C_2(t), \quad (36)$$

where the  $M_i(t)$  are the raw moments of  $J(k, t)$ ,

$$M_i(t) = \int_0^{\infty} k^i J(k, t) dk, \quad (37)$$

and  $C_i(t)$  its cumulants. The first cumulants of a PDF are

$$\begin{aligned} C_1 &= M_1 \\ C_2 &= M_2 - M_1^2 \\ C_3 &= 2M_1^3 - 3M_1M_2 + M_3 \\ C_4 &= -6M_1^4 + 12M_1^2M_2 - 3M_2^2 - 4M_1M_3 + M_4. \end{aligned} \quad (38)$$

From Eq. 36 we see that  $w'(t)$  is the symmetrical of the variance of  $J(k, t)$ , which is a non-negative quantity. It is thus concluded that the decay must be either exponential ( $w'(t) = 0$ ) or sub-exponential ( $w'(t) < 0$ ) for all times, if

$H(k)$  is to be a PDF. This also follows from an examination of Eq. 32, and its effect on Eq. 31, since Eq. 32 implies that in general the function  $J(k, t)$  is progressively “compressed” to the left, as  $t$  increases. If  $H(k) = \delta(k - k_0)$ , no shape change in  $J(k, t)$  occurs,  $w(t)$  is a nonzero constant, and the decay is exponential for all times. If  $H(k)$  is a non-delta distribution, but is equal to zero below some positive value of  $k$ ,  $k_0$ , the “compression” process is effective and ultimately yields a delta function,  $J(k, \infty) = \delta(k - k_0)$ ,  $w(t)$  attains a nonzero constant value, and the decay becomes essentially exponential for sufficiently long times. If  $k_0 = 0$  (with both  $H(0) = 0$  and with  $H(0) > 0$ ), then  $w(t)$  will approach zero for long times, and the decay goes to zero according to a slower-than-exponential function. A more detailed discussion will be presented in Sect. 7.

It is also to be noted that the conditions expressed by Eq. 29 can be rewritten as  $M_n(t) > 0$ , i.e., all moments of  $J(k, t)$  must be positive.

#### 4.2.2

##### Higher Derivatives of $w(t)$

From Eqs. 34 and 37 it follows that

$$\frac{dM_i}{dt} = M_1 M_i - M_{i+1} \quad (i = 2, 3, \dots). \quad (39)$$

Using this identity, one can easily compute the higher derivatives of  $w(t)$ , starting from Eq. 36,

$$\frac{d^2 w}{dt^2} = \frac{d}{dt} (M_1^2 - M_2) = 2M_1^3 - 3M_1 M_2 + M_3 \quad (40)$$

$$\frac{d^3 w}{dt^3} = \frac{d}{dt} (2M_1^3 - 3M_1 M_2 + M_3) = 6M_1^4 - 12M_1^2 M_2 + 4M_1 M_3 - M_4, \quad (41)$$

etc. Comparison with Eq. 38 leads to the compact forms

$$\frac{d^n w}{dt^n} = - \frac{d^{n-1} C_1}{dt^{n-1}} = (-1)^n C_{n+1}(t). \quad (42)$$

Constraints on  $w(t)$  also follow from these equalities. For instance,  $C_3(t)$  should be negative for a so-called negative asymmetric distribution (i.e., a left asymmetric distribution)  $J(k, t)$ , as must happen to any sub-exponential decay for sufficiently long times.

Incidentally, Eq. 42 provides an easy (but sequential) way of obtaining the explicit form of a cumulant of any order.

## 5

### Construction of the Decay from Cumulant and Moment Expansions

Equation 42 implies that a Maclaurin expansion of  $w(t)$  is

$$w(t) = C_1(0) - C_2(0)t + C_3(0)\frac{t^2}{2!} - \dots, \quad (43)$$

where the cumulants of  $J(k, t)$  at time zero are also the cumulants of  $H(k)$ . Insertion of this equation into Eq. 8 gives

$$I(t) = \exp \left[ -C_1(0)t + C_2(0)\frac{t^2}{2!} - C_3(0)\frac{t^3}{3!} + \dots \right], \quad (44)$$

that allows one to reconstruct the decay  $I(t)$  from the cumulants of  $H(k)$ . An analogous equation is used for the analysis of dynamic light-scattering data, in order to recover the distribution of particle sizes from the autocorrelation function [20, 21]. A cumulant analysis (with three terms) of experimental decays was carried out by Fritz et al. [22].

The interesting aspect is that with Eq. 42 we can generalize Eq. 44, by using a Taylor series expansion around any time  $t_0$

$$I(t) = \exp \left[ -C_1(t_0)(t - t_0) + C_2(t_0)\frac{(t - t_0)^2}{2!} - C_3(t_0)\frac{(t - t_0)^3}{3!} + \dots \right], \quad (45)$$

where the cumulants now refer to  $J(k, t)$ .

Similarly, the moment expansion

$$I(t) = 1 - M_1(0)t + M_2(0)\frac{t^2}{2!} - M_3(0)\frac{t^3}{3!} + \dots, \quad (46)$$

can be generalized to give

$$I(t) = I(t_0) \left[ 1 - M_1(t_0)(t - t_0) + M_2(t_0)\frac{(t - t_0)^2}{2!} - M_3(t_0)\frac{(t - t_0)^3}{3!} + \dots \right]. \quad (47)$$

## 6

### Calculation of $H(k)$ from the Cumulants

The probability density function  $H(k)$  can be formally written in terms of the respective cumulants, by means of the analytical inversion formula for Laplace transforms [23, 24]

$$H(k) = \frac{2}{\pi} \int_0^{\infty} \text{Re}[I(i\omega)] \cos(k\omega) d\omega. \quad (48)$$

Using Eq. 44, we see that Eq. 48 becomes

$$H(k) = \frac{2}{\pi} \int_0^{\infty} e^{-\frac{\omega^2}{2!}C_2 + \frac{\omega^4}{4!}C_4 - \dots} \cos\left(C_1\omega - C_3\frac{\omega^3}{3!} + \dots\right) \cos(k\omega)d\omega. \quad (49)$$

Equation 49 allows – at least formally – the calculation of  $H(k)$  from  $w(t)$ . There are in fact two problems with its practical use: (i) With the exception of the delta and Gaussian distributions, all PDFs have an infinite number of nonzero cumulants (Marcinkiewicz theorem [25]). (ii) The cumulant series that appear in Eq. 49 usually have a finite radius of convergence [24].

We now compute the cumulants for the stretched exponential [13] and compressed hyperbola [14] decay laws. In the first case, we consider only a modified form [13],

$$I(t) = \exp\left[1 - \left(1 + \frac{t}{\tau_0}\right)^\beta\right]. \quad (50)$$

The respective cumulants are obtained from a Maclaurin expansion of  $\ln I(t)$ ,

$$\begin{aligned} \ln I(t) &= 1 - \left(1 + \frac{t}{\tau_0}\right)^\beta \\ &= -\beta \left(\frac{t}{\tau_0}\right) - \frac{1}{2!}\beta(\beta-1) \left(\frac{t}{\tau_0}\right)^2 - \frac{1}{3!}\beta(\beta-1)(\beta-2) \left(\frac{t}{\tau_0}\right)^3 - \dots, \end{aligned} \quad (51)$$

hence

$$C_n(0) = \frac{(-1)^{n+1}}{\tau_0^n} \beta(\beta-1)\dots(\beta-n+1). \quad (52)$$

For the compressed hyperbola decay law,

$$\begin{aligned} \ln I(t) &= \frac{1}{\beta-1} \ln\left[1 + (1-\beta) \left(\frac{t}{\tau_0}\right)\right] = \\ &= \frac{1}{\beta-1} \left\{ (1-\beta) \left(\frac{t}{\tau_0}\right) - \frac{1}{2} \left[(1-\beta) \left(\frac{t}{\tau_0}\right)\right]^2 + \frac{1}{3} \left[(1-\beta) \left(\frac{t}{\tau_0}\right)\right]^3 - \dots \right\} \end{aligned} \quad (53)$$

hence

$$C_n(0) = \frac{(n-1)!}{\tau_0^n} (1-\beta)^{n-1}. \quad (54)$$

In both cases, the cumulants are always positive and increase indefinitely with  $n$ , after eventually passing through a minimum.

Consider the truncated Gaussian (i.e., for  $k \geq 0$  only) PDF [24]:

$$H(k) = \sqrt{\frac{2}{\pi\sigma^2}} \frac{\exp\left[-\frac{1}{2}\left(\frac{k-\mu}{\sigma}\right)^2\right]}{1 + \operatorname{erf}\left(\frac{\mu}{\sqrt{2}\sigma}\right)}; \quad (55)$$

It has the following associated decay law,

$$I(t) = \frac{\operatorname{erfc}\left(\frac{\sigma^2 t - \mu}{\sqrt{2}\sigma}\right)}{\operatorname{erfc}\left(-\frac{\mu}{\sqrt{2}\sigma}\right)} \exp\left(-\mu t + \frac{1}{2}\sigma^2 t^2\right), \quad (56)$$

and has an infinite number of cumulants. Its first cumulant (the mean) is

$$\langle k \rangle = \mu + \sqrt{\frac{2}{\pi}} \sigma \frac{e^{-\frac{1}{2}\left(\frac{\mu}{\sigma}\right)^2}}{\operatorname{erfc}\left(-\frac{\mu}{\sqrt{2}\sigma}\right)}. \quad (57)$$

For  $t \ll \mu/\sigma^2$ ,  $I(t)$  coincides with that of a normal distribution, and the first two cumulants of this PDF suffice to describe its behavior,

$$I(t) \simeq \exp\left(-\mu t + \frac{1}{2}\sigma^2 t^2\right). \quad (58)$$

This equation has been used for the analysis of dynamic light-scattering data, in order to recover the distribution of particle sizes from the autocorrelation function [20, 21], and applies to some luminescence decays for not too long times, see Sect. 8. The full Gaussian PDF (or a mixture of Gaussian PDFs) [26–28] and a Gaussian PDF truncated [12] at  $k_0 > 0$  have been used to describe fluorescence decays. The truncated Gaussian reduces to the full Gaussian distribution for large  $\mu/\sigma$  ratios.

Up to now, it was implicitly assumed that all moments and cumulants were finite. For some PDFs, however, not all moments and cumulants are finite. For the Lévy PDFs, for instance, only  $M_1$  can be (but is not always) finite. This is precisely the case of the (unmodified) stretched exponential decay. The form of  $J(k, t)$ , Eq. 32, ensures that, even then, all moments will be finite for  $t > 0$ . The singularity is therefore limited to  $t = 0$ . This is one of the reasons why the expansions Eqs. 45 and 47 are of interest.

## 7

### Decay Function Asymptotics

We will obtain [11] relatively general equations relating the asymptotic behavior of the decay law  $I(t)$  (i.e., for large  $t$ ) to that of the PDF  $H(k)$  for small  $k$ . From Eq. 1, it is indeed obvious that the behavior of  $H(k)$  for small  $k$  will define the shape of the decay  $I(t)$  for long times.

It is convenient to consider separately the cases where the PDF of rate constants is nonzero at  $k = 0$ , or rises from zero immediately afterwards, from the case where  $H(k) > 0$  only for  $k > k_0$ , with  $k_0$  positive. The special case of partial relaxation will also be treated in this section.

Consideration of the asymptotic behavior of a decay function is important, not only because it defines the long time form, that may or may not be experimentally accessible, but also because  $\int_0^{\infty} I(t)dt$  is often computed from the decay law in order to obtain a quantity proportional to the steady-state intensity. This calculation may be meaningless if the major contribution to the above integral corresponds to a time window not experimentally observed, or if the integral diverges.

## 7.1

### $H(0^+) > 0$

#### 7.1.1

##### $H(k)$ Admits a Maclaurin Series Expansion

In this case,

$$H(k) = H(0) + kH'(0) + \frac{k^2}{2!}H''(0) + \dots, \quad (59)$$

and substitution in Eq. 1 gives immediately

$$I(t) = \frac{H(0)}{t} + \frac{H'(0)}{t^2} + \frac{H''(0)}{t^3} + \dots. \quad (60)$$

The effective power dependence with  $t$  for long times (asymptotic behavior) will be determined by the order of the first nonzero term of the Maclaurin series.

#### 7.1.2

##### $H(k)$ is not Analytic at the Origin

A (so-called Tauberian) theorem in probability theory [19] that covers a broad range of cases (including the previous one), is the following, reformulated for our purposes:

If the cumulative distribution function  $U(k)$ ,

$$U(k) = \int_0^k H(u)du, \quad (61)$$

has the asymptotic form

$$U(k) \sim k^p L(k), \quad (62)$$

as  $k \rightarrow 0$ , with  $p > 0$ , where  $L(k)$  is a *slowly varying function*, i.e., a function that obeys

$$\frac{L(\alpha k)}{L(k)} \rightarrow 1, \quad (63)$$

also when  $k \rightarrow 0$ , for any constant  $\alpha$ , then the decay law will have the following asymptotic behavior

$$I(t) \sim U(1/t), \quad (64)$$

when  $t \rightarrow \infty$ .

In most situations of physical interest, the last equation can be replaced by

$$I(t) \sim \frac{1}{t} H\left(\frac{1}{t}\right). \quad (65)$$

Note that PDFs that near the origin vary according to negative power laws ( $0 < p < 1$ ) and therefore rise to infinity, are included.

On the other hand,  $\int_0^{\infty} I(t) dt$  diverges for  $p \leq 1$ .

## 7.2

### $H(0^+) = 0$

In this case,  $H(k) > 0$  only for  $k > k_0$ , with  $k_0$  positive, and the above results are not valid without modification. But they can be applied by shifting the distribution  $H(k)$  to the left, placing it next to the origin, and then moving it back to the right by  $k_0$ , in order to restore the original position. The distribution next to the origin, to which the above results apply, is

$$H_0(k) = H(k + k_0), \quad (66)$$

and the decay law becomes, after restoring the initial position,

$$I(t) = I_0(t) \exp(-k_0 t), \quad (67)$$

where  $I_0(t)$  corresponds to the shifted distribution  $H_0(k)$ . The asymptotic behavior will be that of  $H_0(k)$  times an exponential, hence dominated by the exponential. Note that in this case  $\int_0^{\infty} I(t) dt$  is not divergent even if  $I_0(t)$  has an asymptotic dependence with  $p \leq 1$ , owing to the exponential damping factor.

### 7.3

#### **$H(k)$ Contains $\delta(k)$**

When there is a fraction  $\alpha$  of luminophores not decaying by the mechanism under consideration,  $H(k)$  is given by

$$H(k) = \alpha \delta(k) + (1 - \alpha)H^+(k), \quad (68)$$

where  $H^+(k)$  is the density function of positive rate constants. Insertion of this PDF in the decay law expression gives

$$I(t) = \alpha + (1 - \alpha)I^+(t), \quad (69)$$

where  $I^+(t)$  is the decay law corresponding to  $H^+(k)$ . In this case, the asymptotic form is a numerical constant, and  $\int_0^\infty I(t)dt$  diverges, unless (as must happen in physically acceptable cases) the overall decay contains a multiplicative exponential.

### 7.4

#### **Cases Left Out**

There are some cases that are not covered by the results of the Tauberian theorem presented, namely PDFs  $H(k)$  of rapid variation near the origin, like  $\exp(-1/k)$ . This is the case of the stretched exponential PDF. For  $\beta = 1/2$ , for instance [13],

$$H_{1/2}(k) = \frac{1}{2\sqrt{\pi}k^{\frac{3}{2}}} \exp\left(-\frac{1}{4k}\right). \quad (70)$$

Only for very small  $\beta$ , when [13, 29]

$$H(k) \simeq \frac{\beta}{k^{1+\beta}} \exp\left(-\frac{1}{k^\beta}\right) \simeq \frac{\beta}{e k} \exp\left[-\frac{1}{2}(\beta \ln k)^2\right], \quad (71)$$

does the application of the Tauberian theorem yield the correct result,  $I(t) = \exp(-t^\beta)$ .

The several asymptotic cases discussed are summarized in Table 1, and corresponding specific examples are given in Table 2.

## 8

### **Selected Decay Functions**

As discussed above, PDFs that reduce to the delta function for some value(s) of the parameter(s), such as those of the stretched-exponential and compressed hyperbola decay functions, and the Lorentzian and the Gaussian PDFs, are of special interest and/or of common use. All these functions may



**Table 1** Relation between the type of luminescence decay function, the luminescence decay asymptotic behavior, and the PDF of rate constants

				$H(k)$	$w(t)$	$I(t)$
Exponential				$\delta(k - k_0)$	$k_0$	$e^{-k_0 t}$
Sub-exponential	Asymptotically exponential			$0 \ (k < k_0)$	$\sim k_0$	$\sim e^{-k_0 t}$
	Slower-than-exponential	Maclaurin or Puiseux valid	$H(0) = 0$	$a k^p \ (p > 0, \text{small } k)$	$\sim t^{-1}$	$\sim t^{-(1+p)}$
			$H(0) > 0$	$H_0 + \dots \ (H_0 > 0)$	$\sim t^{-1}$	$\sim t^{-1}$
		Maclaurin or Puiseux invalid	$H(0) = 0$	<i>One-sided Lévy</i>	$\sim t^{-(1-\beta)}$	$e^{-a t^\beta}$
	$H(0) = \infty$		$a k^{-p} \ (1 > p > 0, \text{small } k)$	$\sim t^{-1}$	$\sim t^{-(1-p)}$	

**Table 2** Examples of PDF of rate constants and respective luminescence decay functions

				$H(k)$	$I(t)$
Exponential				Delta	Exponential
Sub-exponential	Asymptotically exponential			Rectangular	$e^{-k_0 t} (1 - e^{-\Delta k t}) / (\Delta k t)$
	Slower-than-exponential	Maclaurin or Puiseux valid	$H(0) = 0$	Gamma	Becquerel
			$H(0) > 0$	Exponential	Hyperbolic
		Maclaurin or Puiseux invalid	$H(0) = 0$	One-sided Lévy	Stretched exponential
	$H(0) = \infty$		Weibull ( $\alpha < 1$ )	Weibull	

be considered as generalizations of the exponential function. Other interesting generalizations of the exponential function will be discussed below, see also Table 2.

There are at least two possible ways to generalize the exponential function. One is to select  $H(k)$  PDFs that are known to reduce to the delta function  $\delta(k - k_0)$  for some value(s) of the parameter(s). This is obviously the case for the Lorentzian and the Gaussian functions. Such a procedure automatically ensures that  $H(k)$  will be a PDF. The other way is to work with the exponential decay law itself, changing it to a functional form that still reduces to the exponential for some value(s) of the parameter(s). This is the case of the stretched exponential function. For the second generalization procedure, one must compute  $H(k)$  to check that it is still a PDF. A slightly different ap-

proach is to take the series expansion of the exponential decay function and to modify it. Distribution functions obtained in this way deserve attention.

## 8.1

### Stretched Exponential (or Kohlrausch) Function

The first use of the stretched exponential function to describe the time evolution of a non-equilibrium quantity is usually credited (with references almost invariably incorrect) to Rudolph Kohlrausch (1809–1858), who in 1854 [13, 30] applied it to the discharge of a capacitor (Leyden jar), after concluding that a simple exponential of time was inadequate [31]. The stretched exponential decay function was used for the first time in luminescence by Werner in 1907 [32], in order to describe the short-time decay of an inorganic phosphor.

The stretched exponential decay function is given by

$$I(t) = \exp \left[ - \left( \frac{t}{\tau_0} \right)^\beta \right], \quad (72)$$

where  $0 < \beta \leq 1$ , and  $\tau_0$  is a parameter with the dimensions of time.

In studies of the relaxation of complex systems, the Kohlrausch function is frequently used as a purely empirical decay law, although there are theoretical arguments to justify its common occurrence. In the field of molecular luminescence, Eq. 72 has firm grounds on several models of luminescence quenching, namely diffusion-controlled contact quenching [33], where  $\beta = 1/2$ , and diffusionless resonance energy transfer by the dipole–dipole mechanism, with  $\beta = 1/6$ ,  $1/3$  and  $1/2$  for one-, two- and three-dimensional systems, respectively [34, 35]. Other rational values of  $\beta$  are obtained for different multipole interactions, e.g.,  $\beta = 3/8$ ,  $3/10$ , for the dipole–quadrupole and quadrupole–quadrupole mechanisms in three-dimensions [36]. In Huber's approximation, energy transport as measured by fluorescence anisotropy shows the same time-dependence as direct energy transfer [6, 37, 38], and is characterized by the same values of  $\beta$ .

RET between donor and acceptor chromophores attached to a polymer chain has been widely used as a tool for studying polymer structure and dynamics. Theory shows [39–45] that the kinetics of donor luminescence quenching and the kinetics of depolarization of luminescence in polymer chains exhibit a Kohlrausch time-dependence, where the parameter  $\beta$  of Eq. 72 depends on the mechanism of RET, the type of chromophore attachment (to the ends of the polymer chain or randomly distributed along the chain), and on the model of polymer chain considered (Gaussian or self-avoiding chain).

The Kohlrausch function is also found to apply to some luminescence decays of disordered [46] and ordered [47] inorganic solids, and of semiconductor nanoclusters [48, 49].

The Kohlrausch decay law is convenient as a fitting function, even in the absence of a model, given that it allows gauging in simple way deviations to the “canonical” single exponential behaviour through the parameter  $\beta$ . Stretched exponentials were used for instance to analyse the fluorescence decay of fluorophores incorporated in a sol–gel matrix [50] and of fluorophores covalently bound to silica surfaces [51] or alumina surfaces [52]. The Kohlrausch decay function was also recently used in the analysis of single-molecule fluorescence [53] and in the fluorescence lifetime imaging of biological tissues [54].

It is striking that a variety of microscopic mechanisms can give rise to stretched exponential relaxation although the origin of this behaviour is not fully understood. In this regard, dynamical models for stretched exponential relaxation developed by several authors [47, 55–58] are conceptually interesting.

A time-dependent rate coefficient  $w(t)$  can be defined for the Kohlrausch decay law, Eq. 72, by using Eq. 7:

$$w(t) = \frac{\beta}{\tau_0} \left( \frac{t}{\tau_0} \right)^{\beta-1}, \quad (73)$$

where  $0 < \beta \leq 1$ . After Williams and Watts [59], the Kohlrausch decay law is often called the “slower-than-exponential” (with respect to an exponential of lifetime  $\tau_0$ ) function. Although sub-exponential, this is however somewhat of a misnomer, as a most characteristic aspect of the function is precisely the existence of two regimes: a faster-than-exponential (with respect to an exponential of lifetime  $\tau_0$ ) initial decay (indeed, the rate constant is infinite for  $t = 0$ ), and a slower-than-exponential decay (with respect to an exponential of lifetime  $\tau_0$ ) for times longer than  $\tau_0$ . These two regimes are very marked for small  $\beta$ , but become indistinct as  $\beta \rightarrow 1$ , see Fig. 1.

The initial part of the Kohlrausch law ( $\beta < 1$ ), resulting from a Lévy distribution of rate constants (see below), with its characteristic long tail, is sometimes “swept under the carpet” by using a  $\tau_0$  smaller than the shortest time of observation, and multiplying the decay law by a factor higher than 1, a procedure that obviously invalidates its correct normalization, but has no other apparent consequences (see however the discussion below).

The slowing down of the decay rate can be shown explicitly by the time-dependent rate coefficient, Eq. 73. As mentioned, this rate coefficient is initially infinite, which is an unphysical result. In the case of diffusion-controlled quenching of fluorescence, this only happens with the Smoluchowski model [60], for which an infinite quenching rate constant at contact is implicitly assumed. The problem no longer exists in the Collins–Kimball model, for instance [33, 60]. In the field of energy transfer in homogeneous

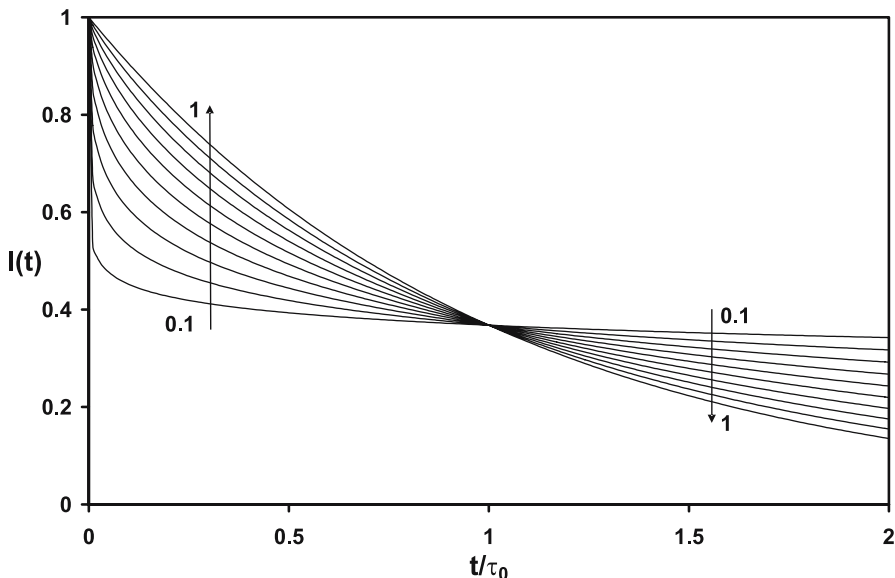


**Fig. 1** The Kohlrausch (stretched exponential) decay function for several values of  $\beta$  (0.1, 0.2, ..., 0.9, 1). The decay is faster than that of an ordinary exponential ( $\beta = 1$ ) for  $t < \tau_0$ , and slower afterwards

media, an initially infinite rate coefficient arises when point particles are assumed [34]. If a distance of closest approach is postulated, then the initial part of the decay becomes exponential, and the decay obeys a stretched-exponential only for longer times [61].

The average rate constant  $\langle k \rangle = w(0)$  is infinite for the Kohlrausch decay law. In general, the time-dependent rate coefficient cannot be infinite; hence this aspect results from the approximate nature of the physical model used, as mentioned for the collisional quenching and energy transfer phenomena.

The necessarily approximate nature of the stretched exponential decay function, owing to its unphysical short-time behavior, was also noted in the field of dielectrics [17, 62].

The average decay time is

$$\bar{\tau} = \tau_0 \frac{\Gamma(2/\beta)}{\Gamma(1/\beta)}, \quad (74)$$

whereas the average time constant is

$$\langle \tau \rangle = \frac{1}{\bar{k}} = \tau_0 \Gamma\left(1 + \frac{1}{\beta}\right). \quad (75)$$

The determination of  $H(k)$  for a given  $I(t)$  amounts to the computation of the respective inverse Laplace transform. The result, first obtained by Pol-

lard [63], is

$$H_{\beta}(k) = \frac{\tau_0}{\pi} \int_0^{\infty} \exp(-k\tau_0 u) \exp[-u^{\beta} \cos(\beta\pi)] \sin[u^{\beta} \sin(\beta\pi)] du, \quad (76)$$

an equivalent integral being

$$H_{\beta}(k) = \frac{\tau_0}{\pi} \int_0^{\infty} \exp\left[-u^{\beta} \cos\left(\frac{\beta\pi}{2}\right)\right] \cos\left[u^{\beta} \sin\left(\frac{\beta\pi}{2}\right) - k\tau_0 u\right] du. \quad (77)$$

For  $\beta = 1$ , one has of course  $H_1(k) = \delta(k - 1/\tau_0)$ . For  $\beta \neq 1$ ,  $H_{\beta}(k)$  can be expressed in terms of elementary functions only for  $\beta = 1/2$  [63],

$$H_{1/2}(k) = \frac{\tau_0}{2\sqrt{\pi} (k\tau_0)^{3/2}} \exp\left(-\frac{1}{4k\tau_0}\right). \quad (78)$$

A form for  $\beta = 1/4$  displaying the asymptotic behavior for large  $k$  was recently obtained [64],

$$H_{1/4}(k) = \frac{\tau_0}{8\pi(k\tau_0)^{5/4}} \int_0^{\infty} u^{-3/4} \exp\left[-\frac{1}{4}\left(\frac{1}{\sqrt{kt_0u}} + u\right)\right] du. \quad (79)$$

The distribution  $H_{\beta}(k)$  is shown in Fig. 2 for several values of  $\beta$ .

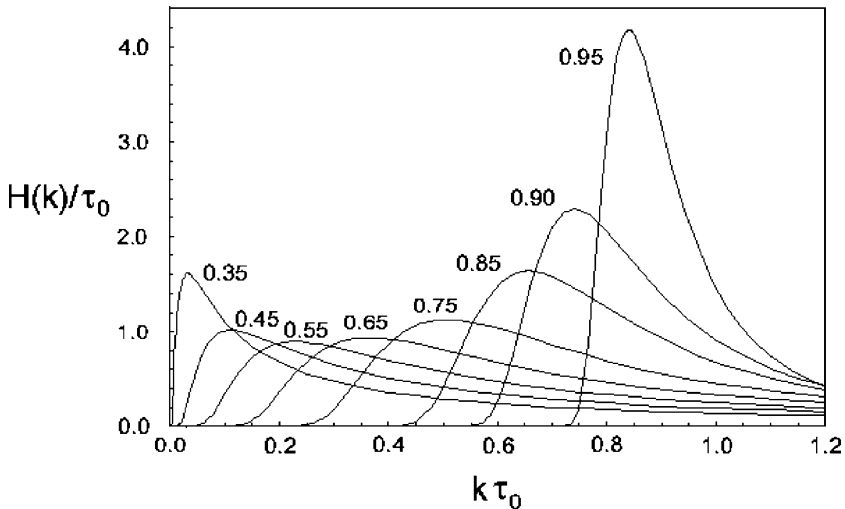


**Fig. 2** Distribution of rate constants (probability density function) for the stretched exponential decay law. The number next to each curve is the respective  $\beta$

In [65], a convergent power series was obtained for  $H_\beta(k)$ ,

$$H_\beta(k) = \frac{\tau_0}{\pi} \sum_{n=1}^{\infty} (-1)^{n+1} \frac{(k\tau_0)^{-(1+n\beta)}}{n!} \Gamma(1+n\beta) \sin(n\beta\pi). \quad (80)$$

It can be seen that the asymptotic form of  $H_\beta(k)$  is

$$H_\beta(k) = \frac{\tau_0}{\pi} \Gamma(1+\beta) \sin(\beta\pi) \frac{1}{(k\tau_0)^{(1+\beta)}}. \quad (81)$$

While the series is convergent for all  $k$ , in practice the terms can increase in magnitude to a tremendous extent and nearly completely cancel each other to yield a small number. Therefore, the asymptotic form is useful only for very large values of  $k$ . Lindsey and Patterson [66] used Eqs. 76 and 80 for the first time in the description of relaxation phenomena.

As mentioned, the stretched exponential decay function has an undesirable short-time behavior (infinite initial rate, faster-than-exponential decay for short times). For this reason, a modified form was proposed [13]

$$I(t) = \exp \left[ \alpha^\beta - \left( \alpha + \frac{t}{\tau_0} \right)^\beta \right], \quad (82)$$

where  $\alpha$  is a nonnegative dimensionless parameter.

## 8.2

### Compressed Hyperbola (or Becquerel) Function

The first quantitative studies of the time evolution of luminescence (following flash excitation), were carried out by Edmond Becquerel (1820–1891) and published in 1861. The functions used by this author for the description of the experimental decays already included an exponential of time, and also a sum of two such exponentials [14, 67]. Becquerel also noticed that for some of his experimental systems (inorganic solids), an empirical decay function of the form

$$I(t) = \frac{1}{(1+at)^2}, \quad (83)$$

gave better fits than a sum of two exponentials. Later on, he proposed a more general equation in the form  $I^m(t+a) = b$  that can be rewritten as

$$I(t) = \frac{1}{(1+at)^p}, \quad (84)$$

with  $p$  taking values between 1 and 2 [67].

This function that decays faster than an hyperbola (for which  $p = 1$ ) can be called *compressed* or *squeezed hyperbola*. But owing to Becquerel pioneering

studies, and reviving a now almost forgotten denomination [68], we shall also call this function the Becquerel decay law.

Using Eq. 7, the time-dependent rate coefficient is

$$w(t) = \frac{1}{\tau_0 + (1 - \beta)t}, \quad (85)$$

where  $0 \leq \beta \leq 1$ . Use of Eq. 8 gives the Becquerel decay function,

$$I(t) = \frac{1}{\left[1 + (1 - \beta) \frac{t}{\tau_0}\right]^{\frac{1}{1-\beta}}}. \quad (86)$$

It should be noted that values of  $\beta$  outside the range defined above yield unphysical results: for  $\beta \leq 0$  the integrated intensity (total intensity) diverges, and for  $\beta > 1$  the intensity becomes zero at a finite value of  $t$ .

The average rate constant takes the following value for the Becquerel function

$$\langle k \rangle = \frac{1}{\tau_0}. \quad (87)$$

Hence the decay can be rewritten as

$$I(t) = \frac{1}{\left[1 + (1 - \beta) \langle k \rangle t\right]^{\frac{1}{1-\beta}}}. \quad (88)$$

For the Becquerel function, we have a time-averaged rate constant

$$\bar{k} = \frac{\beta}{\tau_0}. \quad (89)$$

The average time constant for the Becquerel function is

$$\langle \tau \rangle = \frac{\tau_0}{\beta}. \quad (90)$$

The average decay time is, in the present case, given by

$$\bar{\tau} = \frac{\tau_0}{2\beta - 1}, \quad (91)$$

for  $\beta > 1/2$ . For  $\beta < 1/2$  the average decay time is infinite.

For  $\beta$  close to 1, the decay approaches a single exponential decay with lifetime  $\tau_0$ , while for small  $\beta$  the decay slows down dramatically, see Fig. 3.

From Eq. 88 it follows that for small  $\beta$  the decay becomes hyperbolic

$$I(t) = \frac{1}{1 + \langle k \rangle t}, \quad (92)$$

a result exact for  $\beta = 0$ , and is therefore controlled by a single parameter  $\langle k \rangle$ , while for other values of  $\beta$  there are two independent parameters,  $\beta$  and  $\tau_0$ , or  $\beta$  and  $\langle k \rangle$ , as is always the case for the Kohlrausch function.

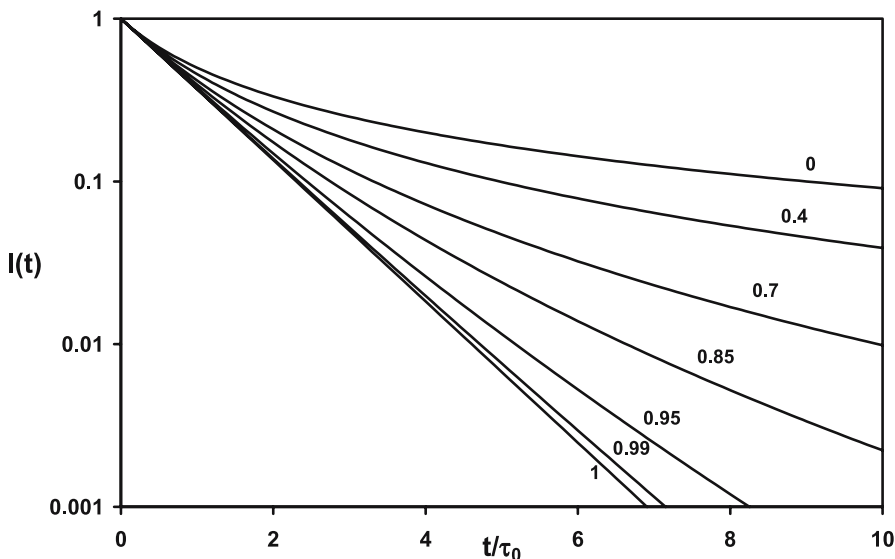


**Fig. 3** Becquerel decay function. Numbers next to each curve are the respective values of parameter  $\beta$ . The decay is hyperbolic for  $\beta = 0$  and exponential for  $\beta = 1$

The Becquerel decay law has also the advantage of possessing a simple inverse Laplace transform,

$$H(k) = \frac{\left(\frac{1}{1-\beta} \langle k \rangle\right)^{\frac{\beta}{1-\beta}} \exp\left(-\frac{1}{1-\beta} \frac{k}{\langle k \rangle}\right)}{(1-\beta) \langle k \rangle \Gamma\left(\frac{1}{1-\beta}\right)}, \tag{93}$$

which is a Gamma distribution, and whose mean and standard deviation are  $\langle k \rangle$  and  $\langle k \rangle \sqrt{1-\beta}$ , respectively. This distribution is shown in Fig. 4 for several values of  $\beta$ .

For  $\beta = 0$ , the distribution of rate constants is exponential. On the other hand, for  $\beta$  sufficiently close to 1 ( $\beta > 0.95$ , say), the rate constant distribution becomes a relatively narrow normal (Gaussian) distribution with mean and standard deviation given by the previous expressions. When  $\beta \rightarrow 1$ , the standard deviation goes to zero, and the distribution becomes  $\delta\left(k - \frac{1}{\tau_0}\right)$ , as could be expected.

The Becquerel decay is initially exponential,

$$I(t) = \exp(-\langle k \rangle t), \tag{94}$$

and the initial decay rate is always finite. This short-time behavior is more realistic than that displayed by the primitive Kohlrausch function, but is shared by the modified Kohlrausch function proposed before [13].



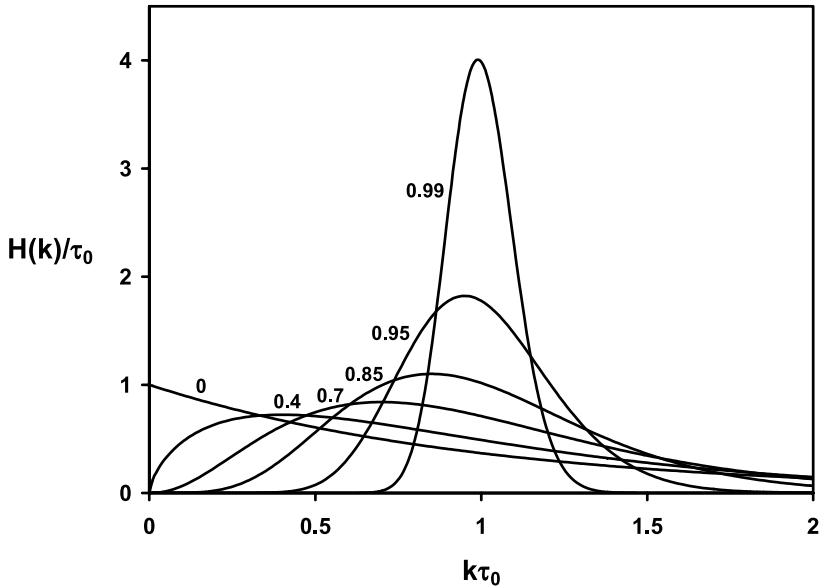


**Fig. 4** Distribution of rate constants (probability density function) for the Becquerel decay law. The *number* next to each curve is the respective  $\beta$

For sufficiently long times, the Becquerel decay becomes a power law,

$$I(t) = [(1 - \beta) \langle k \rangle t]^{\frac{1}{\beta-1}}, \quad (95)$$

and the decay is the slower, the smaller the  $\beta$  parameter, see Fig. 3.

The slowing down of the decay rate can also be seen in the time-dependent rate coefficient, Eq. 85. For  $\beta \neq 1$  it always decays with  $t^{-1}$ , while for the Kohlrausch function the decay of the rate coefficient is slower, with  $t^{\beta-1}$  [13], and only approaches that of the Becquerel function for very small  $\beta$ .

The Becquerel function, as defined here, is a quite flexible decay function, although its less direct relation to the exponential decay has limited its use up to now mainly to the luminescence of phosphors [14]. Nevertheless, there are some recent applications in fluorescence. For instance, Włodarczyk and Kierdaszuk [69] showed that it provides good fits for fluorescence decays that slightly depart from the exponential behavior, implying a relatively narrow distribution of decay times around a mean value.

As discussed in Sect. 3, two possible approaches to fit luminescence decay laws with a discrete sum of terms are the use of exponentials and hyperbolae as base functions. Since the Becquerel decay law interpolates between these two extreme cases, it seems reasonable to assume that a sum of a few Becquerel functions, appropriately weighted, will be a powerful fitting function

for complex decays [14],

$$I(t) = \sum_i \alpha_i (1 + \gamma_i t)^{\frac{1}{\beta_i-1}}, \quad (96)$$

with

$$\sum_i \alpha_i = 1 \quad (97)$$

and

$$\gamma_i = (1 - \beta_i) \langle k_i \rangle = \frac{1 - \beta_i}{\tau_i}. \quad (98)$$

The corresponding distribution of rate constants will be a weighted sum of Gamma density functions.

The average lifetime is

$$\langle \tau \rangle = \sum_i \alpha_i \langle \tau_i \rangle = \sum_i \frac{\alpha_i \tau_i}{\beta_i}, \quad (99)$$

while the average decay time is, for  $\beta_i > 1/2$ ,

$$\bar{\tau} = \frac{\langle \tau^2 \rangle}{\langle \tau \rangle} = \frac{\sum_i \alpha_i \langle \tau_i^2 \rangle}{\sum_i \alpha_i \langle \tau_i \rangle} = \frac{\sum_i \alpha_i \langle \tau_i \rangle \bar{\tau}_i}{\sum_i \alpha_i \langle \tau_i \rangle} = \frac{\sum_i \frac{\alpha_i \tau_i^2}{\beta_i(2\beta_i-1)}}{\sum_i \frac{\alpha_i \tau_i}{\beta_i}}, \quad (100)$$

and the average rate constant and the average rate coefficient are

$$\langle k \rangle = \sum_i \alpha_i \langle k_i \rangle = \sum_i \frac{\alpha_i \beta_i}{\tau_i} \quad (101)$$

$$\bar{k} = \frac{1}{\langle \tau \rangle} = \frac{1}{\sum_i \frac{\alpha_i \tau_i}{\beta_i}}. \quad (102)$$

### 8.3

#### Mittag–Leffler and Heaviside Functions

We now turn our attention to the series expansion of the exponential decay function,

$$e^{-at} = \sum_{n=0}^{\infty} \frac{(-at)^n}{n!} = \sum_{n=0}^{\infty} \frac{(-at)^n}{\Gamma(n+1)}, \quad (103)$$

with the aim of generalizing it. Two simple generalizations are Mittag-Leffler's exponential function, or Mittag-Leffler function  $E_\alpha(x)$  [11, 70–72],

$$E_\alpha(-at) = \sum_{n=0}^{\infty} \frac{(-at)^n}{\Gamma(\alpha n + 1)}, \quad (104)$$

and Heaviside's exponential function,  $e_\alpha(x)$  [72],

$$e_\alpha(-at) = \sum_{n=0}^{\infty} \frac{(-at)^n}{\Gamma(n+1+\alpha)}, \tag{105}$$

where  $0 < \alpha \leq 1$  in the first case, and  $\alpha \geq 0$  in the second case. For our purposes, it is convenient to define a *normalized* Heaviside's exponential function  $\varepsilon_\alpha(x)$ , so that  $\varepsilon_\alpha(0) = 1$ ,

$$\varepsilon_\alpha(x) = \Gamma(1+\alpha) e_\alpha(x) = \alpha \Gamma(\alpha) e_\alpha(x). \tag{106}$$

The  $H(k)$  for these two decay laws are known, and are indeed PDFs. They are displayed in Figs. 5 and 6. The Mittag-Leffler PDF is (with  $a = 1$ ) [64, 71, 73]

$$H_\alpha(k) = \alpha^{-1} k^{-(1+\alpha^{-1})} L_\alpha(k^{-\alpha^{-1}}), \tag{107}$$

where  $L_\alpha(x)$  is the one-sided Lévy PDF given by Eqs. 76 and 77.

For Heaviside's normalized exponential, one has [72] (for  $a = 1$ ) the following PDF,

$$H_\alpha(k) = \begin{cases} \alpha(1-k)^{\alpha-1} & \text{if } k \leq 1 \\ 0 & \text{if } k > 1 \end{cases} \tag{108}$$

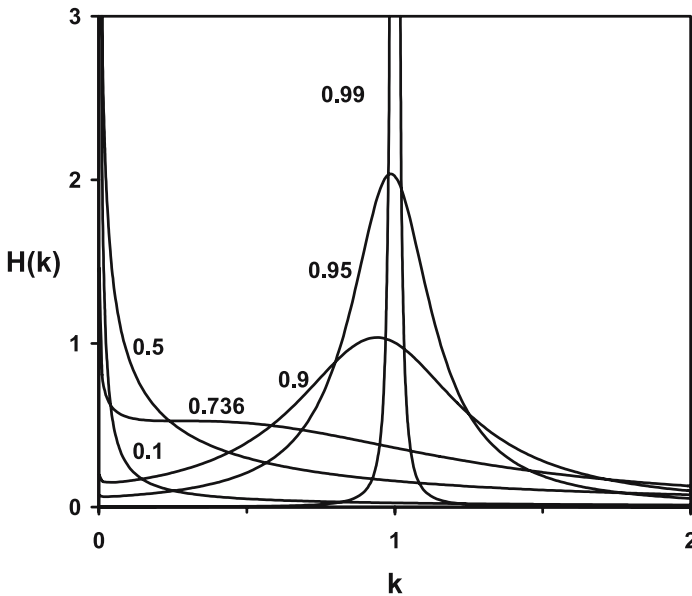


**Fig. 5** Distribution of rate constants (probability density function) for the Mittag-Leffler decay law. The *number* next to each curve is the respective  $\alpha$

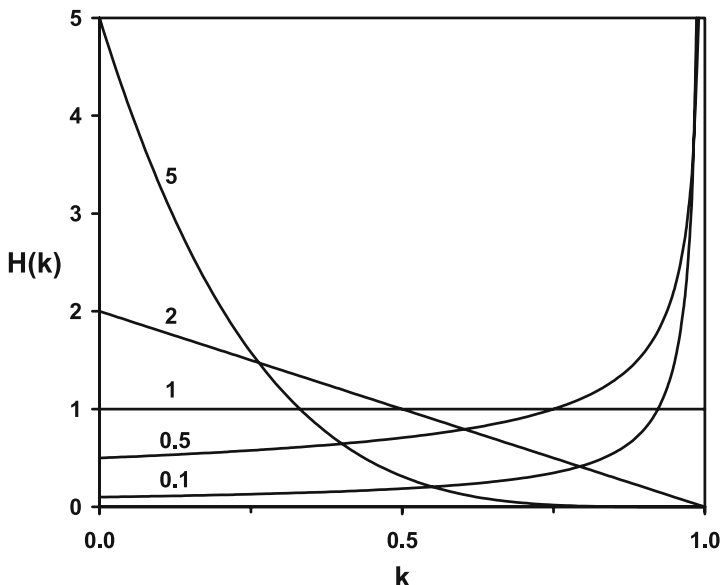


**Fig. 6** Distribution of rate constants (probability density function) for the Heaviside decay law. The *number* next to each curve is the respective  $\alpha$

It can be shown that both generalized exponentials asymptotically decay with  $t^{-1}$ . A simple modification of Heaviside’s normalized exponential PDF is

$$H_{\alpha}(k) = \begin{cases} (\beta + 1) \alpha k^{\beta} (1 - k^{\beta+1})^{\alpha-1} & \text{if } k \leq 1 \\ 0 & \text{if } k > 1 \end{cases} \quad (\beta \geq 0) \quad (109)$$

This function, displayed in Figs. 7 and 8 for two values of parameter  $\beta$ , has  $H_{\alpha}(0) = 0$  for  $\beta > 0$ , and asymptotically decays with  $t^{-(1+\beta)}$ . The Heaviside PDF is an interesting example of a function that approaches the delta function from one side only, and in an unusual way, see Eq. 108 and Fig. 6.

**8.4 Weibull Probability Density Function**

Another interesting generalization of the exponential decay, that appears not to have been used thus far in the analysis of fluorescence decays results from the Weibull PDF [11, 19, 74]

$$H_{\alpha,\beta}(k) = \frac{\alpha}{\beta} \left(\frac{k}{\beta}\right)^{\alpha-1} \exp\left[-\left(\frac{k}{\beta}\right)^{\alpha}\right], \quad (110)$$

where  $\alpha > 0$ . This PDF is displayed in Fig. 9 for a reduced variable  $k/\beta$ . The mean of  $H_{\alpha}(k)$  is  $\beta\Gamma(1 + \alpha^{-1})$ . For  $\alpha = 1$  the distribution is exponential, for

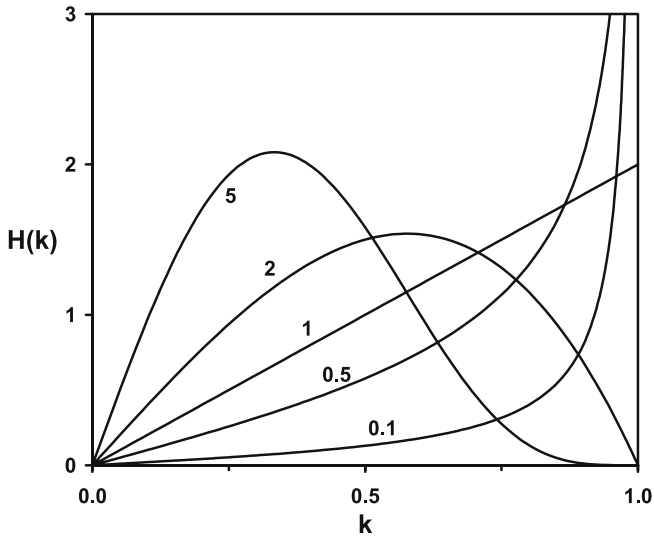


**Fig. 7** Distribution of rate constants (probability density function) for the modified Heaviside decay law, with  $\beta = 1$ . The number next to each curve is the respective  $\alpha$

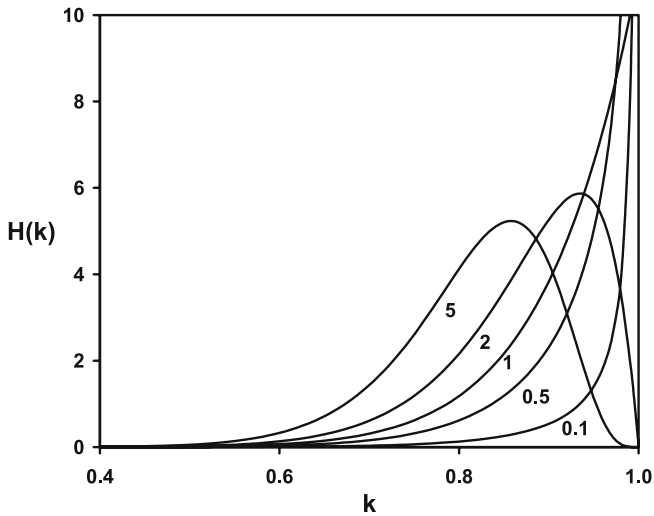


**Fig. 8** Distribution of rate constants (probability density function) for the modified Heaviside decay law, with  $\beta = 10$ . The number next to each curve is the respective  $\alpha$

$\alpha = 2$  it reduces to the Rayleigh distribution, and for  $\alpha \rightarrow \infty$  the delta distribution  $\delta(k - 1)$  is recovered. The asymptotic behavior of the Weibull decay law illustrates several of the cases discussed in Sect. 7 (see Tables 1 and 2). The asymptotic decay is  $I(t) \sim t^{-\alpha}$ , and  $H_\alpha(k) \sim k^{\alpha-1}$ . For  $\alpha < 1$ ,  $H_\alpha(0)$  is in-

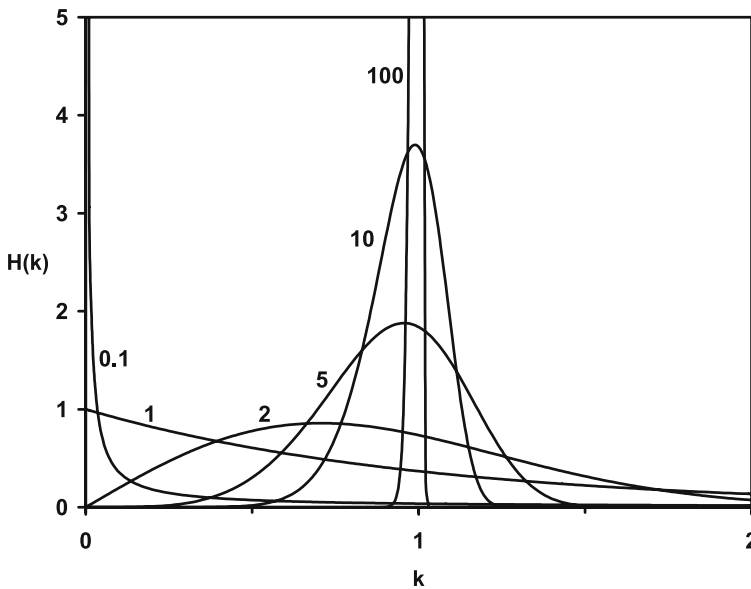


**Fig. 9** Distribution of rate constants (probability density function) for the Weibull decay law. The *number* next to each curve is the respective  $\alpha$

finite. For  $\alpha = 1$ , the decay is hyperbolic and  $H_\alpha(0) > 0$ . In both cases  $\int_0^\infty I(t)dt$  diverges. Finally, for  $\alpha > 1$ ,  $H_\alpha(0) = 0$ , and  $\int_0^\infty I(t)dt$  is finite.

**8.5 Truncated Gaussian Probability Density Function]**

This PDF was already introduced in Sect. 6. Writing  $\tau_0 = 1/\mu$  and the coefficient of variation  $\alpha = \sigma/\mu = \sigma\tau_0$ , Eq. 58 becomes

$$I(t) = \exp \left[ -\frac{t}{\tau_0} + \frac{1}{2}\alpha^2 \left( \frac{t}{\tau_0} \right)^2 \right]. \tag{111}$$

This simple decay function, not widely known, is adequate for  $t/\tau_0 < 10$  (i.e., the full time range of interest) if  $\alpha < 0.25$ . The asymptotic form of the truncated Gaussian is, on the other hand,

$$I(t) = \sqrt{\frac{2}{\pi}} \frac{\exp \left( -\frac{1}{2\alpha^2} \right) \tau_0}{\alpha \operatorname{erfc} \left( -\frac{1}{\sqrt{2}\alpha} \right) t} , \tag{112}$$

and goes as  $t^{-1}$ , as could be expected from the results of Sect. 7. Note that this asymptotic behavior switches to an exponential one if the Gaussian is truncated above zero, however slightly [11].

## 9

### Concluding Remarks

From an analysis of the general form of the decay law, it was concluded that the decay must be either exponential or sub-exponential for all times, if  $H(k)$  is to be a probability density function. Take for instance the hypothetical “compressed exponential” decay law  $I(t) = \exp \left[ - \left( \frac{t}{\tau_0} \right)^2 \right]$ . This decay law is super-exponential, as  $w(t)$  increases monotonically with time. Its  $H(k)$  takes both positive and negative values, and is thus not a PDF. Sub-exponentiality is nevertheless not a sufficient condition. For the hypothetical sub-exponential decay law  $1/[1 + (t/\tau_0) + (t/\tau_0)^2/2]$ , the function  $H(k)$  can be obtained in closed form and is  $2\tau_0 \exp(-k\tau_0) \sin(k\tau_0)$ , taking both positive and negative values. Only decays that are completely monotonous have a PDF of rate constants. A new PDF of rate constants,  $J(k, t)$ , emerged as the central PDF of the problem. Cumulant and moment expansions of the decay can be obtained from this PDF, that is shown to be well-behaved and with all moments finite for  $t > 0$ , even when  $H(k)$  is of the Lévy type. The asymptotic behavior of the decay laws was considered in detail, and the relation between this behavior and the form of  $H(k)$  for small  $k$  was explored. Finally, several generalizations of the exponential decay function, namely the Kohlrausch, Becquerel, Mittag-Leffler and Heaviside decay functions, as well as the Weibull and truncated Gaussian rate constant distributions were analyzed in detail.

The use of such mathematical functions is an efficient way to recover distributions of rate constants from time-resolved fluorescence data. As the number of fitting parameters is small, good chi-squared values and other statistical tests (weighted residuals, autocorrelation function of these residuals, etc.) make one confident in the shape of the recovered distribution. Conversely, the methods that do not require an a priori form of the distribution suffer from the problem of instability which leads to a lack of confidence in the recovered distribution, even if the statistical tests are satisfactory.

### References

1. James DR, Ware WR (1985) A fallacy in the interpretation of fluorescence decay parameters. *Chem Phys Lett* 120:455–459
2. Liu YS, Ware WR (1993) Photophysics of polycyclic aromatic hydrocarbons adsorbed on silica gel surfaces 1. Fluorescence lifetime distribution analysis: An ill-conditioned problem. *J Phys Chem* 97:5980–5986

3. Mollay B, Kauffmann HF (1994) In: Richert R, Blumen A (eds) *Disorder Effects on Relaxational Processes*. Springer, Berlin, pp 509–541
4. Berberan-Santos MN, Choppinet P, Fedorov A, Jullien L, Valeur B (1999) Multichromophoric cyclodextrins, 6. Investigation of excitation energy hopping by Monte Carlo simulations and time-resolved anisotropy. *J Am Chem Soc* 121:2526–2533
5. Berberan-Santos MN, Choppinet P, Fedorov A, Jullien L, Valeur B (2000) Multichromophoric cyclodextrins, 8. Dynamics of homo- and heterotransfer of excitation energy in inclusion complexes with fluorescent dyes. *J Am Chem Soc* 122:11876–11886
6. Bodunov EN, Berberan-Santos MN, Nunes Pereira EJ, Martinho JMG (2000) Eigenvalue spectrum of the survival probability of excitation in nonradiative energy transport. *Chem Phys* 259:49–61
7. Wagner BD, Ware WR (1990) Recovery of fluorescence lifetime distributions: Application to Förster transfer in rigid and viscous media. *J Phys Chem* 94:3489–3494
8. Lee M, Tang J, Hochstrasser RM (2001) Fluorescence lifetime distribution of single molecules undergoing Förster energy transfer. *Chem Phys Lett* 344:501–508
9. Livesey AK, Brochon JC (1987) Analyzing the distribution of decay constants in pulse-fluorimetry using the maximum entropy method. *Biophys J* 52:693–706
10. Siemiarz A, Wagner BD, Ware WR (1990) Comparison of the maximum entropy and exponential series methods for the recovery of distributions of lifetimes from fluorescence lifetime data. *J Phys Chem* 94:1661–1666
11. Berberan-Santos MN, Valeur B (2007) Luminescence decays with underlying distributions: General properties and analysis with mathematical functions. *J Lumin* 126:263–272
12. Verbeek G, Vaes A, Van der Auweraer M, De Schryver FC, Geelen C, Terrell D, De Meutter S (1993) Gaussian distributions of the decay times of the singlet excited state of aromatic amines dispersed in polymer films. *Macromolecules* 26:472–478
13. Berberan-Santos MN, Bodunov EN, Valeur B (2005) Mathematical functions for the analysis of luminescence decays with underlying distributions 1. Kohlrausch decay function (stretched exponential). *Chem Phys* 315:171–182
14. Berberan-Santos MN, Bodunov EN, Valeur B (2005) Mathematical functions for the analysis of luminescence decays with underlying distributions 2. Becquerel (compressed hyperbola) and related decay functions. *Chem Phys* 317:57–62
15. Valeur B (2002) *Molecular fluorescence. Principles and applications*. Wiley-VCH, Weinheim
16. Jameson DM, Gratton E, Hall RD (1984) The measurement and analysis of heterogeneous emissions by multifrequency phase and modulation fluorometry. *Appl Spectrosc Rev* 20:55–106
17. Böttcher CJE, Bordewijk (1978) *Theory of electric polarization vol II*. Elsevier, Amsterdam
18. Widder DV (1946) *The Laplace transform*. Princeton University Press, Princeton
19. Feller W (1971) *An introduction to Probability Theory and its applications vol 2*, 2nd edn. Wiley, New York
20. Koppel DE (1972) Analysis of macromolecular polydispersity in intensity correlation spectroscopy: The method of cumulants. *J Chem Phys* 57:4814–4820
21. Frisken BJ (2001) Revisiting the method of cumulants for the analysis of dynamic light-scattering data. *Appl Opt* 40:4087–4091
22. Fritz R, Kungl A, Rettig W, Springer J (1996) Photochemical fluorescence probes: rate distribution in solid polymers. *Chem Phys Lett* 260:409–417



23. Berberan-Santos MN (2005) Analytical inversion of the Laplace transform without contour integration. Application to luminescence decay laws and other relaxation functions. *J Math Chem* 38:165–173
24. Berberan-Santos MN (2007) Computation of one-sided probability density functions from their cumulants. *J Math Chem* 41:71–77
25. Gardiner CW (1985) *Handbook of Stochastic Methods*, 2nd edn. Springer-Verlag, Berlin
26. James DR, Liu Y-S, de Mayo P, Ware WR (1985) Distributions of fluorescence lifetimes: Consequences for the photophysics of molecules adsorbed on surfaces. *Chem Phys Lett* 120:460–465
27. James DR, Ware WR (1986) Recovery of underlying distributions of lifetimes from fluorescence decay data. *Chem Phys Lett* 126:7–11
28. Alcalá JR, Gratton E, Prendergast FG (1987) Resolvability of fluorescence lifetime distributions using phase fluorometry. *Biophys J* 51:587–596
29. Montroll EW, Bendler JT (1984) On Levy (or stable) distributions and the Williams-Watts model of dielectric relaxation. *J Stat Phys* 34:129–162
30. Kohlrausch R (1854) Theorie des elektrischen Rückstandes in der Leidener Flasche II. *Ann Phys Chem (Poggendorff)* 91:179–214
31. Kohlrausch R (1854) Theorie des elektrischen Rückstandes in der Leidener Flasche. *Ann Phys Chem (Poggendorff)* 91:56–82
32. Werner A (1907) Quantitative Messungen der An- und Abklingung getrennter Phosphoreszenzbanden. *Ann Phys* 24:164–190
33. Rice SA (1985) In: Bamford CH, Tipper CFH, Compton RG (eds) *Chemical Kinetics*, vol 25. Elsevier, Amsterdam
34. Förster T (1949) Experimentelle und theoretische Untersuchung des zwischenmolekularen Übergangs von Elektronenanregungsenergie. *Z Naturforsch* 4a:321–327
35. Sveshnikov BY, Shirokov VI (1962) Change in the mean life-time and yield of luminescence in the process of quenching as a function of the law of molecular interaction. *Opt Spectrosc* 12:576–581
36. Inokuti M, Hirayama F (1965) Influence of energy transfer by exchange mechanism on donor luminescence. *J Chem Phys* 43:1978–1989
37. Huber DL, Hamilton DS, Barnett B (1977) Time-dependent effects in fluorescent line narrowing. *Phys Rev B* 16:4642–4650
38. Huber DL (1981) Dynamics of incoherent transfer. *Top Appl Phys* 49:83–111
39. Fredrickson GH, Andersen HC, Frank CW (1983) Electronic excited-state transport on isolated polymer-chains. *Macromolecules* 16:1456–1464
40. Fredrickson GH, Andersen HC, Frank CW (1985) Macromolecular pair correlation-functions from fluorescence depolarization experiments. *J Polym Sci: Polym Phys Ed* 23:591–599
41. Peterson KA, Fayer MD (1986) Electronic excitation transport on isolated, flexible polymer-chains in the amorphous solid-state randomly tagged or end tagged with chromophores. *J Chem Phys* 85:4702–4711
42. Roy AK, Blumen A (1989) On the direct energy transfer from donors to acceptors in chainlike polymer systems. *J Chem Phys* 91:4353–4359
43. Bodunov EN, Berberan-Santos MN, Martinho JMG (2001) Electronic energy transfer in linear polymers randomly labelled with chromophores. *Chem Phys* 274:243–253
44. Bodunov EN, Berberan-Santos MN, Martinho JMG (2002) Electronic energy transfer in polymers labelled at both ends with fluorescent groups. *J Luminescence* 96:269–278
45. Bodunov EN, Berberan-Santos MN, Martinho JMG (2002) Electronic energy transfer in linear polymer chains. *High Energy Chem* 36:245–249

46. Linnros J, Lalic N, Galeckas A, Grivickas V (1999) Analysis of the stretched exponential photoluminescence decay from nanometer-sized silicon crystals in SiO<sub>2</sub>. *J Appl Phys* 86:6128–6134
47. Chen R (2003) Apparent stretched-exponential luminescence decay in crystalline solids. *J Luminescence* 102–103:510–518
48. Soloviev VN, Eichhöfer A, Fenske D, Banin U (2001) Size-dependent optical spectroscopy of a homologous series of CdSe cluster molecules. *J Am Chem Soc* 123:2354–2364
49. Tang J, Marcus RA (2005) Single particle versus ensemble average: From power-law intermittency of a single quantum dot to quasistretched exponential fluorescence decay of an ensemble. *J Chem Phys* 123:204511
50. Hof M, Schleicher J, Schneider FW (1989) Time resolved fluorescence in doped aerogels and organosilicate glasses. *Ber Bunsenges Phys Chem* 93:1377–1381
51. Wong AL, Harris JM, Marshall DB (1990) Measurements of energy dispersion at liquid-solid interfaces: Fluorescence quenching of pyrene bound to fumed silica. *Can J Phys* 68:1027–1034
52. Métivier R, Leray I, Lefèvre J-P, Roy-Auberger M, Zaner-Szydłowski N, Valeur B (2003) Characterization of alumina surfaces by fluorescence spectroscopy, Part 2. Photophysics of a bound pyrene derivative as a probe of the spatial distribution of reactive hydroxyl groups. *Phys Chem Chem Phys* 5:758–766
53. Lee J, Lee J, Lee M, Lee K-J-B, Ko D-S (2004) Scanning confocal fluorescence microscopy of single DNA-EtBr complexes dispersed in polymer. *Chem Phys Lett* 394:49–53
54. Siegel J, Elson DS, Webb SED, Benny Lee KC, Vlandas A, Gambaruto GL, Lévêque-Fort S, John Lever M, Tadrous PJ, Stamp GWH, Wallace AL, Sandison A, Watson TF, Alvarez F, French PMW (2003) Studying biological tissue with fluorescence lifetime imaging: microscopy, endoscopy, and complex decay profiles. *Appl Optics* 42:2995–3004
55. Huber DL (1996) Dynamical model for stretched exponential relaxation in solids. *Phys Rev E* 53:6544–6546
56. Jurliewicz A, Weron K (1999) A general probabilistic approach to the universal relaxation response of complex systems. *Cellul Mol Biol Lett* 4:55–86
57. Huber DL (2000) Two-state model for sub-exponential fluorescence. *J Luminescence* 86:95–99
58. García-Adeva AJ, Huber DL (2001) Two-state model for sub-exponential fluorescence revisited. *J Luminescence* 92:65–72
59. Williams G, Watts DC (1970) Non-symmetrical dielectric relaxation behaviour arising from a simple empirical decay function. *Trans Faraday Soc* 66:80–85
60. Collins FC, Kimball GE (1949) Diffusion-controlled reaction rates. *J Colloid Sci* 4:425–437
61. Pilling MJ, Rice SA (1976) Long-range energy-transfer by dipole-dipole and exchange interactions in rigid media and in liquids. *J Chem Soc Faraday Trans 2* 72:792–801
62. Macdonald JR (1987) Linear relaxation: Distributions, thermal activation, structure, and ambiguity. *J Appl Phys* 62:R51–R62
63. Pollard H (1946) The representation of  $e^{-x^\lambda}$  as a Laplace integral. *Bull Am Math Soc* 52:908–910
64. Berberan-Santos MN (2005) Relation between the inverse Laplace transforms of  $I(t^\beta)$  and  $I(t)$ : Application to the Mittag-Leffler and asymptotic inverse power law relaxation functions. *J Math Chem* 38:265–270
65. Humbert CP (1945) Nouvelles correspondances symboliques. *Bull Soc Math France* 69:121–129

66. Lindsey CP, Patterson GD (1980) Detailed comparison of the Williams–Watts and Cole–Davidson functions. *J Chem Phys* 73:3348–3357
67. Becquerel E (1867) *La lumière; ses causes et ses effets*, vol 1. Firmin Didot, Paris
68. Curie D (1963) *Luminescence in Crystals*. Methuen, London
69. Wlodarczyk J, Kierdaszuk B (2003) Interpretation of fluorescence decays using a power-like model. *Biophys J* 85:589–598
70. Mittag-Leffler GM (1903) Une généralisation de l'intégrale de Laplace–Abel. *CR Acad Sci Paris Sér II* 136:537–539
71. Berberan-Santos MN (2005) Properties of the Mittag–Leffler relaxation function. *J Math Chem* 38:629–635
72. Wintner A (1959) On Heaviside's and Mittag–Leffler's generalizations of the exponential function, the symmetric stable distributions of Cauchy–Lévy, and a property of the  $\Gamma$ -functions. *J Math Pur Appl IX* 38:165–182
73. Pollard H (1948) The completely monotonic character of the Mittag-Leffler function  $E_\alpha(-x)$ . *Bull Am Math Soc* 54:1115–1116
74. Weibull W (1951) A statistical distribution function of wide applicability. *J Appl Mech* 18:293–297

# Fluorescence as the Choice Method for Single-Molecule Detection

Michel Orrit

MoNOS, Huygens Laboratory, Leiden University,  
Postbus 9504, 2300 RA Leiden, The Netherlands  
[orrit@molphys.leidenuniv.nl](mailto:orrit@molphys.leidenuniv.nl)

1	Introduction . . . . .	106
2	Signal-to-Noise Ratio in Fluorescence . . . . .	106
3	Signal-to-Noise Ratio with other Optical Detection Methods . . . . .	109
4	Conclusion . . . . .	111
	References . . . . .	112

**Abstract** We discuss the specific features of fluorescence that make it the method of choice to optically detect single molecules and other single luminescent nano-objects, such as color centers or semiconductor nanocrystals, in microscopy experiments. The main origin of the high signal-to-background ratio of fluorescence experiments is the resonance enhancement of absorption by the fluorophore with respect to non-resonant Raman scattering of the matrix. As a consequence, other methods with lower differences in resonance factors between probe and matrix will fail to reach single-molecule sensitivity in far-field, even with diffraction-limited excitation volumes. We also briefly discuss signal-to-noise ratios in several new optical methods which do not rely on fluorescent probes.

**Keywords** Fluorescence microscopy · Nano-objects · Single-molecule detection · Signal-to-noise ratio

## Abbreviations

$A$	Beam area at the focus
$E_{sc}$	Scattered wave
$E_{ref}$	Reference wave
$F$	Franck–Condon factor
$\Gamma_{rad}$	Radiative rate
$I_m$	Rate of detected fluorescence photons
$I_R$	Rate of detected Raman scattering photons
$I_s$	Detection rate in counts/s
$M$	Number of incident photons
$N_{abs}$	Number of absorbed photons
$R_d$	Detector dark counts
$\sigma$	Cross-section
$\sigma_F$	Fluorescence cross-section
$T$	Integration time

## 1

### Introduction

Kador and Moerner were the first to establish the feasibility of optically detecting a single molecule in 1989 [1], by applying a doubly modulated absorption method. Soon thereafter, however, fluorescence experiments in solid matrices [2] as well as in liquid solutions [3] have quickly established fluorescence's superiority with respect to signal/noise ratio and to ease of operation. The vast majority of subsequent work on single molecules and, more generally, on single luminescent nano-objects (color centers [4], polymers [5], semiconductor nanocrystals [6], and even metal clusters [7]) has exploited the sensitivity and selectivity of fluorescence, or more generally of photoluminescence.

Conventional optical experiments on large ensembles rely on many techniques besides fluorescence. Since most, if not all, of these spectroscopic techniques can easily be combined with optical microscopy in order to improve spatial resolution, the question of their detection abilities arises. Could we use these techniques to optically detect single molecules? Several new optical techniques have appeared these last years, which do not rely on fluorescence. They have been applied to single absorbing and scattering nano-objects, in particular, to the important class of metal nanoparticles. The latter objects have the advantages of being very sturdy (no blinking, no bleaching), of presenting high saturation intensities, and of existing in various sizes. The latter important feature allows experimentalists to gradually improve their setups to push down detection limits. The absorption of a gold nanoparticle can be detected indirectly via the photothermal effect [8, 9]. Scattering, and interference of the scattered wave with a local oscillator, are related techniques, and open possibilities to detect the weak modification of an incoming beam by a single metal nanoparticle [10–12]. The best result so far has been the photothermal detection of single gold nanoparticles of 1.4 nm diameter, comprising about 70 gold atoms, with a 100 Hz bandwidth [9]. However, neither of these new techniques has been able to reach single-molecule sensitivity so far. What are the specific features of fluorescence that make this method so powerful and unique for the detection of single objects? Wouldn't it be possible to apply for example IR absorption or Raman spectroscopy to single molecules? The purpose of this chapter is to try to answer this question and to explain why fluorescence will remain an irreplaceable tool in single-molecule investigations for many years to come.

## 2

### Signal-to-Noise Ratio in Fluorescence

Optical signals from a single nano-object being weak, we first have to consider their visibility against background. More precisely, as the average of the

background itself can always be subtracted, the limiting factor are fluctuations in the background. Such fluctuations can obviously arise from signals from other structures in the surroundings of the object to be detected, as is the case in biological cells, for example. In the following, we consider the simplest case of a uniform sample, in which only the molecules or objects to be detected are dispersed in a clear matrix. An example can be a mixed molecular crystal, in which, beyond the host, only guest molecules are present at extremely low concentration (less than  $10^{-9}$  molecule/molecule in most single-molecule experiments). In that case, the average background is obviously the same at all positions in the sample, and fluctuations only arise from shot noise in the background. To discuss signal visibility, we take as an example spatial images obtained by scanning a laser spot across the sample where the single luminescent objects (e.g., molecules) are dispersed. A molecule with rate  $I_m$  of detected fluorescence photons during integration time  $T$  will be visible whenever its signal  $I_m T$  clearly dominates the background fluctuations. Background clearly depends on the detection method and on the experimental details. The main background sources in fluorescence experiments are stray and leakage light (with detection rate  $I_s$  in counts/s), fluorescence from impurities other than the one under consideration (e.g., from out-of-focus molecules, or from weak emitters in the focal spot, rate  $I_i$ ), Raman scattering ( $I_R$ ), and detector dark counts ( $R_d$ ). The signal-to-noise ratio for an integration time  $T$  is thus:

$$S/N = I_m \frac{\sqrt{T}}{\sqrt{I_s + I_i + I_R + R_d}} \quad (1)$$

Whereas the molecule's fluorescence rate  $I_m$  and the background sources  $I_s$  and  $I_i$  are all proportional to laser intensity, only the latter background sources and  $I_R$  are proportional to the volume of the excited spot, as  $I_m$  is obviously independent of it for a given laser intensity (this signal arises from only one molecule!). In order to improve the signal-to-noise ratio for a given laser intensity, we must reduce the excited volume, if possible down to the diffraction limit. The excited volume can be further reduced by means of near-field optics, which we exclude from the present discussion. Reaching the diffraction limit is practically necessary for single-molecule detection at room temperature because the absorption cross-section of a typical dye molecule is very small, a few hundredths of  $\text{nm}^2$  (that this cross-section is comparable to the physical area of the molecule is a coincidence, and has no deep physical root). Cryogenic experiments with high spectral resolution and sharp zero-phonon lines tolerate lower-quality optics because of the huge enhancement of the cross-section by resonance with sharp zero-phonon lines at low temperatures [13].

Whereas stray light, sample purity and background from out-of-focus guest molecules can all be reduced by improving the experimental setup and sample preparation, the Raman contribution cannot. Raman scattering has

the same basic physical origin and the same selection rules as fluorescence. The main difference between the two effects is of a resonant nature. In fluorescence, the excited state of the fluorophore is prepared “really” and persists during the excited state lifetime (typically a few ns). In a Raman process, the excited state of the emitter (in our example, a host molecule) is prepared “virtually” only, i.e., the Raman emitter is excited far below its resonance. It therefore “remains” in its excited state only during a very short period  $\Delta t$ , about the inverse of the frequency difference  $\Delta\omega = \omega_{\text{eg}} - \omega_{\text{laser}}$  between laser and host excited state. Because Raman and fluorescence are two sides of the same coin, it is important to discuss the detection limit of a single fluorescent guest molecule in a matrix of Raman scatterers. For this purpose, we compare the absorption (or fluorescence) cross-section of the guest molecule with the Raman scattering cross-section of the host molecule. The fluorescence cross-section can be deduced from the absorption spectrum and the fluorescence yield [13, 14]. The integral of the cross-section over the spectrum can be related to the radiative rate  $\Gamma_{\text{rad}}$  of the guest’s excited state:

$$\int \sigma_{\text{a}}(\omega) d\omega = 3/4\lambda^2 \Gamma_{\text{rad}}. \quad (2)$$

From this expression, we can estimate the molecule’s fluorescence cross-section from the width of the absorption spectrum, which amounts to about  $1000 \text{ cm}^{-1}$  at room temperature, and to about  $\Gamma_{\text{rad}}$  in the best possible case at low temperature (i.e., if we neglect Franck–Condon and Debye–Waller factors [13] for the sake of simplicity). From a typical value for the radiative rate,  $\Gamma_{\text{rad}} \approx 10^{-3} \text{ cm}^{-1}$ , we obtain the order of magnitude of the fluorescence cross-section  $\sigma_{\text{F}}$  at resonance,

- at room temperature:  $\sigma_{\text{F}} \approx 0.1 \text{ nm}^2$
- and for a narrow line at low temperature:  $\sigma_{\text{F}} \approx 100\,000 \text{ nm}^2 = 0.1 \text{ }\mu\text{m}^2$ .

The Raman scattering cross-section can be expressed with transition dipole moments to the high-energy excited states of the scatterer (a host molecule in our example) and with the Franck–Condon factor  $F$  to the vibrational level of the ground electronic state prepared in the Raman Stokes process. Relating the dipole moments to a radiative rate similar to that of the guest, we obtain:

$$\sigma_{\text{R}} = 3/4\pi \left( \frac{\lambda}{2\pi} \right)^2 \frac{\Gamma_{\text{rad}}^2}{\Delta\omega^2} F. \quad (3)$$

We can now readily evaluate the ratio of the two cross-sections:

$$\frac{\sigma_{\text{R}}}{\sigma_{\text{F}}} = \frac{\Gamma_{\text{rad}}}{\Delta\omega} \frac{\Gamma(T)}{\Delta\omega} F, \quad (4)$$

where  $\Gamma(T)$  is the temperature-dependent width of the fluorophore’s absorption spectrum. With  $\Delta\omega \approx 10^4 - 10^5 \text{ cm}^{-1}$  in the case of a host with saturated carbon–carbon bonds (aromatic matrices would give stronger Raman scattering), a typical value of the Franck–Condon factor  $F \approx 0.1$ , we obtain a ratio

of cross-sections of about  $\sigma_R/\sigma_F \approx 10^{-12}$  at room temperature, and about 5–6 orders of magnitude smaller still at low temperature. The number of host molecules in a diffraction-limited focal volume is about  $10^9$ – $10^{10}$ . We therefore conclude that Raman scattering of a diffraction-limited volume is usually negligible against the fluorescence signal of a single molecule of a good fluorophore. Moreover, we see that much of the reduction effect in Eq. 4 stems from the ratio of the radiative rate  $\Gamma_{\text{rad}}$  to the detuning from resonance of the Raman scatterer,  $\Delta\omega$ . In other words, fluorescence dominates Raman scattering because of the resonance difference between fluorophore and scatterer. Raman emission can only take place during the very short virtual lifetime ( $\Delta\omega^{-1} \approx 1$  femtosecond or less) of the excited state, whereas fluorescence emission proceeds during the whole fluorescence lifetime (a few nanoseconds).

This conclusion provides insight into the origin of the sensitivity and selectivity of fluorescence. Those are the two unique properties which make it such a powerful method to detect traces and low concentrations of fluorophores, down to the single-molecule level. Other optical techniques, such as infra-red absorption, or Raman scattering itself, obviously cannot benefit from resonant contrast mechanisms to the same extent as fluorescence. As an example, we can estimate the selectivity of an infrared absorption transition of a guest (say, a single C–D bond stretching) in a matrix with minimal background at the C–D frequency (say, a host with only C–H bonds). Because of the many other vibration modes of the host, such as C–H wagging, combinations, harmonics, for example, which appear in the infrared spectrum, and because of the relatively large width of infrared bands, the background from C–H bonds of the matrix around the C–D frequency cannot be much lower than  $10^{-3}$  of the C–D line maximum. That means that 1000 C–H bonds will already match or dominate the signal of a single C–D bond, in other words, that infrared absorption is much less selective than fluorescence. A single-molecule infrared signal equals that of 1000 host molecules, whereas a fluorescence signal equals the Raman signal of  $10^{12}$  host molecules! An additional problem of infrared absorption would be the difficulty of reaching diffraction limits in infrared imaging, and the much larger focus size due to the large infrared wavelength.

### 3

#### Signal-to-Noise Ratio with other Optical Detection Methods

We now consider detection limits with other optical techniques, based on absorption or on interference of a scattered wave with a reference [10, 12] or with a local oscillator. We first discuss the signal-to-noise ratio in a general interference experiment where the wave (field  $E_{\text{sc}}$ ) scattered by a nano-object (assimilable to a dipole if its dimensions are much less than the wavelength)



interferes with a stronger reference wave (field  $E_{\text{ref}}$ ). The signal then only arises from the interference term  $\text{Re}(E_{\text{ref}}^* E_{\text{sc}})$ , while noise is determined by the photon-noise of the strong reference beam:  $N \propto \sqrt{E_{\text{ref}}^* E_{\text{ref}}}$ . The signal-to-noise ratio is, therefore, independent of the strength of the reference field, at least as long as it is much stronger than the scattered field. The same argument applies to direct absorption as a special case, since absorption can be seen as the interference of the scattered wave with the incident field, which then plays the part of the reference field. For ideal conditions, the detectability of a scatterer or of an absorber does not depend on the strength of the reference field. In other words, the strength of the reference field may be adjusted to adapt the measured signal to detectors, or to other experimental constraints, without any loss (nor gain) of signal-to-noise ratio.

We now proceed to more quantitatively estimate the corresponding signal-to-noise ratio. Without loss of generality, we choose the generic case of an absorption measurement on a single nano-object. The number of absorbed photons  $N_{\text{abs}}$  in a given integration time  $T$ , given by the ratio of the absorption cross-section  $\sigma$  to the beam area  $A$  at the focus, can be compared to the number of incident (and mostly unabsorbed) photons  $M$ , which determines the shot-noise. The signal will be visible when it dominates shot-noise of  $M$ , i.e.,

$$\sigma > \frac{A}{\sqrt{M}}. \quad (5)$$

The number of absorbed photons is limited by the saturation intensity  $M = A I_{\text{sat}} T$ . Typical values for a single molecule at room temperature,  $\sigma \approx 0.1 \text{ nm}^2$ ,  $I_{\text{sat}} \approx 1 \text{ kW cm}^{-2}$  yield a minimum integration time of about 1 s to directly detect the absorption. This should be compared to the typical integration time in single-molecule fluorescence, which may be shorter than 1 millisecond. In addition to the intrinsic weakness of the absorption signal, it is very difficult to eliminate other noise sources, and to reach the photon noise limit in direct absorption measurements. The detection limit of single gold nanoparticles by direct absorption [15] or scattering methods [10] seems to currently lie at diameters of about 5–10 nm.

The signal-to-noise ratio for the detection of absorbing nano-objects in far-field can be enhanced in detection schemes which avoid the detection of the large background of unabsorbed photons, just as is the case with fluorescence. Photothermal detection [16] is a powerful detection method, which has recently been applied to single gold nanoparticles [8, 9, 17]. The detection limit appears to be much lower than with scattering or direct absorption, and it has already been shown that gold nanoparticles with 1.4-nm diameter can be detected with a bandwidth of several tens of Hz. A full discussion of the origin of the photothermal contrast and of the signal-to-noise ratio can be found in the literature [17]. The photothermal method, however, would be

difficult to apply to a single molecule because the excitation intensity required for measurable heating would be much higher than the saturation intensity of a typical absorbing molecule.

## 4 Conclusion

The main advantages of fluorescence methods for the detection of single nano-objects are their ease of application, their sensitivity, and their selectivity. Furthermore, powerful treatment schemes have been designed for the exploitation of fluorescence signals, for example, fluorescence correlation spectroscopy [18]. As we have seen, fluorescence enables the experimentalist to find the needle in the haystack, i.e., to distinguish one fluorescent molecule versus billions of non-fluorescent solvent or matrix molecules, which all contribute a weak but unavoidable Raman scattering signal. The origin of this extreme selectivity is resonance of the laser excitation with the electrons of the fluorophore, and lack of resonance with solvent electrons. Yet, in spite of their power, fluorescence methods have intrinsic limitations:

- i) Fluorophores are a very restricted class of absorbing molecules (namely, they must be rigid, have a large empty gap between excited and ground states, present low intersystem crossing yields, etc.).
- ii) Fluorescence is a slow process. With an excited state lifetime of several nanoseconds and detection yields which most often do not exceed a few percent, the maximum count rate for a single molecule is limited to several kHz. This means that fast processes cannot be studied directly by looking at variations of the fluorescence signal. Correlation [18] and time-resolved spectroscopy [19] have better time resolution, but it comes at the expense of long accumulation times, which rule out real-time observations of single molecules.
- iii) The long dwell time in the excited state, in which the molecule is highly reactive, gives rise to a multitude of possible chemical reactions leading to more or less long-lived products, often non-fluorescent. The ensuing photobleaching and photoblinking processes [20, 21] are the most serious obstacles to the use of single-molecule methods in molecular cell biology.

For all these reasons, new optical detection methods based on other signals than fluorescence are desired. Absorption detection would be complementary to fluorescence, and would apply to a much wider class of nano-objects. Unfortunately, it seems difficult to generalize direct absorption methods to single molecules, because of the large accumulation times they would require, in order to average out photon noise. Beyond fluorescence, other optical methods sidestep the high photon noise of direct absorption measurements, for example photothermal detection. New detection schemes adapted to mi-

croscopy must be developed as optical contrast mechanisms complementary to our workhorse method, fluorescence.

**Acknowledgements** The author gratefully acknowledges financial support of his work by the Stichting voor Fundamenteel Onderzoek der Materie, which is part of the NWO, and by the European Commission (IST contract 2001-33578).

## References

1. Moerner WE, Kador L (1989) Optical detection and spectroscopy of single molecules in a solid. *Phys Rev Lett* 62:2535–2538
2. Orrit M, Bernard J (1990) Single pentacene molecules detected by fluorescence excitation in a p-terphenyl crystal. *Phys Rev Lett* 65:2716–2719
3. Shera EB, Seitzinger NK, Davis L, Keller RA, Soper SA (1990) Detection of single fluorescent molecules. *Chem Phys Lett* 174:553–557
4. Gruber A, Dräbenstedt A, Tietz C, Fleury L, Wrachtrup J, von Borczyskowski C (1997) Scanning confocal optical microscopy and magnetic resonance on single defect centers. *Science* 276:2012–2014
5. Bout DV, Yip WT, Hu DH, Fu DK, Swager TM, Barbara PF (1997) Discrete intensity jumps and intramolecular electronic energy transfer in the spectroscopy of single conjugated polymer molecules. *Science* 277:1074–1077
6. Nirmal M, Dabbousi BO, Bawendi MG, Macklin JJ, Trautman JK, Harris TD, Brus LE (1996) Fluorescence intermittency in single cadmium selenide nanocrystals. *Nature* 383:802–804
7. Peyser PA, Vinson AE, Bartko AP, Dickson RM (2001) Photoactivated fluorescence from individual silver nanoclusters. *Science* 291:103–106
8. Boyer D, Tamarat P, Maali A, Lounis B, Orrit M (2002) Photothermal imaging of nanometer-sized metal particles among scatterers. *Science* 297:1160–1163
9. Berciaud S, Cognet L, Blab GA, Lounis B (2004) Photothermal Heterodyne Imaging of Individual Nonfluorescent Nanoclusters and Nanocrystals. *Phys Rev Lett* 93:257402
10. Lindfors K, Kalkbrenner T, Stoller P, Sandoghdar V (2004) Detection and Spectroscopy of Gold Nanoparticles Using Supercontinuum White Light Confocal Microscopy. *Phys Rev Lett* 93:037401
11. Jacobsen V, Stoller P, Brunner C, Vogel V, Sandoghdar V (2006) Interferometric optical detection and tracking of very small gold nanoparticles at a water-glass interface. *Opt Express* 14:405–414
12. Ignatovich FV, Novotny L (2006) Real-Time and Background-Free Detection of Nanoscale Particles. *Phys Rev Lett* 96:013901
13. Orrit M, Bernard J, Brown R, Lounis B (1996) In: Wolf E (eds) *Progress in Optics XXXV*. Elsevier, Amsterdam, p 61
14. Jackson JD (1975) *Classical Electrodynamics*. Wiley, New York, p 803
15. van Dijk MA, Lippitz M, Orrit M (2005) Detection of Acoustic Oscillations of Single Gold Nanospheres by Time-Resolved Interferometry. *Phys Rev Lett* 95:267406
16. Tokeshi M, Uchida M, Hibara A, Sawada T, Kitamori T (2001) Determination of Suboctomole Amounts of Nonfluorescent Molecules Using a Thermal Lens Microscope: Subsingle-Molecule Determination. *Anal Chem* 73:2112–2116
17. Berciaud S, Lasne D, Blab GA, Cognet L, Lounis B (2006) Photothermal heterodyne imaging of individual metallic nanoparticles: Theory versus experiment. *Phys Rev B* 73:045424

18. Rigler R, Widengren J, Mets U (1992) In: Wolfbeis E (ed) *Fluorescence Spectroscopy*. Springer, Berlin, p 13
19. van Dijk EMHP, Hernando J, Garcia-Lopez JJ, Crego-Calama M, Reinhoudt DN, Kuipers L, Garcia-Parajo MF, van Hulst NF (2005) Single-Molecule Pump-Probe Detection Resolves Ultrafast Pathways in Individual and Coupled Quantum Systems. *Phys Rev Lett* 94:078302
20. Zondervan R, Kulzer F, Orlinskii SI, Orrit M (2003) Photoblinking of rhodamine 6G in poly(vinyl alcohol): radical dark state formed through the triplet. *J Phys Chem A* 107:6770–6776
21. Zondervan R, Kulzer F, Kol'chenko MA, Orrit M (2004) Photobleaching of rhodamine 6G in poly(vinyl alcohol) at the ensemble and single-molecule levels. *J Phys Chem A* 108:1657–1665

**Part B**  
**Molecular and Supramolecular Systems**

# Water-soluble Fluorescent Chemosensors: in Tune with Protons

A. Jorge Parola · João C. Lima · Carlos Lodeiro · Fernando Pina (✉)

Departamento de Química, REQUIMTE-CQFB, Faculdade de Ciências e Tecnologia,  
Universidade Nova de Lisboa, 2829-516 Portugal  
fjp@dq.fct.unl.pt

<b>1</b>	<b>Introduction</b>	118
1.1	Fluorescent Chemosensors	118
1.2	Polyamine-based Receptors	120
1.2.1	The Quenching Mechanism: Exciplex Versus Electron Transfer	121
1.2.2	In Tune with Protons	122
<b>2</b>	<b>Intramolecular Excimer Formation</b>	124
2.1	ON-OFF Switch Driven by Light and pH	124
2.2	A Temperature Sensor	128
<b>3</b>	<b>Intramolecular Energy Transfer</b>	131
3.1	Switching from Energy Transfer to Electron Transfer by the Action of Protons	131
3.2	Antenna Effect	133
<b>4</b>	<b>Electron Transfer</b>	135
4.1	Long Range Electron Transfer Quenching	135
4.2	Exploring Photocatalytic Properties	140
4.2.1	Protonation	140
4.2.2	Sensing Anions	141
4.2.3	Iodide to Iodine Photocatalytic Oxidation	145
	<b>References</b>	147

**Abstract** Development of fluorescent chemosensors able to bind and signal either cations or anions in aqueous media is reviewed. Abundant examples in the literature support the versatility of polyamine-based chemosensors towards applications in water. The chemosensors described have a common structure consisting of a binding polyamine motif linked to a fluorophoric unit. Different sensing mechanisms are explored: photoinduced electron transfer from the amine lone pairs to the fluorophoric unit(s), photoinduced electron transfer between fluorophoric units, energy transfer, excimer and exciplex formation. The protonation equilibria of the polyamine chains render great versatility to the chemosensors since they are at the basis of the different sensing mechanisms and also allows the tuning between cation and anion binding regime.

## Abbreviations

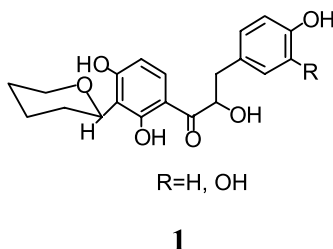
Bpy 2,2'-bipyridine  
CLDA Covalently linked donor-acceptor

CHEF	Chelation enhancement of fluorescence
ET	Energy Transfer
eT	Electron transfer
MLCT	Metal to ligand charge transfer
NMR	Nuclear magnetic resonance
PET	Photoinduced electron transfer
Phen	1,10-Phenanthroline
UV-vis	ultraviolet-visible
Tpy	2,2':6',2''-terpyridine

## 1

### Introduction

The first description of a fluorescent molecule was most likely about Coatline A (R = H) and B (R = OH), Scheme 1, made in the sixteenth century by the physician of Seville (Spain), Nicolás Monardes, who reported the blue colour that is observed from water extracts of the wood of a small tree (Coatli) used in the Aztec culture to treat kidney maladies [1, 2]. Modern fluorescence begins in the middle of the nineteenth century, after the work of Stokes, who proposed the use of fluorescence for the detection of organic substances [3]. In fact, fluorescence has been extensively applied as a powerful analytical tool, but the concept of fluorescent chemosensors only appears after the 1970s.

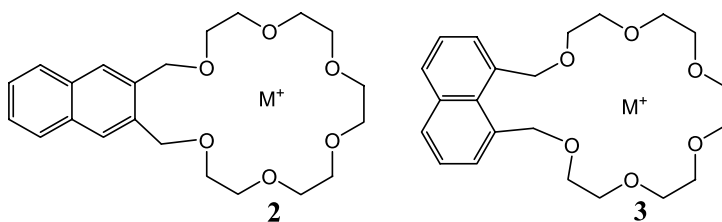


**Scheme 1** Coatline A and B

### 1.1

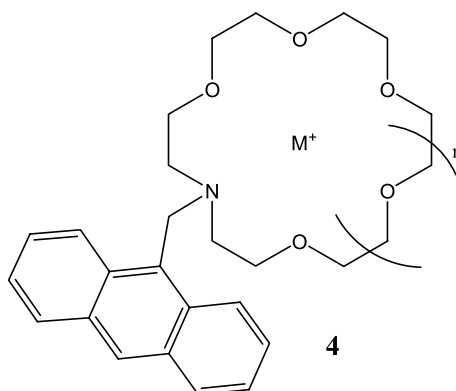
#### Fluorescent Chemosensors

An important contribution to the concept of chemosensors was given by L.R. Sousa in 1977, with the study of the perturbation of the fluorescence and phosphorescence of naphthalene derivatives **2** and **3** by alkali metal cations [4]. While in compound **2** (ethanol glass at 77 K) the fluorescence quantum yield is quenched, and the phosphorescence quantum yield is enhanced by these metals, in compound **3** it is exactly the opposite, the fluorescence is enhanced and the phosphorescence quenched [4].

**Scheme 2**

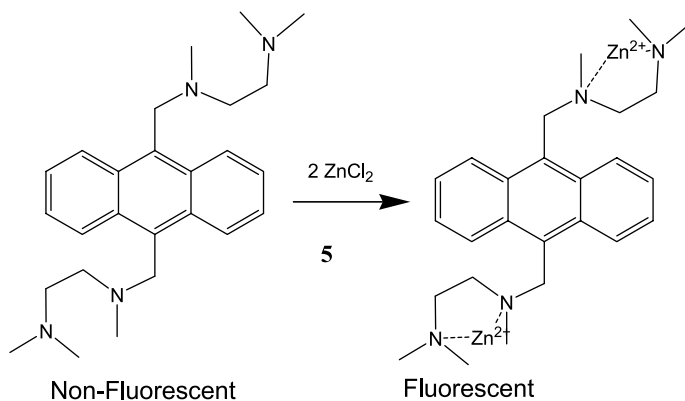
Sousa's work presented for the first time the enhancement of the fluorescence of an aromatic hydrocarbon system by the addition of "perturbers", which are held in a predetermined orientation without the use of a covalent bond [4].

A.P. de Silva, in 1986, introduced the concept of "switching on" to characterize the large perturbation caused by the addition of  $\text{Na}^+$  and  $\text{K}^+$  to methanol solutions of anthracene crown ether derivative **4**. In this compound the anthracene fluorescence is quenched by electron transfer from the lone pair of the nitrogen, and it is recovered on incorporation (recognition) of the alkali metal-ion into the macrocycle [5].

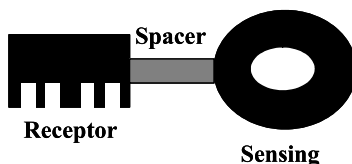
**Scheme 3**

Recovery of the anthracene fluorescence emission upon coordination by an attached ligand was also described by Czarnik in 1988 [6]. This author reported the chelation-enhancement of fluorescence (CHEF) that occurs upon  $\text{Zn}^{2+}$  coordination to anthracene derivative **5**, see Scheme 4. The lack of fluorescence emission in this compound is attributed to a quenching process by electron transfer, taking place from the lone pairs of the amine to the excited fluorophore. Protonation of the amines or coordination of some metal ions such as  $\text{Zn}^{2+}$  or  $\text{Cd}^{2+}$ , prevents the electron transfer process, allowing the fluorophore to exhibit its intrinsic fluorescence.



**Scheme 4**

It was Czarnik [7] who clearly introduced the concept of chemosensor, defined as a molecule containing a binding site (receptor), a fluorophore (sensor), and a mechanism for communication between the two, (through a spacer), see Scheme 5.

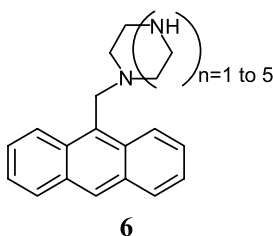
**Scheme 5**

Most of the chemosensors reported in the literature operate in organic solvents, in spite of the fact that water is the ubiquitous solvent, in particular in which concerns biological systems. The present work is focused on water soluble fluorescent chemosensors and the role played by protons in these systems.

## 1.2

### Polyamine-based Receptors

Although chemosensors bearing aromatic hydrocarbons as sensing units and polyoxa or mixed polyoxa and polyaza receptors were previously prepared [8–10], the first water soluble chemosensor possessing a polyamine macrocycle receptor linked to an aromatic hydrocarbon was reported in 1990 by Czarnik and co-workers, Scheme 6 [11]. In this example, protons, as well as  $\text{Zn}^{2+}$  and  $\text{Cd}^{2+}$ , switch ON the fluorescence of the sensor.



### Scheme 6

The presence of the polyamine receptor unit usually renders the sensor water-soluble largely due to the protonation equilibria undergone by the polyamine in water. This results in an increase in complexity due to the presence of species with different protonation degrees, but on the other hand, also confers versatility to the applications of the chemosensor, since their properties can be tuned largely by the pH of the system. In fact, speciation of the sensor leads to the presence of an ensemble of sensors that can be selected for optimum detection performance for a given analyte. For instance, the protonation of the polyamine at acidic pH values renders an anionic sensor while at basic pH the unprotonated forms are ideal to complex metal ions.

The increased complexity of water soluble polyamine-based fluorescence chemosensors implies the use of a set of complementary techniques to fully characterize the speciation behaviour of the sensor with respect to the pH and the presence of the analyte.

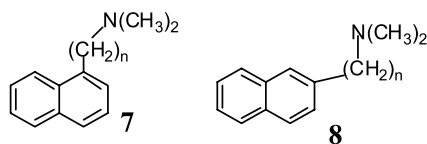
In collaboration with E. Garcia-España we introduced in 1995, as far as we know for the first time, the systematic superposition of the potentiometric, absorption and fluorescence emission titration curves, to study the interaction of polyazacyclophane macrocyclic receptors with the anion hexacyanocobaltate (III) [12]. This approach was later complemented by the use of NMR titrations [13]. These four combined techniques, UV-vis absorption, fluorescence emission, potentiometry, and NMR, as a function of pH, proved to be a powerful tool for investigating the behaviour in water of fluorescent polyamine chemosensors. In particular, this approach permits in the majority of the cases to assign the sequence in which the nitrogen molecules of the polyamine are protonated, clearly identifying the contribution of each species to the fluorescence emission, according to the pH value.

#### 1.2.1

#### The Quenching Mechanism: Exciplex Versus Electron Transfer

In organic solvents, formation of an intermolecular emissive exciplex between naphthalene and triethylamine was reported in 1969 by Kuzmin and Guseva [14]. In addition, intramolecular exciplex formation for naphthylalkylamines (in organic solvents) was described by Chandross and

Thomas, a few years latter, Scheme 7 [15]. The absorption spectra of these compounds are essentially identical to those of 1-methylnaphthalene or 2-methylnaphthalene, indicating that there is no appreciable ground-state interaction between the sensing (naphthalene) and the receptor (amine) units.



**Scheme 7**

An important feature of these systems is the fact that when  $n = 1$ , exciplex emission intensity is very low, due to the restricted overlap. Nevertheless the fluorescence of the naphthalene is quenched efficiently by the amine.

In the work of Kuzmin and Guseva, concerning intermolecular exciplex formation, no alteration on the absorption spectrum in the presence of the amine was observed; on contrary an unstructured emission band at lower energies which was attributed to an exciplex appears. The exciplex emission is displaced to the red by increasing solvent polarity. Furthermore, while the emission intensity of the exciplex in less polar solvents is comparable to the one of the naphthalene, its quantum yield decreases with increasing solvent polarity, and in water no exciplex was observed.

Polyamine-based fluorescence chemosensors systems can in principle undergo quenching through intramolecular exciplex formation or through electron transfer, depending on the solvent polarity. In general, excited aromatic hydrocarbons form exciplexes with amines in non-polar solvents, while undergoing electron transfer to yield radical ion pairs in polar solvents [16–19]. In water the key mechanism through which polyamine-based chemosensors bearing aromatic sensing units are quenched is electron transfer from the lone pairs of the amines to excited fluorophores.

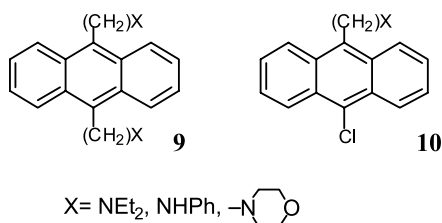
### 1.2.2

#### In Tune with Protons

Water soluble chemosensors can be conveniently prepared by employing linear or cyclic polyamine receptors attached to a fluorophore. The advantage of polyamines, beyond their capacity of conferring solubility to the chemosensor, is their ability to bind not only metal cations, but also anions, depending on pH [9, 10]. One of the consequences of using water as solvent is the lack of exciplex formation, because electron transfer is privileged in comparison with exciplex formation [15–17]. Another one is that protons play an important role in all the processes described.

It is well known that the excited state of a molecule constitutes a new entity exhibiting different chemical and physical properties. In particular the acid-base properties can change greatly [20].

A.P. de Silva and D. Rupasinghe were the first authors to deal with the acid-base characteristics of amines covalently linked to aromatic fluorophores through methylenic spacers [21]. They arrived to the conclusion that in anthracene derivatives **9** and **10**, Scheme 8, the ground and excited state  $pK_a$  values are identical. In these systems, excitation of the fluorophore does not cause significant changes on the acid-base properties of the system due to the presence of the methylenic spacer.



**Scheme 8**

On the other hand electron transfer from the lone pair of the aliphatic amino groups to the excited fluorophore occurs whenever the lone pair is free and blocked upon protonation (or complexation). This was early observed in organic solvents and in water [9, 13, 17, 18, 22]. When nitrogen containing aromatic heterocycles, such as pyridine, bipyridine, terpyridine, or phenanthroline, are included in the receptor unit, their protonation leads to a photoinduced electron transfer from the  $\pi-\pi^*$  excited state of the hydrocarbon fluorophore to the protonated heterocycle. In some cases, when a hydrocarbon fluorophore is connected to a nitrogen containing aromatic heterocycle through a polyamine chain, both quenching effects can occur, defining a pH window where fluorescence emission occurs [23–25]. At acidic pH values, the amino and the N-heterocycle groups are protonated and a photoinduced electron transfer occurs from the excited state of the fluorophore to the protonated heterocycle, while at higher pH values, where the aliphatic amino groups are unprotonated, PET takes place from the aliphatic amine lone pair to the excited state of the fluorophore. Between these two pH values, there is a pH window where PET does not take place and fluorescence emission can be observed [23–25].

The ability of excimer or exciplex formation in bischromophoric systems (e.g., naphthalene-naphthalene, naphthalene-anthracene) as well as the occurrence of energy transfer is also affected by the protonation degree, and this can be used with advantage for the sensorial properties of the chemosensor.

The protonation not only switches ON-OFF the electron transfer quenching but also affects the distribution of conformations of the sensor. For in-

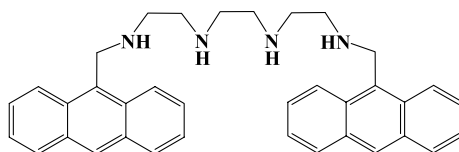
stance, in bischromophoric systems, the fully protonated form is less flexible due to the higher electrostatic repulsions, affecting the excimer or exciplex formation as well as the efficiency of energy transfer.

## 2 Intramolecular Excimer Formation

### 2.1 ON-OFF Switch Driven by Light and pH

Synthesis of bischromophoric species bearing aromatic hydrocarbons at the ends of a polyamine chain is a matter of great interest due to the possibility of excimer formation. Strong excimer formation was reported for methylenic chains possessing two naphthalene units at both terminals, when the two fluorophores are able to find a symmetrical sandwich configuration [26]. Hirayama studied the fluorescence of various diphenylalkanes and their derivatives in fluid solution, at room temperature [27], showing that a three-carbon chain is the shortest that will allow a sandwich configuration.

The first water soluble chemosensor based on excimer emission was claimed by Van Arman and co-workers [28]. These authors reported on the anthracene excimer emission of bis-chromophoric compound **11** upon coordination with  $Zn^{2+}$ .



**11**

#### Scheme 9

Detailed information on these systems can be obtained by the simultaneous use of the techniques referred in Sect. 1.2, as illustrated in Fig. 1 for the bisnaphthalenic system **12** [29, 30]. In this figure, the fluorescence emission titration curve is superimposed to the mole fraction distribution of the several species in solution, obtained by potentiometry. The protonation sequence in this case is easy to predict, and was confirmed by the chemical shifts of the protons ( $^1H$ ) and carbons ( $^{13}C$ ): the first proton goes to one of the terminal nitrogen molecules, the second one to the other terminal nitrogen in order to minimize the electrostatic repulsion, and the third to the central nitrogen. In this case, the absorption spectra are practically independent on the protonation sequence, but in contrast the fluorescence emission is

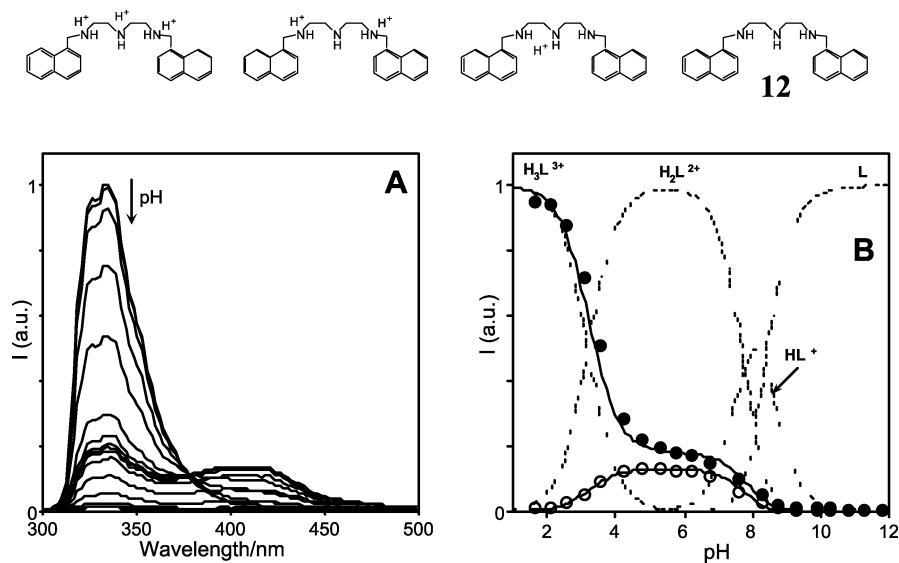


**Fig. 1** **A** pH dependence of the fluorescence emission of compound 12,  $\lambda_{exc} = 280$  nm; **B** Mole fraction distribution of pH speciation of compound 12: (●) fluorescence emission at  $\lambda_{exc} = 280$  nm and  $\lambda_{em} = 334$  nm (○) fluorescence emission at  $\lambda_{exc} = 280$  nm and  $\lambda_{em} = 418$  nm. The protonation sequence at the top was determined by  $^1H$  NMR

dramatically affected, see Fig. 1A. An interesting feature of the system is the observation of a red-shifted and unstructured emission band characteristic of an excimer, Fig. 1A. The fluorescence emission intensity of the monomer ( $\lambda_{exc} = 280$ ,  $\lambda_{em} = 334$  nm) and of the excimer ( $\lambda_{exc} = 280$  nm,  $\lambda_{em} = 418$  nm) are represented in Fig. 1B as a function of pH. The fully protonated species exhibits the highest emission. When a proton is removed from the central nitrogen, the fluorescence emission intensity of the monomer decreases due to the quenching by electron transfer from the lone pair of the amine to the excited fluorophore. It is worth of note that complete quenching can only occur when a second proton is removed from the polyamine chain. However, the most interesting feature of the system is the pH dependence of the excimer emission. The fully protonated species lacks of excimer emission, which is only observed for the di-protonated species. This behaviour can be explained considering that the fully protonated chain is rigid enough to prevent the formation of the symmetrical sandwich configuration. The rigidity of the chain should be dependent on the electrostatic repulsion of the positive charges. Removal of one of these charges, leading to the  $LH_2^{2+}$  species, confers the polyamine chain larger flexibility, allowing excimer formation.

The temperature dependence of the steady state fluorescence was also investigated [30]. As expected, the total fluorescence emission intensity increases with a decrease in temperature, while the contribution from the

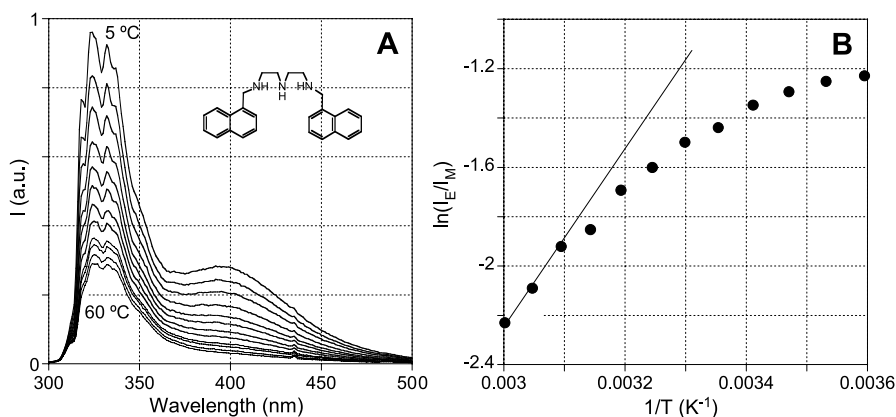


**Fig. 2** **A** Temperature dependence of the fluorescence emission of compound 12 at  $\lambda_{\text{exc}} = 280$  nm, pH = 6.3; **B** Respective Stevens–Ban plot

excimer emission becomes larger for low temperatures, Fig. 2A. In the framework of the Birks kinetic scheme and using the Stevens–Ban plot [31], Fig. 2B, it is possible to calculate the excimer binding energy,  $\Delta H^* = -34$  kJ mol<sup>-1</sup>, and entropy,  $\Delta S^* = -121$  J mol<sup>-1</sup> K<sup>-1</sup>. The values of these two parameters for similar compounds possessing polyamine chains of different lengths and protonation degrees are also reported in [30]. For all the compounds in this series, the binding energy and entropy are negative, showing that the process possesses a favourable enthalpic factor and an unfavourable entropic factor. Moreover, the binding energy for the same chain length becomes more negative with the decrease of the protonation degree of the chain; for the same protonation degree of the chain, the binding energy becomes more negative with increasing chain length. In both cases, decreasing the electrostatic repulsion by reducing the protonation degree of the chain or increasing the chain length leads to a larger flexibility of the chain, allowing more suitable conformations and more stable excimers.

Relevant questions are if the excimer is intra- or intermolecular, if the excimer is pre-formed in the ground state or is formed only upon excitation, and if it is an excimer or an exciplex involving the aliphatic amines.

The mono-chromophoric species 13 was chosen as a model compound, Fig. 3A. In this case, as expected, there is neither excimer formation nor any indication of exciplex emission, since the solvent is water. In addition, if a piperazine unit is introduced in the chain to confer rigidity, as in model compound 14, Fig. 3B, the excimer is not formed in the same range of concentrations used for the systems where the excimer emission is observed, in spite of the existence of two terminal naphthalenes. On the other hand, evidence for excimers formed in the excited state was obtained through time-resolved fluorescence, using the time correlated single photon counting

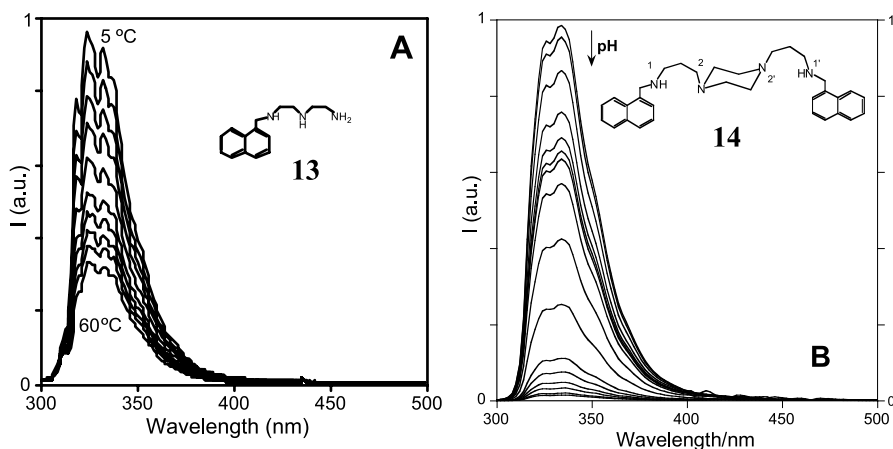


**Fig. 3** **A** Temperature dependence of the fluorescence emission of monochromophoric model compound 13 at  $\lambda_{exc} = 280$  nm, pH = 6.0; **B** pH dependence of the fluorescence emission of rigid model compound 14 at  $\lambda_{exc} = 280$  nm

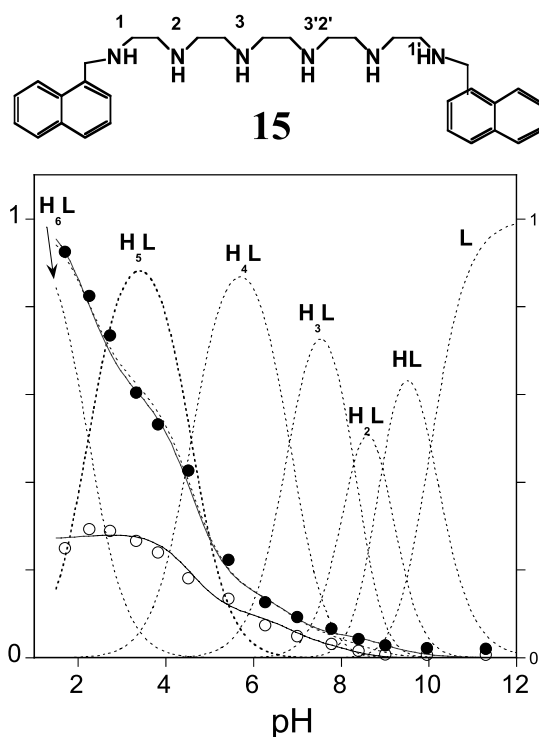


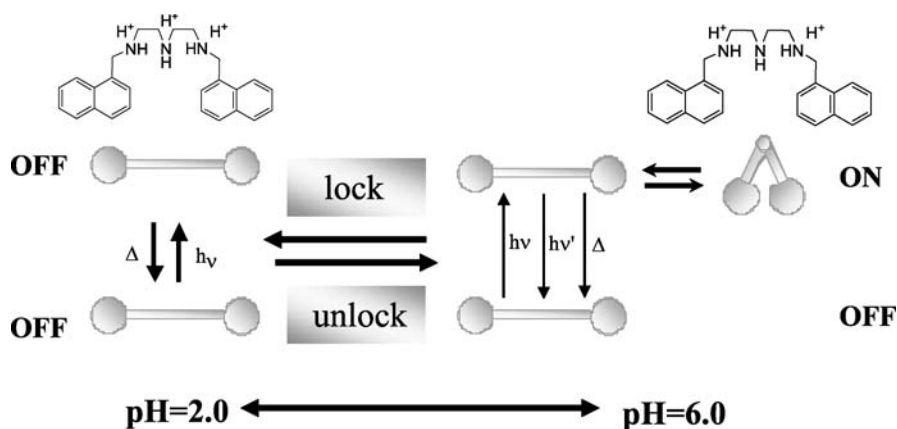
**Fig. 4** pH dependence of the fluorescence emission of compound 15 at  $\lambda_{exc} = 280$  nm and mole fraction distribution of the protonation states: (●) fluorescence emission at  $\lambda_{exc} = 280$  nm (monomer) and  $\lambda_{em} = 334$  nm (excimer)



technique [30]. The fluorescence decays could be fitted with a sum of two exponentials displaying the same decay times at both monomer and excimer emission wavelengths. Moreover, the short decay time at the excimer emission wavelength (418 nm) is associated with a negative pre-exponential (rise time), confirming that the excimer is formed in the excited state at the expenses of the excited monomer [27, 28].

Figure 4 presents the fluorescence emission titration curves superimposed to the mole fraction distribution of the several protonated species obtained by potentiometry, for a system possessing a large chain length, compound 15. As mentioned above, increasing of the chain length leads to a larger flexibility, allowing in this case excimer formation even for the fully protonated form.

In Scheme 10, the ON-OFF properties of compound 12, regarding the output signal of its excimer emission, are summarized. At pH=2.0, the system is locked and there is no chance to form the excimer due to the rigidity of the chain, OFF state. At pH=6.0, the system is unlocked, the excimer emission can be observed and the system is in the ON state.

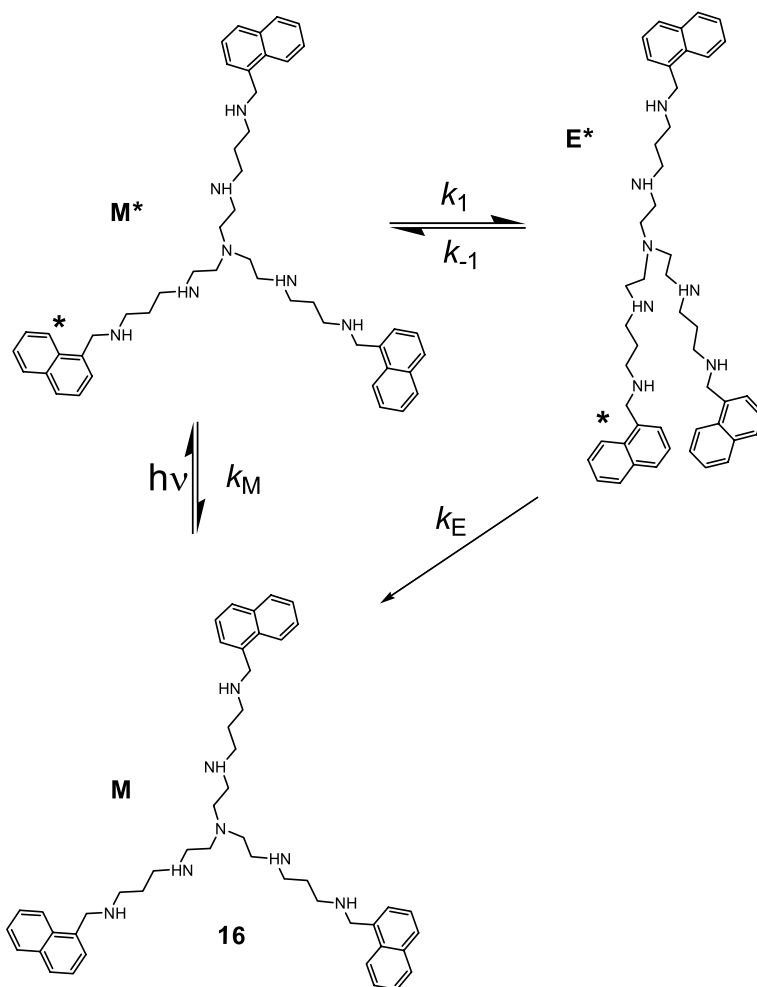


Scheme 10

## 2.2

### A Temperature Sensor

When intermolecular excimers are considered, an obvious way to increase their formation is the increasing of the monomer concentration. In the case of intramolecular excimers, the alternative is to add more fluorophores to the same polyamine chain. On this basis, the tripodal molecule 16 was synthesized, Scheme 11 [32]. In this molecule, at parity of conditions with a bis-chromophoric analogue, the probability of excimer formation can in theory duplicate. Moreover, the triangular pyramidal geometry of the central nitro-

**Scheme 11**

gen pre-organizes the molecule in a way that facilitates the approximation of the naphthalene units.

The results obtained with this system are reported in Fig. 5. The intense excimer band confirms the above predictions. The fully protonated form of **16** ( $\text{LH}_7^{7+}$ ), and the species with six protons show a notably intense excimer emission, slightly greater than the intensity of the monomer. The intense excimer emission confirms also the expected flexibility of the chain in this compound. The studies of the fluorescence emission as a function of the temperature, Fig. 5C, indicate that in the range  $10\text{ }^\circ\text{C}$  to  $50\text{ }^\circ\text{C}$ , the ratio between the maximum intensity of excimer/monomer is a straight line, Fig. 5D, which makes this system a temperature sensor in that region.

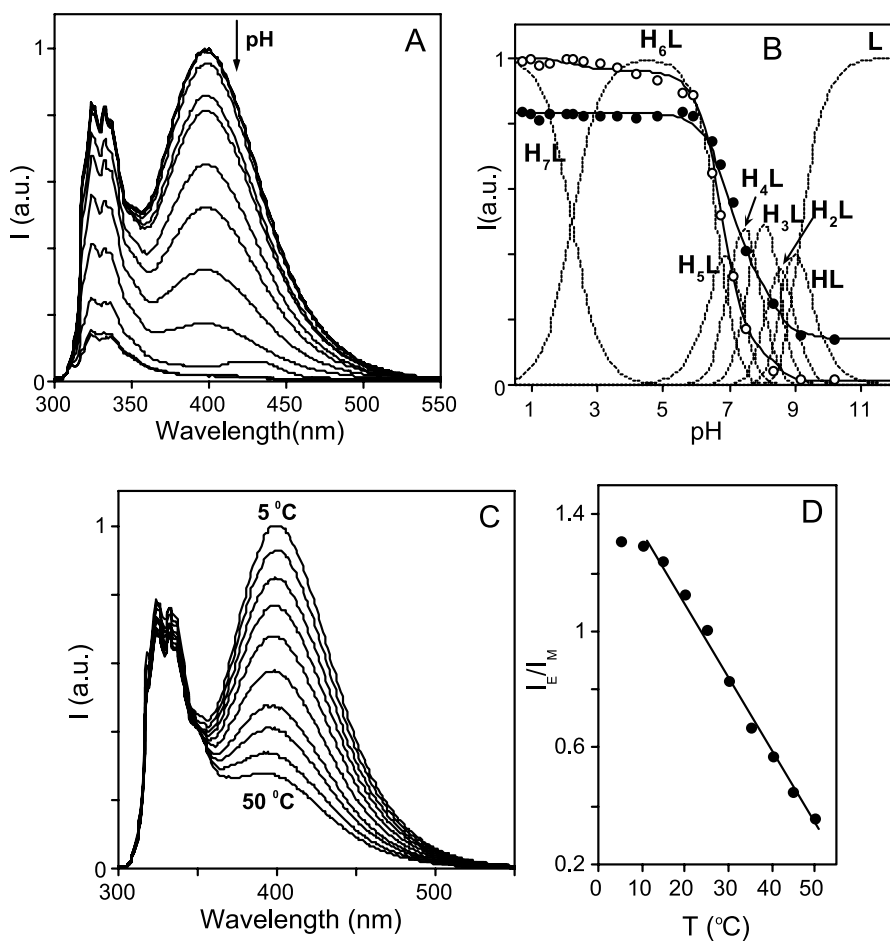


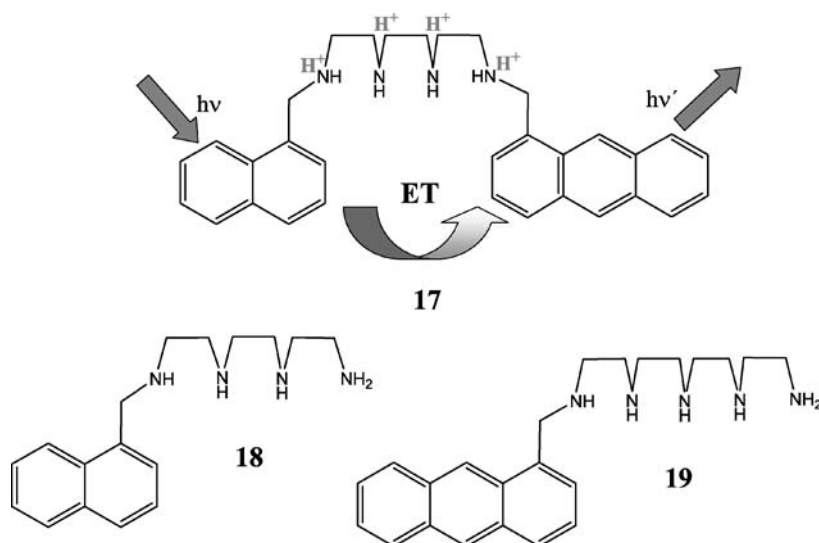
**Fig. 5** **A** Emission spectra of  $0.15 \text{ mol dm}^{-3}$  NaCl aqueous solutions of compound **16** from pH = 0.8 to pH = 10.48 at  $20^\circ\text{C}$  and **B** variation of monomer ( $I_{324}$ ,●) and excimer ( $I_{399}$ ,○) maxima superimposed to the mole fraction distribution of species in solution obtained by potentiometry; **C** Emission spectra of  $0.15 \text{ M}$  NaCl aqueous solutions of **16** at pH = 1.0 as a function of temperature and **D** respective  $I_{399}/I_{324}$  ratio vs.  $T$  showing linear behavior between  $15$  and  $50^\circ\text{C}$

Protons play again a crucial role in this system, since the operation of the temperature sensor is switched OFF above pH=6, due to electron transfer quenching from the amines lone pairs. The sensor operates only in the case of the two most protonated forms. In other words, protons are necessary to activate the sensor.

### 3 Intramolecular Energy Transfer

#### 3.1 Switching from Energy Transfer to Electron Transfer by the Action of Protons

Covalently linked donor-acceptor (CLDA) systems are a subject of great interest because of the theoretical and practical applications of electron (eT) and energy transfer (ET) that can take place in these molecules. The polyamine chains can be used to link donors and acceptors, as shown in Scheme 12 for compound 17 [33–35].



Scheme 12

In order to maximize the energy transfer process, the polyamine chain should be fully protonated; otherwise electron transfer quenches the emission. The reported system allows selective excitation of each fluorophore: anthracene is the sole absorbing moiety at  $\lambda_{\text{exc}} = 360$  nm, while at  $\lambda_{\text{exc}} = 280$  nm the naphthalene moiety absorbs ca. 90% of the excitation light and anthracene less than 10%.

Inspection of Fig. 6 clearly shows that while selective excitation of the anthracene moiety leads to its own fluorescence emission, Fig. 6B, the 90% excitation of naphthalene moiety gives rise to an intense fluorescence emission of the anthracene, and only a minor emission from naphthalene itself, Fig. 6C. This is what should be expected from an efficient energy transfer process. The energy transfer can be confirmed through the excitation spectrum collected

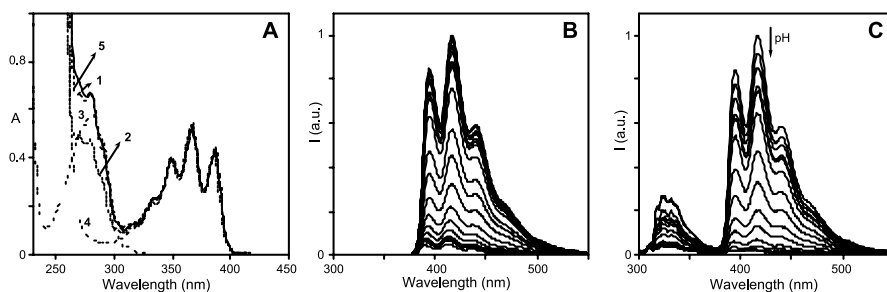
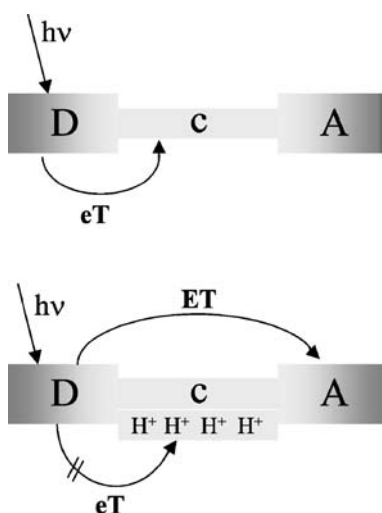


**Fig. 6** **A** Absorption spectrum (1) and respective excitation spectrum at  $\lambda_{em} = 420$  nm (2) of compound 17; absorption spectrum of naphthalene derivative model compound 18 (3), absorption spectrum of anthracene model compound 19 (4), both in the same concentration as 17, and the sum 3 + 4 (5) were represented for comparison purposes. **B** Fluorescence emission spectra upon selective excitation of anthracene at  $\lambda_{exc} = 360$  nm. **C** Fluorescence emission spectrum upon excitation at  $\lambda_{exc} = 280$  nm, 90% naphthalene excitation

at the anthracene emission (420 nm), Fig. 6A, where a large contribution from the naphthalene absorption is clear. The energy transfer (ET) parameters of this system have been calculated: the ET efficiency is  $\eta = 0.94$ , the Förster's critical distance is  $R_0 = 28 \text{ \AA}$ , and the inter chromophoric distance for the fully protonated form,  $R = 19 \text{ \AA}$  [31].

The above referred reductive quenching of hydrocarbon fluorophores by aliphatic amines can be used to control the energy transfer process. On this basis, it is possible to switch from energy transfer to electron transfer by



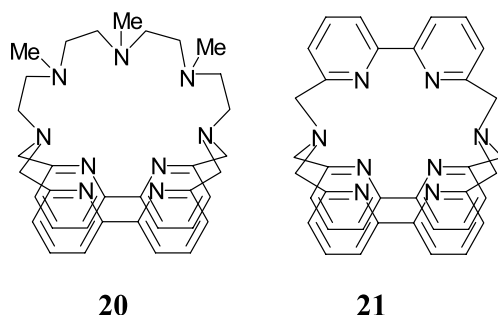
**Scheme 13**

increasing the pH, as shown in Scheme 13. In the absence of protons, the electron transfer is the dominant process and no fluorescence emission can be observed. Protonation of the polyamine bridge prevents the electron transfer and allows the energy transfer to take place.

### 3.2

#### Antenna Effect

During the last few years, the photophysical properties of the Eu(III) and Tb(III) complexes with dipyrindine containing cryptands, such as compound **20** (Scheme 14), have been extensively studied [36–48].



Scheme 14

Lanthanide(III) metal ions present very low molar absorption coefficients, and in spite of their high luminescence quantum yield, can not be used directly as a fluorescent tool. Lanthanides encapsulation into a cryptand cavity containing, for example, bpy, terpyridine or phenanthroline ligands, allows one to overcome this drawback. These ligands give rise to an intramolecular energy transfer between the triplet state of the cryptand and the metal ion, the so-called *antenna effect*.

The use of cryptands as ligands for lanthanide ions is also justified by an efficiently binding to the metal, protecting it from the solvent, especially in aqueous solution where coordinated water is an efficient quencher of the Eu(III) emission. Bis-bipyridine cryptand **20** was synthesized in order to contain a coordinative cleft as potential binding site for metals [49, 50]. The most significant difference from previously reported cryptands based on bipyridine, such as compound **21** [39–44], is the presence of an aliphatic flexible polyamine chain which can easily bind protons in aqueous solutions. These structural features make compound **20** an appropriate ligand for simultaneous binding of Eu(III) and H<sup>+</sup>, sharing the same cavity. This can be illustrated by the diprotonated complex [EuCl<sub>3</sub>H<sub>2</sub>20](ClO<sub>4</sub>)<sub>2</sub>·4H<sub>2</sub>O, that crystallizes from aqueous solutions at acidic pHs containing **20** and Eu(III), see Fig. 7.

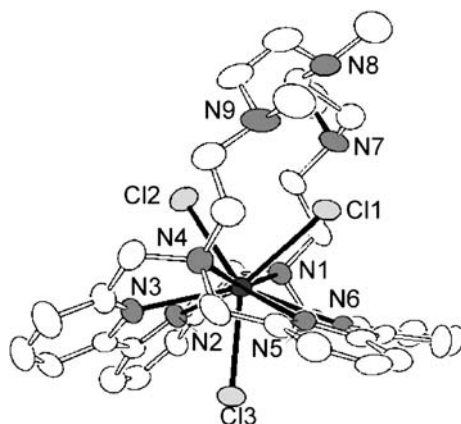


**Fig. 7** Crystal structure of the  $[\text{EuCl}_3\text{H}_2\mathbf{20}]^{2+}$  cation

As can be seen in the X-ray structure of this complex, the polyamine chain is weakly involved in metal coordination and can easily protonate. Moreover, water molecules may reasonably replace the coordinated chloride anions when in aqueous solutions.

As usually observed, the luminescence spectrum of the Eu(III) cryptate of **20** in aqueous solution at  $\text{pH}=6.8$ , in the absence of chloride, shows the characteristic visible emission of the metal ion with a maximum at 617 nm, upon excitation at 306 nm. Figure 8A reports the fluorescence emission spectra of the cryptate at different pH values, while Fig. 8B reports the titration curve obtained by following the fluorescence emission at 617 nm. These results can be explained having in mind that the three central nitrogen atoms of the polyamine chain show a high tendency to bind protons.

Inspection of Fig. 8B shows that the first three constants correspond to protonation of the three non-coordinated amine groups of compound **20** to give the  $[\text{EuH}_n\mathbf{20}]^{(n+3)+}$  ( $n = 1-3$ ) complexes at acidic pHs, while the last two may be attributed to the formation of the hydroxylated  $[\text{Eu}(\text{OH})\mathbf{20}]^{2+}$  and  $[\text{Eu}(\text{OH})_2\mathbf{20}]^+$  complexes at alkaline pHs. Protonation of the aliphatic polyamine chain  $\text{N}2'-\text{N}1-\text{N}2$  prevents the interaction of the methylated amine groups with the metal. For these species, the metal core is less protected from the solvent molecules. The free binding sites are occupied by water molecules, which can act as effective quenchers of the Eu(III) luminescence. This explanation is confirmed by the analysis of the lifetimes of the cryptate complex in water at neutral and acidic pHs [51]. Applying the equation developed by Horrocks and Sudnick [52, 53] to these data, it can be estimated that ca. 2 water molecules are coordinated to the metal at acidic pH values ( $\text{pH}=2$ ) and just one close to neutral pH ( $\text{pH}=6.8$ ) [54]. Concerning the decrease in luminescence at alkaline pH values, this fact can be explained on basis on the formation of the hydroxo-complexes  $[\text{Eu}(\text{OH})\mathbf{20}]^{2+}$

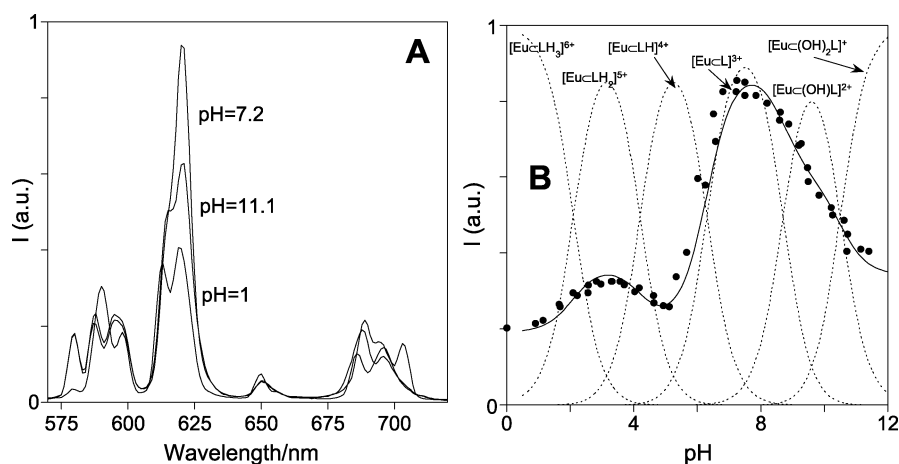


**Fig. 8** **A** Fluorescence emission spectra of the europium cryptate complex in aqueous solutions at pH 1, 7.2 and 11.1; **B** Luminescence emission ( $\bullet$ ) of the Eu(III) complex with **20** ( $\lambda_{\text{exc}} = 260$  nm,  $\lambda_{\text{em}} = 617$  nm,  $[\mathbf{20}] = [\text{Eu}^{3+}] = 5 \times 10^{-5}$  M,  $T = 300$  K) and calculated molar fractions ( $\chi$ ) of the Eu(III) complexes (–) as function of pH

and  $[\text{Eu}(\text{OH})_2\mathbf{20}]^+$ . Generally, binding of hydroxide anions to Eu(III), in fact, give rise to a quenching of the emission [47].

In this case, the quantum yield in aqueous solution at pH 6.8 ( $\Phi = 0.014$  at 300 K), the radiative rate constant ( $k_r = 746$  s $^{-1}$ ), the non-radiative temperature independent rate constant ( $k_{\text{nr}}(\text{OH}) = 1177$  s $^{-1}$ ), and the temperature dependent decay rate constant ( $k_{\text{nr}}(T) \cong 0$ ), are similar to those reported previously for other dipyriddy-containing europium cryptates [55–62] and somewhat lower than those found by Sudnick for  $[\text{Eu}\mathbf{21}]^{3+}$  [52, 53] as expected considering the replacement of a dipyriddy chromophore unit of **21** by an aliphatic more flexible polyamine chain in **20**. The present complex, therefore, still remains an efficient luminescent system, but, at the same time, displays a peculiar feature, which is the pH dependence of the luminescence intensity, with a maximum at neutral pH.

## 4

### Electron Transfer

#### 4.1

#### Long Range Electron Transfer Quenching

According to the experimental data reported in Figs. 1 and 4, the extent of the quenching effect is dependent on the nitrogen distance to the fluorophore. In order to get more insight on this property, a series of compounds have been



synthesized, and the fluorescence emission titration curves superimposed to the potentiometric data, as reported in Figs. 1 and 4 [63]. Fitting of the fluorescence emission can be obtained by a linear combination of the fluorescence contribution of the several species present in solution, according to Eq. 1.

$$I(\text{pH}) = a_n \chi_n + a_{n-1} \chi_{n-1} + \dots + a_0 \chi_0 = \sum_{i=0}^n a_i \chi_i \quad (a_n = 1) \quad (1)$$

In this equation,  $\chi$  represents the mole fraction of the species obtained by potentiometry,  $n$  is the number of nitrogen atoms in the chain, ( $i = n$  refers to the fully protonated species;  $i = 0$  to the completely deprotonated form). The emission from the fully protonated species is normalized to 1 and thus  $a_n = 1$ ; each coefficient  $a_i$  corresponds to the relative emission intensity of the species  $i$  when compared with the unit,  $a_i = I_i/I_0$ .

The quenching constant for each species can be calculated by the Stern-Volmer equation adapted to an intramolecular process, Eq. 2.

$$\frac{I_n}{I_i} = 1 + k_q \tau_n = \frac{1}{a_i} \quad (2)$$

$\tau_n$  (24 ns) is the lifetime of the fully protonated species, and  $k_q$  the quenching rate constant associated to the species  $i$ .

The plot of the quenching rate constants obtained upon removal of a single proton in compounds represented in Fig. 10 vs. a quantity proportional to the chain length (the bond distance between the fluorophore and the virtual middle point of the polyamine chain) are presented in Fig. 9, (black points). An exponential dependency is clearly observed. The pH dependent proton

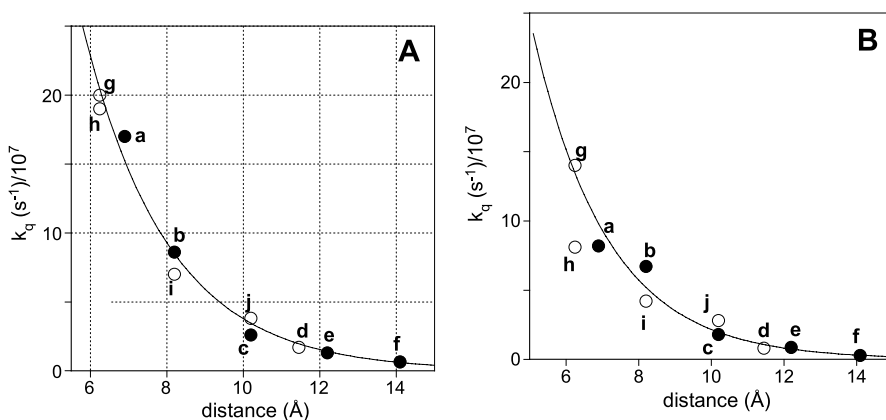


**Fig. 9** Exponential dependence of the quenching rate constants with the distance in water (A) and in deuterated water (B): (●) mono-deprotonated species (○) di-deprotonated (and tri-deprotonated) species

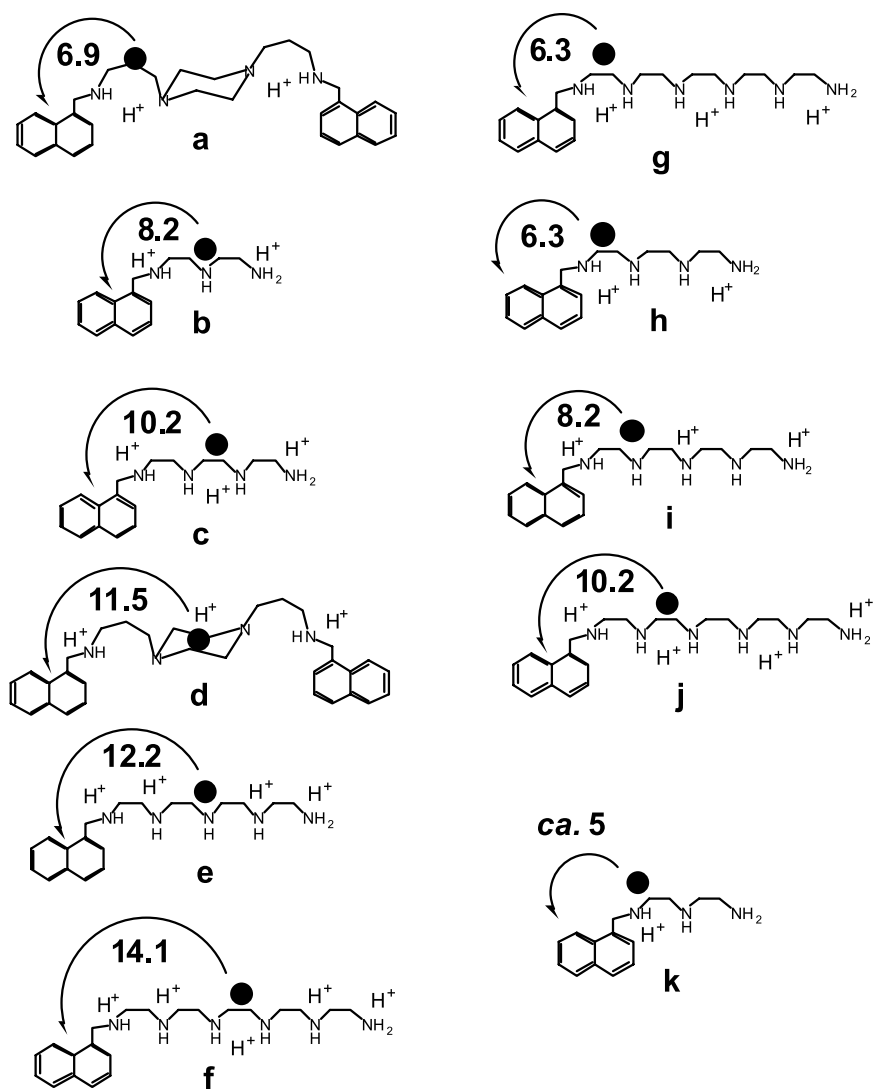


**Fig. 10** Protonation sequence and distance of the electron transferred in order to follow the exponential dependency reported in Fig. 9

distribution in these compounds is mainly determined by electrostatic repulsions, which rule the average position of protons in the chain; that is protons choose to be as far apart as possible. The average proton sequence can be inferred from the shifts that the  $^{13}\text{C}$  and  $^1\text{H}$  NMR resonances undergo with pH. In particular, the carbon nuclei placed in  $\beta$  position and the hydrogen atoms bearing deprotonation move significantly downfield and upfield, respectively [63].

In the cases where the chain consists of an odd number of nitrogen molecules, the first deprotonation affects mainly the central nitrogen. For all the cases where the chain has an even number of nitrogen atoms, the first deprotonation affects mainly the methylenic groups, connected to the two central nitrogen atoms, and because symmetry is preserved, the interpretation is that deprotonation leads to a species where two nitrogen atoms share a single proton, or alternatively, each nitrogen is protonated “half of the time”, see Fig. 10. The distance ( $d$ ) was obtained from a direct measurement of the bond lengths in a space-filling model, and taken from the distance of the naphthalene carbon atom (C1) to the deprotonated nitrogen and by consequence is independent of any conformational assumption. When the electron is transferred from two adjacent nitrogen atoms sharing a proton, the middle distance was taken. This procedure was extended to the compounds whose quenching rate constants result from a second deprotonation (and a third for the species bearing the largest chain), Fig. 9 open circles. In these cases, the observed rate constant will result from the sum of two parcels: (i) the quenching due to the first deprotonated nitrogen (previously calculated); plus (ii) the quenching from the second deprotonated nitrogen. In the case of the species without two protons, the third quenching constant was calculated *mutatis mutandis*.

The obtained exponential dependence for the quenching rate constants, shown in Fig. 9A (and also Fig. 9B), is of general formula  $k_q = k_{q(0)} e^{(-\beta d)}$ , leading to a  $\beta$  factor of  $0.45 \text{ \AA}^{-1}$ , suggesting that electron transfer would occur at longer distances than expected for the aliphatic system. At this point, a mention to the non-rigidity of these systems and its consequences must be made. In fact, in the present case, the strict sense of fixed donor acceptor distances cannot apply, perhaps with the sole exception of compound 4, where a piperazine ring will avoid folded conformations. With all the other compounds, repulsion between positively charged nitrogen atoms will most probably lead to extended conformations. However, a single conformer is not expected to occur in solution and, as a consequence of that, several differently oriented structures are expected to be present, their distribution depending on the pH value of the media. In our previous studies with bischromophoric analogues, shown above, the presence of excimer emission depends on the pH and on the chain length, showing that both factors affect chain flexibility, and that conformational changes occur upon deprotonation. On this basis an electron transfer through space can be questioned, i.e., an exponential decrease of the electron transfer rate constant with the increase in chain length is not compatible with a through-space mechanism, since larger chain lengths favours folded conformations.

In order to account for the role-played by the proton in the electron transfer process we have performed identical experiments in deuterated water. The reported results, in Fig. 9B, show that the quenching rate constants in deuterated water are in average ca. 1.2 times slower than in water ( $\tau_n$  is almost iden-

tical to water; 25 ns). This result suggests isotope sensitivity compatible with an association electron-proton (deuteron) transfer. The dependence with the distance is, however, similar in both media: deuterated water,  $\beta = 0.49 \text{ \AA}^{-1}$ , and water,  $\beta = 0.45 \text{ \AA}^{-1}$ .

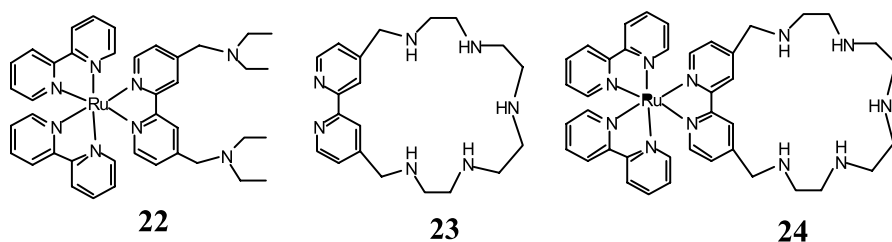
The use of classical and quantum mechanical models to account for the electron transfer phenomenon, in particular their dependence with the distance, is not a simple task. This is true essentially because the series in question lack homogeneity, in the sense that there is no evidence to support that the driving force for the electron transfer process,  $\Delta G^0$ , and the energy required to reorganize nuclear coordinates upon electron transfer,  $\lambda$ , are the same when the nitrogen is completely deprotonated (as in the case of species b and e or i in Fig. 10) or when it shares a proton with an adjacent nitrogen (as in the other cases). At this point of our studies, we can only look to the observed exponential dependence as a trend here expressed by an empirical law. However, despite these limitations, some aspects merit our attention. Independently of the exact meaning of the  $\beta$  factor, it should reflect how the electron transfer process fall-off with the distance. Some comparisons can be made with other covalently-linked bridged redox centers. Typical values for this parameter are found to be  $\beta = 0.9$  [64], 1.01 [65], 0.85 [66], and  $0.5 \text{ \AA}^{-1}$  [67], and tunnelling through vacuum ( $\beta =$  from 2.8 to  $3.5 \text{ \AA}^{-1}$ ) [68, 69]. According to Page and co-workers in the case of the electron tunnelling in biological oxidation-reduction systems a  $\beta$  value of  $0.9 \text{ \AA}^{-1}$  corresponds to a fully packed medium, whereas  $\beta = 2.8 \text{ \AA}^{-1}$  corresponds to the interstitial space in the protein structure outside the united van der Waals atomic radii [70]. These authors have also suggested an intermediate value ( $\beta = 1.4 \text{ \AA}^{-1}$ ), for the electron transfer process occurring in proteins.

The values of  $\beta$ , reported in the present work, are quite low and very similar to those found by Michel-Beyerle, Heitele and co-workers, for the pre-exponential factors of the rate constants in CLDA systems where a pyrene electron acceptor is linked to a dimethylaniline electron donor through a bridge consisting in two terminal methylene groups and different central aromatic fragments [66]. In their case the small value of the  $\beta$  factor was attributed to the presence of aromatic groups in the bridge unit.

In our case the dependence of the quenching rate constants on isotopic substitution suggest that proton movement is involved in the controlling step of electron transfer. In that case, a possible interpretation for the distance dependence is that the quenching rate constant is reflecting the time it takes to deprotonate the nitrogen nearest to the naphthalene moiety, i.e., proton migration through bond. This would also account the fact that conformational changes upon deprotonation are not reflected on the quenching mechanism.

## 4.2 Exploring Photocatalytic Properties

Macrocycles containing endotopic cavities and exotopic coordination sites can be used as ligands in the construction of water soluble fluorescent metal complexes, Scheme 15. These coordination compounds can operate as luminescence chemosensors based on the emission intensity as well as in long lifetime-based sensing for cations and anions. In addition the cavity can be explored as a photocatalytic center capable to host substrates amenable to react upon electron or energy transfer involving the metal center [71].



Scheme 15

The particular usefulness of lifetime based-sensing systems, like the one based on compound **22**, has been pointed out by Lakowicz [72, 73], essentially because they do not depend on probe concentration and remain unaffected by the photobleaching or washout of the probe. Exotopic macrocycles, like compound **23** are ideal precursors for the synthesis of water soluble fluorescent metal complexes such as compound **24** [71].

### 4.2.1 Protonation

The mole fraction distribution curves of the protonated species occurring in compound **24**, are shown in Fig. 8B. As can be seen, on lowering the pH, the compound starts binding protons at about pH 10 and is almost completely protonated at pH 2, where the  $H_5L^{7+}$  species of **24** is present in more than 90%. The protonation constants are consistent with the protonation pattern expected for a polyamine macrocycle [74], although the compound displays a lower basicity, in each protonation stage, due to the presence of a lower number of amine groups available for protonation and to the electrostatic repulsion generated by the coordinated Ru(II) ion. Nevertheless, highly charged species are formed in neutral and acidic solutions, which may interact with anions, as discussed below. The absorption spectrum of compound **24** does not change significantly with pH. In contrast the emission spectrum changes according to the pattern reported in Fig. 11.

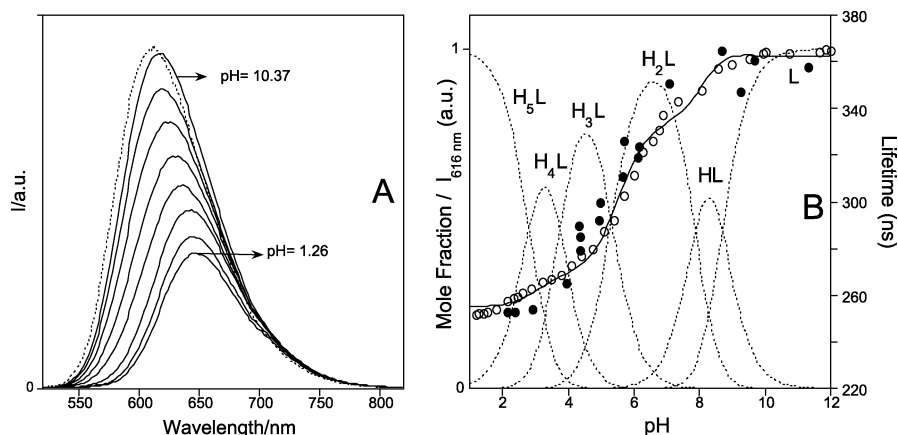


**Fig. 11** Emission spectra of  $1.33 \times 10^{-5}$  M solutions of compound **24** as a function of pH (**A**) and respective emission titration curve obtained at  $\lambda_{em} = 616$  nm and  $\lambda_{ex} = 470$  nm (○) superposed to the lifetime titration curve at  $\lambda_{ex} = 355$  nm (●), together with the representation of the mole fraction distribution of the protonated species. Charges omitted in species labels

The effect of protons is clearly individuated in Fig. 11. At basic pH values ( $\text{pH} > 10$ ), the emission of compound **24** is slightly red-shifted relatively to the parent  $[\text{Ru}(\text{bpy})_3]^{2+}$ , and the obtained ratio of the quantum yields is  $\Phi_L / \Phi_{[\text{Ru}(\text{bpy})_3]^{2+}} = 0.98$ . The increase in the protonation of the amino groups is followed by a significant red-shift of  $\cong 34$  nm (from  $\text{pH} = 10.73$  to  $\text{pH} = 1.26$ ) associated to a notorious decrease in the emission quantum yield. It is interesting to note that an identical behaviour was reported for compound **22**, but the decrease in emission intensity somewhat lower [73]. This effect can be explained by the fact that protonation of the receptor leads to a better electron acceptor, lowering the energy of the MLCT (metal to ligand charge transfer). One additional explanation could be found due to the fact that increase in protonation can gradually give rise to a more distorted excited state geometry which would favour the radiationless processes, leading to a less emissive species, and this is also in agreement with the increase in the Stokes shift. In Fig. 8 (right), the luminescence lifetime dependence with pH, exhibits an identical behaviour to the one found for the titration curve built with luminescence quantum yields. This shows that compound **24** also behaves as a pH based lifetime chemosensor.

#### 4.2.2 Sensing Anions

It is well known that macrocyclic polyamines in their protonated forms are efficient receptors of anionic species in solution [9]. In particular very sta-

ble adducts are formed with  $[\text{Fe}(\text{CN})_6]^{4-}$  and  $[\text{Fe}(\text{CN})_6]^{3-}$ , principally due to the high negative charge of such anions [75–80]. Hence, we expected that also protonated species of compound **24** might be able to form similar adducts. Our principal interest towards such systems results from the fact that the emission of the parent compound  $[\text{Ru}(\text{bpy})_3]^{2+}$  is known to be efficiently quenched by electron transfer from (or to) metal-cyanide complexes [81–83], and thus  $[\text{Ru}(\text{bpy})_3]^{2+}$  could be used as sensor for this type of anions. Compound **24** contains the basic ruthenium sensing unit, but in addition possesses an extra binding polyamine receptor, that is expected to influence the overall process, improving the efficiency in anion sensing. The interaction between this compound and  $[\text{Fe}(\text{CN})_6]^{4-}$  and  $[\text{Fe}(\text{CN})_6]^{3-}$ , have been studied by potentiometry [71].

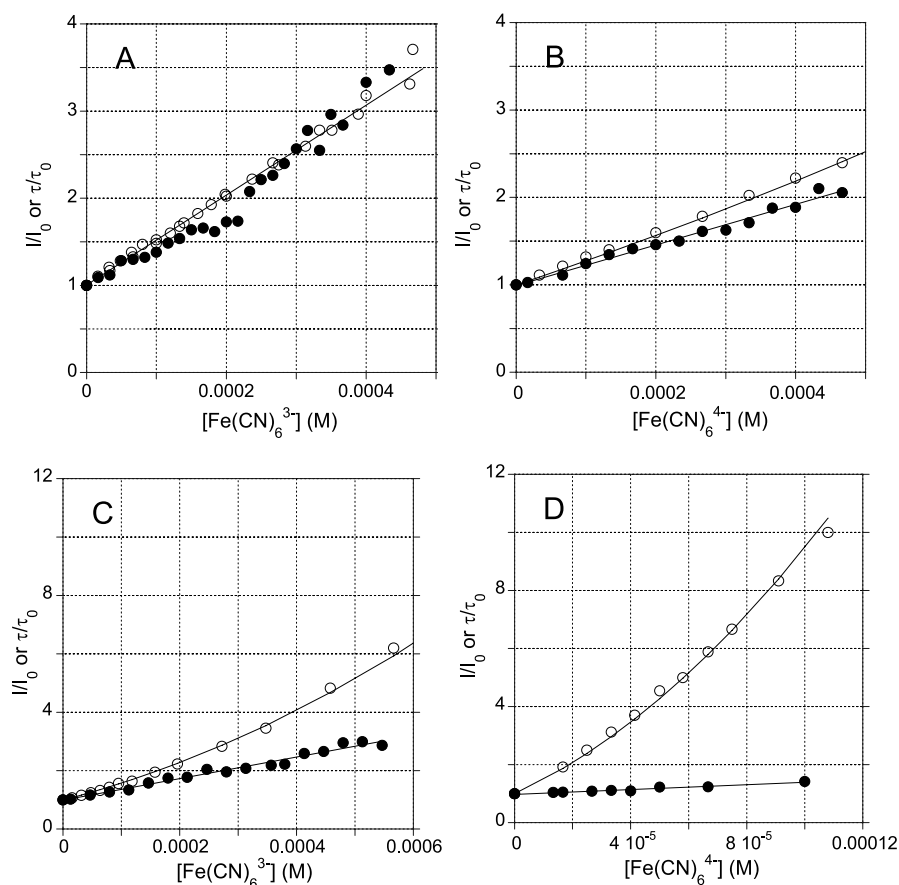


**Fig. 12** Fluorescence intensities (○) and decay times (●) of  $[\text{Ru}(\text{bpy})_3]^{2+}$  (A and B) and **24** in the  $\text{H}_4\text{L}^{6+}$  form (C and D) with  $[\text{Fe}(\text{CN})_6]^{3-}$  and  $[\text{Fe}(\text{CN})_6]^{4-}$  at pH = 4.0 [71]. All the experiments were carried out at 25 °C and air atmosphere

At pH 4.0, compound **24** exists mainly as the form  $\text{H}_4\text{L}^{6+}$ . The Stern–Volmer plots for the adducts involving  $[\text{Ru}(\text{bpy})_3]^{2+}$ , **24** ( $\text{H}_4\text{L}^{6+}$ ) at pH=4.0 with  $[\text{Fe}(\text{CN})_6]^{4-}$  as well as  $[\text{Fe}(\text{CN})_6]^{3-}$  are presented in Fig. 12. Inspection of this figure shows, for the pairs reported in Fig. 12b, Fig. 12c and Fig. 12d, the presence of an upward curvature of  $I_0/I$  in comparison with  $\tau_0/\tau$ , indicating the existence of ion-pair association in the ground state. These systems were treated to take into account both static and dynamic quenching, the resulting constants being reported in Table 1.

**Table 1** Association constants ( $\log K_{\text{ip}}$ ) and quenching rate constants ( $k_{\text{q}}$ ) between  $[\text{Ru}(\text{bpy})_3]^{2+}$  and **24** (with **23** in its  $\text{H}_4\text{L}^{4+}$  form) with  $[\text{Fe}(\text{CN})_6]^{3-}$  and  $[\text{Fe}(\text{CN})_6]^{4-}$  determined from photophysical quenching studies

	Log $K_{\text{ip}}$	$K_{\text{SV}}/\text{M}^{-1}$ <sup>a</sup>	$K_{\text{SV}}/\text{M}^{-1}$ <sup>b</sup>	$k_{\text{q}}/\text{s}^{-1} \text{M}^{-1}$
$[\text{Fe}(\text{CN})_6]^{4-} + [\text{Ru}(\text{bpy})_3]^{2+}$	$\leq 2.5$	2325	1358	$5.8 \times 10^9$ <sup>c</sup>
$[\text{Fe}(\text{CN})_6]^{3-} + [\text{Ru}(\text{bpy})_3]^{2+}$	–	3488	2600	$8.7 \times 10^9$ <sup>c</sup>
$[\text{Fe}(\text{CN})_6]^{4-} + [\text{Ru}(\text{bpy})_2(\text{H}_4\text{L})]^{6+}$	4.7	4164	–	$1.4 \times 10^{10}$ <sup>d</sup>
$[\text{Fe}(\text{CN})_6]^{3-} + [\text{Ru}(\text{bpy})_2(\text{H}_4\text{L})]^{6+}$	3.3	3697	–	$1.3 \times 10^{10}$ <sup>d</sup>

<sup>a</sup> [71]

<sup>b</sup> [77, 78]. All the experiments were carried out at 25 °C and air atmosphere at pH = 4.0

<sup>c</sup> to  $([\text{Ru}(\text{bpy})_3]^{2+}) = 400 \text{ ns}$

<sup>d</sup> to  $([\text{Ru}(\text{bpy})_2(\text{H}_4\text{L})]^{6+}) = 290 \text{ ns}$

The ion-pair association is negligible for the pair between  $[\text{Ru}(\text{bpy})_3]^{2+}$  and  $[\text{Fe}(\text{CN})_6]^{3-}$ . In the case of the pair  $[\text{Ru}(\text{bpy})_3]^{2+}$  and  $[\text{Fe}(\text{CN})_6]^{4-}$ ,  $I_0/I$  is somewhat higher than  $\tau_0/\tau$ , allowing one to calculate an ion-pairing association  $K_{\text{ip}} < 300 \text{ M}^{-1}$ . On the other hand the quenching constants for the dynamic quenching are comparable with those reported by Balzani et al. [81]. The observed differences can be attributed to the differences in ionic strength used by these authors.

As reported previously [81, 82] the mechanism responsible for the observed quenching in the systems involving  $[\text{Ru}(\text{bpy})_3]^{2+}$  and the iron complexes is due to electron transfer from the excited Ru(II) complex to the Fe(III) complex, and vice versa from the Fe(II) complex to the excited Ru(II).

The effect of the polyamine chain in both, ion-pair association constant and dynamic quenching, was studied at pH=4. At this pH value and concentration of the fluorophore ( $1 \times 10^{-5} \text{ M}$ ) ca. four of the five nitrogen atoms of the polyamine macrocycle are protonated. In both systems, **24** with  $[\text{Fe}(\text{CN})_6]^{4-}$  and with  $[\text{Fe}(\text{CN})_6]^{3-}$  the ion pair association dominates the interaction. This is due to the increasing of the charge in the ruthenium complex from 2+ to 6+, and the formation of hydrogen bonding between the



protonated nitrogen molecules of the host and the cyanide ligands of the guest. As expected the ion-pairing association is higher for  $[\text{Fe}(\text{CN})_6]^{4-}$  than for  $[\text{Fe}(\text{CN})_6]^{3-}$ , because of the largest charge in the former. The ion-pair association constants obtained for the **24** and  $[\text{Fe}(\text{CN})_6]^{4-}$  ( $\log K_{\text{ip}} = 4.7$ ) systems is lower than the values obtained by potentiometry ( $\log K_{\text{ip}} = 6.7$ ). This difference can be attributed to the larger influence of the chloride ions from the medium ( $[\text{Cl}^-] = 0.10 \text{ M}$ ) in the case of the fluorimetric measurements ( $[\text{24}] = 1.0 \times 10^{-5} \text{ M}$ ), compared with the potentiometric experiments ( $[\text{24}] = 1.0 \times 10^{-3} \text{ M}$ ).

In which regards the dynamic quenching, Table 1, the values are similar for both adducts and the respective rates seem to indicate that these are controlled by diffusion processes. The small increase of the quenching rate constant from the adducts involving  $[\text{Fe}(\text{CN})_6]^{3-}$  to those with  $[\text{Fe}(\text{CN})_6]^{4-}$  can be attributed to an increase of the driving force for the formation of the encounter complex, due to the increasing of the charge. Our systems involve electron transfer across hydrogen bonds between charged species. They have thus some resemblance with the systems studied by Harriman and Sessler [84–88] and, Nocera [89–91] in which energy/electron transfer in cytosine/guanine H-bonded assemblies and guanidinium/carboxylate salt bridges were studied, respectively. These studies show that both type of bridges influence the rate constants for energy/electron transfer and it cannot be excluded that some kind of mediation involving the hydrogen bonds between the cyanide groups of  $[\text{Fe}(\text{CN})_6]^{3-}$  and  $[\text{Fe}(\text{CN})_6]^{4-}$  and the ammonium groups of **24** may be present in our systems. However, within the time resolution of our equipment (ca. 10 ns), only mono-exponential decays were

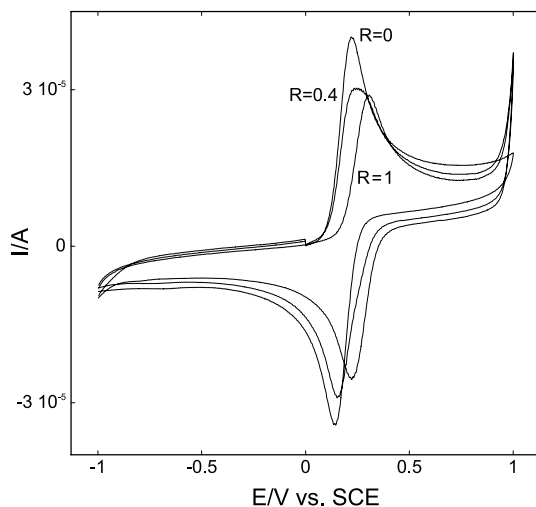


**Fig. 13** Cyclic voltammetry of  $1 \times 10^{-3} \text{ M}$   $[\text{Fe}(\text{CN})_6]^{4-}$  in NaCl 0.1 M and pH = 4.0 as a function of added **24**;  $R = [\text{24}]/[\text{Fe}(\text{CN})_6]^{4-}$

observed which prevents that photoinduced intramolecular electron transfer rate constants could be obtained.

In Fig. 13 are shown the variation of the  $E_{1/2}$  for the iron complex obtained by cyclic voltammetry, as a function of the ratio  $[24]/[\text{Fe}(\text{CN})_6^{4-}]$  for a constant concentration of **24** ( $1 \times 10^{-3}$  M) in NaCl 0.10 M at pH=4. The shift of  $E_{1/2}$ , before and after complexation,  $\Delta E$ , is related to the ratio of the ion-pair association constants of both iron complexes with **24**, by Eq. 3 [92].

$$\Delta E = \frac{RT}{nF} \ln \frac{K_{\text{ip}}(\text{red})}{K_{\text{ip}}(\text{ox})} \quad (3)$$

This equation was used to calculate  $\log K_{\text{ip}}(\text{ox}) = 5.3$  between **24** and  $[\text{Fe}(\text{CN})_6]^{3-}$ , using  $\log K_{\text{ip}}(\text{red}) = 6.7$  obtained from potentiometry carried out in the same conditions of the voltammetry experiments. This value is larger than the one obtained by fluorimetry ( $\log K_{\text{ip}} = 3.3$ ) by the reasons above described, i.e., the influence of the chloride ion.

The results reported above show that the existence of the polyamine chain increases the performance of compound **24** in the sensing the two iron cyanide complexes, when compared with the parent compound  $[\text{Ru}(\text{bpy})_3]^{2+}$ .

### 4.2.3

#### Iodide to Iodine Photocatalytic Oxidation

Aqueous solutions of compound **24**,  $1.55 \times 10^{-4}$  M, in the presence of sodium iodide 0.1 M, lead to the formation of a precipitate. For this reason a mixture water/acetonitrile (9 : 1), at pH=4.3, was used in order to increase the solubility. The absorption spectrum of compound **24** in the presence of  $[\text{I}^-] = 0.1$  M is the summation of the spectra of both components, and thus there is no evidence for the formation of ion-pair charge transfer absorption band. However the fluorescence emission of compound **24** is quenched ca. 5% in the presence of  $[\text{I}^-] = 0.1$  M. In the case of the parent compound  $[\text{Ru}(\text{bpy})_3]^{2+}$  its fluorescence is not affected by addition of the same concentration of iodide. When air equilibrated solutions of compound **24** in the presence of  $[\text{I}^-] = 0.1$  M, at pH=4.3, are irradiated at 436 nm, formation of  $\text{I}_3^-$  is immediately observed by the increasing of its characteristic absorption band centred at 350 nm. The quantum yield of this photo-reaction, based on the total amount of light absorbed by the system is 0.0033. Taking into account that only 5% of the emission of compound **24** is quenched by the iodine the *true* quantum yield is ca. 0.07.

If nitrogen is bubbled in the same solution before irradiation no steady state spectral modifications can be observed. On the contrary saturation of the solutions with dioxygen increase the quantum yield by ca. fivefold. In addition no spectral variations were detected in the absorption spectrum of the parent compound  $[\text{Ru}(\text{bpy})_3]^{2+}$  irradiated in the presence of  $[\text{I}^-] = 0.1$  M.

Formation of iodine from photocatalytic oxidation of iodide is a well established reaction, reported for some other systems, namely for the case of the ion pairs involving iodide and  $\text{Co}(\text{sep})^{3+}$  (sep=sepulchrate=1,3,6,8,10,13,16,19-octaazabicyclo[6.6.6]eicosane) [67]. The experimental results can be accounted for by Fig. 14. Excitation of compound **24** in the MLCT band allows the transfer of one electron from  $\text{I}^-$  to the Ru(II) complex, leading to the formation of an iodine radical and reduced Ru(II) complex (the electron goes to one of the bpy moieties). The iodine radical gives  $\text{I}_3^-$  as a final product by a sequence of well known reactions [81]. The cycle is completed by reoxidation of the reduced bpy moiety of the complex by dioxygen.

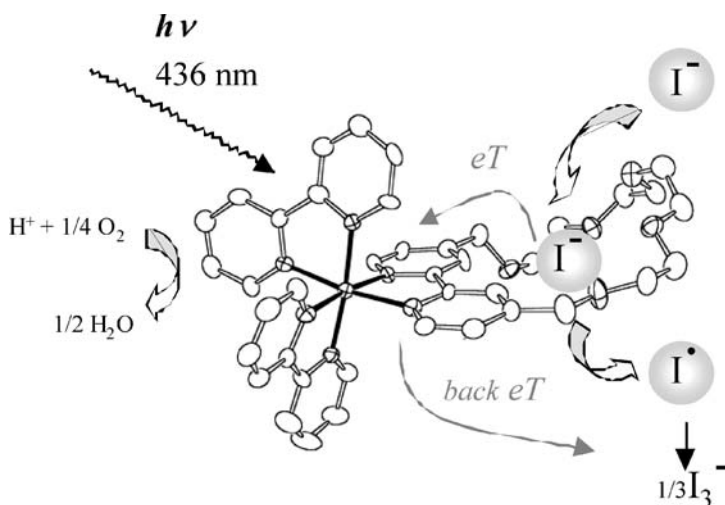
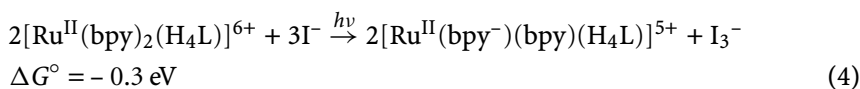


**Fig. 14** Photocatalytic cycle for the oxidation of iodide to iodine by dioxygen using compound **24**

As comproved by the inertness of the parent compound  $[\text{Ru}(\text{bpy})_3]^{2+}$ , the existence of the positively charged macrocyclic receptor seems to be an indispensable requirement to fix the iodide in a position close to the metal, in order to allow the electron transfer process. In the case of **24** (with its polyamine ligand **23** in the  $\text{H}_4\text{L}^{4+}$  form), the net reaction can be accounted by Eq. 4 which is thermodynamically favourable by 0.3 eV.



The relatively low efficiency of this system (0.35 in solution saturated with dioxygen) can be attributed to the fact that only 5% of the excited state can be quenched by iodide. In addition there is evidence, from preliminary flash photolysis experiments, that the back reaction from the reduced Ru(I)

complex to  $I_3^-$  is a competitive process, that decreases the net formation of photo-products.

## References

1. Ulisses Acuña A, Amat-Guerri F (2005) 9th International Conference on Methods and Applications of Fluorescence, Lisbon-Portugal, September book abstracts PL1
2. Beltrami E (1982) *Phytochemistry* 21:2931
3. Stokes GG (1852) *Philos Trans R Soc Lond A* 142:463
4. Sousa LR, Larson JM (1977) *J Am Chem Soc* 99:307
5. De Silva AP (1986) *J Chem Soc Chem Commun*, p 1709
6. Huston ME, Haider KW, Czarnik AW (1988) *J Am Chem Soc* 110:4460
7. Czarnik AW (1994) *Acc Chem Res* 27:302
8. Konopelski JP, Kotzba-Hibert F, Lehn JM, Desvergne JP, Fagès F, Castella A, Bouas-Laurent H, (1985) *J Chem Soc Chem Commun*, p 433
9. Bianchi A, Bowman-James K, García-España E (eds) (1997) *Supramolecular Chemistry of Anions*. Wiley-VCH, New York
10. Fabbrizzi L, Licchelli M, Rabaioni G, Taglietti A (2000) *Coord Chem Rev* 205:85
11. Askaya EU, Huston ME, Czarnik AW (1990) *J Am Chem Soc* 112:7054
12. Bernardo MA, Parola AJ, Pina F, García-España E, Marcelino V, Luis SV, Miravet JF (1995) *J Chem Soc Dalton Trans* 993
13. Bernardo MA, Guerrero JA, García-España E, Luis SV, Llinares JM, Pina F, Ramirez JA, Soriano C (1996) *J Chem Soc Perkin Trans 2* 2335
14. Kuzmin MG, Guseva LN (1969) *Chem Phys Lett* 3:71
15. Chandross EA, Thomas HT (1971) *Chem Phys Lett* 9:393
16. Brimage DRG, Davidson RS (1971) *Chem Commun*, p 1385
17. Cox GS, Turro N, Yang NC, Chen MJ (1984) *J Am Chem Soc* 106:422
18. Konopelski JP, Kotzba-Hibert F, Lehn JM, Desvergne JP, Fagès F, Castella A, Bouas-Laurent H (1985) *J Chem Soc Chem Commun*, p 433
19. Mes GF, van Ramesdonk HJ, Verhoven JW (1984) *J Am Chem Soc* 106:1335
20. Melo MJ, Bernardo MA, Melo EC, Pina F (1996) *J Chem Soc Faraday Trans* 92:957
21. De Silva AP, Rupasinghe RAD (1985) *J Chem Soc Chem Commun*, p 1669
22. De Silva AP, De Silva SA (1986) *J Chem Soc Chem Commun*, p 1709
23. De Silva AP, Gunaratne HQN, McCoy CP (1996) *Chem Commun* 21:2399
24. Fabbrizzi L, Gatti F, Pallavicini P, Parodi L (1998) *New J Chem* 1403
25. Aucejo R, Alarcón J, García-España E, Llinares JM, Marchin KL, Soriano C, Lodeiro C, Bernardo MA, Pina F, Pina J, Seixas de Melo J (2005) *Eur J Inorg Chem* 4301
26. Chandross EA, Dempster CJ (1970) *J Am Chem Soc* 92:3586
27. Hirayama F (1965) *J Chem Phys* 42:3163
28. Sclafani JA, Maranto MT, Sisk T M, Van Arman SA (1996) *Tetrahedron Lett* 37:2193
29. Albelda MT, Bernardo MA, Díaz P, García-España E, de Melo JS, Pina F, Soriano C, Luis SV (2001) *Chem Commun* 1520
30. Melo JS, Albelda MT, Díaz P, Garcia-España E, Lodeiro C, Alves S, Lima JC, Pina F, Soriano C (2002) *J Chem Soc Perkin Trans 2* 991
31. Stevens B, Ban MI (1964) *Trans Faraday Soc* 60:1515
32. Albelda MT, García-España E, Gil L, Lima JC, Lodeiro C, Seixas de Melo J, Melo MJ, Parola AJ, Pina F, Soriano C (2003) *J Phys Chem B* 107:6573
33. Albelda MT, Díaz P, Garcia-España E, Lima JC, Lodeiro C, Melo JS, Parola AJ, Pina F, Soriano C (2002) *Chem Phys Lett* 353:63

34. Albelda MT, Diaz P, Garcia-España E, Lima JC, Lodeiro C, Melo JS, Parola AJ, Pina F, Soriano C (2002) *Chem Phys Lett* 362:179 (erratum)
35. Pina F, Lima JC, Lodeiro C, Melo JS, Diaz P, Albelda MT, Garcia-España E (2002) *J Phys Chem A* 106:8207
36. Izatt RM, Bradshaw JS, Pawlak K, Bruening RL, Tarbet (1992) *Chem Rev* 92:1261
37. Azéma J, Galaup C, Picard C, Tisnès P, Ramos O, Juanes O, Rodríguez-Ubis JC, Brunet E (2000) *Tetrahedron* 56:2673
38. Galaup C, Carrié MC, Tisnès P, Picard C (2001) *Eur J Org Chem* 2165
39. Rodríguez-Ubis JC, Alpha B, Plancherel D, Lehn JM (1984) *Helv Chim Acta* 67:2264
40. Alpha B, Lehn JM, Mathis G (1987) *Angew Chem Int Ed Engl* 26:266
41. Cesario M, Guilhem J, Pascard E, Anklam E, Lehn JM, Pietraskiewicz M (1991) *Helv Chim Acta* 74:1157
42. Bkouche-Waksmann J, Guilhem J, Pascard E, Alpha B, Deshenaux, Lehn JM (1991) *Helv Chim Acta* 75:1163
43. Lehn JM, Regnouf de Vains JB (1992) *Helv Chim Acta* 75:1221
44. Roth C, Lehn JM, Guilhem J, Pascard C (1995) *Helv Chim Acta* 78:1895
45. Barigelletti F, De Cola L, Balzani V, Belsler P, von Zelewsky A, Vögtle F, Ebmeyer F, Grammenudi S (1989) *J Am Chem Soc* 111:4662
46. Balzani V, Ballardini R, Bolletta F, Gandolfi MT, Juris A, Maestri M, Manfrin MF, Moggi L, Sabbatini N (1993) *Coord Chem Rev* 125:75
47. Sabbatini N, Guardigli M, Lehn JM (1993) *Coord Chem Rev* 123:201
48. Balzani V, Credi A, Venturi M (1998) *Coord Chem Rev* 171:3
49. Bazzicalupi C, Bencini A, Bianchi A, Giorgi C, Fusi V, Masotti A, Valtancoli B, Roque A, Pina F (2000) *Chem Commun*, p 561
50. Bazzicalupi C, Bencini A, Berni E, Bianchi A, Giorgi C, Fusi V, Valtancoli B, Lodeiro C, Roque A, Pina F (2001) *Inorg Chem* 40:6172
51. Mallouk TE, Krueger JS, Mayer JE, Dymond CMG (1989) *Inorg Chem* 28:3507
52. Horrocks W, De W, Sudnick DR (1979) *J Am Chem Soc* 101:334
53. Horrocks W, De W, Sudnick DR (1981) *Acc Chem Res* 14:384
54. Izatt RM, Pawlak K, Bradshaw JS, Bruening RL (1991) *Chem Rev* 91:1721
55. Rodríguez-Ubis JC, Alpha B, Plancherel D, Lehn JM (1984) *Helv Chim Acta* 67:2264
56. Alpha B, Lehn JM, Mathis G (1987) *Angew Chem Int Ed Engl* 26:266
57. Cesario M, Guilhem J, Pascard E, Anklam E, Lehn JM, Pietraskiewicz M (1991) *Helv Chim Acta* 74:1157
58. Bkouche-Waksmann J, Guilhem J, Pascard E, Alpha B, Deshenaux, Lehn JM (1991) *Helv Chim Acta* 75:1163
59. Lehn JM, Regnouf de Vains JB (1992) *Helv Chim Acta* 75:1221
60. Roth C, Lehn JM, Guilhem J, Pascard C (1995) *Helv Chim Acta* 78:1895
61. Sabbatini N, Guardigli M, Lehn JM (1993) *Coord Chem Rev* 123:201
62. Balzani V, Credi A, Venturi M (1998) *Coord Chem Rev* 171:3
63. Pina F, Lima JC, Lodeiro C, Melo JS, Diaz P, Albelda MT, Garcia-España E (2002) *J Phys Chem A* 106:8207
64. Smalley JE, Feldberg SW, Chidsey CED, Linford MR, Newton MD, Liu Y-P (1995) *J Phys Chem* 99:131
65. Gloss GL, Calcaterra LT, Green NJ, Penfield KW, Miller JR (1986) *J Phys Chem* 90:3673
66. Finckh P, Heitele H, Volk M, Michele-Beyerle ME (1988) *J Phys Chem* 92:6584
67. Oevering H, Paddon-Row MN, Heppener M, Olivier AM, Cotsaris E, Verhoeven JW, Hush NS (1987) *J Am Chem Soc* 109:3258
68. Moser CC, Keske JM, Warncke K, Farid RS, Dutton PL (1992) *Nature* 355:796
69. Beratan DN, Onuchic JN, Winkler JR, Gray HB (1992) *Science* 258:1740

70. Page CC, Moser CC, Chen X, Dutton PL (1999) *Nature* 402:47
71. Lodeiro C, Pina F, Parola AJ, Bencini A, Bianchi A, Bazzicalupi C, Ciatinni S, Giorgi C, Masotti A, Valtancoli B, de Melo JS (2001) *Inorg Chem* 40:6813
72. Lakowicz JR (ed) (1994) *Probe Design and Chemical Sensing; Topics in Fluorescence Spectroscopy* 4th edn. Plenum Press, New York
73. Murtaza Z, Chang Q, Rao G, Lin H, Lakowicz JR (1997) *Anal Biochem* 247:216
74. Bencini A, Bianchi A, Garcia-España E, Micheloni M, Ramirez JA (1999) *Coord Chem Rev* 188:97
75. Peter F, Gross M, Hosseini MW, Lehn JM, Sessions RB (1981) *J Chem Soc Chem Commun*, p 1067
76. Peter F, Gross M, Hosseini MW, Lehn JM (1983) *Electroanal Chem* 144:279
77. Garcia-España E, Micheloni M, Paoletti P, Bianchi A (1985) *Inorg Chim Acta* 102:L9
78. Bencini A, Bianchi A, Garcia-España E, Giusti M, Mangani S, Micheloni M, Orioli P, Paoletti P (1987) *Inorg Chem* 26:3902
79. Aragón J, Bencini A, Bianchi A, Domenech A, Garcia-España E (1992) *J Chem Soc Dalton Trans* 319
80. Bianchi A, Domenech A, Garcia-España E, Luis S (1993) *Anal Chem* 65:3137
81. Juris A, Gandolfi MT, Manfrin MF, Balzani V (1976) *J Am Chem Soc* 98:1047
82. Mallouk TE, Krueger JS, Mayer JE, Dymond CMG (1989) *Inorg Chem* 28:3507
83. Roundhill DM (1994) *Photochemistry and Photophysics of Metal Complexes*. Plenum Press, New, York
84. Harriman A, Magda DJ, Sessler JL (1991) *J Phys Chem B* 95:1530
85. Harriman A, Magda DJ, Sessler JL (1991) *J Chem Soc Chem Commun*, p 345
86. Harriman A, Kubo Y, Sessler JL (1992) *J Am Chem Soc* 114:388
87. Harrison A, Bing W, Sessler JL (1993) *J Am Chem Soc* 115:10418
88. Harriman A, Bing W, Sessler JL (1995) *J Am Chem Soc* 117:704
89. Turró C, Chang CK, Leroi GE, Cukier RI, Nocera DG (1992) *J Am Chem Soc* 114:4013
90. Roberts JA, Kirby JP, Nocera DG (1995) *J Am Chem Soc* 117:8051
91. Deng Y, Roberts JA, Peng SM, Chang CK, Nocera DG (1997) *Angew Chem Int Ed Engl* 36:2124
92. Bianchi A, Domenech A, Garcia-España E, Luis S (1993) *Anal Chem* 65:3137

## Fluorescence of Fullerenes

Susana Nascimento · Carlos Baleizão · Mário N. Berberan-Santos (✉)

Centro de Química-Física Molecular, Instituto Superior Técnico, 1049-001 Lisboa,  
Portugal  
*mbs@ist.utl.pt*

<b>1</b>	<b>Introduction</b> . . . . .	152
<b>2</b>	<b>Contact Charge-Transfer Complexes with Aromatic Molecules</b> . . . . .	152
2.1	Background . . . . .	152
2.2	Formalism and Methods of Data Analysis . . . . .	154
2.3	Contact CT Pairs: Isotropic and Anisotropic Interactions . . . . .	155
2.4	Application of the Models . . . . .	157
<b>3</b>	<b>Fluorescence Polarization of C<sub>60</sub> and C<sub>70</sub></b> . . . . .	161
3.1	Background . . . . .	161
3.2	Fluorescence Polarization of C <sub>60</sub> . . . . .	163
3.3	Fluorescence Polarization of C <sub>70</sub> . . . . .	165
<b>4</b>	<b>Diels–Alder Monoadducts</b> . . . . .	167
4.1	Photophysical Properties . . . . .	167
4.2	Kinetics of the Diels–Alder Reaction . . . . .	170
<b>5</b>	<b>Heavy-Atom Effects on Methanofullerenes</b> . . . . .	172
5.1	Background . . . . .	172
5.2	Heavy-Atom Effects . . . . .	174
<b>6</b>	<b>Concluding Remarks and Future Perspectives</b> . . . . .	181
	<b>References</b> . . . . .	181

**Abstract** The photophysical properties of fullerenes are selectively reviewed, with an emphasis on fluorescence. It is shown that fullerenes display several unusual photophysical properties, such as their fluorescence anisotropy, and also that they can be used for a more complete understanding of general photophysical processes like charge-transfer complexation and the heavy-atom effect. In spite of the work already carried out, knowledge of the photophysics of fullerenes and derivatives is still incomplete, and much remains to be done in this area.

**Keywords** Fullerenes · C<sub>60</sub> · C<sub>70</sub> · Fluorescence anisotropy · Heavy-atom effect · Contact charge-transfer complex

### Abbreviations

CT Charge transfer  
DA Donor–acceptor 1 : 1 complex

DEM	Diethyl methano[60]fullerene-dicarboxylate
$g(r)$	Radial distribution function
MN	1-methylnaphthalene
N	Maximum coordination number for contact CT complexes
$p$	Fraction of DA pairs with favourable orientation
RSA	Reverse saturable absorption

## 1

### Introduction

The most common fullerenes,  $C_{60}$  and  $C_{70}$ , consist of three-dimensional structures containing a relatively high number of atoms, and can be viewed either as large carbon molecules or as tiny nanoparticles. Their photophysical and photochemical properties result from the many delocalized pi electrons present and also from the high symmetry and curvature of the structures. The photophysics of fullerenes and, in special, of  $C_{60}$  and derivatives has been the subject of considerable investigation in the last 15 years [1–3]. Much attention was paid, in particular, to the triplet state. In fact, the fluorescence quantum yield of these compounds is usually quite low (ca.  $5 \times 10^{-4}$ ), owing to a very efficient intersystem crossing. Nevertheless, many interesting results can be obtained from the study of the usually weak fluorescence of  $C_{60}$ ,  $C_{70}$ , and derivatives. Herein, we review some of the achievements of our group in the field of fullerene photophysics, with an emphasis on fluorescence properties.

## 2

### Contact Charge-Transfer Complexes with Aromatic Molecules

#### 2.1

##### Background

Charge-transfer (CT) bands in electronic absorption spectra are often observed in solutions where the solvent-solute interaction is of the donor-acceptor type. They are also observed when a suitable donor-acceptor pair is dissolved in an inert solvent. However, the existence of a CT band does not imply the existence of a stable charge-transfer complex. Essentially unbound molecular pairs, the so-called contact pairs (which could also be called physical complexes), may also display a modified absorption spectrum, including the appearance of one or more broad, structureless CT bands [4–6]. The binding energy of contact pairs is negligible, that is, smaller than the thermal agitation energy ( $RT = 3 \text{ kJ mol}^{-1}$  at 300 K), and the apparent formation equilibrium constant  $K$  is very small (typically between 0.1 and  $1 \text{ M}^{-1}$ ) and temperature independent. On the other hand, for stable ground-state CT molecular complexes the binding energy is significant, and the formation



equilibrium constant is much larger than the statistical pair value, decreasing with a temperature increase according to the van't Hoff equation.

The existence of CT bands in the absorption spectrum of the contact pair implies that, unlike the ground state, some of its excited states have a significant binding energy. When the lowest excited state is bound, one can speak of an exciplex. However, it may also happen that the lowest excited state of the contact pair is of the locally excited type, the excitation being mainly localized in the donor or in the acceptor. In such a case, all CT bands correspond to transitions to higher excited states. There are, therefore, two types of contact pairs: (i) Those that form exciplexes (exciplex forming contact pairs), whose lowest CT band corresponds to a transition to the first excited state; and (ii) Those that do not form exciplexes, whose CT bands correspond to transitions to higher excited states (simple contact pairs). It should be noted that the energy of (emissive) exciplexes is defined by the relevant band in the observed fluorescence spectrum whose frequency corresponds to the relaxed geometry of the excited complex and not to that of the Franck–Condon state relevant for absorption.

Despite extensive  $\pi$ -electron delocalization, fullerenes are electron-deficient species [7], acting as electron acceptors (A) and giving rise to charge-transfer bands when interacting with a variety of electron donors (D), including amines [8–12], calyx[n]arenes [13–16], crown ethers [17, 18], cyclodextrins [19, 20], and aromatic hydrocarbons [21–26].

The CT interaction of  $C_{60}$  with 1-methylnaphthalene (MN) was studied by Scurlock and Ogilby [21], who reported a very weakly bound or essentially unbound ground-state CT complex with a small equilibrium constant of  $0.08 \pm 0.02 \text{ M}^{-1}$  in toluene. The respective CT band has a maximum located at 425 nm, with a molar absorption coefficient of  $11\,000 \text{ M}^{-1} \text{ cm}^{-1}$  [21]. Later, Sibley et al. [22] studied the interaction of  $C_{60}$  with polycyclic aromatic hydrocarbons, reporting  $K = 0.1 \text{ M}^{-1}$  for the  $C_{60}$ -naphthalene complex and further constants whose values increased by an order of magnitude as the number of aromatic rings of the donor increased. The measured enthalpies of complex formation [22] that were obtained from van't Hoff plots are, nevertheless, dubious because they are always smaller than  $RT$ . The above results point therefore to CT associations essentially of the contact type, although this has not been explicitly recognized. In contradiction with these results, substantially larger equilibrium constants were reported for the same  $C_{60}$  systems with values ranging from 0.7 to  $66 \text{ M}^{-1}$ , depending on the number of aromatic rings of the donor [23]. Again, in a study of the charge-transfer interaction of  $C_{70}$  with aromatic hydrocarbons, Bhattacharya et al. [26] report high equilibrium constants with values ranging from 11 to  $490 \text{ M}^{-1}$ , and significant formation enthalpies with values ranging from  $-21$  to  $-66 \text{ kJ mol}^{-1}$ .

To overcome and clarify the conflicting results in the literature on the interaction of  $C_{60}$  and  $C_{70}$  with aromatic hydrocarbons, namely, naphthalene, 1-methylnaphthalene, and anthracene, a new treatment of the pseudo-

equilibrium of contact pairs and higher complexes was developed and new measurements were carried out [27].

## 2.2

### Formalism and Methods of Data Analysis

The formation of 1 : 1 donor–acceptor CT complexes DA



has an associated concentration equilibrium constant

$$K = \frac{[DA]}{[D][A]}. \quad (2)$$

It is assumed that  $K$  is only a function of temperature, that is, it is proportional to the true (thermodynamic) equilibrium constant written in terms of activities.

Spectrophotometric studies for the evaluation of  $K$  are usually carried out with a small and fixed concentration of D or A and varying the concentration of the other partner in the complex, usually present in large excess. Here, it will always be assumed that A (fullerene) was fixed and at low concentration and that D (aromatic hydrocarbon) is in large excess.

Considering first a wavelength where only the complex DA absorbs, the absorbance is

$$A = \varepsilon_{CT} [DA] l = \varepsilon_{CT} l \frac{K [A]_0 [D]_0}{1 + K [D]_0}, \quad (3)$$

where  $\varepsilon_{CT}$  is the molar absorption coefficient of the complex,  $l$  is the optical path length,  $[A]_0$  is the analytical (total) concentration of acceptor, and  $[D]_0$  is the total concentration of donor. The unknowns are  $\varepsilon_{CT}$  and  $K$ .

For a wavelength where both A and the complex DA absorb one has instead of Eq. 3,

$$A = \varepsilon_A [A] l + \varepsilon_{CT} [DA] l = A_0 \frac{1 + K' [D]_0}{1 + K [D]_0}, \quad (4)$$

where

$$A_0 = \varepsilon_A [A]_0 l, \quad (5)$$

is the absorbance in the absence of donor, and  $K'$  is

$$K' = \frac{\varepsilon_{CT}}{\varepsilon_A} K = \alpha K. \quad (6)$$

A plot of  $A/A_0$  vs.  $[D]_0$  thus enables the determination of  $\varepsilon_{CT}$  and  $K$  as

$$\frac{A}{A_0} = \frac{\frac{1}{K} + \alpha [D]_0}{\frac{1}{K} + [D]_0}. \quad (7)$$

A linearized form of Eq. 4 known as Ketelaar's equation [28] is

$$\frac{[A]_0 l}{A - A_0} = \frac{1}{\varepsilon_{CT} - \varepsilon_A} + \frac{1}{(\varepsilon_{CT} - \varepsilon_A)K [D]_0}. \quad (8)$$

Once the equilibrium constant  $K$  has been determined, the absorption spectrum of the CT complex can be obtained from Eq. 7, rewritten as

$$\varepsilon_{CT}(\lambda) = \frac{1}{[A]_0 l} \left\{ \frac{1}{K [D]_0} [A(\lambda) - A_0(\lambda)] + A(\lambda) \right\}. \quad (9)$$

The spectrum of the CT complex is frequently discussed on the basis of the difference spectrum between the  $D + A$  solution, where the concentration of free  $A$  is  $[A]$ , and the pure  $A$  solution (concentration  $[A]_0$ ), that is  $A(\lambda) - A_0(\lambda)$ . Although this procedure certainly provides evidence of spectral changes accompanying complexation, it is incorrect because it implicitly assumes that in the  $D + A$  solution the concentration of  $A$  in the complex form is negligible, which is not usually the case, cf. Eq. 9. Note also that, because  $K$  is indirectly evaluated from measurements of the absorption spectrum, if there is a solvent effect on the CT absorption, then  $K$  may not be independent of  $[D]$  as assumed. It is therefore important to compute the spectrum of the complex for several concentrations of  $D$ , to confirm that it is essentially independent of  $[D]$ .

## 2.3

### Contact CT Pairs: Isotropic and Anisotropic Interactions

A full treatment of the contact interaction must take into account the possibility of formation of complexes  $D_nA$ , with  $n > 1$ . Only when these are included does a coherent picture (effective multiple equilibrium) emerge. In fact, for sufficiently concentrated solutions, precisely those for which the contact CT pairs are observable, there is the possibility of contact associations of the type  $D_nA$  with  $n > 1$  and up to a maximum coordination number  $N$ . In the case of fullerene-aromatic hydrocarbon systems, simple steric considerations lead to a maximum number of donors around the fullerene of 20 or more. Indeed, considering only the possibility of direct  $\pi$ - $\pi$  interaction between a benzene ring and a hexagon of the fullerene, there are 20 ( $C_{60}$ ) or 25 ( $C_{70}$ ) potential CT sites on each fullerene molecule.

Assuming that all contact complexes have a common molar absorption coefficient  $\varepsilon_{CT}$ , we find that the absorbance at a wavelength where only the CT band is observed is given by [27]

$$A = \varepsilon_{CT} l \left[ 1 - \left( 1 - \frac{K [D]_0}{N} \right)^N \right] [A]_0. \quad (10)$$

For large  $N$ , and for  $[D]_0 \ll [D]_{\max}$ , Eq. 10 reduces to

$$A = \varepsilon_{CT} l [1 - \exp(-K [D]_0)] [A]_0, \quad (11)$$

which for relatively small  $[D]_0$  yields

$$A = \varepsilon_{CT} l K [A]_0 [D]_0. \quad (12)$$

For small  $K$ , Eq. 12 can be obeyed up to very high concentrations of  $D$ , but this fact obviously does not imply that  $K = 0$ , as previously assumed by several authors [4, 5, 28, 29].

For a wavelength where  $A$  also absorbs, Eqs. 10 and 11 become

$$A = \varepsilon_A l \left[ 1 - \left( 1 - \frac{K [D]_0}{N} \right)^N \right] [A]_0 + \varepsilon_{CT} l \left[ 1 - \left( 1 - \frac{K [D]_0}{N} \right)^N \right] [A]_0, \quad (13)$$

$$A = \varepsilon_A l \exp(-K [D]_0) [A]_0 + \varepsilon_{CT} l [1 - \exp(-K [D]_0)] [A]_0. \quad (14)$$

Equation 14 can be rewritten as

$$\frac{A}{A_0} = \exp(-K [D]_0) + \alpha [1 - \exp(-K [D]_0)], \quad (15)$$

where  $\alpha$  is defined by Eq. 6.

If it is now instead assumed that the molar absorption coefficient of the complex  $D_n A$  is given by  $n$  times  $\varepsilon_{CT}$ , then the absorbance at a wavelength where only the CT band is observed is given by

$$A = \varepsilon_{CT} \sum_{n=1}^N n [D_n A] l = \varepsilon_{CT} l K [A]_0 [D]_0, \quad (16)$$

and a linear dependence of the absorbance with  $[D]_0$  is obeyed for the entire donor concentration range. As before, this linear dependence does not imply that  $K = 0$ . For a wavelength where the acceptor also absorbs, Eq. 16 becomes

$$A = \varepsilon_A l \left( 1 - \frac{K [D]_0}{N} \right)^N [A]_0 + \varepsilon_{CT} l K [A]_0 [D]_0, \quad (17)$$

an equation that is to be contrasted with Eq. 13.

A more realistic model should include the possibility of anisotropic interactions. These can be approximately included in the previous model by considering that only a fraction  $p$  of all  $DA$  pairs has a favourable orientation and can give rise to a CT band. For  $D_n A$  complexes, the fraction with at least one  $DA$  pair favourably oriented is given by  $1 - (1 - p)^n$ . Assuming that all contact complexes with at least one  $DA$  pair favourably oriented have a common molar absorption coefficient  $\varepsilon_{CT}$ , the absorbance at a wavelength where

only the CT band is observed is given by [27]

$$A = \varepsilon_{CT} l \left[ 1 - \left( 1 - \frac{pV_m [D]_0}{N} \right)^N \right] [A]_0, \quad (18)$$

where  $V_m$  is a molar volume characteristic of the CT complex [27]. Therefore, a spectrophotometric study will give an effective equilibrium constant  $K = pV_m$  for the DA pairs.

For a wavelength where the acceptor also absorbs, Eq. 18 becomes

$$A = \varepsilon_A l \left( 1 - \frac{pV_m [D]_0}{N} \right)^N [A]_0 + \varepsilon_{CT} l \left[ 1 - \left( 1 - \frac{pV_m [D]_0}{N} \right)^N \right] [A]_0, \quad (19)$$

and again the only difference is that  $pV_m$  is substituted for  $V_m$  (compare with Eq. 14).

Once the equilibrium constant  $K$  is determined, the absorption spectrum of the CT complexes can be obtained from Eqs. 14 or 19 (in the limit of large  $N$ ), rewritten as

$$\varepsilon_{CT}(\lambda) = \varepsilon_A(\lambda) \frac{\frac{A(\lambda)}{A_0(\lambda)} - e^{-K[D]_0}}{1 - e^{-K[D]_0}}. \quad (20)$$

## 2.4

### Application of the Models

The donor-acceptor interaction of  $C_{60}$  and  $C_{70}$  with aromatic hydrocarbons is accompanied by the appearance of at least one CT band in the 400–500 nm region of the electronic absorption spectrum [27]. Figures 1 and 2 display the absorption spectra of solutions of  $C_{60}$  and  $C_{70}$  in toluene-MN mixtures, with the CT interaction being clearly seen. Similar results were obtained in  $CCl_4$ .

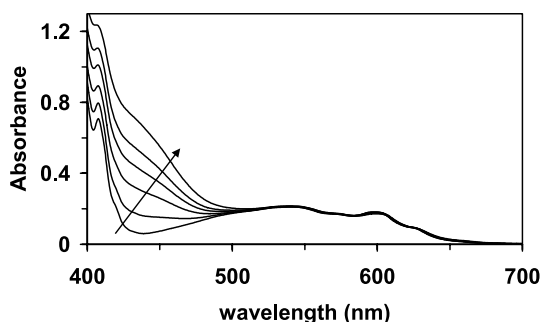


**Fig. 1** Absorption spectra of  $C_{60}$  + MN in toluene-MN solutions. MN concentration increases according to the arrow. The displayed curves correspond to the following MN concentrations: 0, 0.36, 1.01, 1.58, 2.16, and 3.59 M. The concentration of  $C_{60}$  is fixed at  $2 \times 10^{-4}$  M. From [27]

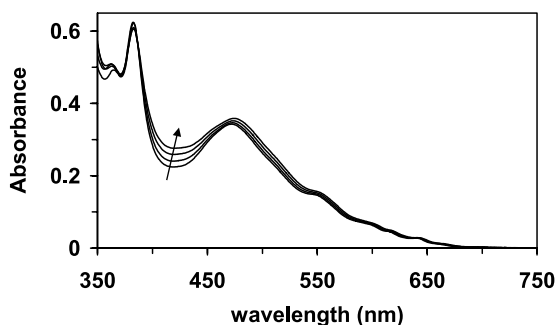


**Fig. 2** Absorption spectra of  $C_{70}$  + MN in toluene-MN solutions. MN concentration increases according to the *arrow*. The displayed curves correspond to the following MN concentrations: 0, 0.86, 2.16, and 3.59 M. The concentration of  $C_{70}$  is fixed at  $2 \times 10^{-5}$  M. From [27]

Formation equilibrium constants  $K$  and CT spectra were estimated using the first method described previously. Data taken at different wavelengths in the spectral range of increasing absorbances were plotted according to Eq. 8, that is, as  $[A]_0/\Delta A$  versus  $1/[D]_0$ . These linear regressions were used for the determination of the initial estimates of  $K$  and  $\varepsilon_{CT}$ . Then, non-linear fits were performed according to Eq. 7. The results are summarized in Tables 1 and 2, and a typical fit is shown in Fig. 3. A global error analysis was performed with all measurements, carried out at several wavelengths, and leads to the conclu-

**Table 1** Formation equilibrium constants of  $C_{60}$ -MN and  $C_{70}$ -MN in toluene at different temperatures (Single DA Complex Model), evaluated at 440 nm. From [27]

		22 °C	44 °C	65 °C
$C_{60}$	$K$ ( $M^{-1}$ )	0.3	0.2	0.2
	$\varepsilon$ ( $10^3 M^{-1} cm^{-1}$ )	6.1	6.1	7.5
$C_{70}$	$K$ ( $M^{-1}$ )	0.1	0.08	0.1
	$\varepsilon$ ( $10^4 M^{-1} cm^{-1}$ )	1.9	2.0	1.8

**Table 2** Formation equilibrium constants of  $C_{60}$ -MN and  $C_{70}$ -MN systems in  $CCl_4$  at room temperature (Single DA Complex Model), evaluated at two different wavelengths. From [27]

	$C_{60}$ 435 nm	445 nm	$C_{70}$ 410 nm	426 nm
$K$ ( $M^{-1}$ )	0.2	0.3	0.6	0.7
$\varepsilon$ ( $10^4 M^{-1} cm^{-1}$ )	0.85	0.65	1.9	1.9

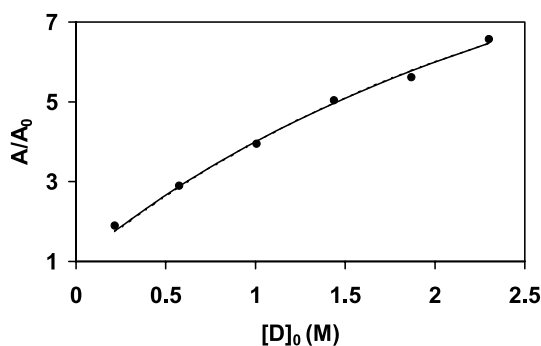


**Fig. 3** Reduced absorbance ( $A/A_0$ ) at 440 nm of  $C_{60}$  + MN in toluene-MN solutions. MN concentration ( $[D]_0$ ) varies from 0.2 to 2.3 M, and  $C_{60}$  concentration is fixed at  $2 \times 10^{-4}$  M. The solid lines corresponding to fits with Eqs. 7 ( $K = 0.25 \text{ M}^{-1}$  and  $\alpha = 15.9$ ) and 15 ( $K = 0.40 \text{ M}^{-1}$  and  $\alpha = 10.1$ ) are very close and cannot be distinguished in the figure. From [27]

sion that the computed equilibrium constants usually have no more than one significant figure, which suffices for most purposes.

The absorption spectra of the fullerene-MN complexes, displayed in Figs. 4 and 5, were obtained from Eq. 9 and found to be essentially independent of the concentration of MN. The smaller spectral changes observed for the  $C_{70}$ -MN solutions (Fig. 2), compared to those of  $C_{60}$  (Fig. 1), are explained by the relatively more similar spectra in the  $C_{70}$  case. The CT bands occur at similar wavelengths for  $C_{60}$  (425 nm,  $\epsilon_{\text{max}} = 7400 \text{ M}^{-1} \text{ cm}^{-1}$ ) and  $C_{70}$  (424 nm,  $\epsilon_{\text{max}} = 19600 \text{ M}^{-1} \text{ cm}^{-1}$ ).

Considering the possibility of multi-equilibrium (contact associations of the type  $D_nA$ ) in concentrated solutions, data were fit to Eq. 15. In all cases, the exponential fitting was satisfactory, as shown in Fig. 3. The shape of the

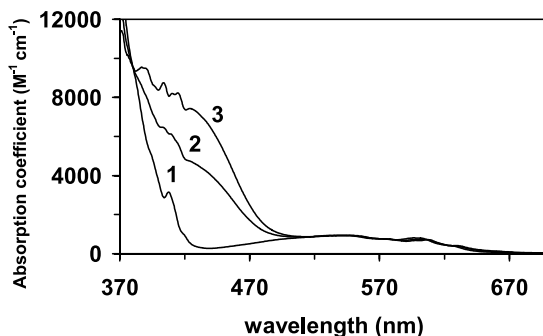


**Fig. 4** Absorption spectrum of the  $C_{60}$ -MN CT complex in toluene calculated according to two models: multi-equilibrium contact complexes (2) and single DA complex (3). The spectrum of  $C_{60}$  (1) is also displayed. From [27]

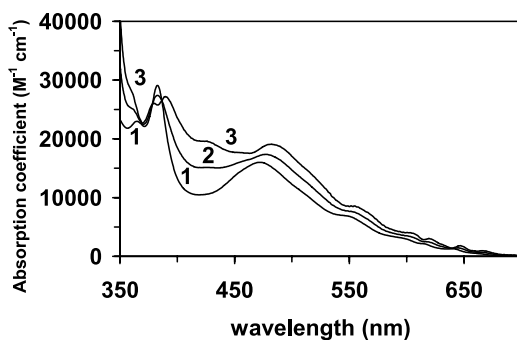


**Fig. 5** Absorption spectrum of the  $C_{70}$ -MN CT complex in toluene calculated according to two models: multi-equilibrium contact complexes (2) and single DA complex (3). The spectrum of  $C_{70}$  (1) is also displayed. From [27]

experimental curves of absorbance versus donor concentration (downward concavity) was not compatible with Eq. 19, and it was concluded that the molar absorption coefficient of the complex  $D_nA$  was not  $n\epsilon_{CT}$  but close to  $\epsilon_{CT}$ , irrespective of the value of  $n$ . This is what can be expected for a low value of the orientational parameter  $p$ ; even for high  $n$ , at most only one D molecule was effective in the CT interaction and the probability of a second molecule of D in the coordinating sphere being favourably oriented at the same time being negligible. A low value of  $p$  was indeed supported by the measured  $K$  values.

The calculated spectra and equilibrium constants for the DA complex do not coincide with those previously obtained by assuming a single equilibrium. The equilibrium constants for the DA complex are slightly higher for the multi-equilibrium model and the absorption coefficients are correspondingly smaller. For  $C_{60}$ -MN system, an equilibrium constant of  $0.4 M^{-1}$  in toluene and  $CCl_4$  was obtained, and in the case of  $C_{70}$ -MN, it was  $0.2 M^{-1}$  in toluene and  $0.7 M^{-1}$  in  $CCl_4$ . The absorption spectra of the fullerene-MN complexes, displayed in Figs. 4 and 5, were obtained from Eq. 20 and found to be essentially independent of the concentration of MN. It was observed that they do not differ much from those obtained for the single complex model, except that the absorption coefficients are somewhat smaller. The CT bands occur at similar wavelengths for  $C_{60}$  (shoulder at 425 nm,  $\epsilon_{max} = 4900 M^{-1} cm^{-1}$ ) and  $C_{70}$  (427 nm,  $\epsilon_{max} = 15\,100 M^{-1} cm^{-1}$ ). The calculated oscillator strengths of the CT bands are  $f = 0.1$  ( $C_{60}$ ) and  $f = 0.2$  ( $C_{70}$ ), corresponding to transition dipole moments of 3 and 4 D, respectively.

The  $K$  values obtained from both models agree with the view that the complexes are of the contact type. In this way, one has in general  $K = pV_m$ . Quantum calculations of the CT interaction between fullerenes and aromatic donors as a function of distance and orientation would be most helpful but are not available at present.



Experiments were also performed with anthracene in toluene. Only a slight increase in absorption intensity was observed for C<sub>70</sub>. Owing to the very small spectral changes, no reliable  $K$  and  $\epsilon_{CT}$  values could be evaluated. However, C<sub>60</sub> undergoes a Diels–Alder reaction with anthracene, even at room temperature, yielding the corresponding Diels–Alder monoadduct, with characteristic absorption bands at 432 and 706 nm [30], see Sect. 4.2 below. In this way, published results [12, 23, 26] on possible C<sub>60</sub>-anthracene and C<sub>70</sub>-anthracene CT complexes appear to be invalid.

As a final critical test on the nature of the CT complexes, the effect of temperature on the equilibrium constant for the fullerene-MN systems in toluene was studied. For both C<sub>60</sub> and C<sub>70</sub>, no significant changes of  $K$  with temperature were observed in the range of 22–65 °C, Table 1, in disagreement with previous studies on related systems [22, 25, 26]. It was thus concluded that the equilibrium constant was essentially temperature independent, as expected for contact complexes.

In this way, we developed a new model for the pseudo-equilibria and absorption spectra of contact complexes; in particular, it implies that a small but non-zero effective equilibrium constant can be defined for contact pairs and all higher-order contact complexes. The model was applied to the interaction of fullerenes with aromatic hydrocarbons, allowing one to show that only contact complexes are formed.

### 3 Fluorescence Polarization of C<sub>60</sub> and C<sub>70</sub>

#### 3.1 Background

The linear polarization of the fluorescence emitted at a right angle with the excitation direction is conveniently measured by the quantity anisotropy,  $r$ , parameter named by Jablonski [31] but in fact pioneered by F. Perrin [32],

$$r = \frac{I_{||} - I_{\perp}}{I_{||} + 2I_{\perp}}, \quad (21)$$

where  $I_{||}$  is the intensity of the fluorescence with vertical polarization and  $I_{\perp}$  is the intensity of the fluorescence with horizontal polarization, the excitation being made with vertically polarized light, as shown in Fig. 6.

For a ground state isotropic distribution of molecules, the fluorescence anisotropy is a direct measure of the angular correlation between the (one-photon) absorption and the emission transition dipoles [33, 34]

$$r(t) = 0.4 \frac{3 \langle \cos^2 \alpha \rangle (t) - 1}{2}, \quad (22)$$

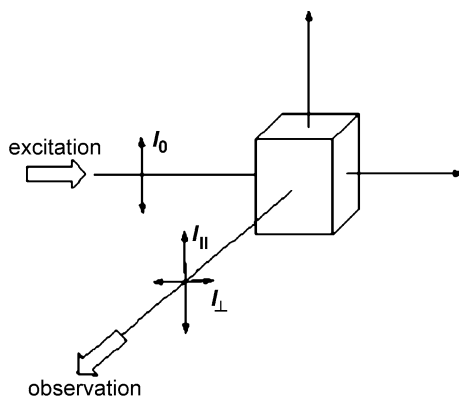


**Fig. 6** Isotropic sample excited with vertically polarized light. The fluorescence emitted in the plane perpendicular to the polarization direction of the excitation can be decomposed into vertically polarized (parallel,  $I_{||}$ ) and horizontally polarized (perpendicular,  $I_{\perp}$ ) components

where  $\alpha$  is the angle between absorption and emission transition dipoles and  $\langle \dots \rangle$  denotes the ensemble average which is in general a function of time. If rotation and energy migration do not occur within the excited state lifetime, the anisotropy in response to excitation by a  $\delta(t)$  pulse is constant in time and identical to that obtained for steady-state excitation. In such a case, both reduce to the fundamental anisotropy  $r_0$  [33, 34]

$$r_0 = 0.4 \frac{3 \langle \cos^2 \alpha \rangle - 1}{2}, \quad (23)$$

where  $\langle \dots \rangle$  is now an average over the angular distribution within the molecular framework. Upper and lower bounds for the fundamental anisotropy are 0.4 (collinear absorption and emission) and  $-0.2$  (orthogonal absorption and emission).

If three mutually perpendicular axes are defined with respect to the molecular framework (molecular frame), these three axes are frequently non-equivalent from the symmetry point of view. In that case, the angle  $\alpha$  is unique for a given pair of excitation and emission wavelengths; in particular it is zero for excitation at the  $0-0$  band of  $S_1$ , provided the emitting  $S_1$  retains the Franck–Condon geometry. Hence, the fundamental anisotropy takes its maximum value, 0.4, when exciting at the  $S_1$   $0-0$  band.

However, if two of the axes of the molecular frame are equivalent,  $x$  and  $y$  say, and if the absorption and the (several equivalent) emission transition moments occur in the  $xy$  plane, then the fundamental anisotropy will have as its maximum value only 0.1 [35, 36]. This was conclusively shown to be the case for benzene (ground state symmetry point group  $D_{6h}$ ) and triphenylene (ground state point group  $D_{3h}$ ) [35–37].

For the even more symmetrical molecules belonging to the tetrahedral, octahedral and icosahedral point groups, where the  $x$ ,  $y$  and  $z$  axes are equivalent, the possibility of intrinsically unpolarized fluorescence arises.

### 3.2

#### Fluorescence Polarization of $C_{60}$

An interesting case is the  $C_{60}$  molecule, which belongs to the icosahedral ( $I_h$ ) point group, as shown by its  $^{13}\text{C}$ -NMR [38, 39], IR absorption [40, 41] and vibrational Raman [41] spectra. The discovery of the weak fluorescence of  $C_{60}$  [42–45] led us to investigate its fundamental polarization [46].

The steady-state fluorescence anisotropy at 140 K determined using a rigid solvent [toluene-ethanol (10 : 1 v/v) mixture] is shown in Fig. 7 together with the absorption spectrum at room temperature. As regards the anisotropy, four distinct regions were defined (A–D in Fig. 7). In regions A (380–410 nm) and C (460–540 nm) the anisotropy was essentially zero, while it was slightly higher than zero in B (410–460 nm) and progressively departs from zero in

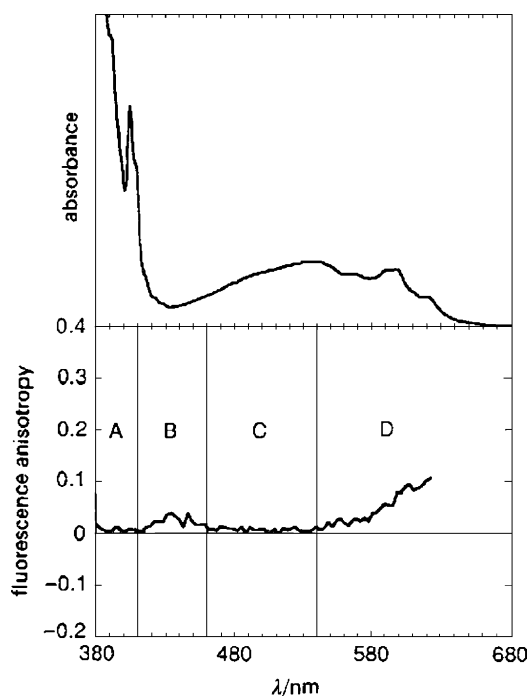


**Fig. 7** Absorption spectrum (room temperature) and steady-state fluorescence anisotropy (140 K) of  $C_{60}$ , in a toluene-ethanol (10 : 1 v/v) mixture. The fluorescence anisotropy was recorded as a function of the excitation wavelength, the emission wavelength being fixed at 740 nm. From [46]

D ( $> 540$  nm). The non-zero value in B was attributed to residual stray light (whose polarization is mainly vertical), which becomes of concern when little exciting light is absorbed, as occurs around the absorption minimum at 438 nm (absorbance = 0.05): this has the effect of increasing the amount of stray light and at the same time the fluorescence becomes weaker. In region D, the progressive increase in the anisotropy was due to the combined effect of stray light, increasingly important as the emission wavelength is approached, and polarized Raman scattering by the solvent (ca.  $3100\text{ cm}^{-1}$ , prominent toluene fundamental), the magnitude of which was found to be comparable to the fluorescence of  $C_{60}$  [46].

The decay of fluorescence anisotropy (Fig. 8) consists of a fast decay component (less than 1 ps, as obtained from the global analysis of the polarized components), identified as polarized Raman scattering, followed by a constant plateau, where  $r = 0.001 \pm 0.005$  for at least 2.7 ns, i.e., the full-time range of the experiment [47]. This result (essentially zero anisotropy) is expected on the basis of the high symmetry of  $C_{60}$ , and agrees with the steady state results obtained in the toluene-ethanol glass [46].

$C_{60}$  was the first carbon molecule to display intrinsically unpolarized fluorescence, owing to its unusually high symmetry.

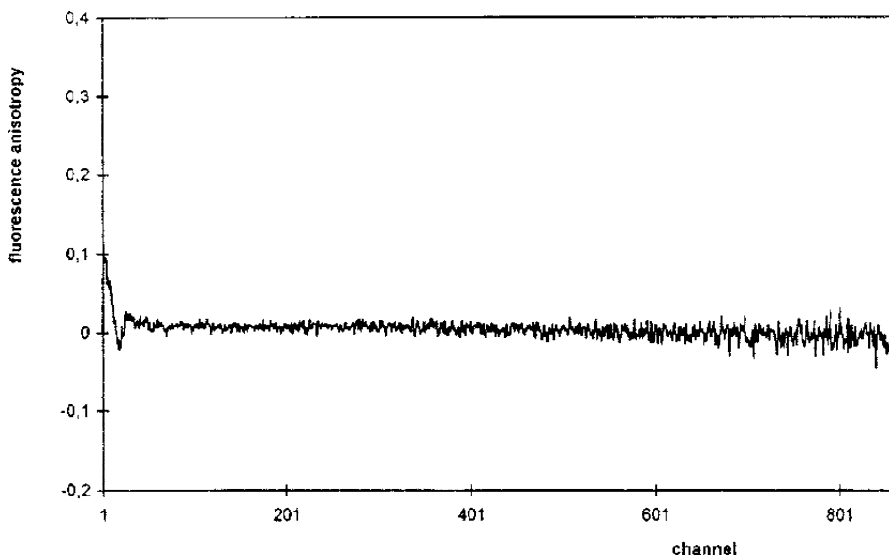


**Fig. 8** Experimental fluorescence anisotropy decay of  $C_{60}$  in the methylcyclohexane-toluene (7 : 2, v/v) mixture glass at 110 K, computed with Eq. 24 using the undeconvoluted polarized components.  $[C_{60}] = 8 \times 10^{-5}$  M. The excitation and emission wavelengths were 595 and 690 nm. The timescale was 2.77 ps/channel. It is seen that, after the impulse duration (FWHM = 35 ps, or 13 channels), the anisotropy has a nearly constant value close to zero ( $0.001 \pm 0.005$ ). From [47]

### 3.3 Fluorescence Polarization of $C_{70}$

From the point of view of symmetry,  $C_{70}$  is again an interesting molecule. The molecule is known to belong to the  $D_{5h}$  point group, thus having two equivalent axes ( $x$  and  $y$ ). The electronic transition moment for  $S_1-S_0$  may, in principle, occur either along the  $z$ -axis or in the  $xy$  plane. In the first case, the fundamental anisotropy of  $C_{70}$  may take values between 0.4 and  $-0.2$ , depending on the excitation wavelength. In the second case, the fundamental anisotropy of  $C_{70}$  may take values only between 0.1 and  $-0.2$ , depending on the excitation wavelength. As mentioned above, cases where 0.1 is the maximum allowed value are known for planar molecules belonging to the  $D_{nh}$  point groups ( $n \geq 3$ ). In these, however, fluorescence anisotropy values cannot be different from 0.1, because all singlet-singlet one-photon transitions are in-plane, whereas in  $C_{70}$  out-of plane ones (i.e., along the  $z$ -axis) are also possible. The first theoretical calculations on the polarization of the electronic transitions of  $C_{70}$  [48] predicted the electronic transition moment for  $S_1 \leftarrow S_0$  to be in the  $xy$  plane. The results obtained by us supported such a conclusion [47], and were later used to calibrate state-of-the-art quantum chemical calculations [49].

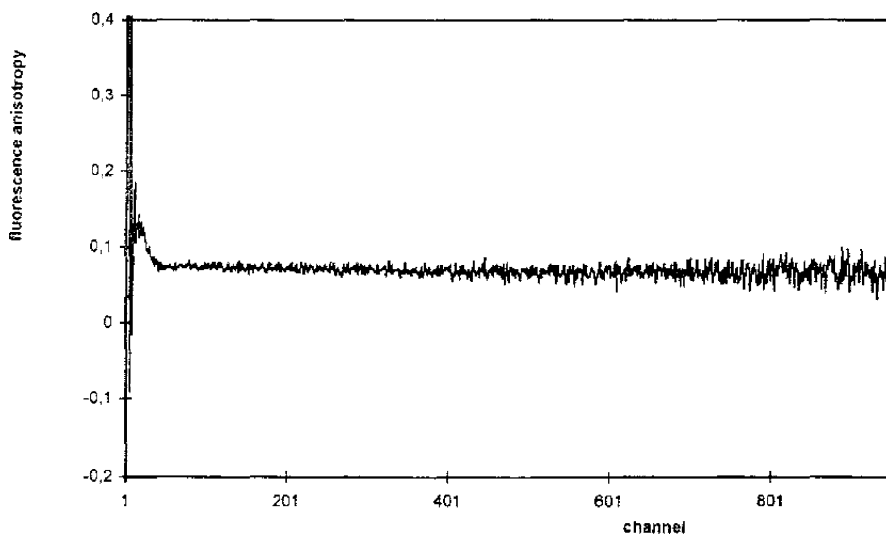


**Fig. 9** Experimental fluorescence anisotropy decay of  $C_{70}$  in the methylcyclohexane-toluene (7 : 2, v/v) mixture glass at 110 K, computed with Eq. 24 using the undeconvoluted polarized components.  $[C_{70}] = 6 \times 10^{-5}$  M. The excitation and emission wavelengths were 595 and 690 nm. The timescale was 2.77 ps/channel. It is seen that, after the impulse duration (FWHM = 35 ps, or 13 channels), the anisotropy has a nearly constant value ( $0.070 \pm 0.005$ ). From [47]

The decay of fluorescence anisotropy of  $C_{70}$  in the methylcyclohexane-toluene mixture glass at 110 K is shown in Fig. 9. As for  $C_{60}$ , it was constant in the whole time range, but now with a non-zero value:  $0.070 \pm 0.005$ . Given the excitation wavelength used (595 nm), this value was in good agreement with that found from the steady-state excitation polarization spectrum recorded under the same conditions (Fig. 10),  $0.08 \pm 0.01$ .

From this spectrum it is also seen that the anisotropy never exceeds 0.1, even when close to the absorption on-set. It was thus concluded that the first electronic transition of  $C_{70}$  is polarized in the  $xy$  plane, in agreement with calculations by the tight-binding model [48]. The same set of calculations predicts the 470 nm transition to be  $z$ -polarized. As can be seen from Fig. 10, this was not the case, negative values of the anisotropy being attained only for wavelengths below 460 nm, with a minimum at 380 nm. This minimum,

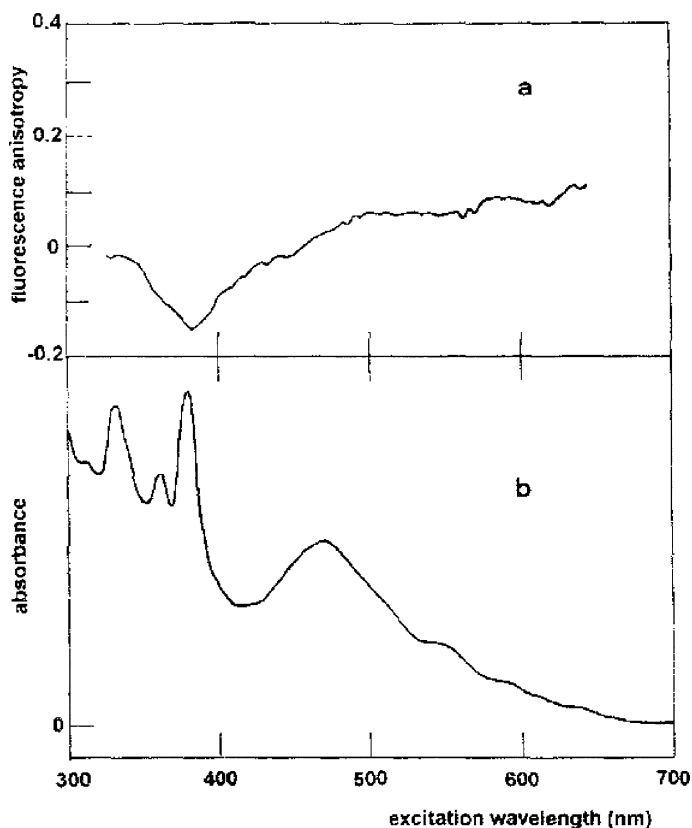


**Fig. 10** **a** Steady-state anisotropy of  $C_{70}$  in the methylcyclohexane-toluene glass at 110 K and **b** absorption spectrum of  $C_{70}$  in methylcyclohexane-toluene at room temperature, both as a function of the excitation wavelength.  $[C_{70}] = 7 \times 10^{-5}$  M. The emission wavelength was 720 nm. The small oscillations observed in (**a**) are due to noise. From [47]

close to  $-0.2$ , coincides with the peak wavelength (378 nm) of a strong absorption band which is therefore  $z$ -polarized. Because the tight-binding model does not take into account configuration interaction nor singlet-triplet splitting [50], the observed wavelength mismatch regarding higher excited states was not altogether surprising. On the other hand, more sophisticated quantum chemical calculations [49] agree with the experimental results.

## 4

### Diels–Alder Monoadducts

#### 4.1

##### Photophysical Properties

Diels–Alder reaction, one of the most widely used reactions in organic chemistry, has also been extensively used for the synthesis of  $C_{60}$  and  $C_{70}$  monoadducts [51–55].

The photophysical properties of six Diels–Alder adducts of  $C_{60}$  [51] or  $C_{70}$  [52, 53] and resin acid derivatives were studied (Fig. 11). A band at 436 nm, characteristic of the monofunctionalization of the  $C_{60}$  core, is observed in the absorption spectra of the  $C_{60}$  monoadducts. Fluorescence studies of all adducts showed an identical behaviour from the point of view of photophysics, resultant of the similarity of their fluorophores which only differ in their functional group. The fluorescence quantum yields obtained for  $C_{60}$  monoadducts were one order of magnitude higher than that of  $C_{60}$ .

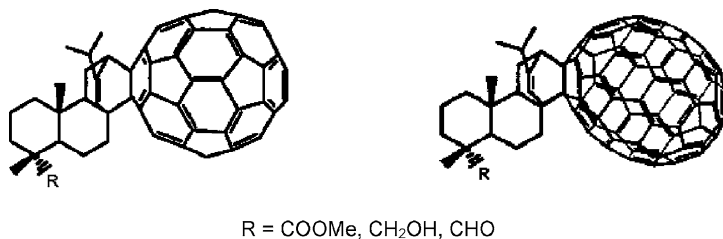


**Fig. 11** Diels–Alder monoadducts of  $C_{60}$  or  $C_{70}$  and resin acid derivatives

In the case of  $C_{70}$  monoadducts, and in comparison with the parent compound, the absorption spectra of these derivatives are generally red-shifted but have similar absorption coefficients (Fig. 12). The addition to the  $\alpha$  bond in these derivatives was seen to be largely dominant due to the similarity of its spectra and absorption coefficients with the published ones for three different monoadduct isomers of  $C_{70}$  [55].

The fluorescence spectra of the  $C_{70}$  Diels–Alder monoadducts, red-shifted with respect to  $C_{70}$ , are characterized by a broad emission between 650 and

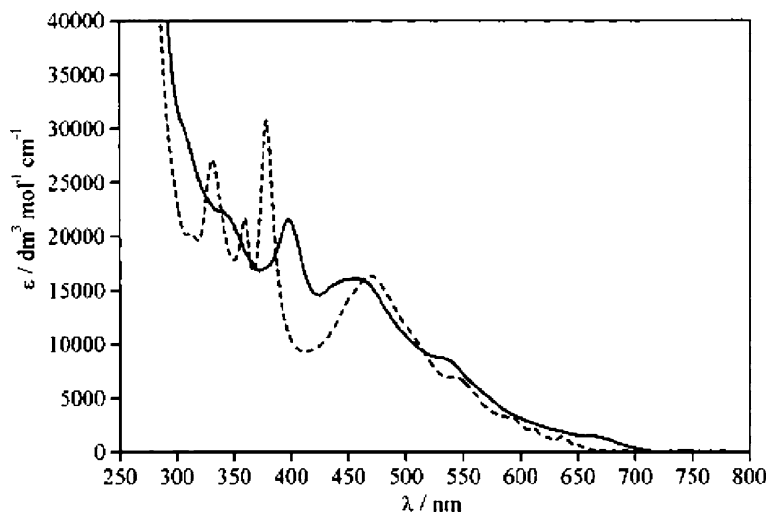


**Fig. 12** UV-Vis absorption spectra of  $C_{70}$  (- - -) and of the Diels-Alder monoadduct with  $R = \text{COOMe}$  (-) in methylcyclohexane at room temperature. From [52]

750 nm with a maximum at ca. 700 nm (see Fig. 13). The determined fluorescence quantum yields were  $7 \times 10^{-4}$  for all the derivatives, which are slightly higher than that of  $C_{70}$ . The lifetime obtained for the three derivatives was

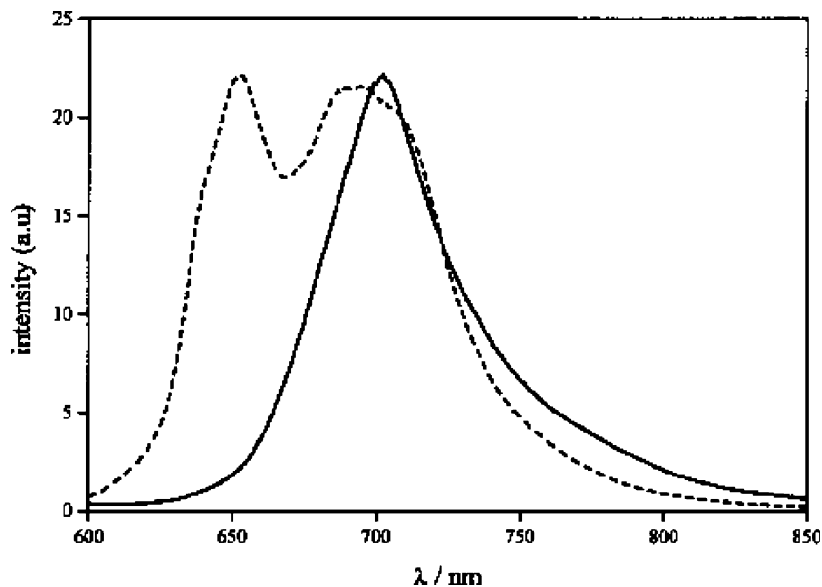


**Fig. 13** Fluorescence spectra of  $C_{70}$  (- - -) and of Diels-Alder monoadduct with  $R = \text{CHO}$  (-) in methylcyclohexane at room temperature. From [52]



1.1 ns and it was shown to be in agreement with efficient intersystem crossing as the main deactivation path for the  $S_1$  state. The analysis of the radiative and non-radiative rate constants revealed that the  $C_{70}$  fluorophore is much less affected by the addition of a group to a [6,6] bond than  $C_{60}$  due to the near invariance of their values relatively to the parent compound.

It was shown that the first electronic transition of all derivatives is polarized in the  $xy$  ("equatorial") plane, while the 400 nm transition is predominantly  $z$  axis polarized [52]. Since the absolute value of anisotropy measured near the absorption onset was close to 0.1 as in  $C_{70}$ , the addition to a [6,6] bond located near the "pole" ( $\alpha$  or  $\beta$ ) did not significantly affect the fluorophore effective symmetry.

The photophysical properties of the triplet state of the  $C_{70}$  Diels–Alder monoadducts were also studied. The phosphorescence spectra of the derivatives were seen to be red-shifted with a maximum at 850 nm (Fig. 14) and the phosphorescence lifetime, with a value of 6.2 ms, was significantly lower than that of  $C_{70}$  (ca. 50 ms) in similar conditions. Quenching of the triplet state of the three derivatives by ground-state molecular oxygen resulted in the formation of singlet oxygen, with a yield close to unity ( $0.9 \pm 0.1$ ) [52].

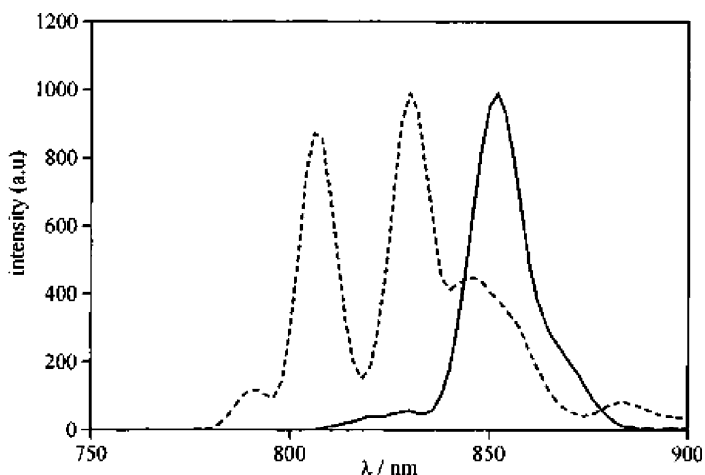


**Fig. 14** Phosphorescence spectra of  $C_{70}$  (---) and of Diels–Alder monoadduct with  $R = \text{COOMe}$  (—) in methylcyclohexane-toluene 7 : 2 (v/v) glass at 110 K. From [52]

The fluorescence spectra, quantum yields and lifetimes of  $C_{70}$  and of  $C_{70}$  monoadduct with  $R = \text{COOMe}$  (Fig. 15) were also measured in a wide range of solvents at room temperature [53]. It was observed that the fluorescence maximum is red-shifted on moving down the halogen series (Fig. 15).

The fluorescence quantum yields determined range from  $5 \times 10^{-5}$  to  $7 \times 10^{-4}$  in methyl iodide and dodecane solvents, respectively. The singlet state lifetimes of the derivative varied from 70 ps to 1.1 ns in the same sol-

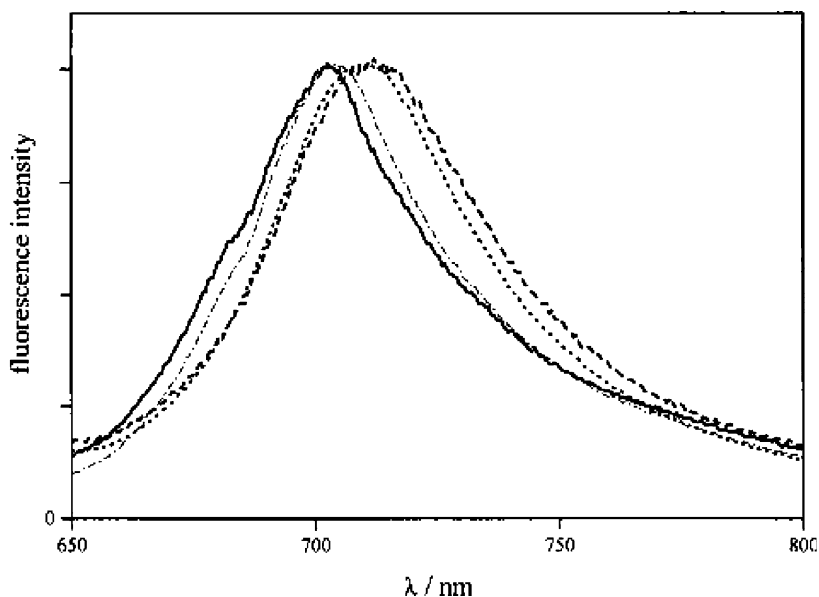


**Fig. 15** Normalized fluorescence spectra of Diels–Alder monoadduct with R = COOMe in methylcyclohexane (–), CCl<sub>4</sub> (· · · · ·), bromobenzene (· · ·) and methyl iodide (– – –). From [53]

vents, the lower values being observed in the bromo and iodo substituted solvents. It was seen that the C<sub>70</sub> monoadduct fluorescence is efficiently quenched by all halogenated solvents used. The quenching of fluorescence was shown to be both static, in chlorinated solvents, and dynamic in bromo and iodo-substituted solvents. In bromo and iodo substituted solvents, the quenching was dynamic and due to the external heavy atom effect, with quenching rate constant values close to  $10^8 \text{ M}^{-1} \text{ s}^{-1}$  and  $10^9 \text{ M}^{-1} \text{ s}^{-1}$ , respectively. As expected, the iodinated quenchers are more effective than the brominated ones.

## 4.2

### Kinetics of the Diels–Alder Reaction

Although mono and multiple C<sub>60</sub> functionalization by the Diels–Alder reaction represent a common synthetic procedure in fullerene chemistry, almost no experimental kinetic data is available. The kinetics of the Diels–Alder reactions between C<sub>60</sub> and the linear acenes anthracene and tetracene were studied, including the dependence with temperature [30]. The reactions were monitored by absorption spectroscopy. For the system C<sub>60</sub>–anthracene, Fig. 16, the absorption spectrum was characterized by four prominent bands that appeared at 436 nm (sharp band), 486 nm (broad band), 640 nm (shoul-

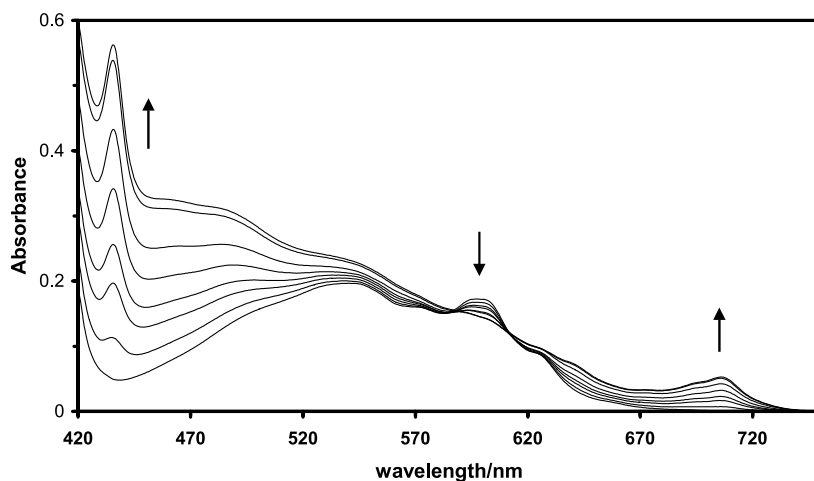


**Fig. 16** Absorption spectra of the reaction mixture C<sub>60</sub>-anthracene as a function of time, for a temperature of 63 °C. The absorption spectrum with the lowest 436 nm absorption corresponds to the starting C<sub>60</sub>-anthracene mixture. The remaining spectra correspond to reaction times of 60, 130, 185, 295, 482, 1523 and 2343 min. From [30]

der) and 706 nm (weak band). For the case of C<sub>60</sub>-tetracene, two prominent absorption features appeared at 640 and 706 nm (Fig. 17). The absorption features observed with anthracene at shorter wavelengths were in the

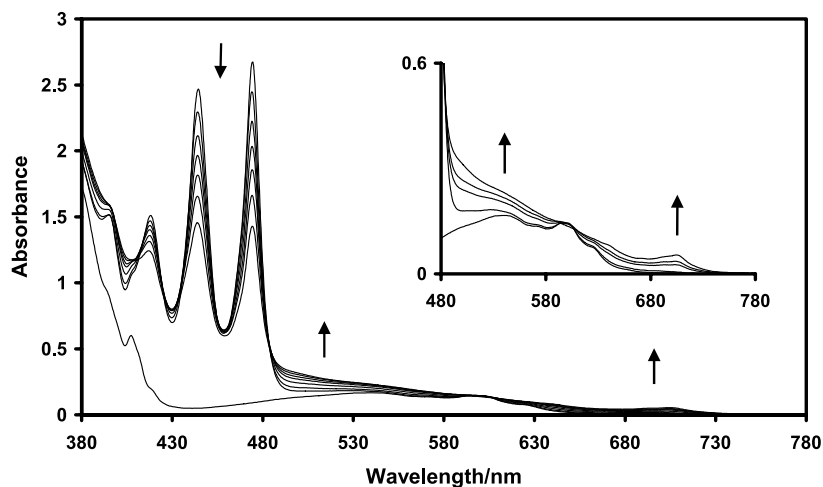


**Fig. 17** Absorption spectra of the reaction mixture C<sub>60</sub>-tetracene as a function of time, for a temperature of 59 °C. The absorption spectrum with the lowest 436 nm absorption corresponds to the pure C<sub>60</sub> solution. The other spectra correspond to the reaction mixture for reaction times of 0, 36, 84, 139, 191, 267 and 408 min. *Inset:* pure C<sub>60</sub> solution and reaction mixture for 0, 84, 139 and 408 min. From [30]

case of tetracene masked by its intrinsic absorption. The formation of the monoadducts was verified by the observation of a progressively increase of the intensity of these bands with time. It was observed that tetracene reacts more readily with  $C_{60}$  than anthracene, due to its lower enthalpy of activation resultant from a lesser aromaticity reduction. The two monoadducts also displayed different kinetics as regards the dissociation back to the reagents. The dependence with the temperature, from the point of view of the reversibility of the Diels–Alder reaction, was only significant for the anthracene monoadduct, which is unstable above room temperature.

## 5

### Heavy-Atom Effects on Methanofullerenes

#### 5.1

##### Background

Methanofullerenes represent the most versatile and widely studied class of fullerene adducts. The monoadducts retain most of the characteristic properties of the unfunctionalized carbon sphere [54]. Monofunctionalization brings a slight reduction to the cage  $\pi$ -electronic system and also a lowering of the cage symmetry and as a result the [60]fullerene derivatives exhibit photophysical properties not identical to those of  $C_{60}$ . Previous studies [2, 3] have shown that for monofunctionalized  $C_{60}$  derivatives, a higher number of transitions in the absorption spectrum are observed, along with a slight increase in the fluorescence lifetime and a substantial increase in the fluorescence quantum yield. The photophysics of monofunctionalized derivatives of  $C_{60}$  remain nevertheless characterised by exceedingly slow radiative transitions and a very fast intersystem crossing, accordingly [60]fullerene monoderivatives are still weakly fluorescent.

All methanofullerenes studied have similar absorption and fluorescence spectra. The absorption spectra of the methano[60]fullerene-dicarboxylates in THF and of  $C_{60}$  in toluene are shown in Fig. 18. The inset displays the weak transitions in the visible. The common absorption spectrum of the methano[60]fullerene-dicarboxylates is clearly different from that of  $C_{60}$  in toluene in the visible region, with the following main distinctive features: (i) A significant red-shift of the  $C_{60}$  406 nm sharp absorption band to 426 nm in all cases; (ii) A significant (50–60 nm) blue-shift of the  $C_{60}$  broad absorption band in the visible (maximum at 535 nm); (iii) The appearance of a new weak band at ca. 688 nm. This last feature is characteristic of mono addition [2, 3]. The spectra of the derivatives in toluene do not show significant shifts with respect to those in THF. Like other  $C_{60}$  monofunctionalized derivatives, the studied mono-methanoderivatives are stronger absorbers in the visible region than  $C_{60}$ , as a result of the cage symmetry reduction.

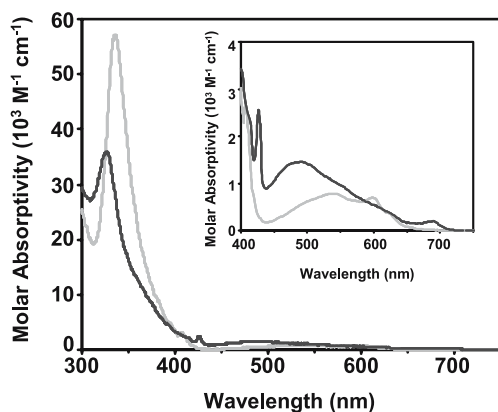


**Fig. 18** Comparison between the absorption spectrum of the methano[60]fullerene-dicarboxylates (*black lines*, in THF) and the absorption spectrum of  $C_{60}$  (*grey lines*, in toluene). The *inset* displays the weak transitions in the visible. From [59]

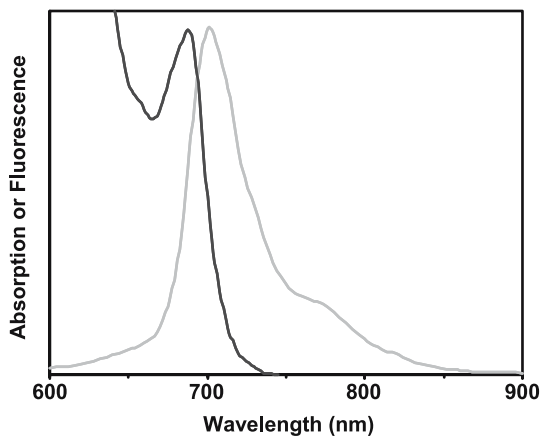


**Fig. 19** Electronic absorption spectrum (*black*) and fluorescence spectrum (*grey*) of the methano[60]fullerene-dicarboxylates in THF, displaying the mirror image relationship. From [59]

The fluorescence spectrum of the methano[60]fullerene-dicarboxylates is shown in Fig. 19. The different addends do not significantly affect it. The fluorescence peak maxima occur at approximately the same emission wavelength as for  $C_{60}$ . However, while in the  $C_{60}$  case the maximum corresponds to a higher vibronic transition, in the derivatives it corresponds to the 0–0 band, and a Franck–Condon progression typical of a small geometry change between the ground and excited states is clearly observed. A good mirror image of the fluorescence and absorption of the  $C_{60}$  derivatives is observed (see Fig. 19), with a small Stokes shift of 11–14 nm.

## 5.2

### Heavy-Atom Effects

The quenching of the fluorescence of fullerenes by the external heavy-atom effect has been the subject of several studies [53, 56, 57]. It was established that in spite of a very efficient intrinsic intersystem crossing (the intrinsic quantum yields of triplet formation being close to 1), fullerenes are still subject to the external heavy atom effect that may significantly increase the intersystem crossing rate constant. For instance, while the fluorescence lifetime of a  $C_{70}$  monoadduct in cyclohexane is 1.1 ns, in bromobenzene it drops to 400 ps, and in methyl iodide it is only 70 ps [53].

A possible application of this effect in the case of the fullerenes is on their use as fast-responding optical limiters of intense laser pulses by reverse saturable absorption (RSA) [53]. In the case of fullerenes, RSA is based on triplet-triplet absorption, and therefore occurs only after intersystem crossing. An increase in the intersystem crossing rate by the heavy atom effect means a faster (picosecond) responding optical limiter, which is required for short laser pulses.

Previous studies of the heavy atom effect on the fluorescence of fullerenes dealt exclusively with the external (intermolecular) effect. In the case of  $C_{70}$  and one monoadduct of  $C_{70}$ , it was concluded that the quenching was dynamic for several brominated and iodinated neutral quenchers. The Stern-Volmer plots obtained in hydrocarbon-quencher mixtures smoothly extrapolate to the results in pure liquid quencher solution, e.g., bromobenzene. In all cases the quenching was below diffusion control, and for this reason (weak) fullerene fluorescence was still detected even in pure iodinated quenchers like iodobenzene. The effect was, as expected, stronger in iodinated quenchers than in brominated ones. A detailed study [57] of the heavy atom effect in the case of  $C_{70}$  and two different quenchers, iodide and bromobenzene, provided evidence for a quenching mechanism with exponential distance dependence. It was later shown [58] that the recovered parameters for this mechanism (effective Bohr radius, quenching rate constant at contact) are dependent on the radial distribution used for the quenchers. In the case of  $C_{60}$  derivatives, including a water-soluble dendrimer [56], a quenching effect similar to that for  $C_{70}$  and derivatives was observed for brominated and iodinated quenchers.

The intramolecular heavy atom effect in fullerenes was investigated in [59]. For this purpose, the fluorophore F (a methano[60]fullerene-dicarboxylate) was covalently attached to one or two chains containing one bromine atom quencher (Q) at the end. Two different compounds (diads) of the FQ type and one compound (triad) of the  $FQ_2$  type were synthesized, Fig. 20, and their fluorescence properties were determined. The use of the diad and polyad designations stems from the fact that in these compounds there are separated sub-units that perform specific photophysical roles, in this case those of flu-

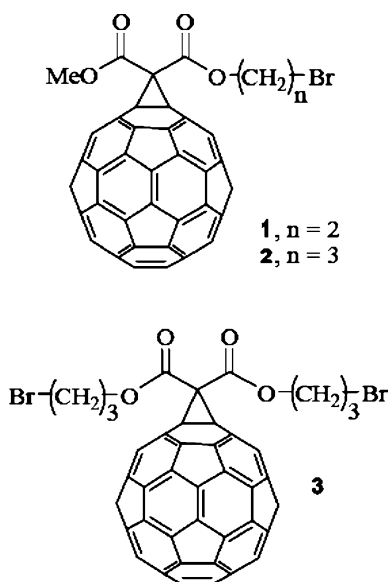


**Fig. 20** Structures of the fullerene diads and triad

orophore and quencher. The effect of a supplementary external heavy atom effect on the polyads was studied by dissolving them in two heavy atom solvents, bromobenzene and iodobenzene.

The fluorescence quantum yields ( $\Phi_F$ ) of the methano[60]fullerene derivatives were measured in THF, and also in bromobenzene and iodobenzene. The value for  $C_{60}$  refers to toluene, as it is insoluble in THF. The diethyl methano[60]fullerene-dicarboxylate (DEM) has identical quantum yields in THF and in toluene, that coincide (within experimental error) with the measured value in chloroform,  $1.0 \times 10^{-3}$ . The values are graphically summarized in Fig. 21, and are also given in Table 3. Several conclusions can be drawn: (i) The substantial increase in the quantum yield upon addition, i.e., when going from  $C_{60}$  to the diethyl dicarboxylate. (ii) It is clear that this increase is no longer observed for the bromoalkyl derivatives, whose quantum yields in THF are similar to that of  $C_{60}$ . This is a direct evidence of an internal heavy atom quenching effect. (iii) In THF, significant differences are observed between the 1/2 pair and 3, i.e., between monobrominated diads and the dibrominated triad, with the dibrominated one experiencing the stronger internal effect. (iv) In bromobenzene all quantum yields decrease significantly, and become comparable. (v) A further decrease occurs in iodobenzene; all quantum yields are again comparable, with the exception of that of  $C_{60}$ , which is distinctly lower. The external heavy atom effect thus follows the expected order, and dominates over the internal one both in bromobenzene and in iodobenzene.

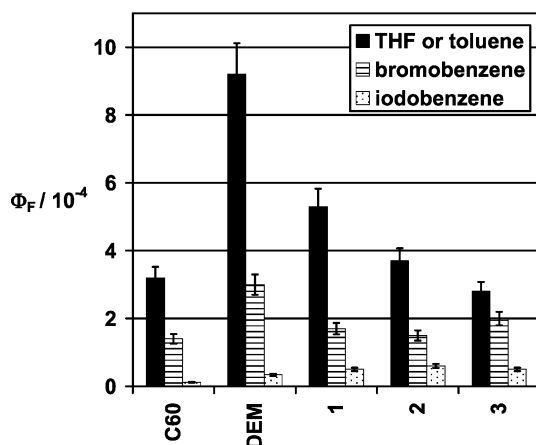


**Fig. 21** Fluorescence quantum yields of C<sub>60</sub> and of the C<sub>60</sub> derivatives. From [59]

**Table 3** Fluorescence quantum yields. From [59]

Compound	$\Phi_F/10^{-4}$		
	Toluene or THF	Bromobenzene	Iodobenzene
C <sub>60</sub>	3.2	1.4	0.12
DEM	9.2	3.0	0.34
1	5.3	1.7	0.5
2	3.7	1.5	0.6
3	2.8	2.0	0.5

The fluorescence decay law of the fullerene moiety in a polyad,  $I(t)$ , is given by the general equation

$$I(t) = \exp(-t/\tau_0) \exp\left(-\int_0^t k(u)du\right), \quad (24)$$

where  $\tau_0$  is the intrinsic fluorescence lifetime, and the time-dependent rate coefficient  $k(t)$  is

$$k(t) = \int_0^\infty N(r, t)k(r)dr, \quad (25)$$

and  $N(r, t)$  is the number of quenchers at a distance  $r$  at time  $t$ . Note that Eq. 24 implies an assumption of additivity of contributions from different quenchers. It is also implicitly assumed in Eq. 24 that the intrinsic fluorescence lifetime is the same, irrespective of the distance between fluorophore



and quencher. This assumption is a reasonable one for fluorescence. In the case of heavy atom quenching, the quenching rate constant falls exponentially with the distance [57],

$$k(r) = \frac{1}{\tau_0} \exp \left[ \frac{2(R_0 - r)}{L} \right], \quad (26)$$

where  $L$  is the effective Bohr radius, with typical values between 1 Å and 2 Å, and  $R_0$  is the critical radius [57], with values typically smaller than 10 Å. For the pair C<sub>70</sub>-bromobenzene, the estimated values for these parameters are [57]  $L = 2.6$  Å and  $R_0 = 5.4$  Å.

In a fluid medium,  $N(r, t)$  is obtained from an appropriate diffusion equation. However, the *rapid diffusion limit* suffices for our purposes. This limit is fulfilled in liquid solutions at room temperature for low quenching efficiencies. In such a case,  $N(r, t)$  is time-independent, and equal to the equilibrium value  $N(r) = N(r, 0)$ , and the decay is thus exponential.

In the intramolecular quenching case,

$$N(r) = N_i f_i(r), \quad (27)$$

where  $N_i = 1$  for the diads and  $N_i = 2$  for the triad, and  $f_i(r)$  is the distance distribution function for a covalently linked (intramolecular) fluorophore-quencher pair. It follows that

$$k_i = N_i \int_0^{\infty} f_i(r) k(r) dr, \quad (28)$$

and if  $f_i(r)$  is the same for the diad and for the triad, one expects a doubling of the quenching rate constant when going from the diad to the triad, in accordance with the starting assumption of additivity of contributions from different quenchers.

In the case of an additional quenching by the solvent, an intermolecular term must be added to the overall quenching rate constant,

$$k = k_i + k_e, \quad (29)$$

where  $k_e$  is the rate constant for the quenching by the solvent. This rate constant can be written again in the form of Eq. 28,

$$k_e = \int_0^{\infty} N_e(r) k(r) dr, \quad (30)$$

where

$$N_e(r) = N f_e(r) = N_A [Q] 4\pi r^2 g(r), \quad (31)$$

and where  $f_e(r)$  is the distance distribution function for an intermolecular fluorophore-quencher pair,  $g(r)$  is the radial distribution function [58], and  $[Q]$  is the external quencher (solvent) concentration.

Using Eq. 31, one finds that the rate constant for external quenching becomes

$$k_e = N_A [Q] \int_0^{\infty} 4\pi r^2 g(r) k(r) dr = k_q [Q], \quad (32)$$

where  $k_q$  is the bimolecular rate constant for quenching. Assuming that the radial distribution function is a step function, i.e., that the quenchers are randomly and independently distributed around the excited molecule,

$$g(r) = \begin{cases} 0 & \text{if } r < d \\ 1 & \text{if } r > d \end{cases} \quad (33)$$

where  $d$  is the distance of closest approach, one obtains from Eqs. 26 and 32 that the bimolecular quenching rate constant is [57]

$$k_q = \frac{\pi N_A L^3}{\tau_0} \left[ 1 + 2\frac{d}{L} + 2\left(\frac{d}{L}\right)^2 \right] \exp\left[\frac{2(R_0 - d)}{L}\right]. \quad (34)$$

For a general  $g(r)$  the bimolecular quenching rate constant can only be obtained numerically [13].

When  $k_e \gg k_i$ , intermolecular quenching is the dominant contribution and all polyads display similar photophysical behavior, irrespective of  $N_i$ .

For a given heavy atom quenching moiety, and for the purposes of comparison with intermolecular quenching (e.g., polyad with a brominated moiety versus brominated solvent), Eq. 28 can be rewritten as

$$k_i = k_q [Q]_{\text{eff}}, \quad (35)$$

where  $k_q$  is the rate constant for intermolecular quenching and  $[Q]_{\text{eff}}$  is an effective quencher concentration defined by Eq. 35.

For  $C_{60}$  and monofunctionalized derivatives, the lifetime is controlled by the non-radiative decay constant, which in turn is practically identical to the intersystem crossing rate constant. In this way, the measured lifetimes directly reflect the enhanced intersystem crossing by the heavy atom effect, when it exists. The fluorescence lifetimes of the studied methano [60]fullerene derivatives were measured in THF, bromobenzene and iodobenzene. The value for  $C_{60}$  (1.1 ns) refers again to toluene, as  $C_{60}$  is insoluble in THF. The diethyl methano[60]fullerene-dicarboxylate has similar lifetimes in THF (1.4 ns) and in toluene (1.5 ns). The values are graphically summarized in Fig. 22, and are also given in Table 4. The following conclusions can be drawn from Fig. 22: (i) The increase in the lifetime upon addition of a group to the fullerene cage, i.e., when going from  $C_{60}$  to the diethyl dicarboxylate, is moderate. (ii) This

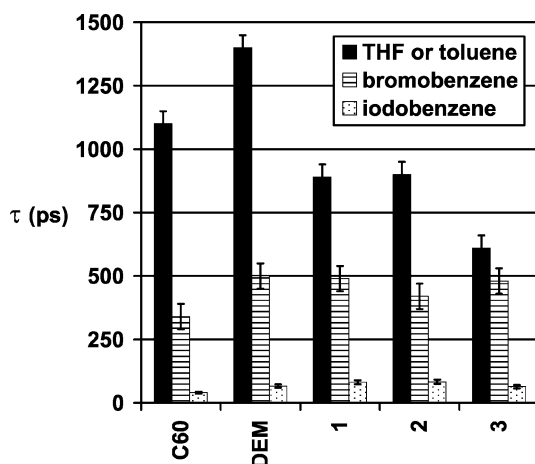


**Fig. 22** Fluorescence lifetimes of C<sub>60</sub> and of the C<sub>60</sub> derivatives. From [59]

**Table 4** Fluorescence lifetimes. From [59]

Compound	τ (ns)		
	Toluene or THF	Bromobenzene	Iodobenzene
C <sub>60</sub>	1.1	0.34	0.040
DEM	1.4	0.50	0.066
1	0.89	0.49	0.081
2	0.90	0.42	0.083
3	0.61	0.48	0.064

increase is no longer observed for the brominated derivatives, whose lifetimes in THF are on the contrary lower than that of C<sub>60</sub>, and also lower than the lifetime of the reference compound, DEM. This is again direct evidence of an internal heavy atom quenching effect. (iii) Within experimental error, no significant difference is observed between diads 1 and 2, that differ in the chain length by one methylene group. (iv) Significant differences are observed in THF between the diads (1 and 2) and the triad 3, i.e., between the monobrominated derivatives and the dibrominated derivative, with the triad experiencing the stronger internal effect. (v) In bromobenzene all lifetimes decrease significantly, and become comparable, with values close to 500 ps, with the exception of that of C<sub>60</sub>, 340 ps, which is distinctly lower. (vi) A further major decrease occurs in iodobenzene; all lifetimes are again comparable, with values between 64 ps and 83 ps, with the exception of that of C<sub>60</sub>, 40 ps, which is distinctly lower. The external heavy atom effect thus follows the expected order, and dominates over the internal one both in bro-

mobenzene and in iodobenzene. These conclusions are in agreement with those reached from the quantum yield data.

In order to compare the relative efficiency of internal and external (bromobenzene) heavy atom effects, an effective quencher concentration,  $[Q]_{\text{eff}}$ , was computed for the intramolecular (internal) effect, see Eq. 35.

As mentioned in the introduction, the intermolecular quenching processes in the case of  $C_{70}$  and derivatives [53], and a  $C_{60}$  derivative [56], were all found to be dynamic (straight Stern–Volmer plot with a common slope for intensities and lifetimes) and well below diffusion control for brominated quenchers. Taking the lifetime of DEM in THF as the reference value, using the previously measured bimolecular rate constant for the quenching of DEM by bromobenzene,  $(1.9 \pm 0.4) \times 10^8 \text{ M}^{-1} \text{ s}^{-1}$ , and using the lifetimes of the  $C_{60}$  derivatives measured in THF, one obtains the following effective quencher concentrations from the Stern–Volmer equation: 2.2 M (1), 2.1 M (2), and 4.9 M (3). Note that the concentration of neat bromobenzene is 9.52 M. The effective concentrations computed appear to be acceptable, given all approximations made. For the diads 1 and 2 the effective concentrations coincide within experimental error, as expected. The value corresponds to one bromine atom in a shell with a thickness of 1.6 Å around the fullerene cage (radius 5.3 Å), which is not unreasonable given the short range of the heavy atom interaction, and the fact that the chain restricts the mobility of the bromine atom. When going from the diads 1 and 2 to the dibrominated triad 3, the effective concentration of quenchers approximately doubles, as expected.

The bromoalkyl methano[60]fullerene-dicarboxylates studied do exhibit an internal heavy atom effect, with the effective quencher concentration doubling when going from the diads to the triad. A corresponding reduction of the fluorescence lifetimes is observed, that are lower than those of both the pristine  $C_{60}$  and the non-brominated diethyl dicarboxylate derivative.

A significant external heavy atom effect is observed in bromobenzene and in iodobenzene. In bromobenzene all quantum yields and lifetimes decrease significantly, and become comparable, as expected for molecules containing the same fluorophore (DEM, 1, 2, and 3) and subject to the same quencher. A further strong decrease occurs in iodobenzene. All quantum yields and lifetimes are again comparable. In spite of having a shorter intrinsic lifetime,  $C_{60}$  has distinctly lower lifetimes in both solvents, when compared to the studied derivatives, showing that it is subject to a stronger quenching effect. The external heavy atom effect follows the expected halogen order, with the iodinated quencher being more effective than the brominated one. The external effect is found to largely surpass the internal one both in bromobenzene and in iodobenzene. With respect to bromobenzene, this is compatible with the higher concentration of quenchers, compared to the effective concentration of the brominated moiety in the intramolecular case. In the case of iodobenzene, this is explained by both the higher concentration of quenchers and the higher quenching efficiency of iodine.

## 6 Concluding Remarks and Future Perspectives

In this chapter, selected results obtained by the authors in the field of fullerene photophysics were reviewed with an emphasis on fluorescence. The topic of thermally activated delayed fluorescence in fullerenes, one of the most characteristic and fruitful aspects investigated [60–65], was deliberately excluded owing to lack of space.

It was shown in this review that fullerenes display several unusual photophysical properties, such as their fluorescence anisotropy, and also that they can be used for a more complete understanding of general photophysical processes like charge-transfer complexation and the heavy-atom effect. In spite of the work already carried out, knowledge of the photophysics of fullerenes and derivatives is still incomplete, and much remains to be done in this area.

**Acknowledgements** S. Nascimento and C. Baleizão were supported by Fundação para a Ciência e a Tecnologia (Portugal) through fellowships SFRH/BD/18622/2004 and SFRH/BPD/28438/2006, respectively. Thanks are due to A. Fedorov, S. Foley, I. Texier, G. Sarova and M. Rae for their important contribution to the described research. Collaboration with the groups of B. Gigante and M.J. Brites (INETI, Lisbon), A.C. Tomé (Universidade de Aveiro), R. Bensasson (Muséum National d'Histoire Naturelle, Paris) and of B. Valeur (CNAM, Paris and ENS Cachan) is gratefully acknowledged.

## References

1. Foote CS (1994) Photophysical and photochemical properties of fullerenes. *Top Curr Chem* 169:347–363
2. Sun YP (1997) In: Ramamurthy V, Shanze KS (eds) *Molecular and Supramolecular Photochemistry*, vol. 1, Organic Photochemistry. Marcel Dekker, New York, pp 325–390
3. Sun YP, Riggs JE, Guo Z, Rollins HW (2000) In: Shinar J, Vardeny ZV, Kafafi ZH (eds) *Optical and Electronic Properties of Fullerenes and Fullerene-Based Materials*. Marcel Dekker, New York, pp 43–81
4. Evans J (1955) Absorption spectra of iodine and bromine in the gas phase and inert solvents. I. Iodine. *J Chem Phys* 23:1424–1426
5. Orgel LE, Mulliken RS (1957) Molecular complexes and their spectra. VII. The spectrophotometric study of molecular complexes in solution; Contact charge-transfer spectra. *J Am Chem Soc* 79:4839–4846
6. Gooding EA, Serak KR, Ogilby PR (1991) Ground-state benzene-oxygen complex. *J Phys Chem* 95:7868–7871
7. Fowler PW, Ceulemans A (1995) Electron deficiency of the fullerenes. *J Phys Chem* 99:508–510
8. Sibley SP, Campbell RL, Silber HB (1995) Solution and solid state interactions of C<sub>60</sub> with substituted anilines. *J Phys Chem* 99:5274–5276
9. Ichida M, Sohda T, Nakamura A (1999) Optical transition and ionicity of C<sub>60</sub>/amine charge-transfer complexes studied by optical spectroscopy. *Chem Phys Lett* 310:373–378

10. Rath MC, Pal H, Mukherjee T (1999) Interaction of ground and excited ( $S_1$ ) states of  $C_{60}$  and  $C_{70}$  with aromatic amines: Exciplex and charge-transfer emissions. *J Phys Chem A* 103:4993–5002
11. Ichida M, Sohda T, Nakamura A (2000) Third-order nonlinear optical properties of  $C_{60}$  CT complexes with aromatic amines. *J Phys Chem B* 104:7082–7084
12. Bhattacharya S, Nayak SK, Chattopadhyay S, Banerjee M, Mukherjee AK (2002) Absorption spectroscopic study of the complexation of  $C_{70}$  with aniline and substituted anilines. *J Phys Chem A* 106:6710–6713
13. Saha A, Nayak SK, Chattopadhyay S, Mukherjee AK (2004) Evidence of reverse micellization of a calix[4]arene through a study of its charge transfer and host-guest complexation with [60]fullerene. *J Phys Chem B* 108:7688–7693
14. Bhattacharya S, Nayak SK, Semwal A, Chattopadhyay S, Banerjee M (2004) Study of host-guest interaction of [70]fullerene with substituted calix[6]arenes by absorption spectrometric method. *J Phys Chem A* 108:9064–9068
15. Bhattacharya S, Nayak SK, Chattopadhyay S, Banerjee M, Mukherjee AK (2001) Spectrophotometric and thermodynamic study of supramolecular complexes of [60]- and [70]fullerenes with a number of calix[n]arenes. *J Chem Soc, Perkin Trans 2* 2292–2297
16. Saha A, Nayak SK, Chattopadhyay S, Mukherjee AK (2004) Study of charge transfer interactions of a resorcin [4]arene with [60]- and [70]fullerenes by the absorption spectrometric method. *J Phys Chem A* 108:8223–8228
17. Saha A, Nayak SK, Chattopadhyay S, Mukherjee AK (2003) Spectrophotometric study of complexation of dicyclohexano-24-crown-8 with [60]- and [70]Fullerenes and other acceptors. *J Phys Chem B* 107:11889–11892
18. Datta K, Banerjee M, Mukherjee AK (2004) Comparative study of the host-guest complexes of [60]- and [70]-fullerenes with  $N,N'$ -Dibenzyl-1,4,10,13-tetraoxa-7,16-diaza-cyclooctadecane in different solvents. *J Phys Chem B* 108:16100–16106
19. Bourdelande JL, Font J, González-Moreno R (1996) Inclusion complex of  $\beta$ -cyclodextrin- $C_{60}$ : photophysical properties in the solid state using diffuse reflectance laser flash photolysis (DRLFP). *J Photochem Photobiol A* 94:215–216
20. Masuhara A, Fujitsuka M, Ito O (2000) Photoinduced electron-transfer of inclusion complexes of fullerenes ( $C_{60}$  and  $C_{70}$ ) in  $\beta$ -cyclodextrin. *Bull Chem Soc Jpn* 73:2199–2206
21. Scurlock RD, Ogilby PR (1995) Excited-state charge-transfer complexes formed between  $C_{60}$  and substituted naphthalenes. *J Photochem Photobiol A* 91:21–25
22. Sibley SP, Nguyen YT, Campbell RL, Silber HB (1997) Spectrophotometric studies of complexation of  $C_{60}$  with aromatic hydrocarbons. *Spectrochim Acta Part A* 53:679–684
23. Datta K, Banerjee M, Seal BK, Mukherjee AK (2000) Ground state EDA complex formation between [60]fullerene and a series of polynuclear aromatic hydrocarbons. *J Chem Soc, Perkin Trans 2* 531–534
24. Bhattacharya S, Nayak SK, Chattopadhyay SK, Banerjee M, Mukherjee AK (2001) Absorption spectroscopic study of EDA complexes of [70]fullerene with a series of methyl benzenes. *Spectrochim Acta Part A* 57:309–313
25. Bhattacharya S, Banerjee M, Mukherjee AK (2001) Study of the formation equilibria of electron donor–acceptor complexes between [60]fullerene and methylbenzenes by absorption spectrometric method. *Spectrochim Acta Part A* 57:1463–1470
26. Bhattacharya S, Nayak SK, Chattopadhyay S, Banerjee M, Mukherjee AK (2002) Study of ground state EDA complex formation between [70]fullerene and a series of polynuclear aromatic hydrocarbons. *Spectrochim Acta Part A* 58:289–298

27. Sarova G, Berberan-Santos MN (2004) Stable charge-transfer complexes versus contact complexes. Application to the interaction of fullerenes with aromatic hydrocarbons. *J Phys Chem B* 108:17261–17268
28. Foster R (1969) *Charge-Transfer Complexes*. Academic Press, London
29. Birks JB (1970) *Photophysics of Aromatic Molecules*. Wiley-Interscience, London
30. Sarova G, Berberan-Santos MN (2004) Kinetics of the Diels–Alder reaction between  $C_{60}$  and acenes. *Chem Phys Lett* 397:402–407
31. Jablonski A (1960) On the notion of emission anisotropy. *Bull Acad Polon Sci, Ser Math Astr Phys* 8:259–264
32. Berberan-Santos MN (2001) Pioneering contributions of Jean and Francis Perrin to molecular luminescence, In: Valeur B, Brochon J-C (eds) *New Trends in Fluorescence Spectroscopy. Applications to Chemical and Life Sciences*. Springer, Berlin
33. Perrin F (1929) La fluorescence des solutions. Induction moléculaire – Polarisation et durée d'émission – Photochimie. *Ann Phys (Paris)* 12:169–275
34. Jablonski A (1961) Über die Abklingungsvorgänge polarisierter Photolumineszenz. *Z Naturforsch A* 16:1–4
35. Feofilov PP (1961) *The Physical Basis of Polarized Emission*. Consultants Bureau, New York
36. Dorr F (1966) Spectroscopy with polarized light. *Angew Chem Int Ed Engl* 5:478–495
37. Hall RD, Valeur B, Weber G (1985) Polarization of the fluorescence of triphenylene. A planar molecule with three-fold symmetry. *Chem Phys Lett* 116:202–205
38. Taylor R, Hare JP, Abdul-Sada AK, Kroto HW (1990) Isolation, separation and characterisation of the fullerenes  $C_{60}$  and  $C_{70}$ : the third form of carbon. *Chem Commun* 1423–1425
39. Ajie H, Alvarez MM, Anz SJ, Beck RD, Diederich F, Fostiropoulos K, Huffman DR, Kraetschmer W, Rubin Y, Schriver KE, Sensharma D, Whetten RL (1990) Characterization of the soluble all-carbon molecules  $C_{60}$  and  $C_{70}$ . *J Phys Chem* 94:8630–8633
40. Kratschmer W, Lamb LD, Fostiropoulos K, Huffman DR (1990) Solid  $C_{60}$ : a new form of carbon. *Nature* 347:354
41. Bethune DS, Meijer G, Tang WC, Rosen HJ, Golden WG, Seki H, Brown CA, Vries MS (1991) Vibrational Raman and infrared spectra of chromatographically separated  $C_{60}$  and  $C_{70}$  fullerene clusters. *Chem Phys Lett* 179:181–186
42. Reber C, Yee L, McKiernan J, Zink JI, Williams RS, Tong WM, Ohlberg DAA, Whetten RL, Diederich F (1991) Luminescence and absorption spectra of carbon ( $C_{60}$ ) films. *J Phys Chem* 95:2127–2129
43. Sibley SP, Argentine SM, Francis AH (1992) A photoluminescence study of  $C_{60}$  and  $C_{70}$ . *Chem Phys Lett* 188:187–193
44. Wang YJ (1992) Photophysical properties of fullerenes and fullerene/*N,N*-diethyl-aniline charge-transfer complexes. *J Phys Chem* 96:764–767
45. Kim D, Lee M, Suh YD, Kim SK (1992) Observation of fluorescence emission from solutions of  $C_{60}$  and  $C_{70}$  fullerenes and measurement of their excited-state lifetimes. *J Am Chem Soc* 114:4429–4430
46. Berberan-Santos MN, Valeur B (1994) Intrinsically unpolarized fluorescence of  $C_{60}$ . *J Chem Soc Faraday Trans* 90:2623–2625
47. Fedorov A, Berberan-Santos MN, Lefèvre JP, Valeur B (1997) Picosecond time-resolved and steady-state studies of the polarization of the fluorescence of  $C_{60}$  and  $C_{70}$ . *Chem Phys Lett* 267:467–471
48. Shumway J, Satpathy S (1993) Polarization-dependent optical properties of  $C_{70}$ . *Chem Phys Lett* 211:595–600

49. Orlandi G, Negri F (2002) Electronic states and transitions in  $C_{60}$  and  $C_{70}$  fullerenes. *Photochem Photobiol Sci* 1:289–308
50. Cioslowski J (1995) *Electronic structure calculations on fullerenes and their derivatives*. Oxford University Press, New York, Oxford
51. Gigante B, Santos C, Fonseca T, Curto MJM, Luftmann H, Bergander K, Berberan-Santos MN (1999) Diels–Alder adducts of  $C_{60}$  and resin acid derivatives: synthesis, electrochemical and fluorescence properties. *Tetrahedron* 55:6175–6182
52. Foley S, Berberan-Santos MN, Fedorov A, McGarvey DJ, Santos C, Gigante B (1999) Photophysical properties of pseudo-dihydro derivatives of  $C_{70}$ . *J Phys Chem A* 103:8173–8178
53. Foley S, Berberan-Santos MN, Fedorov A, Bensasson RV, Leach S, Gigante B (2001) Effect of halogenated compounds on the photophysics of  $C_{70}$ : some implications on optical limiting behaviour. *Chem Phys* 263:437–447
54. Diederich F, Thilgen C (1996) Covalent fullerene chemistry. *Science* 271:317–323
55. Hermann A, Diederich F, Thilgen C, ter Meer H-U, Müller WH (1994) Chemistry of the higher fullerenes: preparative isolation of  $C_{76}$  by HPLC and synthesis, separation, and characterization of Diels–Alder monoadducts of  $C_{70}$  and  $C_{76}$ . *Helv Chim Acta* 77:1689–1706
56. Texier I, Berberan-Santos MN, Fedorov A, Brettreich M, Schönberger H, Hirsch A, Leach S, Bensasson RV (2001) Photophysics and photochemistry of a water-soluble  $C_{60}$  dendrimer: fluorescence quenching by halides and photoinduced oxidation of  $I^-$ . *J Phys Chem A* 105:10278–10285
57. Rae M, Fedorov A, Berberan-Santos MN (2003) Fluorescence quenching with exponential distance dependence. Application to the external heavy-atom effect. *J Chem Phys* 119:2223–2231
58. Bodunov EN, Berberan-Santos MN (2004) Short-range order effects on resonance energy transfer in rigid solution. *Chem Phys* 301:9–14
59. Rae M, Perez-Balderas F, Baleizão C, Fedorov A, Cavaleiro JAS, Tomé AC, Berberan-Santos MN (2006) Intra and intermolecular heavy atom effects on the fluorescence properties of brominated  $C_{60}$  polyads. *J Phys Chem B* 110:12809–12814
60. Berberan-Santos MN, Garcia JMM (1996) Unusually strong delayed fluorescence of  $C_{70}$ . *J Am Chem Soc* 118:9391–9394
61. Salazar FA, Fedorov A, Berberan-Santos MN (1997) A study of thermally activated delayed fluorescence in  $C_{60}$ . *Chem Phys Lett* 271:361–366
62. Baleizão C, Berberan-Santos MN (2006) A molecular thermometer based on the delayed fluorescence of  $C_{70}$  dispersed in a polystyrene film. *J Fluoresc* 16:215–219
63. Baleizão C, Nagl S, Borisov SM, Schäferling M, Wolfbeis OS, Berberan-Santos MN (2007) Optical thermometer based on the delayed fluorescence of  $C_{70}$ . *Chem Eur J* 13:3643–3651
64. Nagl S, Baleizão C, Borisov SM, Schäferling M, Berberan-Santos MN, Wolfbeis OS (2007) Optical Sensing and Imaging of Trace Oxygen with Record Response. *Angew Chem Int Ed* 46:2317–2319
65. Baleizão C, Berberan-Santos MN (2007) Thermally activated delayed fluorescence as a cycling process between excited singlet and triplet states. Application to the fullerenes. *J Chem Phys* 126:204510



# Squeezing Fluorescent Dyes into Nanoscale Containers—The Supramolecular Approach to Radiative Decay Engineering

Werner M. Nau (✉) · Andreas Hennig · Apurba L. Koner

School of Engineering and Science, Jacobs University Bremen,  
Campus Ring 1, 28759 Bremen, Germany  
*w.nau@jacobs-university.de*

1	Introduction . . . . .	186
2	Supramolecular Assemblies and Host Molecules . . . . .	187
3	Polarizability Inside Nanoscale Containers . . . . .	191
4	The Influence of Polarizability on the Photophysical Properties of Fluorescent Dyes . . . . .	195
5	Applications of Supramolecular Radiative Decay Engineering . . . . .	201
6	Stabilization of Aqueous Fluorescent Dye Solutions with Cucurbituril . . . . .	204
7	Recent Developments . . . . .	208
8	Outlook . . . . .	209
	References . . . . .	209

**Abstract** Supramolecular radiative decay engineering allows systematic variations of the radiative decay rates, and therefore changes in the fluorescence lifetimes and intensities. Depending on whether fluorescent dyes are immersed in macrocyclic host molecules with low or high polarizability, reduced or enhanced fluorescence lifetimes may result. Solvatochromic probes to “measure” the polarizability inside such molecular container compounds are now at hand. Cucurbiturils, for example, are water-soluble host molecules, which possess a cavity with an exceptionally low polarizability, close to the gas phase. Placing fluorescent dyes inside cucurbiturils allows one to create in aqueous solution a unique microenvironment, which approaches that of the gas phase and leads to unprecedented photophysical behavior. Accordingly, complexation by cucurbituril leads to prolonged fluorescence lifetimes, for 2,3-diazabicyclo[2.2.2]oct-2-ene (DBO) up to 1  $\mu$ s, the same as that found in the gas phase.

## Abbreviations

DBO 2,3-diazabicyclo[2.2.2]oct-2-ene  
Dbo DBO-labeled asparagine  
FCS fluorescence correlation spectroscopy

FLIM	fluorescence lifetime imaging microscopy
FRET	fluorescence resonance energy transfer
Gly	glycine
Ser	serine
TRF	time-resolved fluorescence
Trp	tryptophan

### Symbols

$\varepsilon$	extinction coefficient
$f$	oscillator strength
$J$	overlap integral
$k_{\text{FRET}}$	fluorescence resonance energy transfer rate constant
$k_{\text{ISC}}$	rate constant for intersystem crossing
$k_{\text{IC}}$	rate constant for internal conversion
$k_{\text{nr}}$	nonradiative decay rate constant
$k_{\text{p}}$	rate constant for photoreaction
$k_{\text{r}}$	radiative decay rate constant
$K$	association (binding) constant
$\kappa^2$	orientation factor
$N_{\text{A}}$	Avogadro number
$n$	refractive index
$P$	polarizability
$R$	donor–acceptor distance
$R_0$	Förster radius
$\phi_{\text{f}}$	fluorescence quantum yield
$\tau_{\text{f}}$	fluorescence lifetime (unquenched)
$\tilde{\nu}$	wavenumber

## 1

### Introduction

Lakowicz has introduced, inspired by early observations in the field of physics [1], the method of radiative decay engineering [2, 3]. Accordingly, when chromophores are positioned in the proximity of a metal surface (but avoiding close contact, which would induce quenching), their radiative decay rate can increase steeply, while nonradiative decay pathways are generally not systematically affected. This results in a shortening of the fluorescence lifetimes and in an impressive increase in the fluorescence intensities, rendering even otherwise nonfluorescent chromophores fluorescent.

Recently, we found similarly that unusual effects on the radiative decay rates can be achieved by placing fluorophores into supramolecular assemblies [4–6], where they may experience extreme environments [4]. These may lead, depending on the choice of the supramolecular host system, to enhanced or reduced radiative decay rates. We have referred to this approach as *supramolecular* radiative decay engineering [7].

The structure of this work is such that a short overview of supramolecular assemblies, and host–guest systems in particular, will be provided first. Alternatively, readers may directly proceed to the next section. It describes our method to probe the polarizability/refractive index in supramolecular environments, which we have identified as the underlying cause of the variations in radiative decay rates [7]. The third section will describe examples and potential applications of the observed effects, focusing on supramolecular assemblies (complexes of fluorophores with cucurbiturils), in which the radiative decay rate is slowed, and where exceedingly long fluorescence lifetimes up to 1  $\mu\text{s}$  result. Cucurbiturils, which are synthetic host molecules with cation receptor properties [8–11] have also additional advantageous effects on fluorescent dye properties, which will also be outlined.

## 2

### Supramolecular Assemblies and Host Molecules

Following the pioneering work of Pedersen, Cram, and Lehn, supramolecular chemistry has matured to a rapidly growing, highly interdisciplinary research area with impact on analytical chemistry, biochemistry, pharmacology, environmental science, and materials science [12–14]. In the area of photochemistry, supramolecular sensor applications have become particularly popular, in which chromogenic or fluorogenic groups are incorporated into supramolecular structures and respond to external stimuli such as pH, metal ions, anions, organic analytes, or biomolecular metabolites [15–17].

Supramolecular assemblies are held together by weak intermolecular interactions [18]. The intermolecular complexes between macrocyclic host molecules and smaller guest molecules present prototypal supramolecular architectures. Owing to the fact that most macrocyclic hosts possess a concave inner cavity to include the guest, they are frequently considered as molecular containers with nanoscale dimensions. The combination of a hydrophobic cavity with water-solubility has further defined the enzyme-mimetic potential of water-soluble macrocyclic hosts [19, 20]. Pertinent examples are cyclodextrins, calixarenes [21], and cucurbiturils, which are also available in different sizes to modulate their selectivity in guest binding (Fig. 1). Additional examples of discrete host systems are crown ethers [14], cryptands, cavitands [22, 23], cyclophanes [24, 25], and hemicarcerands [26], as well as mixed inorganic–organic macrocycles (Fig. 2). Cage molecules like carcerands [27] and cage-type inorganic–organic hybrid assemblies like those devised by Fujita et al. [28] or Raymond and coworkers [29] as well as the self-assembling organic capsules pioneered by Rebek and coworkers [30] (Fig. 3) are also fascinating supramolecular assemblies with host properties, which, however, have not yet been examined with the methodologies described herein.

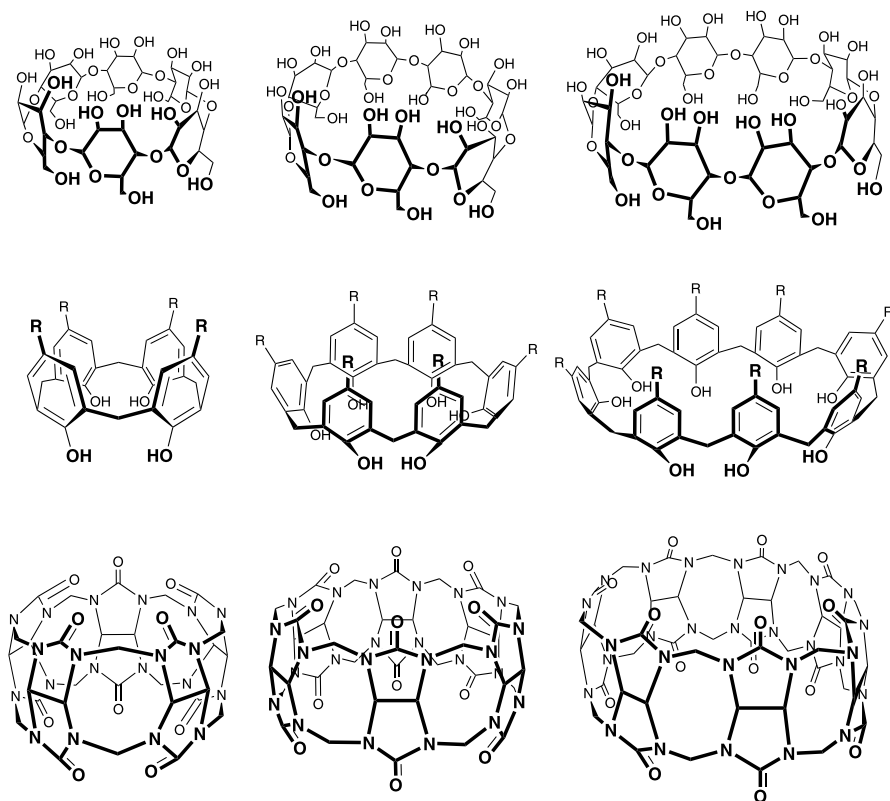


**Fig. 1** Water-soluble macrocyclic host molecules with varying size (from *top to bottom* and *left to right*): cyclodextrins ( $\alpha$ ,  $\beta$ ,  $\gamma$ ), calix[ $n$ ]arenes ( $R = \text{SO}_3^-$ ;  $n = 4, 6, 8$ ) and cucurbit[ $n$ ]urils ( $n = 5, 6, 7$ )

It is very interesting to question whether the inclusion of chromophoric guests, most importantly fluorescent dyes, can affect their photophysical properties and, potentially, lead to unprecedented effects and, ultimately, new applications. In fact, numerous investigations have dealt with variations of fluorescent properties upon complexation [31–34]. In most cases, the effects of inclusion complexation are satisfactorily understood in terms of (i) the relocation of the fluorophore into the more hydrophobic environment of the host cavities or (ii) the geometrical confinement of the chromophore within the host.

The fascinating idea that macrocyclic host molecules might potentially offer to included guests an extreme environment very different from common solvents, and thereby induce novel photophysical effects, is not far fetched. Cram has postulated, for example, that the inner phase of such supramolecules, for example hemicarcerands, could behave as a new phase of matter [26].

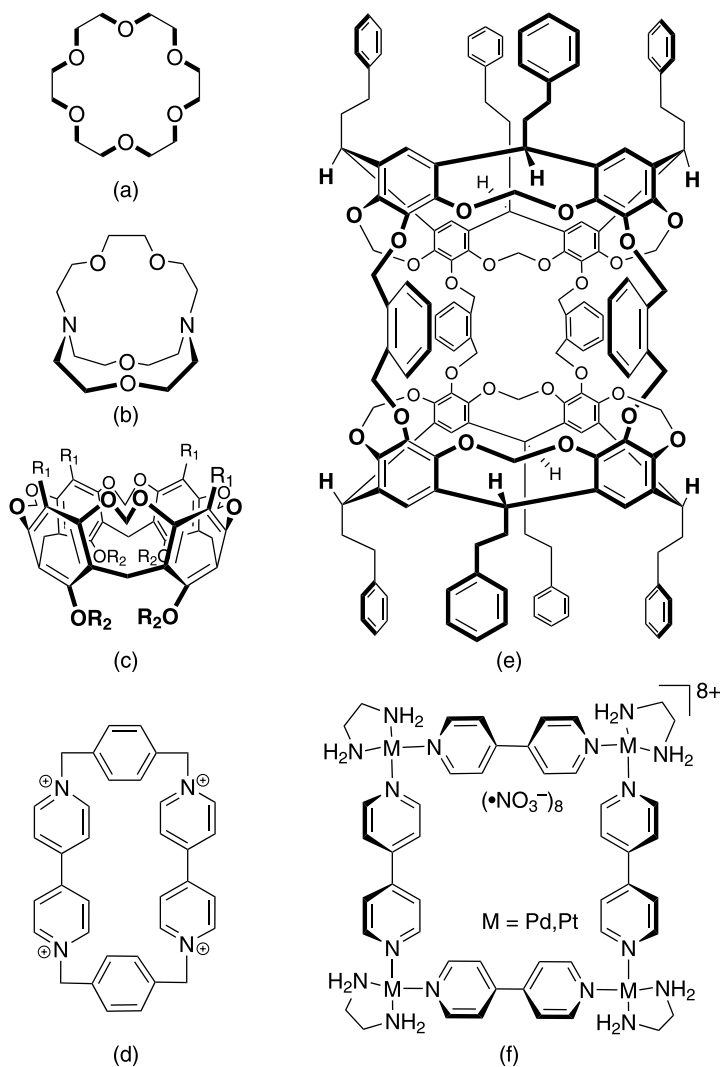
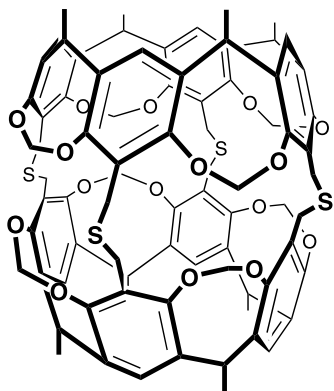
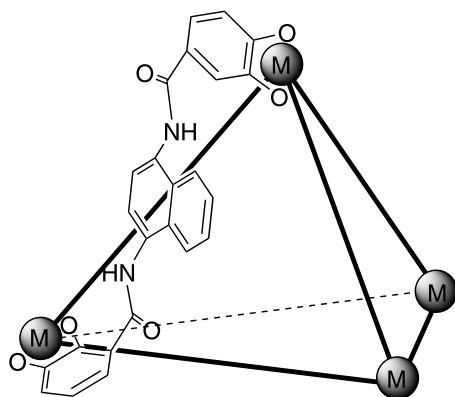


**Fig. 2** Additional examples of macrocyclic hosts: **a** crown ether, **b** cryptand, **c** cavitand, **d** cyclophane, **e** hemicarcerand, and **f** a square inorganic–organic macrocyclic complex, the latter from [28]

We have recently provided the first direct spectroscopic evidence that the inside of molecular containers can indeed impose extreme physical properties, namely an environment with extraordinary polarizability [4], which can have a pronounced influence on photophysical properties, particularly on the radiative decay rate constants [7]. To measure polarizabilities inside host molecules, we have employed new types of solvatochromic probes.

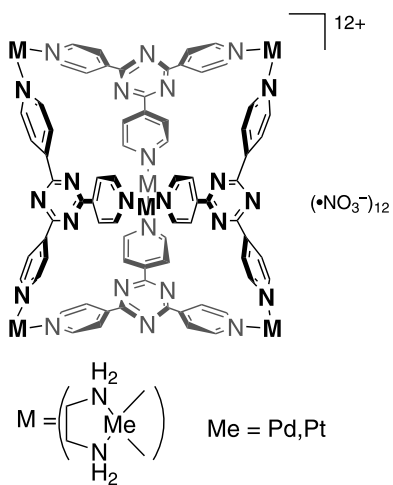


(a)

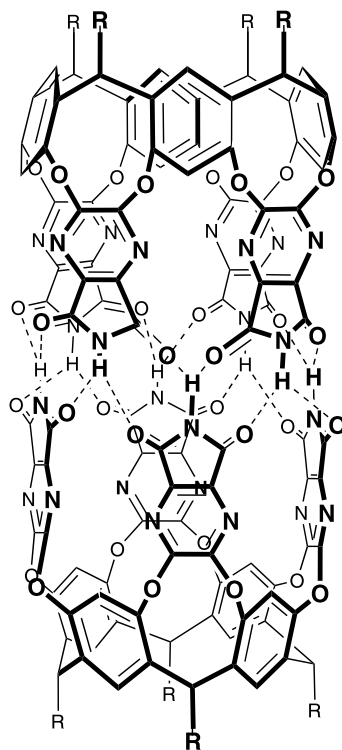


$M = \text{Al}^{3+}, \text{Ga}^{3+}, \text{In}^{3+} \text{ or } \text{Fe}^{3+}$

(c)



(b)



$R = \text{C}_{11}\text{H}_{23}$

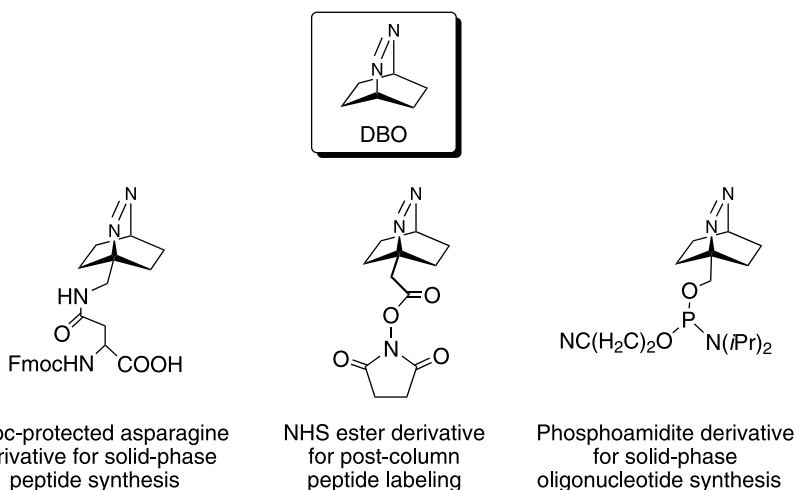
(d)

- ◀ **Fig. 3** Examples of cage-type hosts and self-assembled cages and capsules: **a** carcerand, **b** an octahedral (Fujita type) [28] and **c** a schematic tetrahedral (Raymond type) [29] inorganic–organic macropolycyclic complex, and **d** a self-assembled capsule (Rebek type) [30] composed of two hydrogen-bonded cavitands

### 3 Polarizability Inside Nanoscale Containers

2,3-Diazabicyclo[2.2.2]oct-2-ene (DBO) and its derivatives (Scheme 1), for which we have coined the name fluorazophores, [35] and which are presently commercialized as Puretime™ 325 dyes, are interesting fluorophores owing to their exceedingly long fluorescence lifetime (up to 1  $\mu$ s) [7]. They have found numerous applications in biomolecular and supramolecular chemistry [36–43]. Functionalized derivatives for labeling of peptides and oligonucleotides, for example, are available (Scheme 1). Most importantly, DBO forms supramolecular host–guest complexes with cyclodextrins [44–49], calixarenes [50–52], and cucurbiturils [4, 9, 53, 54], which are of prime interest in the present context (Fig. 1). The small size of DBO and its virtually spherical shape present ideal characteristics to investigate the complexation behavior with macrocyclic hosts, because the (central) position of the chromophore is well defined, that is, DBO can be fully immersed in sufficiently large host cavities.

Recently, we have made the uncommon observation that DBO, as well as other cyclic azoalkanes and some other  $n, \pi^*$ -excited states like biacetyl,



**Scheme 1** Molecular structure of 2,3-diazabicyclo[2.2.2]oct-2-ene (DBO) and its functionalized derivatives suitable for covalent attachment to biopolymers

display environmentally dependent changes of the absorption intensity, i.e., oscillator strength [ $f = 4.32 \times 10^{-9} \int \varepsilon(\bar{\nu})d\bar{\nu}$ ] [4]. The best correlation was observed in both cases (DBO and biacetyl) between the oscillator strength and the (bulk) polarizability. Clear trends of the absorption and emission maxima with varying polarizability were also observed, but the changes of the oscillator strengths were most systematic in nature. Importantly, there was no correlation with the polarity or hydrogen-bond donor abilities of the solvent, such that polarizability effects could be reliably dissected from the more trivial polarity effects [55].

In detail, when the oscillator strength of the near-UV absorption band of DBO was measured in different solvents as well as in the gas phase, a linear correlation between the *inverse* oscillator strength and the polarizability ( $P$ ) of the solvent was found ( $1/f = 3020 - 8320 P$ ,  $r = 0.979$ , 11 data points) [4], which established DBO as a solvatochromic probe for the polarizability of the environment. Note that the bulk polarizability  $P$  is a simple function of the solvent refractive index [ $P = (n^2 - 1)/(n^2 + 2)$ ].

The next step was the application of DBO to sound out the microenvironment, i.e., the micropolarizability, inside macrocyclic hosts by employing the solvatochromic approach [4, 7, 49, 50]. Solvatochromic probes have, in fact, been previously employed to determine the polarity of solvents [55] or inside macrocyclic hosts [31], or to assess hydrogen bond donor properties of the environment [55]. 1-Anilidonaphthalene-8-sulfonate is an example for a polarity-sensitive probe that has been applied to cyclodextrins [32, 33] and water-soluble calixarenes [34] (Fig. 1), providing evidence for a hydrophobic environment inside these hosts (similar to alcohol:water mixtures, but with calixarenes being more hydrophobic).

The determination of polarizabilities inside molecular containers was greatly assisted by the small size and spherical shape of DBO, which allows the formation of tight and “deep” inclusion complexes with a variety of macrocycles. Among the cyclodextrins, the strongest binding of DBO applies for the  $\beta$  homologue composed of 7  $\alpha$ -D-glucose units ( $K$  ca.  $1000 \text{ M}^{-1}$ ) [44, 45]. DBO is too large to be included into cucurbit[6]uril [9], but fits nicely into the next larger homologue, cucurbit[7]uril ( $K$  ca.  $4 \times 10^5 \text{ M}^{-1}$ ) [4]. For *p*-sulfonatocalix[4]arene, a water-soluble calixarene [21], it was recently found that DBO binds in fact stronger ( $K$  ca.  $1000 \text{ M}^{-1}$ ) than all previously studied noncharged guest molecules ( $K$  ca.  $10\text{--}100 \text{ M}^{-1}$ ), which was attributed to the spherical shape complementarity between DBO and the conical host cavity of the calixarene [52].

To extract the polarizabilities inside the various host molecules, DBO solutions with excess host were prepared, and the oscillator strengths of the resulting host-guest complexes were determined and corrected for the degree of complexation, where required. Subsequent correlation according to the established solvatochromic relationship provided the polarizabilities inside a variety of supramolecular container compounds as well as some self-



assembling supramolecular lipidic assemblies (micelles and liposomes), see Table 1. Interestingly, the polarizability inside cyclodextrins was found to be rather unspectacular, similar to that of water and alcohols [7], but the formation of a better shielded 2 : 1 capsule with DBO led to an increase of the polarizability sensed by DBO, which was then similar to that in *n*-hexane [49]. The polarizability inside *p*-sulfonatocalix[4]arene, on the other hand, fell below that of benzene, as would be expected from the partial exposure of the guest

**Table 1** Refractive index and polarizability inside macrocyclic host molecules and different supramolecular environments, determined by using the DBO chromophore as a solvatochromic probe, relative to those in solvents and the gas phase

Environment	Refractive index ( <i>n</i> ) <sup>a</sup>	Polarizability ( <i>P</i> ) <sup>b</sup>
Gas phase	1.000	0.000
Cucurbit[7]uril (axial) <sup>c</sup>	1.17	0.11
Cucurbit[7]uril (equatorial) <sup>d</sup>	1.19	0.12
Perfluorohexane	1.252	0.159
$\beta$ -Cyclodextrin	1.33	0.20
H <sub>2</sub> O	1.333	0.206
SDS micelles <sup>f</sup>	1.34	0.21
<i>n</i> -Hexane	1.375	0.229
Triton XR-100 micelles <sup>f</sup>	1.38	0.23
POPC liposomes <sup>f</sup>	1.38	0.23
DMe- $\beta$ -CD (2 : 1 complex) <sup>e</sup>	1.39	0.24
Calixarene (equatorial) <sup>g,h</sup>	1.41	0.25
Calixarene (axial) <sup>c,g</sup>	1.43	0.26
Benzene	1.501	0.295
Diiodomethane	1.742	0.404
Hemicarcerand <sup>i</sup>	1.86	0.45

<sup>a</sup> Refractive index, converted using the formula  $P = (n^2 - 1)/(n^2 + 2)$

<sup>b</sup> From the empirical relationship ( $1/f = 3020 - 8320 P$ )

<sup>c</sup> H. Bakirci, A.L. Koner, W.M. Nau, unpublished results, measured with the 1-ammoniummethyl derivative of DBO

<sup>d</sup> From a previous publication [4] measured with DBO; the equatorial orientation of DBO was later derived from the crystal structure for the corresponding cucurbit[7]uril · DBO · 3Ag<sup>+</sup> complex (A.L. Koner, M. Dickman, W.M. Nau, unpublished results)

<sup>e</sup> From a previous publication [49] measured with DBO as guest and heptakis-(2,6-di-*O*-methyl)- $\beta$ -cyclodextrin as host

<sup>f</sup> Derived from the absorption spectra of the palmitoyl derivative of DBO in [37]

<sup>g</sup> *p*-Sulfonatocalix[4]arene

<sup>h</sup> From a previous publication [50] measured with DBO; the equatorial orientation of DBO was subsequently corroborated by NMR spectroscopy, cf. previous publication [52]

<sup>i</sup> Value determined using biacetyl as solvatochromic probe, cf. previous publication [4]

to the aqueous environment at the upper and lower opening of the calixarene (Fig. 1) [50]. In some cases, different orientations of the chromophore could be realized through appropriate anchoring groups, for example, an equatorial and axial conformation inside *p*-sulfonatocalix[4]arene (Fig. 4, top), where the azo chromophore experiences a somewhat higher polarizability in the latter arrangement due to the close proximity to the highly polarizable aryl groups.

An exceptionally low polarizability was interpolated for cucurbit[7]uril, even lower than that in perfluorohexane and close to the gas phase. The orientation of the DBO chromophore inside the cucurbituril was further modified through ion-dipole interactions between an ammoniummethyl group attached to the guest and the ureido carbonyl groups of the host (Fig. 4, bottom). In contrast to the calixarene (see above and Fig. 4, top), the axial arrangement of the DBO derivative now suggests a slightly reduced polariz-

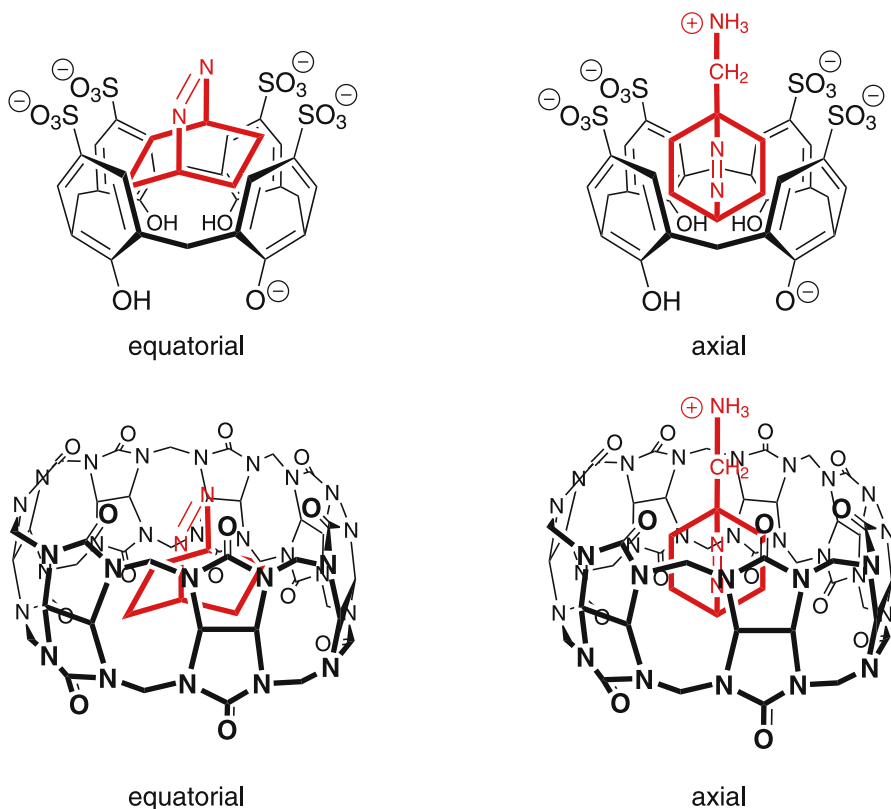


**Fig. 4** Realization of equatorial and axial (with an ammoniummethyl group as anchor) orientations of DBO inside macrocyclic host molecules: *p*-sulfonatocalix[4]arene (*top*) and cucurbit[7]uril (*bottom*), both at neutral pH

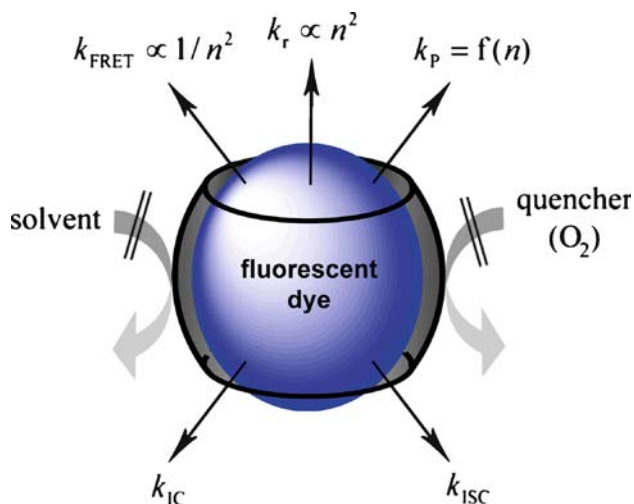
ability compared to that sensed by parent DBO (Table 1); note that the latter is presumed to adapt an equatorial orientation in cucurbit[7]uril. Furthermore, by employing biacetyl as a solvatochromic polarizability probe and using previously reported phosphorescence data for biacetyl [56], an extremely high polarizability was extrapolated for hemicarcerands [4], even higher than that in diiodomethane (Table 1). These results provided strong support for Cram's much debated "new phase of matter" hypothesis [26], because they revealed refractive indices inside supramolecular architectures, which are unheard of in any solvent.

The observed trends, however, are not entirely unexpected, when the molecular structures are closely inspected. The inside of hemicarcerands is dominated by electron-rich  $\pi$ -systems pointing towards the interior, which are known to be highly polarizable; the guest is therefore exposed in all directions to a sea of  $\pi$ -electron density, even more pronounced than if it was immersed in benzene, where the tumbling of the solvent molecules reduces the effective polarizability exerted by the  $\pi$  systems. In contrast, the inside of cucurbit[7]uril is the opposite of electron-rich; all the surrounding bonds are polar, and there are no C–H bonds,  $\pi$  bonds, or lone pair orbitals pointing inwards. Note, in particular, that the concave nature displaces the electron density of the ureido nitrogen lone pairs towards the outside of the cavity; the resonance interaction with the carbonyl groups further withdraws electron density towards the upper and lower portals, away from the inside of the cavity and the centrally positioned guest. The polarizabilities inside nanoscale containers cover therefore a very wide range, and allow the exposure of guest molecules to environments with extremely low and high polarizability.

## 4

### The Influence of Polarizability on the Photophysical Properties of Fluorescent Dyes

The immediate question about the chemical relevance of a low or a high polarizability inside macrocyclic hosts arises. The first interesting area are possible effects on intermolecular interactions or chemical reactions involving supramolecular assemblies. According to the empirical London formula, the contribution of the dispersion interaction to the attraction between any two molecular species depends on their (molecular) polarizability. The importance of the polarizability in host–guest complexation and molecular recognition processes was emphasized early by Castro et al. for cyclophanes as hosts (see Fig. 2); the polarizability of the guest and the resulting dispersion interactions was in fact revealed as the dominant driving force in the complexation of 4,4'-disubstituted biphenyls by cyclobis(paraquat-*p*-phenylene) [24]. The role of the polarizability in the acceleration of reaction rates inside supramolecules has also been demonstrated, for example for nucleophilic



**Scheme 2** Deactivation of singlet-excited states inside molecular containers illustrating the protection from quenchers and solvent-induced quenching as well as rate constants, which are being potentially modulated through the polarizability/refractive index

substitution and elimination reactions in the presence of macrotricyclic ammonium salts [57], for the nucleophilic alkylation and dealkylation inside cyclophanes [58, 59], for the thermal decomposition of diazirines [60, 61], and, according to computational treatments, for the Menshutkin reaction inside carbon nanotubes [62, 63].

The second area, which is more relevant in the present context, are photophysical effects, particularly effects on the properties of fluorescent dyes. Following excitation to the first singlet-excited state the known pathways of deactivation apply (Scheme 2), including radiative decay, fluorescence resonance energy transfer (FRET), photoproduct formation, internal conversion, intersystem crossing, solvent-induced quenching, and quenching by additives or oxygen. Several primary photophysical processes depend on the polarizability/refractive index of the environment [64]. The dependence of the decay rate constants on the refractive index can be analytically expressed for two pertinent rate constants: the FRET rate according to the Förster dipole–dipole mechanism ( $k_{\text{FRET}}$ ), and, more important, the radiative decay rate constant ( $k_r$ ).

The Strickler–Berg equation predicts a dependence of the radiative decay rate on the square of the refractive index (Eq. 1) [65].

$$k_r = 0.668 \langle \tilde{\nu} \rangle_{\text{av}}^2 n^2 f. \quad (1)$$

The validity of this equation was previously tested for fluorophores with allowed electronic transitions; in these cases, the oscillator strength can be considered to remain constant in different environments [66–70]. A direct

relationship between  $k_r$  and  $n^2$  results in these limiting cases, which has been employed to estimate the polarizability in biological microenvironments like lipid membranes [66], reverse micelles [67–69], the interior of the green fluorescent protein [70], and tryptophan residues in proteins [71]. The applicability of Eq. 1 was also successfully tested for DBO, where the additional dependence of the oscillator strength on the polarizability needed to be explicitly taken into account [7].

Assuming that other photophysical rate constants remain constant, one can project a concomitant change of the fluorescence lifetime  $\tau_f$  and of the fluorescence quantum yield  $\phi_f$ . As can be seen from Eq. 2a and b an increase in the fluorescence quantum yield at the expense of a reduced fluorescence lifetime is expected, when the radiative decay rate is increased and vice versa.

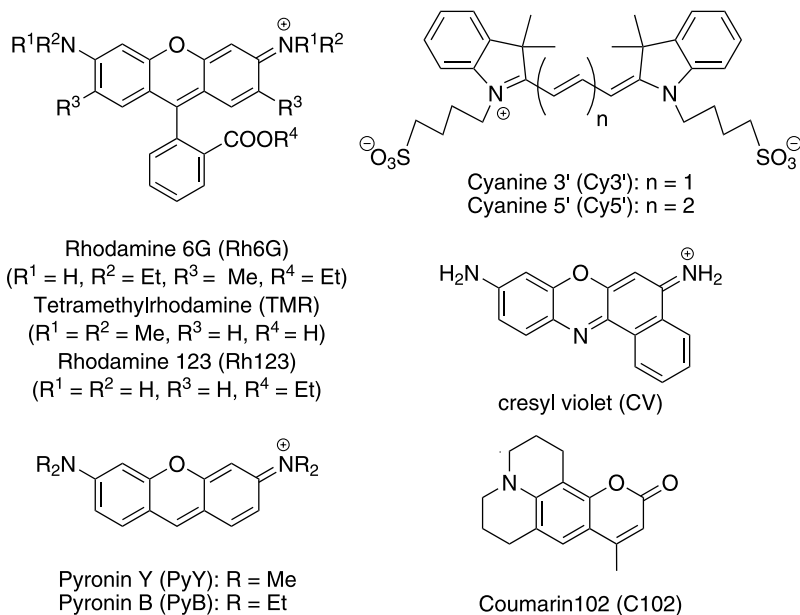
$$\phi_f = \frac{k_r}{k_r + k_{nr}} \quad (2a)$$

and

$$\tau_f = \frac{1}{k_r + k_{nr}}. \quad (2b)$$

The radiative decay rates of DBO in  $\beta$ -cyclodextrin and cucurbit[7]uril provided an independent probe for the polarizabilities projected from the above solvatochromic method (effects on oscillator strength). Accordingly, if the polarizability inside cyclodextrins was similar to water and alcohols, the radiative decay rate should also be comparable, as was found to be the case [7]. If, however, the polarizability inside cucurbiturils was extremely low, in between perfluorohexane and the gas phase, the radiative decay rates should also fall within this uncommon region, therefore resulting in exceedingly slow radiative decay rates and, with other decay rates remaining similar, longer fluorescence lifetimes. Exactly this was observed: The fluorescence quantum yield in deaerated water is 0.26 and the fluorescence lifetime is 415 ns [7]. In the inclusion complex with cucurbit[7]uril, a contrasting observation was made, because the fluorescence quantum yield *decreased* to 0.19, while the fluorescence lifetime increased to ca. 1  $\mu$ s! This corresponds to a decrease in the radiative decay rate constant (simply calculated as  $\phi_f/\tau_f$ ) by a factor of ca. 3! Noteworthy, this decrease in the radiative decay rate is only partially due to the decreased oscillator strength, but also due to a direct effect of the environmental refractive index on the radiative decay rate, thereby demonstrating the influence of the critical  $n^2$  term in Eq. 1.

The 1  $\mu$ s fluorescence lifetime of DBO when included inside cucurbituril is the longest one known for an organic chromophore in aqueous solution [43, 54]. Since then, radiative decay rates of fluorophores included in cucurbituril have been determined for numerous fluorescent dyes, including the commercially important rhodamine, pyronin, oxazine, coumarin, and cyanine dye types (Scheme 3 and Table 2) [5, 6]. In all cases, increased flu-



**Scheme 3** Structures of fluorescent dyes studied in the presence of cucurbit[7]uril, cf. Table 2

orescence lifetimes were observed, often the longest ever observed for the respective dyes, and by calculating the radiative decay rates, several independent estimates for the local refractive index inside the molecular container could be obtained. Because of the allowedness of the respective electronic transitions, the oscillator strength was approximately constant (independent of the presence of CB7) for the fluorescent dyes in Scheme 3 (cf. extinction coefficients in Table 2), such that a simple square-root dependence applied in these cases. The apparent refractive indices (and polarizabilities) experienced by these fluorescent dyes inside cucurbituril could therefore be estimated as

$n_{H_2O} \times \sqrt{k_r^{CB7} / k_r^{H_2O}}$  (last two columns in Table 2). Note that some refractive indices extrapolated by this method are unreasonably low (below 1, the limiting value in vacuum). This is a consequence of the arbitrary choice of water as a reference environment, since gas phase data for these dyes are not available. From the combined data for nine aromatic dyes, a statistically meaningful value ( $1.10 \pm 0.12$ , nine data points) for the refractive index inside cucurbituril was obtained [6], in agreement with the values obtained by the solvatochromic method using DBO (Table 1), and significantly below the refractive index of perfluorohexane (1.25).

It would be of interest to assess the radiative decay rates of fluorophores inside highly polarizable host molecules as well, for example in hemi-

**Table 2** Photophysical parameters of fluorescent dyes (see Scheme 3) with and without 1 mM cucurbit[7]uril (CB7) in H<sub>2</sub>O under air<sup>a</sup>

Fluorescent dye	$\lambda_{\text{abs}}^{\text{max}}$ /nm	$\lambda_{\text{em}}^{\text{max}}$ /nm	$\varepsilon_{\text{max}}/(10^4$ $\text{M}^{-1} \text{cm}^{-1})$	$\phi_{\text{f}}$	Bright- ness <sup>b</sup>	$\tau_{\text{f}}$ /ns	$n_{\text{app}}^{\text{c}}$	$P^{\text{d}}$	
DBO <sup>e</sup>	without CB7	364	419	0.0053	0.26	$1.4 \times 10^{-3}$	415	1.19	0.120
	with CB7	374	427	0.0040	0.19	$7.6 \times 10^{-4}$	725		
Rh6G	without CB7	526	552	8.02	0.89	7.14	4.08	1.24	0.152
	with CB7	535	555	9.24	0.89	8.22	4.76		
TMR	without CB7	553	577	8.78	0.28	2.46	2.15	1.12	0.078
	with CB7	559	582	7.48	0.38	2.84	4.16		
Rh123	without CB7	500	525	6.92	0.83	5.75	4.19	0.84	-0.109
	with CB7	503	532	6.66	0.36	2.40	4.63		
PyY	without CB7	546	565	13.2	0.47	6.20	1.69	1.08	0.053
	with CB7	544	568	13.1	0.63	8.25	3.44		
PyB	without CB7	552	569	9.41	0.36	3.39	1.19	1.14	0.091
	with CB7	556	571	9.93	0.70	6.95	3.10		
C102	without CB7	393	489	2.18	0.66	1.44	6.04	1.30	0.187
	with CB7	405	476	2.36	0.75	1.77	7.19		
CV	without CB7	585	625	3.31	0.36	1.19	2.18	0.98	-0.013
	with CB7	591	628	4.09	0.35	1.43	3.93		
Cy3'	without CB7	545	560	12.0	0.04	0.48	0.46	1.02	0.013
	with CB7	559	571	10.7	0.03	0.32	0.58		
Cy5'	without CB7	642	660	13.8	0.17	2.35	0.63	1.12	0.078
	with CB7	642	657	11.2	0.30	3.36	1.59		

<sup>a</sup> From [6].<sup>b</sup> Calculated as  $\varepsilon_{\text{max}}\phi_{\text{f}}/(10^4 \text{M}^{-1} \text{cm}^{-1})$ .<sup>c</sup> Apparent refractive index experienced by the respective dye inside the cucurbit[7]uril cavity, extrapolated by using the Strickler-Berg formula (Eq. 1), and by using water as reference, i.e.  $n_{\text{H}_2\text{O}} \times \sqrt{k_{\text{r}}^{\text{CB7}}/k_{\text{r}}^{\text{H}_2\text{O}}}$ , cf. text.<sup>d</sup> Calculated from the apparent refractive index as  $P = (n_{\text{app}}^2 - 1)/(n_{\text{app}}^2 + 2)$ <sup>e</sup> From [4, 7].

carcerands, where a strong enhancement would be expected. Unfortunately, the corresponding host-guest complexes cannot be readily prepared through dynamic guest exchange at ambient temperature. However, as far as an acceleration of the radiative decay rate is concerned, the original supramolecular radiative decay engineering near metal surfaces introduced by Lakowicz clearly excels [2, 3]. For this purpose, chromophores are positioned at a certain distance near silver island films on glass slides, silver colloids or silver nanorods, where they experience an uncommon environment from a photophysical point of view, which leads to increased radiative decay rates, i.e., an increased fluorescence intensity and a decreased fluorescence lifetime. The underlying theory for the phenomenon is relatively complex and involves partly counteracting effects like distance-dependent fluorescence quenching

and fluorescence enhancement due to an increased intensity of the incident light (“photonic mode density”), and, potentially, an increased refractive index near the metal particle surface. The resulting enhanced fluorescence intensity (detectable even for otherwise nonfluorescent chromophores like nucleotides) has already been successfully exploited for a wide variety of practical applications in biotechnology like homogeneous and heterogeneous fluorescence immunoassays and hybridization assays [72].

$$k_{\text{FRET}} = \frac{1}{\tau_f} \left( \frac{R_0}{R} \right)^6 \quad \text{where} \quad R_0 = \sqrt[6]{\frac{9000(\ln 10)\kappa^2\phi_f}{128^5 N_A n^4} J}. \quad (3)$$

An impact of the refractive index on the FRET rate and on the Förster radius  $R_0$  (Eq. 3) is also expected. Assuming a limiting fluorescence quantum yield of unity, an  $n^{-2/3}$  dependence should apply to  $R_0$ , i.e., the Förster radius could decrease by up to ca. 35% in supramolecular environments of high refractive index ( $n$  ca. 1.9, cf. Table 1) compared to the gas phase ( $n = 1.0$ ). Although this relationship is presumably difficult to test in discrete supramolecular host-guest systems, corrections for the refractive index are well accepted in the analysis of FRET data in alternative supramolecular assemblies, like lipids and proteins [64]. The dependence of the rate constant of energy transfer ( $k_{\text{FRET}}$  in Eq. 3) on the polarizability can become more complex, since the fluorescence lifetime  $\tau_f$  (in the absence of acceptor) enters the expression, which in turn depends on Eqs. 1 and 2b. However, assuming again  $\phi_f = 1.0$ ,  $\tau_f = 1/k_r$  results from Eq. 2b and therefore  $1/\tau_f \propto n^2$  according to Eq. 1. The net dependence is then expected to be  $k_{\text{FRET}} \propto 1/n^2$ , i.e., the higher the refractive index the slower the rate of fluorescence energy transfer should be. Again, this has not been tested in macrocyclic hosts, and the limitations of the dipole-dipole approximation for describing singlet-singlet energy transfer are well known, which greatly limits the usefulness of the above predictions for FRET. In this context, it should be noted that the positioning of FRET donor/acceptor pairs near metal surfaces, following the strategy introduced by Lakowicz and co-workers, results in enhanced FRET efficiencies [3]; these cannot be accounted for in terms of the above considerations related to refractive index changes alone. Rather, they reflect the involvement of additional surface, size, and shape effects [73].

Finally, it is noteworthy that the encapsulation into macrocyclic hosts displays additional effects on the nonradiative decay rates, in particular on the rates of photochemical reaction pathways. While effects on photochemical reactions may be partly due to polarizability effects as well (akin to the effects on thermal reactions described above), their dissection from polarity effects, or effects related to confinement or specific chemical interactions with the host, is difficult. Supramolecular effects on the photochemical reaction rates are therefore not generally predictable and need to be individually evaluated for different chromophores and hosts. Cyclodextrins and calixarenes,



for example, are quite readily oxidized and may therefore serve as fluorescence quenchers through hydrogen abstraction or charge transfer pathways including exciplex formation [44, 45, 50, 74]. This is generally undesirable, except for selected sensor applications [50, 51], because it will inevitably result in a shortening of the fluorescence lifetime and a reduction in fluorescence intensity by supramolecular inclusion. In contrast, cucurbiturils as hosts are chemically extremely inert and resist even treatment with ozone. This inertness, along with the lower polarity as well as polarizability inside the cavity, reduces chemical reaction pathways of the included chromophores. In general, fluorophores included in cucurbituril display reduced nonradiative decay rates, which reflects their lower reactivity in processes which induce internal conversion, and/or in processes which lead to irreversible chemical transformations (photobleaching, see below) [5, 6, 75].

To conclude this section, the dependence of the radiative decay rate constant on the refractive index (Eq. 1) provides a tool to control fluorescence lifetimes as well as fluorescence intensities (Eq. 2) by a rational choice of the microenvironment. As demonstrated in the previous section, the polarizability inside supramolecules covers an unprecedented large range, from hemicarcerands, in which the polarizability is higher than in diiodomethane, to cucurbit[7]uril, in which the polarizability is close to the gas phase. Accordingly, the radiative decay rate constant should be extremely low inside cucurbit[7]uril and should increase upon changing to more polarizable supramolecules, like cyclodextrins, calixarenes, and ultimately hemicarcerands (see Table 1).

## 5

### Applications of Supramolecular Radiative Decay Engineering

It transpires from the foregoing that supramolecular assemblies offer the unique opportunity to expose chromophores to microenvironments with extreme polarizabilities, such that interesting photophysical effects result. The rational choice of macrocyclic host molecules presents in this sense a genuine approach to engineer the radiative decay rates of fluorescent dyes without changing the solvent. Cucurbiturils, for example, can be used as water-soluble additives. This paves the way for numerous biological and potentially environmental fluorescent sensor and assay applications. The contrast in fluorescence lifetime imaging microscopy (FLIM) of biological samples, for example, depends strongly on a large spread of fluorescence lifetimes [76], and we suggest that cucurbiturils can serve as useful additives and “contrast agents” in FLIM measurements.

An important type of bioassays, known as time-resolved fluorescence (TRF) assays, depends on long luminescence lifetimes as well [77–81]. The principal idea behind using TRF is that long luminescence lifetimes can be selectively detected by employing a time gate, i.e., the emission from the sam-

ple is only detected after a certain delay, i.e., after all short-lived emission has decayed. Such short-lived emission presents a ubiquitous but undesirable background in fluorescence-based measurement. It originates from scattered light, biological autofluorescence, sample container materials, as well as additives and potential inhibitors. In TRF measurements, the short-lived emission is not suppressed, but electronically gated out, which increases the signal to background ratio drastically compared to steady-state detection, owing to the exponential fluorescence decay characteristics [82].

Practically useful TRF assays have until now been based on lanthanide metal ion clathrates, which show sharp emissions with phosphorescence lifetimes in the ms range, corresponding to forbidden atomic transitions [77]. They were employed, among others, for the sensitive detection of DNA and proteins [78], and for a variety of enzyme assays [79–81]. Recently, a novel type of TRF assay based on DBO as a truly fluorescent (rather than phosphorescent) label has been introduced, thereby by-passing the need for rare earth metal ions [82]. Owing to the availability of functionalized DBO derivatives (Scheme 1), new opportunities for substrate design arise, in particular due to the compatibility of the purely organic chromophore during solid-phase peptide and oligonucleotide synthesis. Because the time-gate is applied in the nanosecond rather than in the millisecond range, we have referred to this new technique as Nano-TRF [82]. As an additional asset, Nano-TRF facilitates the use of high-energy lasers or lasers with higher repetition rates.

Supramolecular radiative decay engineering provides a new tool to efficiently expand and improve the sensitivity of Nano-TRF measurements. This method relies on the use of cucurbit[7]uril as an additive to prolong the fluorescence lifetime of the DBO chromophore in polypeptides [54] and in the presence of nucleotides [42, 53]. In both cases the encapsulated fluorescent probe (DBO) is efficiently protected from collision-induced quenching, which is a known deactivation pathway of DBO in oligonucleotides [42] and polypeptides [39–41], owing to the strong quenching by the nucleobase guanine [53] and the amino acids tryptophan (Trp), tyrosine, cysteine, and methionine [39].

A specific example is given for a DBO-labeled polypeptide bearing tryptophan as an efficient quencher (H-Trp-Gly-Ser-Gly-Ser-Dbo-NH<sub>2</sub>, Fig. 5). The interconnecting backbone between DBO and tryptophan is flexible (owing to the presence of the flexible amino acid glycine) [40, 41]. This chain flexibility allows probe/quencher contact during the excited state lifetime, which causes fluorescence quenching. When cucurbit[7]uril (1 mM) is added to the peptide solution, DBO is shielded by the host, which suppresses collision-induced quenching and in addition the fluorophore is placed into the weakly polarizable host cavity, which reduces the radiative decay rate. The fluorescence lifetime of the DBO-labeled peptide increases therefore by nearly two orders of magnitude, from 19.5 ns to 1030 ns in aerated H<sub>2</sub>O (Fig. 5). This lifetime increase is actually due to a composite effect of cucurbit[7]uril, namely the

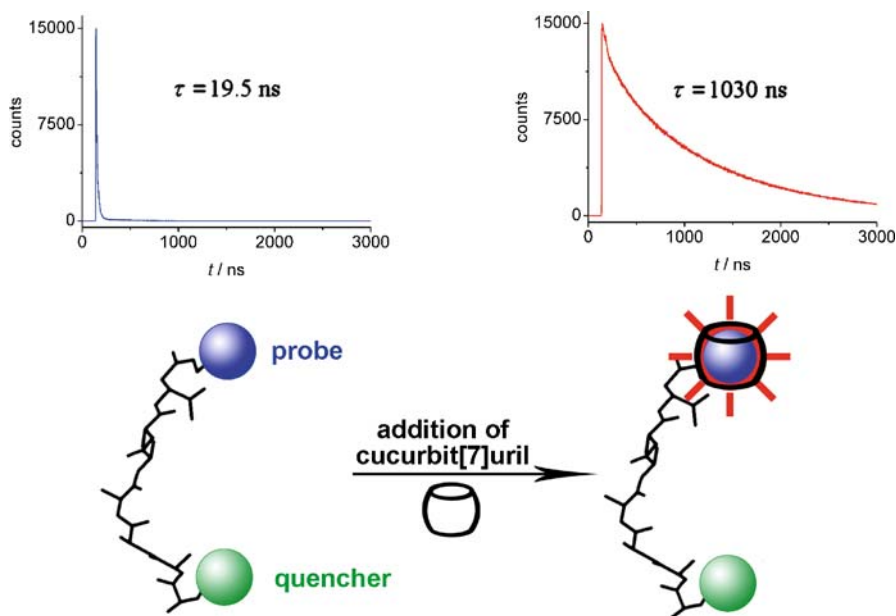


**Fig. 5** Selective complexation of the DBO chromophore in a DBO-labeled peptide (H-Trp-Gly-Ser-Gly-Ser-Dbo-NH<sub>2</sub> where Dbo represents DBO-labeled asparagine, cf. Scheme 1) by the macrocyclic host cucurbit[7]uril (1 mM) and the concomitant effect on the fluorescence lifetimes ( $\lambda_{\text{exc}} = 378$  nm,  $\lambda_{\text{obs}} = 440$  nm, determined by time-correlated single photon counting in D<sub>2</sub>O)

combination of an altered microenvironment and the shielding effect against quenchers. For comparison, in the absence of intramolecular quenchers, i.e., in the corresponding peptide without tryptophan (H-Gly-Ser-Gly-Ser-Dbo-NH<sub>2</sub>), the fluorescence lifetime of DBO increases only ca. three times (from 350 ns to 1030 ns, in aerated water) upon addition of cucurbit[7]uril (1 mM). This exposes solely the environmental effect (polarizability decrease) on the fluorescence lifetime (factor 3 enhancement, note that the slightly different data for DBO in Table 2 refer to the free fluorophore, that is, not covalently attached to a biomolecule).

Owing to the synergetic lifetime-enhancing effects of cucurbituril, fluorescence lifetimes of up to 1  $\mu$ s can be realized for DBO-labeled biomolecules. This allows a highly sensitive detection by the Nano-TRF technique, for example, of a particular peptide substrate. Note the measurement mode illustrated in Fig. 6. Accordingly, when the fluorescence is detected with a time delay of 500 ns and collected in a time window of 2  $\mu$ s, a virtually perfect separation from any short-lived emission, whether it arises from some residual uncomplexed peptide as in the present case study or from additives as in practically relevant screening applications, can be gated out in an elegant and highly efficient manner. In fact, the signal to background ratio in Nano-TRF

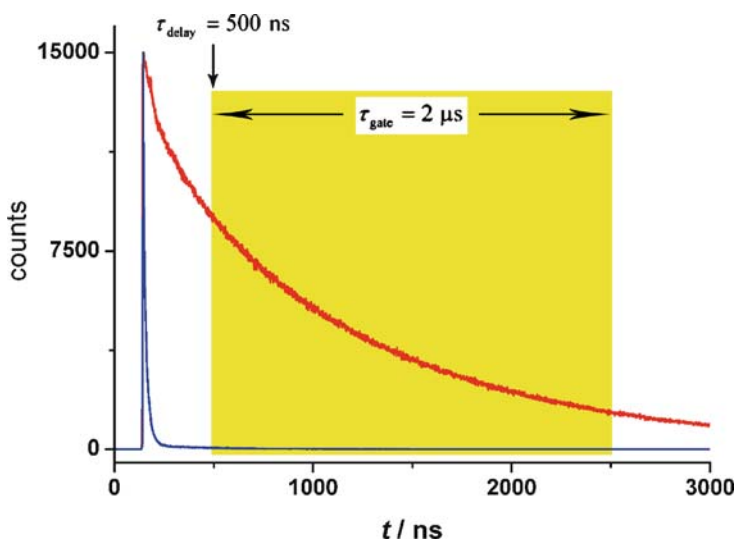


**Fig. 6** Illustration of the Nano-TRF detection mode for the fluorescence decay traces from Fig. 5. Note the virtually perfectly selective fluorescence detection in Nano-TRF mode (*yellow time window*).  $\tau_{\text{delay}}$  is the delay after which fluorescence is recorded and  $\tau_{\text{gate}}$  is the gate time, in which the fluorescence is collected (integrated)

measurements, facilitated by the use of cucurbiturils as fluorescence lifetime-enhancement agents, can be increased by several orders of magnitude [82].

As was demonstrated for the complexation of other fluorescent dyes (Table 2), the increase in fluorescence lifetime upon addition of cucurbit[7]uril is quite general. Although traditional aromatic fluorophores show much shorter fluorescence lifetimes than DBO and present therefore no viable labels for TRF measurements, the complexation by cucurbiturils could be similarly exploited for cationic aromatic dyes in techniques based on nanosecond fluorescence-lifetime measurements, which are employed in another class of emerging assays [83]. The latter have become recently popular and were described as being more robust than conventional steady-state assays in DNA sequencing [84–86], or hybridization assays [87]. Moreover, in the course of our investigations on exploiting cucurbiturils to prolong fluorescence lifetimes of these aromatic fluorescent dyes, we found added value to the use of this macrocyclic host, which is described in the concluding section.

## 6 Stabilization of Aqueous Fluorescent Dye Solutions with Cucurbituril

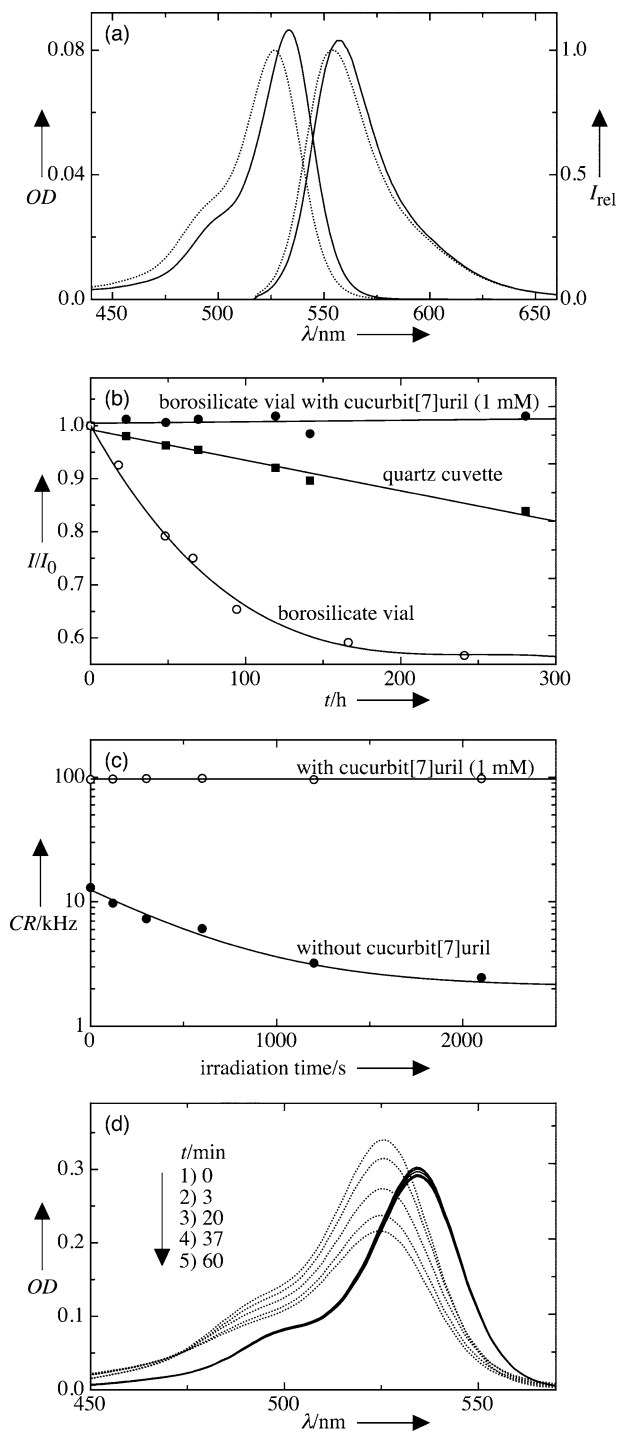
Fluorescent dyes are prone to aggregate in aqueous solution, they tend to be unspecifically adsorbed to material surfaces, and they undergo photo-

bleaching [88–92]. A promising approach to reduce some of these common complications is through molecular encapsulation [93]. Complexation by cucurbituril provides an impressive example in this respect [5, 6], since it can completely suppress aggregation and adsorption, and also reduce photo-bleaching of fluorescent dyes, which leads to several advantageous side effects of supramolecular radiative decay engineering.

To lower the detection limit in fluorescence-based applications, fluorescent dyes have been optimized with respect to their brightness, that is, they show high extinction coefficients characteristic for allowed transitions and exhibit high fluorescence quantum yields; the latter approach unity in some cases. Brightness has been conveniently quantified in terms of the product of extinction coefficient at the absorption maximum and the quantum yield (Table 2). As a first quality criterion for using cucurbit[7]uril as an additive (1 mM), the brightness of the aqueous fluorescent dye solutions increases (with few exceptions, Table 2) [5, 6]. While the increased brightness may be partially due to the protection of the complexed dye from bulk water, which is known to somewhat quench rhodamines and xanthene dyes [94, 95], the effect for the cucurbituril is quite exceptional, because the addition of other macrocyclic hosts like cyclodextrins or calixarenes leads frequently to fluorescence quenching and therefore a reduced brightness [74, 92, 96, 97].

The complexation of fluorescent dyes by cucurbit[7]uril results also in small spectral shifts (Table 2, Fig. 7a), which presents an additional tool, complementing the use of organic solvents, to modulate the absorption and emission characteristics of dyes, for example in the context of dye laser applications. In most cases, a smaller Stokes shift is observed, which is consistent with a smaller geometrical relaxation when the dye is immersed in the rigid and spatially restricted supramolecular environment. The confinement inside the cucurbituril cavity reduces also the radiationless decay rates of the fluorescent dyes [5, 6], which can be rationalized in terms of the limited possibilities to undergo vibrationally or rotationally induced internal conversion [88, 92, 98, 99].

It should be noted here that the spectral shifts upon addition of cucurbit[7]uril, along with NMR spectral shifts and changes in the diffusion coefficients have also been used as criteria that the host does in fact form an inclusion (or partial inclusion) complex with the respective dye [5, 6]. Fluorescein, for example, is an anionic dye, which is not complexed, and therefore does not show the spectral changes and advantageous properties upon addition of cucurbiturils, because these hosts are well-established cation receptors and have little affinity to anions [8–11]. In the case of cationic fluorescent dyes (Scheme 3), the host–guest association constants, determined by UV-Vis spectrophotometric or fluorometric titrations, revealed large binding constants ( $10^4$ – $10^5$  M<sup>-1</sup>, except for rhodamine 123, which showed 1000 M<sup>-1</sup>). This ensures a nearly quantitative complexation of the dyes upon addition of mM cucurbit[7]uril concentrations.



- ◀ **Fig. 7** **a** Absorption and fluorescence spectra of Rhodamine 6G (Rh6G,  $1\ \mu\text{M}$ ) in water in the absence (*dotted lines*) and presence (*solid lines*) of 1 mM cucurbit[7]uril. **b** Temporal evolution of the fluorescence intensity of Rh6G ( $1\ \mu\text{M}$ ) in aerated water under ambient light in different sample containers. **c** Dependence of the registered count rate (CR) of a Rh6G solution ( $10\ \text{nM}$ ) in the time course of an extended FCS measurement. **d** Photobleaching of Rh6G (ca.  $4\ \mu\text{M}$ ) in aerated water in the absence (*dotted lines*) and presence (*solid lines*) of 1 mM cucurbit[7]uril followed through the decrease of the visible absorption with increasing time of pulsed 532-nm Nd-YAG laser irradiation. Reproduced from [5], with permission from Wiley-VCH

A severe complication in the use of fluorescent dyes relates to aggregation and their unspecific adsorption to material surfaces, which inevitably reduce the fluorescence intensity and routinely prevent the storage of aqueous dye solutions over longer periods of time [89–91]. The addition of cucurbit[7]uril has the potential to cure these problems as well, as was impressively demonstrated for rhodamine 6G, the prototype of a water-soluble fluorescent dye [5]. Complexation by cucurbit[7]uril reduces the affinity of the dye towards aggregation, thereby enhancing the fluorescence in particular at higher ( $> 10\ \mu\text{M}$ ) concentrations. Also the tendency to adsorb to various material surfaces is virtually completely suppressed. Note that aqueous rhodamine 6G solutions generally require fresh preparation to reduce loss of active dye due to adsorption effects, and the depletion of fluorescence intensity with time depends strongly on the sample container material employed (Fig. 7b). In contrast, cucurbituril-stabilized solutions retain the initial activity over a period of months when stored in the dark [5].

The “thermal” stabilization (against aggregation and adsorption) has immediate relevance in most applications of fluorescent dyes, e.g., for dye lasers, biolabels, calibration standards, single molecule detection, and scanning confocal microscopy. A pertinent example is the recommended use of rhodamine 6G solutions for referencing diffusion coefficients in fluorescence correlation spectroscopy (FCS). Unstabilized dye solutions show a reduced initial count rate and in addition, the count rate decreases quite readily with time (Fig. 7c). Cucurbituril-stabilized solutions, on the other hand, show not only a nearly 10-times higher initial count rate (since less dye has been lost due to adsorption during sample preparation, that is, dilution, pipetting, etc.), but also no measurable depletion with measurement time (since the dye does not adsorb to the well-plates employed in the FCS measurement). Note the logarithmic intensity scale in Fig. 7c, which shows that the effects are indeed dramatic.

Photobleaching, another recurring problem in fluorescent dye applications, describes the tendency of fluorescent dyes to undergo, in particular under prolonged high-intensity irradiation, irreversible chemical changes upon photoexcitation [89, 100]. Several approaches have been developed to reduce photobleaching and besides classical chemical derivatization of the dye, stabilizing additives, often antioxidants or triplet quenchers, have be-

come popular, regardless of their limited effectiveness. Another approach exploits the use of different (organic) solvents, which, however, is not viable for biological applications. The photostabilizing effect of cucurbit[7]uril was again investigated in detail for rhodamine 6G. For this purpose, stabilization factors were derived from relative quantum yields of photobleaching, which in turn were obtained by monitoring the decrease in absorbance upon prolonged irradiation. The stabilization is already sizeable (by a factor of ca. 1.5) at low irradiation levels (e.g., in a photoreactor), which only leads to excitation to the first singlet-excited state. However, in the high-intensity 532-nm laser irradiation (ca.  $10 \text{ MW cm}^{-2}$ , comparable to the irradiance employed in dye lasers or scanning confocal microscopy), where multi-photon excitation leads also to the population of higher excited states, the stabilization becomes remarkable (factor of 30, Fig. 7d).

Comparable advantageous effects of cucurbit[7]uril on the thermal and photochemical stability have since then been observed for numerous water-soluble fluorescent dyes [6]. The method of supramolecular radiative decay engineering using cucurbiturils is therefore not limited to the prolongation of fluorescence lifetimes, but is complemented by additional benefits, which lead to a stabilization and improved radiative performance of the fluorescent dyes. Some observations upon addition of cucurbit[7]uril, for example the reduction in fluorescence quantum yield of rhodamine 123 (Table 2), or the somewhat enhanced rather than reduced radiative decay rates of the prototypic forms of neutral red [75], show, however, that exceptions to the rule apply.

## 7

### Recent Developments

Since this work was written up for publication, several exciting developments have taken place, which further illustrate the potential of supramolecular radiative decay engineering and cucurbiturils. These include the construction of operational dye lasers with improved beam profile and photostability [101],  $pK_a$  shifts of fluorescent dyes [102], applications of cucurbituril-induced fluorescence enhancements in label-free bio-assays [102, 103], interactions of cucurbit[7]uril with peptide substrates [104], synergetic fluorescence enhancements by cucurbit[7]uril and proteins [105], the photophysical effects on the nucleotide indicator dye acridine orange (M Shaikh et al., submitted for publication), and the confocal microscopy of cucurbit[7]uril-complexed rhodamine 6G immobilized on silica glass surfaces, demonstrating superior probe performance [106].



## 8 Outlook

The recent results establish cucurbiturils as fairly universal stabilizing, intensity-enhancing, and lifetime-prolonging additives for fluorescent dyes. Radiative decay engineering using cucurbituril is expected to find novel and unconventional applications for fluorescent sensors, in bioassays, for the improvement of dye lasers, for storage of calibration solutions, in confocal microscopy as well as FCS, as contrast agents in FLIM, and, more far-fetched, for information storage devices.

## References

1. Amos RM, Barnes WL (1997) *Phys Rev B* 55:7249
2. Lakowicz JR (2001) *Anal Biochem* 298:1
3. Lakowicz JR, Shen Y, D'Auria S, Malicka J, Fang J, Gryczynski Z, Gryczynski I (2002) *Anal Biochem* 301:261
4. Marquez C, Nau WM (2001) *Angew Chem Int Ed* 40:4387
5. Mohanty J, Nau WM (2005) *Angew Chem Int Ed* 44:3750
6. Nau WM, Mohanty J (2005) *Int J Photoenerg* 7:133
7. Mohanty J, Nau WM (2004) *Photochem Photobiol Sci* 3:1026
8. Mock WL (1996) In: Vögtle F (ed) *Comprehensive Supramolecular*, vol 2. Elsevier, New York, p 477
9. Marquez C, Hudgins RR, Nau WM (2004) *J Am Chem Soc* 126:5806
10. Lee JW, Samal S, Selvapalam N, Kim H-J, Kim K (2003) *Acc Chem Res* 36:621
11. Lagona J, Mukhopadhyay P, Chakrabarti S, Isaacs L (2005) *Angew Chem Int Ed* 44:4844
12. Cram DJ (1988) *Angew Chem Int Ed Engl* 27:1009
13. Lehn J-M (1988) *Angew Chem Int Ed Engl* 27:89
14. Pedersen CJ (1988) *Angew Chem Int Ed Engl* 27:1021
15. de Silva AP, Gunaratne HQN, Gunnlaugsson T, Huxley AJM, McCoy CP, Rademacher JT, Rice TE (1997) *Chem Rev* 97:1515
16. Wiskur SL, Ait-Haddou H, Lavigne JJ, Anslyn EV (2001) *Acc Chem Res* 34:963
17. Martínez-Máñez R, Sancenón F (2003) *Chem Rev* 103:4419
18. Lehn J-M (1995) *Supramolecular Chemistry*. VCH, Weinheim
19. Atwood JL, Orr GW, Robinson KD, Hamada F (1993) *Supramol Chem* 2:309
20. Breslow R, Dong SD (1998) *Chem Rev* 98:1997
21. Shinkai S (1990) In: Vicens J, Böhmer V (eds) *Calixarenes*. Kluwer, Dordrecht, p 173
22. Palmer LC, Rebek J Jr (2004) *Org Biomol Chem* 2:3051
23. Purse BW, Rebek J Jr (2005) *Proc Natl Acad Sci USA* 102:10777
24. Castro R, Berardi MJ, Cordova E, Ochoa de Olza M, Kaifer AE, Evanseck JD (1996) *J Am Chem Soc* 118:10257
25. Odermatt S, Alonso-Gomez JL, Seiler P, Cid MM, Diederich F (2005) *Angew Chem Int Ed* 44:5074
26. Cram DJ (1992) *Nature* 356:29
27. Cram DJ, Karbach S, Kim YH, Baczynskyj L, Kallemeyn GW (1985) *J Am Chem Soc* 107:2575
28. Fujita M, Tominaga M, Hori A, Therrien B (2005) *Acc Chem Res* 38:369

29. Fiedler D, Leung DH, Bergman RG, Raymond KN (2005) *Acc Chem Res* 38:358
30. Rebek J Jr (2005) *Angew Chem Int Ed* 44:2068
31. Wagner BD (2003) In: Nalwa HS (ed) *Handbook of photochemistry and photobiology*, vol 3. American Scientific Publishers, Stevenson Ranch, California, p 1
32. Wagner BD, MacDonald PJ (1998) *J Photochem Photobiol A* 114:151
33. Wagner BD, Fitzpatrick SJ (2000) *J Incl Phenom Macro Chem* 38:467
34. Arimura T, Nagasaki T, Shinkai S, Matsuda T (1989) *J Org Chem* 54:3766
35. Nau WM, Wang XJ (2002) *Chem Phys Chem* 3:393
36. Gramlich G, Zhang J, Nau WM (2002) *J Am Chem Soc* 124:11252
37. Gramlich G, Zhang J, Nau WM (2004) *J Am Chem Soc* 126:5482
38. Sonnen AF-P, Bakirci H, Netscher T, Nau WM (2005) *J Am Chem Soc* 127:15575
39. Hudgins RR, Huang F, Gramlich G, Nau WM (2002) *J Am Chem Soc* 124:556
40. Huang F, Nau WM (2003) *Angew Chem Int Ed* 42:2269
41. Huang F, Hudgins RR, Nau WM (2004) *J Am Chem Soc* 126:16665
42. Wang XJ, Nau WM (2004) *J Am Chem Soc* 126:808
43. Nau WM, Huang F, Wang XJ, Bakirci H, Gramlich G, Marquez C (2003) *Chimia* 57:161
44. Nau WM, Zhang XY (1999) *J Am Chem Soc* 121:8022
45. Zhang XY, Gramlich G, Wang XJ, Nau WM (2002) *J Am Chem Soc* 124:254
46. Zhang XY, Nau WM (2000) *Angew Chem Int Ed* 39:544
47. Bakirci H, Zhang XY, Nau WM (2005) *J Org Chem* 70:39
48. Bakirci H, Nau WM (2005) *J Org Chem* 70:4506
49. Bakirci H, Nau WM (2005) *J Photochem Photobiol A* 173:340
50. Bakirci H, Nau WM (2006) *Adv Funct Mater* 16:237
51. Bakirci H, Koner AL, Nau WM (2005) *Chem Commun* 2005:5411
52. Bakirci H, Koner AL, Nau WM (2005) *J Org Chem* 70:9960
53. Marquez C, Pischel U, Nau WM (2003) *Org Lett* 5:3911
54. Marquez C, Huang F, Nau WM (2004) *IEEE Trans Nanobiosci* 3:39
55. Reichardt C (2003) *Solvents and Solvent Effects in Organic Chemistry*. Wiley-VCH, Weinheim
56. Pina F, Parola AJ, Ferreira E, Maestri M, Armaroli N, Ballardini R, Balzani V (1995) *J Phys Chem* 99:12701
57. Schmidtchen FP (1981) *Angew Chem Int Ed Engl* 20:466
58. McCurdy A, Jimenez L, Stauffer DA, Dougherty DA (1992) *J Am Chem Soc* 114:10314
59. Ngola SM, Dougherty DA (1996) *J Org Chem* 61:4355
60. Warmuth R, Kerdelhué J-L, Carrera SS, Langenwaller KJ, Brown N (2002) *Angew Chem Int Ed* 41:96
61. Carrera SS, Kerdelhué J-L, Langenwaller KJ, Brown N, Warmuth R (2005) *Eur J Org Chem* 2005:2239
62. Halls MD, Schlegel HB (2002) *J Phys Chem B* 106:1921
63. Halls MD, Raghavachari K (2005) *Nano Lett* 5:1861
64. Lakowicz JR (1999) *Principles of fluorescence spectroscopy*. Kluwer Academic/Plenum, New York
65. Strickler SJ, Berg RA (1962) *J Chem Phys* 37:814
66. Toptygin D, Brand L (1993) *Biophys Chem* 48:205
67. Lamouche G, Lavallard P, Gacoin T (1998) *J Luminesc* 76/77:662
68. Lamouche G, Lavallard P, Gacoin T (1999) *Phys Rev A* 59:4668
69. Lavallard P, Rosenbauer M, Gacoin T (1996) *Phys Rev A* 54:5450
70. Suhling K, Siegel J, Phillips D, French PMW, Lévêque-Fort S, Webb SED, Davis DM (2002) *Biophys J* 83:3589

71. Toptygin D, Savtchenko RS, Meadow ND, Roseman S, Brand L (2002) *J Phys Chem B* 106:3724
72. Aslan K, Gryczynski I, Malicka J, Matveeva E, Lakowicz JR, Geddes CD (2005) *Curr Opin Biotech* 16:55
73. Gersten JI, Nitzan A (1984) *Chem Phys Lett* 104:31
74. Liu Y, Han B-H, Chen Y-T (2002) *J Phys Chem B* 106:4678
75. Mohanty J, Bhasikuttan AC, Nau WM, Pal H (2006) *J Phys Chem B* 110:5132
76. Suhling K, French PMW, Phillips D (2005) *Photochem Photobiol Sci* 4:13
77. Hemmilä I, Webb S (1997) *Drug Discov Today* 2:373
78. Saha AK, Kross K, Kloszewski ED, Upson DA, Toner JL, Snow RA, Black CDV, Desai VC (1993) *J Am Chem Soc* 115:11032
79. Karvinen J, Laitala V, Mäkinen ML, Mulari O, Tamminen J, Hermonen J, Hurskainen P, Hemmilä I (2004) *Anal Chem* 76:1429
80. Sadler TM, Achilleos M, Rangunathan S, Pitkin A, LaRocque J, Morin J, Annable R, Greenberger LM, Frost P, Zhang YX (2004) *Anal Biochem* 326:106
81. Johansson MK, Cook RM, Xu JD, Raymond KN (2004) *J Am Chem Soc* 126:16451
82. Hennig A, Florea M, Roth D, Enderle T, Nau WM (2007) *Anal Biochem* 360:255
83. Smith JA, West RM, Allen M (2004) *J Fluoresc* 14:151
84. Sauer M, Han K-T, Müller R, Schulz A, Tadday R, Seeger S, Wolfrum J, Arden-Jacob J, Deltau G, Marx NJ, Drexhage KH (1993) *J Fluoresc* 3:131
85. Nunnally BK, He H, Li L-C, Tucker SA, McGown LB (1997) *Anal Chem* 69:2392
86. Flanagan JH Jr, Owens CV, Romero SE, Waddell E, Kahn SH, Hammer RP, Soper SA (1998) *Anal Chem* 70:2676
87. Cosa G, Focsaneanu K-S, McClean JRN, Scaiano JC (2000) *Chem Commun* 8:689
88. Drexhage KH, Hänsch TW, Ippen EP, Schäfer FP, Shank CV, Snavely BB (1973) *Dye Lasers*. Springer, Berlin Heidelberg New York
89. Eggeling C, Widengren J, Rigler R, Seidel CAM (1998) *Anal Chem* 70:2651
90. Dörre K, Brakmann S, Brinkmeier M, Han K-T, Riebeseel K, Schwille P, Stephan J, Wetzel T, Lapczynska M, Stuke M, Bader R, Hinz M, Seliger H, Holm J, Eigen M, Rigler R (1997) *Bioimaging* 5:139
91. Enderlein J, Goodwin PM, van Orden A, Ambrose WP, Erdmann R, Keller RA (1997) *Chem Phys Lett* 270:464
92. Mishra A, Behera RK, Behera PK, Mishra BK, Behera GB (2000) *Chem Rev* 100:1973
93. Arunkumar E, Forbes CC, Smith BD (2005) *Eur J Org Chem* 2005:4051
94. Sinha S, Ray AK, Kundu S, Sasikumar S, Dasgupta K (2002) *Appl Phys B* 75:85
95. Magde D, Wong R, Seybold PG (2002) *Photochem Photobiol* 75:327
96. Rao TVS, Huff JB, Bieniarz C (1998) *Tetrahedron* 54:10627
97. Politzer IR, Crago KT, Hampton T, Joseph J, Boyer JH, Shah M (1989) *Chem Phys Lett* 159:258
98. Acemioglu B, Arik M, Onganer Y (2002) *J Luminesc* 97:153
99. Tatikolov AS, Costa SMB (2002) *Photochem Photobiol Sci* 1:211
100. Eggeling C, Widengren J, Rigler R, Seidel CAM (1999) In: Rettig W, Strehmel B, Schrader S, Seifert H (eds) *Applied Fluorescence in Chemistry, Biology and Medicine*. Springer, Berlin Heidelberg New York, p 193
101. Mohanty J, Pal H, Ray AK, Kumar S, Nau WM (2007) *Chem Phys Chem* 8:54
102. Koner AL, Nau WM (2007) *Supramol Chem* 19:55
103. Hennig A, Bakirci H, Nau WM (2007) *Nat Method* 4:629
104. Hennig A, Ghale G, Nau WM (2007) *Chem Commun* 2007:1614
105. Bhasikuttan AC, Mohanty J, Nau WM, Pal H (2007) *Angew Chem Int Ed* 46:4120
106. Martyn TA, Moore JL, Halterman RL, Yip WT (2007) *J Am Chem Soc* 129:10338

**Part C**  
**Polymers, Semiconductors, Model Membranes and Cells**

# Resonance Energy Transfer in Polymer Interfaces

J. P. S. Farinha (✉) · J. M. G. Martinho (✉)

Centro de Química-Física Molecular, Instituto Superior Técnico, 1049-001 Lisboa, Portugal

*farinha@ist.utl.pt, jgmartinho@ist.utl.pt*

<b>1</b>	<b>Introduction</b>	215
1.1	Polymer Interfaces	216
1.2	Resonance Energy Transfer in Polymer Interfaces	220
<b>2</b>	<b>Resonance Energy Transfer in Restricted Domains</b>	220
2.1	Effect of Restricted Geometry: Donors in Equivalent Locations	223
2.2	Arbitrary Distributions of Donors and Acceptors	224
2.2.1	Spherical Symmetry	225
2.2.2	Planar Symmetry	228
2.2.3	Cylindrical Symmetry	229
<b>3</b>	<b>Interfaces in Block Copolymers</b>	231
3.1	Block Copolymers Films	232
3.2	The Core–Corona Interface in Block Copolymer Micelles	234
<b>4</b>	<b>Interfaces in Polymer Colloids</b>	237
4.1	The Surface of Colloidal Particles	237
4.2	Interface Breadth in Latex Film Formation	239
<b>5</b>	<b>Interfaces in Polymer Blends</b>	243
<b>6</b>	<b>Conclusions</b>	245
	<b>References</b>	247

**Abstract** The properties of polymer materials are often determined by their interfaces. Polymer interfaces are usually much broader than inorganic interfaces, with values from 1 to 10 nm. This range matches the typical length scale of Förster non-radiative resonance energy transfer (FRET). While the use of FRET in polymers was pioneered by Morawetz in the 1980s, the technique has only recently been extended to obtain quantitative detailed information on polymer interfaces and other nanostructured materials. A number of systems with nanodomains and heterogeneous dye concentration profiles, ranging from block copolymer films and micelles, to polymer nanoparticles, latex film formation and polymer blends, have been successfully characterized by FRET.

## 1 Introduction

The properties, reliability and function of multiphase materials are often determined by their interfaces. These are more susceptible to deformation, frac-

ture and chemical degradation than the bulk material. Among the large variety of interfaces that can be envisaged, polymer interfaces merit a particular relevance owing to their scientific and technological importance [1–3]. Unlike inorganic materials where the interfaces are generally very sharp, often characterized by thicknesses of less than a few Å, interfaces between incompatible polymers are much more diffuse. In the few instances where reliable data are available, values ranging from 2 to 8 nm have been found. This range matches the length scale where non-radiative dipole–dipole resonance energy transfer is more sensitive. Resonance energy transfer, which was first described by Förster [4, 5], is also known as Förster resonance energy transfer (FRET). The use of FRET in polymer systems was pioneered by Morawetz [6–12], but with the more recent development of methodologies that allow the calculation of concentration profiles in systems of planar [13, 14], spherical [15–17], or cylindrical [18] symmetry, it has been extended into complex nanostructured materials.

## 1.1

### Polymer Interfaces

The characterization of the interface between domains constituted by different polymers is a challenging topic in polymer science. These interfaces are important because the mechanical properties of materials constituted by different polymers depend upon the adhesion and the transfer of stress across the interface, as, for example, in impact modified plastics. Polymer interfaces are generated in the melt processing of polymer blends, since most polymers do not mix owing to an unfavorable balance between the enthalpy and the entropy of mixing [19]. Upon quenching the polymer melt to room temperature, non-equilibrium, but kinetically stable morphologies develop before the system is able to reach complete phase separation [20–22]. These complex morphologies are composed of microdomains of one phase in the other. They usually do not relax to complete phase separation due to the slow dynamics of the polymer chains (Fig. 1).

In order to improve the material properties, it is usual to use additives that segregate to the interface, thereby reducing the interfacial tension, stabilizing the mixture and improving the interfacial adhesion [23, 24]. Among these, linear diblock copolymers with the molecular structure of each block similar to those of the corresponding homopolymers were shown to be very effective [25, 26]. The block copolymers arrange at the interface so that each block only mixes with the similar homopolymer. This changes the morphology of the mixture and the width of the interface between components, improving the mechanical properties of the blend [27, 28]. In some cases, diblock copolymers can act like surfactants, originating thermodynamically stable bicontinuous microemulsions [28, 29].

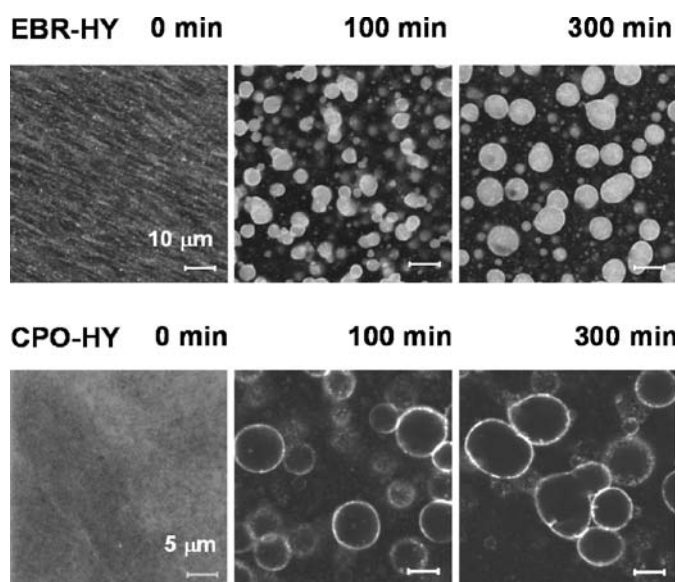


**Fig. 1** Laser scanning confocal microscopy images showing the internal morphology evolution of films of a blend of 74/23.5/2.5 poly(propylene)/poly(ethylene-co-butene)/chlorinated maleated PP (PP/EBR/CPO) in which either the EBR component (*top images*) or the CPO component (*bottom images*) are labeled with a trace amount of HY, an amino-hexyl benzothioxanthene fluorescent dye (*bright areas*). With annealing at 180 °C, EBR microdomains are formed in the film, with the CPO component accumulating at the PP/EBR interface [24]

By themselves, diblock copolymers with an unfavorable interaction between the blocks, display very interesting and rich microstructures in the bulk [30–32]. In this case, complete phase separation is prevented by the covalent linkage between blocks, and the free energy of mixing minimization results in the formation of micro-phase separated domains. Block copolymer phase behavior is primarily determined by three parameters: the overall degree of polymerization  $N$ , the magnitude of the Flory–Huggins interaction parameter  $\chi$  of the polymers, and the volume fractions of the blocks [26]. For immiscible polymers the temperature-dependent  $\chi$  parameter has a value larger than zero but usually small, resulting in some degree of segment interpenetration between the two components at the interface. For block copolymers, the free energy of interface formation balances the entropy penalty for localization of the joints in the interface. This term becomes less important for long polymers, with the interface thickness becoming equivalent in blends and block copolymers.

The product  $\chi N$  controls the degree of segregation. This can be roughly divided in three regimes: weak segregation ( $\chi N \approx 10$ ), strong segregation ( $\chi N \geq 100$ ), and intermediate segregation ( $10 \leq \chi N \leq 100$ ) [33–35]. At low

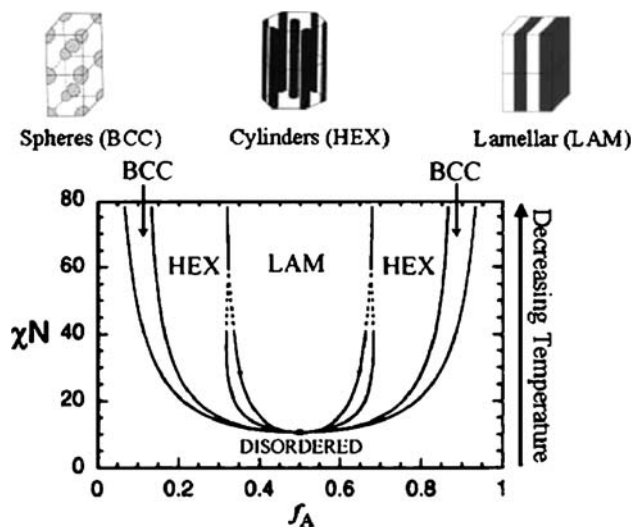


**Fig. 2** Ordered microphases of diblock copolymers as a function of the volume fraction of one block ( $f_A$ ) and  $\chi N$

values of  $\chi N$ , the block copolymers form a single disordered phase in which the chains have unperturbed dimensions. At  $\chi N \approx 10$  the disordered phase evolves to ordered microphases with several rich structures (body centered cubic spheres, hexagonally-packed cylinders, lamellae, ...). By increasing  $\chi N$  above 100, the interface narrows and the major phase-separated structures (bcc spheres, hex cylinders and lamellae, Fig. 2) become dependent on composition only [36, 37].

The theory of block copolymer phase separation began to be developed in the early 1970s, with relevance to the effort of Helfand and co-workers. Using a self-consistent mean-field theory (SCMF), they were able to calculate the free energies, composition profiles and chain conformations in the strong segregation limit [38–40]. Later, Semenov developed a theory that circumvents the numerical calculations inherent to the Helfand approach [41], and Matsen and co-workers further extended the theory to the weak and intermediate segregation regimes [36, 42, 43].

The periodicity of the ordered structures is limited to the range of 10–20 nm owing to difficulties in the synthesis of well characterized long polymer blocks. The interface width, on the other hand, is mainly controlled by the degree of miscibility. In the high segregation limit, the width of the interface is typically smaller than 10 nm [44], and usually agrees well with the predictions of the SCMF theory [21, 32, 43].

In solution, block copolymers self-assemble when the solvent is selective for one of the blocks [45–47], with micelles being formed above the critical micelle concentration (cmc), typically with aggregation numbers of the



order of 100 and spherical geometry. Nevertheless, a wide variety of non-spherical morphologies have been observed [48, 49] with particular prevalence for worm-like micelles [50–52] and vesicles [53, 54]. By increasing the concentration above the cmc, the aggregates arrange to form complex gel structures [32].

Many polymers of industrial importance are prepared as nanometer size spherical particles dispersed in aqueous phase [55, 56]. These dispersions, generally named latexes, are used as base materials for water-based paints and inks, as supports for biomolecules, biovectors for drug delivery, bioseparation, etc [57, 58]. The particles, which can have several morphologies, show a charged hairy layer at the surface [59], with a roughness that depends on the surface charge density, the ionic strength of the aqueous medium and the characteristics of the polymer segments at the interface [60].

In paints and coatings, a strong continuous film has to be formed from the colloidal dispersion [61–63]. After water evaporation and drying, the film is composed of close-packed spherical particles, originating a very large number of sharp interfaces between them. In order to form a homogeneous and mechanically rigid film, the polymer chains have to cross the interface between particles by molecular interdiffusion [62–64]. The width of the interface grows and its strength increases by polymer chain diffusion until being completely healed. To reach this stage, the chains have to diffuse a distance close to its gyration radius.

Interfaces generated in the processes described above have widths with sizes from a few nanometers to some micrometers. Techniques that can give information on these interfaces include X-ray and neutron reflectivity, secondary ion mass spectroscopy (SIMS), X-ray photoelectron spectroscopy (XPS), Fourier transform infrared (FTIR), scanning and transmission electron microscopies (SEM and TEM), and atomic force microscopy (AFM) [21, 32, 65]. The most powerful technique for studying polymer interfaces is probably neutron reflectivity (NR), in which one observes the specular reflection between two thin polymer films. In order to have contrast, selective deuteration of one of the polymer components is necessary [66–69]. This is an important technique for the study of polymer blends and self-assembling block copolymers, but is limited to the lamellar geometry. Small-angle neutron scattering (SANS) and small angle X-ray scattering (SAXS) experiments are both sensitive to the sharpness or diffuseness of the interface between components of different contrast factors, but the interpretation of the data is not as rigorous as in the case of NR, relying in the analysis of deviations from Porod–Law scattering in a region where the scattering intensity is usually very weak. Both NR and scattering techniques require appropriate corrections of the data, because the techniques are sensitive to different artifacts, such as the waviness at the interface, which increases its apparent diffuseness [70]. An alternative approach to studying polymer interfaces is Förster resonance energy

transfer (FRET), which is very sensitive to distances on the order of a few nanometers.

## 1.2

### Resonance Energy Transfer in Polymer Interfaces

Förster resonance energy transfer [4, 5] has been used to study macromolecular systems for more than three decades, since the use of FRET in polymers, and notably in polymer interfaces, was proposed in the 1970s by Morawetz and co-workers [6–10, 71–73]. In most cases, the polymers have to be labeled with a pair of fluorescent dyes (an energy donor and an acceptor). Upon electronic excitation of the donor (D), the energy is transferred to the acceptor (A) by a resonance dipole–dipole coupling mechanism.

The rate of FRET depends mainly on the inverse six power of the separation between D and A. This dependence is the major advantage of the technique. To explore this advantage, one needs to develop models that predict the steady state and/or time resolved fluorescence for the particular distribution of D and A molecules in the system under consideration.

If one mixes two polymer components, one labeled with an energy donor and the other with an acceptor, phase separation leads to localization of the dyes, either in the different domains or at the interface, depending on the sample and the sites chosen for labeling. This can lead to a decrease in the quantum efficiency of energy transfer when separation of D and A labeled domains occurs; or, when phase separation results in the co-localization of both dyes, to an increase in the quantum efficiency of energy transfer. Since the dye distribution mimics the distribution of the polymer components, and the kinetics of FRET between D and A is very sensitive to the D–A distance distribution in a length scale of a few nanometers, these experiments can provide detailed information on the distribution of the labeled polymer components.

In FRET experiments, one usually measures the time-dependent fluorescence intensity decay of D. By fitting the experimental results with a theoretical decay that takes into account the energy transfer processes, it is possible to obtain morphological information on the interface, such as the thickness of the interface between two polymers. In the following sections we will show that this can be done using energy transfer models, which explicitly consider the distribution of donors and acceptors in systems with restricted dimensions.

## 2

### Resonance Energy Transfer in Restricted Domains

The rate of energy transfer,  $w(r)$ , from an electronic excited donor ( $D^*$ ) to an acceptor (A) separated by a distance  $r$  was obtained by Förster for a dipole–

dipole coupling mechanism [4, 5]

$$w(r) = \frac{1}{\tau_D} (R_0/r)^6, \quad (1)$$

where  $\tau_D$  is the donor intrinsic lifetime in the absence of acceptors and  $R_0$  is the critical Förster radius that can be calculated from spectroscopic data of D and A

$$R_0^6 = \frac{9000 (\ln 10) k^2 \phi_f}{128\pi^5 N_A n^4} \int_0^\infty F_D(\lambda) \varepsilon_A(\lambda) \lambda^4 d\lambda. \quad (2)$$

In Eq. 2, the integral accounts for the spectral overlap of the fluorescence spectrum  $F_D(\lambda)$  of the donor (normalized to unity) and the absorption spectrum of the acceptor  $\varepsilon_A(\lambda)$  ( $\text{M}^{-1} \text{cm}^{-1}$ ). The Förster radius also depends on the donor fluorescence quantum yield  $\phi_f$  in the absence of acceptor, the refractive index of the medium in the wavelength range of spectral overlap,  $n$ , and an orientation factor  $k^2$  which, for an individual D–A pair, depends on the angle between the transition dipole moments of the D and A molecules  $\theta_{DA}$  and the angles  $\theta_D$  and  $\theta_A$  between each of these dipoles and the vector connecting their centers:

$$k^2 = (\cos \theta_{DA} - 3 \cos \theta_D \cos \theta_A)^2. \quad (3)$$

The value of  $k^2$  for a single D–A pair is the range of 0 to 4. However, in the more common situation of an ensemble of D–A pairs,  $k^2$  is usually pre-averaged over the distribution of all orientations to give  $\langle k^2 \rangle$  [74]. If the molecules undergo rotational motion on a faster time scale than the fluorescence lifetime,  $\langle k^2 \rangle = 2/3$ , while for randomly oriented dipoles that do not rotate on the timescale of fluorescence,  $\langle k^2 \rangle = 0.476$  [75]. In practice, it is often advantageous to separate the orientation and spectroscopic dependencies of  $R_0$ , writing the rate of energy transfer in terms of the Förster radius for rapidly rotating dipoles  $\langle k^2 \rangle = 2/3$ , as [76]

$$w(r) = \frac{3}{2} \frac{\kappa^2}{\tau_D} (R_0/r)^6. \quad (4)$$

Because of the  $r^{-6}$  dependence in Eq. 4, in systems characterized by a distribution of D–A distances, the donor fluorescence decay corresponds to a distribution of decay times associated with the transfer process for pairs at several distances.

Many systems of interest have a distribution of D–A distances and donor locations. These include simple systems, where D and A have uniform concentrations but are confined to a restricted space; and more complex systems where the D and A concentrations have specific gradients in space, which might arise from diffusion, thermodynamically driven demixing, self-assembling, etc. To obtain in-depth information about the interface between

polymer domains from FRET experiments, the data should be analyzed using a model that takes into account both the restricted dimensions of the interface and the concentration gradients of the components. Here, “restricted dimensions” refer to a space or domain confining the dyes in which at least one dimension is on the order of the length scale of FRET (usually, a few nanometers).

To begin, we will consider a system where there is no restriction or gradient, consisting of isolated donors, each surrounded by  $n_A$  acceptors at a constant distance  $r$ . In this case, the donor survival probability function is still exponential but it decays faster than for the unquenched donor

$$I_D(t) = \exp\left(-\frac{t}{\tau_D}\right) \exp[-w(r)n_A t]. \quad (5)$$

However, if one considers a homogeneous distribution of donors and acceptors in a three dimensional Euclidean space, each donor will be surrounded by acceptors located at different distances, and the donor decay function becomes a stretched exponential as first derived by Förster [4, 77, 78]

$$I_D(t) = \exp\left(-\frac{t}{\tau_D}\right) \exp\left[-P\left(\frac{t}{\tau_D}\right)^{0.5}\right], \quad (6)$$

where  $P$  is proportional to the local concentration of acceptors.

A major advance in using FRET in systems of restricted geometry was due to Klafter and Blumen, who derived the relationship [79]

$$I_D(t) = \exp\left(-\frac{t}{\tau_D}\right) \exp\left[-P\left(\frac{t}{\tau_D}\right)^\beta\right], \quad (7)$$

usually known as the KB equation. This is a general description of the survival probability  $I_D(t)$  of excited donors in infinite media of any dimensionality  $d = 6\beta$ , and generalizes the expressions derived by Förster for three dimensions ( $d = 3$ ) [4, 77, 78], and by Hauser for one ( $d = 1$ ) and two ( $d = 2$ ) dimensions [80]. For donors and acceptors embedded in a fractal lattice, the dimensional parameter  $d$  is equal to the fractal (Hausdorff) dimensionality of the lattice.

The parameter  $P$  is related to the local acceptor concentration as

$$P = c_\Delta \left(\frac{3\kappa^2}{2}\right)^\beta \Gamma(1 - \beta), \quad (8)$$

where  $c_\Delta$  is the number of acceptors in a  $\Delta$ -dimensional sphere of radius  $R_0$ , and  $\Gamma$  is the Gamma function. For donors and acceptors distributed in one, two and three dimensions,  $\Delta$  equals the Euclidean dimension  $d$  of the space where the dyes are distributed. In the case of FRET on a fractal lattice, some assumptions have to be made in order to use the information contained in  $c_\Delta$ .

It was probably El-Sayed and coworkers who first reported the utility of the KB equation as a phenomenological expression to analyze FRET in systems of restricted geometry, that are clearly not of a fractal nature [81]. In this case, the fractional value of  $\beta$  is due to edge effects of the confining space and the value  $6\beta$  is sometimes referred to as the “apparent dimensionality”. The KB equation and similar formulae have been applied to a variety of systems, such as porous solids, [82] surfactant vesicles, [83] and in the simulation of regular lattices with excluded volume [81]. Although the application to systems of restricted geometry is strictly empirical in most cases, the apparent dimension parameter obtained from this equation can give some information on the nature of the domains where donor and acceptor dyes are distributed [84].

## 2.1

### Effect of Restricted Geometry: Donors in Equivalent Locations

We have seen that edge effects become important when the D and A are distributed in a system of restricted geometry, i.e., with at least one dimension on the order of  $R_0$ . The first attempt to rigorously explore these effects was done by Fayer and co-workers for D–D homo-transfer (energy migration) [85–88] and by Klafter, Blumen and co-workers for D–A for FRET [82, 89–91]. The Klafter–Blumen formulation apply to systems in which donors and acceptors are distributed in a restricted volume, but where all donors occupy equivalent positions

$$I_D(t) = \exp\left(-\frac{t}{\tau_D}\right) \varphi(t) \quad (9)$$

$$\varphi(t) = \exp\left(-p \int_V \{1 - \exp[-w(r)t]\} \rho(r) dV\right), \quad (10)$$

where  $\varphi(t)$  is the donor survival probability with respect to FRET,  $V$  is the volume of the nanodomain,  $p$  is proportional to the acceptor concentration,  $\rho(r)$  is proportional to the probability distribution of finding a donor-acceptor pair separated by a distance  $r$ , and  $w(r)$  is the rate of energy transfer defined before. This expression was integrated for a number of interesting cases. For example, when D and A are distributed in the surface of a sphere, the donor survival probability,  $\varphi(t)$ , is given by [17, 89, 92]

$$\varphi(t) = \exp\left[-2\pi C_A \int_0^{2R_s} r \{1 - \exp[-w(r)t]\} dr\right], \quad (11)$$

where  $C_A$  is the acceptor surface density, and  $R_s$  is the radius of the sphere. The distribution of acceptor molecules around each donor is described by the parameters  $p$  and  $\rho(r)$ , with  $\rho(r)$  being difficult to evaluate for many cases.

More recently, new methodologies were developed for computing the survival probabilities whenever the donor and acceptor concentration profiles follow an element of symmetry: planar [13, 14], spherical [15–17], or cylindrical [18]. This theoretical methodology overcame the restriction of equivalent donor positions, and so opened the doors for handling any distribution of donor and acceptor having a plane, a point or an axis of symmetry.

## 2.2

### Arbitrary Distributions of Donors and Acceptors

When the donors in a system do not occupy equivalent positions, the KB formalism described in the previous section cannot be used. In order to calculate the donor fluorescence survival probability in systems with arbitrary distribution functions of donor and acceptor dyes, it is necessary to account for the different acceptor distributions surrounding donor dyes in different locations. These models, known as distribution models for energy transfer, were first derived for planar symmetry, and applied in systems with concentration gradients arising from D and A labeled polymer chains diffusing across an interface [13], and were later extended to reproduce the donor survival probability functions for D and A in simple planar systems [14]. Later, an equivalent model for spherical-symmetric systems was developed and used to analyze experimental results of polymer diffusion in latex films [15]. It was also applied to simple spherical systems of restricted geometry [17] and block copolymer films [16]. A model for cylindrical geometry was obtained only recently, due to the higher mathematical complexity of these systems [18].

The basis of the models that describe FRET is the survival probability of a donor at position  $\mathbf{r}_D$  in the presence of an acceptor at position  $\mathbf{r}_i$

$$f(t, \mathbf{r}_D, \mathbf{r}_i) = \exp[-t \times \omega(|\mathbf{r}_i - \mathbf{r}_D|)] . \quad (12)$$

If we consider that donors and acceptors occupy discrete sites in a restricted space and assume that the acceptors act independently, the donor survival probability  $\varphi$  is given by the product of the donor transition probabilities  $f$  weighted by the distribution function,  $g(\mathbf{r}_i, j)$ , of the number of acceptors,  $j$ , in each site,  $\mathbf{r}_i$

$$\varphi(t, \mathbf{r}_D) = \prod_{\mathbf{r}_i \neq \mathbf{r}_D} \left\{ \sum_j g(\mathbf{r}_i, j) [f(t, \mathbf{r}_D, \mathbf{r}_i)]^j \right\} . \quad (13)$$

If the probability of having one acceptor at  $\mathbf{r}_i$  is small, the probability that  $j$  acceptors exist at the site  $\mathbf{r}_i$  is given by a Poisson distribution with mean equal to the number of acceptors  $n_A(\mathbf{r}_i)$

$$g_i(\mathbf{r}_i, j) = \exp[-n_A(\mathbf{r}_i)] \times \frac{n_A^j(\mathbf{r}_i)}{j!} , \quad (14)$$

and the decay probability of the donor becomes

$$\varphi(t, \mathbf{r}_D) = \prod_{\mathbf{r}_i \neq \mathbf{r}_D} \left\{ \sum_j \exp[-n_A(\mathbf{r}_i)] \times \frac{n_A^j(\mathbf{r}_i)}{j!} f^j(t, \mathbf{r}_D, \mathbf{r}_i) \right\}, \quad (15)$$

which can be rewritten as

$$\varphi(t, \mathbf{r}_D) = \exp \left( - \sum_{\mathbf{r}_i \neq \mathbf{r}_D} n_A(\mathbf{r}_i) \times \{1 - \exp[-t \times \omega(|\mathbf{r}_i - \mathbf{r}_D|)]\} \right). \quad (16)$$

Considering that the donor is inside a continuous restricted space of volume  $V$ , one can write

$$\varphi(t, \mathbf{r}_D) = \exp \left( - \int_V C_A(\mathbf{r}_A) \times \{1 - \exp[-t \times \omega(|\mathbf{r}_A - \mathbf{r}_D|)]\} d\mathbf{r}_A \right), \quad (17)$$

where the integral is performed over the volume elements  $d\mathbf{r}_A$  containing acceptors with number density  $C_A(\mathbf{r}_A)$ .

Donors located at different positions are surrounded by distinct distributions of acceptors, and so the donor decay has to be average over all the donors in the system

$$I(t) = \exp\{-t/\tau_D\} \int_V C_D(\mathbf{r}_D) \times \varphi(t, \mathbf{r}_D) d\mathbf{r}_D, \quad (18)$$

where  $C_D(\mathbf{r}_D)$  is the concentration profile of the donors.

The last two equations describe the donor decay probability when FRET occurs between donors and acceptors heterogeneously distributed in a confined space. The geometric restrictions are introduced by the volume  $V$  over which the integral is calculated and the heterogeneity by position-dependent donor and acceptor concentration profiles. This general formalism can be simplified when the donor and acceptor distributions have spherical, planar or cylindrical symmetry.

### 2.2.1

#### Spherical Symmetry

We now consider the particular case of spherical symmetric distribution functions of donors and acceptors. In this case the survival probability of

a donor located at  $\mathbf{r}_D$  can be integrated in spherical coordinates [15]

$$\varphi(t, \mathbf{r}_D) = \exp \left( - \int_{-\pi}^{\pi} \int_0^{\pi} \int_{R_e}^{\infty} C_A(\mathbf{r}_A) \times \{1 - \exp[-\omega(r)t]\} r^2 \sin \phi \, dr \, d\phi \, d\theta \right), \quad (19)$$

where  $R_e$  is the donor-acceptor encounter distance (their minimum approach distance), usually taken to be the sum of the donor and acceptor van der Waals radii [93]. The acceptor radial position  $r_A$  is related to the vectors defining the donor position  $\mathbf{r}_D$  and the distance  $\mathbf{r}$  between donor and acceptor

$$r_A = |\mathbf{r}_D + \mathbf{r}| = \sqrt{r^2 + r_D^2 + 2\mathbf{r}\mathbf{r}_D \sin \phi \cos \theta}. \quad (20)$$

The function  $\varphi(t, \mathbf{r}_D)$  measures the probability that an excited donor, located at  $\mathbf{r}_D$  “survives” for a time  $t$  before energy transfer occurs. The integration in the donor survival probability function can be further simplified [15] noticing that the acceptor concentration profile  $C_A(r_A)$  is symmetric relative to the origin, while the rate of energy transfer  $\omega(r)$  is symmetric relative to the donor position. The product  $C_A(r_A) \times \{1 - \exp[-\omega(r)t]\}$  is therefore invariant in the volume element defined by the interception of one spherical shell centered in the origin with radius  $r_A$  and width  $dr_A$ , and another centered in the

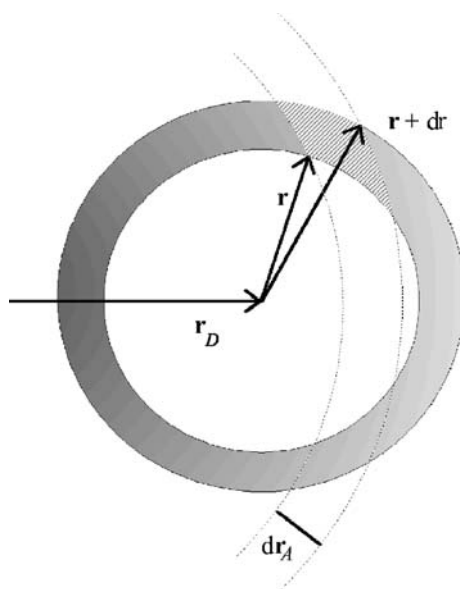


**Fig. 3** Volume defined by the interception of one spherical shell centered in the origin with radius  $r_A$  and width  $dr_A$ , and another centered in the donor position  $r_D$  with radius  $r$  and width  $dr$



donor position  $r_D$  with radius  $r$  and width  $dr$ . This defines a volume element  $dV$  that resembles a concave ring with cross-section as depicted in Fig. 3:

$$dV = 2\pi \frac{r \times r_A}{r_D} dr dr_A. \quad (21)$$

In order to obtain an average concentration of acceptors over each ring of radius  $r$  centered in the donor position, the integral is evaluated over all rings at distances  $r_D - r$  to  $r_D + r$ , for each donor-acceptor separation  $r$ . Integration over all donor-acceptor distances  $r$  finally yields

$$\varphi(t, r_D) = \exp \left( - \frac{2\pi}{r_D} \int_{R_e}^{\infty} \{1 - \exp[-\omega(r)t]\} \times \left[ \int_{r_D-r}^{r_D+r} C_A(r_A) r_A dr_A \right] r dr \right). \quad (22)$$

Equations 18 and 22 allow the determination of the donor decay curve in systems with spherically symmetric donor and acceptor concentration profiles,  $C_D$  and  $C_A$ , and  $w(r)$  given by Eq. 4. The shape of the D and A distributions are typically obtained independently from the morphology of the system.

These expressions can also be used to obtain the donor decay curve for a number of simple situations that cannot be treated with the KF formalism because the donors are in non-equivalent positions. For example, when the acceptors are distributed in the surface of a sphere of radius  $R_s$  and the donors inside [17], the donor and acceptor number density profiles are given by  $C_D(r_D) = C_{D0}H(R_s - r_D)$  for  $0 \leq r_D \leq R_s$  and  $C_A(r_A) = C_{A0}\delta(R_s - r_A)$ , where  $H$  and  $\delta$  are the Heaviside and the delta functions and  $C_{D0}$ ,  $C_{A0}$  are constants. In this case, the integral in  $r_A$  of Eq. 22 has a non-zero value only if the peak of the delta function lies in the domain of integration. Therefore the conditions  $|r_D - r| < R_s$  and  $r_D + r > R_s$  should be simultaneously satisfied ( $R_s - r_D \leq r \leq R_s + r_D$ ) leading to

$$I_D(t) = \exp(-t/\tau_D) \int_0^{R_s} \varphi(r_D, t) 4\pi r_D^2 dr_D \quad (23)$$

$$\varphi(r_D, t) = \exp \left( - \frac{2\pi n_A R_s}{r_D} \int_{R_s-r_D}^{R_s+r_D} \{1 - \exp[-w(r)t]\} r dr \right), \quad (24)$$

which can be expressed in terms of incomplete gamma functions for numerical integration.

Another interesting and useful case that could not be treated with the KB formalism is when both donors and acceptors are uniformly distributed inside a sphere [17]. In this case,  $C_D(r_D) = C_{D0}H(R_s - r_D)$  with  $0 \leq r_D \leq R_s$  and

$C_A(r_A) = C_{A0}H(R_s - r_A)$  with  $0 \leq r_A \leq R_s$ , yielding

$$\varphi(r_D, t) = \exp \left( - 4\pi n_A \int_0^{R_s - r_D} \{1 - \exp[w(r)t]\} r^2 dr - \frac{\pi n_A}{r_D} \int_{R_s - r_D}^{R_s + r_D} \{1 - \exp[w(r)t]\} [R_s^2 - (r_D - r)^2] r dr \right), \quad (25)$$

which can also be expressed in terms of incomplete gamma functions.

### 2.2.2

#### Planar Symmetry

In a system with planar symmetry the distribution functions of donors and acceptors change only along an axis  $z$  perpendicular to the plane. Therefore, if we consider slices perpendicular to the  $z$  axis, the donors in each slice are surrounded by different acceptor concentrations corresponding to different slices and the donor decay can be evaluated as a sum over all slices

$$I(t) = \exp(-t/\tau_D) \int_V C_D(z) \times \varphi(t, z) dz. \quad (26)$$

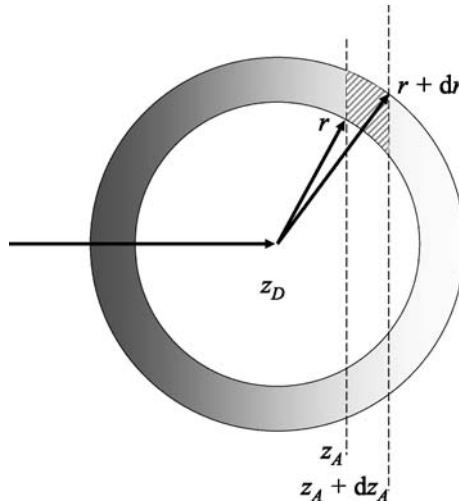


**Fig. 4** Volume element defined by the interception of a vertical slice and width  $dr_A$  position at  $r_A$ , and a spherical shell centered in the donor position  $r_D$  with radius  $r$  and width  $dr$

The donor survival probability for a given slice, positioned at  $z$ , depends on the changing acceptor concentration around it [13]

$$\varphi(t, z) = \exp \left( - \int_0^{2\pi} \int_0^{\pi} \int_{R_e}^{\infty} C_A(z_A) \times \{1 - \exp[-\omega(r)t]\} r^2 \sin \phi \, dr \, d\phi \, d\theta \right), \quad (27)$$

where  $z_A$  is the distance of the acceptor from the plane perpendicular to  $z$  at  $z = 0$ . This equation can be simplified [13, 14] because the distribution function of acceptors is uniform in any thin vertical slice of a spherical shell centered on the donor coordinate (Fig. 4). The volume of the ring defined by the intersection of the spherical shell of radius  $r$  and width  $dr$ , with a slice of width  $dz$  perpendicular to the  $z$  axis is

$$dv = 2\pi r \, dr \, dz. \quad (28)$$

Following a procedure identical to that used for systems with spherical symmetry, we obtain [13]

$$\varphi(t, z) = \exp \left( - 2\pi \int_{R_e}^{\infty} \{1 - \exp[-\omega(r)t]\} \times \left[ \int_{z-r}^{z+r} C_A(z_A) z_A \, dz_A \right] r \, dr \right). \quad (29)$$

Equations 26 and 29 can be used to calculate the donor decay curve for arbitrary planar symmetric donor and acceptor concentration profiles,  $C_D(z)$  and  $C_A(z)$ . The spatial dependence of these concentration profiles can usually be obtained from the local morphology of the system.

### 2.2.3

#### Cylindrical Symmetry

Until recently, research on the morphology of block copolymers focused primarily on their spherical micelles, and films with periodic lamellar structures [66, 94–96]. However, over the past decade there has been increased interest in thin films and cylindrical block copolymer structures to be used as templates in connection with nanotechnology [97]. Cylindrical particles of high axial ratio, such as nanotubes and nanowires, received particular attention. Morphological and other information on these nanostructures can be obtained advantageously from the analysis of FRET. In polymer systems, however, only a few preliminary studies have been published for cylindrical structures [98, 99], probably because, until very recently, the only models available for cylindrical systems pertained to donors located in equivalent positions [90, 91]. The main difficulty in developing appropriate models for cylindrical symmetry reside in the fact that the methodology developed for

spherical and planar symmetric systems cannot be used in cylindrical symmetric systems. In fact, the intersection of spherical shells (representing acceptors at fixed distances from a given donor) and cylinders (the natural objects for specifying dye concentration gradient), are given by complex formulae involving elliptic integrals [100]. Therefore, a general expression for FRET in cylindrical systems is more readily obtained from an equation similar to Eq. 19. Considering the donors located on the surface of a cylinder of radius  $R_D$  and the acceptors on a concentric cylindrical shell of radius  $R_A$  and thickness  $dR_A$ , we find that the distance of the acceptors to a donor at  $\mathbf{r}_D = (R_D, 0, 0)$  is (Fig. 5)

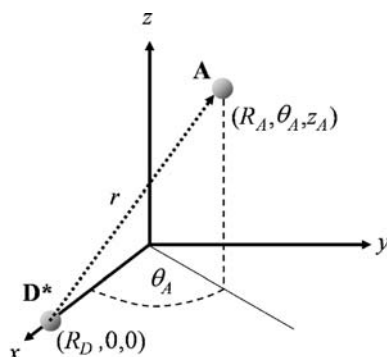


**Fig. 5** Energy transfer from an excited donor, at a distance  $R_D$  from the axis of the cylindrical structure, to an acceptor at a distance  $R_A$  from the axis  $z$

$$r = (R_D^2 + R_A^2 + z_A^2 - 2R_A R_D \cos \theta_A)^{1/2}. \quad (30)$$

The energy transfer probability  $\phi(t, R_D)$  for the donor is then

$$\phi(t, R_D) = 4 \exp \left( - \int_0^\infty dz_A \int_0^\infty R_A C_A(R_A) dR_A \int_0^\pi \{1 - \exp[-w(r)t]\} d\theta_A \right), \quad (31)$$

where the integration is carried out with the volume element  $R_A dR_A d\theta dz$  defined for cylindrical coordinates  $(R_A, \theta_A, z_A)$ , and  $C_A(R_A)$  is the acceptor number density at the cylinder whose radius is  $R_A$ .

The donor survival probability in a cylindrical object of total length  $L$  is obtained by integration over all possible donor positions

$$I_D(t) = \exp \left( - \frac{t}{\tau_D} \right) \int_0^{L/2} 2dz_D \int_0^{2\pi} d\theta_D \int_0^\infty R_D C_D(R_D) \phi(t, R_D) dR_D, \quad (32)$$

or

$$I_D(t) = 2\pi L \exp\left(-\frac{t}{\tau_D}\right) \int_0^{\infty} R_D C_D(R_D) \varphi(t, R_D) dR_D, \quad (33)$$

with  $C_D(R_D)$  being the donor concentration profile. Using Eqs. 30, 31 and 33, one can calculate the donor fluorescence decay profile for virtually any distribution of donors and acceptors obeying cylindrical symmetry [18]. For systems with restricted geometry or finite size,  $C_A(R_A)$  and  $C_D(R_D)$  can be associated with appropriate truncating functions that restrict the domain of integration. The minimum D–A approach distance can be introduced analytically [18] or numerically, by excluding values  $r < R_e$  in the integration.

### 3 Interfaces in Block Copolymers

Most polymers do not mix on a macroscopic scale, but rather form separate phases with domain sizes that usually depend on the processing of the sample [101]. Block copolymers represent a special case in which different polymers are attached at a common junction. If the blocks are similar in length and the two polymers have limited miscibility, they will form separate phases. In this case, however, the degree of phase separation is limited by the covalent bond between the two blocks. When cast into films, these systems self-assemble into periodic structures to satisfy the space-filling requirements of uniform density [30–32]. In a solvent selective for one of the blocks, block copolymers self-assemble to form micelles with a core of insoluble block surrounded by a corona of solvent-swollen soluble block [45–47].

Fredrickson was probably the first to recognize the utility of FRET in the study of block copolymers [102]. In order to study the interface between blocks, two identical copolymers are labeled at the block junction, one with D and another with A. Mixing and subsequent phase separation of the two components leads to confinement of the dyes at the interface, with an increase in the efficiency of FRET between the dyes. FRET can give valuable information on the interface between the two polymers, because it is very sensitive to the D–A distance distribution, which in turn mimics the distribution of the polymer junction points at the interface. The first experiments with junction-labeled block copolymers demonstrated how specific synthetic difficulties could be overcome [103–107], but were not able to extract detailed morphological information on the interface because an appropriate model for the analysis of the experimental donor decays was not available. With the development of models that describe FRET in restricted geometry with arbitrary distributions of donors and acceptors [13, 15, 18], it was possible to

characterize the density profile of the interfacial domain between the blocks in different block copolymer self assembled structures.

### 3.1

#### Block Copolymers Films

In block copolymer films where the blocks are incompatible, the equilibrium structure of the interface between blocks results mainly from the balance between the unfavorable energy of mixing their segments and the entropy loss due to the stretching of the chains to minimize the interfacial area. If the two blocks of a diblock copolymer are approximately the same length, a periodic lamellar structure is formed as represented in Fig. 6 [66, 94, 95, 108]. For increasingly asymmetric diblock copolymers, cylindrical and spherical morphologies are formed [109], with bicontinuous morphologies appearing for block copolymers at the composition boundary between lamellar and cylindrical structures.

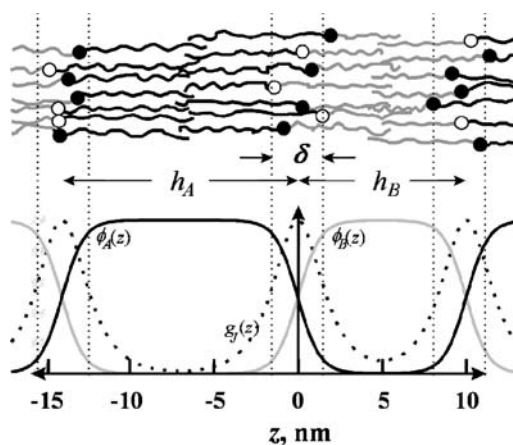


**Fig. 6** Microphase separation in a A-B diblock copolymer originating a lamellar morphology [110]. The copolymer is labeled at the junction between blocks with either a donor ( $\circ$ ) or an acceptor ( $\bullet$ ) so that the dyes concentrate at the interface (*above*), originating the polymer volume fraction profiles  $\phi_A$ ,  $\phi_B$  and junction distribution function  $g_j(z)$  shown *bellow* (calculated with the HT model for period spacing  $H = h_A + h_B = 24$  nm and interface thickness  $\delta = 2.6$  nm)

In the case of a periodic lamellar structure with donor and acceptor dyes attached to the junction points between the blocks, the model for FRET in restricted geometry with planar-symmetric distributions of donors and acceptors (Eqs. 26 and 29) can be used to calculate the donor survival probability. One needs however to know the spatial dependence of the D and A concentration profiles,  $C_D(z)$  and  $C_A(z)$ , which are related to the local morphology of the system. Helfand and Tagami [44] described the interface between blocks

for equilibrium microphase-separated A–B block copolymers in the strong segregation regimen, predicting a junction distribution function  $g_J(z)$  that is a function of the interface thickness  $\delta$

$$g_J(z) = \frac{(2/\pi)}{\delta} \operatorname{sech}(2z/\delta). \quad (34)$$

The interface thickness  $\delta$ , measured along a direction  $z$  perpendicular to the interface, can in turn be expressed in terms of the Flory–Huggins  $\chi$  parameter and the statistical segment length  $b$  averaged for the polymers of the two blocks

$$\delta = \frac{2b}{\sqrt{6\chi}}. \quad (35)$$

Since the bulk-averaged dye concentrations in the film,  $C_{A0}$  and  $C_{D0}$ , can be experimentally determined, these are the natural parameters to define the normalized acceptor and donor distribution functions [110]

$$C_A(z) = \frac{HC_{A0}}{2} g_J(z) \quad (36)$$

$$C_D(z) = \frac{HC_{D0}}{2} g_J(z) \quad (37)$$

where  $H$  is the lamellar period (Fig. 6). Experimentally, one needs only to know the acceptor bulk number density,  $C_{A0}$ , since the donor fluorescence intensity decay is measured in arbitrary units.

This method has been tested in block copolymer systems, namely regarding its sensitivity towards the D/A distribution shape [110] and its relation with the apparent dimension obtained with the KB model [111]. It was also used to determine the interface thickness in a variety of block copolymer films [110–113]. For example, in poly(styrene-*b*-methyl methacrylate) (PS-PMMA) an interface thickness of  $\delta = 4.8$  nm was found, whereas in poly(isoprene-*b*-methyl methacrylate) (PI-PMMA)  $\delta = 1.6$  nm. In addition it was found that there is no influence of the dipole orientation factor in block copolymer films [114, 115], so one can use pre-averaged  $k^2$  values.

Unlike neutron reflectivity, which cannot distinguish between the diffuseness and waviness of the interface, the FRET technique allows one to determine the interface thickness with no capillary wave correction. Nevertheless, the values obtained by FRET compare well with results of neutron reflectivity in thin films of PS-PMMA block copolymers [116, 117] and poly(styrene-*b*-butyl methacrylate) block copolymers (PS-PBMA) [118]. These experiments have been interpreted in terms of an interface thickness of 5.1 nm for PS-PMMA and 7.7 nm for PS-PBMA. For poly(isoprene-*b*-styrene) block copolymer films (PS-PI) an interface thickness of  $\delta = 1.8$  nm was inferred from SAXS measurements [108, 109].

### 3.2

#### The Core–Corona Interface in Block Copolymer Micelles

Applications suggested for block copolymer micelles, for example as surface modification agents [119] and small-molecule delivery vehicles [120], along with the intrinsic interest of self-assembling systems, have prompted the study of block copolymer micelles for many years [121–126]. Several techniques have been used to examine their structure, such as small angle scattering of visible light [127, 128], X-rays [129, 130] and neutrons [131, 132], with transmission electron microscopy also being used, particularly for non-spherical micelles [48, 49, 133]. However, in spite of the strong interest in block copolymer micelles and the effort to characterize their structure, little is known about the interface between their core and corona. While in block copolymer films the interface structure results mainly from the balance between the energy to mix the segments of the two blocks and the entropy loss due to the chain stretching to minimize the interfacial area, in block copolymer micelles it is necessary to consider the solvent effect. The swelling of the (soluble) corona polymer by the solvent leads to the decrease of the core-corona interface thickness because the (insoluble) core polymer segments avoid the contact with the solvent [84].

In early experiments, fluorescence decay curves obtained for junction-labeled block copolymer micelles have been analyzed using the KB equation (Eq. 7). Using this methodology, it was possible to obtain qualitative information about the thickness of the core-corona interface in micelles composed of donor- and acceptor-labeled block copolymers [104, 134, 135]. However, to characterize the density profile of the interfacial domain between the core and corona more deeply it is necessary to use a model that describes FRET in the core-corona interface, accounting for the distribution of donors and acceptors [84]. To use the model for spherical symmetry, described in Sect. 2.2.1, it is necessary to define the shape of the radial variation of the dye concentration. This function is related to the distribution of block junction points at the interface. If a very poor solvent for the core-block is used, swelling of the core does not need to be considered, so that the solvent will only affect the corona and the width of the interface. In this case, the junction point distribution can be described by an inverse hyperbolic cosine function, first derived for interfaces in strongly segregated systems by Helfand and Tagami (HT) [44], modified to account for the curvature of the micelle interface [84]

$$g_j(r) = \frac{1}{n_j \cosh [2(r - R_{\text{core}})/\delta]}, \quad (38)$$

where  $\delta$  is the interface width,  $R_{\text{core}}$  is the radius of the micelle core, and  $n_j$  is a normalization constant. Integration over the micelle volume



yields

$$n_J = 4\pi \int_0^{\infty} \frac{r^2}{\cos h [2(r - R_{\text{core}})/\delta]} dr. \quad (39)$$

A series of donor decay functions simulated with Eqs. 18 and 22 using parameters  $k^2 = 2/3$ ,  $R_0 = 2.3$  nm,  $\tau_D = 45.5$  ns,  $R_e = 0.5$  nm, and junction point distribution functions calculated with Eqs. 38, 39 ( $R_{\text{core}} = 7.6$  nm) [84], showed that for micelle interface thicknesses increasing from 0 to 2.4, the donor decay profile becomes significantly slower (Fig. 7) because a thicker interface dilutes the dyes, increasing their separation and consequently decreasing the overall energy transfer efficiency.

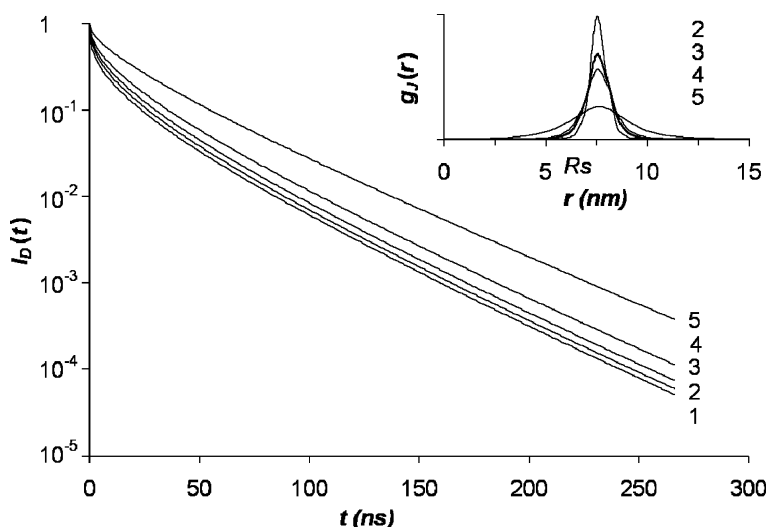


**Fig. 7** Donor fluorescence decay functions simulated with Equations 18 and 22 using  $k^2 = 2/3$ ,  $R_0 = 2.3$  nm,  $\tau_D = 45.5$  ns,  $R_e = 0.5$  nm, and junction point distribution functions calculated with Equations 38 and 39 (inset), for interface thickness values of (1) 0 nm, (2) 0.6 nm, (3) 0.9 nm, (4) 1.2 nm and (5) 2.4 nm

To analyze experimental donor fluorescence decay curves obtained by the single photon timing technique [136], the simulated noise-free simulated donor decay functions are modified to introduce the features characteristic of real experiments [137] and fitted to the experimental curves [138]. Results obtained for polyisoprene-*b*-poly(methyl methacrylate) (PI-PMMA) diblock copolymers in acetonitrile [139] show that the copolymers self-assemble into star-like micelles with a dense core of the insoluble PI-blocks and a soft solvent-swollen corona of the soluble PMMA-blocks. Using block copolymers labeled at the junction with either one donor (phenanthrene) or one acceptor (anthracene), the dyes became confined in the core-corona interface.

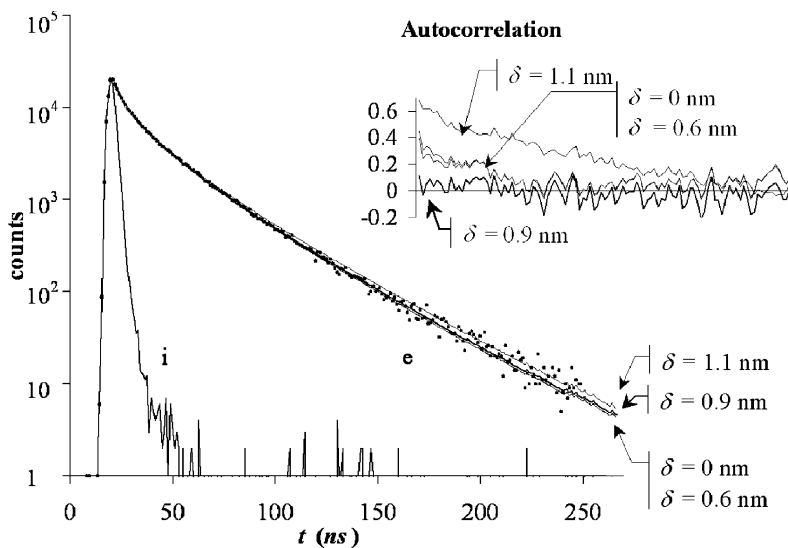


**Fig. 8** Experimental instrument response function (i) and experimental donor decay profile of labeled PI-PMMA block copolymer micelles in acetonitrile (e), fitted with decays simulated for interface thickness of 0, 0.6, 0.9 and 1.1 nm

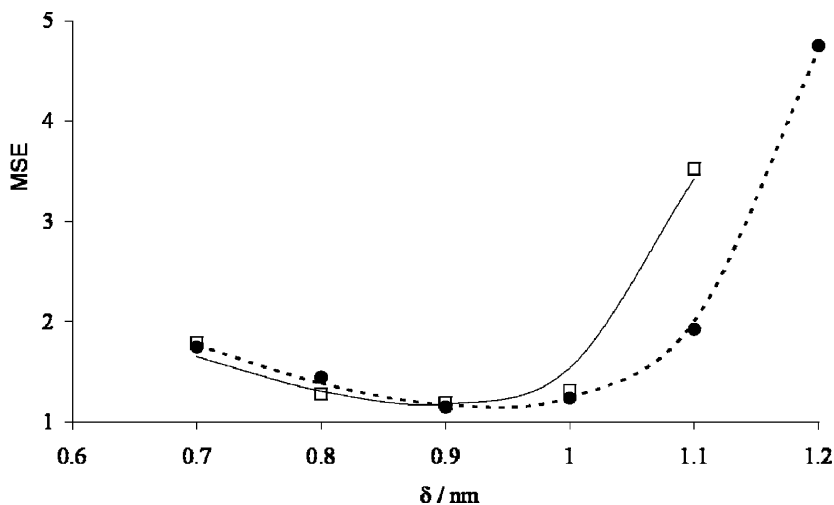


**Fig. 9** Mean square error (MSE) versus simulated interface thickness  $\delta$  for the best fit of an experimental fluorescence decay profile of PI-PMMA block copolymer micelles in acetonitrile, to each of the decays simulated for interface thicknesses  $\delta = 0$  to 1.2 nm and two values of core radius:  $R_{core} = 7.6$  nm ( $\square$ ) and  $R_{core} = 8.7$  nm ( $\bullet$ )

Experimental donor fluorescence decays fitted with simulated donor survival probabilities for interface thickness of 0, 0.6, 0.9 and 1.1 nm (Fig. 8) show that only for interface thickness values of 0.8 to 1.0 nm is it possible to obtain evenly distributed autocorrelation of the weighted residuals [84].

This value of interface thickness is confirmed by the plot of the variation of the mean square error (MSE) with simulated interface thickness (Fig. 9). For thickness values greater than 1.0 nm, good fits are not possible, and the MSE increases steeply. On the other hand, for  $\delta < 0.8$  nm, the MSE values are not very large ( $\chi^2 \approx 2$ ), but the autocorrelation functions are biased. The invariance observed for sharp interfaces results from the interface being much smaller than  $R_0$  – the donor senses an almost two-dimensional distribution of acceptors [84]. The interface thickness for PI-PMMA diblock copolymer micelles in acetonitrile is then  $\delta = (0.9 \pm 0.1)$  nm, a value that is consistent even for different estimates of the core radius (Fig. 9), resulting from fluorescence and light scattering determinations [84, 139].

## 4 Interfaces in Polymer Colloids

### 4.1 The Surface of Colloidal Particles

Polymer colloidal particles, or latex particles, show evidence of a “hairy layer” at the particle/water interface, inherent to the emulsion polymerization process [140–142]. This layer was proposed by Van der Put et al. [143], to explain the salinity dependence of the electrokinetic measurements of sulfate-charged polystyrene particles. Later on, others invoked this surface morphology to interpret the decrease in the electrophoretic mobility [144] and the characteristic relaxation frequency increase [145] of the original and heat-treated particles above the glass transition temperature of the polymer,  $T_g$ . The heat treatment causes some of the chains on the particle surface to collapse, thus creating a surface that more closely conforms to the predictions of the classical model developed for smooth surface particles [146, 147]. In order to use FRET, energy donors and acceptors are adsorbed onto the charged polymer chains at the particle surface. In the first studies of nanoparticle surfaces by FRET, Eq. 7 was used to obtain an “apparent fractal dimension” of the particle surface as  $d = 6\beta \sim 2$ , a value characteristic of a random distribution of dyes on a flat surface [81, 148, 149]. Values slightly lower ( $d = 1.8$ ) were interpreted as being due to the heterogeneous distribution of dyes on the surface [149]. A study of the hairy surface layer was done more recently [150], considering the effect of dye distribution and a polymer density profile across the hairy layer given by Eqs. 38 and 39 (where  $R_{\text{core}}$  is substituted by the radius of the sphere  $R_s$ ). Figure 10 shows a cartoon of a polymer particle with

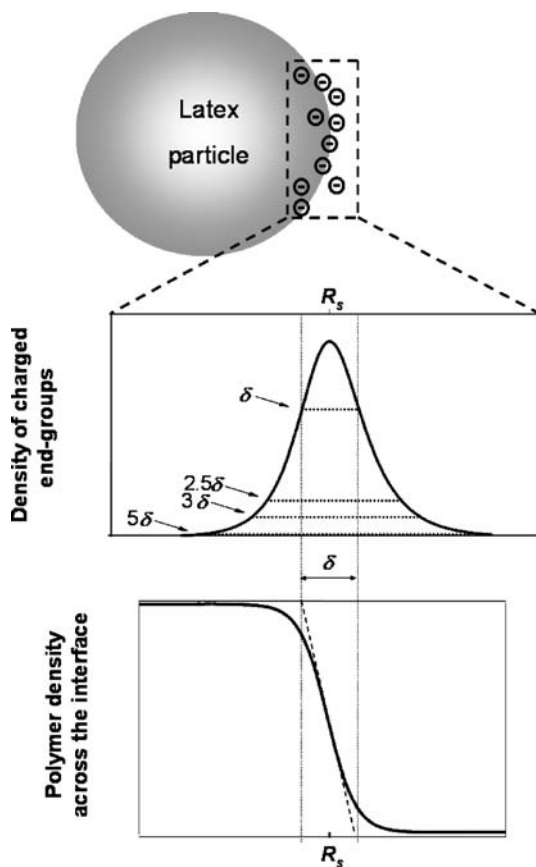


**Fig. 10** Schematic view of the distribution of charged polymer chain end groups at the surface of a latex particle of radius  $R_s$ . The density profile of the charged groups at the interface is described by Equations 38 and 39 (*middle*). The thickness of the interface is defined as  $\delta$  from the intercepts of the tangent line at the inflection point of the polymer density profile (*bottom*). A spherical shell centered in  $R$  with width  $\delta$  contains only about 60% of all the charged groups. To include 90%, 95% and 99% of the charged end groups, it is necessary to consider spherical shells with widths of  $2.5 \delta$ ,  $3 \delta$ , and  $5 \delta$ , respectively (*middle*) [150]

a hairy shell (*top*), and the plots of the density profile of charged groups (*middle*) and the polymer density across the interface (*bottom*).

Since the system has spherical symmetry, Eqs. 18, 22 apply, with the number density profiles given by  $C_i(r) = n_i g_i(r) / C_{i0}$ ;  $i = D, A$ . The polymer distribution profiles  $g_D$ ,  $g_A$  are given by Eqs. 38, 39 and the average number of molecules of donor or acceptor in the hairy particle shell  $n_i$  can be obtained independently. The interface width of two polystyrene particles with a diameter of ca. 100 nm and different surface charge densities ( $1.7 \mu\text{C m}^{-2}$  and  $2.3 \mu\text{C m}^{-2}$ ) were determined by FRET. Two dyes, rhodamine 6G (R6G)

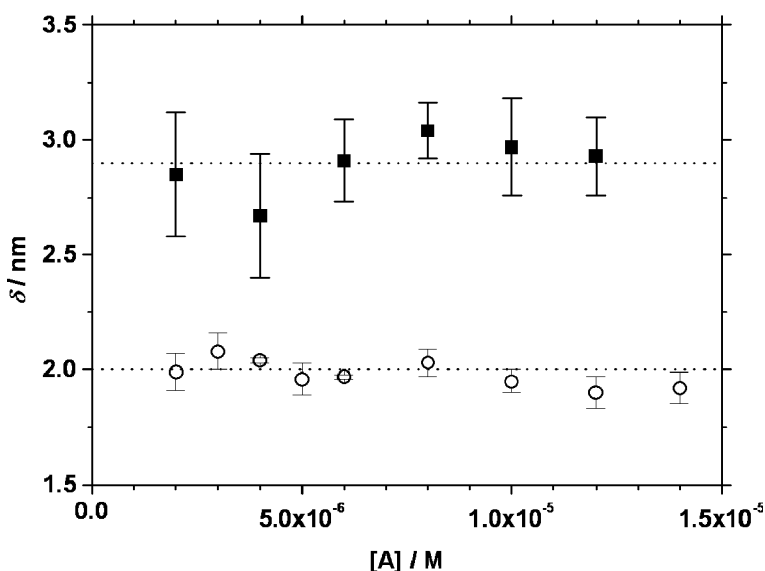


**Fig. 11** Variation of the interface thickness  $\delta$  with the bulk acceptor concentration  $C_{A0}$ . The interface thickness was obtained by fitting the donor decay curves for the less charged latex (○) and the latex with more surface charges (■)

and malachite green carbinol hydrochloride (MG) were adsorbed on the negatively charged surface of the particles. The decay curves of R6G ( $2 \times 10^{-6}$  M) in the presence of several amounts of MG ( $8-72 \times 10^{-6}$  M for the less charged particles and  $4-40 \times 10^{-6}$  M for the other sample) were obtained by the single photon timing technique. The fitting of the donor decays was performed with Eqs. 18, 22, with the interface thickness and the initial acceptor concentration being recovered for each curve. In the fitting procedure, the intrinsic lifetime of R6G,  $\tau_D = 4.5$  ns, and  $R_0 = 6.7 \pm 0.1$  nm were fixed. Figure 11 shows the plot of the particle interface thickness determined as a function of the acceptor concentration.

The interface thickness is lower for the less charged latex ( $\delta = 2.0 \pm 0.1$  nm) than for the more charged one ( $\delta = 2.9 \pm 0.2$  nm). These values correlate well with the surface charge density of the particles. The increase in the hairy layer thickness is mainly due to the electrostatic repulsion between the negatively charged polymer chains in the particle interface [150].

## 4.2

### Interface Breadth in Latex Film Formation

The different stages involved in the formation of a film from a dispersion of polymer nanoparticles, or latex, is schematically shown in Fig. 12 [61–63, 151]. After water evaporation and drying, a large number of sharp inter-

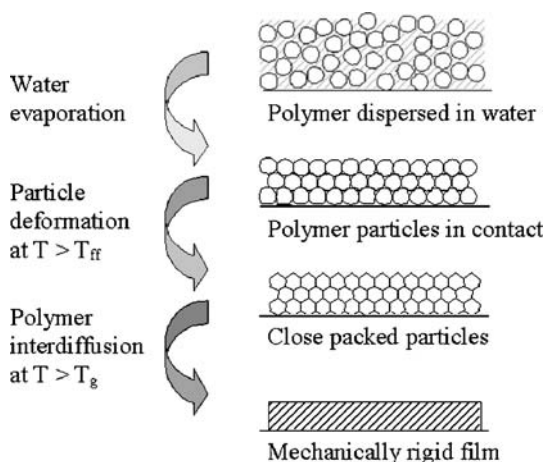


**Fig. 12** Different stages involved in the formation of a film from a dispersion of latex particles

faces are created in the densely close-packed particle arrangement. Particles begin to form a clear and continuous film above the “minimum film formation temperature” (MFFT), by a combination of capillary, osmotic and surface forces that have to overcome the elastic modulus of the latex [61]. In order to form a strong, continuous and transparent film, the polymer chains have to cross the interfaces by molecular diffusion. This process occurs at temperatures above the glass transition temperature of the polymer and is driven by an increase in entropy due to conformational randomization of the polymer chains to attain the ideal conformation of the bulk. During polymer diffusion, the interface width grows until the interface is completely healed.

Two techniques, small angle neutron scattering (SANS) and FRET, were used to study polymer interdiffusion across the interface in latex film formation. SANS was first used by Hahn and coworkers [152, 153], and later applied by Yoo et al. [154, 155], to study the relationship between the depth of interdiffusion and the tensile strength of the film, and its dependence on the molecular weight of the polymer chains. In these studies, the authors prepared films from the mixture of deuterated and non-deuterated particles and followed the diffusion of the test deuterated chains in a matrix of non-deuterated chains. The FRET method, pioneered by Winnik, requires a mixture of particles, some labeled with energy donors and others with acceptors [15, 62–64, 156, 157]. Initially the donors and acceptors are allocated in different particles and the efficiency of energy transfer from donors in one particle to acceptors in another is very small. After polymer diffusion across the interface, the chains from different particles mix and the efficiency of energy transfer increases.

The quantum efficiency of energy transfer after the film has been annealed at temperatures above  $T_g$ , for a period of time  $t_{\text{diff}}$ , is given by,

$$\Phi_{\text{ET}}(t_{\text{diff}}) = 1 - \frac{\int_0^{\infty} I_{\text{DA}}(t) dt}{\int_0^{\infty} I_{\text{D}}(t) dt}, \quad (40)$$

where the integrals of  $I_{\text{DA}}(t)$  and  $I_{\text{D}}(t)$  correspond to the areas under the donor decay curve in the presence and absence of acceptors, respectively. The experimental donor decay curve in the presence of energy transfer has been usually fitted with the empirical equation [62–64]

$$I_{\text{DA}}(t) = A_1 \exp[-t/\tau_{\text{D}} - P(t/\tau_{\text{D}})^{1/2}] + A_2 \exp(-t/\tau_{\text{D}}), \quad (41)$$

where the pre-exponential factor  $A_2$  is proportional to the amount of donors isolated from acceptors which decay with the intrinsic lifetime  $\tau_{\text{D}}$ , while  $A_1$  accounts for the donors that are involved in the energy transfer processes. The increase in the extent of mixing with annealing time has been approximated by the increase in the quantum efficiency of energy transfer, normalized with the values of the initial and fully mixed film

$$f_{\text{m}}(t_{\text{diff}}) \approx \frac{\Phi_{\text{ET}}(t_{\text{diff}}) - \Phi_{\text{ET}}(0)}{\Phi_{\text{ET}}(\infty) - \Phi_{\text{ET}}(0)}. \quad (42)$$

However, the real fraction of mass that has diffuse across the initial boundary  $f_{\text{s}}(t_{\text{diff}})$  is given by,

$$f_{\text{s}}(t_{\text{diff}}) = 1 - \frac{3}{4\pi R_{\text{s}}^3} \int_0^{R_{\text{s}}} 4\pi r^2 g_{\text{D}}(r) dr, \quad (43)$$

where, the donor concentration profiles,  $g_{\text{D}}(r)$ , for Fickian diffusion in a medium with spherical geometry is

$$g_{\text{D}}(r) = \frac{1}{2} \left( \operatorname{erf} \left( \frac{R_{\text{s}} + r}{\theta} \right) + \operatorname{erf} \left( \frac{R_{\text{s}} - r}{\theta} \right) + \frac{\theta}{\sqrt{\pi} r} \left\{ \exp \left[ 1 - \left( \frac{R_{\text{s}} + r}{\theta} \right)^2 \right] - \exp \left[ - \left( \frac{R_{\text{s}} - r}{\theta} \right)^2 \right] \right\} \right), \quad (44)$$

and  $\theta = 2\sqrt{\langle D \rangle t_{\text{diff}}}$  is a parameter measuring the extent of diffusion during a period of time  $t_{\text{diff}}$ , with average diffusion coefficient  $\langle D \rangle$ .  $R_{\text{s}}$  is the radius of the particle and  $\operatorname{erf}(x)$  is the error function. Within this approach the mean diffusion coefficient can be calculated using Eqs. 43, 44.

With the assumption that  $f_m$  closely follows the time evolution of  $f_s$ , (an approximation that could not be clearly justified), this very simple model was systematically used to study the latex film formation [62–64]. The model is very appellative because it is able to predict, at least qualitatively, the evolution of the average diffusion coefficient of the polymer with annealing. However, by using only the efficiency of energy transfer, this simple model disregards most of the information contained in the donor decay function.

In order to improve the methodology for FRET analysis of latex film formation, one should use a model of FRET in restricted geometry (Eqs. 18, 22) with distribution functions of donors and acceptors give by an appropriate diffusion equation (such as Eq. 44), and a model for the close packed arrangement of latex spheres [15, 156–158]. For a latex dispersion composed by a 1 : 1 mixture of donor and acceptor labeled particles, it is reasonable to assume that a given donor-labeled particle is surrounded by 12 “first neighbor particles” half labeled with donor and the others with acceptor. Assuming that energy migration among donors does not compete with the donor–acceptor energy transfer step, the donor decay law, after a  $\delta$ -pulse of excitation light, is given by

$$I_D(t) = 4\pi \exp(-t/\tau_D) \int_{V_s} C_D(r_D) \varphi(t, r_D) r_D^2 dr_D. \quad (45)$$

The decay of a donor at position  $r_D$  is given by Eq. 22, with  $g_D(r)$  given by Eq. 44 and the acceptor density profile

$$g_A(r) = g_D(2R_s - r). \quad (46)$$

Since the initial acceptor concentration, the intrinsic donor lifetime and the critical Förster radius for the donor–acceptor pair in the film are known, the decay curves are only dependent on the average diffusion coefficient. The model cannot be used for fractions of mixing close to one, because the individuality of the particles is lost.

Figure 13 shows the volume fractions of mixing obtained for films of poly(butyl methacrylate) (PBMA) latex annealed at 56, 74 and 90 °C (*top*) and the corresponding diffusion coefficients (*bottom*), for particles with polymer chains randomly labeled with a phenanthrene derivative (donor) or an N-benzophenone derivative (acceptor) [156]. The value of  $R_0 = 2.37$  nm was determined for the same donor–acceptor pair in a homogeneous polymer film of PBMA.

The variation of the average diffusion coefficients with the fraction of mixing is due to the polydispersity of the polymer chains in the particles, with the shorter chains of higher diffusion coefficient contributing more to the fraction of mixing at the early times of annealing [15, 156]. As expected, the average diffusion coefficient increases with temperature and obey the Ar-



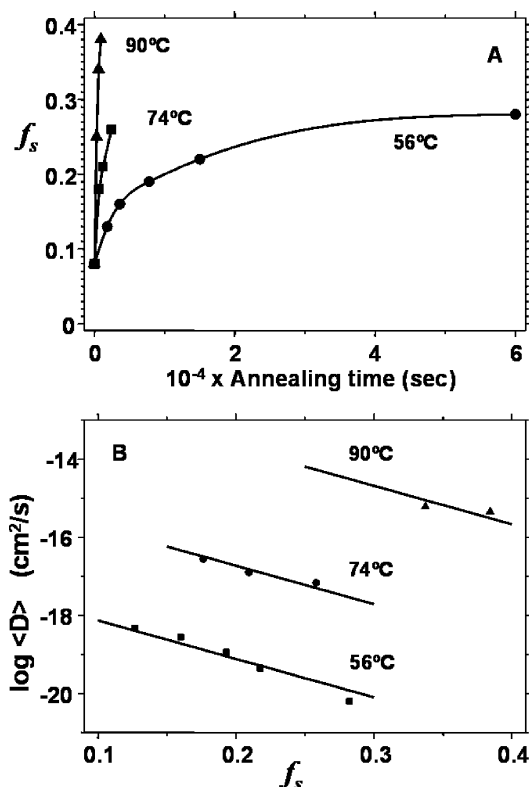


**Fig. 13** Volume fraction of mixing obtained for films annealed at 56, 74 and 90 °C (A) and diffusion coefficients corresponding to the fitted values (B). Multi-linear fit of the data points corresponding to the three annealing temperatures (B) yields a diffusion activation energy of  $38 \pm 5$  kcal mol<sup>-1</sup> [157]

rhenius type equation with activation energy  $38 \pm 5$  kcal mol<sup>-1</sup>. In a recent comparison of the models, it was observed that the simple model can predict fairly well the relative evolution and temperature dependence of the diffusion coefficients. However, the diffusion coefficients calculated by the two models can differ as much as one order of magnitude, though in general the difference might be smaller [156].

## 5 Interfaces in Polymer Blends

Block copolymer interfaces (Sect. 3) and polymer blend interfaces share many common features. The major difference between them lays in the free energy of interface formation, which for block copolymers has an en-

tropy penalty for localization of the joints in the interface. This term becomes smaller as the polymers become longer, and in the limit of very long chains, the interface thicknesses are predicted to be the same in both systems.

Polymer blends have been studied for many years [101]. While a small fraction of polymer mixtures are fully miscible at the molecular level, most polymer blends are not [159]. One often refers to polymer blends as “immiscible” if the blend exhibits two glass transition temperatures identical to that of the individual components. Many polymer blends are not completely immiscible because some segment interpenetration occurs at the interface between the individual domains. In these systems, the volume fraction of the interfacial region is usually too small to be detected by differential scanning calorimetry or by dynamic mechanical analysis. However, FRET, a technique pioneered by Morawetz for the study of polymer blends [6, 11, 12, 72], show that these blends are best described as having limited miscibility.

While specular neutron reflectivity [160–162] is a powerful method for studying polymer–polymer interfaces in polymer blends, if one of the polymers can be deuterated to provide contrast, it is often difficult to distinguish between the segment-density distribution and waviness of the interface [70]. Small angle X-ray scattering (SAXS) and small angle neutron scattering (SANS) are also able, in principle, to provide some information about the interface [163–165]. However, FRET can be advantageously used to determine the thickness of the interface between adjacent phases in polymer blends because, although it requires that the polymers are labeled with donor and acceptor dyes, it avoids the more difficult preparation of deuterated polymers. With an appropriate model for FRET, one can obtain detailed information about the interface between the blend components [166].

One model to study the interface between domains in a binary blend is constituted by a film cast from nanoparticle dispersions of two different polymers. In a film composed of anthracene-labeled poly(2-ethylhexyl methacrylate) (PEHMA) and phenanthrene-labeled poly(butyl methacrylate) (PBMA) latex particles [158, 167], the harder PBMA particles are dispersed as individual spheres in a continuous soft PEHMA matrix [168]. The system can be described by a core-shell type model [166], adapted from the distribution models for FRET in spherical geometry [15–17]. The concentration profiles of the two components depend on the binodal composition and relative amount of the components in each domain, [169–172], and the interfacial region between the polymers [66, 173, 174]. These can be calculated using a combination of Cahn and Hilliard’s theory of phase separation in simple liquids and alloys [170] with the Flory–Huggins description of homogeneous polymer blends [34, 44, 174, 175], as originally proposed by de Gennes [171, 172], and detailed by Anastasiadis [169].

In a blend of two polymers polyA and polyB, the variation in the composition  $\phi$  in a direction perpendicular to the interface is given by [166]

$$\left(\frac{d\phi}{dz}\right)^2 = \frac{36}{N_{\text{polyB}}u_{\text{B}}(1-\phi)\langle r_0^2 \rangle_{\text{polyA}} + N_{\text{polyA}}u_{\text{A}}\phi\langle r_0^2 \rangle_{\text{polyB}}} \\ \times \left\{ N_{\text{polyB}}u_{\text{B}} \left[ \phi^2(1-\phi)\ln\phi - \phi(1-\phi)\phi_{\alpha}\ln\phi_{\alpha} \right] \right. \\ \left. + N_{\text{polyA}}u_{\text{A}} \left[ \phi(1-\phi)^2\ln(1-\phi) - \phi(1-\phi)(1-\phi_{\alpha})\ln(1-\phi_{\alpha}) \right] \right. \\ \left. + \chi N_{\text{polyA}}N_{\text{polyB}}u_{\text{B}} \left[ \phi^2(1-\phi)^2 - \phi(1-\phi)\phi_{\alpha}(1-\phi_{\alpha}) \right] \right\}, \quad (47)$$

where  $\phi_{\alpha}$  and  $\phi_{\beta}$  are the bimodal volume fractions of polyA,  $N_{\text{polyA}}$  and  $N_{\text{polyB}}$  the degrees of polymerization,  $u_{\text{A}}$  and  $u_{\text{B}}$  are the specific monomer volumes, and  $\langle r_0^2 \rangle_{\text{polyA}}$ ,  $\langle r_0^2 \rangle_{\text{polyB}}$  are the average end to end distances of the chains of the two components. The thickness of the interface  $\delta$  is calculate for  $\phi = (\phi_{\alpha} + \phi_{\beta})/2$  in

$$\left(\frac{\phi_{\beta} - \phi_{\alpha}}{\delta}\right)^2 = \frac{36}{N_{\text{polyB}}u_{\text{B}}(1-\phi)\langle r_0^2 \rangle_{\text{polyA}} + N_{\text{polyA}}u_{\text{A}}\phi\langle r_0^2 \rangle_{\text{polyB}}} \\ \times \left\{ N_{\text{polyB}}u_{\text{B}} \left[ \phi^2(1-\phi)\ln\phi - \phi(1-\phi)\phi_{\alpha}\ln\phi_{\alpha} \right] \right. \\ \left. + N_{\text{polyA}}u_{\text{A}} \left[ \phi(1-\phi)^2\ln(1-\phi) - \phi(1-\phi)(1-\phi_{\alpha})\ln(1-\phi_{\alpha}) \right] \right. \\ \left. + \chi N_{\text{polyA}}N_{\text{polyB}}u_{\text{B}} \left[ \phi^2(1-\phi)^2 - \phi(1-\phi)\phi_{\alpha}(1-\phi_{\alpha}) \right] \right\}. \quad (48)$$

The fluorescence donor decay measured for films of a blend of phenanthrene-labeled PBMA and anthracene labeled PEHMA was analyzed using this model to yield an interface thickness  $\delta = 5.8$  nm (Fig. 14) for a Flory–Huggins interaction parameter  $\chi = 0.021$  [166].

These FRET experiments provide a powerful method to determine both the Flory–Huggins  $\chi$  parameter of the two polymers in a blend, and the thickness of the interface between the domains. The model accounts for the polymer binodal compositions in the different blend domains and can be used in systems in which one phase can be prepared in the form of uniform spheres dispersed in a matrix of the other phase.

## 6 Conclusions

Interfaces play an important role in polymeric materials composed of different phases. Even for incompatible polymers, interfaces are quite diffuse, with thickness values in the range of 1 to 10 nm. This length scale matches the range where FRET from a donor dye to an acceptor is more sensitive

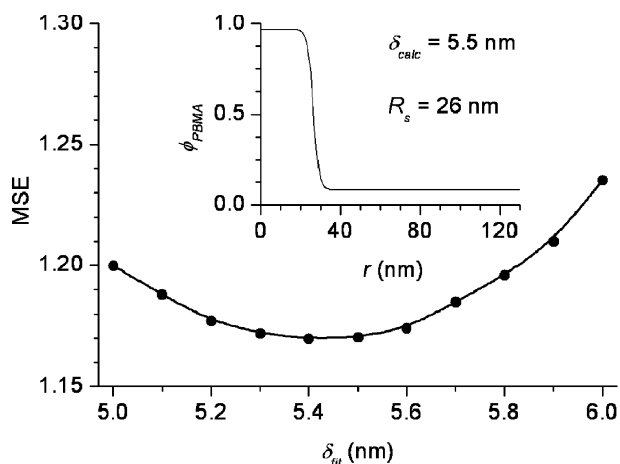


**Fig. 14** Mean square error obtained from fitting an experimental donor decay curve obtained for a film annealed for 1 hour at 60 °C to donor survival probability curves simulated for a PEHMA-PBMA weight ratio of 9.9:1 and several trial  $\delta_{fit}$  interface thickness values, for  $\chi = 0.021$  (corresponding to a calculated interface thickness  $\delta_{calc} = 5.5$  nm and  $R_s = 26$  nm). The interface profile and thickness obtained from thermodynamic calculations are shown in the insert [166]

to their separation. Experiments with FRET in polymer systems have been usually analyzed with models that could only recover qualitative or approximate information when used in nanoheterogeneous systems, such as polymer interfaces. These models, initially developed by Förster [4, 5], Klafter and Blumen [82, 89–91] are only valid for homogeneous distributions of donor and acceptor dyes, either in infinite media (of any dimensionality) or in systems with simple restricted geometry. In systems where the morphology has restricted geometry and/or the components present concentration gradients, the donor and acceptor distributions can not be accommodated by the Förster or KB type models. The more recent development of models that take into account the heterogeneous distribution of donors and acceptors in systems of restricted geometry with planar [13, 14], spherical [15–17], or cylindrical [18] symmetry, allowed the use of FRET to obtain quantitative detailed information on polymer interfaces and other nanostructured materials. These models have been successfully used to analyze FRET experimental results in a number of systems with nanodomains and heterogeneous dye concentration profiles, ranging from block copolymer films, to block copolymer micelles, polymer nanoparticles, latex film formation, and domains in polymer blends.

**Acknowledgements** The authors thank the financial support of FCT (projects POCTI/47885/QUI and POCI/QUI/61054/2004).

## References

1. Jones RAL, Richards RW (1999) *Polymers at Surfaces and Interfaces*. Cambridge University Press, London, UK
2. Wool RP (1995) *Polymer Interfaces: Structure and Strength*. Carl Hanser Verlag, New York
3. Flerer GJ, Stuart MAC, Scheutjens JMHM, Cosgrove T, Vincent B (1993) *Polymers at interfaces*. Chapman & Hall, London, UK
4. Forster T (1949) Experimentelle und Theoretische Untersuchung des Zwischenmolekularen Ubergangs Von Elektronenanregungsenergie. *Z Naturforsch A* 4:321–327
5. Forster T (1948) Zwischenmolekulare Energiewanderung und Fluoreszenz. *Ann Physik Ber* 2:55–75
6. Morawetz H (1988) Studies of Synthetic-Polymers by Nonradiative Energy-Transfer. *Science* 240:172–176
7. Mikes F, Morawetz H, Dennis KS (1984) Characterization of Polymer Compatibility by Nonradiative Energy-Transfer – Applications to Binary-Mixtures of Homopolymers and to Homopolymer Block Copolymer Blends. *Macromolecules* 17:60–63
8. Mikes F, Morawetz H, Dennis KS (1980) Characterization of Polymer Compatibility by Nonradiative Energy-Transfer – Application to Binary-Mixtures Containing Anionically Prepared Polystyrene, Anionically Prepared Poly(Alpha-Methylstyrene), Or Poly(2,6-Dimethyl-1,4-Phenylene Ether). *Macromolecules* 13:969–971
9. Horsky J, Morawetz H (1989) Fluorescence of Solutions of Mixed Donor-Labeled and Acceptor-Labeled Polymers. *Macromolecules* 22:1622–1624
10. Amrani F, Hung JM, Morawetz H (1980) Studies of Polymer Compatibility by Nonradiative Energy-Transfer. *Macromolecules* 13:649–653
11. Morawetz H, Amrani F (1978) New Method for Study of Polymer Compatibility. *Macromolecules* 11:281–282
12. Morawetz H (1999) On the versatility of fluorescence techniques in polymer research. *J Polym Sci A1* 37:1725–1735
13. Farinha JPS, Martinho JMG, Yekta A, Winnik MA (1995) Direct Nonradiative Energy-Transfer in Polymer Interphases – Fluorescence Decay Functions from Concentration Profiles Generated by Fickian Diffusion. *Macromolecules* 28:6084–6088
14. Yekta A, Duhamel J, Winnik MA (1995) Dipole–Dipole Electronic-Energy Transfer – Fluorescence Decay Functions for Arbitrary Distributions of Donors and Acceptors – Systems with Planar Geometry. *Chem Phys Lett* 235:119–125
15. Farinha JPS, Martinho JMG, Kawaguchi S, Yekta A, Winnik MA (1996) Latex film formation probed by nonradiative energy transfer: Effect of grafted and free poly(ethylene oxide) on a poly(*n*-butyl methacrylate) latex. *J Phys Chem* 100:12552–12558
16. Farinha JPS, Martinho JMG (1997) Electronic energy transfer in restricted geometries – Application to the study of spherical and planar interphases of diblock copolymer films. *J Lumin* 72–74:914–917
17. Yekta A, Winnik MA, Farinha JPS, Martinho JMG (1997) Dipole–dipole electronic energy transfer. Fluorescence decay functions for arbitrary distributions of donors and acceptors. 2. Systems with spherical symmetry. *J Phys Chem A* 101:1787–1792
18. Farinha JPS, Spiro JG, Winnik MA (2004) Dipole–dipole electronic energy transfer: Fluorescence decay functions for arbitrary distributions of donors and acceptors in systems with cylindrical symmetry. *J Phys Chem B* 108:16392–16400
19. Rubinstein M, Colby R (2003) *Polymer Physics*. Oxford University Press, New York

20. Bates FS (1991) Polymer–Polymer Phase-Behavior. *Science* 251:898–905
21. Bucknall DG (2004) Influence of interfaces on thin polymer film behaviour. *Prog Mater Sci* 49:713–786
22. Higgins JS, Tambasco M, Lipson JEG (2005) Polymer blends; stretching what we can learn through the combination of experiment and theory. *Prog Polym Sci* 30:832–843
23. Eastwood E, Viswanathan S, O'Brien CP, Kumar D, Dadmun MD (2005) Methods to improve the properties of polymer mixtures: Optimizing intermolecular interactions and compatibilization. *Polymer* 46:3957–3970
24. Ma YC, Farinha JPS, Winnik MA, Yaneff PV, Ryntz RA (2004) Compatibility of chlorinated polyolefin with the components of thermoplastic polyolefin: A study by laser scanning confocal fluorescence microscopy. *Macromolecules* 37:6544–6552
25. Bates FS, Fredrickson GH (1999) Block copolymers – Designer soft materials. *Phys Today* 52:32–38
26. Fredrickson GH, Bates FS (1996) Dynamics of block copolymers: Theory and experiment. *Annu Rev Mater Sci* 26:501–550
27. Reynolds BJ, Ruegg ML, Mates TE, Radke CJ, Balsara NP (2005) Experimental and theoretical study of the adsorption of a diblock copolymer to interfaces between two homopolymers. *Macromolecules* 38:3872–3882
28. Thompson RB, Matsen MW (2000) Improving polymeric microemulsions with block copolymer polydispersity. *Phys Rev Lett* 85:670–673
29. Bates FS, Maurer WW, Lipic PM, Hillmyer MA, Almdal K, Mortensen K, Fredrickson GH, Lodge TP (1997) Polymeric bicontinuous microemulsions. *Phys Rev Lett* 79:849–852
30. Hamley IW (2004) *Developments in Block Copolymers Science and Technology*. Wiley Interscience, New York
31. Lodge TP (2003) Block copolymers: Past successes and future challenges. *Macromol Chem Phys* 204:265–273
32. Hamley IW (1998) *The Physics of Block Copolymers*. Oxford University Press, London, UK
33. Melenkevitz J, Muthukumar M (1991) Density Functional Theory of Lamellar Ordering in Diblock Copolymers. *Macromolecules* 24:4199–4205
34. Leibler L (1980) Theory of Microphase Separation in Block Co-Polymers. *Macromolecules* 13:1602–1617
35. Almdal K, Rosedale JH, Bates FS (1990) Order–Disorder Transition in Binary-Mixtures of Nearly Symmetrical Diblock Copolymers. *Macromolecules* 23:4336–4338
36. Matsen MW, Bates FS (1996) Origins of complex self-assembly in block copolymers. *Macromolecules* 29:7641–7644
37. Adhikari R, Michler GH (2004) Influence of molecular architecture on morphology and micromechanical behavior of styrene/butadiene block copolymer systems. *Prog Polym Sci* 29:949–986
38. Helfand E (1975) Block Copolymers, Polymer-Polymer Interfaces, and Theory of Inhomogeneous Polymers. *Accounts Chem Res* 8:295–299
39. Helfand E, Sapse AM (1975) Theory of Unsymmetric Polymer–Polymer Interfaces. *J Chem Phys* 62:1327–1331
40. Helfand E, Wasserman ZR (1976) Block Copolymer Theory. 4. Narrow Interphase Approximation. *Macromolecules* 9:879–888
41. Semenov AN (1985) Contribution to the Theory of Microphase Layering in Block-Copolymer Melts. *Sov Phys JETP* 61:733
42. Matsen MW, Bates FS (1996) Unifying weak- and strong-segregation block copolymer theories. *Macromolecules* 29:1091–1098

43. Matsen MW, Schick M (1996) Self-assembly of block copolymers. *Curr Opin Colloid Interface Sci* 1:329–336
44. Helfand E, Tagami Y (1972) Theory of Interface Between Immiscible Polymers. 2. *J Chem Phys* 56:3592–3601
45. Riess G (2003) Micellization of block copolymers. *Prog Polym Sci* 28:1107–1170
46. Gast AP (1997) Polymeric micelles. *Curr Opin Colloid Interface Sci* 2:258–263
47. Alexandridis P, Lindman B (2000) *Amphiphilic Block Copolymers: Self-Assembly and Applications*. Elsevier Science B.V., Amsterdam, The Netherlands
48. Zhang LF, Eisenberg A (1996) Multiple morphologies and characteristics of crew-cut micelle-like aggregates of polystyrene-*b*-poly(acrylic acid) diblock copolymers in aqueous solutions. *J Am Chem Soc* 118:3168–3181
49. Zhang LF, Eisenberg A (1995) Multiple Morphologies of Crew-Cut Aggregates of Polystyrene-*B*-Poly(Acrylic Acid) Block-Copolymers. *Science* 268:1728–1731
50. Won YY, Davis HT, Bates FS (1999) Giant wormlike rubber micelles. *Science* 283:960–963
51. Raez J, Barjovanu R, Massey JA, Winnik MA, Manners I (2000) Self-assembled organometallic block copolymer nanotubes. *Angew Chem Int Edit* 39:3862
52. Raez J, Manners I, Winnik MA (2002) Nanotubes from the self-assembly of asymmetric crystalline-coil poly(ferrocenylsilane-siloxane) block copolymers. *J Am Chem Soc* 124:10381–10395
53. Discher BM, Won YY, Ege DS, Lee JCM, Bates FS, Discher DE, Hammer DA (1999) Polymersomes: Tough vesicles made from diblock copolymers. *Science* 284:1143–1146
54. Luo LB, Eisenberg A (2001) Thermodynamic size control of block copolymer vesicles in solution. *Langmuir* 17:6804–6811
55. Sundberg DC, Durant YG (2003) Latex particle morphology, fundamental aspects: A review. *Polym React Eng* 11:379–432
56. Durant YG, Sundberg DC (1997) Progress in predicting latex-particle morphology and projections for the future ACS SYMPOSIUM SERIES 663:44–56
57. Urban D, Takamura K (2002) *Polymer Dispersions and Their Industrial Applications*. Wiley-VCH, New York, USA
58. Pichot C (2004) Surface-functionalized latexes for biotechnological applications. *Curr Opin Colloid Interface Sci* 9:213–221
59. Chow RS, Takamura K (1988) Effects of Surface-Roughness (Hairiness) of Latex-Particles on Their Electrokinetic Potentials. *J Colloid Interface Sci* 125:226–236
60. Farinha JPS, Charreyre MT, Martinho JMG, Winnik MA, Pichot C (2001) Picosecond fluorescence studies of the surface morphology of charged polystyrene latex particles. *Langmuir* 17:2617–2623
61. Keddie JL (1997) Film formation of latex. *Mater Sci Eng R* 21:101–170
62. Wang YC, Winnik MA (1993) Polymer Diffusion Across Interfaces in Latex Films. *J Phys Chem* 97:2507–2515
63. Winnik MA, Wang YC, Haley F (1992) Latex Film Formation at the Molecular-Level – the Effect of Coalescing Aids on Polymer Diffusion. *J Coating Technol* 64:51–61
64. Wang YC, Zhao CL, Winnik MA (1991) Molecular-Diffusion and Latex Film Formation – An Analysis of Direct Nonradiative Energy-Transfer Experiments. *J Chem Phys* 95:2143–2153
65. Hamley IW (2004) *Developments in Block Copolymers: Science and Technology*. Wiley Interscience, New York, USA
66. Stamm M, Schubert DW (1995) Interfaces Between Incompatible Polymers. *Annu Rev Mater Sci* 25:325–356

67. Schubert DW, Stamm M (1997) Neutron reflectometry and small-angle neutron scattering – Two complementary techniques for polymer blend investigations. *Physica B* 234:286–288
68. Russell TP (1996) On the reflectivity of polymers: Neutrons and X-rays. *Physica B* 221:267–283
69. Russell TP (1996) Characterizing polymer surfaces and interfaces. *Mrs Bulletin* 21:49–53
70. Sferrazza M, Xiao C, Jones RAL, Bucknall DG, Webster J, Penfold J (1997) Evidence for capillary waves at immiscible polymer/polymer interfaces. *Phys Rev Lett* 78:3693–3696
71. Morawetz H (1983) Fluorescence Study of Polymer-Chain Interpenetration and of the Rate of Phase-Separation in Incompatible Polymer Blends. *Polym Eng Sci* 23:689–692
72. Morawetz H (1979) Some Applications of Fluorimetry to Synthetic-Polymer Studies. *Science* 203:405–410
73. Chen CT, Morawetz H (1989) Characterization of Polymer Miscibility by Fluorescence Techniques – Blends of Styrene Copolymers Carrying Hydrogen-Bond Donors with Polymethacrylates. *Macromolecules* 22:159–164
74. Baumann J, Fayer MD (1986) Excitation Transfer in Disordered Two-Dimensional and Anisotropic 3-Dimensional Systems – Effects of Spatial Geometry on Time-Resolved Observables. *J Chem Phys* 85:4087–4107
75. Steinber IZ (1968) Nonradiative Energy Transfer in Systems in Which Rotatory Brownian Motion Is Frozen. *J Chem Phys* 48:2411
76. Steinber IZ, Hass E, Katchalsi E (1983) Long-Range Nonradiative Transfer of Electronic Excitation Energy. In: St. Andrews S (ed) *Time-Resolved Spectroscopy in Biochemistry and Biology*. Plenum, New York
77. Galanin MD (1955) The Problem of the Effect of Concentration on the Luminescence of Solutions. *Sov Phys JETP* 1:317–325
78. Forster T (1959) 10th Spiers Memorial Lecture – Transfer Mechanisms of Electronic Excitation. *Discuss Faraday Soc* 7–17
79. Klafter J, Blumen A (1984) Fractal Behavior in Trapping and Reaction. *J Chem Phys* 80:875–877
80. Hauser M, Klein UKA, Gosele U (1976) Extension of Forsters Theory of Long-Range Energy-Transfer to Donor-Acceptor Pairs in Systems of Molecular Dimensions. *Z Phys Chem* 101:255–266
81. Yang CL, Evesque P, Elsayed MA (1985) Fractal-Like, But Nonfractal, Behavior of One-Step Dipolar Energy-Transfer on Regular Lattices with Excluded Volume. *J Phys Chem* 89:3442–3444
82. Levitz P, Drake JM, Klafter J (1989) In: Klafter J, Drake JM (eds) *Molecular Dynamics in Restricted Geometries*. Wiley, New York
83. Mataga N (1989) In: Klafter J, Drake JM (eds) *Molecular Dynamics in Restricted Geometries*. Wiley, New York
84. Farinha JPS, Schillen K, Winnik MA (1999) Interfaces in self-assembling diblock copolymer systems: Characterization of poly(isoprene-*b*-methyl methacrylate) micelles in acetonitrile. *J Phys Chem B* 103:2487–2495
85. Gochanour CR, Andersen HC, Fayer MD (1979) Electronic Excited-State Transport in Solution. *J Chem Phys* 70:4254–4271
86. Gochanour CR, Fayer MD (1981) Electronic Excited-State Transport in Random-Systems – Time-Resolved Fluorescence Depolarization Measurements. *J Phys Chem* 85:1989–1994



87. Loring RF, Andersen HC, Fayer MD (1982) Electronic Excited-State Transport and Trapping in Solution. *J Chem Phys* 76:2015–2027
88. Miller RJD, Pierre M, Fayer MD (1983) Electronic Excited-State Transport and Trapping in Disordered-Systems – Picosecond Fluorescence Mixing, Transient Grating, and Probe Pulse Experiments. *J Chem Phys* 78:5138–5146
89. Klafter J, Blumen A, Drake JM (1989) In: Klafter J, Drake JM (eds) *Molecular Dynamics in Restricted Geometries*. Wiley, New York
90. Levitz P, Drake JM, Klafter J (1988) Direct Energy-Transfer in Pores – Geometrical Cross-Overs and Apparent Dimensionality. *Chem Phys Lett* 148:557–561
91. Blumen A, Klafter J, Zumofen G (1986) Influence of Restricted Geometries on the Direct Energy-Transfer. *J Chem Phys* 84:1397–1401
92. Levitz P, Drake JM, Klafter J (1988) Critical-Evaluation of the Application of Direct Energy-Transfer in Probing the Morphology of Porous Solids. *J Chem Phys* 89:5224–5236
93. Martinho JMG, Farinha JP, Berberansantos MN, Duhamel J, Winnik MA (1992) Test of A Model for Reversible Excimer Kinetics – Pyrene in Cyclohexanol. *J Chem Phys* 96:8143–8149
94. Bates FS, Fredrickson GH (1990) Block Copolymer Thermodynamics – Theory and Experiment. *Annu Rev Phys Chem* 41:525–557
95. Fredrickson GH, Helfand E (1987) Fluctuation Effects in the Theory of Microphase Separation in Block Copolymers. *J Chem Phys* 87:697–705
96. Torikai N, Noda I, Karim A, Satija SK, Han CC, Matsushita Y, Kawakatsu T (1997) Neutron reflection studies on segment distribution of block chains in lamellar microphase-separated structures. *Macromolecules* 30:2907–2914
97. Sidorenko A, Tokarev I, Minko S, Stamm M (2003) Ordered reactive nanomembranes/nanotemplates from thin films of block copolymer supramolecular assembly. *J Am Chem Soc* 125:12211–12216
98. Pekcan O, Winnik MA, Croucher MD (1990) Energy-Transfer Studies on Polymer Membrane Films – Materials with Variable Apparent Dimensionality. *Chem Phys* 146:283–289
99. Tcherkasskaya O, Ni SR, Winnik MA (1996) Effective volume per junction in block copolymer interfaces probed by direct energy transfer. *Macromolecules* 29:4241–4246
100. Lamarche F, Leroy C (1990) Evaluation of the Volume of Intersection of A Sphere with A Cylinder by Elliptic Integrals. *Comput Phys Communicat* 59:359–369
101. Paul D, Bucknall CB (2000) *Polymer Blends*. Wiley, New York
102. Fredrickson GH (1986) Intermolecular Correlation-Functions from Forster Energy-Transfer Experiments. *Macromolecules* 19:441–447
103. Ni SR, Juhue D, Moselhy J, Wang YC, Winnik MA (1992) Energy-Transfer Studies of Donor-Acceptor-Labeled Polystyrene-Block-Poly(Methyl Methacrylate) Diblock Copolymers in Solution. *Macromolecules* 25:496–498
104. Duhamel J, Yekta A, Ni S, Khaykin Y, Winnik MA (1993) Characterization of the Core of Polystyrene Block Poly(Methyl Methacrylate) Polymer Micelles by Energy-Transfer. *Macromolecules* 26:6255–6260
105. Ni SR, Zhang P, Wang YC, Winnik MA (1994) Energy-Transfer Studies of the Boundary-Layer Interphase in Polystyrene Poly(Methyl Methacrylate) Block-Copolymer Films. *Macromolecules* 27:5742–5750
106. Tcherkasskaya O, Spiro JG, Ni SR, Winnik MA (1996) Energy transfer in restricted geometry: Polyisoprene-poly(methyl methacrylate) block copolymer interfaces. *J Phys Chem* 100:7114–7121

107. Tcherkasskaya O, Ni SR, Winnik MA (1996) Direct energy transfer studies of the domain-boundary interface in polyisoprene-poly(methyl methacrylate) block copolymer films. *Macromolecules* 29:610–616
108. Hashimoto T, Shibayama M, Kawai H (1980) Domain-Boundary Structure of Styrene-Isoprene Block Co-Polymer Films Cast from Solution. 4. Molecular-Weight Dependence of Lamellar Microdomains. *Macromolecules* 13:1237–1247
109. Hashimoto T, Fujimura M, Kawai H (1980) Domain-Boundary Structure of Styrene-Isoprene Block Co-Polymer Films Cast from Solutions. 5. Molecular-Weight Dependence of Spherical Microdomains. *Macromolecules* 13:1660–1669
110. Yekta A, Spiro JG, Winnik MA (1998) A critical evaluation of direct energy transfer as a tool for analysis of nanoscale morphologies in polymers. Application to block copolymer interfaces. *J Phys Chem B* 102:7960–7970
111. Farinha JPS, Spiro JG, Winnik MA (2001) Energy transfer in the restricted geometry of lamellar block copolymer interfaces. *J Phys Chem B* 105:4879–4888
112. Rharbi Y, Winnik MA (2001) Interface thickness of a styrene-methyl methacrylate block copolymer in the lamella phase by direct nonradiative energy transfer. *Macromolecules* 34:5238–5248
113. Yang J, Lu JP, Rharbi Y, Cao L, Winnik MA, Zhang YM, Wiesner UB (2003) Energy transfer study of the interface thickness in symmetrical isoprene-methyl methacrylate diblock copolymers. *Macromolecules* 36:4485–4491
114. Yang J, Winnik MA, Pakula T (2005) Numerical simulations of fluorescence resonance energy transfer in diblock copolymer lamellae. *Macromolecules* 38:8882–8890
115. Yang J, Roller RS, Winnik MA, Zhang Y, Pakula T (2005) Energy transfer study of symmetric polyisoprene-poly(methyl methacrylate) diblock copolymers bearing dyes at the junctions: Dye orientation. *Macromolecules* 38:1256–1263
116. Anastasiadis SH, Russell TP, Satija SK, Majkrzak CF (1990) The Morphology of Symmetric Diblock Copolymers As Revealed by Neutron Reflectivity. *J Chem Phys* 92:5677–5691
117. Russell TP, Menelle A, Hamilton WA, Smith GS, Satija SK, Majkrzak CF (1991) Width of Homopolymer Interfaces in the Presence of Symmetrical Diblock Copolymers. *Macromolecules* 24:5721–5726
118. Schubert DW, Weidisch R, Stamm M, Michler GH (1998) Interface width of poly(styrene-*b*-butyl methacrylate) diblock copolymers. *Macromolecules* 31:3743–3745
119. Karymov MA, Prochazka K, Mendenhall JM, Martin TJ, Munk P, Webber SE (1996) Chemical attachment of polystyrene-block-poly(methacrylic acid) micelles on a silicon nitride surface. *Langmuir* 12:4748–4753
120. Kwon GS, Kataoka K (1995) Block-Copolymer Micelles As Long-Circulating Drug Vehicles. *Adv Drug Deliv Rev* 16:295–309
121. Xu RL, Winnik MA, Riess G, Chu B, Croucher MD (1992) Micellization of Polystyrene Poly(Ethylene Oxide) Block Copolymers in Water. 5. A Test of the Star and Mean-Field Models. *Macromolecules* 25:644–652
122. Tuzar Z, Kratochvil P (1993) In: Matijevic E (ed) *Surface and Colloid Science*. Plenum, New York
123. Riess G, Hurtrez G, Bahadur P (1985) In: Mark HF, Bikales NM, Overberg CG, Menges G (ed) *Encyclopedia of Polymer Science and Engineering*. Wiley, New York
124. Rager T, Meyer WH, Wegner G, Winnik MA (1997) Influence of chain length and salt concentration on block copolymer micellization. *Macromolecules* 30:4911–4919
125. Webber SE (1998) Polymer micelles: An example of self-assembling polymers. *J Phys Chem B* 102:2618–2626

126. Liu TB, Zhou ZK, Wu CH, Nace VM, Chu B (1998) Dominant factors on the micellization of BnEmBn-Type triblock copolymers in aqueous solution. *J Phys Chem B* 102:2875–2882
127. Vagberg LJM, Cogan KA, Gast AP (1991) Light-Scattering Study of Starlike Polymeric Micelles. *Macromolecules* 24:1670–1677
128. Farinha JPS, d'Oliveira JMR, Martinho JMG, Xu RL, Winnik MA (1998) Structure in tethered chains: Polymeric micelles and chains anchored on polystyrene latex spheres. *Langmuir* 14:2291–2296
129. Glatter O, Scherf G, Schillen K, Brown W (1994) Characterization of A Poly(Ethylene Oxide) Poly(Propylene Oxide) Triblock Copolymer (Eo(27)-Po39-Eo(27)) in Aqueous-Solution. *Macromolecules* 27:6046–6054
130. Jada A, Hurtrez G, Siffert B, Riess G (1996) Structure of polystyrene-block-poly(ethylene oxide) diblock copolymer micelles in water. *Macromol Chem Phys* 197:3697–3710
131. Mortensen K, Brown W, Almdal K, Alami E, Jada A (1997) Structure of PS-PEO diblock copolymers in solution and the bulk state probed using dynamic light-scattering and small-angle neutron-scattering and dynamic mechanical measurements. *Langmuir* 13:3635–3645
132. Goldmints I, von Gottberg FK, Smith KA, Hatton TA (1997) Small-angle neutron scattering study of PEO-PPO-PEO micelle structure in the unimer-to-micelle transition region. *Langmuir* 13:3659–3664
133. Yu YS, Zhang LF, Eisenberg A (1998) Morphogenic effect of solvent on crew-cut aggregates of amphiphilic diblock copolymers. *Macromolecules* 31:1144–1154
134. Schillen K, Yekta A, Ni SR, Winnik MA (1998) Characterization by fluorescence energy transfer of the core of polyisoprene-poly(methylmethacrylate) diblock copolymer micelles. Strong segregation in acetonitrile. *Macromolecules* 31:210–212
135. Martin TJ, Webber SE (1995) Fluorescence studies of polymer micelles: Intracoil direct energy transfer. *Macromolecules* 28:8845–8854
136. Phillips D, O'Connor DV (1984) Time Correlated Single Photon Counting. Academic, London
137. Farinha JPS, Martinho JMG, Pogliani L (1997) Non-linear least-squares and chemical kinetics. An improved method to analyse monomer-excimer decay data. *J Math Chem* 21:131–139
138. Marquardt DW (1963) An Algorithm for Least-Squares Estimation of Nonlinear Parameters. *J Soc Ind Appl Math* 11:431–441
139. Schillen K, Yekta A, Ni SR, Farinha JPS, Winnik MA (1999) Characterization of polyisoprene-b-poly(methyl methacrylate) diblock copolymer micelles in acetonitrile. *J Phys Chem B* 103:9090–9103
140. De Bruyn H, Gilbert RG, White JW, Schulz JC (2003) Characterization of electrostatically stabilized polystyrene latex; implications for radical entry kinetics. *Polymer* 44:4411–4420
141. Said ZFM (1998) Possible evidence for the existence of a hairy layer at the surface of polymer latex particles. *Polym Int* 47:459–464
142. Seebergh JE, Berg JC (1995) Evidence of A Hairy Layer at the Surface of Polystyrene Latex-Particles. *Colloid Surface A* 100:139–153
143. Vanderput AG, Bijsterbosch BH (1983) Electrokinetic Measurements on Concentrated Polystyrene Dispersions and Their Theoretical Interpretation. *J Colloid Interface Sci* 92:499–507
144. Chow RS, Takamura K (1988) Effects of Surface-Roughness (Hairiness) of Latex-Particles on Their Electrokinetic Potentials. *J Colloid Interface Sci* 125:226–236

145. Rosen LA, Saville DA (1990) The Dielectric Response of Polystyrene Latexes – Effects of Alterations in the Structure of the Particle Surface. *J Colloid Interface Sci* 140:82–92
146. O'Brien RW, White LR (1978) Electrophoretic Mobility of A Spherical Colloidal Particle. *J Chem Soc Faraday Trans II* 74:1607–1626
147. Delacey EHB, White LR (1981) Dielectric Response and Conductivity of Dilute Suspensions of Colloidal Particles. *J Chem Soc Faraday Trans II* 77:2007–2039
148. Nakashima K, Liu YS, Zhang P, Duhamel J, Feng JR, Winnik MA (1993) Picosecond Fluorescence Studies of Energy-Transfer on the Surface of Poly(Butyl Methacrylate) Latex-Particles. *Langmuir* 9:2825–2831
149. Nakashima K, Duhamel J, Winnik MA (1993) Photophysical Processes on A Latex Surface – Electronic-Energy Transfer from Rhodamine Dyes to Malachite Green. *J Phys Chem* 97:10702–10707
150. Farinha JPS, Charreyre MT, Martinho JMG, Winnik MA, Pichot C (2001) Picosecond fluorescence studies of the surface morphology of charged polystyrene latex particles. *Langmuir* 17:2617–2623
151. Eckersley ST, Rudin A (1990) Mechanism of Film Formation from Polymer Latexes. *J Coating Technol* 62:89–100
152. Hahn K, Ley G, Oberthur R (1988) On Particle Coalescence in Latex Films(Ii). *Colloid Polym Sci* 266:631–639
153. Hahn K, Ley G, Schuller H, Oberthur R (1986) On Particle Coalescence in Latex Films. *Colloid Polym Sci* 264:1092–1096
154. Yoo JN, Sperling LH, Glinka CJ, Klein A (1991) Characterization of Film Formation from Polystyrene Latex-Particles Via Sans. 2. High-Molecular-Weight. *Macromolecules* 24:2868–2876
155. Yoo JN, Sperling LH, Glinka CJ, Klein A (1990) Characterization of Film Formation from Polystyrene Latex-Particles Via Sans. 1. Moderate Molecular-Weight. *Macromolecules* 23:3962–3967
156. Ye XD, Farinha JPS, Oh JK, Winnik MA, Wu C (2003) Polymer diffusion in PBMA latex films using a polymerizable benzophenone derivative as an energy transfer acceptor. *Macromolecules* 36:8749–8760
157. Farinha JPS, Wu J, Winnik MA, Farwaha R, Rademacher J (2005) Polymer diffusion in gel-containing poly(vinyl acetate-co-dibutyl maleate) latex films. *Macromolecules* 38:4393–4402
158. Pham HH, Farinha JPS, Winnik MA (2000) Cross-linking, miscibility, and interface structure in blends of poly(2-ethylhexyl methacrylate) copolymers. An energy transfer study. *Macromolecules* 33:5850–5862
159. Krause S, Goh SH (1999) In: Brandrup J, Immergut EH, Gruke E (ed) *Polymer Handbook*. Wiley, New York
160. Zhou XL, Chen SH (1995) Theoretical Foundation of X-Ray and Neutron Reflectometry. *Phys Rep* 257:223–348
161. Geoghegan M, Jones RAL, Sivia DS, Penfold J, Clough AS (1996) Experimental study of surface segregation and wetting in films of a partially miscible polymer blend. *Phys Rev E* 53:825–837
162. Bucknall DG, Butler SA, Higgins JS (1999) Neutron reflectivity of polymer interfaces. *J Phys Chem Solids* 60:1273–1277
163. Foster MD (1993) X-Ray-Scattering Methods for the Study of Polymer Interfaces. *Crit Rev Anal Chem* 24:179–241
164. Tan SS, Zhang DH, Zhou EL (1997) SAXS measurements of the interface in polyacrylate and epoxy interpenetrating networks with fractal geometry. *Polymer* 38:4571–4575

165. Wlochowicz A, Janicki J, Slusarczyk C (1997) Determination of the transition region thickness in polymer blends by the SAXS method. *Compos Interface* 5:1–9
166. Spiro JG, Farinha JPS, Winnik MA (2003) Thermodynamics and morphology of latex blend films. *Macromolecules* 36:7791–7802
167. Feng JR, Winnik MA (1997) Effect of water on polymer diffusion in latex films. *Macromolecules* 30:4324–4331
168. Farinha JPS, Vorobyova O, Winnik MA (2000) An energy transfer study of the interface thickness in blends of poly(butyl methacrylate) and poly(2-ethylhexyl methacrylate). *Macromolecules* 33:5863–5873
169. Anastasiadis SH, Gancarz I, Koberstein JT (1988) Interfacial-Tension of Immiscible Polymer Blends – Temperature and Molecular-Weight Dependence. *Macromolecules* 21:2980–2987
170. Cahn JW, Hilliard JE (1958) Free Energy of A Nonuniform System. 1. Interfacial Free Energy. *J Chem Phys* 28:258–267
171. de Gennes PG (1979) *Scaling Concepts in Polymer Physics*. Cornell University Press, Ithaca, N.Y.
172. de Gennes PG (1980) Dynamics of Fluctuations and Spinodal Decomposition in Polymer Blends. *J Chem Phys* 72:4756–4763
173. Muller M, Binder K, Oed W (1995) Structural and Thermodynamic Properties of Interfaces Between Coexisting Phases in Polymer Blends – A Monte Carlo Simulation. *J Chem Soc Faraday Trans* 91:2369–2379
174. Ermoshkin AV, Semenov AN (1996) Interfacial tension in binary polymer mixtures. *Macromolecules* 29:6294–6300
175. Semenov AN (1994) Scattering of Statistical Structure of Polymer–Polymer Interfaces. *Macromolecules* 27:2732–2735

## Defocused Imaging in Wide-field Fluorescence Microscopy

Hiroshi Uji-i<sup>1</sup> · Ania Deres<sup>1</sup> · Benoit Muls<sup>2</sup> · Sergey Melnikov<sup>1</sup> ·  
Jörg Enderlein<sup>3</sup> · Johan Hofkens<sup>1</sup> (✉)

<sup>1</sup>Department of Chemistry, Katholieke Universiteit Leuven,  
Celestijnenlaan 200F, 3001 Heverlee, Belgium  
*Johan.Hofkens@chem.kuleuven.be*

<sup>2</sup>Unité CMAT, Université Catholique de Louvain,  
Bâtiment Lavoisier Place L. Pasteur 1, 1348 Louvain-la-Neuve, Belgium

<sup>3</sup>Institute for Biological Information Processing I,  
Forschungszentrum Jülich, D-52425 Jülich, Germany

1	Introduction . . . . .	258
2	Instrumentation . . . . .	259
3	Analytical Theory of Defocused Imaging . . . . .	260
3.1	Radiation of a Dipole Near an Interface . . . . .	260
3.2	Simulated Emission Patterns and Image Analysis . . . . .	263
4	Selected Applications . . . . .	267
4.1	Probing the Emitting Chromophore in a Multichromophoric System . . . . .	267
4.1.1	Molecular Orientation of the Dyes in a Multi-Chromophoric System . . . . .	268
4.1.2	Electromagnetic Boundary Condition (EBC) Effect on the Lifetime . . . . .	269
4.2	“3D” Single-Molecule Rotational Diffusion in Polymer . . . . .	272
4.2.1	Defocused Imaging to Track Molecular Rotational Diffusion . . . . .	272
4.2.2	Non-Unidirectional Rotation . . . . .	274
4.2.3	Local Heterogeneity in Time and in Space . . . . .	274
4.2.4	Relaxation Time of the Rotational Diffusion: Comparison Between 2D and 3D Analysis . . . . .	277
	References . . . . .	282

**Abstract** Defocused imaging in wide-field fluorescence microscopy provides information on the 3D orientation of the transition dipole moment of single molecules with nanometer spatial resolution. In this chapter, the theoretical background of defocused imaging will be presented, followed by two experimental applications. As a first example, defocused imaging was used along with fluorescence lifetime measurements to prove the fact that the molecular orientation of dye molecules in a thin film has a significant affect on their fluorescence lifetime. This is attributed to the electromagnetic boundary condition effect. As a second example, the power of the technique for following 3D molecular rotational reorientation (molecular rotational diffusion) in thin polymer films is demonstrated. Since many molecules can be monitored in parallel, both the temporal and the spatial heterogeneity of polymer dynamics can be addressed.

## 1 Introduction

During the last few decades, single molecule spectroscopy (SMS) has been established as a new tool in the ever expanding range of spectroscopic methods to study the physical and chemical behavior of individual molecules [1–21]. SMS is especially useful to study inhomogeneous systems, such as biomolecules [5–7] and polymers [8–21].

A topic of special interest to SMS is the determination of spatial orientation of the adsorption and/or emission dipole moment of individual molecules. Information about the molecular orientation is important for several reasons: on one hand, photophysical parameters of single molecules, such as fluorescence lifetime and observable emission intensity, often depend on the orientation of the molecules. On the other hand, the single-molecule orientation itself can be a probe for studying physical and chemical properties of the local environment in which the molecule is embedded [11–21] and for probing the orientation of labeled biomolecules [22–24].

In the past, several fluorescence techniques have been used for detecting the orientations of single molecules. At room temperature and under ambient conditions, the most popular techniques are polarization-resolved SMS with either confocal far-field microscopy [15–20, 25, 26] or near-field microscopy [27, 28]. The idea of these methods is to detect fluorescence in two detection channels with crossed polarizer, to modulate the excitation polarization or both. Although these yield a highly precise determination of in-plane components (perpendicular to the optical axis) of the absorption/emission dipole moments, it leads to a loss of the out-of-plane information of the molecule under investigation. However, more sophisticated detection schemes have been recently developed for measuring the 3D orientation of single molecules via the orientation of their transition dipole moment [29–34]. Scanning near field optical microscopy [29–31] as well as confocal microscopy, eventually modified by using annular beams [32–34], have been used for this purpose. Also, fluorescence wide-field microscopy has been applied to obtain information about the angular distribution of the fluorescence (and hence 3D orientation) emitted by a single molecule. This was realized by defined image defocusing [21, 35–40] or by introducing aberrations [41]. The latter approach was used by Dickson and co-workers in their study of a polymer (poly(methyl methacrylate)) near the glass transition ( $T_g$ ). In this chapter, we will describe the defocused imaging technique and show how it allows obtaining the full 3D molecular orientation.

In the second and third sections of this chapter, we briefly describe the principle of defocused imaging from both experimental and theoretical point of view, respectively. In section 4, we will show how defocused imaging was applied on two different systems and we will discuss what type of information can be obtained.

## 2 Instrumentation

The typical setup of wide-field fluorescence microscopy is illustrated in Fig. 1. It consists of an optical microscope equipped with an objective with high numerical aperture and a highly sensitive CCD camera. Wide-field illumination for single molecule fluorescence microscopy can be accomplished with stable lasers, such as Ar<sup>+</sup> ion lasers or diode-based solid state lasers. The wide-field illumination can be achieved by focusing the expanded and collimated laser beam onto the back-focal plane of the objective (Köhler illumination mode). The polarization of the excitation light in the sample plane should be circular or scramble in order to excite all molecules with variable dipole orientations. Fluorescence is collected by the same objective and is passed through a dichroic mirror and additional emission filters which remove the excitation light and suppress background such as Raman/Rayleigh scattering. For defocused imaging, very high signal-to-noise ratios will be required in order to determine precisely the molecular orientation, especially for out-of-plane oriented molecules. Therefore, choosing emission filters and reducing stray light are key requirements to perform high quality imaging. The CCD camera should be positioned exactly at the image plane of the microscope's side port. The knowledge of the size of one CCD pixel allows direct conversion into length and thus direct comparison between measured and calculated patterns. To perform defocused imaging, it is ideal that a piezoelectric trans-

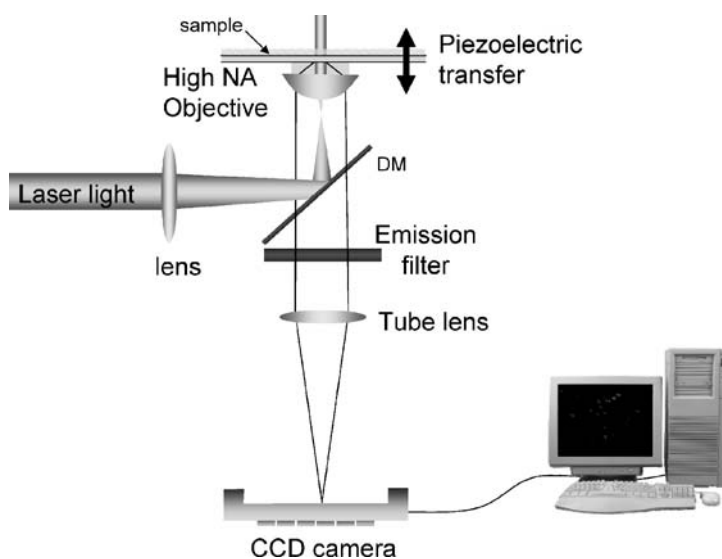


**Fig. 1** Schematic of a typical wide-field fluorescence microscopy for single molecule defocused imaging



ducer with sub-micrometer precision is used for axial positioning of the objective with respect to the sample.

### 3 Analytical Theory of Defocused Imaging

#### 3.1 Radiation of a Dipole Near an Interface

In this section, we will demonstrate how the radiation emitted by a single dipole emitter can be calculated, taking into account the defocusing as well as the significant changes of the dipole emission at an interface [37, 38, 42–44]. The starting point is the emission characteristics of an electric dipole. Below we consider a single molecule emitter within a completely classical electrodynamics framework as a radiating electric dipole. To derive the radiation characteristics of an oscillating electric dipole near a surface, we start with an integral representation of the radiation of a free electric dipole, instead of the usual Hertz vector approach. It is assumed that the dipole is oscillating with an angular frequency  $\omega$  and all parameters (dipole moment, electric, and magnetic field) show a time dependence of the sort of  $\exp(-i\omega t)$ .

The emission geometry near an interface is depicted in Fig. 2. For an oscillating electric dipole with amplitude vector  $\mathbf{p}$  in a medium with refractive index  $n_0$  and distance  $|z_0|$  above the interface, the amplitude of the electric

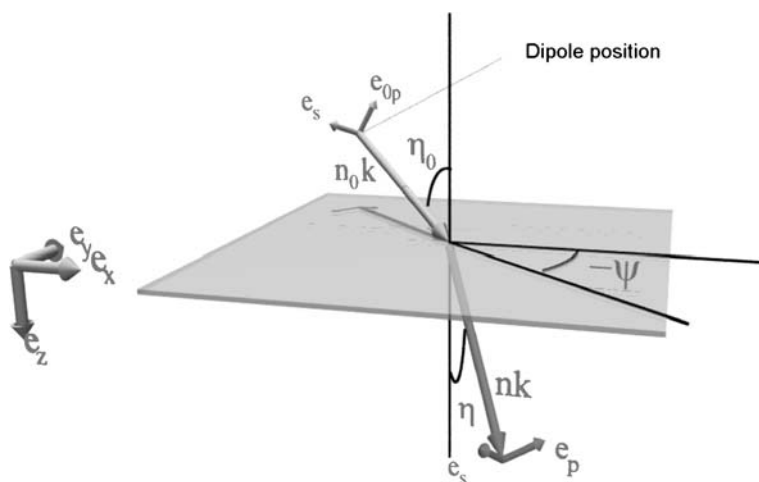


**Fig. 2** Geometry of a dipole emitter and its reflected and transmitted electromagnetic field at an interface dividing regions of different refractive index

field  $E_D$  can be given by the plane-wave representation

$$E_D = \frac{ik_0^2}{2\pi\epsilon} \int \frac{d^2\mathbf{q}}{\omega_0} [\mathbf{e}_{0p} (\mathbf{e}_{0p} \cdot \mathbf{p}) + \mathbf{e}_s (\mathbf{e}_s \cdot \mathbf{p})] \times \exp [i\mathbf{q} \cdot (\boldsymbol{\rho} - \boldsymbol{\rho}_0) + i\omega_0 |z - z_0|] , \quad (1)$$

where  $(\boldsymbol{\rho}_0, z_0)$  and  $(\boldsymbol{\rho}, z)$  are the coordinates of the dipole and the target point where the electric field is computed, respectively;  $\omega_0$  is the  $z$  component of the wave vectors of the plane wave,  $\omega_0 = (n_0^2 k_0^2 - |\mathbf{q}|^2)^{1/2}$ ;  $\mathbf{k}_0$  is the vacuum wave vector of the emitted light,  $\mathbf{k}_0 = (\mathbf{q}, \pm\omega_0)$ .

It is obvious how to obtain the contribution of the reflected field to the complete dipole field amplitude:

$$E_R = \frac{ik_0^2}{2\pi\epsilon} \int \frac{d^2\mathbf{q}}{\omega_0} [\mathbf{e}_{0p} R_p (\mathbf{e}_{0p} \cdot \mathbf{p}) + \mathbf{e}_s R_s (\mathbf{e}_s \cdot \mathbf{p})] \times \exp [i\mathbf{q} \cdot (\boldsymbol{\rho} - \boldsymbol{\rho}_0) + i\omega_0(z + z_0)] . \quad (2)$$

Equivalently, the transmitted field amplitude is given by

$$E_T = \frac{ik_0^2}{2\pi\epsilon} \int \frac{d^2\mathbf{q}}{\omega_0} [\mathbf{e}_p T_p (\mathbf{e}_{0p} \cdot \mathbf{p}) + \mathbf{e}_s T_s (\mathbf{e}_s \cdot \mathbf{p})] \times \exp [i\mathbf{q} \cdot (\boldsymbol{\rho} - \boldsymbol{\rho}_0) + i\omega_0 z_0 + i\omega |z|] , \quad (3)$$

where  $\omega = (n^2 k_0^2 - |\mathbf{q}|^2)^{1/2}$ ;  $\mathbf{e}_{0p}$ ,  $\mathbf{e}_p$ , and  $\mathbf{e}_s$  are the unit vectors of the  $p$ - and  $s$ -polarization that are transversal to the plane-wave propagation:

$$\begin{aligned} \mathbf{e}_{0p} &= (\cos \psi \cos \eta_0, \sin \psi \cos \eta_0, -\sin \eta_0) \\ \mathbf{e}_p &= (\cos \psi \cos \eta, \sin \psi \cos \eta, -\sin \eta) \\ \mathbf{e}_s &= (-\sin \psi, \cos \psi, 0) ; \end{aligned} \quad (4)$$

$R_{p,s}$  and  $T_{p,s}$  are usual Fresnel reflection and transmission coefficients for plane  $p$  and  $s$  waves incident at angle  $\eta_0$  with respect to the  $z$  (optical) axis. The angles  $\eta_0$  and  $\eta$  are connected by Snell's law,  $n \sin \eta = n_0 \sin \eta_0$ . The two-dimensional vector  $\mathbf{q}$  is the integration variable over which the integrations in Eqs. 1–3 have to be performed, and the integration extends over the complete  $\mathbf{q}$  plane.

Concerning the orientation of the dipole, two different cases have to be considered: a dipole orientation vertical to the interface and a dipole orientation parallel to the interface. Then, neglecting any constant factor, the angular distribution of the electric-field  $E(\eta, \psi)$  connected with light radiation into the glass along direction  $\mathbf{k} = (\sin \eta \cos \psi, \sin \eta \cos \psi, \cos \eta)$  and solid angle  $\sin \eta d\eta d\psi$  is written as,

$$E(\eta, \psi) = \mathbf{e}_p \left[ \cos \beta E_p^\perp(\eta) + \sin \beta E_p^\parallel(\eta) \cos \psi \right] + \mathbf{e}_s \sin \beta E_s^\parallel(\eta) \sin \psi , \quad (5)$$

where  $\beta$  is the angle between the molecule's emission dipole axis and the optical axis (being perpendicular to the interface).

Below, we will consider two different configurations which correspond to realistic experimental conditions; the case that the dye molecule is directly adsorbed at an air-glass interface, and the case that the molecule is embedded in glass-former such as a polymer. In the former case (dye on glass), the transmitted field amplitude is given in Eq. 5:

$$E_p^\perp(\eta) = \sin \eta T_p \exp(inz \cos \eta) ,$$

$$E_{p,s}^\parallel(\eta) = \pm \cos \eta T_{p,s} \exp(inz \cos \eta) . \tag{6}$$

In the latter case, the angular distribution of radiation drastically changes due to the self-interaction of the emitting dipole with its back-reflected electromagnetic field at the glass/air interface along direction  $k$  into the glass. In this configuration, each component can be given by,

$$E_p^\perp(\eta) = \sin \eta [\exp(-inz \cos \eta) + R_p(\eta) \exp(inz \cos \eta)]$$

$$E_{p,s}^\parallel(\eta) = \cos \eta [\exp(-inz \cos \eta) \mp R_{p,s}(\eta) \exp(inz \cos \eta)] . \tag{7}$$

Thus the electric field of the vertical dipole depends only on the polar angle  $\eta$  and is polarized along  $e_p$  in all directions. For the parallel dipole orientation, the angular distribution also depends on the azimuthal angle  $\psi$  between the dipole orientation and the direction of emission.

After the angular distribution of the dipole emission into the glass has been found, the next step is to find an expression for the way in which this emission is imaged onto the chip of a CCD camera. The image geometry is shown schematically in Fig. 3. It is assumed that the camera is positioned at the back focal plane (image plane) of the imaging optics (consisting of the objective and a tube lens) and that the imaging optics are perfectly free of aberrations when an object lying within the focal plane is imaged on the con-

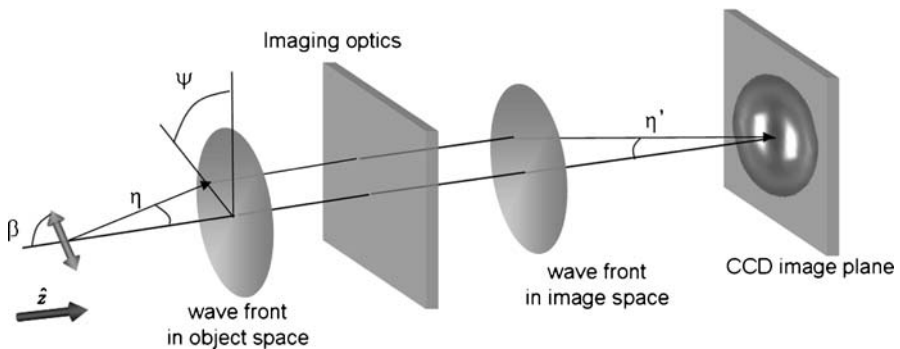


**Fig. 3** Geometry representing imaging from an interface onto a CCD camera

jugated image plane. The electric and magnetic field amplitudes can be found from the general theory developed by Richards and Wolf [45]. In this approach, the core idea is to develop the electric and magnetic field amplitudes in image space into a superposition of plane waves and to find a connection between the plane-wave amplitudes and polarizations and the intensity and polarization of the light incident onto the objective. Following reference 31, the electric and magnetic fields on the surface of the CCD chip are given by

$$\begin{Bmatrix} E_j \\ B_j \end{Bmatrix} = \int_0^{\eta'_{\max}} d\eta' \sin \eta' \sqrt{\frac{n' \cos \eta'}{n \cos \eta}} \begin{Bmatrix} e_j \\ b_j \end{Bmatrix} \times \exp(ik\delta z \cos \eta), \quad (8)$$

and

$$\begin{aligned} \begin{Bmatrix} e_x \\ e_y \end{Bmatrix} &= \frac{i \sin \beta}{2} \begin{Bmatrix} \cos \eta' (J_0 - J_2 \cos 2\psi) E_p^{\parallel} + (J_0 + J_2 \cos 2\psi) E_s^{\parallel} \\ -\cos \eta' J_2 \sin 2\psi E_p^{\parallel} + J_2 \sin 2\psi E_s^{\parallel} \end{Bmatrix} \\ &\quad + i \cos \beta \cos \eta' J_1 E_p^{\perp} \begin{Bmatrix} \cos \psi \\ \sin \psi \end{Bmatrix} \\ \begin{Bmatrix} b_x \\ b_y \end{Bmatrix} &= \frac{in' \sin \beta}{2} \begin{Bmatrix} J_2 \sin 2\psi E_p^{\parallel} - \cos \eta' J_2 \sin 2\psi E_s^{\parallel} \\ (J_0 - J_2 \cos 2\psi) E_p^{\parallel} + \cos \eta' (J_0 + J_2 \cos 2\psi) E_s^{\parallel} \end{Bmatrix} \\ &\quad + i \cos \beta n' J_1 E_p^{\perp} \begin{Bmatrix} -\sin \psi \\ \cos \psi \end{Bmatrix}, \quad (9) \end{aligned}$$

where  $n'$  is the refractive index of the imaging medium between the objective lens and the CCD camera (usually that of air), and the  $J_{0,1,2}$  denotes Bessel functions of the first kind with functional argument  $k' \rho' \sin \eta'$ ; the  $k, k'$  are the wave vectors in glass and air, respectively. The connection between  $\eta$  and  $\eta'$  is given by Abbe's law,  $n \sin \eta = Mn' \sin \eta'$ , where  $M$  is the imaging magnification, so  $\eta'_{\max}$  is determined as  $\eta'_{\max} = \arcsin(NA/Mn')$ , where  $NA$  denotes the numerical aperture of the objective. The root factor in Eq. 8 ensures that energy is conserved on imaging. In the equation, the defocusing length,  $\delta z$ , (how much the imaging objective is moved out of focus toward the sample) was introduced. Finally, the position-dependent detectable light intensity on the CCD camera is given by the  $z$  component of the Poynting vector

$$S = (c/8\pi) \mathbf{e}_z \cdot (\mathbf{E} \times \mathbf{B}^*). \quad (10)$$

### 3.2

#### Simulated Emission Patterns and Image Analysis

The emission pattern strongly depends on molecular orientation as well as defocusing value and thickness of the polymer in the case that molecules

are fixed in a polymer thin film [37, 38]. The angle of molecular orientation is redefined as illustrated in Fig. 4:  $\theta$  is the out-of-plane angle between the emission dipole (the arrow) and the optical axis ( $z$ -axis), and  $\phi$  indicates the in-plane (in  $xy$  plane) dipole orientation. Figure 5 presents an example of simulated patterns which shows how the emission pattern changes depending on molecular orientation. The calculation exploited Eqs. 8–10 for determining the energy flow distribution as seen by the CCD camera. At  $\theta = 90$  degree (completely in-plane-orientation), the emission pattern exhibits a bilaterally symmetric two-lobe pattern, the symmetric axis of which is parallel to the dipole moment axis. Such a symmetric pattern changes into

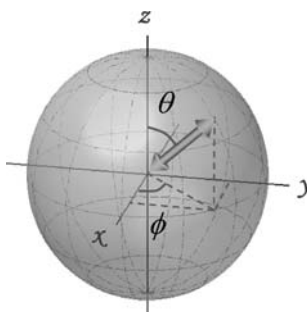


**Fig. 4** Definition of angular coordinates:  $\theta$  is out-of-plane angle (inclination angle between the emission dipole (gray arrow) and optical axis ( $z$ -axis)), and  $\phi$  indicates the in-plane (the  $xy$  image plane) angle

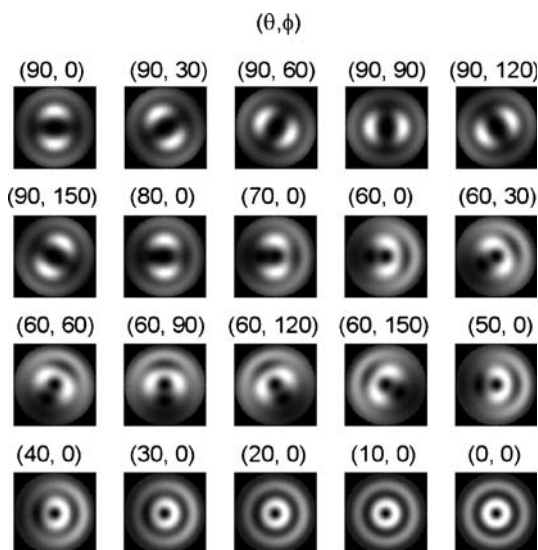


**Fig. 5** Calculated defocused patterns for 20 different molecular orientations

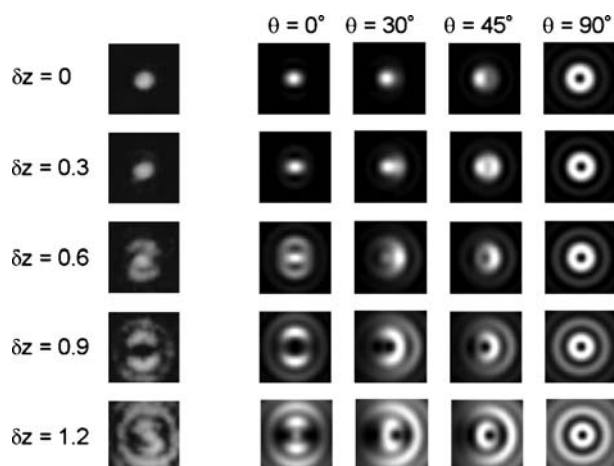


**Fig. 6** Comparison of measured images of a single molecule (*left*) and theoretically calculated patterns for four different out-of-plane angles (*right*) as indicated. The defocused values are indicated at the *left*

an asymmetric ringed pattern as the out-of-plane angle ( $\theta$ ) decreases. At 0 degrees (complete out-of-plane), the pattern has a symmetric circular ring shape.

The defocused pattern strongly depends on the defocused value,  $\delta z$ , in Eq. 8 [37, 38]. For comparison of theoretical calculations with experimental results, series of five images are shown in Fig. 6. These images are calculated with increasing defocusing values from 0 to 1.2  $\mu\text{m}$  in steps of 300 nm. The left columns show the experimental results and the other four images, from left to right, display the calculated images for completely in-plane, inclined, and vertical dipole orientation, respectively. One can find a fair correspondence between the measured images and the patterns calculated for the complete in-plane orientation. The optimal defocusing value for orientation measurements is about 1  $\mu\text{m}$ . For this value, the bipolar character of the images is clearly discernible, but the fluorescence emission is not yet spread over an image area sufficiently large to severely worsen the signal-to-noise ratio, which is the case for larger defocusing values.

In many examples in single molecule spectroscopy, fluorescent molecules are embedded in different kinds of thin films, such as polymer films, bilayers, and so on. As stated before, the precise shape of the defocused patterns, especially for the in-plane orientation, is very sensitive to both the defocusing value and the film thickness. Therefore, it is worth investigating the dependence of defocused pattern on the thickness of matrix. A set of calculations for varying values of film thickness (at the fixed defocusing value of 1.2  $\mu\text{m}$ ) is displayed in Fig. 7. The figure clearly shows the dramatic changes in pattern shape with varying film thickness.

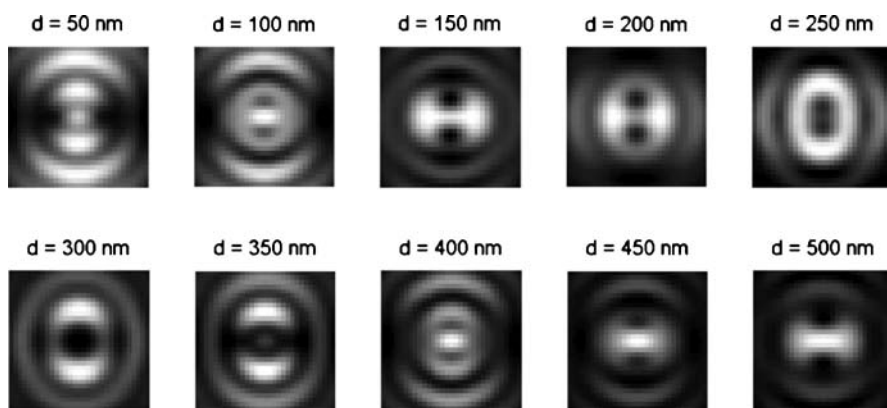


**Fig. 7** Calculated defocused images for a fixed defocusing value of  $1.2\ \mu\text{m}$  with varying polymer thickness. Above every pattern, the value  $d$  of the film thickness is indicated

The next step is to analyse experimentally obtained images in order to determine the exact 3D orientation of the emitting dipole. This can be achieved by a pattern matching routine using pre-calculated emission patterns to roughly determine the molecular orientation, followed by precise fitting with a non-linear least-square algorithm [37, 38]. Figure 8a shows a full CCD image of an experimentally obtained defocused image of fluorescent dyes embedded in thin polymer film ( $\sim 100\ \text{nm}$  thickness). The defocused value was about

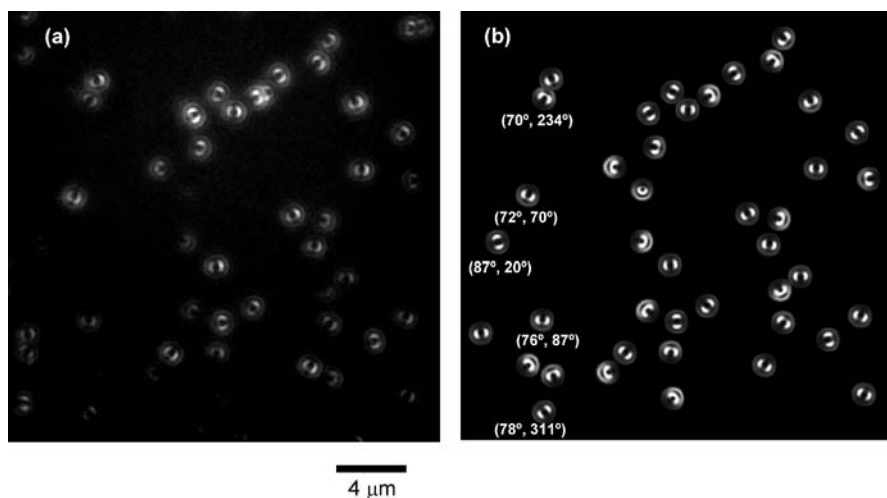


**Fig. 8** An example of analysis. **a** Measured defocused image of the perylene diimide dyes embedded in a thin polymer film. Defocusing was achieved by moving the objective  $1\ \mu\text{m}$  toward the sample. **b** Composite image displaying all analyzed molecules and their fitted emission patterns

1  $\mu\text{m}$ ; i.e. the objective was first set to sharp focus and then moved toward the sample by an amount of 1  $\mu\text{m}$ . In the image, though various emission patterns are observed, most of them show distinctive bi-modal patterns that reflect in-plane emission dipole orientations. The fluorescence intensity varies from molecule to molecule. Especially molecules oriented out of plane are not excited efficiently [47] and therefore show lower emission intensity. The center position of the defocused pattern corresponds to the spatial coordinate of the corresponding single molecule, and can be determined by the image analysis. The result of the fitting procedure described above on an experimental image is shown in Fig. 8b.

## 4 Selected Applications

### 4.1 Probing the Emitting Chromophore in a Multichromophoric System

The defocused imaging technique can be applied to study the orientation of fluorescent dyes embedded in thin polymer films. This is of great importance for applications in nanotechnology and nano-electronics because the photo-physical and photochemical properties of the dyes strongly depend on the molecular orientation with respect to the optical axis and the position of the dyes in the film. One of the properties that is influenced by the orientation and the distance to the interface is the fluorescence lifetime. Indeed, the fluorescence lifetime cannot only fluctuate as a direct manifestation of the single molecule environment, but it also depends on the position and orientation of the single molecule with respect to the boundaries of the film, an effect known as the influence of the electromagnetic boundary conditions (EBC effect). In this section, we will show how the combination of the defocused imaging technique with single molecule fluorescence lifetime measurements allows correlating orientation and fluorescence lifetime [39].

We decided to focus on a first generation multichromophoric dendrimer with four perylene imide chromophores at the rim (G1R4). The chemical structure and its 3D model are depicted in Fig. 9. In such a multichromophoric system energy transfer processes are possible. A model developed to describe energy transfer in this system invokes energy hopping between different chromophores. It was suggested that, at any moment in time, the emission of a single dendrimer originates from the chromophore that has the lowest energy (fluorescent trapping site) due to the heterogeneous nature of the polymer matrix used to immobilize the dye. Due to polymer dynamics and/or consecutive photobleaching, each of the chromophores in the dendrimer can in time become the fluorescent trapping site. The 3D orientation of the chromophores with respect to each other is well-defined



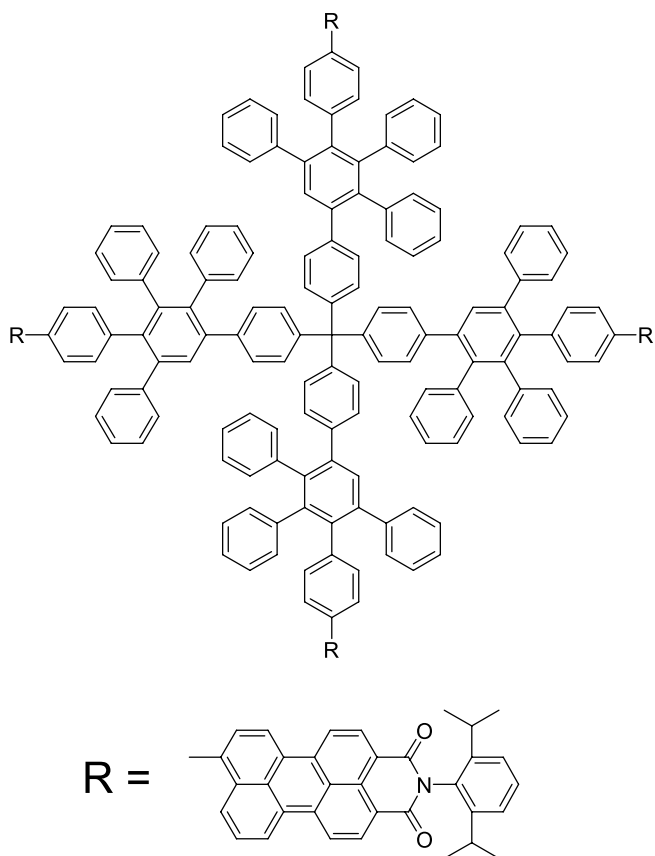


**Fig. 9** Chemical structure of a dendrimer with four perylene imide chromophores

for the G1R4 dendrimer, due to the rigidity of the polyphenylene core structure. The chromophores can be considered as being in a tetrahedral geometry. Hence, probing the dipole orientation of the emitting chromophore of a single dendrimer molecule in combination with fluorescence lifetime measurements should allow validating the earlier discussed hopping model and should allow demonstrating the EBC effect.

#### 4.1.1

##### Molecular Orientation of the Dyes in a Multi-Chromophoric System

To perform the experiments, G1R4 dendrimers at single molecule concentration were embedded in thin (10–25 nm) zeonex (poly(norbornene)) films. The defocused patterns shown in Fig. 10 are a set of the observed emission patterns during the indicated period. One can see that the emission pattern of a single G1R4 molecule changes as function of time. The patterns pro-

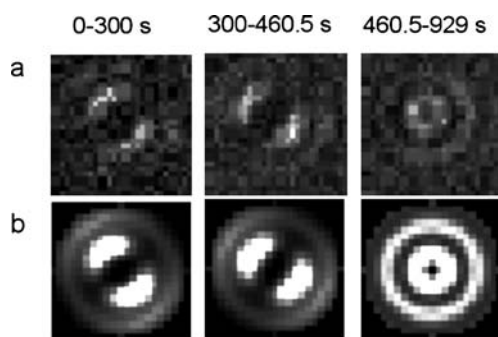


**Fig. 10** **a** Defocused emission patterns of a single G1R4 molecule embedded in a 25 nm thick zeonex film recorded with 1  $\mu\text{m}$  defocusing depth and with 0.5 second integration time. **b** Corresponding simulated patterns

vide direct evidence that different chromophores of the G1R4 emit in time, as different dipole orientations are observed. In this series, only three different orientations were observed. This is most likely because one chromophore bleached during the image scan and/or alignment. On the basis of simulated patterns (Fig. 10b) following the sequence in Fig. 10a, the first and second pattern are attributed to a chromophore with an emission dipole oriented in-plane with angle  $\phi = 40$  and  $70$  degrees, respectively, with respect to the  $x$ -axis. The third pattern indicates an out-of-plane orientation with almost  $0$  degree for the inclination angle  $\theta$ .

#### 4.1.2

##### Electromagnetic Boundary Condition (EBC) Effect on the Lifetime

Since defocused imaging gives direct evidence for the hopping model between the tetrahedral orientated chromophores in individual G1R4 molecules, the EBC effect for a single molecule of G1R4 should result in discrete changes in the fluorescence lifetime. By means of a scanning confocal optical microscope with polarization-sensitive FIFO (first-in, first-out) mode detection, the fluorescence intensity, the degree of polarization  $P$ , and the fluorescence lifetime of a G1R4 molecule were simultaneously determined. Such a data set is shown in Fig. 11: (a) the fluorescence intensity recorded in the two orthogonal polarization channels, (b) the degree of polarization, and (c) the fluorescence lifetime trajectory of a single G1R4. Four different emissive levels are observed in the intensity trajectory. The levels clearly have different polarization values. Thus, each level is related to one of the four different emitting chromophores. The lifetime trajectory shows an increase of the fluorescence lifetime from 4.8 ns for the highest emissive level to approximately 7 ns for the other three lower levels. Such anticorrelated behavior between the lifetime and intensity can be attributed to the EBC effect. 40% of the 158 investi-

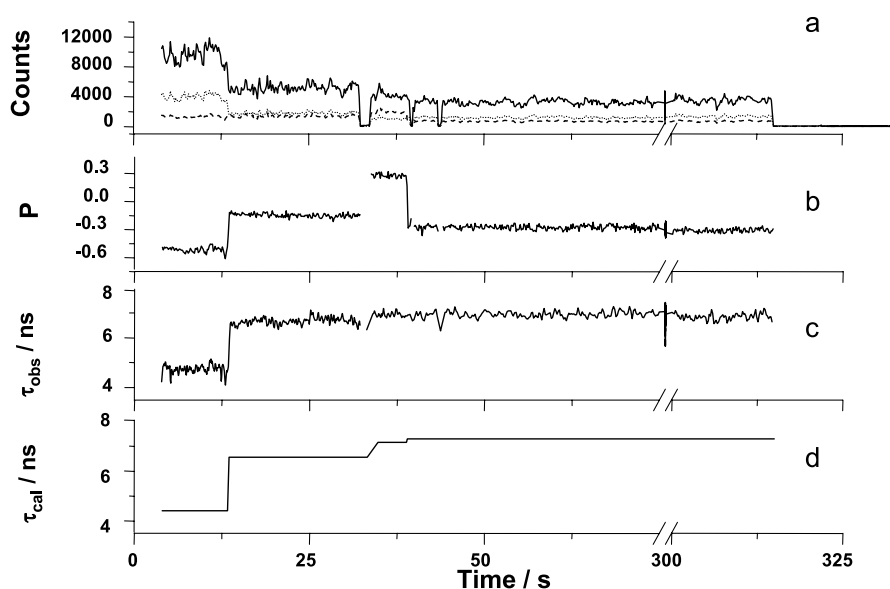


**Fig. 11** **a** Fluorescence intensity (counts) **b** degree of polarization ( $P$ ) and **c** lifetime ( $\tau_{\text{obs}}$ ) trajectories for a single G1R4 dendrimer in 10 nm thick zeonex film. The two gray trajectories in **a** correspond to the intensity detected in the two orthogonal polarization channels. **d** A simulated fluorescence lifetime trace ( $\tau_{\text{cal}}$ ), which was calculated for a dendrimer located 4 nm away the polymer surface

gated molecules show EBC-type lifetime fluctuations. The largest observed fluctuation in a 10 nm film is from 4 to 12 ns, in good agreement with the calculated lifetimes obtained for parallel and perpendicular oriented chromophores. The emission of a chromophore oriented more or less in-plane is indeed expected to give a shorter lifetime and higher emissive rate than a chromophore oriented more perpendicularly with respect to the air interface [11–13]. Figure 12 shows typical spectra taken from a series of emission spectra recorded simultaneously with the intensity trajectories for the single molecule. No large changes in the spectral position or shape were observed. Only the intensity of the spectra changes in function of time. The absence of jumps in the simultaneously recorded emission spectra ensures that the lifetime jumps are not connected to other processes in the matrix. As mentioned above, the structure of a G1R4 in a polymer film resembles a tetrahedron. The four chromophores of the system can thus be placed in such a way that three of them are similarly oriented more perpendicularly with respect to the interface, while in comparison the fourth chromophore is oriented in a more parallel fashion. Figure 11d shows a simulation of the lifetime change of G1R4 for such an orientation, clearly confirming this assumption. Both defocused imaging and lifetime measurements confirm the “hopping to a fluorescent trap” model for G1R4.

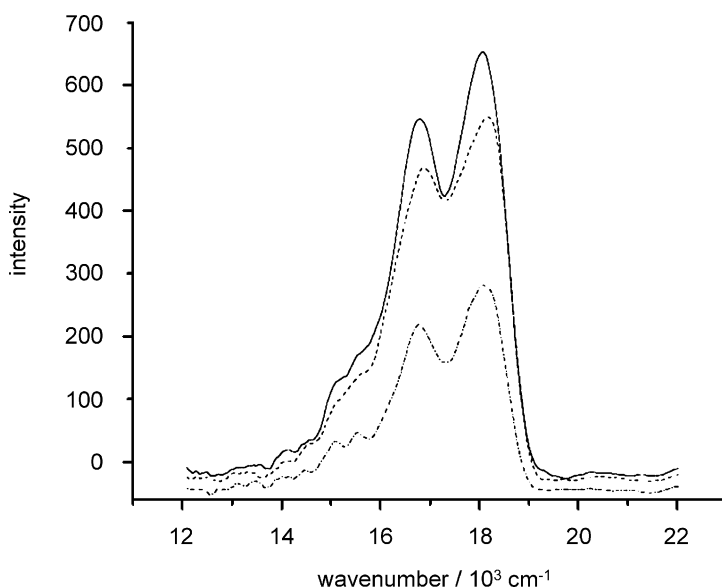


**Fig. 12** Emission spectra taken from a spectral series that was simultaneously recorded with the trajectories shown in Fig. 11. The spectra were recorded after 3 s (*line*), 12 s (*dot*), and 15 (*bar dot*). The integration time for each spectrum is 3 s

An important parameter related to the hopping model presented for G1R4 is the relative inhomogeneous character of the environment acting on the single molecule. In contrast to the results discussed above, for a more homogeneous local environment, the energies of the four chromophores are nearly identical. In the later case, each individual chromophore has now a certain probability to emit at any given moment in time. Because of the finite integration time, the detected signal then results in an averaging of the fluorescence of the different chromophores. Such an example is given in Fig. 13. Although the first, second and third patterns could be assigned as more or less in-

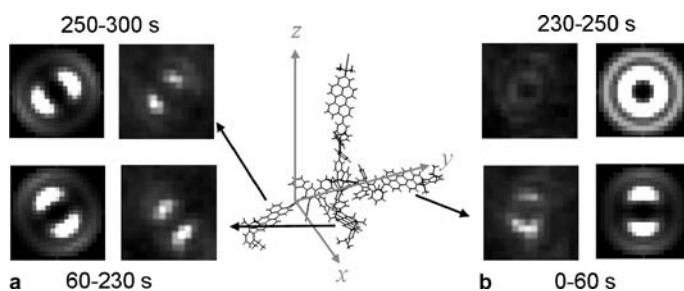


**Fig. 13** Series of emission patterns (**a**) and corresponding computed patterns (**b**) for a single G1R4 molecule in a 25 nm thick zeonex film. Images are taken at 1  $\mu\text{m}$  defocusing and with 10 s integration time

plane orientation, the third pattern is a combination of patterns of some different in-plane orientations according to the calculation, indicating multiple emitters in this time interval. Notice the different features between the out-of-plane orientation shown in Fig. 10 and the averaged pattern in Fig. 13: the size of inner rim is clearly different. The switching in the time between distinct patterns related to chromophores acting as fluorescent traps and the average pattern (even at 0.5 s time resolution) indicates that the homogeneity of the polymer surrounding this particular molecule fluctuates as a result of polymer dynamics. These results indicate the potential of defocused wide field imaging for following polymer dynamics, a topic discussed in detail in the next section.

## 4.2

### "3D" Single-Molecule Rotational Diffusion in Polymer

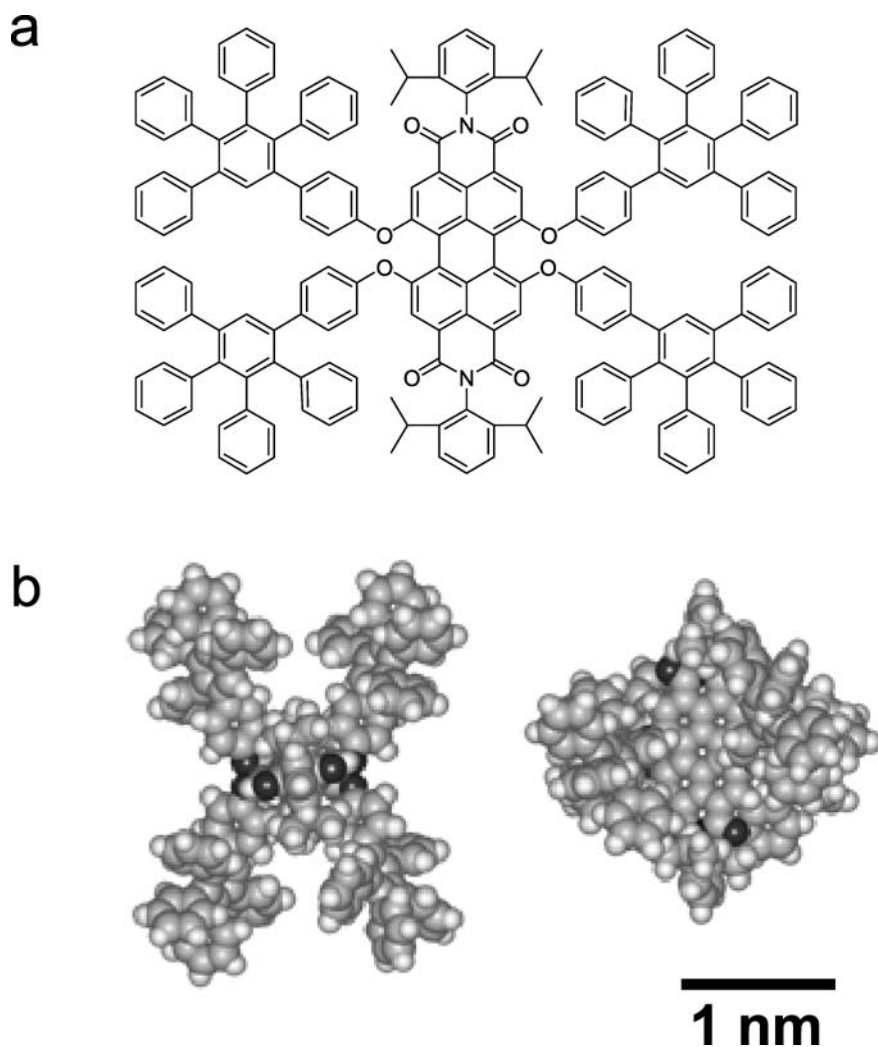
The physical properties of polymers, especially the dynamics close to the glass transition, are complex. Although many experimental and theoretical studies have been performed, the physical origin is not completely understood. Many theories that describe polymer properties near the glass transition are based on a microscopic picture [48, 49] that now can be evaluated experimentally by applying single molecule techniques. Segmental relaxation of a polymer above  $T_g$  can be probed by the rotational diffusion, induced by the relaxation process, of a probe molecule embedded in the polymer under study [15–21]. The rotation of single molecules is typically followed by measuring the degree and orientation of linear polarization of fluorescence, resulting from the projection of the emission dipole orientation on a two-dimensional plane as stated in the Introduction.

In this section, we will show that defocused imaging is a powerful method to study polymer relaxation processes by detecting 3D rotational motions of probe molecules in a polymer thin film [21]. It should be noted that defocused imaging offers some advantages: it allows for highly parallel data collection by looking at many molecules in the field of view, it gives exact information on 3D orientation as mentioned above, and it is easy to come back to focused images in order to determine the exact locations of probe molecules. Since the defocused imaging requires relatively many photons to obtain a good signal-to-noise ratio, we used an extremely robust perylendiimide dye (Fig. 14) as probe molecule. The excellent photostability of the molecule allows us to image for an extended period of time (more than 30 min in a nitrogen atmosphere).

#### 4.2.1

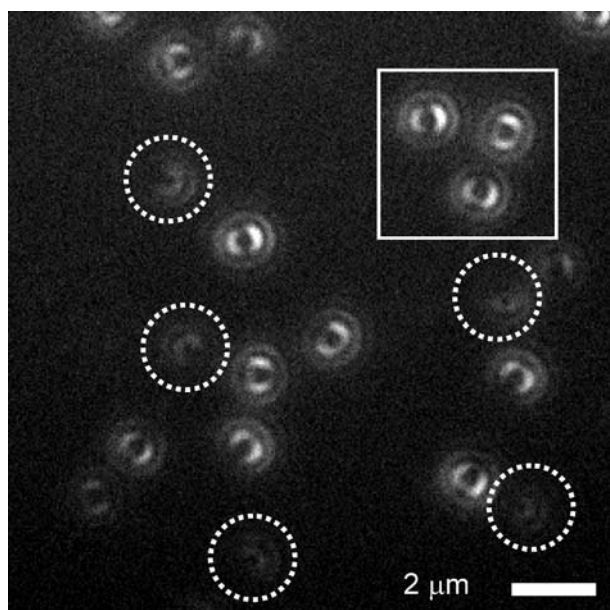
##### Defocused Imaging to Track Molecular Rotational Diffusion

Figure 15 shows a defocused image of the perylendiimide chromophores in a thin (100 nm) poly(methyl acrylate) (PMA) film. A video containing about



**Fig. 14** **a** Chemical structure of the perylene diimide substituted with polyphenylene groups in the bay positions. **b** 3D representation of the compound from different view points: along the vertical axis of the plane of the perylene diimide core (*right*) and along the long axis of the core (*left*)

2000 images, recorded with an integration time of 1 s, was obtained. In the image, shown in Fig. 15, the two-lobe pattern is dominant (75%). Twenty-five percent of molecules show substantial out-of-plane contribution, as indicated by the dashed white circles. This difference is due to the preferential excitation of the molecules with an in-plane orientation.



**Fig. 15** A defocused image of the perylenediimide derivative embedded in a 50 nm thick film of PMA with 1  $\mu\text{m}$  defocusing toward the sample. The *white dashed circles* indicate molecules that are substantially oriented out of plane. The *white square* indicates the molecules discussed in Figs. 17–19

#### 4.2.2

##### Non-Unidirectional Rotation

The sequence displayed in Fig. 16a consists of snapshots of an individual molecule showing rotational diffusion in a PMA film as function of time. An image is shown every 1.4 s (with 1 s integration and 0.4 second interval time). The sequence A represents experimental data, the sequence B shows the corresponding calculated patterns. By fitting each emission pattern as a function of time, transition dipole orientation trajectories are obtained (Fig. 16b). The first derivative of such trajectory clearly shows that the rotational diffusion is not unidirectional but random instead. This is to be expected since the dynamics of the probe molecule are driven by polymer segmental motions and hence result from relaxations of the polymer chains which should be random.

#### 4.2.3

##### Local Heterogeneity in Time and in Space

Wide-field imaging allows us to collect data of many molecules in parallel. Therefore, local heterogeneity of polymer can be studied on the nanometer

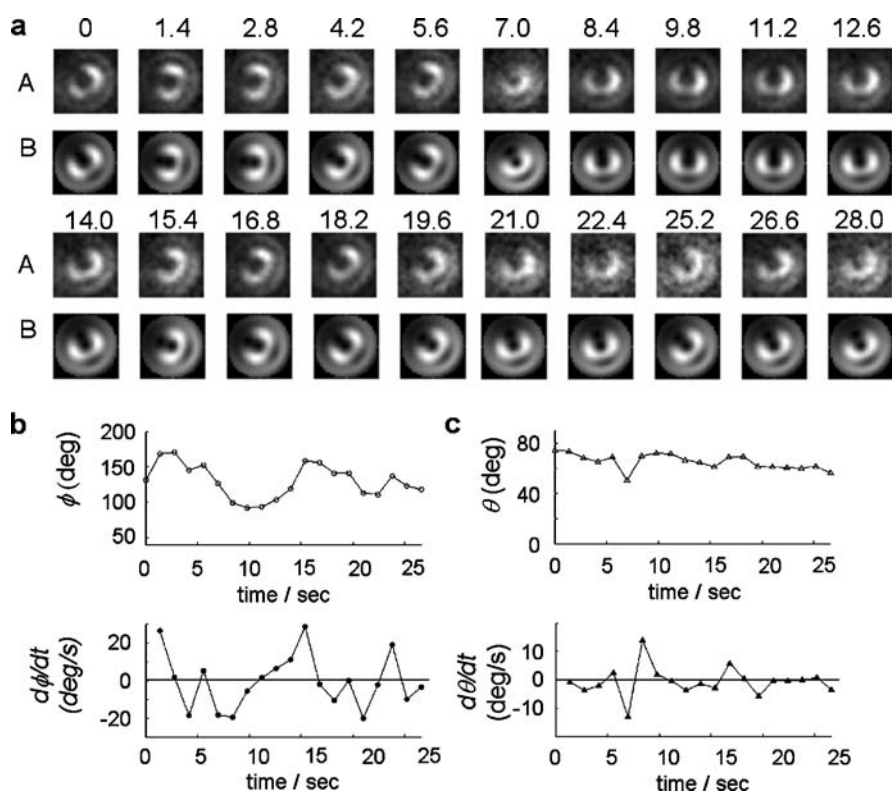


**Fig. 16** a Snapshots of experimentally observed emission patterns (sequence A) and corresponding computed patterns (sequence B) as a function of time. Transition dipole orientation trajectories and their first time derivatives are shown for the in plane (b) and out of plane component (c), respectively

scale. Figure 17 shows three molecules which locate relatively close to each other in space (as highlighted by the white square in Fig. 15). Figure 17b–d shows the projection maps for molecules 1–3 shown in Fig. 17a, respectively. Two different behaviors can be observed in the trajectories. Molecule 2 (Fig. 17c) exhibits fast rotation with no preference for any orientation. On the other hand, molecules 1 and 3 are temporarily locked in one orientation and occasionally jump to a completely different orientation occur (Fig. 17b and d). For example, molecule 1 is first oriented in the region indicated by the black line but undergoes a jump in orientation, indicated by the blue line, after 970 s. Molecule 3 shows an even more complex behavior: though it is locked in three different orientations for 1760 s, it starts rotating in rather wide range of angles afterwards. From that point on, completely different rotational dynamics are observed. This clearly reflects temporal heterogeneity of polymer relaxations. Most interestingly, molecule 3 passes through the initial region on the projection map, observed between 0 and 190 s and indicated in black,



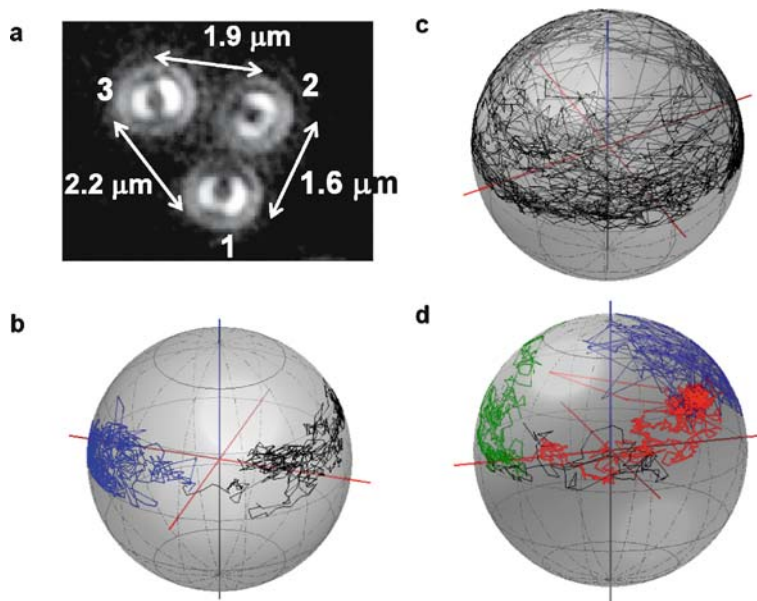


**Fig. 17** Spatial and temporal heterogeneity of dynamics at 295 K. **a** A zoom of the three molecules indicated by the white square in Fig. 15. Molecules are separated between 1.6 and 2.2  $\mu\text{m}$ . **b–d** Projection maps for molecules 1–3, respectively. The *red* lines indicate the *x–y* image plane and the blue line is the optical (*z*) axis: 0–960 s (*black*) and 960–2380 s (*red*) in **b**, 0–190 s (*black*), 190–895 s (*green*), 895–1763 s (*red*), and 1763–2940 (*blue*) in **d**

when jumping from the green region into the red region after 890 s. These results clearly indicate temporal heterogeneity and may point to a memory effect in polymer relaxation at the dimension of the probe molecule, meaning approximately 3 nm.

A more quantitative evaluation of the phenomenon seen in the projection maps can be obtained by constructing time trajectories of the dipole orientation and analyzing the observed fluctuations by correlation functions. Figure 18 shows the time trajectories of the dipole orientation and their first derivatives for the three molecules in Fig. 17. Several important observations can be made for these molecules. First, the analysis of the rotational movement of these molecules clearly indicates spatial heterogeneity on a micrometer scale. Secondly, molecule 1 (Fig. 18a,b) shows no large changes in rotation rate during the observation time of 2500 s. The behavior of molecule 2 (Fig. 18c,d) is in striking contrast with the behavior of molecule 1. Clear changes in the rotational rate can be observed, both for the in and the out of plane part of the rotation. This difference between these molecules is also reflected in the correlation function of the rotational movement (vide infra). Molecule 3 (Fig. 18e,f) shows a wide variety of behaviors. Changes of the rota-

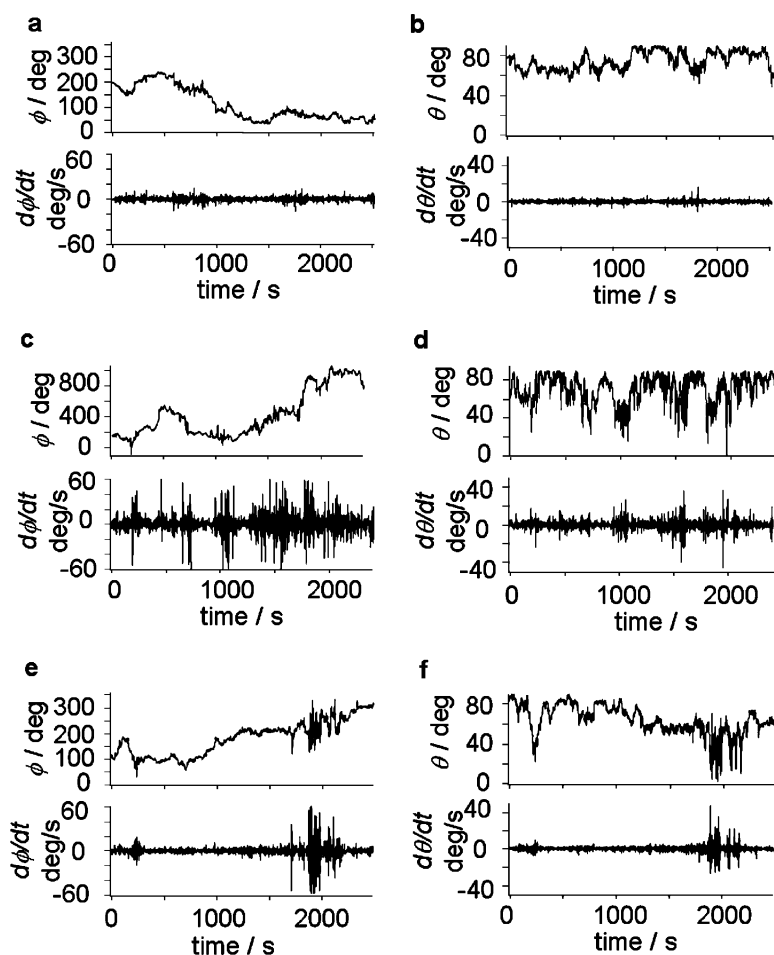


**Fig. 18** Transition dipole orientation trajectories in plane and out of plane and their time derivatives for molecule 1 (a) and (b), 2 (c) and (d), and 3 (e) and (f)

tion rate for both in and out of plane rotation components occur after 1800 s. These changes correspond to the wide angular distribution observed in the projection map in Fig. 17d after 1800 s, indicated in blue.

#### 4.2.4

##### Relaxation Time of the Rotational Diffusion: Comparison Between 2D and 3D Analysis

In order to evaluate our experimental technique and in order to compare the results obtained with data reported earlier in literature, we first estimate the in plane component of the rotational diffusion using a similar analysis as

reported in [17–19]. The autocorrelation function was calculated using

$$C(t) = \langle A(t')A(t' + t) \rangle / \langle A(t')A(t') \rangle, \quad (11)$$

where  $A(t) = \cos(2\phi(t))$ . The decay of  $C(t)$  is then fitted with a Kohlrausch-Williams-Watt (KWW) stretched exponential function:

$$C(t) = \sum_i \exp \left[ - (t/\tau_{i\text{KWW}})^{\beta_{i\text{KWW}}} \right]. \quad (12)$$

The averaged time scale of rotational diffusion ( $\tau_C$ ) is estimated by  $\tau_C = \int_0^\infty C(t) dt$ . The correlation functions and the fitting results of the three molecules in Figs. 17 and 18 are illustrated in Fig. 19. The individual molecules show significantly different behavior. The correlation function of molecule 1 and 3 can be fitted with a stretched exponential decay with a  $\beta_{\text{KWW}}$  close to one. The  $\tau_C$  was estimated to be 164 and 230 seconds for molecule 1 and 3, respectively. These values are more than twice slower than the correlation times of rhodamine 6G and rubrene embedded in PMA in the earlier reports [17–19, 50]. This is not surprising since it is known that rotation of large probes is more hindered and can deviate from the collective relaxation of surrounding matrix, resulting in high  $\beta_{\text{KWW}}$  value and large  $\tau_{\text{KWW}}$  [50]. On the other hand, molecule 2 shows a much faster average de-

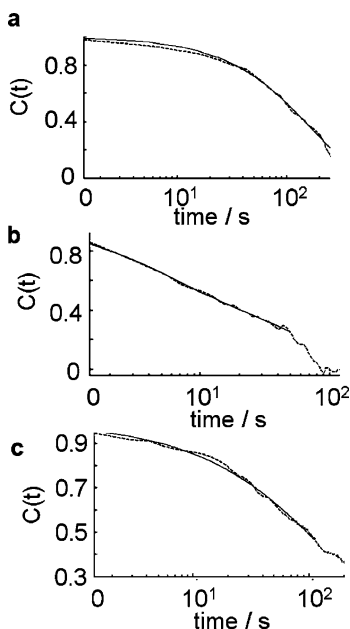


**Fig. 19** Correlation functions of the in-plane transition dipole orientation of molecule 1 (a) ( $\tau_C = 164$  s,  $\tau_{\text{KBB}} = 160$  s,  $\beta_{\text{KBB}} = 0.95$ ), 2 (b) ( $\tau_C = 47$  s,  $\tau_{1\text{KBB}} = 4.2$  s,  $\beta_{1\text{KBB}} = 1.0$  and  $\tau_{2\text{KBB}} = 49$  s,  $\beta_{2\text{KBB}} = 0.65$ ), and 3 (c) ( $\tau_C = 231$  s,  $\tau_{\text{KBB}} = 169$  s,  $\beta_{\text{KBB}} = 0.65$ )

cay of  $\tau_C = 47$  s actually consisting of two components, yielding  $\tau_{1\text{ KBB}} = 4.2$  s ( $\beta_{1\text{ KBB}} = 1.0$ ) and  $\tau_{2\text{ KBB}} = 44$  s ( $\beta_{2\text{ KBB}} = 0.7$ ). This smaller value of  $\tau_{2\text{ KBB}}$  can be related to spatially heterogeneous dynamics present in polymers, especially in the very poly-disperse PMA matrix used. However, interfacial effects at the air/polymer or polymer/glass interfaces where the probe molecule might exhibit different dynamics can not be excluded. The  $\tau_{1\text{ KBB}}$  might represent a shorter second relaxation regime of the polymer. Note that the mismatch between the correlation function and the exponential at the initial part of molecule 1 might also indicate the presence of this faster polymer relaxation regime. However, it was recently argued that for the approach described above, e.g. analyzing a 3D rotation by only considering the in plane contribution by calculating the linear dichroism, even an isotropic rotational diffusion can lead to non-exponential correlation functions [51]. If so, the obtained stretched exponential behavior of the correlation functions might be the result of a complex mixture of an analysis artifact and polymer dynamics. Indeed, assume one is interested in the probability that the dipole orientation, within time  $t$ , changes its polar angle from  $\theta_0$  to  $\theta_1$ , and its in-plane angle by  $\phi$ , as shown in Fig. 20.

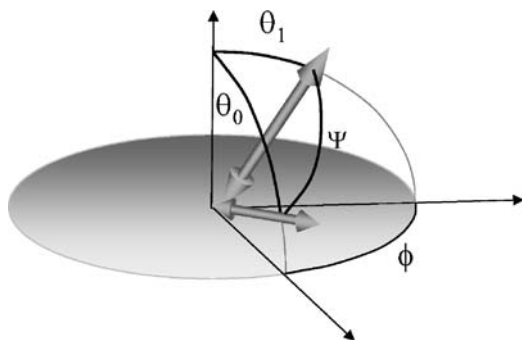


**Fig. 20** Schematic representation of the angular changes in a time interval  $t$  for a 3D rotational diffusion of the transition dipole. The in plane projection of the transition dipole is also shown

For an isotropic rotator, the associated probability distribution is given by:

$$P(\theta, \phi, t|\theta_0) = \sum_{n=0}^{\infty} \sum_{m=-n}^n \frac{2n+1}{4\pi} \frac{(n-|m|)!}{(n+|m|)!} \dots P_n^m(\cos \theta) P_n^m(\cos \theta_0) \times \exp [i\phi - n(n+1)D_{\text{rot}}t] , \quad (13)$$

where  $P_n^m$  are associated Legendre polynomials.  $D_{\text{rot}}$  is the rotational diffusion constant. Knowing this distribution, one can compute the average of

the  $\cos 2\phi$  as

$$\begin{aligned}
 \langle \cos 2\phi \rangle &= \int_0^\pi d\theta \sin \theta \int_0^\pi d\theta_0 \sin \theta_0 \int_0^{2\pi} d\phi P(\theta, \phi, t | \theta_0) \cos 2\phi \\
 &= \int_0^\pi d\theta \sin \theta \int_0^\pi d\theta_0 \sin \theta_0 \sum_{n=2}^{\infty} \frac{2n+1}{2} \frac{(n-2)!}{(n+2)!} P_n^2 \\
 &\quad \times (\cos \theta) P_n^2(\cos \theta_0) \exp[-n(n+1)D_{\text{rot}}t] \\
 &= 8 \sum_{n=1}^{\infty} (4n+1) \frac{(2n-2)!}{(2n+2)!} \exp[-2n(2n+1)D_{\text{rot}}t], \tag{14}
 \end{aligned}$$

which is a complicated infinite series of exponential decays. As stated above, it is difficult to interpret the physical meaning.

A very recent report claims, however, that the above mentioned effect is minimal when one uses high NA objective lenses [52]. The authors state that to best compare to ensemble measurements of reorientation dynamics it would be ideal to measure the full three-dimensional orientation of the molecule. They also mention that single molecule techniques capable of measuring the 3-D orientation require many photons to determine the orientation and thus limit the length of the trajectories and impairing useful correlation analysis. Here, we demonstrate measurements of long trajectories of the full 3D orientation with high signal-to-noise ratio that allow correlation analysis.

The 3D rotational diffusion equation for an isotropic rotational diffusion with diffusion constant  $D_{\text{rot}}$  on the other hand is simply is given by

$$\frac{\partial h(\Psi, t)}{\partial t} = D_{\text{rot}} \frac{1}{\sin \Psi} \frac{\partial}{\partial \Psi} \sin \Psi \frac{\partial h(\Psi, t)}{\partial \Psi}, \tag{15}$$

where  $h(\Psi, t)$  is the orientation distribution function.  $\Psi$  is angular change as defined by  $\Psi = \arccos(\mathbf{n}_t \cdot \mathbf{n}_{t+\delta t})$ , where  $\mathbf{n}_t$  is the unit orientation vector of the molecular dipole moments at time  $t$ . The average of  $\langle \cos(\Psi) \rangle$  over  $\Psi$  as function of time,

$$\langle \cos(\Psi) \rangle = \int_0^\pi d(\Psi) \sin(\Psi) h(\Psi, t) \cos(\Psi) = \exp(-2D_{\text{rot}}t) \tag{16}$$

shows a single exponential decay. The relaxation time is given by  $\tau = 1/2D_{\text{rot}}$ .

54 of the molecules shown in Fig. 21 were analyzed using the mathematics for a 3D isotropic rotor as outlined above (Eqs. 15 and 16). The images were taken with 200 ms integration time and no interval time between the different frames. Although in this contribution trajectories are analyzed with 1000 data points to demonstrate the method, it is possible to obtain trajectories with

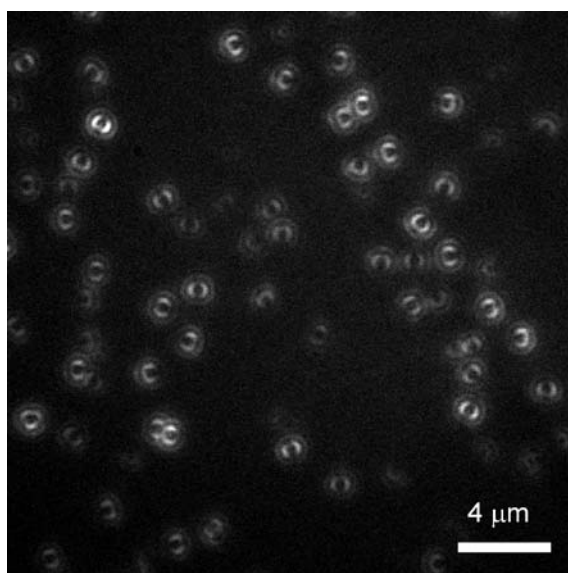


**Fig. 21** The defocused image used for the statistical analysis of 54 of the molecules embedded in 100 nm PMA film. The movie was taken with 200 ms integration time per frame and no interval time between frames

more than 10 000 data points by recording longer movies with shorter integration times. Note that for the image in Fig. 21 a sample film of more than 100 nm was used to rule out the earlier discussed interfacial effects.

Figure 22 shows typical decays and fitting results. Again, two different time scales were found in the correlation functions. The obtained values of the diffusion coefficients for 40 of the 54 molecules, showing a clear bi-exponential decay, are shown in Fig. 23. Note that the difference between the fast and the slow rotational component is nearly two orders of magnitude. The fast

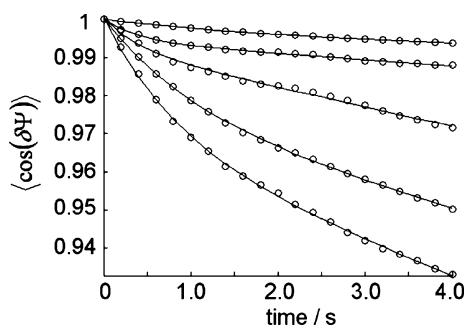


**Fig. 22** Typical autocorrelation functions ( $\circ$ ) and bi-exponential fits (*solid line*) for 4 molecules from Fig. 21

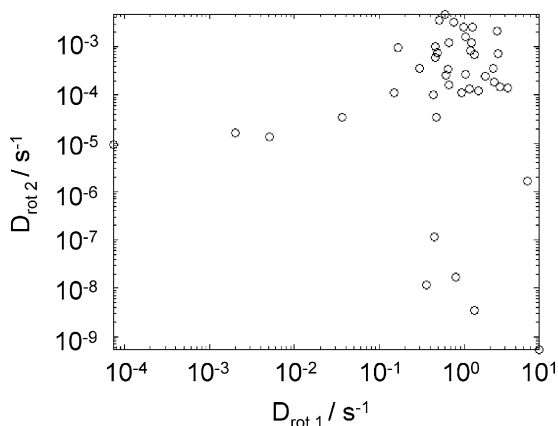


**Fig. 23** The distribution of diffusion coefficients for 40 of the molecules shown in Fig. 21

component of most molecules is distributed between 0.1 s and 10 s and the slow decay between several hundreds to thousands of seconds. From a phenomenological point of view, it is well known that fast local rearrangements of a polymer (referred to as the Johari-Goldstein  $\beta$  process, or secondary relaxation) are followed by the main slower relaxation, commonly termed as  $\alpha$  process. This process involves cooperative molecular motions. The observed relaxation time scale may reflect different relaxation regimes of polymer relaxation dynamics. Namely, the observed fast relaxation of molecular rotation might reflect the  $\beta$ -process polymer relaxation and the slower rotational diffusion could reflect the collective polymer motion. The tentative assignment made here to different relaxation regimes will be further investigated in detail by using a variety of fluorescent probes with different sizes and aspect ratios in well-defined mono-disperse polymer matrixes.

## References

1. Ambrose WP, Goodwin PM, Jett JH, Van Orden A, Werner JH, Keller RA (1999) *Chem Rev* 99:2929
2. Moerner WE, Fromm DP (2003) *Rev Sci Instrum* 78:3597
3. Kulzer F, Orrit M (2005) *Annu Rev Phys Chem* 55:585
4. Enderlein J, Böhmer M (2003) *Chem Phys Chem* 4:792
5. Smith DE, Perkins TT, Chu S (1995) *Phys Rev Lett* 75:4146
6. Chu S (2003) *Phil Trans R Soc Lond A* 361:689
7. Smith DE, Babcock HP, Chu S (1999) *Science* 283:1724
8. Barbara PF, Gesquiere AJ, Park SJ, Young JL (2005) *Acc Chem Res* 38:602
9. Sartori SS, De Feyter S, Hofkens J, Van der Auweraer M, De Schryver FC, Brunner K, Hofstraat JW (2003) *Macromolecules* 36:500
10. Huser T, Yan M, Rothberg LJ (2000) *Proc Natl Acad Sci USA* 97:11187

11. Vallee RAL, Tomczak N, Kuipers L, Vancso GJ, van Hulst NF (2003) *Phys Rev Lett* 91:038301
12. Vallee RAL, Marsal P, Braeken E, Habuchi S, De Schryver FC, Van der Auweraer M, Beljonne D, Hofkens J (2005) *J Am Chem Soc* 127:12011
13. Vallee RAL, Cotlet M, Hofkens J, De Schryver FC, Müllen K (2003) *Macromolecules* 36:7752
14. Biju VP, Ye JY, Ishikawa MJ (2003) *Phys Chem B* 107:10729
15. Ha T, Laurence TA, Chemla DS, Weiss S (1999) *J Phys Chem B* 103:6839
16. Tomczak N, Vallée RAL, van Dijk EMHP, García-Parajó M, Kuipers L, van Hulst NF, Vancso GJ (2004) *Eur Polym J* 40:1001
17. Deschenes LA, Vanden Bout DA (2001) *J Phys Chem B* 105:11978
18. Deschenes LA, Vanden Bout DA (2001) *Science* 292:255
19. Deschenes LA, Vanden Bout DA (2002) *J Chem Phys* 116:5850
20. Zhou Q, Kor J (2005) *Phys Soc* 47:S190
21. Uji-i H, Melnikov S, Deres A, Bergamini G, De Schryver F, Herrmann A, Müllen K, Enderlein J, Hofkens J (2006) *Polymer* 47:2511
22. Ishijima A, Kojima H, Higuchi H, Harada Y, Vale R, Funatsu T, Yanagida T (1996) *Biophys J* 70:383
23. Kinoshita K (1999) *FASEB J* 13:S201
24. Warahaw DM, Hayes E, Gaffney D, Lauzon AM, Wu JR, Kennedy G, Trybus K, Lowey S, Verger C (1998) *Proc Natl Acad Sci USA* 95:8034
25. Trautman JK, Macklin JJ (1996) *Chem Phys* 205:221
26. Macklin JJ, Trautman JK, Harris TD, Brus LE (1996) *Science* 272:255
27. Ambrose WP, Goodwin PM, Martin JC, Keller RA (1994) *Phys Rev Lett* 72:160
28. Bopp MA, Meixner AJ, Tarrach G, Zschokke-Gränacher I, Novotny L (1996) *Chem Phys Lett* 263:721
29. Ruiters AGT, Veerman JA, Garcia-Parajo MF, Van Hulst NF (1997) *J Phys Chem A* 101:7318
30. Veerman JA, Garcia-Parajo MF, Kuipers L, Van Hulst NF (1999) *J Microsc* 194:477
31. Veerman JA, Levi SA, Van Veggel FCJM, Reinhoudt DN, Van Hulst NF (1999) *J Phys Chem A* 103:11264
32. Sick B, Hecht B, Novotny L (2000) *Phys Rev Lett* 85:4482
33. Novotny L, Beversluis MR, Youngworth KS, Brown TG (2001) *Phys Rev Lett* 86:5251
34. Piwonski H, Stupperich C, Hartschuh A, Sepiol J, Meixner A, Waluk J (2005) *J Am Chem Soc* 127:5302
35. Jasny J, Sepiol J (1997) *Chem Phys Lett* 273:439
36. Sepiol J, Jasny J, Keller J, Wild UP (1997) *Chem Phys Lett* 273:444
37. Böhmer M, Enderlein J (2003) *J Opt Soc Am B* 20:554
38. Patra D, Gregor I, Enderlein J (2004) *J Phys Chem A* 108:6836
39. Schroeyers W, Vallee RAL, Patra D, Hofkens J, Habuchi S, Vosch T, Cotlet M, Müllen K, Enderlein J, De Schryver FC (2004) *J Am Chem Soc* 126:14310
40. Brokmann X, Ehrensperger MV, Hermier JP, Triller A, Dahan M (2005) *Chem Phys Lett* 406:210
41. Bartko AP, Xu K, Dickson RM (2002) *Phys Rev Lett* 89:026101
42. Enderlein J, Ruckstuhl T, Seeger S (1999) *Appl Opt* 38:724
43. Enderlein J (2000) *Opt Lett* 25:634
44. Patra D, Gregor I, Enderlein J (2005) *Appl Phys Lett* 87:101103
45. Richards B, Wolf E (1959) *Proc R Soc Lond A* 235:358
46. Piwonski H, Stupperich C, Hartschuh A, Sepiol J, Meixner A, Waluk J (2005) *J Am Chem Soc* 127:5302



47. Fourkas JT (2001) *Opt Lett* 26:211
48. Schilling R (2003) In: Randons G, Just W, Haeussler P (eds) *Collective Dynamics of Nonlinear and Disordered System*. Springer, Berlin
49. Götze WJ (1999) *Phys* 11:A1
50. Inoue T, Cicerone MT, Ediger MD (1995) *Macromolecules* 28:3425
51. Hinze G, Diezemann G, Basche T (2004) *Phys Rev Lett* 23:203001
52. Wei CYJ, Kim YH, Darst RK, Rossky PJ, Vanden Bout DA (2005) *Phys Rev Lett* 95:173001

# Dynamics of Excited States and Charge Photogeneration in Organic Semiconductor Materials

Kim G. Jespersen<sup>1</sup> · Yuri Zaushitsyn<sup>1</sup> · Sebastian Westenhoff<sup>2</sup> · T. Pullerits<sup>1</sup> · Arkady Yartsev<sup>1</sup> · Olle Inganäs<sup>3</sup> · Villy Sundström<sup>1</sup> (✉)

<sup>1</sup>Department of Chemical Physics, Lund University, Box 124, 22100 Lund, Sweden  
*villy.sundstrom@chemphys.lu.se*

<sup>2</sup>Cavendish Laboratory, University of Cambridge, Madingley Road,  
Cambridge CH3 0HE, UK

<sup>3</sup>Biomolecular and Organic Electronics, Linköping University, 58183 Linköping, Sweden

1	Introduction . . . . .	285
2	Excited-State Dynamics and Energy Transfer . . . . .	287
3	Light-Induced Charge Generation in Neat Polymers . . . . .	289
4	Light-Induced Charge Generation in Polymer–Fullerene Blends . . . . .	295
	References . . . . .	296

**Abstract** Organic semiconductor materials are attracting increasing interest for application as active materials in large-area displays, light-emitting diodes, transistors, photodetectors, solar cells, etc. Elementary processes like excitation energy transfer, charge photogeneration, charge transport, and photoluminescence quenching are at the basis of the function of the materials. In order to design new materials and optimize their function, a detailed knowledge of the various light-induced processes is required. In this contribution we discuss how ultrafast spectroscopy can be used to study excited-state relaxation and quenching, energy transfer, and charge generation in neat conjugated polymers as well as in polymer–C60 blends.

## 1 Introduction

Conjugated polymers, or organic semiconductors, are attracting great interest as new materials for applications in, for example, solar cells, light-emitting diodes (LEDs), lasers, displays, sensors, and transistors. Traditional inorganic and novel organic semiconductors are used in very much the same applications, based on their light-to-charge (e.g., solar cell) and charge-to-light (e.g., LED) converting properties, but the underlying mechanisms are very different. Due to their standing as intermediate between traditional semiconductors and molecules and their heterogeneous nanostructure, the properties and processes of conjugated polymers are highly complex and in many

cases far from being understood. However, a great deal of progress has been achieved during the past few years, as a result of combining new and powerful experimental and theoretical methods. As an example, ultrafast spectroscopy has been widely applied and provides direct access to the timescale of elementary processes such as energy transfer and charge photogeneration.

As the notion organic semiconductor may suggest, and as has in fact been suggested [1, 2], light absorption could be described by a semiconductor band picture and thought of as a direct charge generating process, without any excited-state intermediates. However, an overwhelming number of experimental and theoretical results show that the major primary photoexcitation in conjugated polymers is a neutral strongly bound exciton [3–6].

Following the formation of an exciton by light absorption, this exciton can migrate along the polymer chain on which it was formed. If many polymer chains are in close contact, like in a solid-state film of a neat conjugated polymer, the energy may as well jump to a neighboring chain. Time-resolved fluorescence spectral diffusion and time-resolved fluorescence or absorption anisotropy, combined with Monte Carlo simulations, have proven particularly powerful tools to study energy transfer on both isolated chains and thin polymer films [7–9]; both intra- and interchain transfer are efficient and proceed on the subpicosecond to tens (and hundreds) of picoseconds timescale. Downhill energy transfer from high-energy segments to segments at lower energy is fastest,  $\sim 1$  ps or less, while transfer among segments at the bottom of the density of states can be much slower ( $\sim 10$ – $100$  ps). Interchain transfer in a solid film can be very fast ( $< 1$  ps) due to short distances, favorable geometry, and many more possible transfer pathways [9].

As mentioned above, the exciton formed by light absorption is generally quite strongly bound, implying that breaking it up into an electron–hole pair requires extra energy or a lowering of the potential barrier separating the bound exciton from the geminate electron–hole pair, by applying an external electric field. Different conjugated polymers have chemically very different repeat units, and the nanostructure could vary a lot depending on structural properties and method of manufacture. Therefore, it should not be surprising if the exciton binding energy varies among the broad spectrum of conjugated polymers that are studied today. We will discuss results for a polymer where exciton binding is strong and no exciton breaking into charge pairs occurs unless a strong electric field is applied, or excess photon energy ( $\sim 1$  eV) is used to excite the molecules. Such a polymer is obviously a good material for light-emitting devices. An external electric field applied to such a polymer lowers the binding energy, but charge pair formation is still an activated process and therefore quite slow—it proceeds throughout the excited-state lifetime of the polymer. Much faster charge pair formation, subpicosecond to a few picoseconds, can be achieved by high photon energy excitation (UV light) or by sequential two-photon excitation (obtained under exciton annihilation conditions), by opening up relaxation pathways surmounting the

exciton binding potential barrier. We will also discuss a qualitatively different situation where exciton breaking occurs at a low yield ( $\sim 5\%$ ) in the absence of an external electric field and at low photon energy excitation. This is the expected behavior in the semiconductor band picture. However, also in this case charge pair formation is slow ( $\sim 50\text{--}100$  ps), in contrast to the expected instantaneous formation for a direct ground state–charge pair excitation. A detailed analysis of this situation shows that charge generation occurs at a small number of low binding energy sites and that the charge generation time is limited by energy transfer to these dissociation sites. These two distinct charge photogeneration behaviors could represent two limiting cases, and the charge generation characteristics of a particular polymer could be obtained as a suitable linear combination of the two.

## 2

### Excited-State Dynamics and Energy Transfer

The nature of the excited state, relaxation processes, and excited-state energy migration and quenching are related processes connected to the temporal evolution of the excited state, and determining, e.g., if it has strong emission or is more prone to charge separation. Energy migration is a basic property of a material and is strongly related to inhomogeneity and the presence of traps. Energy transfer has been studied by many groups for many different polymers, both in thin solid films and for polymers in solution.<sup>1</sup> This work shows that energy transfer occurs along polymer chains, as well as between polymer chains when they are closely packed in a solid film. Depending on the nature of the polymer spectroscopic unit and distances between polymer chains, the site-to-site energy transfer is on the subpicosecond to a few picoseconds timescale [7–11]. Faster processes ( $< 100$  fs), assigned to exciton relaxation or localization within a single spectroscopic unit, have also been observed [9].

In our work we have used energy migration, probed by, e.g., fluorescence depolarization, as a tool to study polymer conformations. As excitation energy migrates along and between polymer chains, the measured fluorescence or transient absorption signal depolarizes because different segments have different orientations. Thus, time-resolved polarized measurements can be used to probe the degree of conformational disorder of a polymer. As the exciton migrates between different polymer segments it will sample the distribution of density of states representing the inhomogeneously broadened spectrum of the polymer. If a high-energy site is initially excited by a short pulse of light, the spectral evolution (red shift) of the fluorescence spectrum monitors the migration of the exciton toward lower energy sites. Consequently, time-resolved anisotropy and spectral migration reflect the

<sup>1</sup> See *Photochem Photobiol* 144, and references therein.

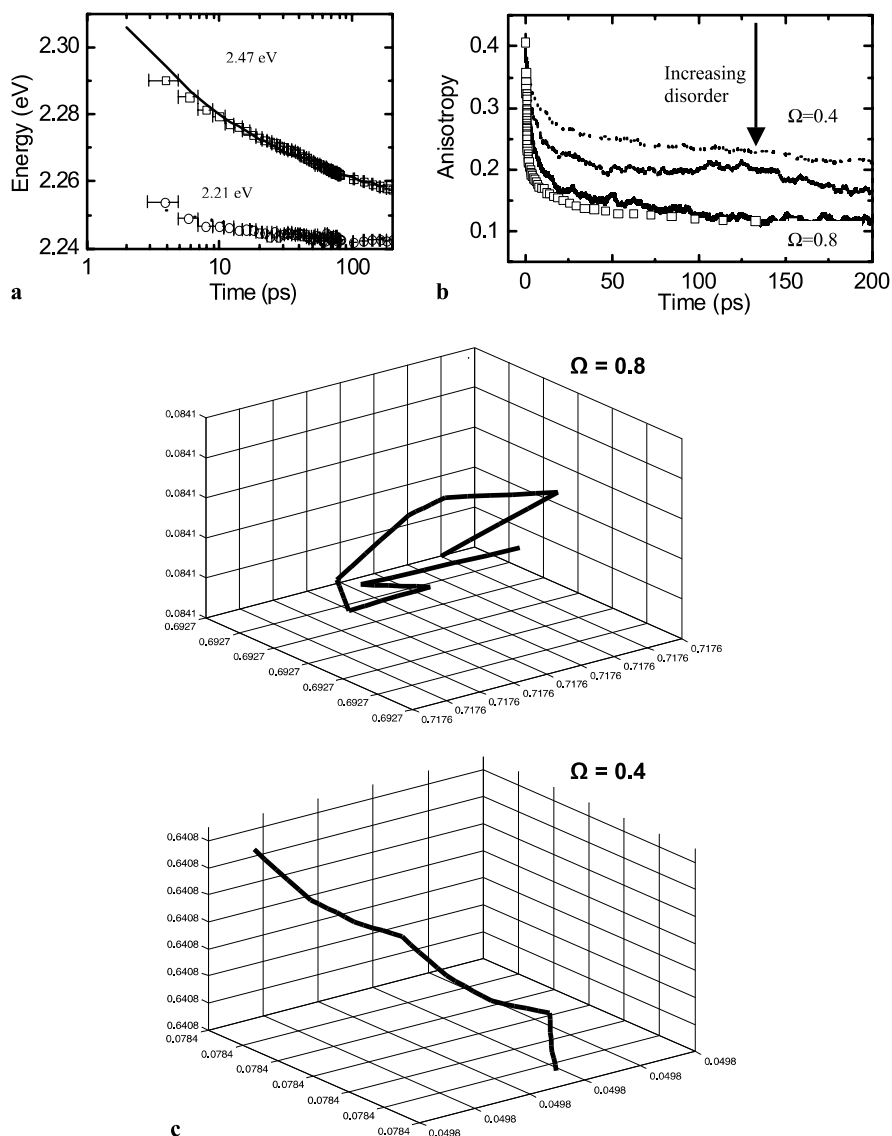


**Fig. 1** **a** Time-dependent fluorescence spectral migration of PDOPT in chloroform measured at two different energies, 2.47 and 2.21 eV (*symbols*) and results of the corresponding Monte Carlo simulations (*lines*). Good agreement between experiment and simulation was obtained with a size of the spectroscopic unit of 7.4 monomer units and a disorder parameter  $\Omega = 0.8$  (perfect order is for  $\Omega = 0$ ). **b** Transient absorption anisotropy of PDOPT in chloroform measured at 2.47 eV (*open squares*) and Monte Carlo simulations for various degrees of disorder (*dotted lines*; a high value of anisotropy corresponds to low disorder). A good agreement between experiment and simulation was obtained with the same size of the spectroscopic unit and the same disorder as in (**a**). **c** Typical polymer conformations for two values of the disorder parameter

same process, and by simultaneously monitoring both phenomena we can get detailed insight into the energy transport and conformational properties of the polymer. By comparing the results of ultrafast measurements and Monte Carlo simulations on computer-generated polymer chains, we could obtain information regarding the conformational properties of several polymers [7–9, 11]. Figure 1a and b illustrates the results of a low molecular weight poly[3-(2,5-dioctylphenyl)thiophene] (PDOPT) in dilute chloroform solution. The simulations yield a descriptive microscopic picture of exciton migration and lead to an effective conjugation length of 7.4 monomer units and a measure of the disorder of the chains ( $\Omega$ ). Typical conformations for two values of the disorder parameter  $\Omega$  are shown in Fig. 1c.

During the migration of the exciton it may encounter an impurity or nonfluorescing species (dimer, aggregate, etc.) and if energy transfer to this species occurs, luminescence is quenched. Our recent work resulted in detailed insights into the mechanism of photoluminescence quenching. It was concluded that in thin polymer films with densely packed chains having strong intermolecular interactions, aggregates formed by chains in close approach act as nonluminescent traps [12, 13].

### 3

#### Light-Induced Charge Generation in Neat Polymers

Many different theoretical models have been proposed over the years to describe charge photogeneration in conjugated polymers. According to the semiconductor model, carriers are directly generated by the optical excitation and thermalize to form charged polarons, which later bind into polaron excitons due to the Coulomb interaction. The initial generation step in this model is field independent, while the field dependence of the generation efficiency comes from the competition between the Coulomb interaction and the external field preventing exciton formation, and/or from breaking of already formed excitons. Onsager-type models are similar, in the sense that they describe exciton dissociation in terms of charge pair dissociation and consider primary exciton dissociation as being field independent. Arkhipov et al. [14] took into consideration the excess vibrational energy stored in a polymer segment after excitation with a high-energy photon, and proposed a model where photogeneration of free mobile charges occurs in two steps involving three species: a neutral exciton, a geminately bound electron–hole (e-h) pair, and separated charges. These three species are separated by electric-field-dependent potential barriers, which may be overcome by excess thermal energy and/or by applying an external electric field that lowers the barriers. Thus, if a neutral exciton is created close to the bottom of its potential well a substantial electric field is required for its dissociation. If, on the other hand, sufficient excess energy is delivered to the polymer segment via the optical ex-

citation, exciton dissociation is facilitated by the excess energy delivered to the phonon bath and is predicted to have a significantly lower electric field dependence than the dissociation originating from the thermalized exciton [14]. According to this model, hot exciton dissociation is expected to occur within a time window set by vibrational cooling of a polymer segment, i.e., the few picoseconds timescale. Fully dissociated mobile charges contributing to the photocurrent are formed by breaking the geminate e-h pairs held together by the mutual Coulombic attraction energy. Charge photogeneration could also be thought of as autoionization of a hot Franck-Condon state, which after thermalization forms a charge pair. This process was first discovered by Geacintov and Pope [15] and theoretically explained by Jortner [16]. The timescale of exciton dissociation in this case is set by redistribution of excess vibrational energy into the heat bath, i.e.,  $\sim 100$  fs.

In order to contribute toward reaching a general picture of charge photogeneration in conjugated polymers, we have performed systematic studies of two different types of polymers that, on the basis of previous studies, appear to represent two quite different limits of charge generation behavior: a ladder-type poly(para-phenylene) (MeLPPP) and poly[3-(2'-methoxy-5'-octylphenyl)thiophene] (POMeOPT). Exciton dissociation was investigated as a function of excitation photon energy, electric field strength, and excitation power density, with the aim of obtaining exciton binding energies, and the dependence of exciton breaking on excess vibrational energy and excitation density.

Using electric field modulated femtosecond transient absorption spectroscopy [6, 17], we have studied charge pair generation in thin films of MeLPPP and POMeOPT. We will briefly summarize the results and then present a picture of photoinduced charge generation that emerges. Upon exciting MeLPPP with a femtosecond pulse into the  $S_0 \rightarrow S_1$  transition (3.1 eV) with low excess vibrational energy, an external electric field is required for the formation of a discernable number of charge pairs. The temporal evolution of the electron-hole concentration is characterized by a rise time of approximately 30 ps, implying that charge pairs are formed throughout the exciton lifetime from thermally relaxed excitons (see Fig. 2a). The charge generation exhibits a threshold-like electric field dependence with an onset at  $\sim 0.7 \times 10^6$  V/cm, showing that there is a substantial potential barrier (several tenths of an eV) between the exciton and charge pair states, which is reduced by the electric field. The charge pair generation rate is not constant in time, but decreases with time as  $\gamma(t) \propto (t_0/t)^{0.4}$ , typical for a random system, as a result of a distribution of interchain distances and segment orientations leading to a distribution of charge transfer rates (dotted line in Fig. 3).

Upon exciting the polymer at 4.66 eV, i.e., with almost 2 eV of excess energy, an instantaneous generation of charge pairs superimposed on a much slower more gradual response, reminiscent of that with 3.1-eV excitation, is observed (Fig. 2b). The instantaneous charge pair generation has a weaker

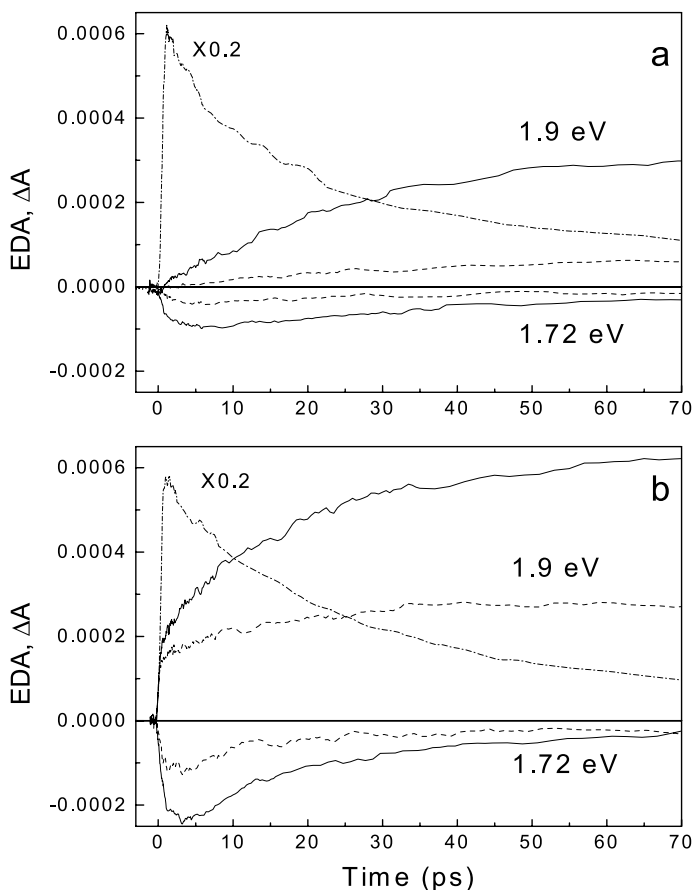


**Fig. 2**  $\Delta A$  and EDA (electric field modulated differential absorption) kinetics measured at two different probe energies with 3.1 eV (**a**) and 4.66 eV (**b**) excitation. *Solid lines* show EDA kinetics at  $2.2 \times 10^6$  V/cm applied field and *dashed lines* those at  $1.5 \times 10^6$  V/cm. *Dash-dot lines* show  $\Delta A$  kinetics measured at 1.72 eV without applied voltage. The  $\Delta A$  kinetics are divided by a factor of 5

electric field dependence without the threshold behavior observed for lower (3.1 eV) photon energy excitation, and the time dependence of the slow (> 500 fs) charge generation rate is much more pronounced (solid line in Fig. 3). The rate decreases by a factor of  $\sim 10$  as compared to a factor of 2 with low excess energy excitation during the first 5 ps after excitation.

These results suggest that with  $\sim 2$  eV excess energy excitation of MeLPPP photogeneration occurs from a hot Franck–Condon exciton state, prior to complete cooling. Using the potential energy surface diagram of Fig. 4 the following picture of charge generation in MeLPPP can be given. The threshold-type voltage dependence of the charge pair generation efficiency with 3.1-eV



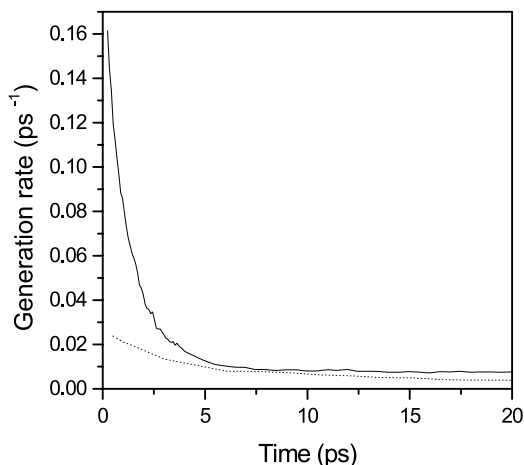


**Fig. 3** Time dependence of the charge pair generation rate with 4.66 eV (*solid line*) and 3.1 eV (*dotted line*) excitation

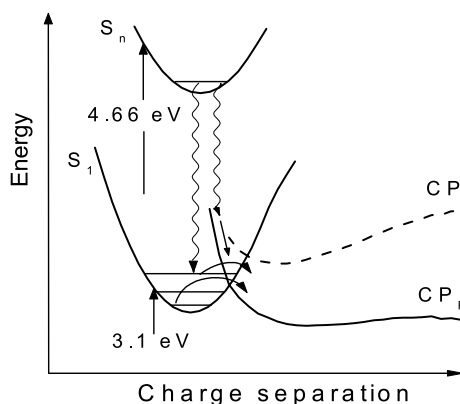


**Fig. 4** Charge pair generation model.  $S_1$  and  $S_n$  are electronic states localized within a single conjugated polymer segment. CP is the charge pair state and  $CP_F$  is that modified by the applied electric field

excitation shows that a barrier exists between the exciton and the charge pair states, and that this barrier is reduced by the electric field. With 4.66-eV excitation, the charge pair states may be populated by three different processes: (a) branching during the relaxation of the higher energy excited state to the charge pair and the  $S_1$  exciton state, (b) thermally activated barrier crossing from the hot  $S_1$  state, and (c) barrier crossing from the thermalized  $S_1$  state. Process (a) accounts for the very fast  $< 100$  fs charge pair formation observed with 4.66-eV excitation and would correspond to the autoionization

proposed by Geacintov and Pope [15]. Process (b) corresponds to the strongly time-dependent charge pair generation and would correspond to the vibrational energy assisted charge generation discussed by Arkhipov et al. [14]. Finally, process (c) is the slow, almost time-independent, process observed with low excess energy (3.1 eV) excitation. The model is significantly simplified, since it accounts for neither different carrier separation directions relative to the electric field, nor effects related to the structural disorder and polymer morphology. Nevertheless, we believe that it explains the basic features of photodissociation in MeLPPP and conjugated polymers with similar properties.

For the polythiophene POMeOPT, the charge photogeneration behavior is quite different from that of MeLPPP. Although the timescale of charge generation from singlet excitons is similar for the two polymers, there are several differences in the charge formation dynamics. As revealed by the electric field dependence of the charge generation yield, the exciton breaking in POMeOPT is barrierless: at zero applied external field there is appreciable charge pair formation at low excitation photon energy, and the electric field dependence of the charge formation yield is much more gradual than that for MeLPPP (Fig. 5) [18]. Despite the barrierless nature of exciton breaking in POMeOPT, excess vibrational energy deposited in the polymer through direct optical excitation or excitation annihilation does not change the charge generation yield or dynamics. Comparison of charge generation and energy transfer times (the latter obtained from time-resolved absorption and fluorescence anisotropy) shows that the two processes occur on a similar timescale, suggesting that charge generation is controlled by energy migration to sites with particularly low exciton binding energy.

Combining these results with those already available in the literature, a general picture of charge generation is beginning to emerge. The resulting

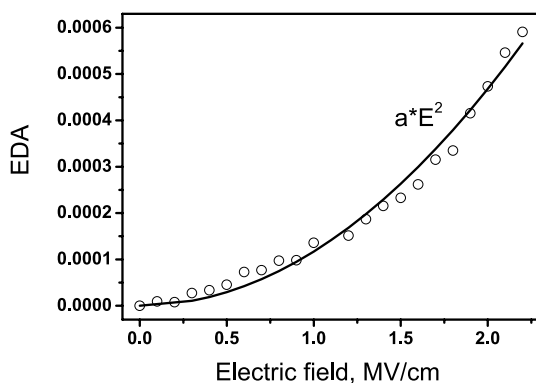


**Fig. 5** Voltage dependence of charge pair formation in POMeOPT (circles). The solid line is a parabolic fit:  $EDA = a \cdot E^2$ , where  $a = 1.17 \times 10^{-4} (\text{MV}/\text{cm})^{-2}$

scenario includes differences in polymer properties as well as different experimental conditions. The different charge generation behavior of MeLPPP and POMeOPT can be understood as being a result of the presence of sites with low exciton binding energy in POMeOPT [18]. In POMeOPT, being a flexible and disordered polymer, strong interaction between chains may give rise to aggregates or donor-acceptor structures, while this tendency is lower in the stiff ladder structure of MeLPPP. Thus, we suggest that in POMeOPT, sites with particularly low energy barriers toward charge separation are formed where there is strong interaction between polymer chains, while in MeLPPP the exciton binding energy has a finite value (several tenths of an eV) with a distribution characteristic of the random nature of the polymer. This will give rise to the following dynamical characteristics of charge photogeneration:

1. In a polymer with high exciton binding energy, the energy barrier may be overcome and charge pairs formed by applying an external electric field or by depositing sufficient ( $> 1$  eV) excess vibrational energy in the polymer, by direct optical excitation or by exciton annihilation. Charge pair generation has a threshold type of electric field dependence, signaling that a substantial energy barrier has to be overcome for breaking the exciton.
2. For a polymer with high exciton binding energy, the field-assisted charge pair generation is slow and occurs throughout the exciton lifetime with a time-dependent rate characteristic of a disordered material with a distribution of exciton binding energies and electron transfer times. With substantial excess vibrational energy a component of ultrafast ( $< 100$  fs) charge generation appears in competition with vibrational relaxation and cooling. Charge generation from hot  $S_1$  states occurs with a strongly time-dependent rate.
3. In a polymer with sites having low ( $\sim 0$  eV) exciton binding energy, charge pair generation occurs in the absence of an external electric field and applying a field increases the charge pair yield.
4. The dynamics of charge pair formation in a polymer with low barrier sites is controlled by energy migration, since the excitons have to move to a dissociation site for charge pair generation. A similar picture has previously been proposed [19], but with the difference that the dominating part of the charge generation was thought to occur during downhill energy migration. This would place charge generation on the  $\sim 1$  ps timescale, clearly different from the slow charge generation from thermalized exciton states observed here.
5. In a polymer with low barrier dissociation sites, excess vibrational energy may not increase the charge pair yield. This puzzling behavior may be understood as a result of weak excess energy dependence of the barrierless exciton dissociation and dissipation of excess energy during energy migration to dissociation sites.

It should once more be emphasized that the above picture is in an early stage of development and more results including several more polymers will certainly add other features and more details to this picture.

#### 4 Light-Induced Charge Generation in Polymer–Fullerene Blends

The generally low yield of charge photogeneration in a neat conjugated polymer means that it requires blending with an electron accepting material in order to obtain efficient materials for light-to-charge conversion devices. Mixtures of various polymers and fullerene derivatives have been explored and solar cells constructed with light-to-charge conversion efficiencies of 2–3%. In order to obtain more efficient materials the factors limiting conversion efficiency have to be better understood. In this work, time-resolved spectroscopy is a powerful tool since it may provide direct insight into the processes of charge photogeneration, formation of free mobile charges, and charge recombination. We have studied these processes in a low-bandgap polyfluorene/fullerene (APFO3/PCBM) blend [20] and find that charge generation is very fast ( $< 100$  fs, see Fig. 6), in analogy with what has been found previously for other polymer/PCBM blends [21]. Charge separation into free mobile charges then occurs on the 10–100-ps timescale with a morphology-dependent yield. Geminate and nongeminate charge recombination occurs on a nanosecond and slower timescale [20]. Nongeminate recombination is ex-

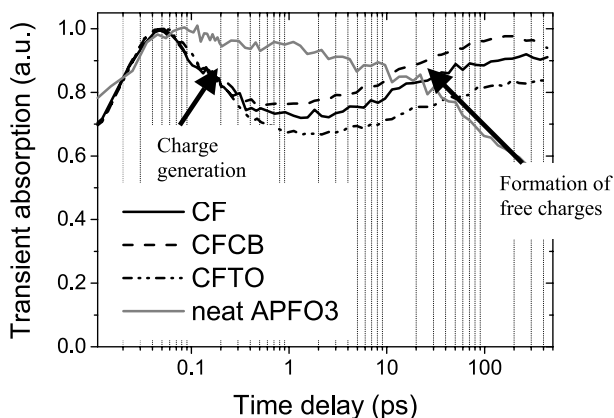


**Fig. 6** Transient absorption kinetics for solar cell blends cast from mixtures of different solvents (chloroform = CF, chlorobenzene = CB, toluene = TO) and neat APFO3 measured at an excitation intensity of  $1.4 \times 10^{13}$  ph/cm<sup>2</sup>. The probing wavelength is 1000 nm corresponding to the spectral region of excited-state absorption and photoinduced absorption by charge-separated species. The time delay axis is logarithmic

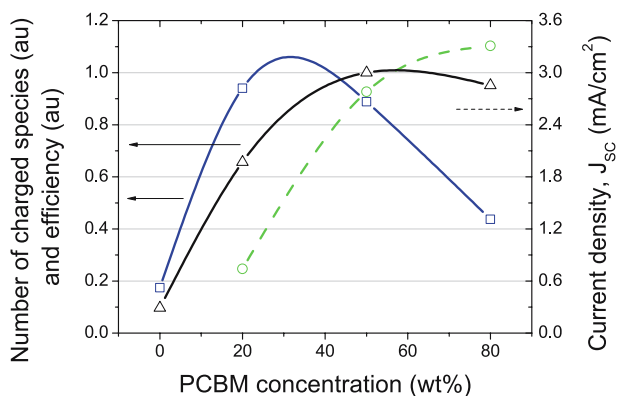


**Fig. 7** Number of charged species generated (□), charge formation efficiency (Δ), and the short circuit current density  $J_{SC}$  (○-). The data points are connected via an arbitrary function

citation intensity dependent and becomes quite fast (nanoseconds) at higher intensities. We could also show that optimal charge formation is obtained with 20–50 wt % PCBM as illustrated by the results in Fig. 7 [22]. This is in contrast to the maximum short circuit current density obtained at ~80 wt % PCBM, as determined by steady-state current density–voltage characterization. This suggests that the solar cell performance of these interpenetrating polymer networks containing PCBM is limited by charge transport rather than by formation of charges.

**Acknowledgements** This work was financed by the Strategic Research Foundation SSF, the Swedish Research Council, the K&A Wallenberg Foundation, and the Crafoord Foundation.

## References

1. Miranda PB, Moses D, Heeger AJ (2001) *Synth Met* 119:619
2. Moses D, Wang J, Heeger AJ, Kirova N, Brazovski S (2002) *Synth Met* 125:93
3. Bäessler H, Arkhipov VI, Emelianova EV, Gerhard A, Hayer A, Im C, Rissler J (2003) *Synth Met* 135–136:377
4. van der Horst JW, Bobbert PA, Pasveer WF, Michels MAJ, Brocks G, Kelly PJ (2002) *Comput Phys Commun* 147:331
5. Schweitzer B, Bäessler H (2000) *Synth Met* 109:1
6. Gulbinas V, Zaushitsin Y, Hertel D, Sundström V, Bäessler H, Yartsev A (2002) *Phys Rev Lett* 89:7401
7. Grage MML, Wood P, Ruseckas A, Pullerits T, Mitchell W, Burn PL, Samuel IDW, Sundström V (2003) *J Chem Phys* 118:7644
8. Grage MML, Pullerits T, Ruseckas A, Theander M, Inganäs O, Sundström V (2001) *Chem Phys Lett* 339:96

9. Grage MML, Zaushitsyn Y, Yartsev AP, Chachisvilis M, Sundström V, Pullerits T (2003) *Phys Rev B* 67:5207
10. Ruseckas A, Theander M, Valkunas L, Andersson MR, Inganäs O, Sundström V (1998) *J Lumin* 76-77:474
11. Westenhoff S, Daniel C, Friend RH, Silva C, Sundström V, Yartsev A (2005) *J Chem Phys* 122:094903
12. Ruseckas A, Namdas E, Ganguly T, Theander M, Svensson M, Andersson MR, Inganäs O, Sundström V (2001) *J Phys Chem* 105:7624
13. Ruseckas A, Namdas E, Theander M, Svensson M, Zigmantas D, Yartsev AP, Andersson MR, Inganäs O, Sundström V (2001) *Photochem Photobiol* 144:3
14. Arkhipov VI, Emelianova EV, Bäessler H (1999) *Phys Rev Lett* 82:1321
15. Geacintov NE, Pope M (1965) *J Chem Phys* 47:1194
16. Jortner J (1968) *Phys Rev Lett* 20:244
17. Gulbinas V, Zaushitsyn Y, Bäessler H, Yartsev AP, Sundström V (2003) *Phys Rev B* 70:5215
18. Zaushitsyn Y, Gulbinas V, Zigmantas D, Fengling Z, Inganäs O, Yartsev A, Sundström V (2004) *Phys Rev B* 70:075202
19. Graupner W, Cerullo C, Lanzani G, Nisoli M, List EJW, Leising G, De Silvestri S (1998) *Phys Rev Lett* 81:3259
20. Zhang F, Björström C, Jespersen KG, Svensson M, Andersson MR, Yartsev A, Sundström V, Magnusson K, Moons E, Inganäs O (2006) *Adv Funct Mater* 16:667
21. Brabec CJ, Zerza G, Cerullo G, De Silvestri S, Luzzati S, Hummelen JC, Sariciftci NS (2003) *Chem Phys Lett* 340:232
22. Jespersen KG, Zhang F, Sundström V, Yartsev A, Inganäs O (2006) *Organ Electron* 7:235

# Resonance Energy Transfer in Biophysics: Formalisms and Application to Membrane Model Systems

Luís M.S. Loura<sup>1,2</sup> (✉) · Manuel Prieto<sup>3</sup>

<sup>1</sup>Faculdade de Farmácia, Universidade de Coimbra, Rua do Norte, 3000-295 Coimbra, Portugal

<sup>2</sup>Centro de Química de Évora, Rua Romão Ramalho 59, 7000-671 Évora, Portugal  
*lloura@ff.uc.pt*

<sup>3</sup>Centro de Química-Física Molecular, Instituto Superior Técnico, Av. Rovisco Pais, 1049-001 Lisboa, Portugal

1	Introduction . . . . .	301
2	Intramolecular RET . . . . .	302
3	RET in Infinite Planar or Quasi-2D Geometry (Uniform Probe Distribution) . . . . .	303
4	Considerations Regarding Homotransfer . . . . .	305
5	Non-uniform Probe Distribution . . . . .	306
6	Applications . . . . .	310
6.1	One-Component Lipid Bilayers . . . . .	310
6.2	Two-Component Lipid Bilayers . . . . .	311
6.3	Three-Component Lipid Bilayers (Raft Models) . . . . .	312
6.4	Lipid-Protein/Lipid-Peptide Interaction . . . . .	313
6.5	Lipid-DNA Interaction . . . . .	317
7	Conclusions . . . . .	318
	References . . . . .	320

**Abstract** Useful models for resonance energy transfer (RET) are reviewed for several geometries relevant to membranes (planar, bilayer, multilayer) and uniform donor and acceptor probe distribution. Extensions for non-uniform distribution of fluorophores are presented and discussed. Selected examples of quantitative applications of RET to these systems are described. It is illustrated how information about lipid phase separation (phase composition, domain size, partition coefficients, kinetics of lipid demixing) lipid-peptide (domain induction/membrane aggregation), lipid-protein (lipid selectivity in the annular region) and lipid-DNA (lipoplex structural characterization) interactions can be recovered from time-resolved RET data.

**Keywords** Energy transfer · Lipid domains · Rafts

**Abbreviations**

$A_i$	Relative amount of donor in phase $i$
BOBO-1	Benzothiazolium, 2,2'-[1,3-propanediyl]bis[(dimethyliminio)-3,1-propanediyl-1(4 <i>H</i> )-pyridinyl-4-ylidenemethylidene]bis[3-methyl]-tetraiodide
BODIPY	<i>n</i> -(4,4-Difluoro-5,7-dimethyl-4-bora-3a,4a-diaza- <i>s</i> -indacene-3-yl)methyl iodoacetamide
BODIPY-PC	2-(4,4-Difluoro-5-octyl-4-bora-3a,4a-diaza- <i>s</i> -indacene-3-pentanoyl)-1-hexadecanoyl PC
$C$	Dimensionless acceptor concentration (Eq. 8)
$C_i$	Same as $C$ , for phase $i$
CTB	Cholera toxin subunit B
$d$	Distance (donor-acceptor)
DiIC <sub>1</sub> (7)	1,1',3,3,3',3'-Hexamethylindotricarbocyanine
DiIC <sub>12</sub> (3)	1,1'-Didodecyl-3,3,3',3'-tetramethylindocarbocyanine
DiIC <sub>18</sub> (3)	1,1'-Dioctadecyl-3,3,3',3'-tetramethylindocarbocyanine
DOTAP	1,2-Dioleoyl-3-trimethylammonium-propane
$E$	RET efficiency
$f(C)$	Acceptor concentration distribution function
$F(l,t,R_e)$	Auxiliary function in $i_{DA,trans}(t)$ (Eq. 10)
GPI	Glycosylphosphatidylinositol
$I(\lambda)$	Normalized donor emission spectrum
$i_D(t)$	Donor decays in absence of acceptor
$i_{D0}(t)$	DNA probe decay inside free DNA (Eq. 20)
$i_{DA}(t)$	Donor decays in presence of acceptor
$i_{DA,cis}(t)$	Donor decays in presence of acceptor, planar geometry
$i_{DA,trans}(t)$	Donor decays in presence of acceptor, bilayer geometry
IAEDANS	<i>n</i> -(Iodoacetyl)aminoethyl-1-sulfonaphthylamine
$k$	$2/R_0^2$
$k_D$	Intrinsic donor decay rate coefficient
$K_{pD}$	Partition coefficient
$K_S$	Relative association (selectivity) constant
$k_T$	RET rate coefficient
$l$	Distance between planes of donors and acceptors in $i_{DA,trans}(t)$
$l_1, l_2$	Same as $l$ , for double- <i>trans</i> geometry
ld	Liquid disordered phase
lo	Liquid ordered phase
LUV	Large unilamellar vesicles
Lys	Lysine
mcp	Major coat protein
$n$	Refractive index
$n_2$	Number of acceptors per unit area
$n_{acceptor}$	Concentration of acceptor
$n_{lipid}$	Concentration of unlabeled lipid
$N_A$	Number of acceptors surrounding a given donor
NBD	<i>N</i> -(7-Nitrobenz-2-oxa-1,3-diazol-4-yl)
NBD-cholesterol	22-NBD-23,24-bisnor-5-colen-3 $\beta$ -ol
ORB	Octadecylrhodamine B
PA	Phosphatidic acid
PC	Phosphatidylcholine



PE	Phosphatidylethanolamine
PG	Phosphatidylglycerol
PS	Phosphatidylserine
PSM	Palmitoylsphingomyelin
Rh	<i>N</i> -(Lissamine-rhodamine B)
$\langle r \rangle$	Steady-state fluorescence anisotropy
$r_1$	Anisotropy of the directly excited molecule
$r_2$	Anisotropy of the molecule excited by RET
$R$	Distance (donor–acceptor)
$R_e$	Distance of closest approach between donor and acceptor molecules
$R_i$	Distance (donor– <i>i</i> th acceptor)
RET	Resonance energy transfer
$R_0$	Förster critical distance
$T_m$	Main transition temperature
$x_{\text{chol}}$	Cholesterol mole fraction
$X_\beta$	lo phase fraction
$\varepsilon(\lambda)$	Acceptor molar absorption spectrum
$\Phi_D$	Donor quantum yield in the absence of acceptor
$\gamma$	Incomplete gamma function, fraction of free DNA
$\Gamma$	Complete gamma function
$\kappa^2$	Orientation factor
$\lambda$	Wavelength
$\mu$	Probability of occupation of annular site
$\rho_{\text{annular}}$	Probability of RET to acceptors in the annular region
$\rho_{\text{random}}$	Probability of RET to acceptors in the bulk
$\tau$	Lifetime of excited state
$\tau_0$	Lifetime of excited state of donor in the absence of acceptor
$\tau_i$	Same as $\tau_0$ , for phase <i>i</i>

## 1

### Introduction

Spectroscopic techniques in general, and fluorescence spectroscopy in particular, have become indispensable tools in the study of micro-heterogeneous media. At the present time there is a very fast evolution of microscopy techniques, both optical or related to the several variants of atomic force. However, their resolution is still unable to reveal nanoscopic details. From the measurement of properties such as the excitation or emission spectra, fluorescence lifetimes and fluorescence anisotropy, information regarding the molecular conformation and dynamics can be obtained [1]. Despite the usefulness of these parameters in the study of the immediate vicinity of the studied fluorophore, they are not informative regarding the spatial organization features concerning the embedding medium. Resonance energy transfer (RET), however, is a photophysical process that relies upon a distance-dependent dipole–dipole interaction between different molecules, and is a very useful tool for structural characterization (distances, topology)

in the 1–10 nm scale. This chapter reviews the formalisms of RET for different possibilities of acceptor probe distribution geometry, and illustrates them with quantitative applications to the study of model systems of biological membranes. These quasi-2D media are chosen because: (i) the study of biological membranes, namely the organization of multicomponent bilayers (lipid membranes with reconstituted proteins, or lipid mixtures such as raft models), is a very active field in biophysics and biochemistry and, (ii) upon varying the membrane composition (both lipid and peptide/protein components), the membrane preparation procedure and the studied chromophores, many geometrical arrangements can be materialized. Emphasis is given on the data analysis methodologies and the information that can be gained through them. Outside the scope of this review is RET in the rapid diffusion limit.

## 2 Intramolecular RET

RET between donor–acceptor pairs for which the donor–acceptor distance is the same, such as verified in a solution of a two-chromophore species, is often termed “intramolecular” RET. For this process to be efficient, there must be spectral overlap between emission of one of the chromophores, which acts as donor, and absorption of the other, which acts as acceptor. The rate constant of energy transfer between a donor molecule, with fluorescence lifetime  $\tau$ , and an acceptor molecule, separated by a distance  $R$ , is given by [2]:

$$k_T = \frac{1}{\tau} \left( \frac{R_0}{R} \right)^6, \quad (1)$$

where  $R_0$  is the critical distance, which can be calculated from

$$R_0 = 0.2108 \left[ \kappa^2 \Phi_D n^{-4} \int_0^\infty I(\lambda) \varepsilon(\lambda) \lambda^4 d\lambda \right]^{1/6}, \quad (2)$$

where, in turn,  $\kappa^2$  is the orientation factor (see [3] for a detailed discussion),  $\Phi_D$  is the donor quantum yield in the absence of acceptor,  $n$  is the refractive index,  $\lambda$  is the wavelength,  $I(\lambda)$  is the normalized donor emission spectrum, and  $\varepsilon(\lambda)$  is the acceptor molar absorption spectrum. As is clear from Eq. 2,  $R_0$  can be calculated from spectroscopic data. If the  $\lambda$  units used in Eq. 2 are nm, then the calculated  $R_0$  has Å units. A quantification of the extent of RET is given by the RET efficiency,  $E$ , which is defined by:

$$E = 1 - \int_0^\infty i_{DA}(t) dt / \int_0^\infty i_D(t) dt. \quad (3)$$

In this equation,  $i_D(t)$  and  $i_{DA}(t)$  are the donor decays in absence and presence of acceptor (respectively). The effect of RET on donor fluorescence is the reduction of lifetime and quantum yield (note that, in this simple case, the donor decay law remains exponential, albeit faster than in the absence of acceptor). The relationship between the donor lifetime in absence and presence of acceptor fluorophore ( $\tau_0$  and  $\tau$ , respectively) is given by:

$$E = 1 - \tau/\tau_0 = R_0^6 / (R^6 + R_0^6) , \quad (4)$$

where  $R$  is the donor–acceptor separation. An expression identical to Eq. 4 can be written for the fluorescence quantum yield. From both steady-state and time-resolved data,  $R$  is easily computed. This is the basis of the use of intramolecular RET as a “spectroscopic ruler” [4].

A slightly more complex situation is verified if there is an ensemble of donor–acceptor pairs with separation distance not fixed, resulting e.g. from flexibility of the molecule to which they are attached and/or a distribution of macromolecule conformations. In this case, formalisms invoking a donor–acceptor distance distribution can be used to interpret the now-complex decay data. These are out of the scope of this chapter, but a good review is given in [1].

### 3

#### RET in Infinite Planar or Quasi-2D Geometry (Uniform Probe Distribution)

Now let us consider the more complex situation of each donor having more than one acceptor within transfer distance. If a given donor molecule is now surrounded by  $N_A$  acceptors ( $R_i$  being the distance between the donor and acceptor molecule  $i$ ) and  $R_0$  is the same for every donor–acceptor pair, then  $i_{DA}(t)$  is given by:

$$i_{DA}(t) = \exp\left(-\frac{t}{\tau_0}\right) \prod_{i=1}^{N_A} \exp\left[\left(-\frac{t}{\tau_0}\right) \left(\frac{R_0}{R_i}\right)^6\right]. \quad (5)$$

This equation is useful for numeric simulation of decay laws for systems where analytical solutions are too complex, i.e. restricted geometries or non-uniform probe distribution (see [5] for an example of the latter). Basically, the process consists of selecting a donor and computing its interaction with all the acceptors at their different distances, and then repeating the process for all the donors in order to obtain an ensemble average value for all the system. However, in order for this equation to have practical use in data analysis, one must calculate the product on the right, which can be replaced by integration assuming a random distribution of acceptors. This procedure is also valid if there is a distribution of equivalent donors. The result for an infinite two-dimensional system (or any system with donors and acceptors in

the same plane, i.e. *cis* transfer), assuming that: (i) there is no homotransfer between donors, (ii) the fraction of excited acceptors is negligible, and (iii) translational diffusion is negligible, is [6, 7]:

$$i_{\text{DA},\text{cis}}(t) = \exp\left(-\frac{t}{\tau_0}\right) \exp\left\{-\pi R_0^2 n_2 \gamma\left[\frac{2}{3}, \left(\frac{R_0}{R_e}\right)^6 \left(\frac{t}{\tau_0}\right)\right] \left(\frac{t}{\tau_0}\right)^{1/3}\right\} \\ \cdot \exp\left\{\pi R_e^2 n_2 \left(1 - \exp\left[-\left(\frac{R_0}{R_e}\right)^6 \left(\frac{t}{\tau_0}\right)\right]\right)\right\}, \quad (6)$$

where  $n_2$  is the number of acceptors per unit area,  $\gamma$  is the incomplete gamma function, and  $R_e$  is the distance of closest approach between donor and acceptor molecules. In the case that  $R_e \ll R_0$  (in practice, if  $R_e < R_0/4$ ), the incomplete gamma term in Eq. 6 can be replaced by  $\Gamma(2/3)$  (where  $\Gamma$  is now the complete gamma function), the last exponential term in that equation can be omitted, and Eq. 6 reduces to the much simpler form:

$$i_{\text{DA},\text{cis}}(t) = \exp\left(-t/\tau_0 - C(t/\tau_0)^{1/3}\right), \quad (7)$$

where

$$C = \Gamma(2/3) n \pi R_0^2. \quad (8)$$

Frequently, donors and acceptors are located in parallel planes separated by a distance  $l$ , as a result of different transverse membrane locations. In this case, the result for the donor decay law is [8]:

$$i_{\text{DA},\text{trans}}(t) = \exp\left(-t/\tau_0 - kCl^2 F(l, t, R_e)\right), \quad (9)$$

where

$$F(l, t, R_e) = \int_0^{\frac{l}{\sqrt{l^2 + R_e^2}}} \frac{1 - \exp\left(\left(-t/\tau_0\right) \left(R_0/l\right)^6 \alpha^6\right)}{\alpha^3} d\alpha \quad (10)$$

and  $k = 2/R_0^2$ . If  $R_e \ll R_0$ , the upper limit in the integral in Eq. 10 becomes 1.

If each donor can transfer energy to two distinct planes of acceptors, then  $i_{\text{DA}}(t)$  is obtained by multiplying the intrinsic donor decay by the survival probability terms pertinent to each acceptor plane. For example, if a donor located inside the membrane is able to transfer energy to acceptors located in both lipid/water interfaces, in planes which are separated from that of the donor by  $l_1$  and  $l_2$  (and  $R_{e1}$  denotes the exclusion radius for donors and the  $i$ th plane of acceptors,  $i = 1, 2$ ), the overall donor decay is given by:

$$i_{\text{DA}}(t) = \exp\left[-t/\tau_0 - kC \left(l_1^2 F(l_1, t, R_{e1}) + l_2^2 F(l_2, t, R_{e2})\right)\right]. \quad (11)$$

## 4 Considerations Regarding Homotransfer

RET can occur between like fluorophores, provided that there is overlap between emission and absorption of the fluorescent species. Unlike RET between different fluorophores (heterotransfer), homotransfer does not lead to a reduction in donor fluorescence intensity or lifetime, because the donor excited state population is not diminished during the act of transfer. In practice, the sole observable that reflects the phenomenon is fluorescence anisotropy [1], which is reduced as a consequence of homotransfer. Measurement of fluorescence anisotropy requires polarizers and, because these lead to a considerable reduction in the detected emission, often a larger amount of fluorophore (relative to that which would be used in an intensity measurement) is needed for a given precision. When instrumentation is not a problem, the decrease in anisotropy is quite clear. For example, the steady-state anisotropy for a dimer of two identical static molecules with energy migration between them is given by:

$$\langle r \rangle = \frac{1 + (R_0/R)^6}{1 + 2(R_0/R)^6} r_1 + \frac{1 + (R_0/R)^6}{1 + 2(R_0/R)^6} r_2, \quad (12)$$

in which  $R$  is the distance between the molecules,  $r_1$  is the anisotropy of the directly excited molecule, and  $r_2$  is the anisotropy of the molecule excited by RET. The latter is usually very small (less than 4% of the former; [9]) and as such often neglected (e.g. [10]). Taking  $r_2 = 0$ , if the two molecules are separated by distance  $R = R_0$ , the measured anisotropy will only be 2/3 of that of the monomer, which is a significant decrease.

Despite having an obvious advantage of only requiring a single fluorophore, the use of homotransfer is more restricted than that of heterotransfer. The rationalization of the extent of depolarization due to homotransfer is more complicated than that of quenching due to heterotransfer, because: (i) there is the possibility of back-transfer to the directly excited donor, or transfer to any donor, eventually involving a large number of transfer steps, and (ii) fluorescence anisotropy being the relevant observable, in addition to RET, another source of depolarization is fluorophore rotation. If rotation and RET occur in the same timescale, the two phenomena are coupled. This is why most theories for homotransfer assume static dipoles (see [11, 12] for theory reviews and discussion), even the user-friendly numerical simulations of Snyder and Freire [13]. In some works, the experimental anisotropy decay is assumed to be the product of a rotational depolarization term by a RET depolarization term obtained from a static-dipole theory (e.g. [14]) and, therefore, the RET rate can be recovered e.g. from the faster component in the anisotropy decay [15, 16]. It must be understood that this independence of rotation and transfer constitutes an approximation (unless the time scales for the two phenomena are very distinct), whose severity is not easy

to ascertain. The coupling of rotation and RET in the measured anisotropy is therefore the main obstacle to quantitative data analysis of homotransfer.

## 5 Non-uniform Probe Distribution

The kinetics of RET become considerably more complex if probe distribution is not uniform. Efforts have been developed to obtain general exact models for arbitrary probe distributions for systems with planar, spherical or cylindrical symmetry [17–19]. However, these symmetry restrictions are sometimes not met in membrane systems (e.g. in the case of nanoscale phase separation), for which more approximate models are the only feasible option. In other, more symmetrical geometries (e.g. RET from a cylindrical protein with donor on the cylinder axis), models specifically derived for the recovery of a physical parameter of the system (e.g. distance between the protein fluorophore and the membrane surface, or protein–lipid selectivity constant) have been applied successfully. Some are reviewed below.

Non-uniform component distribution and phase separation are common occurrences in lipid mixtures. The molecules that bear the donor and acceptor fluorophores in a RET experiment in such a system will naturally have non-uniform distributions, following their “preference” or partition between the coexisting phase domains. Let us consider that there are only two phases or types of domains present (the most common experimental situation). If these are sufficiently large to be infinite in the RET scale (i.e., complications resulting from RET involving molecules in different domains, or boundary effects, are negligible; this is the case if the domains are larger than  $\sim 5\text{--}10R_0$ ), then the donor decay law is simply a linear combination of the hypothetical decay laws in each phase, weighed by the relative amount of donor ( $A_i$ ) in each phase [20]:

$$i_{\text{DA, phase separation}}(t) = A_1 i_{\text{DA, phase1}}(t) + A_2 i_{\text{DA, phase2}}(t), \quad (13)$$

$i_{\text{DA}}(t)$  within each phase is given e.g. by Eqs. 6, 9, or 11, for *cis*, *trans*, or double-*trans* geometries, respectively. Note that usually the donor lifetimes are different in the two phases, as are the acceptor surface concentrations (and possibly also the distances of the donor and acceptor planes, for *trans* or double-*trans* geometries) The decay of donor in presence of acceptor is globally analyzed together with that in the absence of acceptor:

$$i_{\text{D}}(t) = A_1 \exp(-t/\tau_1) + A_2 \exp(-t/\tau_2), \quad (14)$$

where  $\tau_1$  and  $\tau_2$  are the donor lifetimes in each phase. The recovered parameters are usually  $\tau_1$ ,  $\tau_2$ ,  $A_2/A_1$  (from which the donor partition coefficient  $K_{\text{pD}}$  is obtained), and the acceptor concentrations in the two phases,  $C_1$  and  $C_2$  (from which the acceptor partition coefficient  $K_{\text{pA}}$  is obtained) [20].

A particular case of this formalism is the “isolated donors” situation, which corresponds to  $C_2 = 0$  [21].

Being strictly valid for infinite phase separation, this model can be applied to nanoscale phase separation; in this case, the recovered acceptor partition coefficient (“RET”  $K_{pA}$ ) will not be equal to the true coefficient recovered from independent (acceptor fluorescence intensity, anisotropy or lifetime) measurements (“non-RET”  $K_{pA}$ ), and is affected (being closer to unity than the non-RET value) by the fact that donors in one phase are sensitive to acceptors in the other. This fact contains important information regarding the domain size, as seen in Sects. 6.2 and 6.3.

The phase separation model of Eq. 13 assumes that there are two non-equivalent donor populations, one surrounded by acceptor concentration  $C_1$ , and the other sensing an acceptor concentration  $C_2$ . One could consider a more general formalism, taking into account a continuous probability function  $f(C)$  of having donors with a mean local concentration  $C$  of acceptors in their surroundings, rather than a discrete function [22]. In this model, the RET donor decay laws expressed by Eqs. 6 or 9 (for *cis* or *trans* geometry, respectively) are locally valid and the decay law is expressed as a Fredholm integral equation of the first kind regarding recovery of the function  $f(C)$ . For example, for *cis* RET geometry (and assuming that all donors have the same lifetime in absence of acceptor), one would have:

$$i_{DA}(t) = \int_0^{\infty} f(C) \exp(-t/\tau_0 - C(t/\tau_0)^{1/3}) dC. \quad (15)$$

Although it constitutes a potentially useful formalism, there are two main problems with the mean concentration model. First, the recovery of  $f(C)$  leads to an ill-conditioned problem that requires special numerical techniques or rigorous acceptance criteria for the solutions [5, 22]. Second (and perhaps most important), it was pointed out [17] that in the derivation of Eq. 15 it is assumed that each donor is surrounded by a uniform concentration of acceptors, and for this equation to be valid, the local acceptor distributions must be uniform in the RET scale ( $\sim 2R_0$ ), that is, the acceptor non-uniform distribution profiles must be smooth.

Of course, a way to test the validity of an analytical model is to carry out numerical simulations. These are also useful when analytical derivation of the decay law is too complex, due to restricted geometry of the system or a complicated acceptor distribution function. One proceeds as follows:

- i) Randomly generate coordinates for a large number of donor and acceptor molecules in a geometrical arrangement simulating the system of interest
- ii) Using these coordinates, evaluate the excitation survival probability of each donor using Eq. 5
- iii) Calculate, for each time interval, the overall excitation survival probability of the donor population by averaging over the ensemble

Snyder and Freire [13] calculated RET efficiency curves (and concentration depolarization ratios for homotransfer) as a function of acceptor concentration in this way for uniform and non-uniform (resulting from a heuristic potential function) probe distribution, and fitted their numerical results to simple analytical expressions, which can be conveniently used to analyze experimental data.

A special case of non-uniform distribution that has generated interest in membrane studies is the preferential location of certain lipids around a protein (in the so-called annular region). In a typical experiment, a protein fluorophore (extrinsic covalently-linked probe, tryptophan, tyrosine) acts as donor and a fluorescently labeled lipid acts as acceptor. These kind of experiments have been carried out now for some three decades. In an early work, Yguerabide and coworkers developed a model to calculate the transverse distance between the membrane and special protein sites (where the donor fluorophores reside [23]), assuming a cylindrical protein with the donor on the axis (but uniform distribution of acceptors), which was later extended by this author to non-axially located fluorophores [24].

Gutierrez-Merino derived approximate analytical expressions for the average rate of RET ( $\langle k_T \rangle$ ) in membranes undergoing phase separation or protein aggregation [25, 26] and extended this formalism to the study of protein–lipid selectivity [27]. His model has proved useful to the study of the lipid annulus around the oligomeric acetylcholine receptor [28, 29]. However, there are some limitations to the model, namely, the simplification that underlies the formalism, which consists of considering RET only to neighboring acceptor molecules. On the other hand, as the experimental observable is the average RET efficiency, given by:

$$\langle E \rangle = \langle k_T / (k_T + k_D) \rangle, \quad (16)$$

where  $k_D$  is the donor intrinsic decay rate coefficient, the relation with  $\langle k_T \rangle$  is not straightforward. It is proposed that if the setting of experimental conditions is such that  $\langle E \rangle$  is low (namely,  $\langle k_T \rangle$  is much smaller than  $k_D$ ), then  $\langle E \rangle \approx \langle k_T \rangle / k_D$  [25]. However, low accurate RET efficiencies are difficult to measure experimentally.

In a recent study [30], RET from a protein-located donor (in the center of the bilayer) to a labeled-phospholipid acceptor, with fluorophores located on both lipid/water interfaces, was modeled assuming a single layer of annular lipid. The model assumes two populations of energy transfer acceptors, one located in the single annular lipid shell around the protein and the other outside the shell. The donor fluorescence decay curve has RET contributions from both populations:

$$i_{DA}(t) = i_D(t) \rho_{\text{annular}}(t) \rho_{\text{random}}(t). \quad (17)$$

Here  $i_D$  and  $i_{DA}$  are the donor fluorescence decay in the absence and presence of acceptors, respectively, and  $\rho_{\text{annular}}$  and  $\rho_{\text{random}}$  are the RET contributions



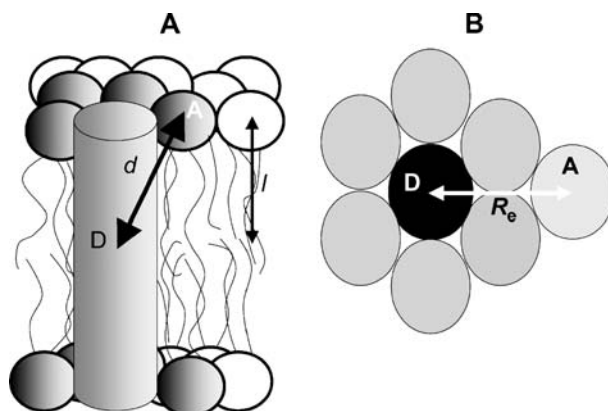


**Fig. 1** Molecular model for the RET analysis (**a** side view; **b** top view). Protein–lipid organization presents a hexagonal geometry. Donor fluorophore ( $D$ ) from the mutant protein is located in the center of the bilayer, whereas the acceptors ( $A$ ) are distributed in the bilayer surface. Two different environments are available for the labeled lipids (acceptors): the annular shell surrounding the protein, and the bulk lipid. Energy transfer to acceptors in direct contact with the protein has a rate coefficient dependent on the distance ( $d$ ) between donor and annular acceptor (Eq. 19).  $R_e$  is the distance of closest approach between donor and acceptor molecules and  $l$  is the transverse distance between the donor and acceptor planes. Energy transfer toward acceptors in the bulk lipid is given by Eq. 9 (see text for details). Reprinted with permission from [30]. © 2004 Biophysical Society

arising from energy transfer to annular labeled lipids and to uniformly distributed labeled lipids outside the annular shell, respectively. If the donor is located at the center of the bilayer and the acceptors are distributed in both bilayer leaflets, all at the same depth in the membrane (or the lipid/water interface), we can assume that the energy transfer to each of these acceptors is described by the rate constant given by Eq. 1, with  $R$  replaced by  $d$  as defined in Fig. 1a.

Considering an hexagonal type geometry for the protein–lipid arrangement (Fig. 1), each donor protein will be surrounded by 12 annular lipids. In bilayers composed of both labeled and unlabeled phospholipids, these 12 sites will be available for both of them. The probability  $\mu$  of one of these sites being occupied by labeled phospholipid is given by:

$$\mu = K_S \frac{n_{\text{acceptor}}}{n_{\text{acceptor}} + n_{\text{lipid}}} . \quad (18)$$

Here,  $n_{\text{acceptor}}$  is the concentration of labeled lipid, and  $n_{\text{lipid}}$  is the concentration of unlabeled lipid.  $K_S$  is the relative association constant, which reports the relative affinity of the labeled and unlabeled phospholipids. Using a binomial distribution, the probability of each occupation number (0–12 sites occupied simultaneously by labeled lipid), and finally the RET contribution

arising from energy transfer to annular lipids is computed:

$$\rho_{\text{annular}}(t) = \sum_{i=0}^{12} \exp(-ik_{\text{T}}t) \frac{12!}{(12-i)!i!} \mu^i (1-\mu)^{12-i}. \quad (19)$$

The RET contribution from acceptors uniformly distributed outside the annular region in two different planes at the same distance to the donor plane (from the center of the bilayer to both leaflets) is given by the latter term of Eq. 9, in which  $C$  must be corrected for the presence of labeled lipid molecules in the annular region, which therefore are not part of the uniformly distributed acceptors pool.

## 6 Applications

In this section, we illustrate the formalisms described above with selected examples from our recent work, for different types of membrane systems.

### 6.1

#### One-Component Lipid Bilayers

RET from octadecylrhodamine B (ORB) to 1,1',3,3',3'-hexamethylindotri-carbocyanine (DiIC<sub>1</sub>(7)) in fluid 16 : 0,16 : 0 phosphatidylcholine (PC) large unilamellar vesicles (LUV) [31] ( $m : n$  denotes a chain with  $m$  carbon atoms and  $n$  double bonds) was measured in both steady-state and time-resolved conditions. Both probes were incorporated in the outer LUV leaflet by an injection procedure, and neither of them underwent significant translocation to the inner leaflet. Hence, a planar RET geometry was expected. In this study, a modified Eq. 7 was derived for biexponentially decaying donors, and the decays were globally analyzed, with linkage of donor lifetimes and pre-exponential ratio. A linear dependence of the recovered  $C$  parameter as a function of acceptor concentration was verified, as expected from Eq. 8. However, analysis of the decays for the same system but below the main transition temperature ( $T_{\text{m}}$ ) was not successful, pointing to probe aggregation in the gel phase, possibly on line defects in the gel phase structure. In a later publication [32], the gel phase results were successfully rationalized with the mean concentration model (together with data obtained using the lipid analogs  $N$ -(7-nitrobenz-2-oxa-1,3-diazol-4-yl) (NBD)-16 : 0,16 : 0 phosphatidylethanolamine (PE) as donor and  $N$ -(lissamine-rhodamine B) (Rh)-16 : 0,16 : 0 PE as acceptor, in the same lipid system), supporting this hypothesis. This analysis methodology was also used in the RET study of interactions between the fluorescent sterol dehydroergosterol and the polyene antibiotic

filipin in small unilamellar vesicles of 16 : 0,16 : 0 PC [33], revealing the formation of both filipin–sterol and filipin–filipin aggregates.

## 6.2

### Two-Component Lipid Bilayers

Two-component lipid systems often have ranges of pressure and temperature for which there is coexistence of two lipid phases. Whereas Eq. 13 may be applied to all biphasic systems, experimentally one can distinguish between gel/fluid and fluid/fluid phase separation types. In one gel/fluid heterogeneity study [34], mixtures of 12 : 0,12 : 0 PC/18 : 0,18 : 0 PC, were investigated for two different temperatures and compositions inside the phase coexistence range. The short-tailed RET donor, NBD-12 : 0,12 : 0 PE, and a short-tailed RET acceptor, 1,1'-didodecil-3,3',3'-tetramethylindocarbocyanine (DiIC<sub>12</sub>(3)), were shown to prefer the fluid phase (rich in short-tailed phospholipid) by both intrinsic anisotropy, lifetime and RET measurements, in agreement with published reports. The other studied RET acceptor, long-tailed probe 1,1'-dioctadecil-3,3',3'-tetramethylindocarbocyanine (DiIC<sub>18</sub>(3)), was expected to prefer the gel (rich in long-tailed phospholipid), on account of hydrophobic matching considerations [35]. While intrinsic lifetime studies indeed indicated preferential partition of DiIC<sub>18</sub>(3) into a rigidified environment, RET analysis pointed to an increased donor-acceptor proximity as a consequence of phase separation. These apparently conflicting results were rationalized on the basis of segregation of DiIC<sub>18</sub>(3) to the gel/fluid interphase. In order that fluid-located donors sense these interphase-located acceptors, fluid domains should be small (not exceed ~10–15 nm). This work shows that membrane probes that apparently prefer the gel phase may show a non-random distribution in this medium (in agreement with the study described above for pure DPPC gel phase LUV), and tend to locate in an environment that simultaneously leads to less strict packing constraints and to favorable hydrophobic matching interactions.

A very important type of phase separation in binary lipid mixtures is liquid ordered (lo)/liquid disordered (ld) phase separation, which occurs e.g. in mixtures of some PC lipids and cholesterol. Regarding this type of heterogeneity, two studies were recently carried out in the 14 : 0,14 : 0 PC/cholesterol system. The phase diagram for this mixture has been determined [36]. The main focus was to probe the small domains using the formalisms described above. In one study [37], 22-NBD-23,24-bisnor-5-colen-3 $\beta$ -ol (NBD-cholesterol) was used as donor and ORB was used as acceptor. It was expected that NBD-cholesterol would mimic the behavior of cholesterol and partition preferably to the lo phase. However, using both steady-state fluorescence and time-resolved RET, values much less than unity were obtained for the lo/ld partition coefficients for both probes, pointing to preference for the cholesterol-poor phase. It is concluded that, in particular, NBD-cholesterol is not a suitable cholesterol ana-

log and its distribution behavior in PC/cholesterol bilayers is in fact opposite to that of cholesterol. However, additional photophysical measurements revealed that both probes aggregate in the lo phase, preventing further characterization of the lipid domain structure.

In the other study [20], NBD-14 : 0,14 : 0 PE and Rh-14 : 0,14 : 0 PE were used as donor and acceptor, respectively. Although Rh-14 : 0,14 : 0 PE prefers the ld (or  $\alpha$ ) phase, NBD-14 : 0,14 : 0 PE prefers the lo (or  $\beta$ ) phase, as determined by fluorescence intensity and anisotropy variations, respectively. Accordingly, RET efficiency decreases as a consequence of phase separation. For cholesterol mole fractions  $x_{\text{chol}} = 0.15$  and  $x_{\text{chol}} = 0.20$  (the studied samples with smaller lo phase fraction  $X_{\beta}$  in the lo/ld coexistence range), the experimental  $C_{\alpha}$  value (which would always be expected to be larger than  $C_{\beta}$ ) is smaller than expected, while the opposite is true for  $C_{\beta}$ . This, together with numerical simulations of decays in biphasic systems, suggests that in this region of the phase diagram, the lo domains, dispersed in ld phase, should be very small (of the order of magnitude of  $R_0$ , that is, a few nanometers).

### 6.3

#### Three-Component Lipid Bilayers (Raft Models)

The putative existence of lipid rafts (domains enriched in (glyco)sphingolipids, cholesterol, specific membrane proteins and glycosylphosphatidylinositol (GPI)-anchored proteins) has raised, since its proposal [38], considerable interest in the membrane biophysics community, because of their possible implication in a variety of cell processes (e.g. [39, 40]). The ternary lipid system palmitoylsphingomyelin (PSM)/palmitoyloleoylphosphatidylcholine (16 : 0,18 : 1 PC)/cholesterol is a model for lipid rafts. Previously, the phase diagram for that mixture was obtained [41] and established the composition and boundaries for lipid rafts. This allowed us to study this ternary system along a tie-line in the lo/ld coexistence range [42], similarly to the binary system study described above. This time, NBD-16 : 0,16 : 0 PE and Rh-18 : 1,18 : 1 PE were used as donor and acceptor, respectively, and were shown to prefer the lo and ld phases, respectively, from measurements of the variations of fluorescence lifetime and intensity (respectively) along the tie-line. From this, a decrease of RET efficiency was expected, and indeed observed, in the ld/lo phase coexistence range. For some samples, small amounts of raft marker ganglioside  $G_{M1}$  (and excess cholera toxin subunit B, CTB) were added. Figure 2 shows the variation of RET efficiency along the studied tie-line.

From this study, and taking into account the experimental and theoretical studies carried out previously concerning the binary system, it was concluded that: (i) the rafts on the low lo fraction range of the raft region are small (below 20 nm; this is apparent in the slow drop of RET efficiency for low  $X_{10}$ ), whereas on the other side the domains are larger (as seen from the fact that

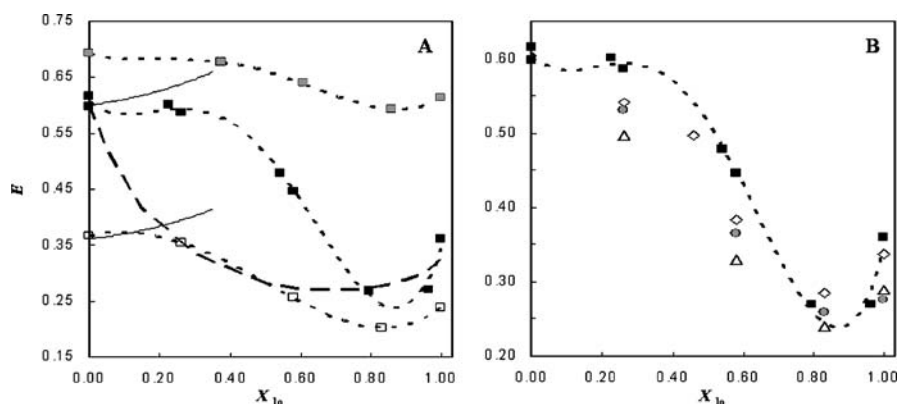


**Fig. 2** Variation of  $E$  of the donor/acceptor pair NBD-DPPE/Rh-DOPE in PSM/POPC/chol LUV, as a function of  $X_{1o}$ , along the tie-line that crosses the point of composition 1 : 1 : 1 in the phase diagram [41]. **a** Effect of acceptor concentration and comparison with the binary system DMPC/chol. The *dotted lines* are merely guides for the eye. The *thin continuous lines* are the values of  $E$  calculated for a uniform distribution of donor and acceptor molecules in pure hypothetical pure  $l_d$  phase for acceptor/lipid ratios of 1 : 200 and 1 : 500. The different data sets correspond to 1 : 200 acceptor lipid ratio (■) and 1 : 500 acceptor/lipid ratio (□). For comparison, the values for the binary system DMPC/chol along the  $l_d/l_o$  tie-line at 30 °C are also shown (■ [20]). The theoretical line for infinite phase separation (large domains) for the 1 : 200 acceptor/total lipid mole ratio is also shown (*thin broken line*). **b** Effect of raft markers. The different data sets correspond to 1 : 200 acceptor lipid ratio, with 0 mol%  $G_{M1}$  and 2 mol%  $G_{M1}$ /no CTB indistinguishable (■), 2 mol%  $G_{M1}$  and excess CTB (◇), 4 mol%  $G_{M1}$  and no CTB (●), 4 mol%  $G_{M1}$  and excess CTB (△). Reprinted with permission from [42], © 2005, with permission from Elsevier

the theoretical infinite phase regime is obtained). (ii) From the extent of the reduction in RET efficiency on the large domain region, the domains reach larger sizes in the ternary system ( $> 75 \sim 100$  nm) than in binary systems phosphatidylcholine/cholesterol (between  $\sim 20$  and  $\sim 75\text{--}100$  nm). (iii) The raft marker ganglioside  $G_{M1}$  in small amounts (and excess cholera toxin subunit B) does not affect the general phase behavior of the lipid system, but can increase the size of the rafts on the small-to-intermediate domain region (decreasing the RET efficiency relative to the values without these components). In sum, lipid–lipid interactions alone can originate lipid rafts on very different length scales, and this behavior can be probed by RET.

## 6.4

### Lipid–Protein/Lipid–Peptide Interaction

Characterization of lipid/membrane protein or peptide interactions is a fundamental area of research in biophysics, and one in which the contribution of RET is paramount. The first step is usually the determination of the extent of interaction, as measured e.g. by the peptide lipid/aqueous phase partition co-

efficient [43]. This is often achieved using fluorescence methodologies other than RET, such as variation of fluorescence intensity, lifetime or anisotropy of the protein chromophore (frequently tryptophan). However, if this cannot be realized, the increased efficiency of RET between tryptophan in the peptide and a membrane-bound acceptor probe reveals partition of the peptide to the bilayer. In this way, the extent of interaction of HIV fusion inhibitor T1249 with 16 : 0,18 : 1 PC/cholesterol vesicles could recently be established, using dehydroergosterol as acceptor, despite the fact that the fluorescence parameters of the peptide are almost unchanged in the presence of the vesicles [44].

However, the specific features of the RET interaction are usually exploited in the study of two other problems regarding lipid-protein interaction: (i) protein compartmentalization or aggregation in the bilayer; (ii) protein selectivity for certain lipid components in the annular region. The application of RET to both these questions will be illustrated with recent works using M13 major coat protein (M13 mcp). This molecule is the main protein component of the filamentous bacteriophage M13, with about 2800 copies. It contains a single hydrophobic transmembrane segment of approximately 20 amino acid residues, in addition to an amphipathic N-terminal arm and a heavily basic C-terminus with a high density of cationic lysine (Lys) residues (see [45] for a review).

The first RET study [46] was performed using protein derivatized with *n*-(iodoacetyl)aminoethyl-1-sulfonaphthylamine (IAEDANS) as donor and with *n*-(4,4-difluoro-5,7-dimethyl-4-bora-3a,4a-diaza-*s*-indacene-3-yl)methyl iodoacetamide (BODIPY) as acceptor, due to the good overlap between IAEDANS emission and BODIPY absorption ( $R_0 = 49 \text{ \AA}$ ). Both donor and acceptor chromophores were labeled in a position located near the bilayer midplane, so that the formalism for RET in a plane (Eq. 6) were used. Energy transfer studies were performed for the labeled protein incorporated in pure 18 : 1,18 : 1 PC bilayers, mixtures of zwitterionic/anionic lipids with the same acyl chains (18 : 1,18 : 1 PC/18 : 1,18 : 1 phosphatidylglycerol (PG) (80/20 mol/mol), and 18 : 1,18 : 1 PE/18 : 1,18 : 1 PG (70/30 mol/mol)), and in mixtures of two PCs with one component with a hydrophobic length significantly longer or shorter than that of the protein (respectively 22 : 1,22 : 1 PC/18 : 1,18 : 1 PC (60/40 mol/mol), and 14 : 1,14 : 1 PC/18 : 1,18 : 1 PC (60/40 mol/mol)), creating considerable hydrophobic mismatch. It was intended to study the influence of electrostatic interactions and hydrophobic mismatch in the aggregation and compartmentalization properties of M13 mcp.

The results are shown in Fig. 3. The high RET efficiencies obtained in 22 : 1,22 : 1 PC/18 : 1,18 : 1 PC and 14 : 1,14 : 1 PC/18 : 1,18 : 1 PC bilayers can only be explained by protein segregation in the bilayer or severe aggregation (Fig. 3b). In this case, additional data from fluorescence self-quenching studies helped to establish that segregation into 18 : 1,18 : 1 PC-enriched domains (rather than aggregation) is the major phenomenon in these lipid mixtures.

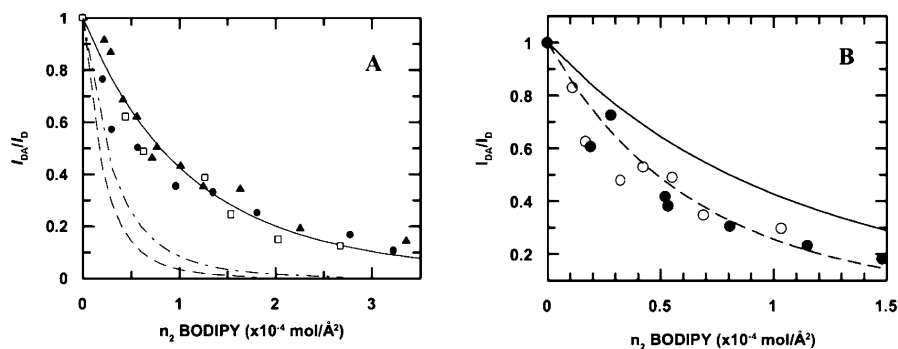


**Fig. 3** Quenching ratios ( $I_{DA}/I_D = 1 - E$ ) of IAEDANS-M13 mcp RET to BODIPY-M13 mcp. **a**  $\blacktriangle$  Experimental data for 18 : 1,18 : 1 PC,  $\bullet$  18 : 1,18 : 1 PC/18 : 1,18 : 1 PG (80/20 mol/mol), and  $\square$  18 : 1,18 : 1 PE/18 : 1,18 : 1 PG bilayers (70/30 mol/mol). *Solid line* represents theoretical expectation (Eqs. 6 and 3) for an uniform distribution of acceptors. Simulation for total co-localization of M13 coat protein considering 20% (---) and 30% (-.-.-) of the total surface area available. **b** *Solid line* represents theoretical expectation for a random distribution of acceptors. --- Simulation for a segregation of major coat protein considering 60% of the total surface area available.  $\bullet$  Experimental data for 22 : 1,22 : 1/18 : 1,18 : 1 (60/40 mol/mol).  $\circ$  Experimental data for 14 : 1,14 : 1/18 : 1,18 : 1 (60/40 mol/mol).  $I_{DA}$  and  $I_D$  were obtained by integration of donor decays. Reprinted with permission from [46]. © 2003 Biophysical Society

Although the results can be reasonably explained on the basis of protein segregation to 60% of the total bilayer area (Fig. 3b), this rationalization should be considered an oversimplification, and is presented as an illustration. Indeed, the measured efficiencies are only reporting the average BODIPY-M13 mcp surface density that each IAEDANS-labeled protein is sensing. Probably there will be M13 coat protein interacting with the mismatching phospholipids, but the majority of the proteins will be preferentially surrounded by 18 : 1,18 : 1 PC, and microdomains enriched in 18 : 1,18 : 1 PC, and M13 coat protein should be formed.

In this work we also studied whether similar heterogeneities could be induced by the presence of positively charged M13 mcp in bilayers composed of mixtures of anionic and neutral phospholipids. Due to the basic character of the M13 mcp C-terminal, it is reasonable to consider the possibility of anionic phospholipid-enriched domain induction by M13 coat protein incorporation in the bilayer. The formation of these domains could actually help explain some of the mechanisms involved in the creation of the phage assembly site. Assuming that the hypothetical domains were composed by all the protein and negative lipid content in the sample, and that the protein would be uniformly distributed inside them, one can, integrating Eq. 6, obtain theoretical curves describing the energy transfer within these domains. These plots are compared with the experimental data points for M13 coat protein incorporated in 18 : 1,18 : 1 PC/18 : 1,18 : 1 PG (80/20 mol/mol) and

18 : 1,18 : 1 PE/18 : 1,18 : 1 PG (70 : 30 mol/mol) in Fig. 3a. It is concluded that the segregation of M13 coat protein to a PG-rich phase in the mixed systems, induced by electrostatic interactions between the positively charged protein and the negatively charged phospholipid, is ruled out. In fact, this process would lead to a greater local surface density of acceptor, and therefore, a very significant increase of energy transfer efficiencies should be observed, in contrast to the data.

On the whole, from this study, it is concluded that for the M13 mcp the hydrophobic matching conditions on the protein–lipid interface are more important than electrostatic interactions between the protein and the phospholipids, for the protein lateral distribution on the bilayer.

In the second study [30], the protein selectivity for the acceptor (18 : 1,18 : 1 PE derivatized with NBD at the head group) was measured in bilayers of either 18 : 1,18 : 1 PC, 22 : 1,22 : 1 PC, or 14 : 1,14 : 1 PC. In a second set of measurements, several probes were used as acceptors, all studies being made in 18 : 1,18 : 1 PC vesicles. The probes used as acceptors were phospholipids of identical acyl chains (18 : 1 and 12 : 0) and different head groups (PC, PE, phosphatidylserine (PS), PG, and phosphatidic acid (PA)) classes, derivatized with NBD at the 12 : 0 chain. The complete set of experiments is described in Table 1, where the recovered selectivity constants ( $K_S$ , Eq. 18) are summarized.

Regarding the hydrophobic matching experiment, the lower value recovered in 18 : 1,18 : 1 PC relative to those in 14 : 1,14 : 1 PC and 22 : 1,22 : 1 PC bilayers confirms the larger protein selectivity towards the hydrophobic matching unlabeled phospholipid (18 : 1,18 : 1 PC). On the other hand, from the varying acceptor head group experiment, a larger selectivity for the anionic labeled phospholipids (especially the 18 : 1,(12 : 0-NBD) PA and 18 : 1,(12 : 0-NBD) PS probes) is inferred.

**Table 1** Relative association constants of labeled phospholipids towards M13 major coat protein

Labeled phospholipid	Bilayer composition	$K_S$	$K_S/K_S(\text{PC})^a$
((18 : 1) <sub>2</sub> -PE-NBD)	DOPC ((18 : 1) <sub>2</sub> PC)	1.4	–
((18 : 1) <sub>2</sub> -PE-NBD)	DEuPC ((22 : 1) <sub>2</sub> PC)	2.1	–
((18 : 1) <sub>2</sub> -PE-NBD)	DMoPC ((14 : 1) <sub>2</sub> PC)	2.9	–
(18 : 1-(12 : 0-NBD)-PE)	DOPC	2.0	1.0
(18 : 1-(12 : 0-NBD)-PC)	DOPC	2.0	1.0
(18 : 1-(12 : 0-NBD)-PG)	DOPC	2.3	1.1
(18 : 1-(12 : 0-NBD)-PS)	DOPC	2.7	1.3
(18 : 1-(12 : 0-NBD)-PA)	DOPC	3.0	1.5

<sup>a</sup>  $K_S(\text{PC})$  is the relative association constant of (18 : 1-(12 : 0-NBD)-PC)

Reprinted with permission from [30]. © 2004 Biophysical Society



## 6.5

### Lipid–DNA Interaction

It has been almost two decades since it was reported for the first time that plasmid DNA and cationic liposomes aggregate due to electrostatic attractive forces and form small complexes able to transfer DNA to the cells [47]. Since then, cationic liposomes have become the most widely used non-viral DNA delivery system for gene therapy studies [48]. Many efforts have been made to fully characterize cationic liposome–DNA complexes (lipoplexes), because it is the only way to understand, improve, and control the transfection efficiency of these non-viral based vectors. Electron microscopy and X-ray diffraction used in parallel revealed a multilamellar structure of lipid bilayers with sandwiched DNA, with a constant interlayer spacing invariant with the charge ratio, and depending on cationic liposomes formulations [49, 50]. Recently [51], a RET study was carried out in 1,2-dioleoyl-3-trimethylammonium-propane (DOTAP)/pUC19 plasmid DNA complexes with different charge ratios. 2-(4,4-Difluoro-5-octyl-4-bora-3a,4a-diaza-s-indacene-3-pentanoyl)-1-hexadecanoyl PC (BODIPY-PC) was the membrane dye and acceptor, and benzothiazolium, 2,2'-[1,3-propanediyl]bis[(dimethyliminio)-3,1-propanediyl-1(4*H*)-pyridinyl-4-yl-idenemethylidyne]]bis[3-methyl]-, tetraiodide (BOBO-1) was the DNA intercalator and RET donor. BOBO-1 (which has four positive charges) binds with very high affinity to negatively charged DNA. Addition of DOTAP leads to formation of lipoplexes. If the amount of DOTAP added is not sufficiently high, this binding is not quantitative, and a fraction  $\gamma$  of BOBO-1 molecules are intercalated inside “free” DNA, i.e., DNA not complexed by DOTAP. These molecules do not sense acceptors in their surroundings. In these circumstances, the overall decay of BOBO-1 fluorescence is expressed by an “isolated donors” formalism:

$$i_{DA}(t) = (1 - \gamma)i_D(t) \exp(-kCl^2F(l, t, 0)) + \gamma i_{D0}(t). \quad (20)$$

In this equation,  $i_D(t)$  is the decay of BOBO-1 molecules that reside in lipoplexes, in the absence of acceptor. On the other hand,  $i_{D0}(t)$  is the decay of the BOBO-1 population that is intercalated inside free DNA. If one assumes that BOBO-1 distributes equally between free DNA and DOTAP-complexed DNA, the  $\gamma$  parameter reflects the fraction of free DNA, which is an important parameter regarding the efficiency of a given lipid formulation. The RET model is better visualized in Fig. 4.

If one fixes  $i_D(t)$  and  $i_{D0}(t)$  to the values measured in the absence of acceptor, and uses the  $C$  value computed from the experimental labeled lipid:total lipid ratio, the only parameters left are  $l \approx d_1 \approx d_2 =$  distance between the donor plane and the two acceptor planes (see Fig. 4; note that the fact that there are two equivalent acceptor planes is taken into account by simply by multiplying  $C$  by a factor of two in Eq. 20), and the free DNA fraction  $\gamma$ .

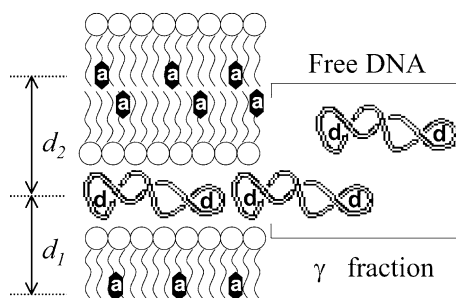


**Fig. 4** Schematic representation of the multilamellar structure of lipoplexes with the fluorescent probes (acceptor on the lipid (BODIPY-PC) and donor on the DNA (BOBO-1)). Reprinted with permission from [51]. © 2003 Biophysical Society

The strategy of data analysis was as follows. From literature X-ray studies, it was known that the distance  $l$  does not depend on the cationic lipid:DNA ratio [50]. In this way, a high DOTAP/DNA charge ratio (4 in our study) was chosen as a system for which there was no free DNA ( $\gamma = 0$ ). This ratio was confirmed (i) by agarose gel experiments and, (ii) because RET efficiency between DNA-bound BOBO-1 and membrane lipid probe BODIPY-PC did not increase for higher DOTAP/DNA ratios, pointing to complete coverage of DNA. For this sample,  $l$  is the only fitting parameter in the RET model, and  $l = 27 \text{ \AA}$  is conveniently recovered from RET efficiency data (Fig. 5a). This  $l$  value is in turn fixed for analysis of lipoplexes with less DOTAP (DOTAP/DNA charge ratios 0.5 and 2 in our study), for which the free DNA fraction  $\gamma$  is now the sole parameter (Figs. 5b and 5c).

This study shows that RET allows structural characterization of lipoplexes, with determination of the lamellar repeat distance (in agreement with diffraction techniques), the amount of free DNA (susceptible to enzyme degradation, and probably the most relevant predicting observable regarding transfection efficiency), and the lowest DOTAP/DNA ratio for which all DNA is protected (this knowledge is important to minimize cytotoxicity resulting from unnecessarily high cationic lipid amount in the lipoplex formulation).

## 7

### Conclusions

Application of quantitative RET methodologies in membrane biophysics allows the detection and size estimation of phase separation in membranes, much below the present day microscopy resolution, and this is especially relevant since in living cells these liquid-ordered domains are nanoscopic (“rafts”). Other topology related problems such as lipid-protein interaction

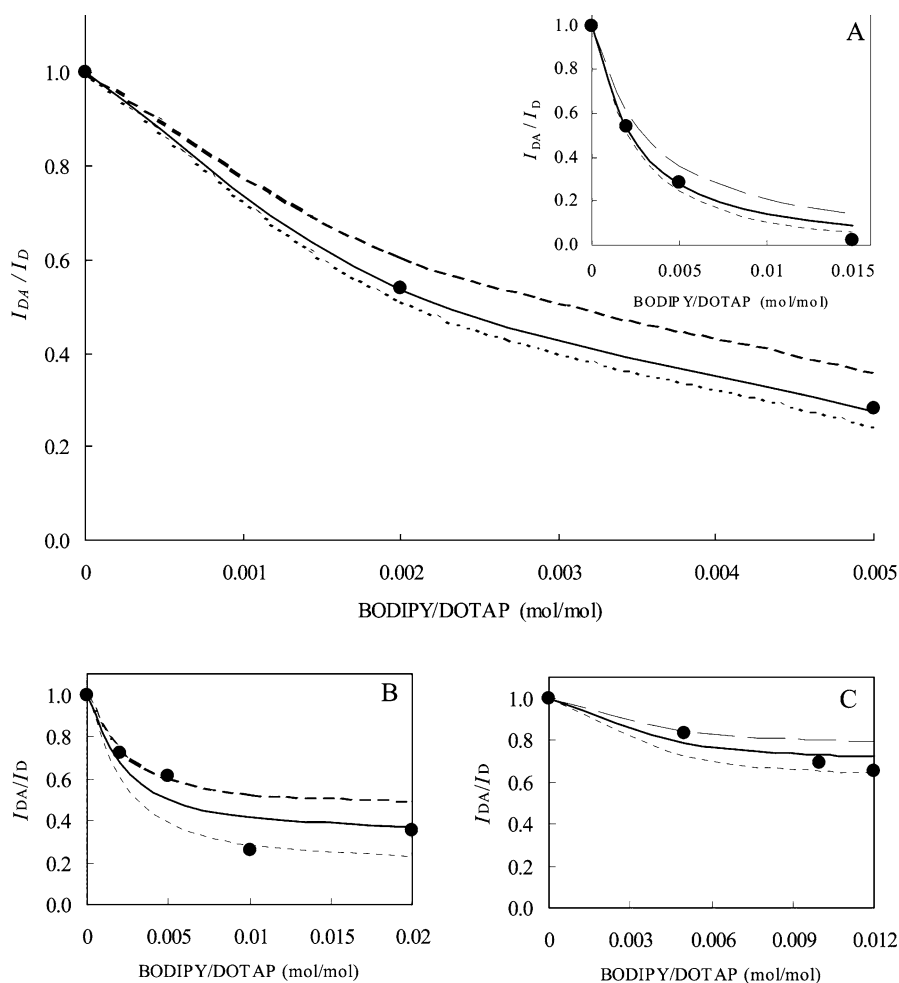


**Fig. 5** RET quenching ratios ( $I_{DA}/I_D = 1 - E$ ), for BOBO-1/BODIPY-PC pairs in DOTAP/DNA complexes with charge ratios (+ / -) of **A** 4 (*larger plot* is a zoom of *inset*), **B** 2, and **C** 0.5. ● Experimental data. For fitting curves using the model described in the text, the assumed fitting parameters were: **A**  $\gamma = 0$  (fixed),  $l = 32 \text{ \AA}$  (---),  $l = 27 \text{ \AA}$  (—),  $l = 22 \text{ \AA}$  (⋯); **B**  $l = 27 \text{ \AA}$  (fixed),  $\gamma = 0.20$  (—),  $\gamma = 0.30$  (---),  $\gamma = 0.10$  (⋯); **C**  $l = 27 \text{ \AA}$  (fixed),  $\gamma = 0.50$  (—),  $\gamma = 0.60$  (---),  $\gamma = 0.40$  (⋯). Reprinted with permission from [51]. © 2003 Biophysical Society

and the structure of lipid–DNA complexes can also be addressed in great detail. This requires both the acquisition of time-resolved data and its global analysis in the framework of simpler models assuming infinite-phase separation on the RET range. Deviations to the decay laws contain topological information, and inference about domain sizes can be obtained from simulation methodologies.

**Acknowledgements** This work was supported by POCTI projects (FCT, Portugal).

## References

1. Lakowicz JR (1999) Principles of fluorescence spectroscopy, 2nd edn. Plenum, New York
2. Förster T (1949) Experimentelle und theoretische Untersuchung des Zwischenmolekularen Übergangs von Elektronenanregungsenergie. *Z Naturforsch* 4a:321–327
3. Dale RE, Eisinger J, Blumberg WE (1979) The orientational freedom of molecular probes. The orientation factor in intramolecular energy transfer. *Biophys J* 26:161–193
4. Stryer L (1978) Fluorescence energy transfer as a spectroscopic ruler. *Ann Rev Biochem* 47:829–846
5. Loura LMS, Prieto M (2000) Resonance energy transfer in heterogeneous planar and bilayer systems: theory and simulation. *J Phys Chem B* 104:6911–6919
6. Tweet AG, Bellamy WD, Gaines GL Jr (1964) Fluorescence quenching and energy transfer in monomolecular films containing chlorophyll. *J Chem Phys* 41:2068–2077
7. Wolber PK, Hudson BS (1979) An analytical solution to the Förster energy transfer problem in two dimensions. *Biophys J* 28:197–210
8. Davenport L, Dale RE, Bisby RH, Cundall RB (1985) Transverse location of the fluorescent probe 1,6-diphenyl-1,3,5-hexatriene in model lipid bilayer membrane systems by resonance energy transfer. *Biochemistry* 24:4097–4108
9. Berberan-Santos MN, Valeur B (1991) Fluorescence depolarization by electronic energy transfer in donor–acceptor pairs of like and unlike chromophores. *J Chem Phys* 95:8048–8055
10. Runnels LW, Scarlata SF (1995) Theory and application of fluorescence homotransfer in melittin oligomerization. *Biophys J* 69:1569–1583
11. Kowski A (1983) Excitation energy transfer and its manifestation in isotropic media. *Photochem Photobiol* 4:487–508
12. Van de Meer BW, Coker G III, Chen S-YS (1994) Resonance energy transfer: theory and data. VCH, New York
13. Snyder B, Freire E (1982) Fluorescence energy transfer in two dimensions. A numeric solution for random and non-random distributions. *Biophys J* 40:137–148
14. Medhage B, Mukhtar E, Kalman B, Johansson LB-Å, Molotkovsky JG (1992) Electronic energy transfer in anisotropic systems. Part 5. Rhodamine-lipid derivatives in model membranes. *J Chem Soc Faraday Trans* 88:2845–2851
15. Gautier I, Tramier M, Duriex C, Coppey J, Pansu RB, Nicolas J-C, Kemnitz K, Coppey-Moisan M (2001) Homo-FRET microscopy in living cells to measure monomer–dimer transition of GFP-tagged proteins. *Biophys J* 80:3000–3008
16. Sharma P, Varma R, Sarasij RC, Ira, Gousset K, Krishnamoorthy G, Rao M, Mayor S (2004) Nanoscale organization of multiple GPI-anchored proteins in living cell membranes. *Cell* 116:577–589
17. Farinha JPS, Martinho JMG, Yekta A, Winnik MA (1995) Direct nonradiative energy-transfer in polymer interphases – fluorescence decay functions from concentration profiles generated by Fickian diffusion. *Macromolecules* 28:6084–6088
18. Yekta A, Winnik MA, Farinha JPS, Martinho JMG (1997) Dipole–dipole electronic energy transfer. Fluorescence decay functions for arbitrary distributions of donors and acceptors. II. Systems with spherical symmetry. *J Phys Chem A* 101:1787–1792

19. Farinha JPS, Spiro JG, Winnik MA (2004) Dipole–dipole electronic energy transfer. Fluorescence decay functions for arbitrary distributions of donors and acceptors. III. Systems with cylindrical symmetry. *J Phys Chem B* 108:16392–16400
20. Loura LMS, Fedorov A, Prieto M (2001) Fluid–fluid membrane microheterogeneity: a fluorescence resonance energy transfer study. *Biophys J* 80:776–788
21. Ballet PM, Van der Auweraer M, De Schryver FC, Lemmetyinen H, Vourimaa E (1996) Global analysis of the fluorescence decays of *N,N'*-dioctadecyl rhodamine B in Langmuir–Blodgett films of diacyl phosphatidic acids. *J Phys Chem* 100:13701–13715
22. Liu YS, Li L, Ni S, Winnik M (1993) Recovery of acceptor concentration distribution in a direct energy transfer experiment. *Chem Phys* 177:579–589
23. Shaklai N, Yguerabide J, Ranney HM (1977) Interaction of haemoglobin with red blood cell membranes as shown by a fluorescent chromophore. *Biochemistry* 16:5585–5592
24. Yguerabide J (1994) Theory for establishing proximity relations in biological membranes by excitation energy transfer measurements. *Biophys J* 66:683–693
25. Gutierrez-Merino C (1981) Quantitation of the Förster energy transfer for two-dimensional systems. I. Lateral phase separation in unilamellar vesicles formed by binary phospholipids mixtures. *Biophys Chem* 14:247–257
26. Gutierrez-Merino C (1981) Quantitation of the Förster energy transfer for two-dimensional systems. II. Protein distribution and aggregation state in biological membranes. *Biophys Chem* 14:259–266
27. Gutierrez-Merino C, Munkonge F, Mata AM, East JM, Levinson BL, Napier RM, Lee AG (1987) The position of the ATP binding site on the  $(Ca^{2+} + Mg^{2+})$ -ATPase. *Biochim Biophys Acta* 897:207–216
28. Antollini SS, Soto MA, de Romanelli IB, Gutiérrez-Merino C, Sotomayor P, Barrantes FJ (1996) Physical state of bulk and protein-associated lipid in nicotinic acetylcholine receptor-rich membrane studied by laurdan generalized polarization and fluorescence energy transfer. *Biophys J* 70:1275–1284
29. Bonini IC, Antollini SS, Gutiérrez-Merino C, Barrantes FJ (2002) Sphingomyelin composition and physical asymmetries in native acetylcholine receptor-rich membranes. *Eur Biophys J* 31:417–427
30. Fernandes F, Loura LMS, Koehorst R, Spruijt RB, Hemminga MA, Fedorov A, Prieto M (2004) Quantification of protein–lipid selectivity using FRET: Application to the M13 major coat protein. *Biophys J* 87:344–352
31. Loura LMS, Fedorov A, Prieto M (1996) Resonance energy transfer in a model system of membranes: application to gel and liquid crystalline phases. *Biophys J* 71:1823–1836
32. Loura LMS, Fedorov A, Prieto M (2000) Membrane probe distribution heterogeneity: a resonance energy transfer study. *J Phys Chem B* 104:6920–6931
33. Loura LMS, Castanho MARB, Fedorov A, Prieto M (2001) A photophysical study of the polyene antibiotic filipin Self-aggregation and filipin–ergosterol interaction. *Biochim Biophys Acta* 1510:125–135
34. Loura LMS, Fedorov A, Prieto M (2000) Partition of membrane probes in a gel/fluid two-component lipid system: a fluorescence resonance energy transfer study. *Biochim Biophys Acta* 1467:101–112
35. Mouritsen OG, Bloom M (1984) Mattress model of lipid–protein interactions in membranes. *Biophys J* 46:141–153
36. Almeida PFF, Vaz WLC, Thompson TE (1992) Lateral diffusion in the liquid phases of dimyristoylphosphatidylcholine/cholesterol lipid bilayers: a free volume analysis. *Biochemistry* 31:6739–6747

37. Loura LMS, Fedorov A, Prieto M (2001) Exclusion of a cholesterol analog from the cholesterol-rich phase in model membranes. *Biochim Biophys Acta* 1511:236–243
38. Simons K, Ikonen I (1997) Functional rafts in cell membranes. *Nature* 387:569–572
39. Simons K, Toomre D (2000) Lipid rafts and signal transduction. *Nat Rev Mol Cell Biol* 1:31–39
40. Anderson RGW, Jacobson K (2002) A role for lipid shells in targeting proteins to caveolae, rafts and other lipid domains. *Science* 296:1821–1825
41. de Almeida RFM, Fedorov A, Prieto M (2003) Sphingomyelin/phosphatidylcholine/cholesterol phase diagram: boundaries and composition of lipid rafts. *Biophys J* 85:2406–2416
42. de Almeida RFM, Loura LMS, Fedorov A, Prieto M (2005) Lipid rafts have different sizes depending on membrane composition: a time-resolved fluorescence resonance energy transfer study. *J Mol Biol* 346:1109–1120
43. Santos NC, Prieto M, Castanho MA (2003) Quantifying molecular partition into model systems of biomembranes: an emphasis on optical spectroscopic methods. *Biochim Biophys Acta* 1612:123–135
44. Veiga AS, Santos NC, Loura LMS, Fedorov A, Castanho MARB (2004) HIV fusion inhibitor peptide T-1249 is able to insert or adsorb to lipidic bilayers. Putative correlation with improved efficiency. *J Am Chem Soc* 126:14758–14763
45. Stopar D, Spruijt RB, Wolfs CJAM, Hemminga MA (2003) Protein–lipid interactions of bacteriophage M13 major coat protein. *Biochim Biophys Acta* 1611:5–15
46. Fernandes F, Loura LM, Prieto M, Koehorst R, Spruijt RB, Hemminga MA (2003) Dependence of M13 major coat protein oligomerization and lateral segregation on bilayer composition. *Biophys J* 85:2430–2441
47. Felgner PL, Gadek TR, Holm M, Roman R, Chan HW, Wenz M, Northrop JP, Ringold GM, Danielsen M (1987) Lipofection: a highly efficient, lipid-mediated DNA-transfection procedure. *Proc Natl Acad Sci USA* 84:7413–7417
48. Huang L, Hung M-C, Wagner E (eds) (1999) *Nonviral vectors for gene therapy*. Academic Press, San Diego
49. Lasic DD, Strey H, Stuart MCA, Podgornik R, Frederik PM (1997) The structure of DNA–liposome complexes. *J Am Chem Soc* 119:832–833
50. Radler JO, Koltover I, Salditt T, Safinya CR (1997) Structure of DNA–cationic liposome complexes: DNA intercalation in multilamellar membranes in distinct interhelical packing regimes. *Science* 275:810–814
51. Madeira C, Loura LM, Aires-Barros MR, Fedorov A, Prieto M (2003) Characterization of DNA/lipid complexes by fluorescence resonance energy transfer. *Biophys J* 85:3106–3119

# Measuring Diffusion in a Living Cell Using Fluorescence Correlation Spectroscopy. A Closer Look at Anomalous Diffusion Using HIV-1 Integrase and its Interactions as a Probe

Jo Vercammen · Goedele Maertens · Yves Engelborghs (✉)

Laboratory of Biomolecular Dynamics, University of Leuven, Celestijnenlaan 200G,  
3001 Leuven, Belgium

*Yves.Engelborghs@fys.kuleuven.be*

1	Introduction to Fluorescence Correlation Spectroscopy (FCS) . . . . .	324
2	HIV-1 Integrase . . . . .	330
3	The Integrase Interactor LEDGF/p75 . . . . .	331
4	HIV-IN Diffusion in the Cell . . . . .	331
5	HIV-IN Diffusion in the Presence of LEDGF/p75 . . . . .	334
6	Conclusions . . . . .	336
	References . . . . .	337

**Abstract** Fluorescence correlation spectroscopy is a powerful technique for observing the diffusion of fluorescent molecules. In buffer solution the autocorrelation analysis of the intensity fluctuations allows the calculation of the diffusion coefficient, and therefore the size of the molecule, as well as its interactions. In living cells, however, the situation is more complicated because the viscosity of the medium varies a lot from spot to spot. Moreover, the analysis of the autocorrelation curve is not always straightforward and the chosen analysis method can sometimes be questioned. Autocorrelation curves obtained from living cells can be fitted equally well with a multicomponent model or with an anomalous diffusion model (Wachsmuth et al., *J Mol Biol*, 298:677, 2000). The latter model introduces a global anomaly parameter that describes the heterogeneity of the hindrance of the medium to the diffusing molecules in the cell. By applying the two models on a system of interacting proteins in living cells, we could compare the advantages and disadvantages of both models. This article will give an introduction to fluorescence correlation spectroscopy as well as HIV-1 integrase, whose protein fragments have been used as a model in this study. HIV-1 integrase has been shown to interact with a cellular protein, called lens epithelium-derived growth factor or LEDGF/p75. This interaction will be used as a starting point for the comparison of the two models.

**Keywords** Anomalous diffusion · FCS · HIV-1 integrase · LEDGF

## Abbreviations

ACF autocorrelation function  
APD avalanche photodiode

Ct	C terminus
$D$	diffusion coefficient
$D_{\text{app}}$	apparent diffusion coefficient
EGFP	enhanced green fluorescent protein
FCS	fluorescence correlation spectroscopy
FCCS	fluorescence cross correlation spectroscopy
fpm	fluorescence per molecule
IBD	integrase binding domain
IN	integrase
LEDGF	lens epithelium-derived growth factor
LTR	long terminal repeat
LSM	laser scanning microscope
Nt	N terminus
PIC	preintegration complex
scFCS	single color FCS
SEM	standard error of mean

## 1

### Introduction to Fluorescence Correlation Spectroscopy (FCS)

Compared to classical relaxation techniques, where a perturbation of the equilibrium—e.g. by a temperature or a pressure jump—is necessary to observe the relaxation to the new equilibrium position, FCS is novel since it monitors small spontaneous deviations from thermal equilibria in an open system without any need for perturbation. It can be shown that the fluctuations are governed by the same kinetic laws as observed when the equilibrium is macroscopically perturbed [14, 27].

We have used the ConfoCor2/LSM 510 combination to perform FCS measurements (Fig. 1). This instrument consists basically of an inverted confocal microscope, a laser source, optical filters, and avalanche photodiodes (APDs) as the detector. The laser source is used to excite fluorescent molecules in the sample solution. The ConfoCor2 has three lasers from which five excitation wavelengths can be filtered: 454, 488, 514, 543, and 633 nm. The laser light is directed through optical fibers, reflected by the dichroic mirror, and passed through a 40 $\times$  magnification water objective lens. The objective generates a focussed laser beam in which the fluorescent molecules are excited. The emitted fluorescence is then captured through the same objective and passes through the same dichroic mirror. The optical fluorescence is then focussed on a pinhole, which determines the confocal volume. Behind the pinhole the photons are detected with a highly sensitive APD detector. The open confocal volume, which is used to detect fluorescence fluctuations, has a typical size of about 0.2 fL. This small volume allows us to perform measurements at different positions inside a single living cell.



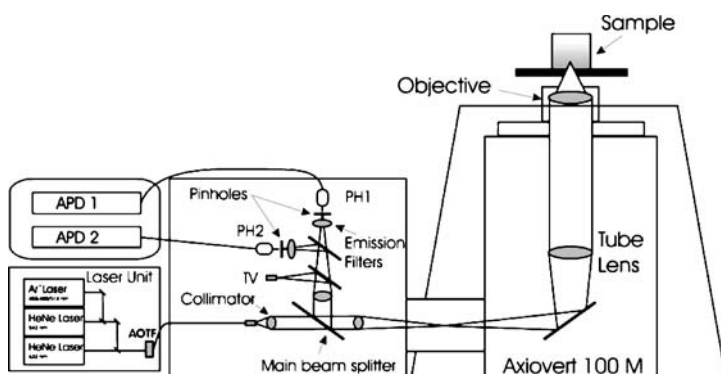


**Fig. 1** Instrumental setup of the ConfoCor2 (Zeiss). The instrument consists of an inverted confocal microscope equipped with units for scanning, FCS, and fluorescence cross correlation spectroscopy (FCCS). Three different laser sources (one Ar<sup>+</sup> and two He-Ne lasers) can separately excite the sample. The emission light is collected by the APDs after using an appropriate filter set for two different colors

When fluorescence intensity fluctuations are detected, the normalized autocorrelation function (ACF) can be calculated on the basis of the following relation:

$$G(\tau) = \frac{\langle F \rangle^2 + \langle \delta F(t) \cdot \delta F(t + \tau) \rangle}{\langle F \rangle^2}, \quad (1)$$

where  $\langle F \rangle$  is the mean fluorescence intensity of the measurement and  $\delta F(t)$  is the deviation of the fluorescence intensity at time  $t$ , or in the case of  $\delta F(t + \tau)$  at a time interval  $\tau$  later. In the case where the fluctuations are solely due to number fluctuations as a result of diffusion in and out of the confocal volume, the autocorrelation curve can be described by the following ACF:

$$G(\tau) = 1 + \frac{1}{\langle N \rangle} \left[ \frac{1}{1 + \tau/\tau_d} \right]_{x,y} \left[ \frac{1}{1 + \tau/S^2\tau_d} \right]_z^{1/2} = 1 + \frac{1}{\langle N \rangle} f(\tau, \tau_d), \quad (2)$$

where  $\langle N \rangle$  is the average number of molecules in the confocal volume and  $S$  is the structure parameter. This parameter equals the ratio of the radius of the confocal volume in the  $z$  direction ( $\omega_z$ ) to that of the  $x$ - or  $y$ -direction ( $\omega_x$ ). The radius is defined as the distance from the center where the intensity of the Gaussian beam profile has decreased to  $1/e^2$  in the axial or the lateral direction [18].

The diffusion time is related to the diffusion coefficient ( $D$ ) in the following manner:

$$\tau_d = \frac{\omega_{x,y}^2}{4D}, \quad (3)$$

and the diffusion coefficient for a sphere with radius  $r$  is:

$$D = \frac{kT}{6\pi\eta r}, \quad (4)$$

with  $kT$  the kinetic energy of the molecules and  $\eta$  the viscosity of the medium. The parameters  $\omega$  and  $S$  can be obtained by calibrating the instrument with a dye of known  $D$ .

It is clear from Eq. 2 that the amplitude of the autocorrelation curve is inversely proportional to the number of molecules present in the confocal volume. The concentration of the solution can be calculated from the average number of molecules and the volume (assuming a cylindrical shape) using Eq. 5:

$$\text{Vol.} = 2\pi \cdot \omega_x^2 \omega_z \quad \text{and} \quad \text{Conc.} = \frac{\langle N \rangle}{\text{Vol.} \cdot N_A}. \quad (5)$$

Depending on the properties of the measured fluorophore, photophysical processes will be visible during the FCS measurement. During FCS measurements the conversions to the triplet state will be seen as a process occurring in the microsecond timescale (1–10  $\mu\text{s}$ ), and this process will cause an additional shoulder in the autocorrelation curve (Fig. 2). In almost all cases we have to use a model which includes a triplet state of the fluorophores. The amount of triplet state is characteristic for each fluorophore and can change with a different environment, e.g., it increases when the light intensity increases. For FCS measurements we prefer to have a low contribution of triplet state because this process leads to a decrease of signal, which can be used to look at the diffusion of the molecules.

When a species displays intersystem crossing to the triplet state, Eq. 2 has to be changed and an additional factor due to the triplet fraction has to be included:

$$G(\tau) = 1 + \frac{1}{\langle N \rangle} \cdot \frac{1 - T + T e^{-\tau/\tau_T}}{(1 - T)} f(\tau, \tau_d), \quad (6)$$

where  $T$  is the fraction of molecules in the triplet state and  $\tau_T$  is the corresponding triplet relaxation time.

For the complete evaluation of the ACF, the curve has to be fitted with the model that is suited to the investigated process. Depending on the number of different fluorescent species, the curve has to be fitted to a model with different components with a different diffusion coefficient (Fig. 3). Usually the maximum number of components is three, as a higher number of variables to fit the curve generally do not contribute to a better fit.

When two particles are present in the solution the autocorrelation curve can be fitted with a model with two diffusing particles (provided they have

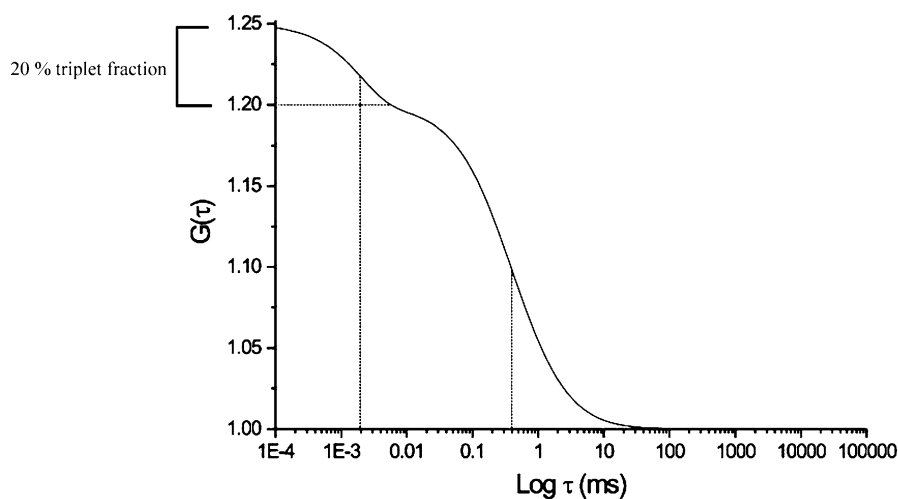


**Fig. 2** Simulated autocorrelation curve corresponding to a sample with an average of five molecules in the open volume, with a diffusion time of  $400 \mu\text{s}$ ; 20% of the fluorescence signal is lost due to the triplet fraction in the sample. The relaxation time of this process is  $2 \mu\text{s}$ . The *dotted lines* indicate the triplet relaxation time and diffusion time, respectively

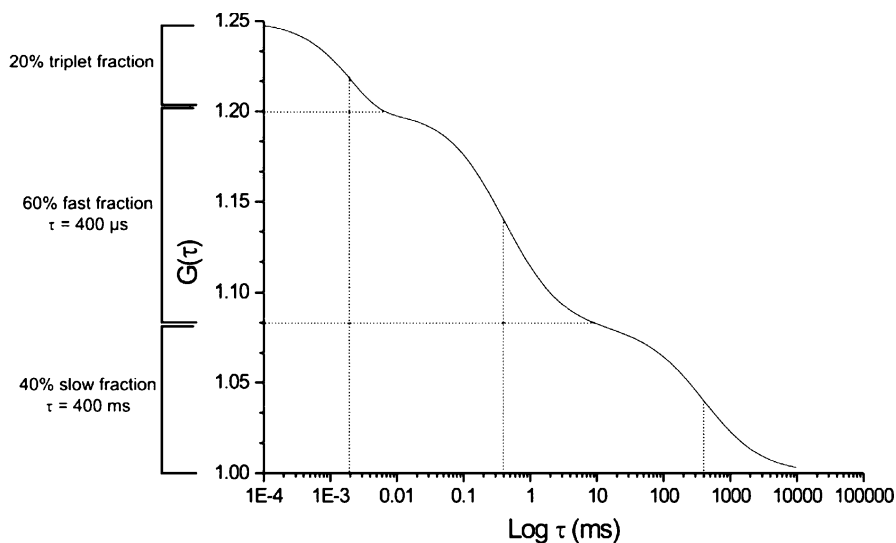


**Fig. 3** Simulated autocorrelation curve corresponding to a sample with two diffusing species with equal molecular brightness. There are on average five molecules in the open volume, containing a fast fraction (60%) with a diffusion time of  $400 \mu\text{s}$  and a slow fraction (40%) with a 1000-fold slower diffusion time. The contribution of the triplet fraction is 20% of the total signal with a triplet relaxation time of  $2 \mu\text{s}$ . The *dotted lines* indicate the triplet relaxation time and diffusion times

the same brightness):

$$G(\tau) = 1 + \frac{1}{\langle N \rangle} \cdot \frac{1 - T + T e^{-\tau/\tau_T}}{(1 - T)} \cdot \{(1 - y)f(\tau, \tau_{d,1}) + yf(\tau, \tau_{d,2})\} . \quad (7)$$

When the brightness differs then we have to correct for that as well:

$$G(\tau) = 1 + \frac{1}{\langle N \rangle} \cdot \frac{1 - T + T e^{-\tau/\tau_T}}{(1 - T)} \cdot \frac{\{(1 - y)f(\tau, \tau_{d,1}) + y\alpha^2 f(\tau, \tau_{d,2})\}}{(1 - y + \alpha y)^2} , \quad (8)$$

where  $\alpha = \text{fpm1}/\text{fpm2}$  (fpm = fluorescence per molecule = brightness).

Next to pure random diffusion, other models can also be applied to describe the autocorrelation curve. These models are usually related to specific phenomena. When a conformational change occurs while the particle is diffusing, and this leads to a change in brightness, an appropriate kinetic factor has to be introduced. A protonation model has been used to describe the decay times of internal and external protonation, which result in a change of fluorescence. This model has been used to describe the protonation of green fluorescent protein [6]. When measuring inside cells, we have to consider that the medium is very crowded. The concentration of proteins inside cells is usually about 200 mg/ml [15]. Therefore simple diffusion is not possible. Other molecules and structures will hinder the fluorophores when they move through the protein network. When studying diffusion in the cytosol and the nucleus of living cells, the autocorrelation curve can usually be fitted with two diffusing components, corresponding to a nonhindered or unrestricted fraction and a part with a restricted mobility, which is interacting with cellular components. A second way of describing the same autocorrelation curves is by using an anomalous diffusion model [28] (Eq. 9). This model introduces an anomaly parameter  $\alpha$ , corresponding to the amount of hindrance when the molecules travel through the cell. With both methods we can generate information on the mobility inside cells as well as the interaction of certain proteins with other components in the cell:

$$G(\tau) = 1 + \frac{1}{\langle N \rangle} \left( \left[ \frac{1}{1 + \left(\frac{\tau}{\tau_d}\right)^\alpha} \right] \cdot \left[ \frac{1}{1 + \left(\frac{\tau}{S^2 \tau_d}\right)^\alpha} \right]^{1/2} \right) . \quad (9)$$

The anomaly parameter  $\alpha$  in the equation for anomalous diffusion gives rise to a more stretched autocorrelation curve. This parameter equals 1 for free diffusion and decreases with increasing obstacle concentration [28] (in fact these authors use another nomenclature so that  $\alpha = 2/d_w$  and discuss anomaly in terms of  $d_w$ ). However, when the obstacles form cages, dead ends, and cavities smaller than the focal volume, we expect to observe a fast component due to free diffusion and an additional slower component of trapped molecules that take longer to leave the focus [23]. From the fitting we calculate an apparent diffusion coefficient ( $D_{\text{app}}$ ) since the calculated diffusion

coefficient is a function of time when  $\alpha < 1$ . For normal diffusion there is a linear relationship between  $\omega_1^2$  and  $\tau$  ( $\omega_1^2 = 4D\tau$ ); however, with anomalous diffusion this relationship is time dependent.

Anomalous diffusion is dependent on the concentration of obstructing molecules [22, 29]; when the concentration is below the percolation threshold  $c_{o,p}$ , obstruction in molecular motion by an excluded volume interaction will be observed. This can be seen by the nonlinear relationship between the mean square displacement and time. At obstacle concentrations below the percolation threshold, diffusion is anomalous at short distances and normal at long distances.

Anomalous diffusion has been studied by various groups, and the origin of anomalous diffusion is still being discussed. Computer simulations have been introduced to describe anomalous diffusion as a function of the size and concentration of the obstacles [22]. The group of Nilsson describe anomalous diffusion as a measure of cytoplasmic (or nuclear) crowding [29]; thus, not the presence of immobile structures but rather the presence of a highly concentrated protein/lipid/carbohydrate solution lies at the origin of anomalous diffusion. This last study combined computer simulations with actual measurements in solution and in the cytoplasm of mammalian cells. The fact that anomalous diffusion behavior is due to macromolecular crowding and not to the presence of immobile structures, such as microtubules and actin, was supported by experiments where addition of nocodazole (depolymerization of microtubules), filipin III (destroys endoplasmic reticulum network), or latrunculin (depolymerization of actin network) did not reduce the observed anomalous diffusion behavior. Diffusion in mitotic cells also displayed a certain degree of anomaly [29]. However, not all intracellular immobile structures were destroyed (Golgi network and mitochondria remained unaffected), so whether a dramatic effect on anomalous diffusion would be observed is questionable under these conditions.

Nowadays is not yet clear which model is the most appropriate to describe intracellular diffusion. Some groups have fitted their FCS data to an anomalous diffusion model [25, 28]; however, both groups concluded that both the two-component and the anomalous diffusion models fit the data equally well. Some reports fit to the one- or two-component model [8, 17, 19, 20], while other reports use both fitting models [24, 25, 28]. The conclusion from Wachsmuth and coworkers, who measured diffusion along a straight line in the same focal plane of a cell, is that diffusion changes a lot from spot to spot within one cell [28]. This can be expressed by the diffusion coefficient as well as by the anomaly parameter. In agreement with these observations, we also observed a relatively large variation in the observed diffusion coefficient of integrase [13]. While anomalous diffusion uses the anomaly parameter  $\alpha$ , the two-component model uses the second diffusion coefficient to display the heterogeneity; in fact, both fitting models convey this observation equally well.

When looking at protein–protein interactions, one wants to see differences in diffusion coefficients when a protein is interacting with other proteins. Therefore, a large shift in diffusion coefficient can be used to determine the amount of interaction, using single color FCS (scFCS) [13]. Thus, as long as there is a significant shift in diffusion coefficient, scFCS can measure the interaction between two macromolecules; however, additional techniques are necessary to support the results. Specific knockdown of one of the protein partners should result in an increase in the diffusion coefficient, as well as deletion or point mutagenesis, which results in loss of binding, and should be used as a control. For fluorescence cross correlation spectroscopy (FCCS) no shift in diffusion coefficient should be observed, as it is the concomitant movement of two macromolecules, each labeled with a spectrally distinct label, through the open confocal volume element that gives a positive signal for the interaction. In this regard, the discovery of monomeric red fluorescent proteins (mRFPs) will be very useful in the future [21].

## 2

### HIV-1 Integrase

Integration of the viral DNA of the human immunodeficiency virus type 1 (HIV-1) into the genome of a human cell is an essential step in the retroviral replication cycle. Genetic studies have shown that retrovirus integration requires two viral components: integrase (encoded by the 3' end of the *pol* gene) and DNA sequences at the ends of the viral long terminal repeats (LTRs) (for a review see [1]). In the cytoplasm the integrase forms a nucleoprotein complex with the viral DNA. This is followed by two enzymatic reactions. In the 3' processing reaction, integrase removes a dinucleotide from each 3' end of the reverse transcribed viral DNA, resulting in viral DNA 3' ends terminating with a CA dinucleotide. The processed DNA is transported into the nucleus as part of a preintegration complex (PIC). During the second reaction, the DNA strand transfer, integrase carries out a concerted cleavage–ligation reaction. The recessed 3'-OH ends are covalently joined to the host chromosome, producing a gapped intermediate. Gap repair of the inserted DNA is probably carried out by cellular DNA repair enzymes.

Integrase is a 32-kDa protein, composed of three structurally and functionally distinct domains (Fig. 4). The N-terminus contains the “HHCC” zinc fingerlike motif. Evidence suggests that binding of zinc has a prominent role in the self-assembly of integrase into an active multimeric complex [9, 30]. Some studies have suggested that the N-terminus is involved in protein–protein interactions, whereas other experiments indicated that it contributes to substrate specificity [2]. The central core and the C-terminal domain are DNA binding domains. The central core contains the catalytic triad, the D,D-35-E motif, which is responsible for the specific binding of the substrate and

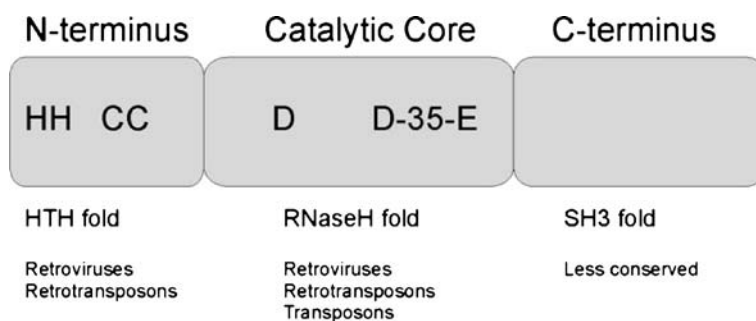


**Fig. 4** Schematic presentation of the HIV-IN domains

the enzymatic activity of integrase. The C-terminal domain has a nonspecific DNA binding activity. In solution, integrase has been shown to form monomers, dimers, and tetramers [4, 7, 26]. However, the active complex present in the PIC is a multimer, as required for the enzymatic reactions of integrase [5, 30]. Recent studies have shown that integrase forms a stable complex with the cofactor called lens epithelium-derived growth factor (LEDGF) and that this complex accomplishes the coordinated integration of at least an octamer [3].

### 3

#### The Integrase Interactor LEDGF/p75

LEDGF/p75 is a 60-kDa protein of 530 amino acids. It shares 325 NH<sub>2</sub>-terminal residues with the alternative splice variant p52. Both LEDGF/p75 and p52 proteins are nuclear, chromatin-associated, and display a different nuclear distribution pattern during interphase and mitosis [12, 16]. LEDGF/p75 interacts with HIV-IN and forms stable complexes. This protein also stimulates the enzymatic activity of HIV-1 IN *in vitro* [3]. The interaction domain of LEDGF has been identified in the C-terminal region of this protein and is called the integrase binding domain (IBD) (residues 347–471). Mutations at this region on the LEDGF of IN protein will therefore affect the interaction of these two proteins in a cell.

### 4

#### HIV-IN Diffusion in the Cell

The diffusion of proteins was followed by using enhanced green fluorescent protein (EGFP) as a marker protein. Upon expression of EGFP in HeLa cells, there is a diffuse distribution of the protein throughout the whole cell. When

measuring the diffusion coefficient with FCS, a two-component model had to be used in order to obtain satisfactory results, as determined by visual inspection of the fitted ACC, the residuals, and the chi-square value. Fast diffusion in the nucleus was comparable to that in the cytoplasm, giving  $D_{\text{nucleus}} = 23.0 \pm 1.0 \mu\text{m}^2/\text{s}$  (standard error of mean, SEM) and  $D_{\text{cytoplasm}} = 25.1 \pm 1.2 \mu\text{m}^2/\text{s}$ . When the diffusion of recombinant EGFP was measured in solution, we obtained a diffusion coefficient of  $57.7 \pm 2.6 \mu\text{m}^2/\text{s}$ . Diffusion of EGFP is thus 2.5 times slower in the cell compared to aqueous buffer solution, which is in agreement with earlier reports. The residence time of the second component in the confocal volume was in the millisecond time range, giving an apparent  $D_{\text{nucleus, slow}} = 0.72 \pm 0.10 \mu\text{m}^2/\text{s}$  and  $D_{\text{cytoplasm, slow}} = 0.85 \pm 0.09 \mu\text{m}^2/\text{s}$ , and displayed a large variation, most probably due to partial interaction with intracellular structures and/or much larger soluble molecules.

Next to EGFP, we measured the diffusion of full-length EGFP-IN and the deletion mutants EGFP-IN/Nt (the N-terminal domain), EGFP-IN core (the core domain), and EGFP-IN/Ct (the C-terminal domain) (Fig. 5). The diffusion of these fusion proteins could be measured with FCS in order to see differences in mobility. HeLa cells were seeded in eight-well Nunc LabTek cover glasses one day before transfection. Transfection of the HeLa cells was performed at 80% confluency using Lipofectamine 2000 (Gibco). Twenty-four hours posttransfection, cells were washed twice with OptiMem to reduce background fluorescence and FCS was performed.

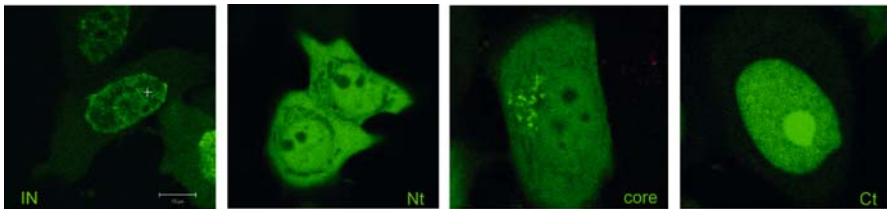


**Fig. 5** Expression of different IN domains in HeLa cells. From left to right: EGFP-IN, EGFP-IN/Nt, EGFP-IN/core, EGFP-IN/Ct

Before the start of each measurement, the cells were visualized with the laser scanning confocal microscope module (LSM 510) attached to the ConfoCor2. During the focusing in the cell, minimal laser power was used to reduce bleaching of the fluorophores. Fifteen measurements of 20 s duration were performed at each spot in the cytoplasm or nucleus. The FCS measurements were performed at a low laser power ( $\sim 15 \mu\text{W}$  at the sample). After each measurement, cells were again visualized with the LSM to check for the cell morphology and displacement. In a few cases, the cell had moved or had changed its shape—those measurements were discarded. The measurements were fitted and the average  $D$  of the fast fraction was determined (Fig. 6, Table 1). For the EGFP-IN/Nt, almost all measurements could be fitted to



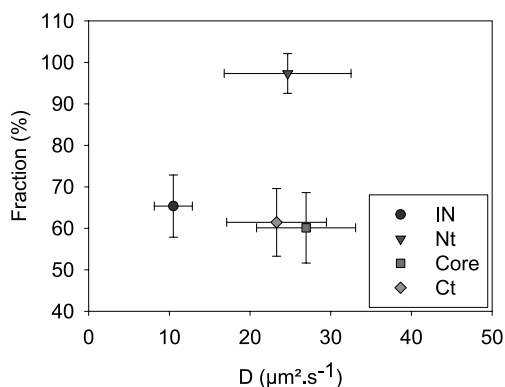


**Fig. 6** Diffusion of EGFP-IN deletion mutants fitted with a two-component model. The average  $D_{\text{fast}}$  and fraction (%) for measurements in the nucleus are presented together with their standard deviations. The separate IN domains (the IN N-terminal domain fragment (IN/Nt), central domain (IN/core), and C-terminal domain fragment (IN/Ct)) move  $2.3 \pm 0.2$  times faster than the full-length protein. Although the deletion mutants have a similar  $D_{\text{fast}}$ , IN/core and IN/Ct have a slightly larger fraction of slowly moving molecules (39.6 and 38.6%, respectively), while the IN/Nt is almost completely moving free (2.6% slowly moving molecules)

**Table 1** Results of two-component and anomalous diffusion model fitting. The average diffusion coefficients are given with their standard error of mean (SEM). For the anomalous diffusion model, the diffusion coefficient is given as an apparent diffusion coefficient ( $D_{\text{app}}$ ) obtained from the point where  $\tau = \tau_d$

	$D_{\text{fast}} \pm \text{SEM}$ ( $\mu\text{m}^2/\text{s}$ )	$(1-y) \pm \text{SEM}$ (%)	$D_{\text{slow}} \pm \text{SEM}$ ( $\mu\text{m}^2/\text{s}$ )	$D_{\text{app}} \pm \text{SEM}$ ( $\mu\text{m}^2/\text{s}$ )	Anomaly ( $\alpha$ )	No. of measure- ments
EGFP-IN (60 kDa)	$10.5 \pm 0.4$	$65.4 \pm 1.3$	$0.42 \pm 0.07$	$6.26 \pm 0.42$	$0.60 \pm 0.01$	33
EGFP-IN/Nt (33 kDa)	$23.4 \pm 0.6$	$97.3 \pm 0.6$	$1.00 \pm 0.08$	$25.48 \pm 0.54$	$0.94 \pm 0.01$	59
EGFP-IN/Core (45.5 kDa)	$26.3 \pm 0.8$	$60.4 \pm 1.2$	$2.21 \pm 0.10$	$11.96 \pm 0.54$	$0.70 \pm 0.01$	50
EGFP-IN/Ct (37.5 kDa)	$23.3 \pm 1.9$	$61.4 \pm 1.2$	$2.09 \pm 0.11$	$10.48 \pm 0.32$	$0.70 \pm 0.01$	46
EGFP-IN/core + p75	$10.4 \pm 0.5$	$67.9 \pm 2.5$	$0.37 \pm 0.07$	$7.47 \pm 0.50$	$0.66 \pm 0.02$	20
EGFP-IN/core + p52	$26.5 \pm 0.8$	$56.9 \pm 1.8$	$1.37 \pm 0.13$	$10.57 \pm 0.61$	$0.59 \pm 0.02$	22

one component. Some measurements had to be fitted to the two-component model; however, in this case, 94–98% of fast diffusing molecules were still found with a  $D$  corresponding to the cases where a one-component fit was

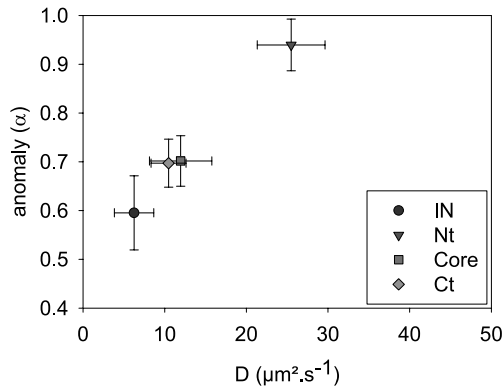


**Fig. 7** Diffusion of EGFP-IN deletion mutants fitted with an anomaly model. The apparent diffusion coefficient and anomaly parameter ( $\alpha$ ) for measurements are presented together with their standard deviations. The central domain (IN/core) and C-terminal domain (IN/Ct) move  $1.79 \pm 0.01$  times faster than the full-length integrase. The N-terminal domain moves 4.07 times faster than the full-length integrase and has almost no anomalous diffusion ( $\alpha \approx 1$ )

used. For EGFP-IN, EGFP-IN/core, and EGFP-IN/Ct, only the two-component model gave satisfactory fits. The same data are also fitted with an anomalous diffusion model (Fig. 7, Table 1) and show a difference between the full-length integrase and the different integrase domains. The difference is that the N-terminal domain has a higher apparent diffusion coefficient than IN/Ct and IN/core. This difference was not seen in the fitting with a model for two components. However, the latter domains are also involved in the DNA binding of integrase and this may be reflected in a difference in apparent diffusion coefficient.

## 5

### HIV-IN Diffusion in the Presence of LEDGF/p75

We were curious to see whether overexpression of LEDGF/p75, and hence recruitment of the IN/core domain to the nucleus, would also affect the diffusion characteristics of the latter. Unlike LEDGF/p75, the splice variant p52 does not interact with HIV-1 IN [12]. As p52 overexpression does not influence the IN/core intracellular distribution, we had to use HcRed1 fusions to be sure to measure in a cell that expressed both p52 and EGFP-IN/core. Hence, we also used HcRed1-fused LEDGF/p75 to work under the same conditions. When this fusion protein was expressed with EGFP-IN/core there was a good colocalization of both proteins in the nucleus (Fig. 8).

As LEDGF/p75 determines the HIV-1 IN intracellular distribution [10–12], we speculated that the reduced diffusion rate of the full-length protein was

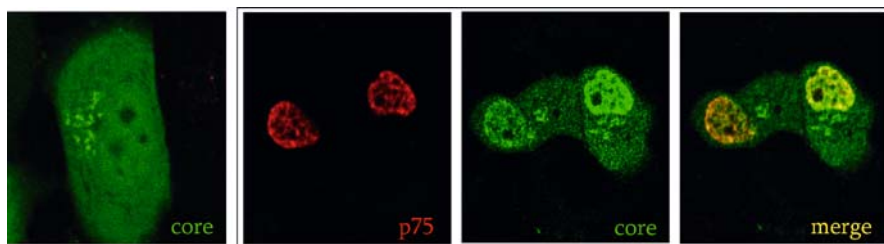


**Fig. 8** Colocalization of EGFP-IN/core with LEDGF/p75. EGFP-IN/core is distributed throughout the whole cell at endogenous levels of LEDGF/p75 (*left panel*). Upon coexpression with HcRed1-LEDGF/p75, the IN/core is recruited to the nucleus and displays a nuclear distribution pattern equal to the full-length HIV-1 IN (*right three panels*)

due to its interaction with LEDGF/p75. The IN/core domain is both essential and sufficient for the interaction with LEDGF/p75. This IN/core domain displayed a reduced affinity for the cellular protein as it became recruited to the nucleus and displayed the characteristic irregular distribution pattern typical of HIV-1 IN, only upon overexpression of LEDGF/p75 [12].

When HcRed1-p75 was coexpressed, the  $D_{\text{fast}}$  of EGFP-IN/core was reduced by a factor of 2.5, corresponding to the  $D$  of the full-length viral protein (Fig. 9, Table 1). Our control experiment demonstrates that this shift in  $D$  was specific, as coexpression of HcRed1-p52 with EGFP-IN/core did not influence the diffusion behavior of the latter. Hence, we can say that the specific interaction between IN (core domain) and LEDGF/p75 results in a slower diffusion that can be measured in living cells. To further show that the shift in  $D$  of IN compared with IN/core is due to the interaction

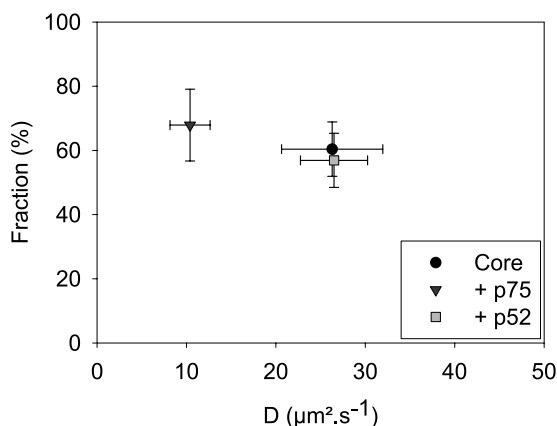


**Fig. 9** Influence of LEDGF/p75 and p52 on  $D_{\text{fast}}$  of EGFP-IN/core. Using a two-component model to fit the data allows a 2.5-fold shift of  $D_{\text{fast}}$  to be seen. We conclude that this shift is due to the protein–protein interaction of LEDGF/p75 with the core domain of integrase

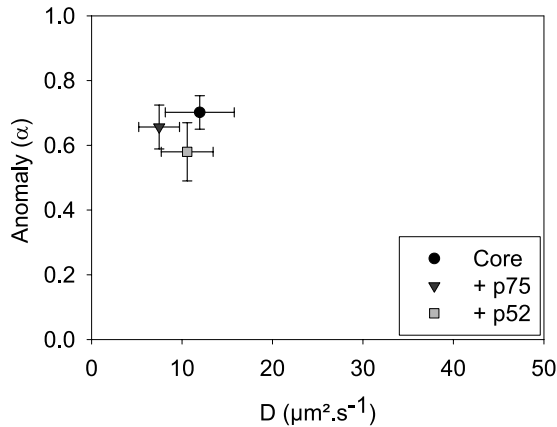


**Fig. 10** Influence of LEDGF/p75 and p52 on  $D_{\text{app}}$  of EGFP-IN/core. The anomalous diffusion model shows a 1.6-fold shift for  $D_{\text{app}}$  when LEDGF/p75 is present and a small shift of 1.1 for  $D_{\text{app}}$  when p52 is overexpressed in cells

with LEDGF/p75, we transiently knocked down LEDGF/p75 using specific siRNA and measured the diffusion of full-length HIV-1 IN. IN diffused faster when LEDGF/p75 levels were reduced and displayed a diffusion behavior similar to the IN/core domain, both in the cytoplasm and the nucleus (data not shown).

When the same data are fitted with a model for anomalous diffusion, there is also a small shift in the apparent diffusion coefficient upon overexpression of p52 (factor 1.1). This is, however, smaller than the shift upon overexpression of LEDGF/p75, where we observe a 1.6-fold difference. Nevertheless, the anomalous diffusion model makes the shift in diffusion coefficient less pronounced (Fig. 10, Table 1).

## 6 Conclusions

The interactions between integrase and LEDGF/p75 were studied using FCS in living cells. The observed autocorrelation curves could be fitted equally well with a two-component system as with the model for anomalous diffusion, since the chi-square values were comparable. We performed this analysis because we wanted to see if the anomaly model would be better (or not) for distinguishing known protein-protein interactions, and whether this fit would give more accurate results.

For the EGFP-IN/Nt deletion mutant it was interesting to see that we could almost fit the data with a one-component model, which corresponded to an anomaly parameter close to 1. For all the other proteins the anomaly

parameter varied between 0.6 and 0.7, and was close to the fraction of fast component in the two-component fit.

We can thus conclude that the anomaly factor for a given cell type is different for different proteins and can even be different for proteins with similar size. The anomaly factor also varies inside the cell from spot to spot, as was demonstrated before [28]. The anomaly factor is therefore not characteristic of the medium alone, but of the interactions between the diffusing protein and the medium.

When using a two-component fit, a true diffusion coefficient ( $D_{\text{fast}}$ ) is attributed to the fast moving fraction. The slow moving molecules are thus considered as obstructed molecules and have no contribution to the fast diffusion coefficient of the measured protein. In the case of anomalous diffusion, the average diffusion time (for a given  $\omega_1$ ) can be used to calculate an apparent diffusion coefficient ( $D_{\text{app}}$ ). For  $\alpha = 1$ ,  $D_{\text{app}}$  equals the fast diffusion coefficient, but for  $\alpha < 1$ , it is smaller than the fast diffusion coefficient, and it does not reflect the known interactions between integrase and LEDGF/p75 as well. If we look at proteins of comparable size,  $D_{\text{app}}$  is dependent on the anomaly in the cell, whereas  $D_{\text{fast}}$  is an independent parameter. Therefore, in the case of the HIV-1 proteins,  $D_{\text{fast}}$  is a more accurate measure of the size changes due to specific interactions and  $D_{\text{slow}}$  reflects more the interactions with all the cellular components.

## References

1. Brown PO, Coffin J, Hughes S, Varmus H (1997) Integration in retroviruses. Cold Spring Harbor Laboratory Press, Cold Spring Harbor, USA, p 161
2. Cai ML, Zheng RL, Caffrey M, Craigie R, Clore GM, Gronenborn AM (1997) Nat Struct Biol 4:839
3. Cherepanov P, Maertens G, Proost P, Devreese B, Van Beeumen J, Engelborghs Y, De Clercq E, Debyser Z (2003) J Biol Chem 278:372
4. Deprez E, Tauc P, Leh H, Mouscadet JF, Auclair C, Brochon JC (2000) Biochemistry 39:9275
5. Engelman A, Bushman FD, Craigie R (1993) EMBO J 12:3269
6. Haupts U, Maiti S, Schwille P, Webb WW (1998) Proc Natl Acad Sci USA 95:13573
7. Jenkins TM, Engelman A, Ghirlardo R, Craigie R (1996) J Biol Chem 271:7712
8. Kim SA, Heinze KG, Waxham MN, Schwille P (2004) Proc Natl Acad Sci USA 101:105
9. Lee SP, Xiao JM, Knutson JR, Lewis MS, Han MK (1997) Biochemistry 36:173
10. Llano M, Vanegas M, Fregoso O, Saenz D, Chung S, Peretz M, Poeschla EM (2004) J Virol 78:9524
11. Maertens G, Cherepanov P, Debyser Z, Engelborghs Y, Engelman A (2004) J Biol Chem 279:33421
12. Maertens G, Cherepanov P, Pluymers W, Busschots K, De Clercq E, Debyser Z, Engelborghs Y (2003) J Biol Chem 278:33528
13. Maertens G, Vercammen J, Debyser Z, Engelborghs Y (2005) FASEB J 19:1039
14. Magde D (1977) Mol Biol Biochem Biophys 24:43
15. Minton AP (2000) Curr Opin Struct Biol 10:34

16. Nishizawa Y, Usukura J, Singh DP, Chylack LT Jr, Shinohara T (2001) *Cell Tissue Res* 305:107
17. Politz JC, Browne ES, Wolf DE, Pederson T (1998) *Proc Natl Acad Sci USA* 95:6043
18. Rigler R, Mets U, Widengren J, Kask P (1993) *Eur Biophys J Biophys Lett* 22:169
19. Ruan Q, Cheng MA, Levi M, Gratton E, Mantulin WW (2004) *Biophys J* 87:1260
20. Ruchira, Hink MA, Bosgraaf L, van Haastert PJ, Visser AJ (2004) *J Biol Chem* 279:10013
21. Saito K, Wada I, Tamura M, Kinjo M (2004) *Biochem Biophys Res Commun* 324:849
22. Saxton MJ (1994) *Biophys J* 66:394
23. Saxton MJ (1996) *Biophys J* 70:1250
24. Schmiedeberg L, Weisshart K, Diekmann S, Meyer Zu HG, Hemmerich P (2004) *Mol Biol Cell* 15:2819
25. Schwille P, Haupts U, Maiti S, Webb WW (1999) *Biophys J* 77:2251
26. Sherman PA, Fyfe JA (1990) *Proc Natl Acad Sci USA* 87:5119
27. Thompson NL (1991) *Fluorescence correlation spectroscopy*, 1st edn. Plenum, New York
28. Wachsmuth M, Waldeck W, Langowski J (2000) *J Mol Biol* 298:677
29. Weiss M, Elsner M, Kartberg F, Nilsson T (2004) *Biophys J* 87:3518
30. Zheng R, Jenkins TM, Craigie R (1996) *Proc Natl Acad Sci USA* 93:13659

# Pushing the Complexity of Model Bilayers: Novel Prospects for Membrane Biophysics

Nicoletta Kahya<sup>1,2</sup> (✉) · Dennis Merkle<sup>1</sup> · Petra Schwillé<sup>1</sup>

<sup>1</sup>Institute of Biophysics, Biotechnology Center, Dresden University of Technology,  
Tatzberg 47–49, 01307 Dresden, Germany

<sup>2</sup>Present address:

Philips Research Eindhoven, High Tech Campus II, 5656 AE Eindhoven,  
The Netherlands

*nicoletta.kahya@philips.com*

1	Introduction . . . . .	340
2	Biomimetic Membranes for Optical Microscopy . . . . .	341
3	Domain Assembly in Giant Unilamellar Vesicles . . . . .	343
4	Giant Unilamellar Vesicles from Native Cellular Membranes . . . . .	347
4.1	GUVs from Bacterial Membranes . . . . .	348
4.2	Lipid Domains in Native Membranes . . . . .	350
4.3	A Minimal System for Membrane Tube Formation . . . . .	351
4.4	Protein Reconstitution in GUVs . . . . .	353
5	Future Directions . . . . .	356
	References . . . . .	357

**Abstract** As an interface between different biological compartments, membranes guarantee an efficient exchange of matter, energy and/or signals. For this purpose, such an interface has to be designed as a very dynamic system, yet with a non-random distribution of its components, lipids and proteins. A delicate balance of lipid and protein interactions is the basis of tightly regulated mechanisms to concentrate molecules at the site of interest at a specific time and, thereby, exclude unwanted components. In order to elucidate this highly intricate architecture, the top-down approach—by looking at the intact cell—is best complemented by a bottom-up strategy, by building the whole complexity starting from a minimal number of components. Within this framework, model membranes are key systems to isolate the biological machinery and identify its function. In this paper, we review research on biomimetic membranes for optical microspectroscopy. In particular, we focus on giant unilamellar vesicles (GUVs), and their application to studies on domain assembly and on membrane curvature and deformations. In order to build complexity, efforts must be made towards mimicking cellular compositions, by using GUVs with native lipid compositions, to reconstitute (complexes of) membrane proteins and to include components of an artificial cytoskeleton underneath the bilayer. Novel exciting avenues lie ahead in the arena of membrane biophysics, many of which are strongly coupled to the promising developments of optical technologies.

**Abbreviations**

AFM	atomic force microscopy
APP	amyloid precursor protein
BACE	beta-site-amyloid cleaving enzyme
BBMs	brush border membranes
Biot-DOPE	dioleoyl-phosphoethanolamine
BLM	black lipid membranes
DOPC	dioleoyl-phosphatidylcholine
DPPC	dipalmitoyl-phosphatidylcholine
DPPS	dipalmitoyl-phosphatidylserine
EPC	egg phosphatidylcholine
FCS	fluorescence correlation spectroscopy
FRAP	fluorescence recovery after photobleaching
FRET	fluorescence resonance energy transfer
GP	generalized polarization
GUVs	giant unilamellar vesicles
L <sub>d</sub>	liquid-disordered phase
L <sub>o</sub>	liquid-ordered phase
LUVs	large unilamellar vesicles
PE	phosphatidylethanolamine
PC	phosphatidylcholine
PI	phosphatidylinositol
PLFE	polar lipid fraction E
PS	phosphatidylserine
SM	sphingomyelin
SPT	single particle tracking
SUVs	small unilamellar vesicles
TBLE	total brain lipid extract

**1****Introduction**

As an interface between different biological compartments, membranes guarantee an efficient exchange of matter, energy and/or signals. For this purpose, such an interface has to be designed as a very dynamic system, yet with a non-random distribution of its components, lipids and proteins. Up to 1000 structurally different lipids have been identified in eukaryotic cells [1]. According to recent estimates, membrane proteins, which occupy on average one third of the mass of membranes, correspond to roughly one third of all membrane proteins encoded in the entire human genome [2]. Such a structural variety brings about a large spatial and temporal heterogeneity in the lipid and protein organization, which may be related to the way cells cope with the need to regulate biological processes at and around membranes in space and time.

The highly intricate architecture of cellular membranes represents a drawback in assigning biological function to lipids and proteins in the top-down



approach, by looking at the intact cell, mainly because of the large number of interfering events simultaneously occurring at the spot of interest. Complementing this approach with a bottom-up strategy is, therefore, highly desirable. Within this context, model membranes are key systems to isolate the biological machinery and identify its function.

From a methodological point of view, tracking lipids and proteins in space and time represents a big challenge. The small size of lipids makes it difficult to follow their trajectories in real time and in a non-invasive way (i.e. the size of the label is often comparable to the size of the lipid itself). This is the main reason why to assign biological significance to a lipid remains a challenge. On the other hand, membrane proteins may be easier to track but the biological implications of their lateral organization and association/dissociation behaviors are, in many cases, not well understood [3]. Furthermore, the problem of how lipids organize in space and time is tightly coupled to the problem of membrane protein distribution and association. In recent years, optical microscopy techniques have greatly contributed to broadening our knowledge of membranes, in particular with the development of single-molecule methodologies (Single Particle Tracking [4]—SPT—and Fluorescence (Cross)-Correlation Spectroscopy [5]—FCS) and Fluorescence Resonance Energy Transfer (FRET) [6].

In this paper, we focus on biomimetic membranes for optical microspectroscopy. After a brief overview of the model membranes available (Sect. 2), we focus on giant unilamellar vesicles (GUVs), which provide free-standing spherical closed bilayers with diameters between 10 and 100  $\mu\text{m}$ . Here, we present a few applications of GUVs to studies on domain assembly and on membrane curvature and deformations (Sect. 3). Continuing along the line of a bottom-up approach to characterize submicron membrane heterogeneity with close-to-native systems, efforts must be made towards an improvement of the complexity of biomimetic membranes. Possible steps in this direction are to use GUVs with native lipid compositions, to reconstitute (complexes of) membrane proteins and to include components of an artificial cytoskeleton underneath the bilayer. A few indications of these improving strategies are given in Sect. 4. Finally, as described in Sect. 5, novel exciting avenues lie ahead in the arena of membrane biophysics, many of which are strongly coupled to the promising developments of optical technologies.

## 2

### **Biomimetic Membranes for Optical Microscopy**

In order to study events occurring at and around membranes by means of optical microscopy, the bilayer has to span the illumination spot in the focal plane, whose lateral dimension goes with the half of the wavelength of light ( $\sim 250$  nm in the visible range). Here, we briefly provide an overview of the

most suitable model membranes developed through the years, starting from the most simple monolayers up to the most biomimetic giant vesicles.

Monolayers [7] provide a regular and stable structure and their composition can be accurately controlled. However, their ability to mimic biomembranes can be questioned, as they lack the second leaflet to form a bilayer. The first successful attempt to make membranes with a bilayer lipid arrangement was reported by Müller et al. [8] with the Black Lipid Membranes (BLMs). Two compartments are separated by a thin partition (septum) and communicate through an aperture (100–200  $\mu\text{m}$  in diameter) in this partition. An organic solution of lipids is brushed over the hole and then the compartments are filled with an aqueous medium. Dispersion of the solvent in the aqueous medium eventually leaves a bilayer on the hole. In practice, however, there are many technical limitations, which prevent the formation of an ideal BLM and lead to an irregular bilayer structure [9]. A very interesting alternative to BLMs is represented by bilayers assembled at the interface between a solid substrate and an aqueous phase. The early concept was based on the fusion of small unilamellar vesicles (SUVs), which can be deposited onto the hydrophilic surface of a clean polar substrate, such as glass or mica. This results in a supported membrane [10] floating on an ultra-thin ( $\sim 1\text{--}2$  nm) water layer. In general, the absence of a “bulk aqueous medium” between the bilayer and the solid substrate may give rise to secondary lipid–substrate interactions and, thereby, to artifacts. In particular, many membrane proteins protrude from the bilayer surface into the water phase, much further than 1–2 nm, implying their soluble residues interact with the solid substrate. Secondary interactions of this nature have been shown to cause a lack of protein lateral dynamics, which may lead to hindered conformational changes and lateral association/dissociation, and, in the end, to partial or complete loss of functionality. Some of these drawbacks have been partially solved by designing a tethered bilayer [10], which is composed of a solid substrate, a tethering layer (e.g. a soft polymer cushion) and a lipid bilayer. The soft and hydrophilic polymer should keep the lipid bilayer far apart from the rigid support, and thereby, preserve membrane fluidity. However, membrane proteins embedded in such a lipid matrix interact with the polymer and appear to be only partially mobile [11].

Supported lipid bilayers have been extensively exploited in various optical microscopy techniques, including imaging, SPT, and Fluorescence Recovery After Photobleaching (FRAP). Their big advantage is their accessibility with surface techniques, which makes them the most interesting model bilayers for combined studies of optical imaging and spectroscopy and high spatial resolution surface techniques, such as Atomic Force Microscopy (AFM). We and others have shown that optical microscopy can be successfully combined with AFM [12]. The latter technique can be in fact employed to study the organizational structure, with nanoscopic resolution, of supported bilayers on the basis of topographical variations (for instance between different

lipid phases [13]). Further information about the dynamics involved in lipid–lipid and lipid–protein interactions can be acquired, on a much faster time scale, by using sensible fluorescence techniques, like FCS [12]. As an example, we recently used a combined approach of AFM, fluorescence imaging and FCS in order to investigate the effects of ceramide inclusion in heterogeneous lipid bilayers, both from a structural and a dynamical point of view [14].

Finally, from a technological point of view, supported membranes provide an enormous potential for the production of biosensors, membrane chips [15] and membrane protein microarrays [16], constructed by lateral patterning of the bilayer–substrate architectures either with microlithography techniques [17] or by blotting and stamping the desired patterns [18]. Nevertheless, important properties of integral membrane proteins in a supported planar membrane—lateral mobility, association/dissociation behavior—seem to be far from those observed in the native cell membrane [11].

Potentially, the artifacts present in supported membranes are absent in Giant Unilamellar Vesicles (GUVs), which is a rapidly emerging model in membrane research [19]. GUVs are spherical closed single bilayers, freely floating in aqueous solution. They are suitable for single-molecule optical microscopy and exhibit a cell-like curvature, as their size ranges from 10 to 100  $\mu\text{m}$  in diameter. GUVs micromanipulation gives membrane researchers a unique opportunity to monitor a single colloidal particle exposed to controlled mechanical, thermal and/or (bio)chemical perturbations.

### 3

#### Domain Assembly in Giant Unilamellar Vesicles

Since they span the laser focus in the optical microscope and provide single free-standing bilayers, GUVs—as prepared according to the electroformation method [20–22]—are ideally suited for a wide range of applications, from studies of membrane thermal undulations up to mimicking biological processes of increasing complexity. Data on molecular diffusion coefficients and the analysis of the diffusion behavior helps to define the membrane organization in space and time, including the molecular packing and degree of conformational order. Lipid probes have been shown to diffuse in single-component GUVs in a Brownian-like fashion and the corresponding FCS curves are well fitted to a single-component 2D Brownian diffusion model [23, 24]. Diffusion coefficients in fluid membranes are on the order of  $\sim 1\text{--}20 \mu\text{m}^2/\text{s}$ , depending on the temperature, lipid composition and on the ionic strength/type of buffer. These values are consistent with those obtained with other techniques, such as SPT [25], FRAP [26] and diffusion NMR [27, 28].

Model membranes provide the minimal system to study the mechanism of lateral organization of lipids for both short- and long-range order. More

than 15 years ago, a new aspect of cell membrane structure was presented, which was based on the preferential packing of sphingolipids and cholesterol into dynamic clusters called lipid rafts [29, 30]. These microdomains would serve as functional platforms to which proteins can be selectively included or excluded. Domain assembly has been observed by us and other groups in the case of ternary lipid mixtures [24, 31–33]. Relatively simple mixtures of a low melting temperature ( $T_m$ ) lipid, a high  $T_m$  lipid, such as sphingomyelin, and cholesterol, exhibit a very complex phase behavior, as demonstrated by the various versions of phase diagrams based on different techniques [34, 35]. Liquid–liquid immiscibility has been observed over a wide range of lipid compositions and temperatures in the form of round micrometer-sized domains [35, 36]. We have explored several regions of the phase diagram for dioleoyl-phosphatidylcholine (DOPC), sphingomyelin (SM) and cholesterol (see Fig. 1) by combining confocal imaging and FCS [24]. On one hand, confocal imaging would give a static picture of the domain morphology, provided that sufficient contrast is reached by the preferential partitioning of the fluorescent probe in one lipid phase over the other. On the other hand, FCS would

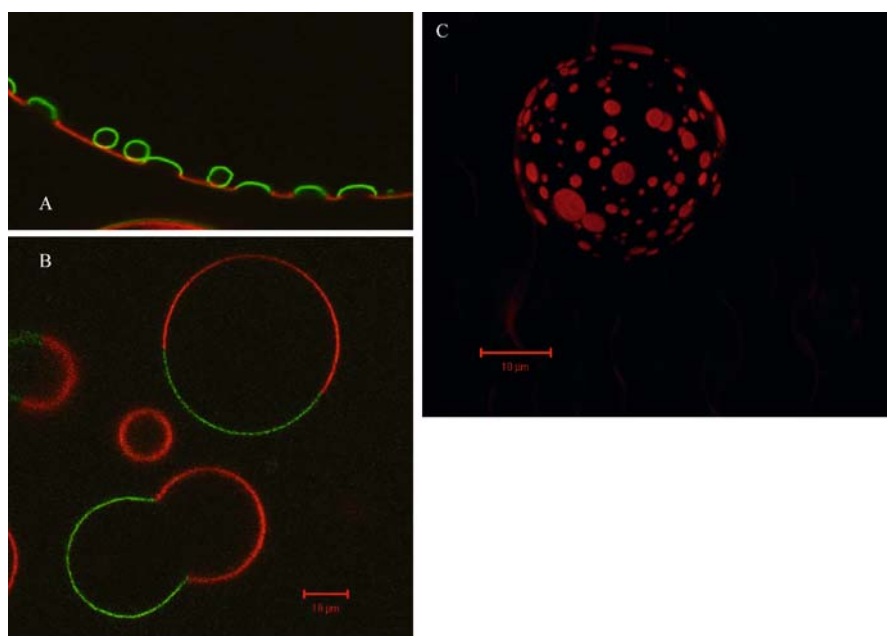


**Fig. 1** **A** and **B** Fluorescence confocal images of GUVs composed of sphingomyelin/dioleoylphosphatidylcholine/cholesterol 1 : 1 : 1 and 0.1% of GM1. *Red*: fluorescence from DiI-C<sub>18</sub> (0.1%). *Green*: fluorescence from GM1-bound AlexaFluor488-labeled cholera toxin B subunit. **C** Three dimensional projection of a stack of confocal images (thickness of 0.4  $\mu\text{m}$ ). The lipid composition is the same as in (**A** and **B**). *Red*: fluorescence from DiI-C<sub>18</sub> (0.1%)

give information on the lateral lipid diffusion and, hence, phase assignment and composition. FCS also helps to detect distinct phases, for instance in the case of low imaging contrast given by the fluorescent probe.

Although far from the real native membrane system, model membranes allow for a detailed investigation of the physico-chemical properties of lipids and lipid–lipid interactions. As an example, we studied in detail the effect of cholesterol on lipid mobility of equimolar mixtures of DOPC and SM [24]. Here, cholesterol induces formation of immiscible lipid phases, a liquid-disordered one,  $L_d$ , (characterized by high lipid mobility) and a liquid-ordered one,  $L_o$  (with low lipid mobility). Lipid mobility changes dramatically upon changing the amount of cholesterol (in mixtures with equimolar amounts of DOPC and SM). This suggests a change in the composition of the liquid domains, even if the domain morphology remains qualitatively unchanged. Cholesterol mostly affects the lipid packing of the  $L_o$  phase, enriched in SM, as shown by the steep increase of the lipid lateral diffusion rate by almost one order of magnitude [24]. By contrast, cholesterol plays little or no role in the mobility and packing of lipids in the  $L_d$  phase, which is enriched in DOPC.

The conclusions drawn from employing optical imaging necessarily rely on the ability of lipid probes to prefer one lipid phase to the other. However, the phase assignment is not straightforward as the partition coefficient of a probe strongly depends on the lipid composition of the bilayer. We found, for example, that the lipid analog DiI-C<sub>18</sub> prefers the  $L_d$  to the  $L_o$  phase in DOPC/SM/cholesterol mixtures but it mainly associates with the  $L_o$  phase in DOPC/DSPC/cholesterol mixtures [37]. In this respect, FCS offers an independent and reliable tool to assign lipid phases. Alternatively, one can exploit the spectral differences in the emission spectrum of a dye, Laurdan, which equally partitions in all of the lipid phases. Its emission spectrum is sensitive to the alignment of the acyl chains within a bilayer, thereby allowing for discriminating a solid phase (relatively blue emission) from a  $L_d$  phase (relatively red emission) [31].

Theoretical calculations have demonstrated that domain assembly may induce local membrane curvature deformations [38, 39]. By applying fluorescence microscopy to GUVs, in which domain assembly have been achieved by mixing SM, DOPC and cholesterol (i.e. lipids mainly present in the outer leaflet of the plasma membrane), Baumgartner et al. [40] have shown a direct correlation between domain composition and local bilayer curvature. Parameters, such as line tension and local curvature of different domain shapes and patterns can be optically resolved and systematically investigated. This approach may be used in more advanced studies of the influence of membrane additives and/or proteins on membrane curvature and can be used to test the function and composition of biological machines in local membrane bending in crucial processes, such as endo- and exocytosis and viral infection.

A direct correlation between membrane composition, domain assembly and local curvature has been observed also in GUVs, whose composition mimicked the inner leaflet of the plasma membrane. Whether rafts are present at the inner leaflet of the plasma membrane is an open question. However, intriguing hypotheses have been brought forward on the effect of local accumulation of certain lipids at the site of the membrane curvature deformations. We prepared GUVs from dipalmitoyl-phosphatidylcholine (DPPC) and dipalmitoyl-phosphatidylserine (DPPS), in order to investigate the differential packing ability of lipids that differ only by the headgroup structure (see Fig. 2; N. Kahya, unpublished results). For certain PC:PS ra-

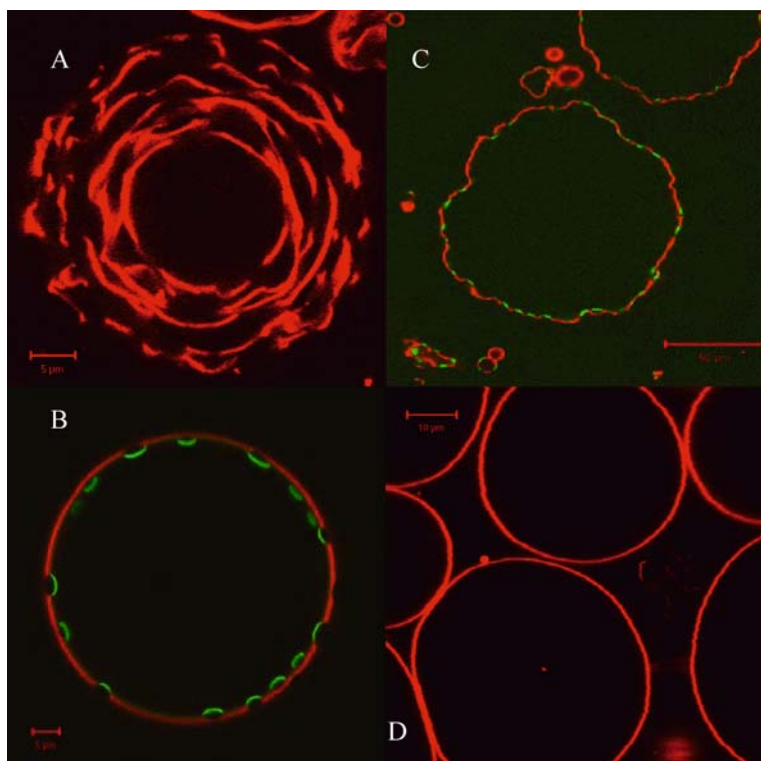


**Fig. 2** **A** Confocal image of a multilamellar vesicle composed of dipalmitoyl-phosphatidylcholine/dipalmitoyl-phosphatidylethanolamine 3 : 1 and 0.1% of DiI-C<sub>18</sub> (red). **B** Confocal image of GUVs composed of dipalmitoyl-phosphatidylcholine/dipalmitoyl-phosphatidylserine 3 : 1, 0.1% of DiI-C<sub>18</sub> (red) and membrane-bound AlexaFluor488-labeled Annexin V (green). **C** Confocal image of a GUV composed of dipalmitoyl-phosphatidylcholine/dipalmitoyl-phosphatidylserine/cholesterol 3 : 1 : 0.2, 0.1% of DiI-C<sub>18</sub> (red) and membrane-bound AlexaFluor488-labeled Annexin V (green). **D** Confocal image of a GUV composed of dipalmitoyl-phosphatidylcholine/dipalmitoyl-phosphatidylserine/cholesterol 3 : 1 : 0.5, and 0.1% of DiI-C<sub>18</sub> (red)

tios, phase separation was optically resolved in the fluorescence microscope, by exploiting the preferential partitioning of DiI-C<sub>18</sub> into the PC-enriched domains (see Fig. 2A). Such vesicles are stable over time and exhibit peculiar shapes and local curvature. The phase assignment was confirmed by adding AlexaFluor488-labeled Annexin V (Fig. 2B). The green-labeled protein only bound to PS-enriched regions, which were exactly complementary to the PC-enriched ones. Note the local membrane deformations induced by distinct domain compositions. Strikingly, adding cholesterol to the lipid mixture had the effect of relaxing local membrane deformations (see Fig. 2C). Further additions of cholesterol caused lipid mixing and, thereby disappearance of the large, optically resolved domains (Fig. 2D). Although further systematic studies are needed to quantify the effect of the lipid headgroup on domain assembly and membrane curvature, these results already show intriguing correlations between lipid structure, clustering and bilayer curvature, which could be relevant to important biological processes.

## 4

### Giant Unilamellar Vesicles from Native Cellular Membranes

The use of complex synthetic lipid mixtures for the formation of GUVs has shed light upon many biological phenomena, such as, lipid sorting and dynamics. Furthermore, the reconstitution of proteins in GUVs has provided valuable insight into protein–lipid interactions, as well as, protein functionality in membranes. None the less, the eukaryotic cell has many different membranes that serve various functions beyond being a simple “barrier of the cell.” Complex and diverse lipid mixtures also provide encapsulation for various cellular compartments and organelles, such as the Golgi, endoplasmic reticulum, lysosome, nuclear membrane and mitochondria, to name a few (reviewed in [41]). The lipid composition of these various membranes plays important roles in how each organelle or “barrier” functions. For example, what kinds of molecules can be transported through the membranes, how the lipids sort themselves and hence how the proteins found in those membranes sort themselves and function can all be affected by the composition of the lipids in the membrane. While GUV studies using synthetic lipid mixtures are useful, it is difficult to achieve the level of complexity, with respect to lipid content, found in natural cellular membranes. The major lipid constituents found in cellular membranes include; phosphatidylcholine (PC), phosphatidylethanolamine (PE), phosphatidylserine (PS), phosphatidylinositol (PI), cholesterol, sphingomyelin (SM), cardiolipin, and glycolipid, among other triglycerides, free fatty acids and cholesterol esters [41]. Since every cellular organelle and plasma membrane can contain a diverse composition of the lipids listed above, it is easily understood how GUVs formed from na-

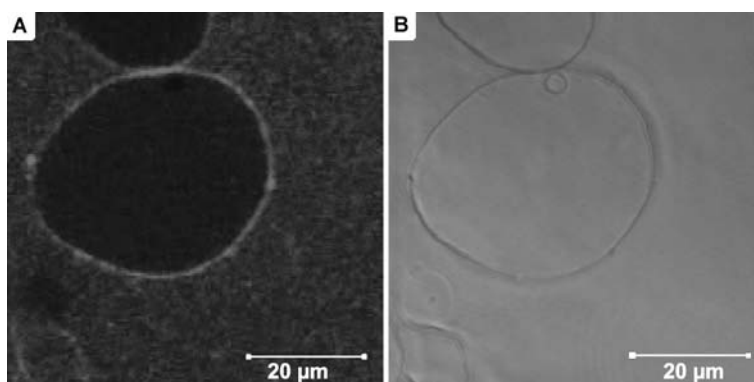


**Fig. 3** GUV grown from extracted porcine brain membranes and visualized using confocal scanning microscopy. **A** The membrane is stained with a primary mouse monoclonal antibody against the transmembrane Na/K-ATPase and detected via a secondary goat anti-mouse antibody conjugated to Cy5. **B** Phase contrast image of the same GUV as in (A)

tive membranes can be advantageous for the study of such specific protein and lipid systems (see Fig. 3). Furthermore, since the membranes of cellular organelles exhibit characteristic distributions of lipids, it is desirable to achieve as close as possible such native lipid patterns when examining model membrane systems.

#### 4.1

##### GUVs from Bacterial Membranes

One of the earliest examples of GUVs produced from native membranes came from Bagatolli et al., (2000); the group examined the fluorescence properties of the polarity-sensitive membrane probe Laurdan (6-lauroyl-2-(dimethylamino)naphthalene), as well as the effects of temperature and pH, in the polar lipid fraction E (PLFE) from the thermoacidophilic archaibacterium *Sulfolobus acidocaldarius*. Laurdan is an excellent membrane probe due to its polar-sensitivity and has been employed in previous studies looking at defined shape hysteresis at the phase transition temperature in single component GUVs as well as in fluorescence images of solid and fluid lipid domains in GUVs composed of binary mixtures of monopolar diester phospholipids [42]. *S. acidocaldarius* live at high temperatures (65–80 °C) and in acidic environments (pH 2–3) while maintaining a nearly neutral intracellular pH. PLFE is the major component of the *S. acidocaldarius* plasma membrane and, compared to vesicles formed from standard diester lipids, liposomes from PLFE display high thermal stability due to a tight and rigid membrane packing.

Bagatolli et al. prepared GUVs of PLFE at 65 °C by the electroformation method [20–22] at pH 7.23, as well as at pH 2.86; the GUVs are negatively



charged at both pH levels. Next Bagatolli examined the effect of temperature on the Laurdan generalized polarization (GP) in the PLFE GUVs by scanning two-photon fluorescence images at the center cross section, as well as the top and bottom surfaces of the target vesicles, as they were cooled from 66.0 to 12.0 °C (at 0.18°/min) for pH 7.23 and from 64.8 to 12.7 °C (at 0.15°/min) for pH 2.86. Results at pH 7.23 demonstrate that there is a small but steady increase in the average GP from 66.0 to 52.0 °C, followed by an abrupt increase at approximately 50 °C. Below this temperature, the average GP continuously shows a slight increase. At pH 2.86, Bagatolli observed a similar effect with the average GP exhibiting an abrupt change near 50 °C; however, this change is much less pronounced compared to the case of pH 7.23. Interestingly, the PLFE GUVs at pH 7.23 demonstrated lipid domain formation at temperatures below 20 °C. Furthermore, the Laurdan is segregated from these lipid domains which had a snowflake-like appearance and were immobile within the vesicle from 12.8–23.2 °C. These domains shrunk between 24 and 28 °C and eventually disappeared at 29.2 °C. At pH 2.86, the PLFE GUVs also demonstrated domains at lower temperatures, however, these domains displayed irregular shapes. None the less, the immobility of these domains again demonstrates the rigid and tight packing of the PLFE lipids indicating that at lower temperatures these membranes undergo very little lateral diffusion.

This study demonstrated the effectiveness of Laurdan as a membrane probe due to its highly sensitive emission spectrum with respect to environmental polarity and the physical state of the membrane. While previous studies showed Laurdan had an emission dipole aligned perpendicular to the membrane surface of monopolar diester phospholipids, the emission dipole in the bipolar tetraether PLFE GUVs was shown to be mainly aligned parallel to the membrane surface. This would suggest that the naphthalene ring of the Laurdan resides in the PLFE polar headgroup region and the lauroyl tail inserts into the PLFE hydrocarbon core with the emission dipole of the chromophore aligned parallel to the membrane surface. In such a state, Laurdan is in close proximity to bound water molecules at the polar headgroups of the membrane, resulting in extensive solvent relaxation and hence the low GPs observed in the PLFE GUVs. The chromophore orientation can be attributed to the unique chemical structure and tight packing of the PLFE lipids and suggests that the abrupt change in GP around 50 °C is likely due to a temperature-induced conformational change of the polar headgroups in the PLFE membrane. Tighter membrane packing would hinder such headgroup conformational changes and hence the GP change at 50 °C of the pH 2.86 PLFE GUVs is not so pronounced. These results show how natural membranes can aid in the characterization of membrane probes with respect to how they behave in various lipid environments. Furthermore, these results improved the understanding of the plasma membrane of thermoacidophilic archaeobacteria.

## 4.2

### Lipid Domains in Native Membranes

The existence of glycosphingolipid-enriched domains (rafts) in synthetic lipid vesicles has been extensively studied. However, it was not until 2001 that the existence of such “rafts” was also demonstrated in native membranes [26]. Dietrich and colleagues isolated and purified brush border membranes (BBMs) from the renal cortical tissue of adult Sprague Dawley rats and formed GUVs via electrosweeling. These GUVs were directly compared to Laurdan-labeled GUVs from a raft forming a 1 : 1 : 1 mixture of DOPC/sphingomyelin/cholesterol with 1 mol % GM1 ganglioside. GM1 localizes to the glycosphingolipid fractions of such raft mixtures. Such a “raft mixture” of lipids is believed to be a good approximation to that composition found in detergent-resistant membranes from cells (i.e. cellular raft fractions). Round domains, indicating a fluid-phase state, on the order of 10  $\mu\text{m}$  in dimension were observed in polar sections of these lipid raft GUVs as they were cooled through 25  $^{\circ}\text{C}$ , as seen by scanning two-photon fluorescence microscopy.

Interestingly, GUVs formed from BBMs also demonstrated round domains similar to those seen in the synthetic raft mixture GUVs, however, these domains formed upon cooling to 45  $^{\circ}\text{C}$ , indicating a remarkable domain stability. Furthermore, upon removal of cholesterol from the BBM lipid extracts, domain formation in these GUVs was inhibited until cooling to 24  $^{\circ}\text{C}$  and displayed irregular shapes similar to gel domains observed in the fluid–gel coexistence region of binary phospholipid mixtures [23, 32]. These data suggest that sphingomyelin-enriched gel-like phases occur in the absence of cholesterol. This study demonstrated that formation of fluid-phase coexistence can also exist in natural multi-component lipid mixtures and is not restricted to simple synthetic lipid mixtures. While the domains observed in this study were on the order of 10  $\mu\text{m}$ , such rafts in biomembranes play a role as disperse, regulatory elements, and are likely far smaller (reviewed in [43]). In the plasma membrane lipids are in constant contact with proteins, especially the cytoskeleton. These interactions likely play critical roles in how rafts are organized and positioned in cells such that they can play a role in cellular signalling events. The native state of the plasma membrane is therefore likely to be close to a state of coexistence between different domains that can be regulated via subtle changes in local lipid, protein and/or other small molecule compositions to trigger domain formation, growth and rearrangement. In addition, the fact that lipid composition can affect the size, shape, formation and deformation of rafts in GUVs indicates that the partitioning of molecules in and out of these domains can be yet another important aspect for cellular regulation and signalling.

### 4.3

#### A Minimal System for Membrane Tube Formation

Dynamic tubular networks between the membranes of various cellular compartments, such the Golgi, the endoplasmic reticulum and the plasma membrane, participate in various cellular transport events (for examples see [44–47]). The formation and movement of such membrane tubes involves the microtubule based cytoskeleton as well as several classes of motor proteins of the dynein and kinesin families, which can directly bind membranes via lipid interaction domains [48, 49]. While many previous studies have demonstrated that membrane tubes can be pulled from membranes, using a variety of techniques including; hydrodynamic flow [50], micropipette manipulation [51] and optical tweezers [52], it was not until 2002 that Roux and colleagues directly demonstrated that motor proteins were capable of binding native lipid bilayers and subsequently generating membrane tubes [53]. Roux et al. showed that kinesin-coated beads, microtubules and ATP provided a minimal system for membrane tubule generation from Golgi-membrane formed GUVs.

Golgi membranes were purified from rat livers from which the Golgi lipids were isolated using standard protocols [54, 55]. From these Golgi lipid extracts GUVs were produced via the electroformation technique. GUVs were also formed from a mixture of egg phosphatidylcholine (EPC), cholesterol and a biotinylated form of dioleoyl-phosphoethanolamine (Biot-DOPE). Initially, Roux et al. [53] attached biotinylated kinesins (containing the motor domain of *Drosophila melanogaster* kinesin) to these EPC biotinylated GUVs via 100 nm streptavidin-coated polystyrene beads. The GUV-kinesin-coated bead complexes were then microinjected in a chamber coated with polymerized microtubules, in the presence of 1 mM ATP. Membrane tubes began to form from these GUVs within 10 min after injection and followed the path of the underlying microtubule network. Furthermore, side branching events of the lipid tubes were observed at the intersections of individual microtubules resulting in the formation of a network of lipid tubes extending up to 50  $\mu\text{m}$  from the GUVs. Tubes did not form in the absence of ATP, and in addition, the tube formation was dependent upon the use of streptavidin coated beads, since using streptavidin alone resulted in the kinesin attaching to the GUVs with no tubule growth. The tube networks formed were examined via transmission electron microscopy and indicated that single tubes were on the order of  $40 \pm 10$  nm in diameter which is in good agreement with the estimated size of similar tubes formed in vivo. In addition, it was often observed that two or more membrane tubes aligned along a single microtubule. The tubular networks formed in two phases; the first phase represented the emergence of tubes from a vesicle up until the formation of tubule networks, and the second phase corresponds to a progressive densification of the tube networks. The first growth phase (phase I) occurred at an average velocity of

$340 \pm 40$  nm/s, a value comparable to the speed of a kinesin coated bead moving along a microtubule in the absence of membranes, and the length of the tubes increased linearly with time. Upon entering the second growth phase (phase II), the average velocity decreased by a factor of two with the growth of the tubes slowing with time and eventually stopping. Phase II also displayed a greater fluctuation in the instantaneous velocity at the tip of the growing tubules.

Roux then examined the influence of lipid composition of the GUV membranes on the generation of tubes [53]. The addition of cholesterol to the GUVs did not significantly change the growth, velocity or diameter of the tubes formed. Interestingly, when the GUVs were prepared from a more complex lipid mixture, i.e. from isolated Golgi membranes (50% phosphatidylcholine, 20% phosphoethanolamine, 6% phosphatidylserine, 12% phosphatidylinositol, 8% sphingomyelin, and cholesterol), the kinetic parameters of tube formation were similar to the ones found with the EPC GUVs while the Golgi lipid GUVs also gave rise to networks consisting of bundles of membrane tubes. Finally, Roux et al. determined whether the tubes could be obtained by binding the kinesin-coated beads to membrane proteins instead of lipids [53]. To do this, the purified rat liver Golgi membranes were incubated with N-hydroxysuccinimide-biotin, which biotinylates amino groups on proteins. Again, the addition of kinesin-coated beads led to the formation of tube networks resembling those described above, with the exception that phase I of tube growth was not observed. Instead the tubules formed at a growth rate velocity observed in phase II and the tubes formed were also present in bundles.

The study by Roux and colleagues was an elegant example of how the use of GUVs can aid in understanding complex cellular signalling events [53]. For example, the fact that the growth velocity of the tubules during phase I was not significantly lower than that of free kinesin-coated beads moving on microtubules, suggests that the force experienced by an individual motor while pulling a tube is less than 1 pN. From static arguments, Roux and colleagues estimated a required force of approximately 12 pN to pull a tube, and since each bead contained 10–20 kinesins, the estimated load per motor is on the order of 1 pN or less. The fact that tubes pulled from Golgi membranes did not display phase I growth velocity may be due to high initial tension in these membranes. The velocity fluctuations observed in phase II may be due to fluctuations in tension or in the number of motors working at a given time during the tube pulling. While the exact nature of how motor proteins bind to membranes is still not clear, it has been demonstrated that some kinesin motors (KIF13A) can directly interact with coat proteins, which are large cytosolic complexes that are recruited on to membranes during the formation of transport intermediates in cells [56]. It is interesting that Roux observed a requirement for the kinesin-coated beads in order to promote membrane tube growth [53]. The formation of membrane patches (or rafts) containing coat

protein complexes or other motor protein anchoring sites may serve similar functions *in vivo* as the beads did in this study. Furthermore, this work demonstrated that the action of motor proteins is sufficient to produce membrane tubules from native membrane lipid bilayers.

#### 4.4

#### **Protein Reconstitution in GUVs**

The plasma membrane is a complex mixture, which can be thought to exist as a general three-layer compound system [41]. Its center is formed by a liquid crystalline lipid/protein layer, the outside is covered by a macromolecular film formed by oligosaccharides of the glycolipid headgroups and the branched polypeptide/oligosaccharide headgroups of glycoproteins, and on the intracellular side the bilayer is coupled to the membrane associated cytoskeleton (reviewed in [41]). It is therefore easily understood how a model membrane system is not a native membrane system in the absence of proteins. Proteins play critical roles throughout all types of cellular membranes, and therefore they play integral roles in how membranes behave. There exist several methods that have allowed the incorporation of membrane proteins into GUVs. The following section will briefly describe the most common methodologies employed to reconstitute membrane proteins into GUVs and will be followed by an elegant example of how these methods have led to a deeper understanding for how proteins function in membranes.

Several methods to produce proteo-GUVs have been developed and one of the simplest techniques consists of dehydration of biological membranes or preformed proteoliposomes in the presence of added exogenous lipids followed by rehydration of the lipids with a buffer [57, 58]. The major advantage of such a technique is that such vesicles can be prepared with a wide range of buffers, however, the vesicles produced from the rehydration are very heterogeneous with many multilamellar vesicles forming as well. None the less, this method has proved useful in experiments in which lipid tubes have been pulled from vesicles that have been rehydrated from a multilamellar lipid base [59, 60]. Using micropipettes these nanotubes can be extended to inflate new GUVs and even to create vast lipid tubule networks.

The most common method for the production of GUVs of constant size and unilamellarity is the electroformation method in which a dry lipid film is rehydrated in the presence of an alternating current electric field [22]. This methodology can include drying the membrane protein with the lipid such that it incorporates into the GUVs upon electroswelling. This was first achieved by Manneville and colleagues [61] for bacteriorhodopsin. Another methodology for the incorporation of membrane proteins into electroformed GUVs is to fuse the GUVs with small preformed proteoliposomes. This method was developed by Kahya et al. [62] and was also used to reconstitute bacteriorhodopsin into GUVs. A technique, which applies both principles

discussed above, involves the partial dehydration of preformed proteoliposomes followed by controlled rehydration via electroformation. This method is ideal since often the drying of a membrane protein in the presence of organic solvents leads to denaturation and inactivation of the protein. Meanwhile, vesicle fusion of proteoliposomes with GUVs can limit the amount of protein that can be incorporated and also requires other molecules, such as fusogenic peptides, to facilitate the fusion event. On the other hand, partial dehydration of proteoliposomes containing the protein of interest can result in consistent GUVs with a homogeneous distribution of the reconstituted transmembrane protein throughout the vesicle. This later technique was developed by Girard et al. [63] and was used to incorporate the  $\text{Ca}^{2+}$ -ATPase as well as bacteriorhodopsin into GUVs. More recently, a similar technique has been developed to examine raft partitioning of human placental alkaline phosphatase in GUVs [64] as well as the proteolytic activity of the  $\beta$ -secretase, beta-site-amyloid cleaving enzyme (BACE) [65], which will be discussed in more detail below. It is worth noting that the formation of proteoliposomes can be achieved using various methods (for examples see [66, 67]).

BACE is a membrane spanning aspartic protease, which cleaves the amyloid precursor protein (APP) during the initial stage of proteolytic processing leading to the formation of the neurotoxic  $\beta$ -amyloid peptide ( $A\beta$ ) [68]. The  $A\beta$  peptide is the major constituent of amyloid plaques in brains of patients suffering from Alzheimer disease [69, 70]. It is believed that APP is cleaved by BACE ( $\beta$ -cleavage) which then can lead to further processing by the  $\gamma$ -secretase to produce the  $A\beta$  peptide [68]. It is hence favorable to limit the contact between two such membrane proteins as APP and BACE by confining them into distinct cellular compartments, separate cellular trafficking routes and/or via partitioning into distinct membrane microdomains, i.e. lipid rafts [65]. Studies demonstrating that decreased cholesterol and sphingolipid levels, both of which are raft constituents, correlate with reduced  $\beta$ -cleavage implicate lipid rafts in APP processing [71]. In addition, ceramides, which have also been implicated in lipid domain organization, have been proposed as  $\beta$ -cleavage modulators [72]. In an elegant study by Kalvodova et al. [65], GUVs and LUVs of defined lipid composition were reconstituted with BACE and examined with respect to the lipid requirements for  $\beta$ -cleavage.

In order to incorporate BACE into GUVs, Kalvodova and colleagues first reconstituted BACE into LUVs by mixing liposomes with concentrated BACE, under mild detergent conditions and shaking for 15–45 min at 32 °C [65]. The sample was then loaded onto a Sephadex G-50 gel filtration column in order to purify the proteoliposomes. To form the proteo-GUVs, the prepared BACE-vesicle suspension was deposited onto ITO-coated coverslips and put under vacuum at 4 °C overnight. The dehydrated and fused liposomes were subsequently rehydrated in buffer under an alternate electric field for 3–4 h, producing numerous GUVs on the order of 10–150  $\mu\text{m}$ . The yield of the BACE in the preformed LUVs, by weight, was typically 15–30% and immu-

noelectron microscopy revealed that virtually all the BACE was found to be membrane associated. Furthermore, the specific activity of the vesicle reconstituted BACE was found to be 3-fold higher than that of the purified BACE in 0.02% Triton X-100, as judged by its ability to cleave a soluble fluorogenic substrate, which mimics the cleavage site of APP.

Kalvodova et al. examined the activity of the reconstituted BACE in complex lipid mixtures [65]. This was achieved by dissection of a total brain lipid extract (TBLE) and examining which lipid species are capable of supporting BACE activity. Since interpretation of the effects caused by a particular lipid species in such complex mixtures as brain membranes can be very problematic, various simple lipid mixtures of defined headgroup compositions were examined and compared to the activity of BACE reconstituted into a total brain lipid extract. The activity of BACE reconstituted in glycerophospholipids and glycerophospholipid:cholesterol vesicles was examined first since glycerophospholipids are the most abundant phospholipids in living cells. In vesicles containing pure PC, BACE activity was several-fold lower than that of BACE in TBLE vesicles. Inclusion of cholesterol still resulted in a five-fold lower BACE activity as compared to the TBLE-BACE LUVs. It has been demonstrated that many membrane proteins require PE for their activity [73], however in the case of BACE, the inclusion of up to 20% PE did not significantly affect the proteolytic activity in the PC vesicles. On the other hand, a strong effect of negatively charged phospholipids (i.e. PS) on the activity of PC-BACE vesicles was observed. PC:PS (at 80:20, w/w) supported BACE activity to approximately  $58 \pm 4\%$  of the TBLE LUVs and mixtures of PC:PE:PS and PC:PE:phosphatidic acid (PA) brought the specific activity of BACE back to the full level of TBLE.

The activity of BACE was then examined in vesicles from glycerophospholipids, sphingolipids and cholesterol. Proteoliposomes consisting of PC:PE:SM:gangliosides were supplemented with increasing amounts of cholesterol, substituting for SM, such that the molar ratios of cholesterol to sphingolipid were 0:0.4:2.5. An increase in BACE activity was observed with increasing cholesterol:sphingolipid molar ratios, however, the activity did not exceed  $36 \pm 1\%$  of the original TBLE-BACE activity. When sphingolipids were replaced with cerebrosides the activity increased to  $46 \pm 4\%$  of the TBLE-BACE LUVs, and furthermore, the addition of cerebrosides, as well as synthetic C8-glucosyleceramide greatly enhance the activity of purified solubilized BACE. This effect was not observed with any other lipids in the solubilized state.

The effect of negatively charged glycerophospholipids (i.e. PS) in vesicles composed of glycerophospholipids, sphingolipids, and cholesterol were also examined. There was a clear trend of increasing BACE activity with increasing amounts of PS, however, in mixtures with differing sphingolipid content, the response to the addition of PS varied. This suggests that the ratio of sphingolipid to phospholipids (and perhaps cholesterol) may play

critical roles in BACE regulation *in vivo*. Again, the addition of cerebrosides revealed higher BACE activities in these mixtures. Furthermore, methyl- $\beta$ -cyclodextrin was used to deplete cholesterol from the TBLE proteoliposomes resulting in a dramatic (up to four-fold) reduction in BACE activity.

Finally, BACE-GUVs were examined with respect to the portioning of BACE. From cellular extracts, BACE has been found to be partially associated with detergent resistant membrane (DRMs) fractions, and hence the authors examined the putative raft association of BACE by probing the partitioning of fluorescence labelled BACE between the  $L_o$  and  $L_d$  phases in GUVs. In pure DOPC vesicles ( $L_d$  phase only) there is a homogeneous distribution of BACE. In mixtures containing both  $L_d$  and  $L_o$  phases, BACE partitions into the  $L_o$  phase. In GUVs composed of DOPC:SM:cholesterol, in which microscopic domains on the order of several  $\mu\text{m}$  in diameter were formed, about 15–20% of BACE portioned into the  $L_o$  phase, whereas the addition of 1 mol % of GM1 which was subsequently crosslinked with cholera toxin subunit B, resulted in redistribution of BACE such that the partitioning between  $L_o$  and  $L_d$  phases was approximately equal [65].

The results of Kalvodova and colleagues have implications far too broad to discuss in detail here. None the less this study shows the importance of lipid content for the activity of reconstituted membrane proteins in both GUVs and smaller vesicles. This work underscores that while native membranes are the ideal physiological hosts for membrane proteins, at times simple lipid mixtures are required for a better understanding of how individual lipid components affect protein activity and partitioning in various lipid phases. It is clear that no one approach is superior for the study of lipid significance in biology, but that a multitude of techniques needs to be employed to access the finer details of these complex lipid–protein systems, these native membrane states.

## 5

### Future Directions

The obvious next step in GUV research as a “model membrane” would be the reconstitution of membrane proteins in their native membrane environment. This can be achieved by extracting native membranes from cellular fractions, without the removal of the proteins. Recently, we explored such options with respect to the trans-membrane receptors, ion channels and ATPases found in all eukaryotic cells. Such proteins include the Na/K-ATPase, the voltage-gated sodium channel, inositol 1,4,5-triphosphate receptor, CD44, L1CAM and the Na/Ca exchanger, just to name a few. The work described here is focused on the Na/K-ATPase (reviewed in Decollogne et al. [74]). These proteins play critical cellular roles from generating energy, maintaining osmotic balance within a cell, participating in cellular signalling, to anchoring cytoskeletal



components to the plasma membrane. We recently began investigations on these proteins, from porcine brain extracts, in GUVs (D. Merkle, N. Kahya, unpublished results). The brain extracts containing both membrane proteins and the native porcine brain membranes were produced as previously described [75].

Briefly, fresh porcine brain was homogenized and pelleted to produce a crude membrane extract. The crude membrane extract was then demyelinated via centrifugation through a 1 M sucrose bed. This starting membrane fraction still contained many anchored cytoskeletal components and hence was further extracted using 0.1 N NaOH (this step removes all non-integral membrane-associated proteins). The final extracted membranes were then repeatedly washed in buffer and pelleted via centrifugation, snap frozen in liquid nitrogen and stored at  $-80^{\circ}\text{C}$ . All experiments from such membrane fractions were completed within days of the extraction procedure. GUVs were grown from the porcine brain extracts using the electroformation technique and produced many unilamellar vesicles on the order of 10–100  $\mu\text{m}$  (Fig. 3). In order to demonstrate the presence of Na/K-ATPase, we then incubated the GUVs with a mouse monoclonal antibody directed against Na/K-ATPase, extensively washed the GUV sample and then incubated the GUVs with a secondary goat-anti-mouse antibody which was conjugated to the Cy5 fluorescent dye. Each antibody was incubated for 1 h and the wash steps were on the order of  $10\times$  the sample volume of the GUV growth chamber (approximately 200  $\mu\text{L}$ ). As can be seen in Fig. 3A, the GUVs are stained brightly with the Cy5 antibody only at the membrane border. While there is some background signal due to unbound antibody, it is clear that the antibody is localizing at the membrane of the GUV, and furthermore, the background fluorescence is even less inside the GUV. The presence of Na/K-ATPase in these fractions was also confirmed via immunoblot analysis and GUVs incubated in the absence of primary antibody, or with a non-specific primary mouse monoclonal antibody did not show this localized fluorescence at the membrane of the GUV (data not shown). While these results are preliminary and will be greatly expanded upon, these data represent the next critical step in further validating GUVs as model membrane systems and extending their applications into completely native membrane states.

**Acknowledgements** We thank Lucie Kalvodova and Salvo Chiantia for useful discussions.

## References

1. Cullis PR, Hope MJ, Tilcock CPS (1986) *Chem Phys Lipids* 40:127
2. Iwata S, Kaback HR (2004) *Curr Opin Struct Biol* 14:387
3. de Kruijff B (1985) Lipid polymorphism and membrane function. In: Martonosi AN (ed) *The Enzymes of Biological Membranes*, Vol 1. Membrane Structure and Dynamics, 2nd edn. Plenum Press, New York, pp 131–204

4. Schütz GJ, Schindler H, Schmidt T (1997) *Biophys J* 73:1073
5. Schwille P, Koriach J, Webb WW (1999) *Cytometry* 36:176
6. Almeida PF, Vaz WL, Thompson TE (1992) *Biochemistry* 31:7198
7. Lipp MM, Lee KYC, Zasadzinski JA, Waring AJ (1996) *Science* 273:1196
8. Müller P, Rudin DO, Tien HT, Wescott WC (1962) *Nature* 194:979
9. Meseth U (1998) PhD Thesis. Ecole Polytechnique Federale de Lausanne, Switzerland
10. Sackmann E (1996) *Science* 271:43
11. Wagner ML, Tamm LK (2000) *Biophys J* 79:1400
12. Shaw JE, Epand RF, Epand RM, Li Z, Bittman R, Yip CM (2006) *Biophys J* 90:2170
13. Chiantia S, Kahya N, Schwille P (2005) *Langmuir* 21:6317
14. Chiantia S, Kahya N, Ries J, Schwille P (2006) *Biophys J* 90:4500
15. Sinner EK, Knoll W (2001) *Curr Opin Chem Biol* 5:705
16. Fang Y, Frutos AG, Lahiri J (2002) *J Am Chem Soc* 124:2394
17. Groves JT, Ulman N, Boxer SG (1997) *Science* 275:651
18. Hovis JS, Boxer SG (2000) *Langmuir* 16:894
19. Menger FM, Keiper JS (1998) *Adv Mater* 10:888
20. Angelova MI, Dimitrov DS (1988) *Prog Colloid Polym Sci* 76:59
21. Dimitrov DS, Angelova MI (1987) *Prog Colloid Polym Sci* 73:48
22. Angelova MI, Soleau S, Meleard Ph, Faucon JF, Bothorel P (1992) *Prog Colloid Polym Sci* 89:127
23. Koriach J, Schwille P, Webb WW, Feigenson GW (1999) *Proc Natl Acad Sci USA* 96:8461
24. Kahya N, Scherfeld D, Bacia K, Poolman B, Schwille P (2003) *J Biol Chem* 278:28109
25. Schütz GJ, Schindler H, Schmidt T (1997) *Biophys J* 73:1073
26. Dietrich C, Bagatolli LA, Volovyk ZN, Thompson NL, Levi M, Jacobson K, Gratton E (2001) *Biophys J* 80:1417
27. Vist MR, Davis JH (1990) *Biochemistry* 29:451
28. Filippov A, Oradd G, Lindblom G (2004) *Biophys J* 86:891
29. Simons K, van Meer G (1988) *Biochemistry* 27:6197
30. Simons K, Toomre D (2000) *Nat Rev Mol Cell Biol* 1:31
31. Parasassi T, Gratton E (1995) *J Fluor* 5:59
32. Bagatolli LA, Gratton E (2000) *Biophys J* 78:290
33. Samsonov AV, Mihalyov I, Cohen FC (2001) *Biophys J* 81:1486
34. De Almeida RFM, Fedorov A, Prieto M (2003) *Biophys J* 85:2406
35. Veatch SL, Keller SL (2003) *Biophys J* 85:3074
36. Bagatolli LA, Gratton E (1999) *Biophys J* 77:2090
37. Scherfeld D, Kahya N, Schwille P (2003) *Biophys J* 85:3758
38. Lipowski R, Dimova R (2003) *J Phys Condens Matter* 15:S31
39. Benvegnu DJ, McConnell HM (1992) *J Phys Chem* 96:6820
40. Baumgart T, Hess ST, Webb WW (2003) *Nature* 425:821
41. Sackmann E (1995) In: *Handbook of Biological Physics, Vol 1A. Structure and Dynamics of Membranes: From Cells to Vesicles*. Elsevier, Amsterdam, pp 1–19
42. Bagatolli LA, Gratton E, Khan TK, Lee-Gau Chong P (2000) *Biophys J* 79:416
43. Jacobson K, Dietrich C (1999) *Trends Cell Biol* 9:87
44. Keller P, Toomre D, Diaz E, White J, Simons K (2001) *Nat Cell Biol* 3:140
45. Stephens DL, Pepperkok R (2001) *J Cell Sci* 114:1053
46. Polishchuk RS, Polishchuk EV, Marra P, Saverio A, Roberto B, Luini A, Mironov AA (2000) *J Cell Biol* 148:45
47. Hirschberg K, Miller CM, Ellenberg J, Presley JF, Siggia ED, Phair RD, Lippincott-Schwartz J (1998) *J Cell Biol* 143:1485

48. Allan VJ, Schroer TA (1999) *Curr Opin Cell Biol* 11:476
49. Hirokawa N (1998) *Science* 279:519
50. Waugh RE (1982) *Biophys J* 38:19
51. Evans E, Yeung A (1994) *Chem Phys Lipids* 73:39
52. Raucher D, Sheetz MP (1999) *Biophys J* 77:1992
53. Roux A, Cappello G, Cartaud J, Prost J, Goud B, Bassereau P (2002) *Proc Natl Acad Sci USA* 99:5394
54. Slusarewicz P, Hui N, Warren G (1994) In: *Cell Biology: A Laboratory Handbook*, Vol 1. Academic Press, San Diego, pp 509–516
55. Brugger B, Sandhoff R, Wegehingel S, Gorgas K, Malsam J, Helms JB, Lehmann WD, Nickel W, Wieland FT (2000) *J Cell Biol* 151:507
56. Nakagawa T, Setou M, Seog D, Ogasawara K, Dohmae N, Takio K, Hirokawa N (2000) *Cell* 103:569
57. Ajouz B, Berrier C, Besnard M, Martinac B, Ghazi A (2000) *J Biol Chem* 275:1015
58. Darzon A, Vandenberg CA, Schonfeld M, Ellisman MH, Spitzer NC, Montal M (1980) *Proc Natl Acad Sci USA* 77:239
59. Davidson M, Karlsson M, Sinclair J, Sott K, Orwar O (2003) *J Am Chem Soc* 125:374
60. Karlsson M, Sott K, Davidson M, Cans AS, Linderholm P, Chiu D, Orwar O (2002) *Proc Natl Acad Sci USA* 99:11573
61. Manneville J-B, Bassereau P, Ramaswamy S, Prost J (2001) *Phys Rev E* 64:021908
62. Kahya N, Pécheur E-I, de Boeij WP, Wiersma DA, Hoekstra D (2001) *Biophys J* 81:1464
63. Girard P, Pécréaux J, Lenoir G, Falson P, Rigaud J-L, Bassereau P (2004) *Biophys J* 87:419
64. Kahya N, Brown DA, Schwille P (2005) *Biochemistry* 44:7479
65. Kalvodova L, Kahya N, Schwille P, Ehehalt R, Verkade P, Drechsel D, Simons K (2005) *J Biol Chem* 280:36815
66. Brown DA (2001) *Proc Natl Acad Sci USA* 98:10517
67. Schroeder RJ, Ahmed SN, Zhu Y, London E, Brown DA (1998) *J Biol Chem* 279:1150
68. Hussain I, Powell D, Howlett DR, Tew DG, Meek TD, Chapman C, Gloger IS, Murphy KE, Southan CD, Ryan DM, Smith TS, Simmons DL, Walsh FS, Dingwall C, Christie G (1999) *Mol Cell Neurosci* 14:419
69. Selkoe DJ (1994) *Curr Opin Neurobiol* 4:708
70. Selkoe DJ (2001) *Physiol Rev* 81:741
71. Ehehalt R, Keller P, Haas C, Thiele C, Simons K (2003) *J Cell Biol* 160:113
72. Puglielli L, Ellis BC, Saunders AJ, Kovacs DM (2003) *J Biol Chem* 278:19777
73. Bogdanov M, Sun J, Kaback HR, Dowhan W (1996) *J Biol Chem* 271:11615
74. Decollogne S, Bertrand IB, Ascensio A, Drubaix I, Lelievre LG (1993) *J Cardiovasc Pharmacol* 22:S96
75. Davis JQ, Bennett V (1986) *J Biol Chem* 261:16198

**Part D**  
**Nanotubes, Microparticles and Nanoparticles**

# Photoluminescence Properties of Carbon Nanotubes

Bing Zhou · Yi Lin · Barbara A. Harruff · Ya-Ping Sun (✉)

Department of Chemistry and Laboratory for Emerging Materials and Technology,  
Clemson University, P.O. Box 340973, Clemson, SC 29634-0973, USA  
*syaping@clemson.edu*

1	Introduction . . . . .	363
2	Functionalization and Dispersion of Carbon Nanotubes . . . . .	364
3	Luminescence from Modified/Functionalized Carbon Nanotubes . . . . .	367
3.1	General Features and Properties . . . . .	367
3.1.1	Effect of Dispersion . . . . .	370
3.1.2	Effect on Raman Spectra . . . . .	372
3.2	Luminescence Polarization . . . . .	373
3.3	Potential Applications . . . . .	375
4	Defect-Derived vs Bandgap Emissions . . . . .	377
	References . . . . .	378

**Abstract** Carbon nanotubes, upon surface modification through defects-targeted functionalization, exhibit strong photoluminescence in the visible and into the near-IR region. In this chapter, the general features and polarization characteristics of the photoluminescence are highlighted, mechanistic issues addressed, and potential applications explored. The similarities and differences between the defect-derived emission and the bandgap fluorescence (emission from individualized single-walled carbon nanotubes) are also discussed.

## 1 Introduction

Carbon nanotubes have attracted much interest for their novel properties [1–3]. As predicted theoretically, the electronic states in semiconducting single-walled carbon nanotubes (SWNTs) are characterized by sharp spikes in the density of states (DOS) [4]. Experimentally, electronic transitions in these nanotubes are featured as broad absorption bands in the near-infrared region, corresponding to the first ( $S_{11}$ ) and second ( $S_{22}$ ) van Hove singularity pairs [5]. The bandgap fluorescence mirroring the  $S_{11}$  absorption band was reported and studied first by O’Connell et al. and then by a number of other research groups for SWNTs mostly produced from the high-pressure carbon monoxide disproportionation (HiPco) process [6–14]. An accurate quantum yield value for the fluorescence is still being determined or decided, with current numbers ranging from 0.001 to 0.1%, presumably depending

on the degree of nanotube bundling/aggregation, surface doping, etc. [6–11]. There is apparently a required condition for the observation of bandgap fluorescence in SWNTs, namely that the nanotubes must be dispersed very well to minimize internanotube quenching effects [6, 7, 11]. Recently, there were reports on the detection of bandgap fluorescence for suspended SWNTs in an ambient environment [12] and also for nanotubes produced by the laser ablation method [8, 9, 13, 14].

Even before the first report on bandgap fluorescence from semiconducting SWNTs, both single- and multiple-walled carbon nanotubes (MWNTs) were found, upon their surface modification or functionalization, to be strongly emissive in the visible and near-IR regions [15]. In that report, Sun and coworkers referred to the emission as luminescence because the nature of the emissive excited state was not known. The luminescence was bright, with quantum yields of up to more than 10% under some conditions [15]. While there were questions on the assignment of the strong emission to carbon nanotube species [16], several other research groups confirmed the observation and assignment in subsequent investigations [17, 18]. For example, Guldi and coworkers reported that the luminescence was associated with carbon nanotube samples from different production methods, including laser ablation and arc discharge, and with heavily oxidized nanotubes [17]. Similarly, Wong and coworkers reported strong visible luminescence from carbon nanotubes that were functionalized with Wilkinson's catalyst [18]. Mechanistically, Sun and coworkers suggested that the broad visible luminescence could be attributed to the presence of passivated surface defects on carbon nanotubes, which serve as trapping sites for the excitation energy. The passivation, as a result of the surface modification and functionalization with oligomeric and polymeric species, stabilizes the emissive sites in their competition with other excited-state deactivation pathways [15, 19, 20].

The defect-derived luminescence of surface-modified or functionalized carbon nanotubes represents an interesting optical property of carbon nanotubes because surface defects should be considered as the norm rather than exception in typical SWNTs and MWNTs. It may find many applications, such as luminescence imaging with visible and near-IR colors and nanotube sensors based on luminescence quenching properties. In this article, we will discuss the characteristics of the defect-derived luminescence and its dependence on the surface modification and functionalization of the carbon nanotubes, and some mechanistic and application-relevant issues.

## 2

### **Functionalization and Dispersion of Carbon Nanotubes**

It was about a decade after the discovery of carbon nanotubes that it was realized that these nanotubes are in fact strongly luminescent under well-

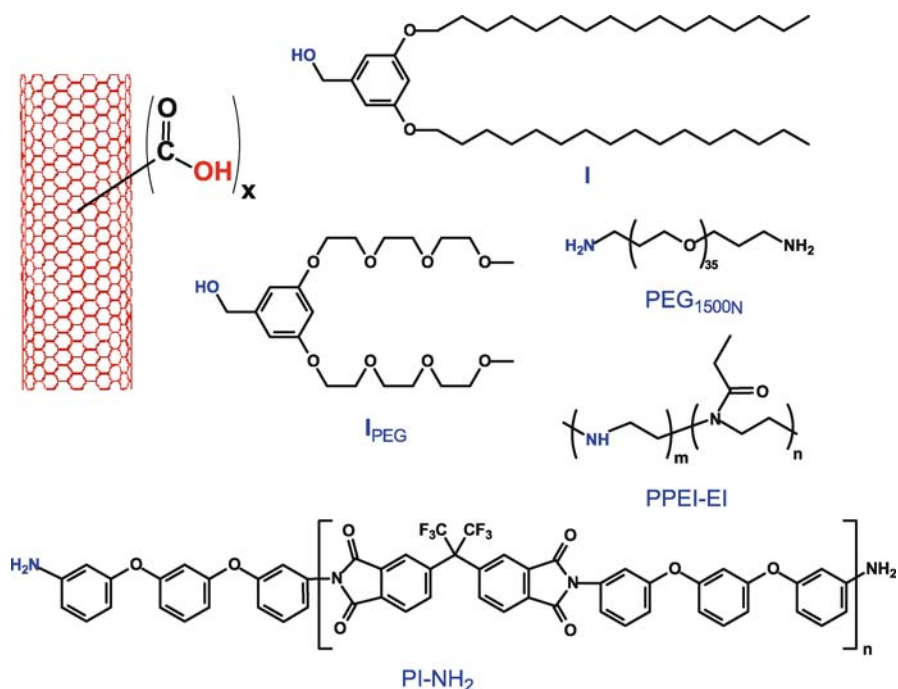
defined conditions [15]. The revealing of the luminescence was a direct result of the significant advance in the chemical modification and functionalization of carbon nanotubes for their solubilization and dispersion at the individual nanotube level [20, 21].

As-produced carbon nanotubes are generally insoluble in common organic solvents and water [22]. The insolubility is due to the fact that these species are relatively large in size and also significantly bundled (strong van der Waals interactions between adjacent nanotube graphitic surfaces). The bundling of nanotubes has made it difficult to observe many of their intrinsic properties, including the bandgap fluorescence and the defect-derived luminescence, due to their sensitivity to internanotube quenching [6, 15].

The field of chemical functionalization of carbon nanotubes has become very active and diversified, driven primarily by application needs in the processing of nanotube-based materials. The functionalization leads to the homogeneous dispersion (the exfoliation of nanotube bundles, especially for SWNTs) and solubilization of the nanotubes. The chemical functionalization methods may be classified roughly into two categories: noncovalent and covalent modifications [21, 23–26]. The noncovalent functionalization methods usually take advantage of the hydrophobic or  $\pi$ - $\pi$  interactions between functional molecules (such as surfactants and some polymers) and the nanotube surface. The reagents in covalent methods target either the nanotube graphitic sidewall [23–25] or surface defect sites (carboxylic acid moieties from oxidative acid treatment of the defect carbons on nanotubes, see below) [21, 26]. Compared to noncovalent functionalization, covalent methods have provided a higher degree of flexibility in functional group selection and generally higher efficiency in the resulting nanotube dispersion and solubilization.

The nanotube sidewall chemistry is largely derived from the previously well-developed graphite and fullerene chemistry, since the reactivity of nanotube  $sp^2$  carbons, as a result of  $\pi$ -orbital misalignment and curvature-induced pyramidalization, is in fact intermediate between those two carbon allotropes [26]. A less attractive feature of the dispersion and solubilization via the sidewall chemistry in some applications is that it disrupts the nanotube graphitic surface and thus alters the nanotube electronic structure, again making it difficult to observe and study many intrinsic properties of the underlying carbon nanotubes. The functionalization targeting nanotube surface defects (including open ends) seems to preserve the nanotube electronic structure much better [26, 27].

Experimentally, a typical estimate of the population of defects on the nanotube surface suggests that the defects represent a few percent of the nanotube carbons [28, 29]. After oxidative treatment, these defect nanotube carbons are converted into oxygen-containing groups (especially carboxylic acid moieties). These functional groups on the nanotube surface may be derivatized with a variety of reagents in functionalization reactions. For example, Sun and coworkers have explored many oligomeric and polymeric molecules con-



**Scheme 1** Oligomeric and polymeric molecules for defect-derivatized functionalization of carbon nanotubes

taining hydroxyl or amino groups for esterification or amidation reactions with the nanotube-bound carboxylic acids (Scheme 1) [21].

The functionalization of carbon nanotubes with the selected oligomeric or polymeric molecules typically improves dramatically their solubility in common organic solvents and/or water, depending upon the properties of the molecules. For example, solubility of carbon nanotubes in both water and organic solvents was afforded by functionalization with amine-terminated oligomeric polyethylene glycol (PEG<sub>1500N</sub>) [30] or poly(propionyl-ethyleneimine-*co*-ethyleneimine) (PPEI-EI) (Scheme 1) [31]. The nanotube-equivalent solubilities for the functionalized carbon nanotubes are usually on the order of a few mg/mL to as high as about 100 mg/mL with the right functional groups and functionalization reactions [32]. The soluble functionalized carbon nanotubes are generally in individual nanotubes or thin bundles, which can be probed and visualized by imaging with state-of-the-art electron microscopy techniques (Fig. 1) [35].

The solubility has allowed characterization and investigations in the solution phase. For example, nanotube carbons in a soluble functionalized sample of SWNTs were recently detected in solution by <sup>13</sup>C NMR [33]. It has also been shown that the solubilization by functionalization targeting defect sites



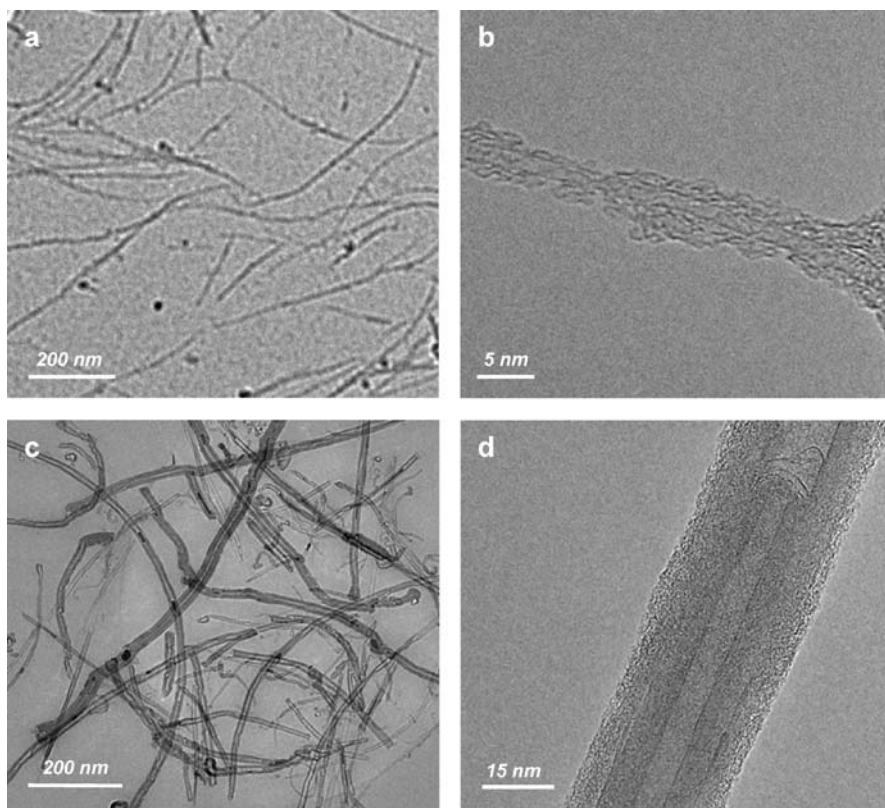


**Fig. 1** TEM images of **a,b** a PPEI-EI-functionalized SWNT sample and **c,d** a polyimide (PI)-NH<sub>2</sub>-functionalized MWNT sample

largely preserves the electronic structures and optical transitions in SWNTs, especially the observation that the bandgap absorptions associated with the van Hove singularity pairs are little changed when measured in both the solution phase and solid state (Fig. 2) [34].

### 3

## Luminescence from Modified/Functionalized Carbon Nanotubes

### 3.1

#### General Features and Properties

The solubilization of carbon nanotubes via chemical functionalization has provided great opportunities for studying the optical properties of nanotubes in the solution phase under the condition of homogeneous dispersion. The most relevant was the discovery by Sun and coworkers that polymer-

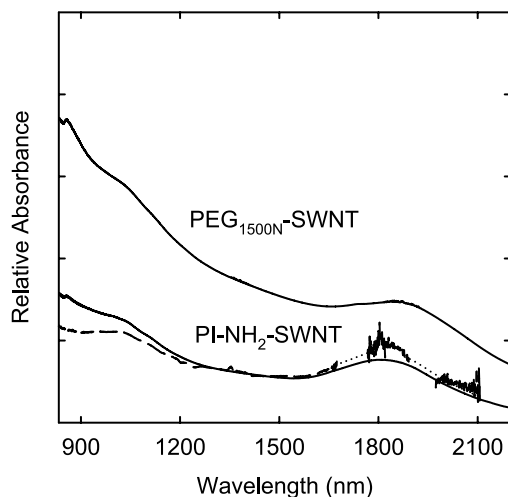


**Fig. 2** Absorption spectra of PEG<sub>1500N</sub>-SWNT in the solid state (—) and PI-NH<sub>2</sub>-SWNT in DMF solution (---, the dotted line region was subject to overwhelming solvent background) and the solid state (—) (Reproduced from [20] with permission. © 2005 American Chemical Society)

functionalized carbon nanotubes are luminescent or strongly luminescent in homogeneous organic or aqueous solution, exhibiting broad luminescence emission bands in the visible and extending well into the near-IR region (Fig. 3) [15]. The luminescence of functionalized carbon nanotubes is not specific to any particular polymeric or oligomeric functionality on the nanotube surface. In fact, the luminescence has been observed in all well-functionalized carbon nanotube samples with diverse functional groups [15, 17–20]. Much effort was made to eliminate other possible explanations for the observed strong luminescence emission. For example, a fluorescence contribution from the polymers or oligomers used in the functionalization was ruled out because these molecules have no absorption at the excitation wavelength. The possibility of luminescent impurities and small aromatic species induced from the solubilization was also excluded in various control experiments.

The luminescence excitation spectra of functionalized carbon nanotubes monitored at different emission wavelengths are consistent with the broad UV-Vis absorption spectra. However, the emission spectra are strongly dependent on excitation wavelengths in a progressive fashion. The excitation wavelength dependence indicates the presence of significant inhomogeneity or a distribution of emitters in the sample (nanotubes of different diameters, in particular) or emissive excited states (trapping sites of different energies) [15, 18–20].

The observed luminescence quantum yields are generally high. As shown in Fig. 4, for example, the luminescence quantum yields of PPEI-

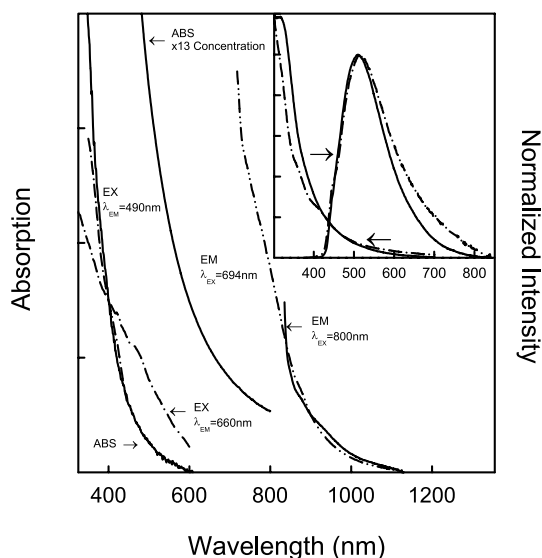


**Fig. 3** Absorption (ABS), luminescence emission (EM), and luminescence excitation (EX) spectra of PPEI-EI-MWNT in room-temperature chloroform. *Inset*: A comparison of absorption and luminescence (440 nm excitation) spectra of PPEI-EI-MWNT (—) and PPEI-EI-SWNT (---) in homogeneous chloroform solutions at room temperature (Reproduced from [15] with permission. © 2000 American Chemical Society)

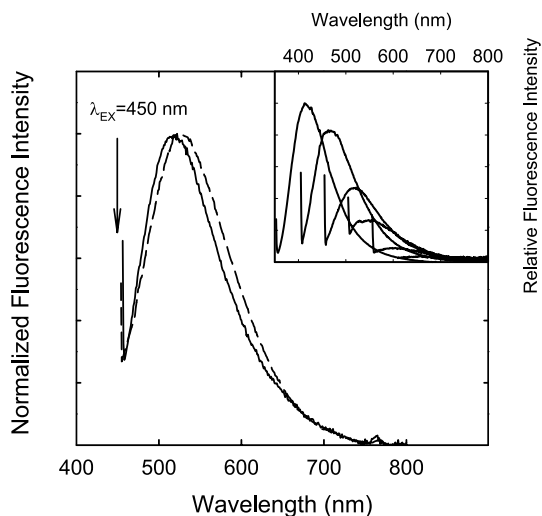


**Fig. 4** Luminescence emission spectra (normalized, 450 nm excitation) of PPEI-EI-SWNT (—) and PEG<sub>1500</sub>N-SWNT (---) in aqueous solution. *Inset*: Spectra of PPEI-EI-functionalized SWNTs excited at 350, 400, 450, 500, 550, and 600 nm (intensities shown in relative quantum yields) (Reproduced from [20] with permission. © 2005 American Chemical Society)

EI-functionalized SWNTs (PPEI-EI-SWNT) and PEG<sub>1500N</sub>-functionalized SWNTs (PEG<sub>1500N</sub>-SWNT) at 450-nm excitation are 4.5 and 3%, respectively [20]. Generally speaking, the luminescence quantum yields of SWNTs and MWNTs are on the same order of magnitude. The luminescence decays of functionalized nanotubes are relatively fast and nonexponential, with average lifetimes on the order of a few nanoseconds. The nonexponential nature of the luminescence decays is consistent with the presence of multiple emissive entities in the sample and the observed excitation wavelength dependence of luminescence.

### 3.1.1

#### Effect of Dispersion

There is ample experimental evidence suggesting that the defect-derived luminescence is sensitive to the degree of functionalization and dispersion of the carbon nanotubes. The higher observed luminescence quantum yields are generally associated with better-functionalized carbon nanotubes, as supported by results from experiments of repeated functionalization and the defunctionalization of functionalized carbon nanotubes [20, 21]. The repeated functionalization reactions of a carbon nanotube sample with the same polymer results in a substantial increase in the luminescence quantum yield of the final functionalized nanotube sample. Conversely, the luminescence can be quenched or eliminated upon a partial or complete defunctionalization process, through thermal evaporation or acid/base hydrolysis to remove the functional groups from the nanotube surface. The polymer-functionalized carbon nanotube samples obtained from different functionalization routes may have different luminescence quantum yields due to the nature of the functionalization reactions with respect to the nanotube dispersion. It is commonly observed that the amidation/esterification of carbon nanotubes through the acyl chloride route [27, 31] is more effective than other reactions (such as diimide-activated coupling [36]) in the functionalization, corresponding to a higher degree of nanotube dispersion in the resulting sample.

The functionalization of carbon nanotubes for their solubilization is likely more than just dragging the nanotubes into aqueous or common organic solution through covalently wrapping the nanotube with oligomeric or polymeric molecules. In the functionalization reaction, the functional groups exfoliate the nanotube bundles by either reducing the bundle size or completely disintegrating the bundle into individual nanotubes (thus, the degree of nanotube dispersion is greatly enhanced) [35]. Better-functionalized carbon nanotubes and the associated better dispersion result in higher luminescence quantum yields. Conversely, stronger luminescence serves as an indication that the underlying nanotubes are better dispersed, which may be verified or supported by other complementary techniques such as high-

resolution electron microscopy or atomic force microscopy. In fact, because of the sensitivity of fluorescence spectroscopy, the luminescence measurements may be used as an experimental tool for probing the dispersion of carbon nanotubes.

Lin et al. have demonstrated the sensitivity of the defect-derived luminescence to the nanotube dispersion [20]. In a comparison of nonfunctionalized and functionalized SWNTs, the former were dispersed in DMF with the assistance of polyimide under sonication. The latter (SWNTs functionalized with polyimide) were dissolved in DMF to afford another solution. At the same equivalent nanotube content, the two solutions had comparable optical densities at the same excitation wavelength (450 nm). However, the luminescence measurements of the two solutions revealed that the latter was much more luminescent than the former (Fig. 5). This is a piece of evidence strongly in support of the conclusion that the dispersion of carbon nanotubes plays a critical role in their luminescence.

Effective exfoliation to obtain individually dispersed nanotubes is a necessary prerequisite to observe strong defect-derived luminescence. This requirement seems the same as that for the detection of bandgap fluorescence [6] because both emissions are subject to the internanotube quenching effect. Again, the high quantum yield of defect-derived luminescence combined with the sensitivity to nanotube bundling may be exploited as a convenient, effective, and noninvasive technique to monitor the dispersion of carbon nanotubes in polymer and other matrices.

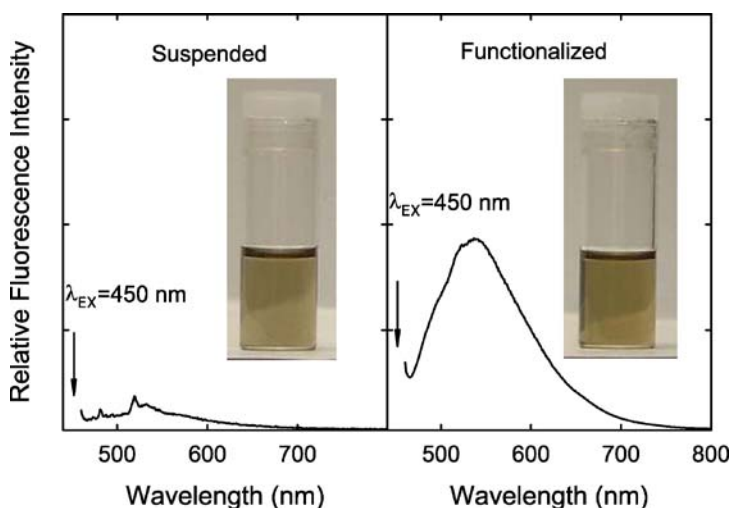


**Fig. 5** Luminescence emission spectra and pictures from SWNTs dispersed with the aid of polyimide in DMF (*left*) and the PI-NH<sub>2</sub>-SWNT in DMF solution (*right*). The nanotube and polymer contents in the two samples were comparable (Reproduced from [20] with permission. © 2005 American Chemical Society)

### 3.1.2 Effect on Raman Spectra

The strong luminescence in functionalized carbon nanotubes often becomes overwhelmingly interfering in the Raman characterization of the nanotube samples. Resonant Raman spectroscopy has been identified as one of the most important experimental tools for probing and studying carbon nanotubes because of the sensitivity of Raman features to the nanotube diameter, chirality, environmental effect, etc. For example, a typical Raman spectrum of a pristine SWNT sample shows characteristic peaks that include the radial breathing mode (100–300  $\text{cm}^{-1}$ ), D band ( $\sim 1300 \text{ cm}^{-1}$ ), G band ( $\sim 1600 \text{ cm}^{-1}$ ), and D\* band ( $\sim 2600 \text{ cm}^{-1}$ ). However, for functionalized carbon nanotubes, these characteristic Raman bands are generally obscured or overwhelmed by the strong luminescence background, which essentially turns the Raman spectrum into a luminescence spectrum [20, 21]. The extent of luminescence interference in Raman measurements is consistent with the intensities in directly measured luminescence spectra. Better-functionalized nanotube samples with better solubility and dispersion are usually associated with more intensive luminescence interference, which often buries the Raman features completely. For example, the Raman spectrum of I-MWNT is simply a broad curve (Fig. 6) [21].

The luminescence background in Raman spectra could be removed by reducing the degree of nanotube functionalization. Typically, a chemical or thermal defunctionalization process may be used to remove the functional groups from the nanotube surface. The characteristic Raman features of car-

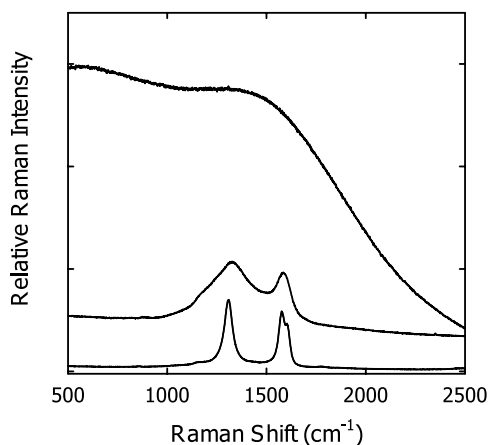


**Fig. 6** Raman spectra (785 nm excitation) of the I-MWNT sample before (*top*) and after (*middle*) thermal defunctionalization in a TGA scan to 650 °C. The spectrum of the pristine MWNT sample (*bottom*) is also shown for comparison (Reproduced from [21] with permission. © 2002 American Chemical Society)

bon nanotubes are restored upon the defunctionalization, as shown in Fig. 6 for I-MWNT.

### 3.2 Luminescence Polarization

The luminescence emission of functionalized carbon nanotubes is highly polarized, both in solution at ambient temperature and in polymer thin films. The anisotropy values  $r$  were calculated for the nanotube luminescence in terms of the well-established equations [37]:

$$P = (I_{HH}I_{VV} - I_{HV}I_{VH}) / (I_{HH}I_{VV} + I_{HV}I_{VH}) \quad (1)$$

$$r = 2P / (3 - P) . \quad (2)$$

At each excitation wavelength, the anisotropy values are essentially independent of emission wavelengths. Shown in Fig. 7 are typical luminescence anisotropy results for the functionalized SWNTs, where each value is averaged over all emission wavelengths [19].

The luminescence anisotropy values are strongly dependent on the excitation wavelengths, exhibiting obvious increases with progressively longer excitation wavelengths, approaching the limiting anisotropy value of 0.4 (Table 1). The excitation wavelength dependence of the anisotropy value is less significant in polymer films than in solution [38].

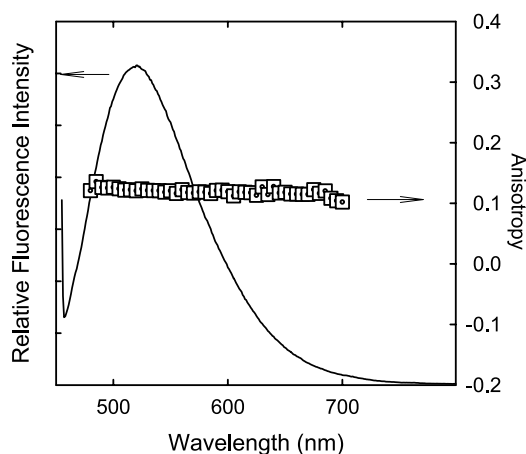


**Fig. 7** Luminescence anisotropy values at different emission wavelengths for I<sub>PEG</sub>-MWNT in room-temperature chloroform solution with 450 nm excitation. The luminescence spectrum at the same excitation wavelength is also shown for comparison (Reproduced from [19] with permission. © 2002 Elsevier Science B. V.)

**Table 1** Luminescence anisotropy ( $r$ ) values at different excitation wavelengths [38]

Excitation wavelength (nm)	400	425	450	475	500	525	550	575	600
$r_{\text{solution}}^a$	0.052	0.069	0.10	0.12	0.14	0.15	0.16	0.18	0.19
$r_{\text{film}}$	0.32	0.34	0.35	0.35	0.37	0.38	0.39	0.39	0.39

<sup>a</sup> From repeating the experiments reported in [19]

The luminescence emission is likely associated with excited-state energy trapping sites (well-passivated nanotube surface defects). The luminescence polarization indicates that the absorption and emission dipole moments are correlated. The excitation wavelength dependence of luminescence polarization seems to suggest that the excitation is at least partially localized in a distribution of electronic states in the functionalized carbon nanotubes. For functionalized carbon nanotubes embedded in a polymeric matrix, the anisotropy values are generally larger than those in solution. This may be attributed to the more restrictive environment in the films toward rotational diffusion, thus minimizing or completely eliminating the depolarization induced by molecular motion.

The absorption and emission dipole moments are close to being parallel for the functionalized carbon nanotubes dispersed in a polymeric matrix. However, the orientation of parallel dipoles with respect to the nanotube structure cannot be revealed from only the luminescence anisotropy results. The alignment of the luminescent carbon nanotubes is required. Alignment has been achieved by uniaxial mechanical stretching of PVA thin films embedded with functionalized SWNTs. The large aspect ratio of carbon nanotubes makes them good candidates for alignment by mechanical stretching, as already reported in the literature (see, for example, [39]). Experimentally, the nanotube-embedded PVA films (about 100 microns in thickness) can usually be stretched to five- to sevenfold. The observed dichroic ratios are strongly in favor of the film stretching direction (Fig. 8), indicating that the electronic absorption responsible for the luminescence properties is along the nanotube long axis [38]. When combined with the luminescence anisotropy results, an obvious conclusion is that both the absorption and emission dipole moments are coaxial with the functionalized carbon nanotubes. It should be noted that the measurement of luminescence emissions from the stretched films is a more sensitive alternative to the direct determination of absorption polarization with reference to the film stretching direction.

The alignment of the functionalized SWNTs in the stretched PVA film has also been evaluated in terms of the dependence of the observed dichroic ratio on the draw ratio [38]. As shown in Fig. 9 for stretching with a film draw ratio



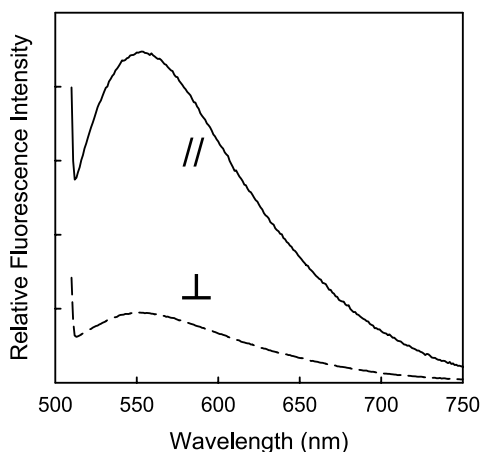


**Fig. 8** Luminescence emission spectra of PPEI-EI-SWNT in stretched PVA film (draw ratio  $\sim 5$ ) excited with polarized light parallel ( $\parallel$ , -) and perpendicular ( $\perp$ , - -) to the stretching direction

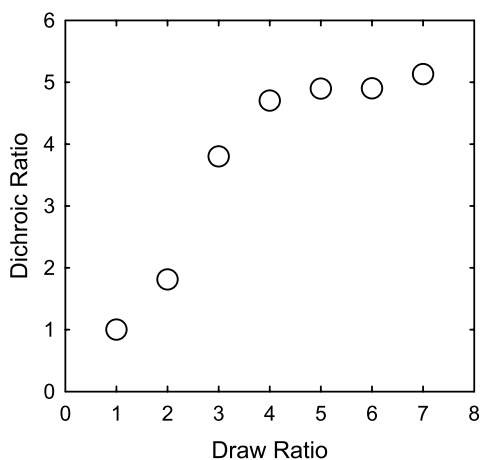


**Fig. 9** The observed dichroic ratio for PPEI-EI-SWNT in stretched PVA film as a function of the draw ratio (500 nm excitation)

of 1 to 7, the dichroic ratio initially increases rapidly with increasing draw ratio and then reaches almost a plateau.

### 3.3

#### Potential Applications

The bright defect-derived luminescence in functionalized carbon nanotubes may find applications in luminescence imaging. Shown in Fig. 10 are confocal

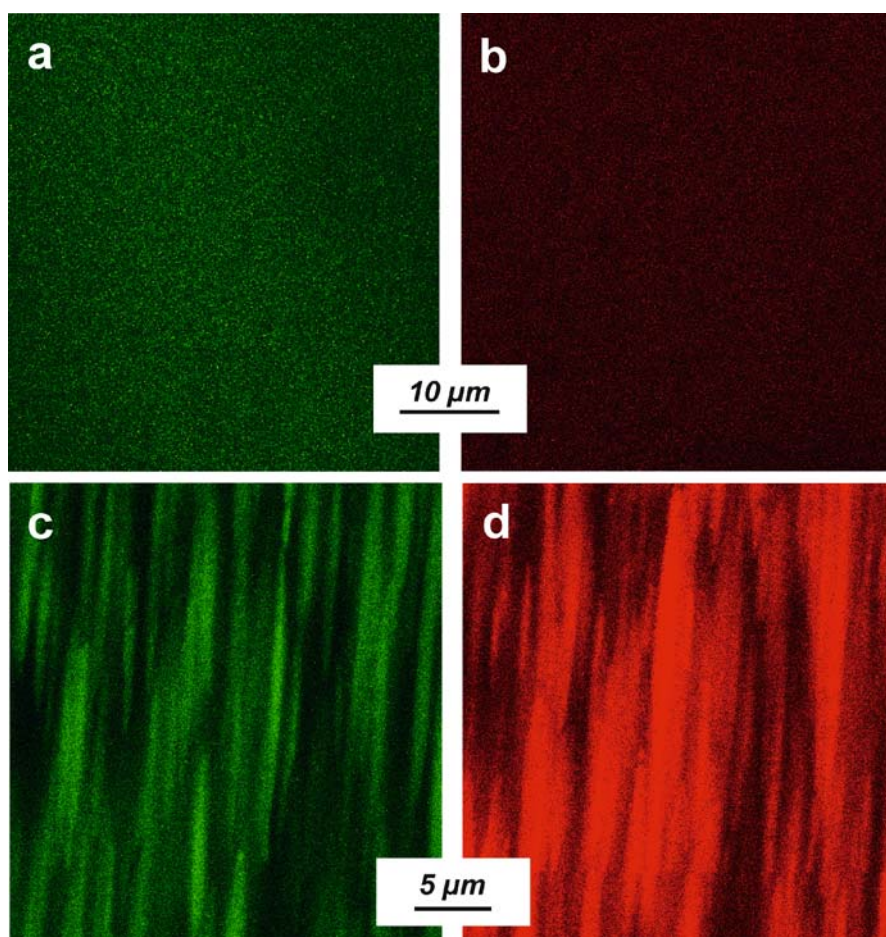


**Fig. 10** Confocal microscopy images of PPEI-EI-SWNT in PVA film **a,b** before and **c,d** after mechanical stretching to a draw ratio of about 5. **a,c**: 514 nm excitation, > 530 nm detection; **b,d**: 633 nm excitation, > 650 nm detection

microscopy images of the PVA film dispersed with PPEI-EI-SWNT. The confocal images at different depths beneath the film surface suggest that these are representative of the whole film matrix (no surface effects). The compatibility of the functionalized nanotubes with, and their good dispersion in, the PVA matrix are also reflected in the confocal images, with bright and homogeneous emissions (spatial resolution about  $0.5\ \mu\text{m}$ ) across the whole film. The emission light intensity as expressed by the color intensity from across the film is uniform, without obvious deviation (such as bright or dark spots from local aggregation, localized enrichment, or absence of functionalized nanotubes, etc.). Different excitation wavelengths can be used (such as 458 and 633 nm in Fig. 10). For the stretched films, while the nanotubes remain well dispersed ac-

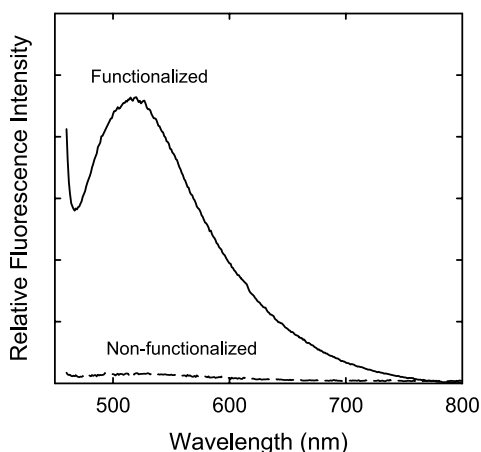


**Fig. 11** Luminescence emission spectra from polyimide nanocomposites embedded with nonfunctionalized SWNTs (- - -) and the polyimide-functionalized SWNTs (PI-NH<sub>2</sub>-SWNT) (-). The nanotube and polymer contents in the two samples were comparable

ording to confocal microscopy images (Fig. 10), their preferential orientation along the stretching direction is also well illustrated in the images.

The defect-derived luminescence may be used as a tool to probe the dispersion of functionalized carbon nanotubes in polymeric composites. In a recent demonstration, polymeric nanocomposites embedded with functionalized carbon nanotubes and with purified nanotubes (nonfunctionalized) were compared [40]. Characterization by using TEM and SEM techniques suggests that in the former the nanotubes are much better dispersed. In luminescence measurements, the nanocomposites with functionalized carbon nanotubes exhibit strong luminescence at variable excitation wavelengths from 450 to 600 nm, whereas those with purified SWNTs at the same nanotube loading are essentially nonemissive in the visible and near-IR regions (Fig. 11).

## 4

### Defect-Derived vs Bandgap Emissions

The two emissions of carbon nanotubes are obviously different in origin, but complementary in some properties. As observed by Kappes et al., in the measurement of bandgap fluorescence there was a significantly stronger and structureless luminescence background toward the visible region, with the intensity increasing smoothly toward the excitation wavelength for stable dispersions of acid-treated SWNTs [8]. This suggests the coexistence of the two kinds of emissions in the same carbon nanotube sample.

The bandgap emission is likely much weaker and very sensitive to any effects on the electronic structure of SWNTs (easily quenched or diminished by

doping or chemical treatment). For example, the emission spectrum of dispersed SWNTs after the acid treatment is weak and poorly structured [8]. However, the defect-derived luminescence is much improved by the same procedure that induces or generates more defect sites. The excellent surface passivation is critical to the observation of strong defect-derived luminescence [20].

The bandgap emission is strongly dependent on the nanotube diameter ( $d$ ) and diameter distribution [6, 8]. It has been reported that the quantum efficiency of SWNTs from arc-discharge production ( $d \sim 1.5$  nm) is weaker in bandgap fluorescence because of their larger average diameter than that of SWNTs produced by the HiPco method ( $d \sim 0.7$ – $1.2$  nm) [8]. The bandgap emission is more prominent in the small-diameter nanotubes with an upper diameter limit of 1.5 nm. For example, the observed quantum yield of SWNTs from the laser ablation production ( $d \sim 1.4$  nm) is on the order of  $1 \times 10^{-5}$ , two orders of magnitude lower than that of the HiPco nanotubes. SWNTs from arc discharge are predicted to have an even lower quantum yield, which may actually represent a technical challenge in the observation of their bandgap fluorescence.

A shared requirement between the two kinds of emissions is that the emission is highly sensitive to the nanotube dispersion. For the bandgap emission, dispersion is often assisted by the use of surfactants with the carbon nanotubes and also ultrahigh-speed centrifugation. The functionalization is effective in the exfoliation of nanotube bundles to the level of individual nanotubes and very thin bundles, but it is hardly applicable to the investigation of bandgap fluorescence. Despite extensive efforts on the elucidation of the two kinds of emission, there are still significant technical and mechanistic issues for both. For example, the accurate determination of quantum yield for the bandgap fluorescence remains difficult because of the wavelength region, while the nature and properties of the emissive excited states for the defect-derived luminescence require further investigation.

**Acknowledgements** We thank Dr. L.F. Allard, Dr. C.E. Bunker, Prof. D.L. Carroll, Dr. J.W. Connell, and Prof. A.M. Rao for fruitful collaborations. We also thank Dr. J. Riggs, Dr. Z.-X. Guo, Dr. K. Fu, Dr. W. Huang, B. Martin, L. Qu, S. Fernando, Dr. K. Henbest, W. Wang, Dr. S.-Y. Xie, S. Taylor, X. Wang, and M. Veca for experimental assistance. Financial support from the National Science Foundation, NASA, USDA, and the Center for Advanced Engineering Fibers and Films (NSF-ERC at Clemson University) is gratefully acknowledged.

## References

1. Haddon RC (2002) Special issue on carbon nanotubes. *Acc Chem Res* 35
2. Dresselhaus MS, Dai H (2004) Advances in carbon nanotubes. *MRS Bull* 29
3. Baughman RH, Zakhidov AA, de Heer DH (2002) *Science* 297:787

4. Dresselhaus MS, Dresselhaus G, Eklund PC (1996) Science of fullerenes and carbon nanotubes. Academic, New York
5. Kataura H, Kumasawa Y, Maniwa Y, Umezu I, Suzuki S, Ohtsuka Y, Achiba Y (1999) *Synth Met* 103:2555
6. O'Connell MJ, Bachilo SM, Huffman CB, Moore VC, Strano MS, Haroz EH, Rialon KL, Boul PJ, Noon WH, Kittrell C, Ma J, Hauge RH, Weisman RB, Smalley RE (2002) *Science* 297:593
7. Bachilo SM, Strano MS, Kittrell C, Hauge RH, Smalley RE, Weisman RB (2002) *Science* 298:2361
8. Lebedkin S, Hennrich F, Skipa T, Kappes MM (2003) *J Phys Chem B* 107:1949
9. Lebedkin S, Arnold K, Hennrich F, Krupke R, Renker B, Kappes MM (2003) *New J Phys* 5:140
10. Jones M, Engtrakul C, Metzger WK, Ellingson RJ, Nozik AJ, Heben MJ, Rumbles GP (2005) *Phys Rev B* 71:115426
11. Graff RA, Swanson JP, Barone PW, Baik S, Heller DA, Strano MS (2005) *Adv Mater* 17:980
12. Lefebvre J, Fraser JM, Finnie P, Homma Y (2004) *Phys Rev B* 69:075403
13. Hennrich F, Krupke R, Lebedkin S, Arnold K, Fischer R, Resasco DE, Kappes MM (2005) *J Phys Chem B* 109:10567
14. Arnold K, Lebedkin S, Kiowski O, Hennrich F, Kappes MM (2004) *Nano Lett* 12:2349
15. Riggs JE, Guo Z, Carroll DL, Sun YP (2000) *J Am Chem Soc* 122:5879
16. Zhao B, Hu H, Niyogi S, Itkis ME, Hamon MA, Bhowmik P, Meier MS, Haddon RC (2001) *J Am Chem Soc* 123:11673
17. Guldi DM, Holzinger M, Hirsch A, Georgakilas V, Prato M (2002) *Chem Commun*, p 1130
18. Banerjee S, Wong SS (2002) *J Am Chem Soc* 124:8940
19. Sun YP, Zhou B, Henbest K, Fu K, Huang W, Lin Y, Taylor S, Carroll DL (2002) *Chem Phys Lett* 351:349
20. Lin Y, Zhou B, Martin RB, Henbest KB, Harruff BA, Riggs JE, Guo ZX, Allard LF, Sun YP (2005) *J Phys Chem B* 109:14779
21. Sun YP, Fu K, Lin Y, Huang W (2002) *Acc Chem Res* 35:1096
22. Bahr JL, Mickelson ET, Bronikowski MJ, Smalley RE, Tour JM (2001) *Chem Commun*, p 93
23. Bahr JL, Tour JM (2002) *J Mater Chem* 12:1952
24. Hirsch A (2002) *Angew Chem Int Ed* 41:1853
25. Tasis D, Tagmatarchis N, Georgakilas V, Prato M (2003) *Chem A Eur J* 9:4001
26. Niyogi S, Hamon MA, Hu H, Zhao B, Bhowmik P, Sen R, Itkis ME, Haddon RC (2002) *Acc Chem Res* 35:1105
27. Chen J, Hamon MA, Hu H, Chen Y, Rao AM, Eklund PC, Haddon RC (1998) *Science* 282:95
28. Kuznetsova A, Mawhinney DB, Naumenko V, Yates JT, Liu J, Smalley RE (2000) *Chem Phys Lett* 321:292
29. Hu H, Bhowmik P, Zhao B, Hamon MA, Itkis ME, Haddon RC (2001) *Chem Phys Lett* 345:25
30. Huang WJ, Fernando S, Allard LF, Sun YP (2003) *Nano Lett* 3:565
31. Lin Y, Rao AM, Sadanadan B, Kenik EA, Sun YP (2002) *J Phys Chem B* 106:1294
32. Fernando KAS, Lin Y, Sun YP (2004) *Langmuir* 20:4777
33. Kitaygorodskiy A, Wang W, Xie SY, Lin Y, Fernando KAS, Wang X, Qu LW, Chen B, Sun YP (2005) *J Am Chem Soc* 127:7517

34. Zhou B, Lin Y, Li H, Huang W, Connell JW, Allard LF, Sun YP (2003) *J Phys Chem B* 107:13588
35. Lin Y, Hill DE, Bentley J, Allard LF, Sun YP (2003) *J Phys Chem B* 107:10453
36. Huang W, Lin Y, Taylor S, Gaillard J, Rao AM, Sun YP (2002) *Nano Lett* 2:231
37. Lakowicz RJ (1999) *Principles of fluorescence spectroscopy*, 2nd edn. Kluwer/Plenum, New York
38. Zhou B, Lin Y, Veca LM, Fernando KAS, Harruff BA (2006) *J Phys Chem B* 110:3001
39. Rozhin AG, Sakakibara Y, Kataura H, Matsuzaki S, Ishida K, Achiba Y, Tokumoto M (2005) *Chem Phys Lett* 405:288
40. Zhou B, Lin Y, Hill DE, Wang W, Veca LM, Qu L, Liu Y, Qu LW, Pathak P, Meziani MJ, Diaz J, Connell JW, Watson KA, Allard LF, Sun YP (2006) *Polymer* 47:5323

## Fluorescence Correlation Spectroscopic Studies of a Single Lipopolyamine–DNA Nanoparticle

Noppadon Adjimatera<sup>1</sup> · Aleš Benda<sup>2</sup> · Ian S. Blagbrough<sup>1</sup> · Marek Langner<sup>3</sup> · Martin Hof<sup>2</sup> · Teresa Kral<sup>2,4</sup> (✉)

<sup>1</sup>Department of Pharmacy and Pharmacology,  
University of Bath, Bath BA2 7AY, UK

<sup>2</sup>J. Heyrovský Institute of Physical Chemistry,  
Academy of Sciences of the Czech Republic,  
Dolejškova 3, 182 23 Prague 8, Czech Republic  
kral@jh-inst.cas.cz

<sup>3</sup>Institute of Physics, Wrocław University of Technology,  
Wybrzeże Wyspiańskiego 27, 50-370 Wrocław, Poland

<sup>4</sup>Department of Physics and Biophysics,  
Wrocław University of Environmental and Life Sciences,  
Norwida 25, 50-375 Wrocław, Poland

1	Introduction . . . . .	383
2	Principles of Fluorescence Correlation Spectroscopy . . . . .	383
3	Simultaneous Lifetime and FCS Data Acquisition . . . . .	386
4	Dyes for Efficient DNA Labelling . . . . .	387
5	Calf Thymus DNA Classical FCS Studies . . . . .	389
5.1	Calf Thymus DNA–PicoGreen Interaction Study . . . . .	389
5.2	Calf Thymus DNA Condensation by Lipopolyamines . . . . .	392
5.3	Point-like Molecule Detection in DNA Condensation . . . . .	393
6	Simultaneous Lifetime and FCS Studies of Plasmid DNA . . . . .	395
6.1	Plasmid DNA–PicoGreen Labelling Study . . . . .	395
6.2	Simultaneous Lifetime and FCS Analysis of Plasmid DNA Through the Condensation Process . . . . .	401
7	Conclusions . . . . .	407
	References . . . . .	411

**Abstract** We have studied lipopolyamine–DNA complex formation by fluorescence correlation spectroscopy (FCS). Two lipopolyamines,  $N^4, N^9$ -dioleoylspermine and  $N^1$ -cholesteryl spermine carbamate, were used to condense linear calf thymus DNA and two plasmid DNAs: pGL3 (5.3 kilobase pairs) and pEGFP (4.7 kilobase pairs). PicoGreen® (PG), a high-affinity DNA intercalating agent that only fluoresces when intercalated, was used in our FCS study. In this study, the ConfoCor I set-up upgraded with TimeHarp 200 was used. FCS directly visualizes the condensation process by tracking changes in diffusion coefficients and particle numbers. We were able to define the fluorescent signalling

behaviour of PG through the process from dye binding to dye release and then dye quenching. Dye release was suggested as the indicator for DNA conformational change, but not for nanoparticle formation. Dye quenching, through the observation of life-time change, is a more important event accurately and sensitively reporting that a single nanoparticle exists.

**Keywords** DNA condensation · FCS · Fluorescent lipopolyamines · Non-viral gene therapy · PicoGreen · Polyamines · TTTR data

### Abbreviations

$A$	Correction factor
$C$	Molarity
CR	Count rate
ct DNA	Calf thymus DNA
$D$	Diffusion coefficient
DNA	Deoxyribonucleic acid
DNase	Nuclease
dsDNA	Double-stranded DNA
EthBr	Ethidium bromide
$F_0$	Fluorescence intensity in the absence of quencher
$F_q$	Fluorescence intensity in the presence of quencher
FCS	Fluorescence correlation spectroscopy
$G(\tau)$	Autocorrelation function
HEPES	4-(2-Hydroxyethyl)-1-piperazine-ethanesulphonic acid
$k_B$	Boltzmann constant
$M$	Molecular mass
N/P	Ammonium/phosphate ratio
$N_A$	Avogadro's number
NaCl	Sodium chloride
NVGT	Non-viral gene therapy
$\eta$	Dynamic viscosity
pEGFP	pEGFP plasmid DNA
PG	PicoGreen®
pGL3	pGL3 plasmid DNA
PN	Particle number
$r_h$	Hydrodynamic radius
ssDNA	Single-stranded DNA
$\tau$	Correlation time
$\tau_D$	Diffusion time
$\tau_0$	Lifetime of the fluorophore in the absence of quencher
$\tau_q$	Lifetime of the fluorophore in the presence of quencher
$\tau_{tr}$	Triplet decay time
$T$	Triplet fraction
$T_C$	Thermodynamic temperature
TCSPC	Time-correlated single photon counting
TTTR	Time-tagged time-resolved
$V$	Confocal volume
$\omega_1$	Lateral radius of detection volume
$\omega_2$	Axial radius of detection volume
$\chi$	Fit parameter



## 1

### Introduction

DNA binding by lipopolyamines plays an important role in gene delivery success. DNA condensation affords nanoparticles with the appropriate size to enter cells, as well as giving protection from nucleases (DNases), and these are important properties when considering serum stability for *in vivo* applications. Disassociation of DNA at the right time is crucial, possibly after escaping from the endosome and just before reaching or right after entering a nucleus. However, the association and dissociation between these lipopolyamines and DNA are still not well understood [1–7].

Fluorescence correlation spectroscopy (FCS) is a relatively new non-invasive technique with single-molecule sensitivity to study molecular diffusion, large conformational changes and molecular interactions based on fluorescence and confocal microscopy. In conventional fluorescence spectroscopy, a relatively large volume of sample is illuminated by an excitation light. Thus, the fluorescence signal is recorded from the whole ensemble of molecules leading to averaged information. The single-molecule sensitivity of fluorescence confocal microscopy overcomes this limitation and provides non-averaged information about the sample. FCS was used to study the dynamic processes on the molecular scale, including DNA nanoparticle formation [8–14]. One advantage of the FCS approach is that it works at low concentrations (difficult to attain by other technologies) and consequently opens measurement possibilities at physiologically relevant levels.

## 2

### Principles of Fluorescence Correlation Spectroscopy

Fluorescence approaches, like ethidium bromide (EthBr) quenching during DNA condensation [15] and DNA detection on gels using EthBr, are among many commonly used bulky fluorescence techniques applied in non-viral gene therapy (NVGT) research. Their advantage is simplicity; on the other hand they require rather large amounts of sample and provide only averaged information about the system. Decreasing the effective detection volume to femtolitre size (Fig. 1) by using confocal optics and nanomolar concentrations of samples bring us to a single-molecule level. This opens new dimensions in the NVGT research field. Standard fluorescence parameters (spectra, lifetime, anisotropy) can be obtained in a non-averaged, molecule by molecule, evaluated manner. Moreover, changes in local concentrations and brightness of the studied molecules due to diffusion, chemical reactions, photophysical events and other effects lead to pronounced fluctuations in the overall detected fluorescence intensity. Thus, the temporal evolution of the detected fluorescence intensity carries information about concentrations, dif-

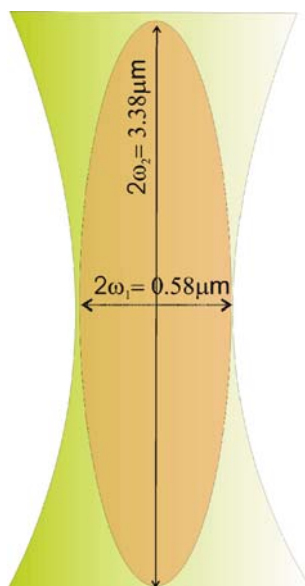


**Fig. 1** Illustration showing a confocal volume in FCS (typical volume is around  $1 \times 10^{-15}$  l) enabling single molecule sensitivity. The dimension of the volume element was determined by using standard fluorophores (Rhodamine-6G and Alexa Fluor 488)

fusion coefficients, brightness, photophysical parameters, chemical equilibria etc.

FCS analysis fluctuations in the fluorescence signal over time arise mainly from diffusion of fluorescent species in and out of the detection volume. This small volume improves the signal-to-noise ratio and thus enables single-molecule sensitivity. The highly focused laser beam creates a diffraction-limited Gaussian–Lorentzian intensity profile with minimum lateral radius  $\omega_1 = 0.29 \pm 0.05 \mu\text{m}$ . The detection in the axial dimension ( $\omega_2$ ) is limited by a pinhole in the image plane of the microscope and was found to be  $\omega_2 = 1.69 \pm 0.02 \mu\text{m}$ . The size of the detection volume is  $0.9 \pm 0.1$  fl.

The dimensions of the volume element were determined by using the standard fluorophores Rhodamine-6G and Alexa Fluor 488, given the standard diffusion coefficient ( $D$ ) at  $25^\circ\text{C}$  of both dyes is  $2.8 \times 10^{-10} \text{m}^2/\text{s}$ . Molecules diffuse through this illuminated volume over time, and give out photons which are recorded by the detection unit. Fluctuations in the detected fluorescence intensity are analysed by means of the autocorrelation function  $G(\tau)$ . To obtain real physical parameters from  $G(\tau)$ , one needs to apply a proper physical model. At this step first approximations take place. The detection volume is for bulk measurements approximated as a 3D Gaussian. Assuming small point-like non-interacting molecules freely diffusing in a space much larger than the detection volume, showing only the triplet state, the  $G(\tau)$  takes

the form:

$$G(\tau) = 1 + (1 - T + Te^{-\tau/\tau_{tr}}) \left( \frac{1}{PN(1 - T)} \right) \frac{1}{1 + (\tau/\tau_D)} \left( \frac{1}{1 + (\tau/\tau_D) (\omega_1/\omega_2)^2} \right)^{1/2}, \quad (1)$$

where  $T$  is the triplet fraction,  $\tau_{tr}$  is the triplet decay time,  $PN$  is the apparent particle number,  $\tau_D$  is the diffusion time, and  $\omega_1$  and  $\omega_2$  are the lateral and axial radii of the detection volumes. The derivation of equations for the applied models makes use of the natural laws applied in classical methods of perturbation kinetics, as the only difference is in the source of fluctuations.

The parameters  $PN$  and  $\tau_D$  are related to macroscopic values of concentration  $c$  and diffusion coefficient  $D$  via:

$$\tau_D = \frac{\omega_1^2}{4D}, \quad (2)$$

and

$$PN = \pi c \omega_1^2. \quad (3)$$

The diffusion coefficient for spherically symmetric molecules is related to the hydrodynamic radius  $r_h$  via the Einstein–Stokes equation:

$$D = \frac{k_B T_C}{6\pi\eta r_h}, \quad (4)$$

where  $k_B$  is the Boltzmann constant,  $T_C$  is the thermodynamic temperature and  $\eta$  is the dynamic viscosity. The hydrodynamic radius  $r_h$  can be calculated from the molecular mass  $M$  using:

$$r_h = \sqrt[3]{\frac{3M}{4\pi\rho N_A}}, \quad (5)$$

where  $\rho$  is the mean density of the molecule and  $N_A$  is Avogadro's number.

The translational diffusion coefficient ( $D$ ) depends largely on the shape of the molecule. For rod-like molecules, such as DNA,  $D$  can be estimated as:

$$D = \frac{Ak_B T_C}{3\pi\eta L}, \quad (6)$$

where  $L$  corresponds to the length of the rod (for DNA it is the rise per base pair (0.34 nm) multiplied by the number of base pairs),  $d$  is the diameter of the rod (2.38 nm for DNA) and  $A$  represents a correction factor:

$$A = \ln(L/d) + 0.312 + 0.565/(L/d) - 0.1/(L/d)^2. \quad (7)$$

It means that the diffusion coefficient of a 1000-bp DNA is approximately five times smaller and thus the diffusion time five times larger for a rod-like molecule than a spherical one. The DNA diffusion coefficient decreased by

increasing the DNA size, indicating the complex hydrodynamic properties of DNA with respect to translational diffusion [16, 17].

### 3 Simultaneous Lifetime and FCS Data Acquisition

The present state of the art in lasers, optics, photon detection and signal processing units enables many different single-molecule sensitivity set-ups. We applied an upgraded ConfoCor 1 fluorescence microscope to our NVGT research [18]. The basis is an inverted confocal epifluorescence microscope Axiovert 100. A pulsed picosecond 470-nm diode laser is coupled via an optical fibre to the back port of the microscope. Excitation light is reflected at a dichroic mirror to an overfilled water immersion objective, which focuses the light into a diffraction-limited spot (radius 250 nm). Emitted light is collected through the same objective, passes the dichroic mirror, is spatially filtered using a pinhole, and is detected by fast APD. Photon detection events are counted by a MicroTime 200 PCI board using the time-tagged

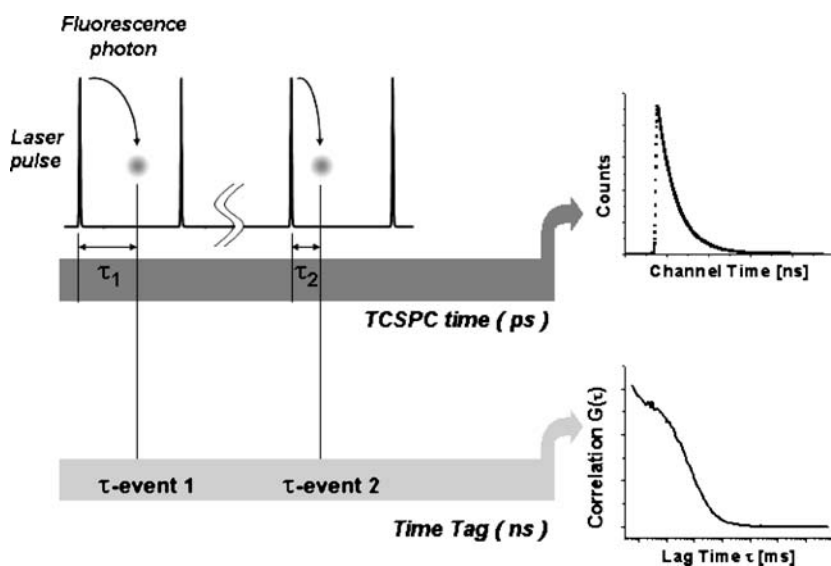


**Fig. 2** The TTTR data acquisition mode enables monitoring of the full arrival kinetics of individual photons. The time tag (100 ns resolution) tells us the arrival time of the photon from the beginning of the experiment, and this information is used for calculation of the intensity trace and autocorrelation function  $G(\tau)$ . Time resolved means a time difference (40 ps resolution) between the laser pulse and detection of the photon. From this the fluorescence lifetime decay histogram is constructed. This simultaneous FCS and lifetime measurement helps to give more detailed information about the sample

time-resolved (TTTR) mode and saved to hard disk for further offline analysis.

The TTTR mode is advanced time-correlated single photon counting (TC-SPC). In classical TCSPC, photon arrival times after the excitation (laser pulse) are measured and displayed as histograms. In TTTR mode, one measures and saves not only the time between excitation and emission (40 ps resolution), but also the arrival time from the beginning of the experiment (100 ns resolution), detector number (useless in a one-detector set-up) and sample position (again useless for a fixed set-up) (Fig. 2). Information-rich TTTR data can be analysed in many ways. We applied fluorescence lifetime determination from TCSPC times and FCS analysis of intensity fluctuations. The major advantages of this approach are that from a single measurement we simultaneously obtain information about the molecule microenvironment (carried in the fluorescence lifetime) and its diffusion properties, concentration and brightness (carried in the intensity fluctuations). Thus, we can directly correlate changes in one parameter with another.

## 4

### Dyes for Efficient DNA Labelling

The study of DNA intercalation with EthBr was first reported by Webb's research group [19, 20], using the FCS technique. The DNA binding constant of EthBr and the DNA diffusion coefficient were reported using FCS. Kral et al. [21, 22] recently studied DNA condensation by using EthBr and propidium iodide (PI) in FCS. The count rate (CR), diffusion time ( $\tau_D$ ), and particle number (PN) observed by FCS at the single-molecule level, and their correlations, can be used to differentiate the nature of DNA/oligonucleotide–polycation interactions [21–25].

Although EthBr is a commonly used dye in DNA condensation studies, it was found to have effects on DNA structure at high concentrations. The helical axis of DNA was dislocated + 1.0 Å and the helix was twisted by 10°, giving rise to an angular unwinding of -26°, and the intercalated base pairs were tilted relative to one another by 8° [26]. Manning's theory of counterion condensation of polyelectrolytes [27] suggested that EthBr intercalation lengthens the DNA by about 0.27 nm [28]. This possible DNA conformation alteration is generally not a concern in steady-state fluorescence spectroscopy with a larger population to be measured, but this is detectable within the sensitivity of FCS. Additionally, the higher rate of EthBr release from DNA may also lead to a significant reduction in fluorescence, making fluorescence analysis more complex. This in turn leads to the search for new fluorescent dyes that can be used without significant change in DNA conformation and also possess high extinction coefficients (which allow them to be used at low concentrations), to avoid interference in the DNA condensation behaviour mediated by NVGT vectors.

Recently, a new unsymmetrical monomethine cyanine dye, PicoGreen® (PG) (Fig. 3), was introduced as a patented fluorescent dye from Roth, Haughland and co-workers at Molecular Probes [29, 30]. Its chemical structure was recently reported by Vitzthum and co-workers, confirmed by NMR and MS techniques and named as [2-[*N*-bis(3-dimethylaminopropyl)amino]-4-[2,3-dihydro-3-methyl-(benzo-1,3-thiazol-2-yl)-methylidene]-1-phenyl-quinolinium]<sup>+</sup> (Fig. 3a) [31]. However, this name could also be (Chem Abs 9th CI): 2-[bis(3-dimethylaminopropyl)amino]-4-(3-methyl-2(3*H*)-benzothiazolylidene)methyl-1-phenyl-quinolinium [32] [178918-98-4] and/or 2-[bis(3-dimethylaminopropyl)amino]-1-phenyl-4(1*H*)-quinolinylidene)methyl)-3-methyl-benzothiazolium [33] [771577-99-2]. The charge due to quaternization of the aromatic N atoms is delocalized, probably equally well shown residing on the *N*-methyl-benzothiazolium (Fig. 3a) [33] and on the *N*-phenyl-quinolinium (Fig. 3b) [32], in a solvent- and environment-dependent manner. There is also a contribution from the third mesomer, including the lone-pair electrons on the anilino tertiary amine, as its ammonium ion (Fig. 3c) [34].

From DNA intercalation structure-activity relationship considerations, PG carries three positive charges, i.e. one on nitrogen in the conjugated, mesomeric, heteroaromatic system and two at the 3-dimethylaminopropyl residues. The cationic side chain of PG (compared to EthBr) contributes to

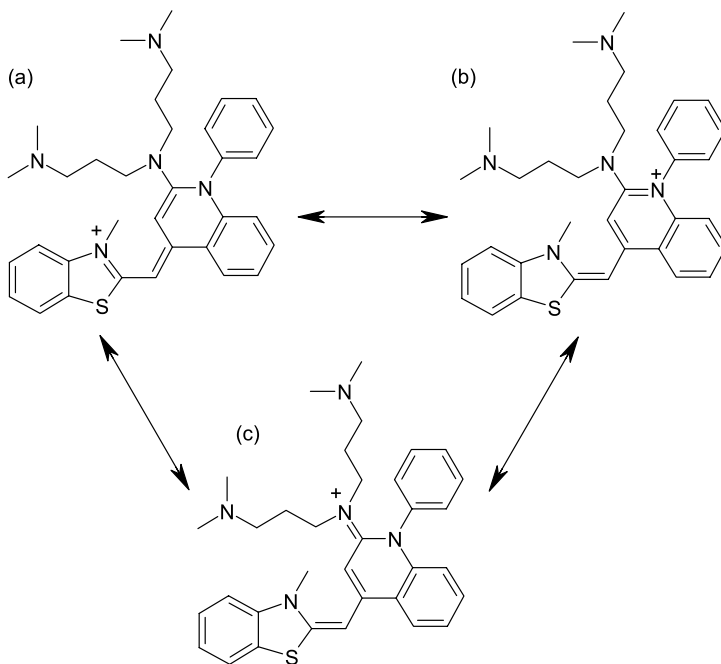


**Fig. 3** PicoGreen® (PG), an unsymmetrical monomethine cyanine dye containing a polyamine side chain to improve DNA-binding affinity with three mesomers (a, b and c)

higher affinity for double-stranded DNA (dsDNA). Biphasic-mode binding was reported for PG interaction with dsDNA. Base-pair intercalation happens at a low dye/base pair ratio, and external binding (minor groove) was found at a higher dye/base pair ratio. At low dye/base pair ratio, PG shows no base sequence specificity. However, the fluorescence intensities of PG–DNA complexes were related to the DNA sequence at higher ratios. The increase in fluorescence intensity of PG upon binding to DNA is about 1000-fold (extinction coefficient  $70\,000\text{ M}^{-1}\text{ cm}^{-1}$ ) and this makes the background fluorescence from free dye negligible. A small red shift of the peak absorption (from 498 nm for free dye to 500 nm for the bound dye) was observed for PG [35]. Re-equilibration can be reached in seconds upon PG labelling on dsDNA. These favourable kinetics also make PG one of the most efficient and versatile DNA probes [36]. Interestingly, PG binds selectively to single-stranded DNA (ssDNA) (low affinity) and dsDNA (high affinity) at 525 nm, unlike EthBr at 610 nm. Thus, the use of PG with EthBr simultaneously at dual wavelength (525 and 610 nm) was recently established as a novel efficient tool to determine the DNA unwinding condition (ss:dsDNA ratio) [37, 38]. The low affinity of PG for ssDNA helps to ensure that fluorescence detection mainly arises from dsDNA–PG interactions.

In NVGT research, PG was used to determine the quantity of free DNA (uncomplexed DNA) to assess the DNA condensation property of gene vectors [39–42]. Currently, there is no study using low-concentration PG to assess complexed DNA during DNA condensation.

## 5

### Calf Thymus DNA Classical FCS Studies

#### 5.1

##### Calf Thymus DNA–PicoGreen Interaction Study

Calf thymus DNA (ct DNA) is a linear DNA with minimum kilobase pairs (kbp) = 13 (MW 8580 MDa). Also, as calculated from:  $L = N_{\text{DNA}} \times a$ , given  $N_{\text{DNA}}$  is the average number of DNA monomers (base pair) and  $a$  = monomer length (i.e. 0.34 nm rise per base pair for DNA duplex), its contour length is 4.4  $\mu\text{m}$ . PG was used in our study to monitor ct DNA. In comparison with EthBr, PG intercalation affinity to dsDNA is higher, and it also has a higher absorption extinction coefficient. PG labels nucleic acid uniformly and without any concentration dependence or artefacts [43]. Free PG also has no significant fluorescence unless intercalated, thus background fluorescence is negligible. In our experiments, fluorescence fluctuation was observed and recorded over the increase of PG concentration (i.e. labelling ratio). Experimental  $G(\tau)$  functions were satisfactorily fitted to a theoretical diffusion model with a single fluorescent type. Typical normalized autocorrelation functions  $G(\tau)$  are plotted as shown in Fig. 4.

When ct DNA is labelled with PG the diffusion time remains constant throughout the whole dye concentration range, showing that the plasmid conformation is not altered by the dye association (Fig. 5). The fluorescence intensity per plasmid particle rises monotonically. The apparent PN saturates at ten dye molecules per 1 kbp of the ct DNA. PN calculated from  $G(\tau)$  of PG molecules bound to ct DNA was  $43.1 \pm 8.1$ . This may be explained from the DNA length, as ct DNA (contour length =  $4.4 \mu\text{m}$ ) is considerably bigger than the confocal element ( $\omega_1 = 0.58 \mu\text{m}$ ,  $\omega_2 = 3.4 \mu\text{m}$ ). In a recent paper [44], it was proposed that long DNA may have internal conformation diffusion of its chain (segmental motion). This leads to a high number of fluctuations in the fluorescence intensity, i.e. lower  $G(\tau)$ , especially when considering that the laser focus could excite at least one part of the entire chain, and thus finally to a higher PN.

Furthermore, at concentrations where apparent PN stabilizes the fluorescence intensity, “count rate” (Fig. 5) is still rising thus indicating that all particles are labelled only after a certain amount of dye is added. Further increase of the fluorophore quantity makes only the fluorescence intensity rise. These results show that the ideal dye/DNA ratio should give a sufficient fluorescence signal with less interference in DNA conformation from intercalating

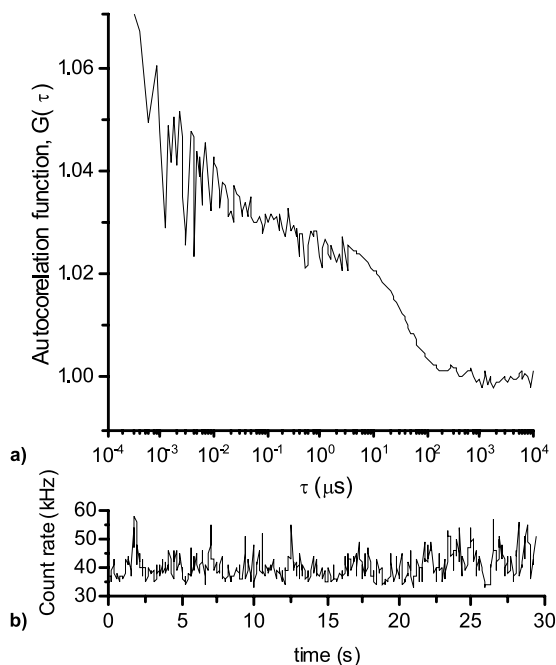


**Fig. 4** Examples of normalized autocorrelation functions  $G(\tau)$  (a) and the relative count rates (b) for ct DNA (1 nM,  $200 \mu\text{l}$ ) intercalated with PG ( $1.1 \times 10^{-6}$  M,  $30 \mu\text{l}$ );  $C_{\text{dye}}/C_{\text{kbp}}$  is 13. The nature of multi-labelling DNA (long-chain molecules) causes an overestimation of PN (apparent PN) compared to the PN of singly labelled small molecules



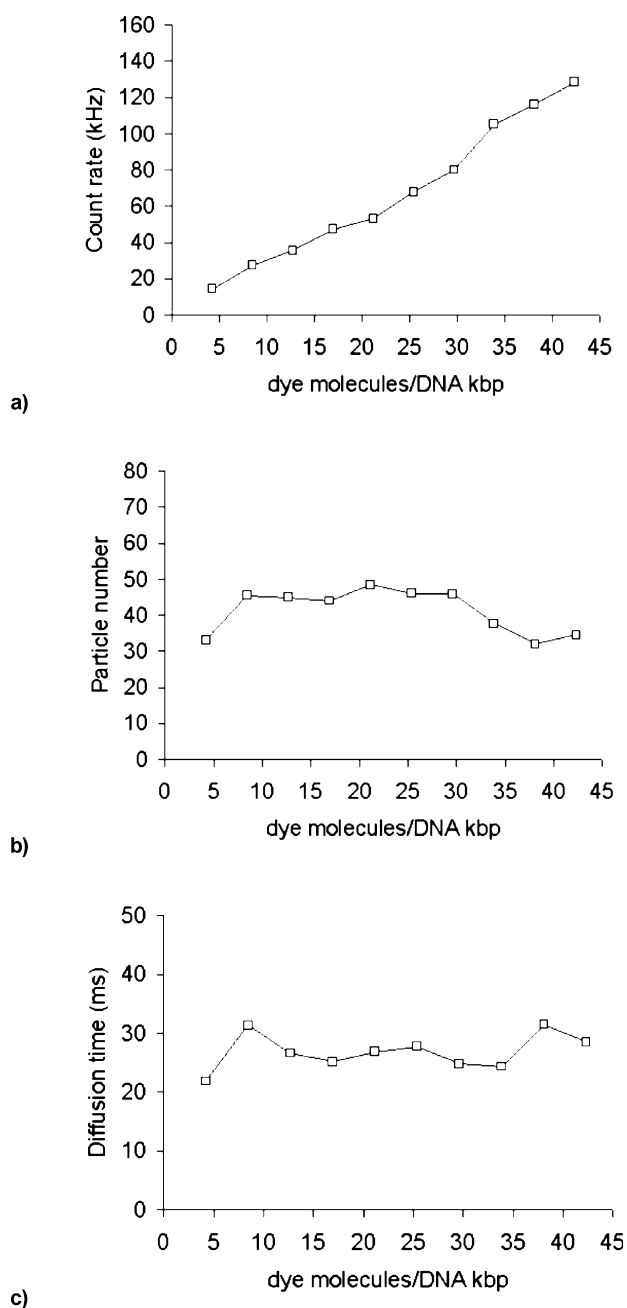


**Fig. 5** PG labelling calibration using ct DNA. Different volumes of PG (1.1  $\mu\text{M}$ ) were added to 200  $\mu\text{l}$  of 1 nM DNA and incubated for 10 min.  $G(\tau)$  was recorded at each dye labelling ratio. FCS parameters were calculated and plotted against dye concentration, i.e. **a** count rate (CR), **b** particle number (PN) and **c** diffusion time ( $\tau_D$ )

dyes. This suggests that PG has no influence over the hydrodynamic properties of DNA molecules. Additionally, PG can be used at a very low level (i.e. 5–40 dye molecules/kbp) compared to the similar study using EthBr [21, 22, 24]. The stability of the dye and DNA complexes after dilution is also important for a titration study of DNA condensation. The high stability of PG-labelled DNA samples means that the volume addition of DNA condensing agent does not affect the accuracy of the measurement [35].

The diffusion coefficient of ct DNA was calculated by considering DNA as a rod-like molecule [21, 22, 24]. Considering the characteristics of DNAs, ct DNA has a high  $\tau_D$  which is due to its significantly greater size than circular plasmids; different length DNAs diffuse differently in solution. The  $D$  of ct DNA from calculation ( $5.3 \times 10^{-13} \text{ m}^2/\text{s}$ ) shows a similar result to that found in FCS experiments ( $7 \times 10^{-13} \text{ m}^2/\text{s}$ ). The deviation of  $\tau_D$  found in our FCS studies and from calculation was noticeably high for ct DNA, which may suggest that the long DNA may diffuse differently from the shorter one with some additional mechanism. The other contribution factor is also from the polydispersity of ct DNA, which means that a different length of linear DNA was measured at once. However, the DNA condensation process is regarded as an all-or-nothing process; it is possible to monitor nanoparticle formation using ct DNA [45, 46].

## 5.2

### Calf Thymus DNA Condensation by Lipopolyamines

Lipopolyamine vectors have been regarded as efficient DNA condensing agents in NVGT. These molecules have a lipophilic moiety (mainly long chain hydrocarbon or steroidal lipids) and positively charged amine group(s), such as spermine or synthetic polyamines [47–52]. Two lipopolyamines were synthesized and used in these experiments. Both are designed to incorporate a spermine backbone conjugated with a lipophilic moiety, i.e. the oleoyl group (amide link) (Fig. 6a) [47, 49, 50] and the cholesteryl group (carbamate link) (Fig. 6b) [52]. Both our novel DNA condensing agents show effective condensation (i.e. yielding 10% fluorescence reduction in a fluorometric assay at ammonium/phosphate (N/P) ratio as low as 1.5–2.0) and high transfection rate. One aim of this study is to understand more on the mechanism of how these two vectors interact with DNA at a single-molecule level (in this case, specifically regarded as a single nanoparticle) by FCS using PG.

From the calibration curves (Fig. 5a–c), the optimal dye ratio used for ct DNA labelling was in the range of 5–40. PG was prepared in 1 : 200 dilution (according to the manufacturer's protocol). In the DNA condensation experiment, the PG volume added was 30  $\mu\text{l}$  (which is equivalent to a dye/kbp ratio = 35). Fluorescence fluctuation was monitored while adding  $N^4, N^9$ -dioleoylspermine or  $N^1$ -cholesteryl spermine carbamate in a solution sample containing PG-labelled DNA.

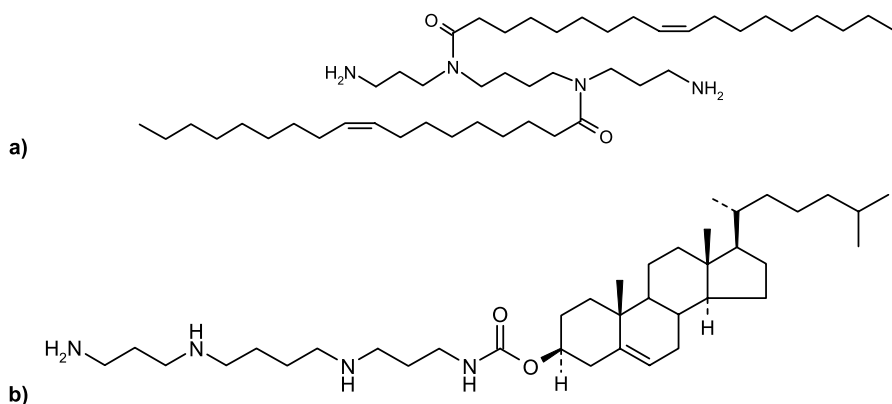


**Fig. 6** **a**  $N^4,N^9$ -Dioleoylspermine, **b**  $N^1$ -cholesteryl spermine carbamate. The aim of this study is to understand more of the mechanisms by which these two vectors interact with DNA at a single molecule level (in this case, specifically regarded as a single nanoparticle) by FCS using PG

When the N/P ratio was increased (Fig. 7), DNA phosphate groups were gradually neutralized by positively charged ammonium groups of  $N^4,N^9$ -dioleoylspermine and  $N^1$ -cholesteryl spermine carbamate.  $G(\tau)$  was recorded and FCS parameters (diffusion coefficient and PN) were then calculated throughout the DNA condensation process. The indication of DNA condensation occurrence is the dramatic decrease of  $\tau_D$  and PN, particularly for a system with macromolecules where a single monitored molecule is not small enough to fit in the confocal volume. From Fig. 7, the diffusion coefficient ( $D$ ) continuously increased upon the addition of lipopolyamines in both DNA condensation experiments. As faster movement of DNA resulted from condensation, we conclude that smaller (compacted) DNA nanoparticles have been formed. The PN also decreased while measured CR remained constant.

### 5.3

#### Point-like Molecule Detection in DNA Condensation

PN is a direct parameter to prove the number of fluorescent molecules, which here reports on the DNA concentration. In the model with point-like molecules, PN is described by the equation  $PN = C \times V \times N_A$ , where  $C$  = molarity of detected molecules,  $V$  = confocal volume, and  $N_A = 6.023 \times 10^{23}$ . By using this equation, and as the DNA concentrations used in our experiments were kept constant at 1 nM, the theoretical PN to be achieved is around 1. The PN achieved at N/P = 1.0–1.5 for ct DNA condensed by  $N^4,N^9$ -dioleoylspermine was 0.7. This evidence confirms that DNA was condensed into a point-like molecule by the  $C_{18}$ -substituted lipopolyamine, which fulfils the assumptions of FCS and validates the use of FCS as a sensitive method in DNA formula-

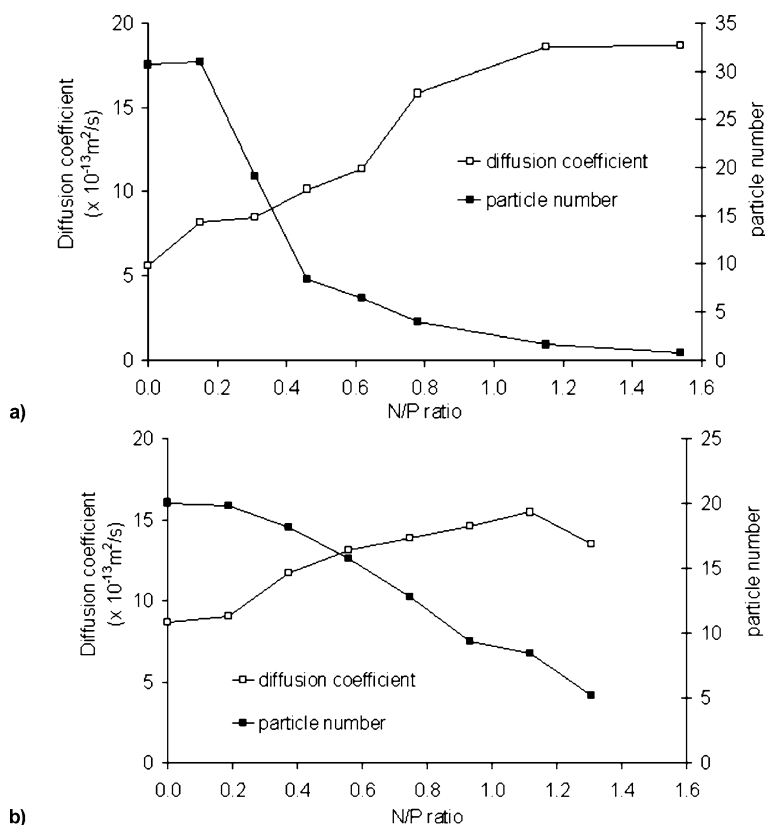


**Fig. 7** FCS study of DNA nanoparticle formation: ct DNA (1 nM, 200  $\mu\text{l}$ ) was condensed with lipopolyamines, using PG as a reporter probe. **a** ct DNA condensation by  $N^4, N^9$ -dioleoylspermine (PG at dye/kbp = 13), **b** ct DNA condensation by  $N^1$ -cholesteryl spermine carbamate (PG at dye/kbp = 13)

tion studies (which is indeed a point-like molecule, when compared to the typical confocal volume). This result is in agreement with other physical studies on DNA particle size, when completely condensed at the nanoscale level. Similar results were also found for DNA condensation with  $N^1$ -cholesteryl spermine carbamate, with a decrease in  $\tau_D$  and PN. The PN value achieved at  $N/P = 1.5\text{--}2.5$  for ct DNA condensed by  $N^1$ -cholesteryl spermine carbamate was 5.2. From a comparison of this PN result with that obtained with  $N^4, N^9$ -dioleoylspermine, we conclude that  $N^1$ -cholesteryl spermine carbamate is a poorer DNA condensing agent than  $N^4, N^9$ -dioleoylspermine. Additionally, the condensation occurred at a higher  $N/P$  ratio ( $N/P = 1.5\text{--}2.5$ ) than the condensation achieved with  $N^4, N^9$ -dioleoylspermine ( $N/P = 1.0\text{--}1.5$ ). Considering the positive-charge number of  $N^4, N^9$ -dioleoylspermine is less than that of  $N^1$ -cholesteryl spermine carbamate (i.e. 2 compared to 2.4), we conclude that

the more efficient DNA condensation is possibly due to the respective regio-chemical distribution of these two positive charges together with their lipid moieties ( $C_{18}$  vs cholesterol).

Point-like molecules obtained from ct DNA condensation by  $N^4, N^9$ -dioleoylspermine have an average  $\tau_D$  of 12.0 ms ( $D = 1.8 \times 10^{-12} \text{ m}^2/\text{s}$ ). These nanoparticles diffuse about three times faster than free DNA ( $D = 0.71 \times 10^{-12} \text{ m}^2/\text{s}$ ). A similar diffusion behaviour of ct DNA complexed with  $N^1$ -cholesteryl spermine carbamate was also found at 14.0 ms ( $D = 1.3 \times 10^{-12} \text{ m}^2/\text{s}$ ), although the PN has not fulfilled the point-like molecules hypothesis (i.e. not approximating to 1.0). The change in the magnitude of the diffusion coefficient ( $D$ ) between free and condensed DNA, mediated by both our two lipopolyamines and at appropriate N/P ratios to achieve full DNA condensation, provides evidence for the dramatic change that is DNA condensation. Moreover,  $D$  is, in general for point-like molecules, a rather insensitive parameter and could incorporate some error (about 10%). On the other hand, PN is much more sensitive, and it accurately shows differences between both condensing agents. Thus,  $N^4, N^9$ -dioleoylspermine is a more efficient DNA condensing agent (PN approaching 1.0) than  $N^1$ -cholesteryl spermine carbamate.

In the steady-state EthBr fluorescence quenching study, it was shown that there is no significant difference in the condensation of ct DNA and plasmids. However, FCS is a single-molecule technique with high sensitivity, and it is possible to observe the difference of linear (and big) ct DNA behaviour and plasmid (circular) DNA in a 1-fl confocal volume.

## 6

### Simultaneous Lifetime and FCS Studies of Plasmid DNA

Titration experiments of chromophore–DNA complexes using classical FCS yield information about changes in diffusion behaviour (caused by conformational changes) during condensation. These changes can be accompanied by changes in dye environment, which can be reflected in fluorescence lifetime change. Therefore, in our study, we have applied simultaneous lifetime and FCS analysis [18] to monitor the behaviour of PG on plasmid DNA at low labelling ratio (40 dye/kbp) through its condensation process. The set-up used (pulsed laser and TTTR data storage) allows the simultaneous monitoring of DNA condensation (through FCS analysis) and PG lifetime (through the time-resolved mode).

#### 6.1

##### Plasmid DNA–PicoGreen Labelling Study

pGL3 DNA (5.3 kbp, contour length  $1.8 \mu\text{m}$ ) and pEGFP (4.7 kbp, contour length  $1.6 \mu\text{m}$ ) are two circular plasmids used in simultaneous lifetime and FCS

experiments. It was expected that the smaller size of both plasmids (compared to linear ct DNA) would result in a higher diffusion coefficient and smaller PN when they are detected using FCS and PG.

pGL3 and pEGFP were prepared in HEPES buffer (20 mM NaCl, pH 7.4) in 1 nM concentration and used in 200  $\mu\text{l}$  volumes. Increasing amounts of PG (as a 1.1  $\mu\text{M}$  solution) were added to both plasmids to perform a measurement simulating the different states of PG binding. Experimental  $G(\tau)$  functions were satisfactorily fitted to a theoretical diffusion model with two-population fluorescent types, which show (more than 95%) a major population of a slow diffusing species. Typical normalized autocorrelation functions  $G(\tau)$  are shown in Fig. 8.

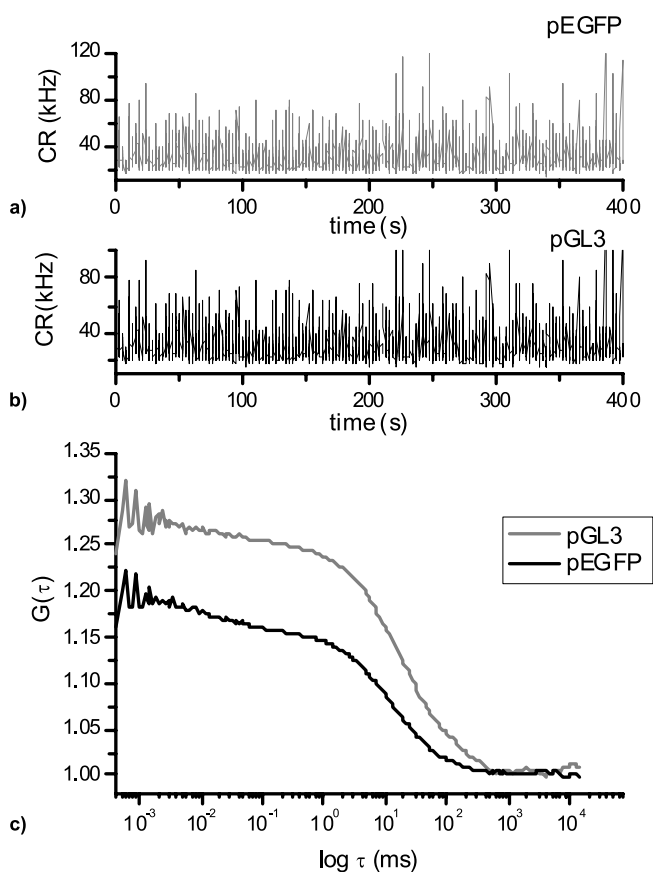


**Fig. 8** Examples of CR plots and normalized  $G(\tau)$  constructed from TTTR data. The CR tracking (**a** pEGFP, **b** pGL3) and  $G(\tau)$  (**c**) for pGL3 (1 nM, 200  $\mu\text{l}$ ) intercalated with PG (1.1  $\mu\text{M}$ , 18  $\mu\text{l}$ ) (*black line*) and pEGFP (1 nM, 200  $\mu\text{l}$ ) intercalated with PG (1.1  $\mu\text{M}$ , 18  $\mu\text{l}$ ) (*grey line*);  $C_{\text{dye}}/C_{\text{kbp}}$  are 18 and 21, respectively. The nature of multi-labelling DNA (long-chain molecules) causes an overestimation of PN (apparent PN)

According to the  $G(\tau)$  obtained from TTTR data analysis, both PG-labelled plasmids show similarity in their autocorrelation functions (Fig. 8). These similar diffusion coefficients correspond to the similar size and structure of pGL3 and pEGFP. Both DNAs also show the overestimated PN, higher than the theoretical PN (calculated by the real concentration of DNA used) as previously discussed for ct DNA. This is caused by the size of multi-labelled plasmid DNA, which is too big to fit the confocal volume. This leads to a multiplicity of observed PG on a single DNA molecule.

The FCS parameters (Fig. 9), calculated from  $G(\tau)$  and the confocal volume obtained from Alexa Fluor 488 calibration, are complementary to the lifetime

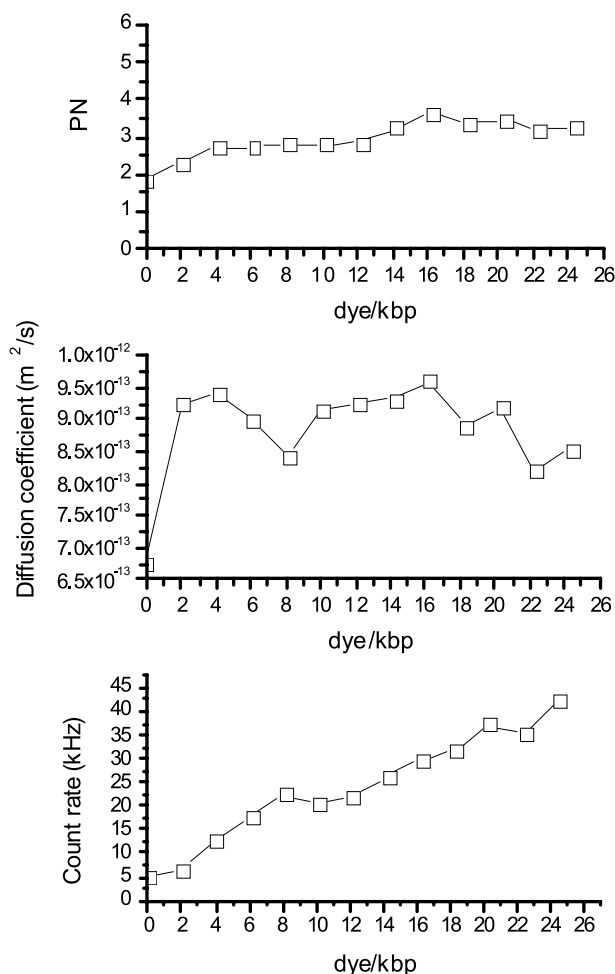


**Fig. 9** FCS parameters from TTTR data acquisition, i.e. PN, CR and diffusion time (or coefficient), of PG-labelled pGL3 ( $\square$ ) were analysed from  $G(\tau)$ . PG was added to DNA solutions achieve different dye/kbp ratios

information of fluorescent PG. The constant increase of CR when more PG was added confirmed that PG intercalation is the most preferable binding mode in the low-labelling condition (less than 40 kbp). This is important to DNA probe selection which the unity of binding mode may simplify for data interpretation. The constant PN at a value of 3–5 and diffusion coefficient ( $1 \times 10^{-12} \text{ m}^2/\text{s}$ ) suggest that DNA-bound PG molecules do not alter the DNA hydrodynamic property (i.e. do not induce DNA bending or even condensation).

In Fig. 10, the PN and diffusion coefficient ( $1.5 \times 10^{-12} \text{ m}^2/\text{s}$ ) of labelled pEGFP were similar to those of pGL3 ( $1 \times 10^{-12} \text{ m}^2/\text{s}$ ). However, the PN of PG-labelled pEGFP was slightly increased and finally attained a constant level.

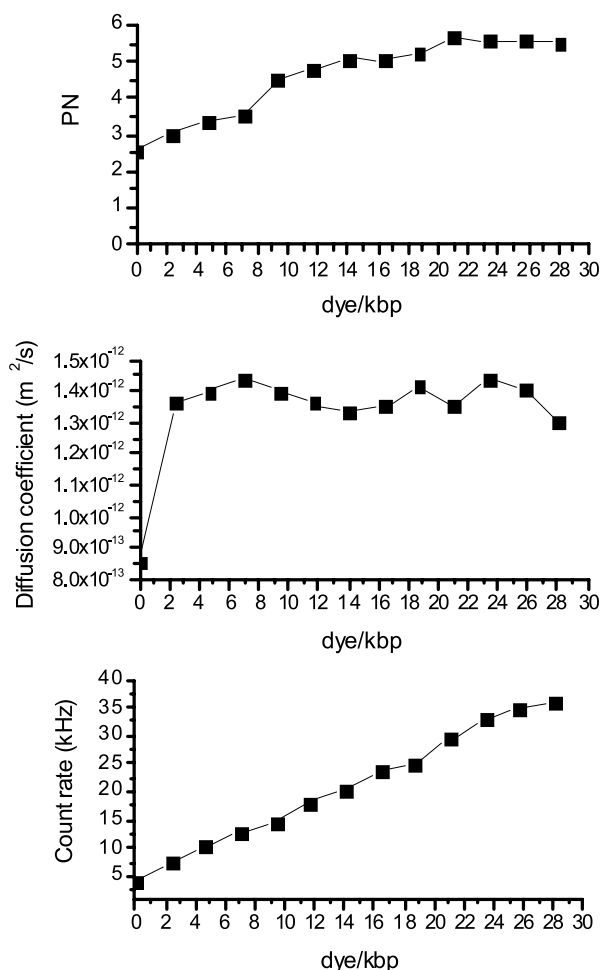


**Fig. 10** FCS parameters from TTTR data acquisition, i.e. PN, CR and diffusion time (or coefficient), of PG-labelled pEGFP (■) were analysed from  $G(\tau)$ . PG was added to DNA solutionsto achieve different dye/kbp ratios



This increased PN may result from the DNA labelling distribution of PG, where initially PG molecules are localized at preferential binding sites on DNA (apparent lower PN), then PG molecules are randomly distributed over the DNA double helical chain, so the apparent PN becomes slightly higher, and finally, PN reaches its constant value. However, this possible DNA base-preference of PG binding was not found in pGL3. According to the literature [38], PG also shows higher affinity to GC than AT. This slight increase of PN does not affect PG fluorescence in DNA when it is used to monitor the DNA condensation process.

To understand the nature of DNA binding of PG, fluorescence TTTR data were recorded at different PG dye/kbp ratios using pGL3 and pEGFP. The

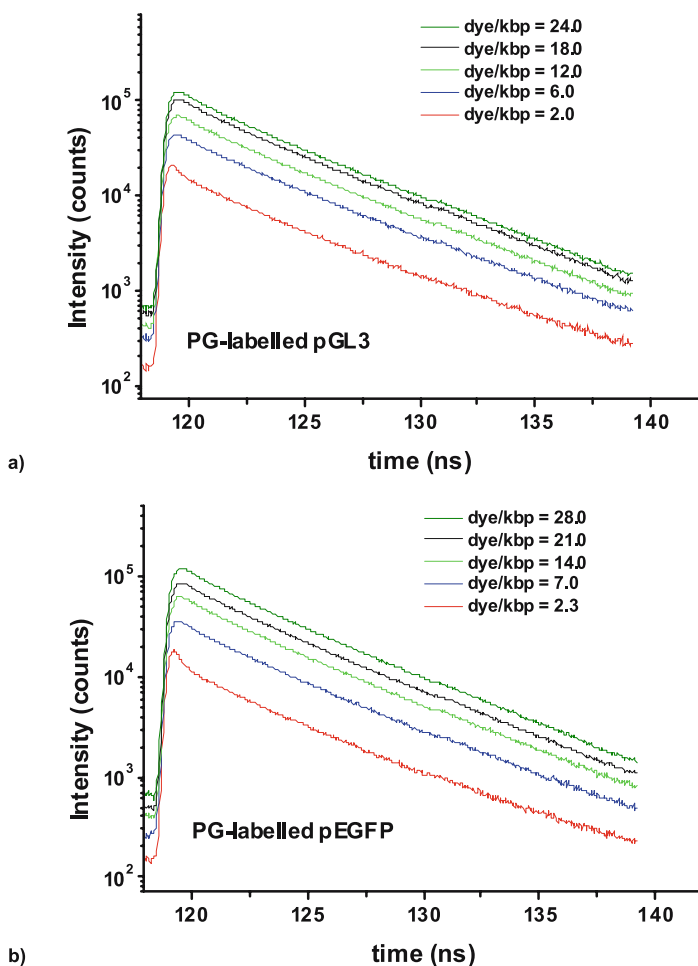


**Fig. 11** Fluorescence decay profiles for PG bound to circular plasmid DNA (a pGL3 and b pEGFP) obtained from TTTR data acquisition

intensity decay was obtained from TTTR data and fitted by MicroTime 200 (Fig. 11 plotted in OriginPro 7.0). A tail fitting was used in this experiment at constant channels. PG-labelled DNA fluorescence lifetime decay was best fitted by a two-exponential model. From this fitting calculation, there are two populations of DNA-bound PG fluorescent species: (a)  $\tau = 4$  ns (intensity fraction 97%) and (b)  $\tau = 1$  ns. Considering that the fraction of other PG species (with  $\tau = 1$  ns) is very small, we concluded that the  $\tau = 4$  ns species is the major fluorescent PG (Fig. 12). This corresponds well to the previous study

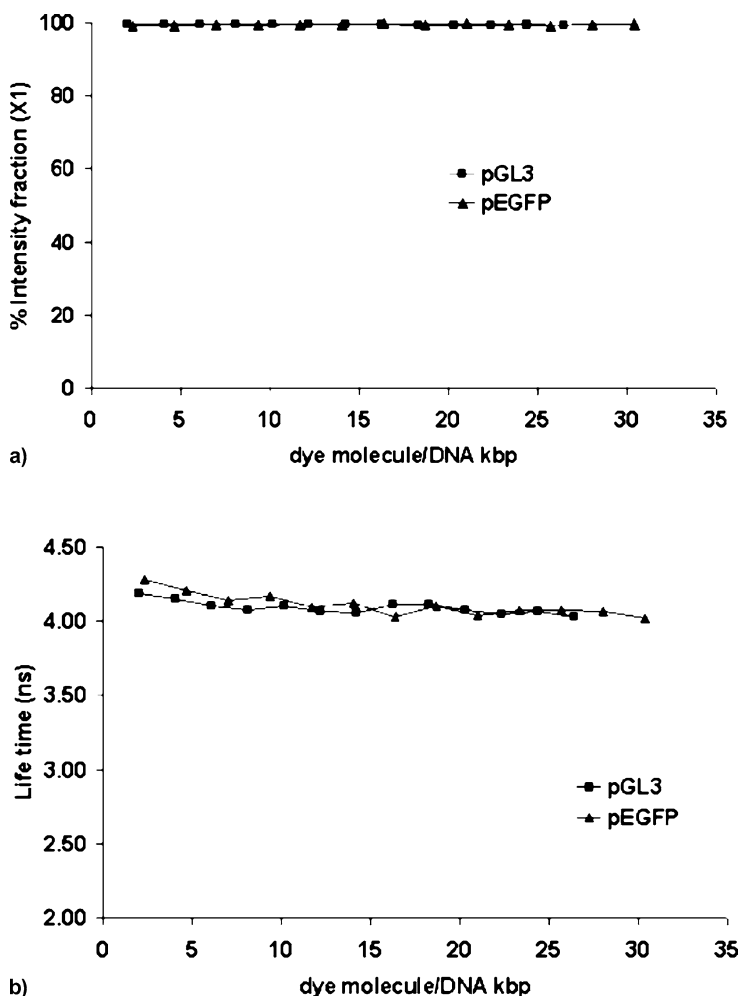


**Fig. 12 a** Major fraction of fluorescent species (97%) and **b** lifetime of the major fluorescent population over a range of dye labelling ratios. The major fluorescent species of DNA-bound PG shows a consistent lifetime, indicating that there is no dye relocation or dye environment change

by fluorescence lifetime measurement with a streak camera by Schweitzer and Scaiano [38], who also showed that PG is adequately fitted by mono-exponential decays when complexed to dsDNA (within  $\pm 5\%$  error). In terms of model fitness, the two-exponential model has improved the  $\chi^2$  value over the mono-exponential model, but a three-exponential model failed to improve the  $\chi^2$  value further. Thus, we used the two-exponential model throughout our experiments.

Figure 12 reveals that the majority of PG, in the range of 0–30 dye molecules/kbp, is bound to both plasmid DNAs through a single and unified mechanism. PG-labelled DNAs show negative in the circular dichroism study [53], indicating that majority of dyes are intercalated between DNA base pairs. This is also supported by the PG concentration used in our study, which is much lower than the saturation of acridine dye intercalation (i.e. 500 dye molecules/kbp). However, our model also indicates the presence of short-lived PG (1 ns), though in very small numbers. The constant lifetime of DNA-bound PG at 4 ns also confirms that there is no change in the environment surrounding PG intercalating sites. This ensures that there is no major change in DNA conformation due to PG intercalation, which is a desirable property of a good fluorescent probe for DNA.

## 6.2

### **Simultaneous Lifetime and FCS Analysis of Plasmid DNA Through the Condensation Process**

Two lipopolyamines,  $N^4, N^9$ -dioleoylspermine (Figs. 13 and 14) and  $N^1$ -cholesteryl spermine carbamate (Figs. 15 and 16), were used in this study to condense pGL3 and pEGFP. The FCS parameters were obtained from  $G(\tau)$  (derived from TTTR data) and show efficient condensation of both plasmids.

DNA conformational change toward a condensed DNA was reflected in lower PN values with increased N/P charge ratios. More structured DNA would have less segmental movement, thus reducing the PN value. Based on our previous study, these two lipopolyamines can achieve the point-like molecule condition (DNA was seen as one nanoparticle), because the observed PN (= 1.0 for both plasmids) is approaching the theoretical PN = 0.6 (for 1 nM DNA). Complete DNA condensation was also illustrated by the increase of the diffusion coefficient ( $D$ ) of fluorescently labelled plasmid.

PG lifetime data, additional information obtained from TTTR data, can be used to explain the behaviour of PG when DNA is condensed. The fluorescence decay profile of DNA-bound PG was fitted by employing the two-exponential model. The decay plots are shown in Figs. 17 and 18. The major population of fluorescent species in condensed DNA was also found to be 97% consistently through the condensation process, with lifetime at 4 ns, which is the same as previously noted in the experiments (without

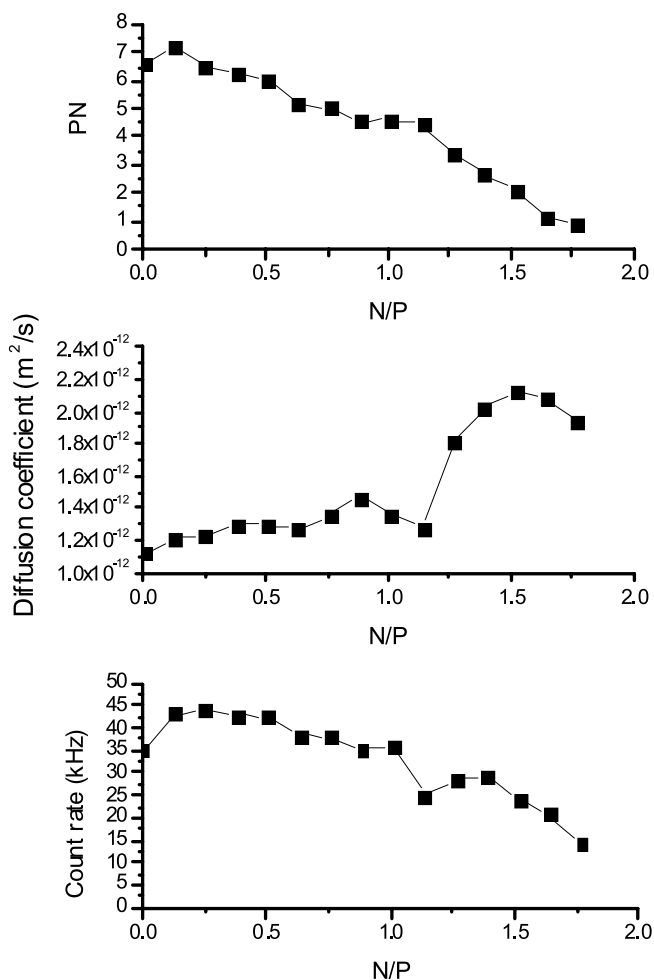


**Fig. 13** FCS parameters derived from TTR data acquisition during the condensation process of pGL3 by  $N^4, N^9$ -dioleoylspermine; PG used at 18 dye/kbp

lipopolyamines) shown in Fig. 12. This emphasized that most PG molecules remain in the same binding site and there was no migration to other binding sites (i.e. minor groove).

The lifetime values (Fig. 19b) found in our DNA experiments were decreased from 4 to 3.0–3.5 ns at the last stage of DNA condensation. We conclude that even though PG still maintains its binding sites, there might be some changes in the surrounding environment of the DNA base pairs, and this promotes fluorescence loss at a quicker rate (i.e. fluorescence quenching). This quenching was probably due to DNA packing into nanoparticles in the condensed DNA environment.

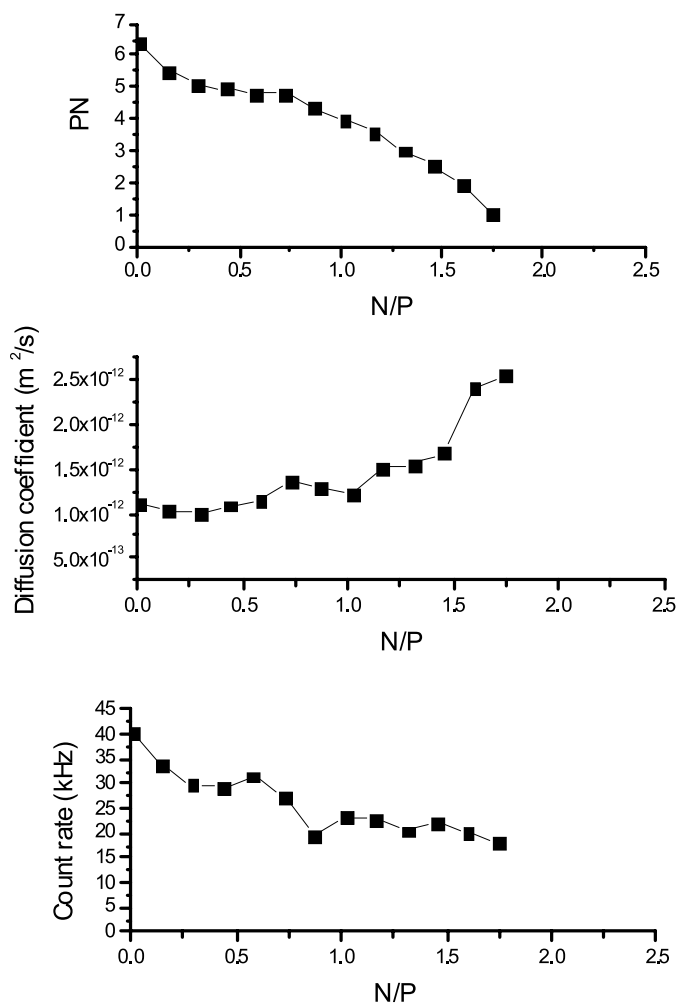


**Fig. 14** FCS parameters derived from TTTR data acquisition during the condensation process of pEGFP by  $N^4,N^9$ -dioleoylspermine; PG used at 21 dye/kbp

Both CR and lifetime were normalized to the percentage of fluorescence decrease. This use of lifetime (time unit) as a fluorescence unit was based on the relationship of fluorescence quantum yield and lifetime, as described in the equation:

$$\frac{F_0}{F_q} = \frac{\tau_0}{\tau_q} \quad (8)$$

The CR values were reported as % relative CR, which included both dye release (physical loss of dye from DNA) and dye quenching (no physical loss of

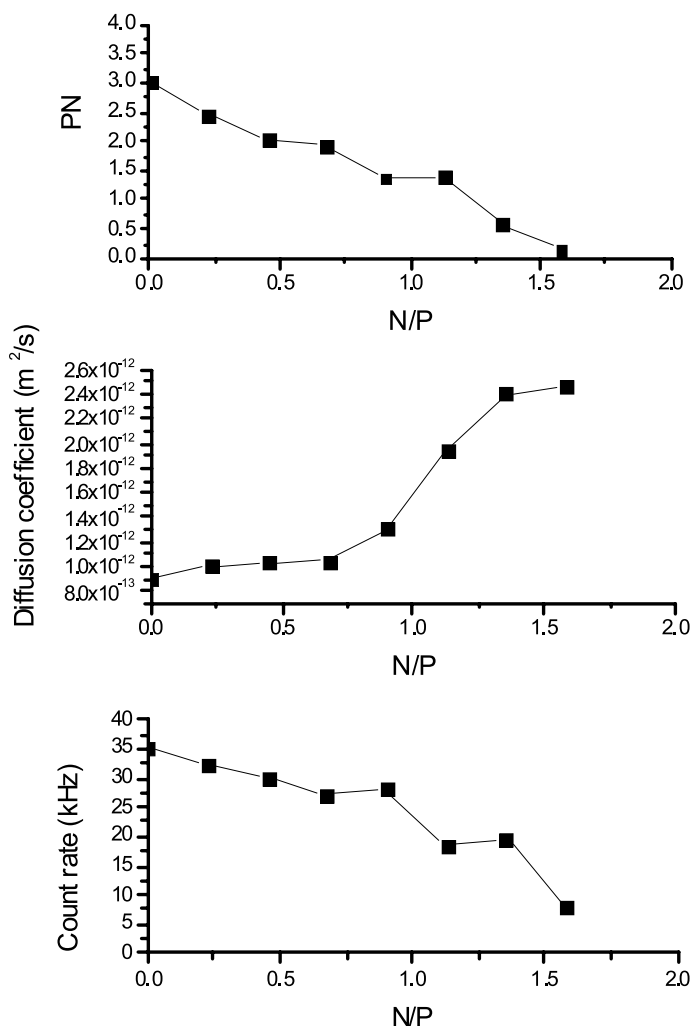


**Fig. 15** FCS parameters derived from TTTR data acquisition during the condensation process of pGL3 by  $N^1$ -cholesteryl spermine carbamate; PG used at 18 dye/kbp

dye, but shorter lifetime). During the first stage of DNA condensation, only the dye release process leads to CR loss. The dye release process does not decrease the decay time of PG, because only the fluorescent species (intercalated PG) was monitored. This is supported by Figs. 20 and 21, in which lifetime is found to be constant during the dye release process. At the stage of nanoparticle formation, dynamic quenching of PG is proposed as the process leading to fluorescence loss. The quenching process acts on the excited population and thus decreases the mean decay time of the excited-state population.

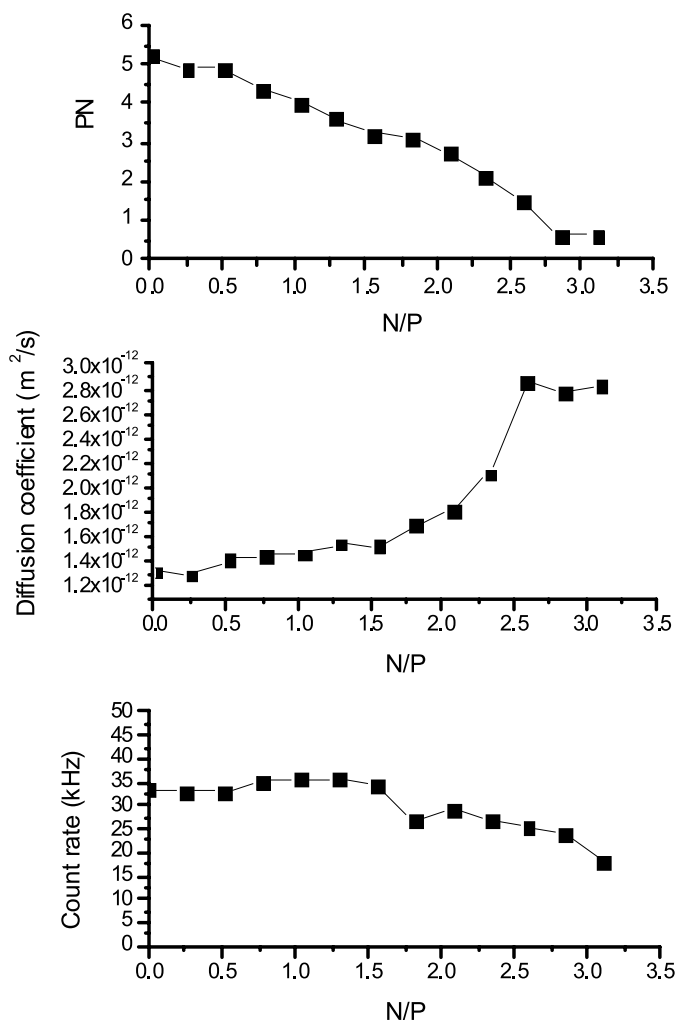


**Fig. 16** FCS parameters derived from TTTR data acquisition during the condensation process of pEGFP by  $N^1$ -cholesteryl spermine carbamate; PG used at 21 dye/kbp

The behaviour of PG on DNA during condensation is shown in our model (Fig. 22). PG efficiently binds to DNA (step I dye binding) with a single binding mode (intercalation), a 4-ns lifetime, and no interference in DNA hydrodynamics. Upon adding the lipopolyamine DNA condensing agent to the DNA–PG complex, a small fraction of PG molecules were excluded from the complex. However, the degree of PG release also depends on the condensing agent used (step II dye release). This does not indicate the end point of DNA nanoparticle formation. On the addition of further lipopolyamine, the circular plasmid DNA was transformed into a single nanoparticle (step III dye quenching).

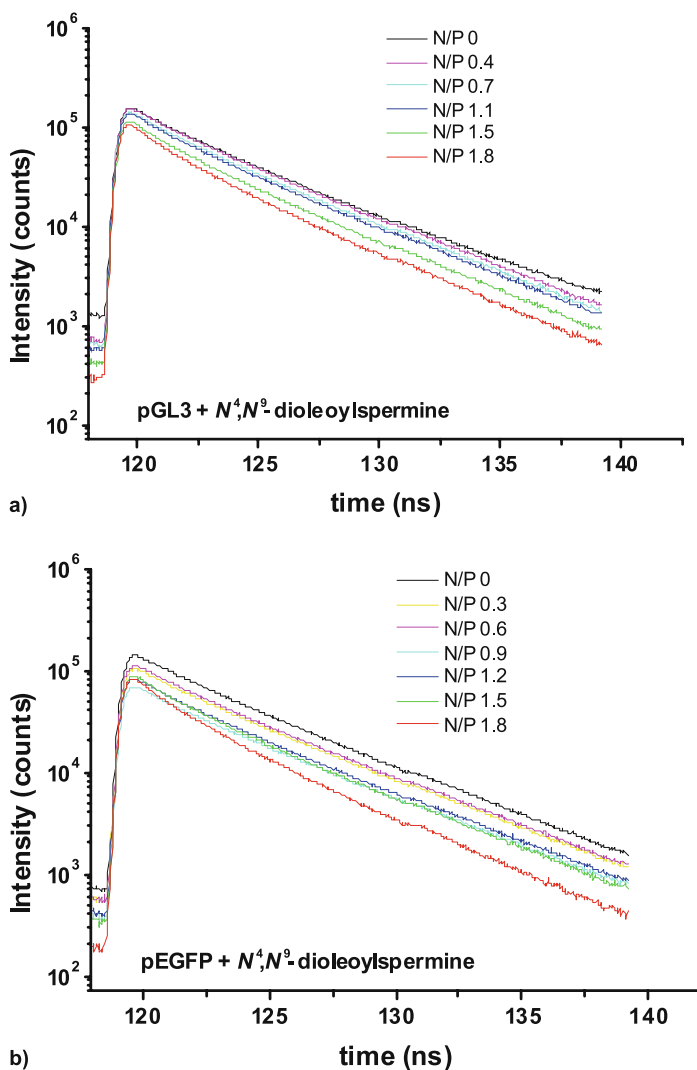


**Fig. 17** Fluorescence decay profiles for PG bound to circular plasmid DNA (**a** pGL3 and **b** pEGFP), obtained from TTTR data acquisition, which undergoes DNA condensation using  $N^4,N^9$ -dioleoylspermine

Dye quenching, as determined by lifetime analysis, is an effective indicator of nanoparticle formation. In step III, the measured PN, a reliable parameter for FCS measurement, approached the theoretical PN. Key advantages in the use of PG in these DNA condensation studies are, at the low concentrations employed (essentially 100 nM), its single (97%) mode of binding to DNA (intercalation) and, in comparison with other dyes such as EthBr, its high affinity for DNA.



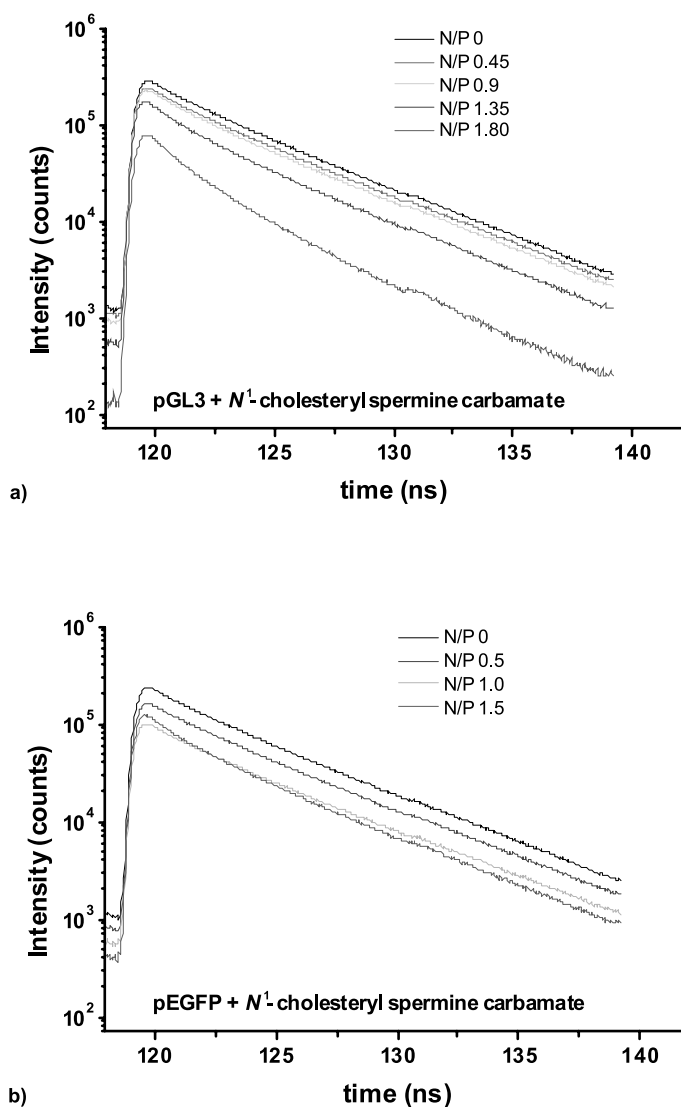


**Fig. 18** Fluorescence decay profiles for PG bound to circular plasmid DNA (**a** pGL3 and **b** pEGFP), obtained from TTR data acquisition, which undergoes DNA condensation using  $N^1$ -cholesteryl spermine carbamate

## 7

### Conclusions

Employing the reported FCS experiments, we were able to monitor lipopolyamine–DNA complex formation at the single-molecule level. In comparison to

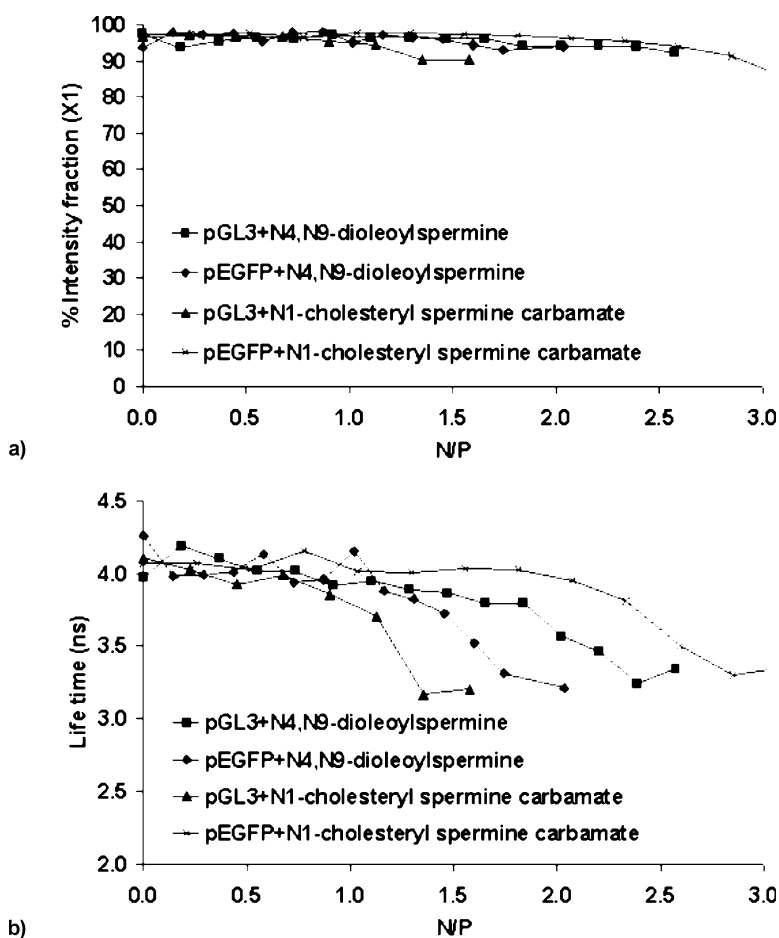


**Fig. 19** Intensity fraction **a** of major fluorescent species of DNA-bound PG shows there is no change of the intensity fraction of the major population (4.0-ns dye species) during the DNA condensation process. **b** Lifetime changes (4.0-ns dye species) during the DNA-condensation process.

other DNA markers, the PG used in our FCS study has several advantages: it does not change the hydrodynamic properties of DNA, and it does not influence the lipopolyamine concentrations necessary for condensation. Additionally, due to its high brightness, PG requires tenfold lower staining when compared with previously used markers. PG has a higher affinity than EthBr and other related dyes for dsDNA, in part because of the polyamine moiety structural modification which efficiently forms salt bridges with DNA phosphate anions; taken together with DNA intercalation, this is known as biphasic binding. Finally, the count rate is practically invariant in the condensation process, indicating that dye release does not interfere with the condensation process. As

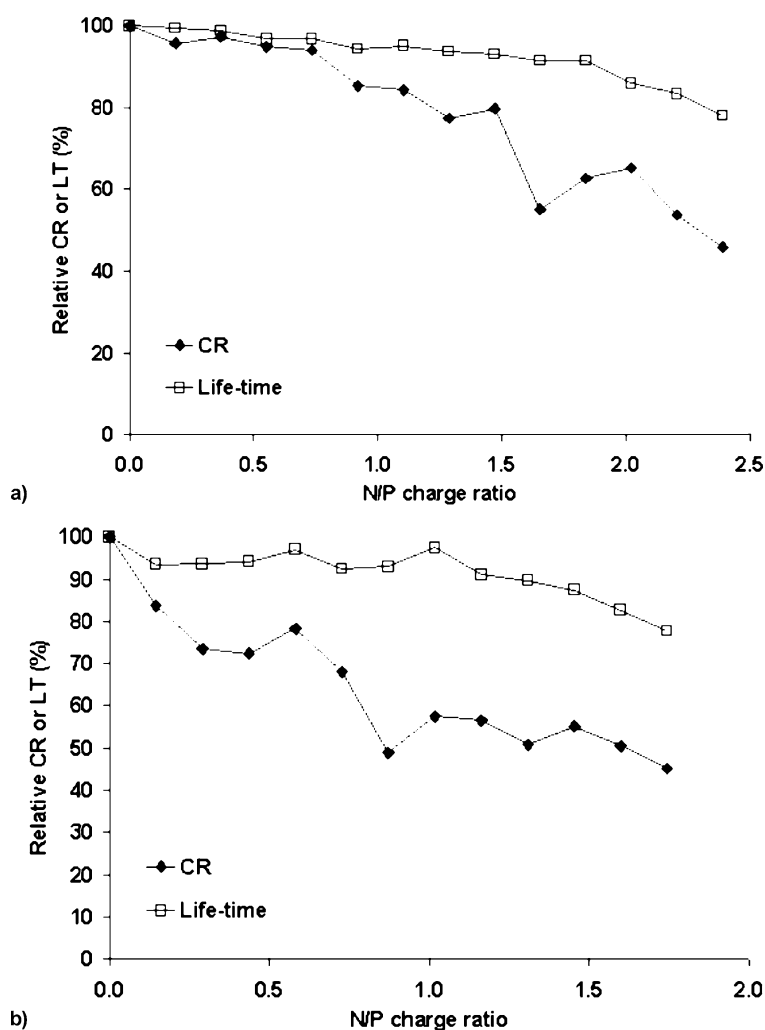


**Fig. 20** Lifetime and CR change during the DNA condensation process of **a** pGL3 +  $N^4,N^9$ -dioleoylspermine and **b** pEGFP +  $N^4,N^9$ -dioleoylspermine

demonstrated using two newly designed lipopolyamines, FCS directly visualizes the condensation process by tracking changes in diffusion coefficients and PNs. In the experiments reported herein, the PN value, which is the most accurate read-out parameter of a FCS experiment, gives quantitative information on the packing density of DNA–lipopolyamine aggregates. Thus, direct information on the quality of condensing molecules can be derived. From this analytical platform, FCS provides detailed information on and insight into DNA and its interaction with gene carriers, which is crucial in the development of safe and effective non-viral gene delivery vectors.

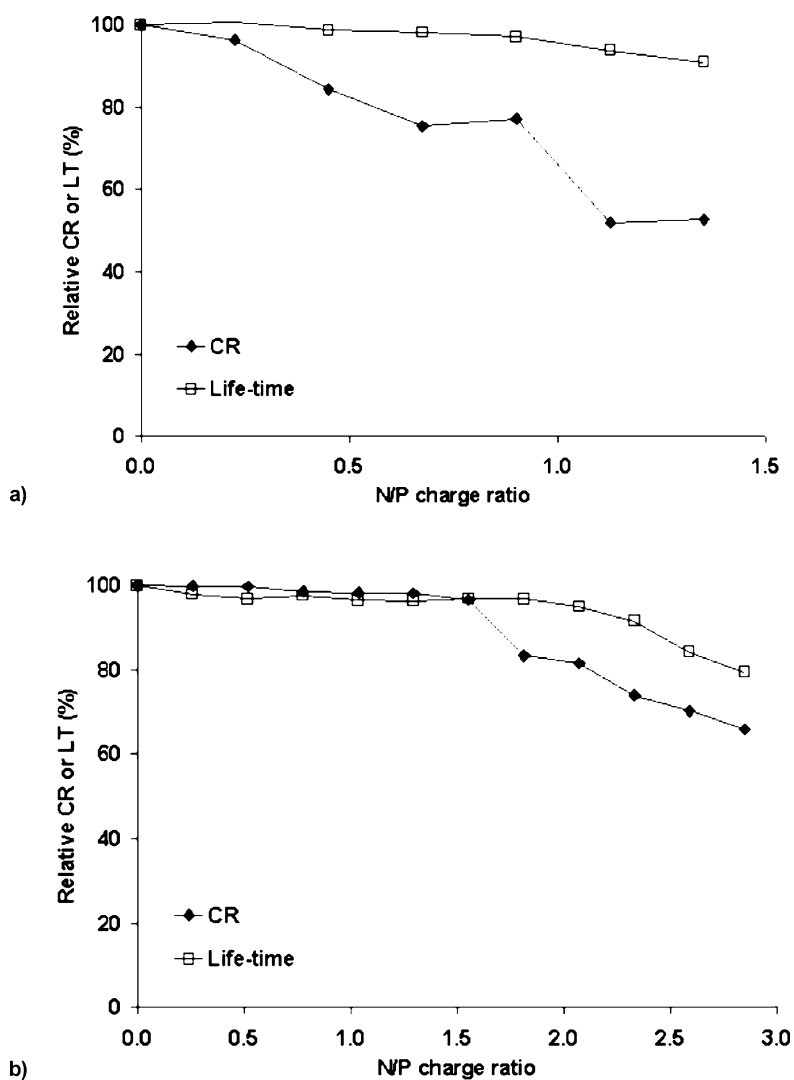


**Fig. 21** Lifetime and CR change during the DNA condensation process of **a** pGL3 +  $N^1$ -cholesteryl spermine carbamate and **b** pEGFP +  $N^1$ -cholesteryl spermine carbamate

In this study, the ConfoCor I set-up upgraded with TimeHarp 200 was used. It offers access to simultaneous lifetime and FCS analysis (TTTR data format). pGL3 and pEGFP condensation with  $N^4, N^9$ -dioleoylspermine and  $N^1$ -cholesteryl spermine carbamate were used as models. We were able to define the fluorescent signalling behaviour of PG through the process from dye binding to dye release, and then dye quenching. Dye release was suggested as the indicator for DNA conformational change, but not for nanoparticle formation.

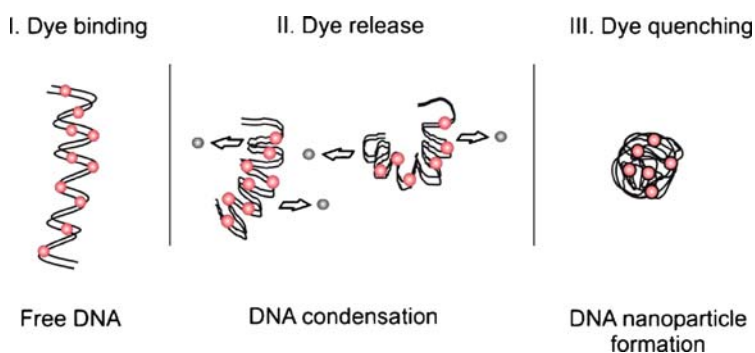


**Fig. 22** PG behaviour through the DNA condensation process

Dye quenching, through the observation of lifetime change, is a more important event accurately and sensitively reporting that a single nanoparticle exists.

**Acknowledgements** We acknowledge support of the Ministry of Education of the Czech Republic via grant LC06063 (AB, MH), the Academy of Sciences of the Czech Republic via grant IAA400400621 (TK), and the Universities UK for an ORS award (partial studentship support to N.A.).

## References

1. Bloomfield VA (1991) *Biopolymers* 31:1471–1481
2. Zabner J, Fasbender AJ, Moninger T, Poellinger KA, Welsh MJ (1995) *J Biol Chem* 270:18997–19007
3. Bloomfield VA (1996) *Curr Opin Struct Biol* 6:334–341
4. Bloomfield VA (1997) *Biopolymers* 44:269–282
5. Godbey WT, Wu KK, Mikos AG (1999) *Proc Natl Acad Sci USA* 96:5177–5181
6. Wiethoff CM, Middaugh CR (2003) *J Pharm Sci* 92:203–217
7. Blagbrough IS, Geall AJ, Neal AP (2003) *Biochem Soc Trans* 31:397–406
8. Thompson NL (1991) Fluorescence correlation spectroscopy. In: Lakowicz JR (ed) *Topics in fluorescence spectroscopy*. Kluwer, New York, p 337
9. Eigen M, Rigler R (1994) *Proc Natl Acad Sci USA* 91:5740–5747
10. Walter NG, Schwille P, Eigen M (1996) *Proc Natl Acad Sci USA* 93:12805–12810
11. Welz C, Fahr A (2001) *Appl Spectrosc Rev* 36:333–397
12. Rigler R, Elson ES (2001) *Fluorescence correlation spectroscopy: theory and applications*. Springer, Berlin
13. Enderlein J (2004) Single molecule spectroscopy: basics and applications. In: Hof M, Hutterer R, Fidler V (eds) *Fluorescence methods and applications: advanced methods and their applications to membranes, proteins, DNA, and cells*. Springer, Berlin Heidelberg, pp 104–122
14. Brock R (2004) Fluorescence correlation spectroscopy in cell biology. In: Hof M, Hutterer R, Fidler V (eds) *Fluorescence methods and applications: advanced methods and their applications to membranes, proteins, DNA, and cells*. Springer, Berlin Heidelberg, pp 245–262

15. Geall AJ, Blagbrough IS (2000) *J Pharm Biomed Anal* 22:849–859
16. Bjorling S, Kinjo M, Foldes-Papp Z, Hagman E, Thyberg P, Rigler R (1998) *Biochemistry* 37:12971–12978
17. Lukacs GL, Haggie P, Seksek O, Lechardeur D, Freedman N, Verkman AS (2000) *J Biol Chem* 275:1625–1629
18. Benda A, Hof M, Wahl M, Patting M, Erdmann R, Kapusta P (2005) *Rev Sci Instrum* 76:033106
19. Magde D, Webb WW, Elson E (1972) *Phys Rev Lett* 29:705
20. Magde D, Elson EL, Webb WW (1974) *Biopolymers* 13:29–61
21. Kral T, Langner M, Benes M, Baczynska D, Ugorski M, Hof M (2002) *Biophys Chem* 95:135–144
22. Kral T, Hof M, Langner M (2002) *Biol Chem* 383:331–335
23. Jurkiewicz P, Okruszek A, Hof M, Langner M (2003) *Cell Mol Biol Lett* 8:77–84
24. Kral T, Hof M, Jurkiewicz P, Langner M (2002) *Cell Mol Biol Lett* 7:203–211
25. Van Rompaey E, Engelborghs Y, Sanders N, De Smedt SC, Demeester J (2001) *Pharm Res* 18:928–936
26. Sobell HM, Tsai CC, Jain SC, Gilbert SG (1977) *J Mol Biol* 114:333–365
27. Manning GS (1978) *Q Rev Biophys* 11:179–246
28. Nordmeier E (1992) *J Phys Chem* 96:6045–6055
29. Singer VL, Jones LJ, Yue ST, Haugland RP (1997) *Anal Biochem* 249:228–238
30. Millard PJ, Roth BL, Thi HPT, Yue ST, Haugland RP (1997) *Appl Environ Microbiol* 63:2897–2905
31. Zipper H, Brunner H, Bernhagen J, Vitzthum F (2004) *Nucleic Acids Res* 32:e103
32. Eriksson M, Karlsson HJ, Westman G, Akerman B (2003) *Nucleic Acids Res* 31:6235–6242
33. Petty JT, Bordelon JA, Robertson ME (2000) *J Phys Chem B* 104:7221–7227
34. Zipper H, Buta C, Lammle K, Brunner H, Bernhagen J, Vitzthum F (2003) *Nucleic Acids Res* 31:e39
35. Yan X, Grace WK, Yoshida TM, Habbersett RC, Velappan N, Jett JH, Keller RA, Marrone BL (1999) *Anal Chem* 71:5470–5480
36. Yan XM, Habbersett RC, Yoshida TM, Nolan JP, Jett JH, Marrone BL (2005) *Anal Chem* 77:3554–3562
37. Beach L, Schweitzer C, Scaiano JC (2003) *Org Biomol Chem* 1:450–451
38. Schweitzer C, Scaiano JC (2003) *Phys Chem Chem Phys* 5:4911–4917
39. Tsai JT, Furstoss KJ, Michnick T, Sloane DL, Paul RW (2002) *Biotechnol Appl Biochem* 36:13–20
40. Choi JS, Nam K, Park J, Kim JB, Lee JK, Park J (2004) *J Control Release* 99:445–456
41. Kasper FK, Seidlits SK, Tang A, Crowther RS, Carney DH, Barry MA, Mikos AG (2005) *J Control Release* 104:521–539
42. Singh R, Pantarotto D, McCarthy D, Chaloin O, Hoebeke J, Partidos CD, Briand JP, Prato M, Bianco A, Kostarelos K (2005) *J Am Chem Soc* 127:4388–4396
43. Kral T, Widerak K, Langner M, Hof M (2005) *J Fluoresc* 15:179–183
44. Lumma D, Keller S, Vilgis T, Radler JO (2003) *Phys Rev Lett* 90:218301(1)–218301(2)
45. Kleideiter G, Nordmeier E (1999) *Polymer* 40:4025–4033
46. Yoshikawa K, Yoshikawa Y, Kanbe T (2002) *Chem Phys Lett* 354:354–359
47. McLaggan D, Adjimatera N, Blagbrough IS, Sepčić K, Jaspars M, MacEwan DJ, Scott RH (2006) *BMC Biotechnol* 6:6
48. Ahmed OAA, Pourzand C, Blagbrough IS (2006) *Pharm Res* 23:31–40
49. Adjimatera N, Neal AP, Blagbrough IS (2004) Fluorescence techniques in non-viral gene therapy. In: Hof M, Hutterer R, Fidler V (eds) *Fluorescence methods and applications*:

- advanced methods and their applications to membranes, proteins, DNA, and cells. Springer, Berlin Heidelberg, pp 201–228
50. Ahmed OAA, Adjimatera N, Pourzand C, Blagbrough IS (2005) *Pharm Res* 22:972–80
  51. Blagbrough IS, Adjimatera N, Ahmed OAA, Neal AP, Pourzand C (2004) Spermine and lipopolyamines as gene delivery agent. In: Beadle DJ, Mellor IR, Usherwood PNR (eds) *Neurotox'03: neurotoxicological targets from functional genomics and proteomics*. Society of Chemical Industry, London, pp 147–159
  52. Geall AJ, Taylor RJ, Earll ME, Eaton MAW, Blagbrough IS (2000) *Bioconjug Chem* 11:314–326
  53. Cosa G, Focsaneanu KS, McLean JRN, McNamee JP, Scaiano JC (2001) *Photochem Photobiol* 73:585–599

# Morphology-Dependent Resonance Emission from Individual Micron-Sized Particles

Trevor A. Smith (✉) · Adam J. Trevitt · Philip J. Wearne · Evan J. Bieske · Lachlan J. McKimmie · Damian K. Bird

School of Chemistry, The University of Melbourne, 3010 Victoria, Australia  
trevoras@unimelb.edu.au

<b>1</b>	<b>Introduction</b> . . . . .	415
1.1	Morphology-Dependent Resonances . . . . .	416
<b>2</b>	<b>Experimental Details</b> . . . . .	419
<b>3</b>	<b>Results and Discussion</b> . . . . .	422
3.1	PPV-Coated Silica Micro-spheres . . . . .	423
3.2	Dye-Doped Micro-spheres . . . . .	424
3.3	Polystyrene Micro-spheres in the QIT . . . . .	426
<b>4</b>	<b>Conclusions</b> . . . . .	427
	<b>References</b> . . . . .	428

**Abstract** We report on the observation and application of morphology-dependent resonances (MDR) (or whispering gallery mode) emission from individual micron-sized particles. MDR emission has been observed through confocal and two-photon fluorescence microscopes and when the particles are trapped in a quadrupole ion trap. The emission has been collected as a series of optical section slices through the micron particles, and the emission resolved temporally using two-photon excitation.

**Keywords** Whispering gallery mode emission · Morphology-dependent resonances · Fluorescent micro-particles

## 1 Introduction

Luminescent nanometre- and micrometre-sized particles are used in a range of applications such as specialist paints, photovoltaic devices, pharmaceutical and formulation science, analytical applications and micro-cavity lasers. Such particles can be inherently luminescent (e.g. quantum dots), or non-emissive particles can be made luminescent through a number of techniques. Porous particles such as Latex micro-spheres can be doped throughout with fluorescent dyes [1, 2], or other (e.g. non-porous) particles can be outer-coated with luminescent species, including dyes, quantum dots [3, 4] and polymers [5].



Luminescent micro-particles, whether inherently emissive, doped or coated, can exhibit interesting emission characteristics. In addition to the normal emission spectrum of the fluorophore, the spectral profile of a luminescent particle can be significantly altered if the dielectric particle acts as an optical micro-cavity. In such a case, the micro-cavity can give rise to highly structured enhancement of emission, which has attracted considerable interest in recent years [6]. A micro-sphere can act as a three-dimensional optical cavity able to support optical resonances, commonly known as morphology-dependent resonances (MDRs). As a consequence of the optical confinement, the spectroscopic properties of an individual micro-sphere are strongly dependent on the particle's composition, size and shape.

In this paper we report on the spatial, temporal and spectral emission characteristics of a range of individual, micron-sized polymer particles doped with fluorescence dyes, or  $\text{SiO}_2$  particles coated with conjugated photoluminescent polymers. These systems are shown to exhibit MDR emission when excited through a confocal or multi-photon microscope. We also report on the detection of MDR emission from micron-sized particles isolated in a quadrupole ion trap.

The highly structured MDR emission spectra have been analysed in terms of Mie theory, leading to the accurate determination of the particles' size and refractive index. We have also analysed this emission as a function of position within the spherical particles using confocal and two-photon fluorescence microscopy, and as a function of time using time-resolved fluorescence imaging techniques following short laser pulse excitation.

## 1.1

### Morphology-Dependent Resonances

Optical micro-cavities can confine light within small volumes by resonant circulation (Fig. 1). In the simplest case, considered classically, an optical beam is confined and circulates in an equatorial path within a spherical dielectric cavity by successive total, or near total, internal reflections at the interface formed between the sphere and the surrounding medium. Classically, resonant circulation occurs when the optical path length of one orbit of the sphere is equal to an integer number of optical wavelengths, thus producing standing light waves within the spherical confines. The total internal reflection enables

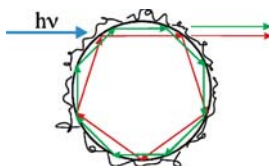


**Fig. 1** MDR schematic

the particles to act as very high- $Q$  optical cavities. As a result of the high confinement of these modes, the theoretical [7]  $Q$  value can exceed  $10^5$ , even for a small sphere of diameter  $5 \mu\text{m}$  at optical frequencies.

The result of this optical confinement is that for individual fluorescently labelled micro-spheres, the fluorescence emission profile is dominated by the appearance of sharp peaks or MDRs. These MDRs are also known as whispering gallery modes (WGM), so-named due to the resemblance of this modal behaviour to the acoustic effect noted in some cathedrals, where one can whisper along the wall and be heard all along the inside perimeter of the dome [8]. As a consequence of these MDRs, the spectroscopic properties of an individual micro-sphere are dependent on its composition, size and shape. The wavelengths of the MDR peaks allow the radius and the refractive index to be accurately determined [9]. In addition to the size and shape of the micro-sphere itself, the MDR locations are sensitive to changes (e.g. through refractive index) in the surrounding medium, making micro-sphere systems attractive prospects for biosensory applications [10].

The mathematical description of these MDR features is attributed to Mie [11] who considered the scattering of a plane, x-polarized electromagnetic wave by a sphere. Incident, x-polarized electromagnetic radiation upon a sphere is both scattered by and coupled into the sphere. The tangential components of the electric and magnetic fields must be continuous across the surface for the incident, scattered and internal radiation. The expression of each field in spherical harmonics becomes the summation of partial waves, each partial wave weighted by an appropriate coefficient. For example, the electric field of the scattered light,  $E_{\text{sca}}$ , is represented as:

$$E_{\text{sca}} = \sum_{n=1}^{\infty} E_n \left( ia_n N_{\text{eln}}^{(3)} - M_{\text{oln}}^{(3)} \right), \quad (1)$$

where  $N_{\text{eln}}^{(3)}$  and  $M_{\text{oln}}^{(3)}$  are the vector spherical harmonic solutions to the spherical vector wave equation,  $a_n$  and  $b_n$  are the expansion coefficients and the subscripts  $l$  and  $n$  are the quantum numbers corresponding to the Bessel,  $j_n$ , and Legendre,  $h_n^{(1)}$ , functions. For non-absorbing spheres, which is the limit that we impose for our experiments, the scattering efficiency is:

$$Q_{\text{sca}}(x, m) = \frac{2}{x^2} \sum_{n=1}^{\infty} (2n+1) \{ |a_n|^2 + |b_n|^2 \} \quad (2)$$

where

$$a_n = \frac{j_n(x) [mxj_n(mx)]' - m^2 j_n(mx) [xj_n(x)]'}{h_n^{(1)}(x) [mxj_n(mx)]' - m^2 j_n(mx) [xh_n^{(1)}(x)]'}$$

and

$$b_n = \frac{j_n(x) [mxj_n(mx)]' - j_n(mx) [xj_n(x)]'}{h_n^{(1)}(x) [mxj_n(mx)]' - j_n(mx) [xh_n^{(1)}(x)]'}$$

Note the dependence of  $Q_{\text{sca}}$  on the size parameter  $x = \frac{2\pi a}{\lambda}$ , where  $a$  is the sphere radius,  $\lambda$  is emission wavelength and  $m$  is the ratio of the refractive index of the particle to that of the surrounding medium. Each MDR mode, which corresponds to either the  $a_n$  or  $b_n$  coefficient dominating the expression for  $Q_{\text{sca}}$ , can be uniquely labelled by its mode *order*, mode *number* and mode *polarization*. The boundary conditions imposed by the spherical surface on the propagation of radiation results in the transverse magnetic (TM) and transverse electric (TE) modes ( $a_n$  and  $b_n$ , respectively), which lead to the domination by sharp resonances appearing in the scattering efficiency curve or the measured emission profile.

The different mode designations of the MDRs of a dielectric sphere correspond to modes with different numbers of reflections around the circumference, and the mode orders correspond to the radial location within the particle, with lower mode orders residing close to the perimeter and higher order modes penetrating closer to the centre of the particle. As an example, Fig. 2 shows the electric field intensity within a dielectric sphere for a TE MDR with mode order = 2 and mode number = 11 (denoted as  $\text{TE}_{11}^2$ ).

MDR emission has been observed in numerous studies when light, coupled into a spherical micro-cavity either directly from a laser or via an external coupling element such as an optical fibre, a dielectric prism, microstrip transmission lines or a dielectric waveguide [7], is collected and spectrally resolved. More complex optical cavities than spheres can also be envisaged [12], giving rise to many current and potential applications, which have been reviewed in detail elsewhere [12]. MDR modes can be observed in Raman scattering [13, 14] and within the bandwidth of elastically scattered femtosec-

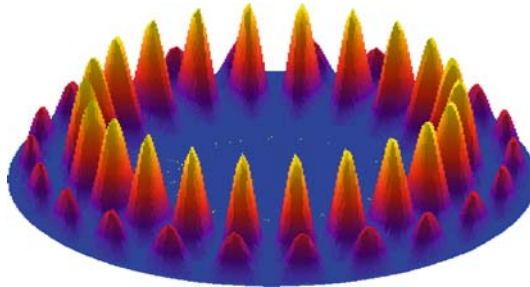


**Fig. 2** Cross-sectional representation of the internal electric field intensity for the  $\text{TE}_{11}^2$  MDR

ond laser pulses [15]. They are observed more readily in the emission spectra of fluorescent species doped throughout spherical micro-cavities.

In addition to doped micro-cavities, spherical particles coated with fluorescent outer layers can also exhibit MDRs in their emission spectrum. This is due to the fact that the resonant circulation of the confined light field resulting from the nearly totally internally reflected light results in an evanescent field that penetrates outside the particle beyond the particle/surrounding medium interface. The distance this evanescent field can penetrate into the outer medium is dependent on the refractive indices of the particle core and the surrounding medium, the wavelength of light, and the mode order. Typically the field can penetrate the outer medium tens of nanometres, which exceeds the typical thickness of many common luminescent material coatings, such as dyes, semiconductor nanocrystals or polymers. This evanescent field can photo-excite fluorophores in close proximity (adsorbed) to the surface of the particle, giving rise to structured emission over the emission band of the luminescent coating. The detection of MDR emission therefore provides a convenient and sensitive way of detecting the success of surface coating of micro-particles.

The wavelengths of the MDR peaks are extremely sensitive to the particle diameter, the refractive indices of the particle and its surrounding medium, and on optical dispersion [16]. This sensitivity can be exploited in biosensory applications where small changes in these parameters, resulting from changes in the local environment, lead to appreciable modification of the MDR spectrum. For example, changes in the (effective) size of the particle or in the refractive index, due to the adsorption of biomolecules, polymers or other species to the surface of the particle, can be detected with high sensitivity. MDR emission has been used in this way for the detection of unlabelled protein molecules [17, 18].

## 2

### Experimental Details

Several luminescent micro-particles have been investigated, as described below. A new conjugated polymer that we have developed, poly(2,5-dipropoxy sulfonato *para* phenylene) vinylene (DPS-PPV, Fig. 3) [5], is a highly photoluminescent ( $\phi_f \sim 20\%$ ), water-soluble, conjugated polymer that is a derivative of the mono-sulfonated form of the (MPS-PPV) polymer used by others in emission quenching studies. DPS-PPV was coated onto silica micro-particles in a similar manner to that described elsewhere [3] for coating quantum dots to silica. The colloidal silica used in this work was synthesized by the Stöber method [19] and the particles were  $\sim 5 \mu\text{m}$  in diameter.

In brief, the following procedure was followed: Prior to DPS-PPV deposition, an initial modification of the silica surface was performed through

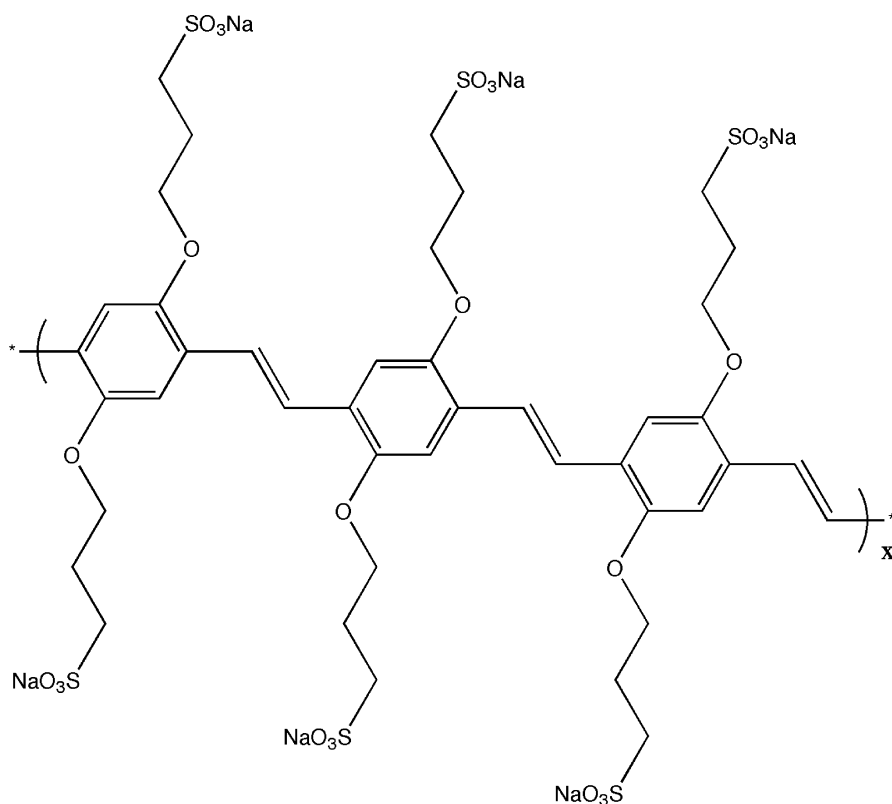


**Fig. 3** Chemical structure of poly(2,5-dipropoxy sulfonato *para* phenylene) vinylene used to coat silica micro-spheres

adsorption of polyethylenimine (PEI). This cationic polyelectrolyte adsorbs onto the negatively charged silica particles through electrostatic interactions. Then, 100  $\mu\text{L}$  of the PEI-coated  $\text{SiO}_2$  particles were pipetted into a micro-centrifuge tube and sonicated for 1 min. DPS-PPV, synthesized as described elsewhere (Ramachandran et al., submitted for publication), was adsorbed onto the PEI-coated silica particles by mixing the addition of 100  $\mu\text{L}$  of polymer solution added to the silica suspension and sonication for 1 min. The resulting solution was centrifuged under moderate power for 15 min and the supernatant decanted to remove excess polymer from the solution. Milli-Q water was added and the purification process repeated until no fluorescence was detected in the surplus solution, indicating that no free polymer was present. The transfer of DPS-PPV to the aqueous phase was readily observed to occur within a few minutes by observing the fluorescence under a UV lamp. The luminescent polymer-coated silica particles were dried onto microscope coverslips for spectral studies.

Whispering gallery mode emission was recorded using a modified confocal fluorescence microscope (Olympus FV500 scan unit, IX71 frame, Fluoview software) with a multi-line argon ion laser (Melles Griot) as the excitation source. The FV500 scan box was modified by activating the fourth channel but with the photomultiplier tube removed. The confocally isolated emission was allowed to exit the FV500 through an aperture made in the back plate behind where the PMT would normally reside. Optical filters further isolated the emission from scattered light and NIR emission from LEDs within the scan box. The emission was subsequently directed to a 0.5 m spectrograph (SPEX) and detected with a liquid nitrogen CCD camera. Confocal fluorescence images were collected as a function of focal plane through the micron-sized particles using the Z-scan facility of the Fluoview software.

Time-resolved fluorescence imaging was achieved via two-photon excitation of Fluoresbrite Yellow Green (YG) micro-spheres of 10  $\mu\text{m}$  diameter (Polysciences, Warrington) [20] dried onto a microscope coverslip. A cavity-dumped titanium:sapphire laser (Coherent Mira 900f/PulseSwitch) operating at a two-photon excitation wavelength of 820 nm and a pulse repetition rate of  $\sim 5.4$  MHz, was used as the excitation source. This radiation was incident on an Olympus FV300/IX71 confocal microscope that was modified to allow for the emission to be detected at right angles to the in-built photomultiplier tubes, using an ultra-fast single photon detector (micro-channel plate EMI-132/100, Eldy, St. Petersburg, Russia, or PMC-100, Becker and Hickl, Germany). For single-photon counting a complete electronic system for recording fast light signals by time-correlated single photon counting (SPC-830, Becker and Hickl) was incorporated with the computer-controlled laser scanning microscope and measures individual anode pulses from the detector relative to the arrival of an excitation laser pulse. The SPC-830 was synchronized with the frame, line and pixel clock of the FV300 scan unit following necessary hardware modifications to the microscope driver electronics: the signal was picked off from the cable between the I/O and memory boards in the controller PC with pins 6 and 8 being GND and pin 7 providing the master pixel trigger signal, which must be buffered into  $< 10 \text{ M}\Omega$  (K. Hyakumura, personal communication. Olympus, Japan). Time-resolved images were collected as a function of focal plane depth through the micron-sized particles using the Z-scan facility of the Fluoview software. The microscope objective lens used was an Olympus UPLSAPO 100 $\times$  with a numerical aperture of 1.4. A photon count time of 60 s was used and, accounting for losses through the scan system and objective, the illumination power was a few milliwatts at the sample.

The quadrupole ion trap (QIT) uses an optically open electrode structure [21]. Essentially the design replaces the solid ring electrode with a series of a thin rod electrodes, resulting in a wide solid viewing angle into the QIT and therefore efficient light collection (Fig. 4) [22]. The QIT operates by generating an oscillating quadrupole field, which results in charged particles being constrained by a three-dimensional harmonic potential between the

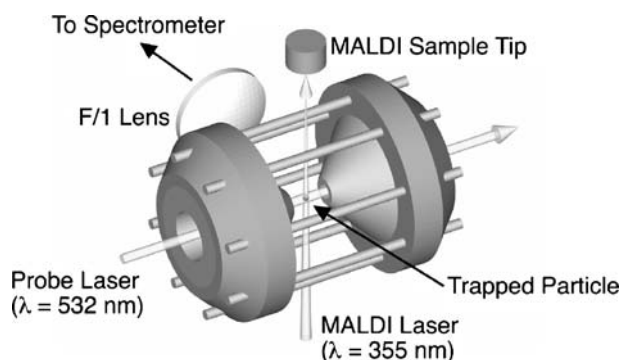


**Fig. 4** Schematic diagram of the QIT showing the ring of rod electrodes and the excitation and emission coordinates

two cap electrodes, generated by applying an alternating potential to the two end-cap electrodes while grounding the ring electrode (Fig. 4). At appropriate drive frequencies and voltages an individual charged particle (or an ensemble of charged particles) can be confined indefinitely.

Fluorescently labelled polystyrene micro-spheres (diameter  $\phi \sim 7 \mu\text{m}$ , from Bangs Laboratories, Fishers, IN) [1], were used as received and introduced into the QIT using a matrix-assisted laser desorption/ionization (MALDI) process with 3-hydroxypicolinic acid (3-HPA) as the absorbing matrix. To prepare a MALDI sample, 3–4 drops of an aqueous suspension of the polystyrene particles were mixed with 3–4 drops of a saturated solution of 3-HPA in an acetonitrile/water mixture on a stainless steel sample tip. The sample was then dried under nitrogen and placed above the QIT situated in a vacuum chamber. A single 7 ns laser pulse, 3rd harmonic ( $\lambda = 355 \text{ nm}$ ) from a Q-switched Nd:YAG laser, irradiated the sample, ejecting charged particles into the quadrupole trap. By systematically varying the trap driving voltage and frequency, particles were ejected until only one remained. Using He buffer gas ( $\sim 100 \text{ mTorr}$ ) the remaining particle's motion was damped so that its oscillation amplitude was less than 0.1 mm. About 2 mW from a continuous wave 532 nm Nd:YVO<sub>4</sub> laser irradiated the trapped particle. Scattered light/fluorescence was collected at right angles to the incident laser beam using a 25 mm diameter F/1 lens and directed through an edge filter to remove 532 nm light and then into a spectrometer (SPEX, resolution  $\sim 0.03 \text{ nm}$ ) equipped with a LN<sub>2</sub> cooled CCD detector interfaced to a personal computer.

### 3 Results and Discussion

In this work we have investigated a number of fluorescent spherical particles, both isolated on the surface of microscope coverslips and isolated in the QIT.

### 3.1 PPV-Coated Silica Micro-spheres

DPS-PPV was coated onto  $\sim 5 \mu\text{m}$  diameter silica micro-spheres as described above and excited with the argon ion laser 488 nm line. The emission spectrum of DPS-PPV in bulk solution is broad and reasonably structureless, spanning from 520 nm to beyond 700 nm as shown by the solid line (a) in Fig. 5. The highly structured MDR emission of a single DPS-PPV-coated micro-sphere is shown as (b) in Fig. 5. The overall shape of the MDR experimental spectrum closely resembles that of the bulk fluorescence emission spectrum and exhibits numerous peaks over the entire emission band. Also shown (c in Fig. 5) is the calculated spectrum with the resonance peak assignment. Nineteen of the main peaks were assigned, with all the calculated peak positions falling within  $\sim 0.2 \text{ nm}$  of the corresponding measured peak position. The assigned spectrum shows the TM and TE peaks associated with minima (zero values) in the denominators of the expressions for the parameters  $a_n$  and  $b_n$  of Eq. 2, respectively, leading to a marked increase in the magnitude of the  $a_n$  or  $b_n$  value and single peaks in the Mie spectrum. The calculated spectrum returns a value for the particle radius of 2575 nm, in excellent agreement with the anticipated particle diameter of  $\sim 5 \mu\text{m}$ . The refractive index recovered from this analysis is 1.412 at 590 nm, which is also in good agreement with a value of 1.45846 reported elsewhere for fused silica [23]. The slightly lower value may reflect the ef-

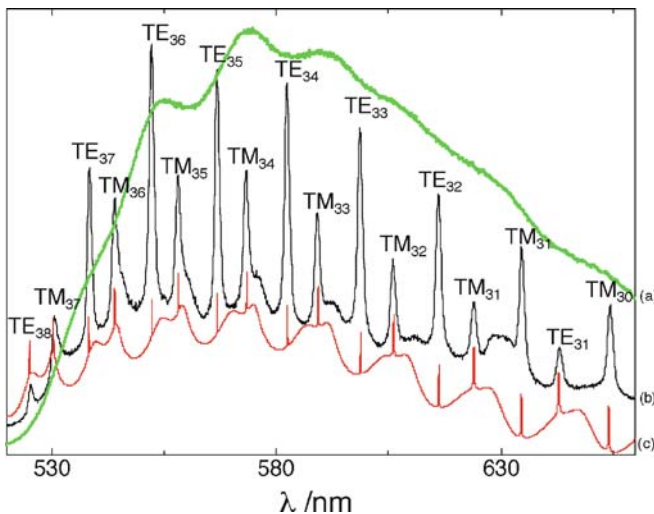


**Fig. 5** Emission spectrum of DPS-PPV-coated silica micro-spheres: *a* bulk solution, *b* single particle spectrum and *c* the fitted peaks corresponding to particle radius of 2.575  $\mu\text{m}$  and refractive index of 1.412



fect on the refractive index of the polymer coating or the actual material property of the silica micro-sphere. The ability to detect the presence of the adsorbed polymer illustrates the power of MDRs to report on the success (or otherwise) of particle surface coatings, in addition to minute increases in the particle's size.

### 3.2

#### Dye-Doped Micro-spheres

Scanning confocal fluorescence images were recorded as a function of z-distance (optical sectioning) through  $\sim 7\ \mu\text{m}$ -sized fluorescent particles. Figure 6 shows the confocal images corresponding to the optical sections at the top of the particle (left) and at a distance of  $3.5\ \mu\text{m}$  (i.e. half way) into the particle (right). The emission is clearly concentrated around the circumference of the micro-sphere. Since the optical sectioning is undertaken in the confocal mode, the converging and diverging cone of focus overlaps with most of the particle and the light is coupled into the cavity modes even when the excitation is focussed at the middle of the sphere. However, the confocal detection volume restricts the emission from the optical focal plane, and the confocal image from the focal plane half way through the particle produces the clear equatorial ring of enhanced emission seen on the right in Fig. 6.

Two-photon excitation of fluorescence is known to confine the fluorescence emission from a much smaller focal volume than conventional confocal fluorescence microscopy [24]. Using this imaging mode may reduce the amount of light coupled into the cavity modes when the excitation is focussed in the centre of the sphere and thus allow for a more precise interpretation of the modes to be made due to the highly localized point excitation. In order to characterize this method, we performed scanning two-photon time-

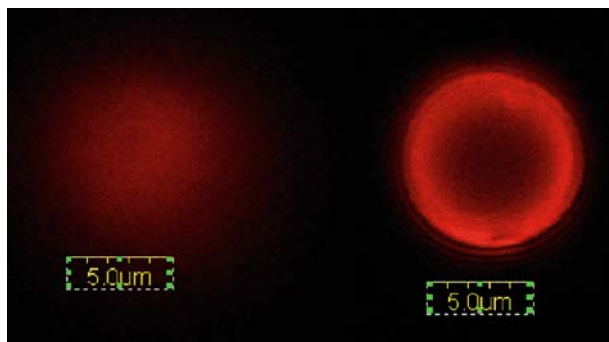


**Fig. 6** Confocal optical sectioning through dye-doped micro-spheres. *Left*: optical slice from top of particle, *Right*: optical section from approximately half the diameter of the particle

resolved imaging of  $10\ \mu\text{m}$  diameter fluorescent micro-spheres as a function of the optical sectioning depth through the particle using the techniques described in Sect. 2. The emission was detected non-confocally, that is, in the “direct”, “non-descanned” mode. An example of the time-resolved images recorded is shown in Fig. 7, which is a  $256 \times 256$  pixel pseudo-coloured image, with each pixel representing a spatially resolved fluorescence lifetime derived from a single-exponential fit from the corresponding photon count histogram recorded at that pixel. Each histogram comprises 256 time bins that may each contain up to  $2^{16}$  individual photon counts. It is clear that the enhanced emission around the circumference of the sphere, as illustrated in Fig. 6, exhibits significantly different fluorescence decay behaviour compared to the central region of the micro-sphere. The optical confinement of femtosecond laser pulses in micro-cavities has been measured [25] in a scattering experiment, but the present experiment records the *emission* initiated by these short pulses, and so is evident over much longer time-scales. The variation in the temporal emission properties may be due to the optical confinement itself or the effects of the surface on the radiative and non-radiative pathways available to the fluorophore. The experimentally recorded emission decay profile will be a complex convolution of the emission from each of the cavity modes excited and the temporal residence behaviour of the excitation within the cavity.

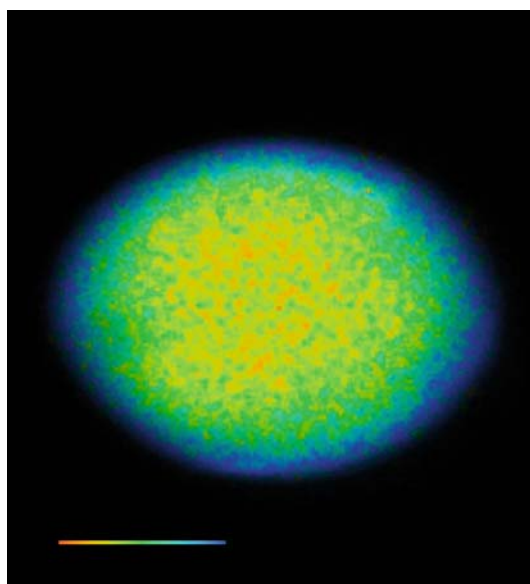


**Fig. 7** Two-photon, time-resolved fluorescence image of  $\sim 10\ \mu\text{m}$  particle at an optical section corresponding to approximately  $5\ \mu\text{m}$ , i.e. half way through the particle. Pseudo-colour map corresponds to decay times of 2.0–2.4 ns (red to blue)

### 3.3 Polystyrene Micro-spheres in the QIT

Here we demonstrate the use of a quadrupole ion trap (QIT) suited to the confinement of single micro-spheres. A single fluorescently labelled polystyrene sphere is trapped and its MDR-dominated emission spectra are collected over several days. An analysis of the MDR spectrum allows the temporal stability of the particle's size and refractive index to be monitored.

Figure 8 displays the fluorescence emission spectra obtained from a single trapped micro-sphere at one-day intervals, over three days. By modelling the emission spectra using Mie theory it is possible to extract the particle's radius and refractive index. These data are summarized in Table 1.

Over the three-day experimental period there is a systematic shift in the spectral positions of all the MDR peaks corresponding to an increase in the radius and decrease in the refractive index. It is most plausible that slow evaporation of solvent molecules from the micro-sphere results in a small but measurable expansion of the sphere and corresponding decrease in refractive index.

Another noticeable feature of the data in Fig. 8 is the change in relative peak *intensities* between the spectra. The inset in Fig. 8 shows a group of three MDR peaks of different mode order. The change in relative peak intensities can be explained by considering input coupling resonance. Using the fitted parameters in Table 1, the nearest MDR to the input wavelength ( $\lambda = 532.07$  nm) is calculated. For spectrum A, the nearest MDR is  $TE_{57}^1$  at  $532.3 \pm 0.3$  nm. For spectrum B the input resonance remains closest to  $TE_{57}^1$  at  $531.5 \pm 0.3$  nm. However, for spectrum C the input wavelength is close to both  $TE_{57}^1$  at  $531.3 \pm 0.3$  nm and  $TE_{47}^3$  at  $532.8 \pm 0.3$  nm. Correspondingly,

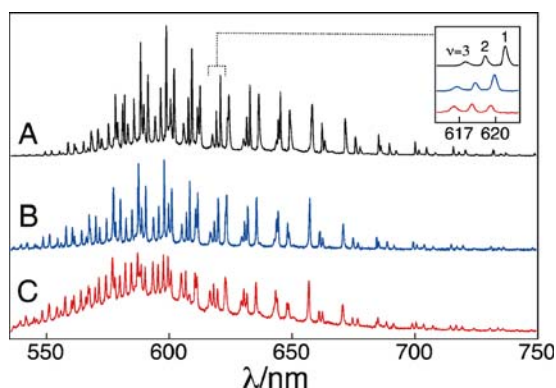


**Fig. 8** Fluorescence emission spectra from a polystyrene micro-particle monitored over 3 days. *Inset*: A group of three MDRs with different mode orders showing the systematic shift of the MDRs and also the variation in relative intensities

**Table 1** Particle radius and refractive index values recovered from fitting the MDR positions from Fig. 8. Note that the refractive indices are corrected for dispersion

Time(spectrum) (h)	Particle radius (nm)	Refractive index (at 532 nm)
0 (A)	$3399 \pm 6$	$1.584 \pm 0.015$
24 (B)	$3404 \pm 5$	$1.580 \pm 0.014$
48 (C)	$3428 \pm 7$	$1.566 \pm 0.019$

the output intensities show that whereas for spectra A and B the first order resonances are most intense, for spectrum C the third order resonances are of comparable intensities to the first order resonances. This is consistent with the input and output MDR correlation observed in emission from dye-labelled micro-droplets [26]. The input coupling efficiency is maximized when the input wavelength overlaps with an MDR of the cavity. In the case of spectrum A the overlap is good, resulting in strong output MDR intensities. In the case of spectrum C, the input wavelength is almost out of resonance with the cavity and therefore the output MDRs are weaker in intensity compared to the broad baseline profile of the fluorophore.

## 4

### Conclusions

Morphology-dependent resonance (or whispering gallery mode) emission has been detected from a range of micro-spheres both doped and coated with fluorophores. These micro-particles have been studied both by optical sectioning using confocal microscopy, two-photon time-resolved fluorescence imaging, and by being isolated within a quadrupole ion trap. Emission is enhanced around the circumference of the sphere and this emission exhibits different average fluorescence decay behaviour compared with the central region of the sphere. Isolation within a QIT removes any effects of the immobilizing substrate and allows for controlled adsorption of molecules to the same particle to be monitored over lengthy periods of time. Assignment of the resonance peaks provides highly accurate determination of the particles' size and refractive index, and assignment of the mode number, order and polarization.

The MDRs of a dielectric micro-sphere therefore provide a uniquely sensitive monitoring tool for the measurement of small changes in micro-sphere size and refractive index. Such sensitivity is potentially useful in the observation of adsorbing monolayers and also for probing the temporal stability of micro-sphere systems under various pressures, temperatures and gas environments.

**Acknowledgements** The authors acknowledge the financial assistance of the Australian Research Council (ARC), the Victorian Institute for Chemical Sciences (VICS) and the Rowden White Foundation (University of Melbourne). We also thank Daniel Gómez and Paul Mulvaney for valuable assistance and discussions.

## References

1. Bangs Laboratories (2007) Bangs Laboratories, Fisher IN, USA, <http://www.bangslabs.com/>, last visited: 16 August 2007
2. Schiro PG, Kwok AS (2004) Cavity-enhanced emission from a dye-coated microsphere. *Opt Express* 12:2857–2863
3. Gómez DE, Pastoriza-Santos I, Mulvaney P (2005) Tunable whispering gallery mode emission from quantum-dot-doped microspheres. *Small* 1:238–241
4. Rakovich YP, Yang L, McCabe EM, Donegan JE, Perova T, Moore A, Gaponik N, Rogach A (2003) Whispering gallery mode emission from a composite system of CdTe nanocrystals and a spherical microcavity. *Semicond Sci Technol* 18:914–918
5. Ramachandran G, Smith TA, Gómez DE, Ghiggino KP (2005) Fluorescence studies on the conjugated polyelectrolyte DPS-PPV [poly(2,5-dipropoxy sulphonato *para* phenylene) vinylene] in aqueous solution. *Synth Metal* 152:17–20
6. Barber PW, Chang RK (1988) Optical effects associated with small particles. World Scientific, Singapore
7. Zhang JQ, Grischkowsky D (2003) Whispering gallery mode cavity for teraHertz pulses. *J Opt Soc Am B* 20:1894–1904
8. von Klitzig W, Long R, Ilchenko VS, Hare J, Lefèvre-Seguin V (2001) Tunable whispering gallery modes for spectroscopy and CED experiments. *New J Phys* 3:14.11–14.14
9. Eversole JD, Lin H-B, Huston AL, Campillo AJ, Leung PT, Liu SY, Young K (1993) High-precision identification of morphology-dependent resonances in optical processes in microdroplets. *J Opt Soc Am B* 10:1955–1968
10. Noto M, Khoshsima M, Keng D, Teraoka I, Kolchenko V, Arnold S (2005) Molecular weight dependence of a whispering gallery mode biosensor. *Appl Phys Lett* 87:223901/1–223901/3
11. Mie G (1908) Beitrage zur Optik truber Medien, speziell kolloidaler, Metallosungen. *Ann Phys (Leipzig)* 25:377–445
12. Vahala KJ (2003) Optical microcavities. *Nature* 424:839–846
13. Hartmann I, Popp J, Lankers M, Trunk M, Kiefer W (1995) Theory for morphology dependent resonances in the Raman spectra of optically levitated dielectric microspheres. *J Mol Struct* 349:203–206
14. Hartmann I, Lankers M, Popp J, Trunk M, Urlaub E, Kiefer W (1997) Simulation of morphology-dependent resonances in the Raman spectra of optically levitated microspheres. *J Raman Spect* 28:547–550
15. Sbankski O, Roman VE, Kiefer W, Popp J (2000) Morphology-dependent resonances in a dielectric microsphere and femtosecond laser pulses. *J Chinese Chem Soc* 47:863–864
16. Popp J, Lankers M, Trunk M, Hartmann I, Urlaub E, Kiefer W (1998) High-precision determination of size, refractive index, and dispersion of single microparticles from morphology-dependent resonances in optical processes. *Appl Spect* 52:284–291
17. Vollmer F, Braun D, Libchaber A, Khoshsima M, Teraoka I, Arnold S (2002) Protein detection by optical shift of a resonant microcavity. *Appl Phys Lett* 80:4057–4059

18. Arnold S, Khoshsima M, Teraoka I, Holler S, Vollmer F (2003) Shift of whispering gallery modes in microspheres by protein adsorption. *Opt Lett* 28:272–274
19. Stöber W, Fink A, Bohn E (1968) Controlled growth of monodisperse silica spheres in the micron size range. *J Coll Int Sci* 26:62–69
20. Polysciences (2007) Online catalog. Polysciences, Warrington PA, USA, <http://www.polysciences.com/shop/viewCatalog.asp?dept%5Fid=401505>, last visited: 16 August 2007
21. Schlemmer S, Illemann J, Wellert S, Gerlich D (2001) Nondestructive high-resolution and absolute mass determination of single charged particles in a three-dimensional quadrupole trap. *J Appl Phys* 90:5410–5418
22. Trevitt AJ, Wearne PJ, Bieske EJ (2007) Calibration of a quadrupole ion trap for particle mass spectrometry. *Int J Mass Spectrom* 262:241–246
23. Opticsland (2007) Fused silica. Del Mar Ventures, San Diego, CA, <http://www.sciner.com/Opticsland/FS.htm>, last visited: 16 August 2007
24. Denk W, Strickler JH, Webb WW (1990) Two-photon laser scanning fluorescence microscopy. *Science* 248:73–76
25. Siebert T, Sbanski O, Schmitt M, Engel V, Kiefer W, Popp J (2003) The mechanism of light storage in spherical microcavities explored on a femtosecond time scale. *Opt Comm* 216:321–327
26. Eversole JD, Lin H-B, Campillo AJ (1995) Input/output resonance correlation in laser-induced emission from microdroplets. *J Opt Soc Am B* 12:287–296

## New Plastic Microparticles and Nanoparticles for Fluorescent Sensing and Encoding

Sergey M. Borisov<sup>1</sup> · Torsten Mayr<sup>2</sup> · Alexander A. Karasyov<sup>1</sup> · Ingo Klimant<sup>2</sup> · Pawel Chojnacki<sup>1</sup> · Christoph Moser<sup>2</sup> · Stefan Nagl<sup>1</sup> · Michael Schaeferling<sup>1</sup> · Matthias I. Stich<sup>1</sup> · Anna S. Kocincova<sup>1</sup> · Otto S. Wolfbeis<sup>1</sup> (✉)

<sup>1</sup>Institute of Analytical Chemistry, Chemo- and Biosensors, University of Regensburg, POB 100102, 93040 Regensburg, Germany  
*otto.wolfbeis@chemie.uni-r.de*

<sup>2</sup>Institute of Analytical Chemistry, Graz University of Technology, Technikerstrasse 4, 8010 Graz, Austria

<b>1</b>	<b>Materials and Methods for Making Polymer Beads</b>	432
1.1	Polymers	432
1.2	Dyes	433
1.2.1	Lipophilic Fluorescent Organic Dyes	434
1.2.2	Lipophilic Phosphorescent Metal–Ligand Complexes	436
1.3	Making Dyed Beads	437
<b>2</b>	<b>Chemical Sensing with Addressable Micro- and Nanospheres</b>	438
2.1	Oxygen-Sensitive Beads	439
2.2	pH-Sensitive Microbeads	440
<b>3</b>	<b>Dyed Polymer Microparticles and Their Use in Sensor Layers</b>	442
<b>4</b>	<b>Luminescence Lifetime Encoded Microbeads as Carriers for Multiplexed Bioassays</b>	446
<b>5</b>	<b>Dyed Polymer Microparticles and Their Use in Pressure-Sensitive and Temperature-Sensitive Paints (PSPs and TSPs)</b>	449
5.1	Beads for Use in TSPs	451
5.2	Beads for Use in PSPs	452
5.3	Use of the Microparticles for Simultaneous Imaging of Oxygen and Temperature	453
<b>6</b>	<b>Phosphorescent Polymeric Nanospheres as Labels for Homogeneous Protein Assays and Protein Arrays Using Luminescence Lifetime Imaging</b>	454
	<b>References</b>	461

**Abstract** We report on the progress that has been made in the area of luminescence sensing and encoding by making use of microparticles and nanoparticles prepared from plastic materials. These are quite different from particles built up from metal sulfides (such as the so-called quantum dots, “Q-dots”; see Michalet et al., *Science* 307:538, 2005),

other semiconductor materials, metal nanoparticles (mainly gold) (see DL Feldheim, CA Foss (eds) *Metal Nanoparticles: Synthesis, Characterization, and Applications*, p 338, Marcel Dekker, 2002), or glass and its modifications including certain sol-gels. Plastic nanoparticles may contain magnetic beads in order to facilitate separation from the sample solution. All the particles described here are doped with fluorescent dyes, which is in contrast to particles where the material itself displays intrinsic luminescence. Unlike the case of Q-dots, the color of plastic beads can be varied to a wide extent irrespective of their size, as can be the decay times and even anisotropy. This, in fact, is a most attractive feature of such beads and makes them superior in many cases despite the undisputed utility of other types of particles in certain fields.

The area of beads was almost exclusively occupied until 10 years ago by polystyrene beads (also referred to as latex beads) 0.1–5  $\mu\text{m}$  in diameter. They are widely used in bioassays and flow cytometry because they can be manufactured with good reproducibility (usually by emulsion polymerization) and because they are rather inert. Other applications include agglutination tests, particle capture ELISAs (e.g., Abbott's IMx and AxSym), solid-phase assays (often used for pregnancy testing), scintillation proximity assays, luminescent oxygen channeling immunoassay (LOCI), and bead-FRET assays. Nanoparticles have been used for labeling purposes, particularly in the context of protein arrays and DNA arrays. In recent years, beads have been fluorescently dyed for purposes of encoding, for example in combination with optical fiber arrays and in microwells, and in methods for homogeneous multiplexed high-throughput screening. The analytical information may be the color of the fluorescence, its intensity (or—even better—the ratio of two intensities), decay time, anisotropy, or combinations thereof.

In the first section we will describe dyes for doping plastic particles. The second section will report on chemical sensing with addressable micro- and nanospheres, and the third on the use of dyed microparticles in sensing pH values. We will also report on luminescence lifetime encoded microbeads as carriers for multiplexed bioassays (Sect. 4), the use of dyed polymer microparticles in simultaneous sensing of oxygen and temperature (Sect. 5), and on nanobead labels for homogeneous protein assays and protein arrays (Sect. 6).

## 1

### Materials and Methods for Making Polymer Beads

#### 1.1

##### Polymers

Dyes can be attached to beads in various ways but noncovalent dyeing is preferred because of its simplicity and reproducibility. Covalent dyeing, in contrast, requires both the dye and the beads to have a reactive group through which a covalent bond can be formed between the polymer and the dye. This situation is often undesirable because excess reactive groups on the surface of beads may compromise their properties and often make them more prone to aggregation. Table 1 lists polymers that have been used in beads, along with the respective solvents and typical sizes. Depending on how the beads are made [1–3], the method for dyeing them can vary to a large extent. Polystyrene (PS) and poly(decyl methacrylate) (PDMA) beads, for example, are



**Table 1** Representative organic polymers for use in beads, respective solvents (if any), and typical sizes

Organic polymer	Solvent	Typical bead size	Manufactured via
Polystyrene (PS)	Toluene, chloroform	0.1–5 $\mu\text{m}$	Emulsion polymerization
Polyacrylonitrile (PAN)	DMF <sup>a</sup>	40–200 nm	Precipitation from solution
Poly(decyl methacrylate) (PDMA)	THF <sup>b</sup> /H <sub>2</sub> O	0.15–10 $\mu\text{m}$	Emulsion polymerization
Polyacrylamide	–	20–100 nm	Emulsion polymerization
Ormosil <sup>c</sup>	–	100–800 nm	Polymerization

<sup>a</sup> Dimethylformamide

<sup>b</sup> Tetrahydrofuran

<sup>c</sup> Organically modified siloxanes

preferably dyed by swelling them in a solvent containing the fluorescent dye, while polyacrylonitrile (PAN) beads are doped by coprecipitation with the respective dye. Polyacrylamide and ormosil nanoparticles, on the other hand, are usually dyed during the polymerization process.

Most bead materials are hydrophobic. Hence, dyes are only soluble in such polymers (and are retained by the particles) if they are lipophilic to a large extent. The exceptions are polyacrylamide beads (which are more compatible with hydrophilic dyes) and ormosil particles (suitable for amphiphilic dyes).

## 1.2

### Dyes

Dyes for use in polymer beads are expected to have as many as possible of the following properties:

- Strong absorbance
- High emission quantum yield
- Good photostability
- Good solubility in the polymer but insolubility in water
- Narrow emission bands if unambiguous multiplexing and encoding is desired
- Wide emission bands if resonance energy transfer assays are desired
- Varying degrees of anisotropy (in order to make them amenable to polarization assays or encoding)
- Varying decay time (in order to make them amenable to encoding via decay time)

The quality of a dye in terms of its luminescence intensity is best represented by its *brightness* ( $B_s$ ), which is the product of molar absorbance ( $\epsilon$ )

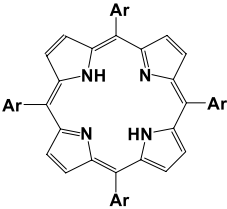
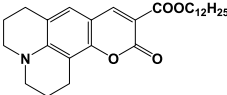
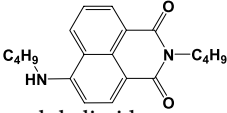
and quantum yield (referred to as QY or  $\Phi$ ). Brightnesses exceeding 30 000 are desirable, while one of below 10 000 renders a dye practically useless (unless other properties make it useful). The width of the luminescence emission band is often expressed by the acronym FWHH, which stands for full width (in terms of wavelength) at half height. Values of  $< 10$  nm are desirable in the case of multicolor multiplexing and encoding but are achieved by lanthanide-derived fluorophores only. Good organic dyes have FWHHs of 30 nm [4, 5]. Ruthenium diimine complexes have rather wide bands ( $>60$  nm FWHH) while metalloporphyrins have narrower FWHHs but—like many organic dyes—suffer from side bands or shoulders that can occur on either side of the main emission band [6].

### 1.2.1

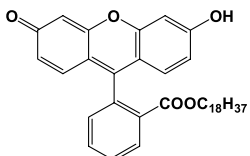
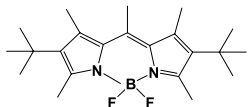
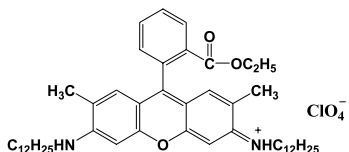
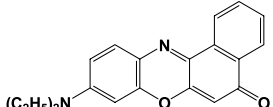
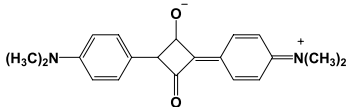
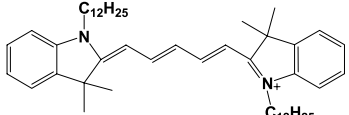
#### Lipophilic Fluorescent Organic Dyes

Table 2 gives a list of typical lipophilic organic dyes that cover the visible and near-infrared (NIR) part of the spectrum. Dyes that require excitation in the ultraviolet (UV) are clearly less attractive in practice because most organic

**Table 2** Chemical structures, spectral data, and quantum yields of the lipophilic dyes used for dyeing polystyrene beads

Chemical structure and name	Absorption/emission maxima (in nm); [solvent]; molar absorption (in $\text{cm}^{-1} \text{M}^{-1}$ ); quantum yields
 <p>Porphyrins</p>	419, 514/652 [benzene] 470 000, 18 700 0.13
 <p>Coumarins</p>	436/480 [ethanol] 47 000 0.77
 <p>naphthalimides</p>	444/520 [ethanol]      420/485 [toluene] 16 600                      14 800 0.66                         0.84

**Table 2** (continued)

Chemical structure and name	Absorption/emission maxima (in nm); [solvent]; molar absorption (in $\text{cm}^{-1} \text{M}^{-1}$ ); quantum yields	
 <p>Fluoresceins</p>	515/543 [ethanol] 98 000 0.88	
 <p>Bora-dipyrroles (Bodipy)</p>	521/561 [acetonitrile] 77 000 0.44	525/567 [THF] 77 500 0.37
 <p>Rhodamines</p>	530/556 [ethanol] 105 000 0.95	
 <p>Phenoxazines</p>	540/595 [ethanol] 23 000 0.3	487/525 [hexane] 22 000 0.6
 <p>Squaraines</p>	628/654 [dichloromethane] 310 000 0.45	
 <p>Cyanines</p>	644/665 nm [ethanol] 180 000 0.4	

polymers display UV-excitable fluorescence that may interfere, as does the UV-excitable autofluorescence of many biological samples.

Like practically all organic fluorophores, the dyes of Table 2 have decay times in the order of several nanoseconds. The naphthalimides have

a high QY, but low absorbances and thus smaller brightness compared to the dyes with absorbance exceeding  $100\,000\text{ cm}^{-1}\text{ M}^{-1}$ . The same is true for the 7-aminocoumarins and all other dyes absorbing at below 500 nm, since their absorbances do not exceed values of  $60\,000\text{ cm}^{-1}\text{ M}^{-1}$  in general. Porphyrins absorb efficiently in the violet ( $\varepsilon > 150\,000\text{ cm}^{-1}\text{ M}^{-1}$ ) and moderately in the green to red part of the spectrum, but have a low QY. The rhodamines ( $\varepsilon$  up to 600 000) cover the 500 to 600 nm range. The long-wave cyanine and squaraine dyes (580 to 800 nm) display much larger absorbances and some are fully compatible with the 635-, 670-, or 780-nm diode lasers [7].

### 1.2.2

#### Lipophilic Phosphorescent Metal–Ligand Complexes

Unlike organic fluorophores, the luminescence (often of the phosphorescence type) of metal–ligand complexes (MLCs) decays rather slowly ( $> 1\ \mu\text{s}$ ) and this enables additional options in bead-based assays, encoding, and authentication. Numerous MLCs are known but few meet the criteria of brightness ( $\text{QY} \times \varepsilon$ ), stability, and solubility. Solubility is a particular issue when it comes to dyeing organic beads with MLCs that carry (usually positive) charges. In such a case the counterion plays an important role since—in the worst case—it can prevent the dye from becoming incorporated into the bead. It is quite useful to replace small anions by larger, preferably organic anions, such as perchlorate, hexafluorophosphate, 3-(trimethylsilyl)propylsulfonate, dodecyl sulfate, or tetraphenyl borate [8], to mention a few.

The MLCs that have been used so far strongly vary in terms of their properties. Ruthenium-derived labels have moderate quantum yields and absorbances [9], so their brightnesses rarely exceed a value of 10 000. The same is true for MLCs of osmium and rhenium, and particularly for cyclometalated complexes of platinum and iridium [10], whose absorbances in the visible region rarely exceed  $5000\text{ cm}^{-1}\text{ M}^{-1}$ . Metalloporphyrins, like many ruthenium MLCs, are prone to quenching by oxygen but have a much larger brightness, in particular when excited via the Soret band at around 410 nm. On the other hand (and unlike ruthenium dyes) they tend to aggregate and to form side bands [6]. Certain lanthanides, notably the trivalent ions of europium and terbium, possess fairly strong emission at room temperature but their absorbances are low and in the UV, and some display a strongly temperature-dependent luminescence. However, their Stokes shifts are rather large and their decay times rather long. Consequently, time-resolved measurements become possible.

All existing europium(III) labels require UV excitation, typically between 330 and 370 nm. At present, this can be accomplished with comparably expensive (UV) light sources only, and this causes a strong luminescence background in the UV and near visible. Fortunately, the emission of the Eu labels

is extremely red-shifted, with peaks between 610 and 620 nm. A lanthanide label that may be excited by the recently available blue (or UV) light-emitting diodes (LEDs) with peak wavelengths of 365 or 380 nm, or the 405-nm diode laser is therefore highly desirable.

Chelate complexes of the lanthanide ion europium(III) have been widely used in all kinds of binding assays (Wu M, Wolfbeis OS (2003) unpublished results) because of their long decay times, which are in the range from several microseconds to even milliseconds. As a result, so-called gated measurements become possible. In such a measurement, the sample is excited with a short pulse of UV light, and the emission is gathered only after a delay of several hundred nanoseconds, during which the short-lived background luminescence is allowed to decay and therefore cannot interfere. After the delay time, the measurement gate is opened, typically for a period during which the intensity of the Eu label has dropped to 20 or 10% of its initial value.

The europium-tetracycline complex (EuTc) appears to be the first lanthanide complex with an absorption maximum at 405 nm, thereby exactly matching the line of the 405-nm diode laser. The citrate salt of EuTc has been used [11] to dye beads made from cross-linked polyacrylamide. Attempts to dye PS failed since the complex is virtually insoluble in all organic solvents and nonpolar polymers. The resulting beads display pink fluorescence ( $\lambda_{\text{max}} = 616$  nm) if excited with light of wavelengths between 370 and 440 nm. If carboxy groups are present on the surface of the beads, they can be surface-modified with species of high binding affinity, e.g., biotin.

### 1.3

#### Making Dyed Beads

Most polymer beads are obtained by emulsion polymerization [12]. Such beads are usually dyed by swelling them in a solvent containing the luminescent dye. In a typical process for dyeing 5- $\mu\text{m}$  PS particles, they are first suspended in water/methanol (1 : 1, v/v), swollen by addition of 2% (v/v) dichloromethane, and dyed by slow addition of the lipophilic dye dissolved in dichloromethane. The resulting beads are weakly blue or green and display a strong fluorescence that is not quenched by oxygen, proteins, or ions, such as halides. Similar procedures are used for dyeing PDMA beads which are swollen in THF/water mixtures. In some cases (mostly for preparation of dyed polyacrylamide or ormosil particles) the dye is added during the polymerization process.

The process is quite different when dyed PAN nanobeads are obtained. The dye and PAN are dissolved in dimethylformamide (DMF) to obtain a typically 0.5% w/w solution of the polymer in DMF. Under vigorous stirring, a 3 $\times$  volume excess of water is added to the solution to produce nanoparticles of a size between 40 and 200 nm.

## 2 Chemical Sensing with Addressable Micro- and Nanospheres

Nano- and microspheres are popular tools for many bioanalytical applications. A combination of optical sensor technology and microsphere approaches was first presented by Kopelman et al. [13–16]. They designed the so-called PEBBLE sensors, which are nanoscale spherical devices consisting of sensor molecules entrapped in a chemically inert matrix. PEBBLES have been used for the intracellular determination of pH, oxygen, glucose, calcium, magnesium, potassium, and selected ionic species such as chloride, sodium, or zinc. Later on, strategies were developed to insert sensor particles into living cells. However, procedures such as shotgunning, pico-injection, or the use of liposomes as trackers are complicated and frequently require sophisticated equipment. An alternative solution consists in the attachment of sensor beads directly onto the surface of the cell through which they are enriched. This enables the measurement of differences of pH or oxygen concentration between the cell interior and the environment without interference in the susceptible cell interior.

Coupling of functional sensor beads onto the walls of living cells requires them to possess receptors that are capable of binding to their surface. In this respect, the beads become multifunctional in that they combine the functions of analyte recognition and sensing. Depending on the respective bead size, the sensor microparticles may also be coated with the cells or the cells can be covered with sensing nanobeads (Fig. 1).

Coating the surface of a sensor bead with receptors can be achieved by various methods, primarily by covalent coupling or by adsorption. Covalent coupling, despite being more complicated, has many advantages. It allows

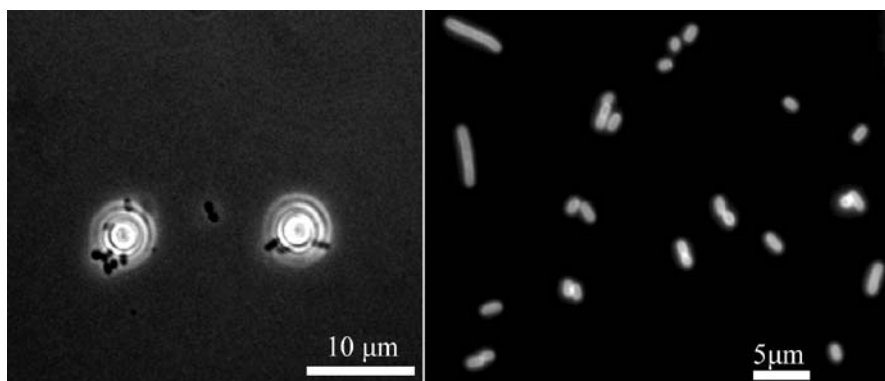


**Fig. 1** Confocal image (Nomarski illumination) of microbeads coated with anti-*Escherichia coli* IgG catching bacteria (left), and fluorescence image of *E. coli* cells coated with polyelectrolyte nanobeads containing a pH indicator (right)

better control of coating level and uniformity, reduces leaching, and does not require a large excess of protein.

Coupling biologically active molecules onto the polymeric beads requires functional groups, located on their surface, which are susceptible to protein terminals, primarily amino and carboxy groups. If the beads are provided with biological recognition systems, such as antibodies, aptamers, or receptor proteins, they can be applied to various sensing schemes including site-specific monitoring, as markers in immunoassays, or for quantification of enzyme activity in the direct vicinity of a live cell.

In order to better understand any processes occurring inside living cells, it is almost mandatory to monitor physiological parameters, such as oxygen or pH, in situ. We have therefore designed pH-sensitive and oxygen-sensitive beads, and their synthesis and application is presented in this section.

## 2.1

### Oxygen-Sensitive Beads

PS copolymerized with 5% of acrylic acid was chosen as a matrix for the oxygen-sensitive nanobeads because of its lipophilic properties that enable dye encapsulation and the formation of an active layer of carboxy groups on the surface of the beads. The microbeads consist of a PS core with a surface modified by polyethylene glycol and carboxy groups, thus making the beads amenable to coating with proteins. Such beads are commercially available and can be homogeneously stained with luminescent probes over the entire volume.

Platinum(II) *meso*-tetra(pentafluorophenyl)porphine (Pt-TFPP), a phosphorescent dye that is quenched by oxygen (Fig. 2), is retained by the polymeric matrix due to its lipophilicity. However, a significant proportion of the dye remains on the surface of nanobeads (or close to it). Therefore, proteins may exert an undesired effect on the luminescence of the probe. Moreover, positively charged proteins may cause aggregation of carboxylated

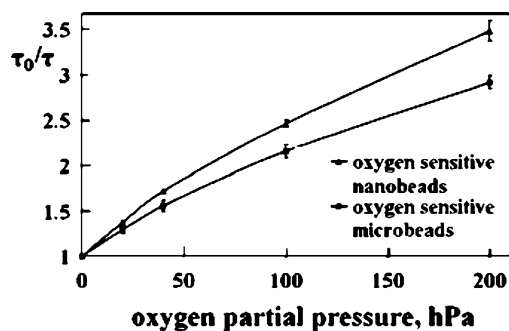


Fig. 2 Calibration curves of the oxygen-sensitive sensor beads

nanobeads. This, in turn, can alter their properties because the phosphorescence lifetime increases due to shielding of the probe by the protein (from oxygen). The effect is, however, dependent on the bead size and is more pronounced in the case of nanobeads. We have found that it is negligible in the case of oxygen-sensitive microbeads, which do not suffer from significant interference by BSA.

## 2.2

### pH-Sensitive Microbeads

pH-sensitive nanobeads were obtained by doping poly(acrylonitrile-*co*-acrylic acid) with carboxyfluorescein (CF). Both materials were first dissolved in DMF and then precipitated as fluorescently doped nanobeads by addition of water [18]. CF enables the measurement of pH in the physiological range. The fluorescence intensity at 530 nm may serve as the analytical signal, which in addition may become a reference signal if a second (reference) dye is added, for example a ruthenium complex whose luminescence is independent of pH (Fig. 3).

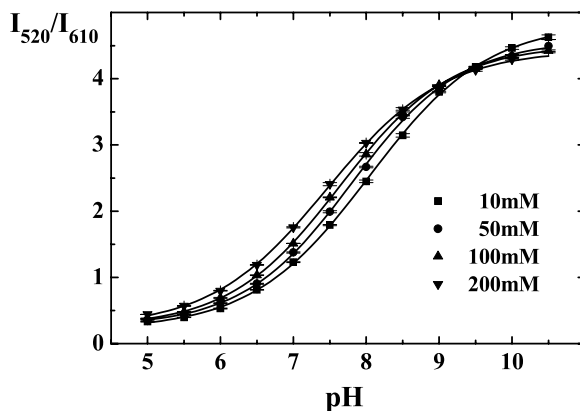


**Fig. 3** Calibration curves of pH-sensitive nanobeads at ionic strengths between 10 and 200 mM. Excitation at 485 nm

In order to obtain microscale pH-sensitive beads, a second strategy was developed. A lipophilic fluorescein derivative [19] served as a pH probe and was incorporated into the water-insoluble cationic polyelectrolyte Eudragit RL100 ([www.roehm.de](http://www.roehm.de)). This is a copolymer composed of esters of acrylic acid and methacrylic acid that also contains quaternary ammonium groups. It can be dispersed in water as a nanosuspension. The lipophilic fluorescein pH probe accumulates in the nanobeads because of the aliphatic C<sub>18</sub> side chain. The polyelectrolyte nanoparticles thus obtained adhere to the nanobeads due to



electrostatic interaction with the negatively charged carboxy groups on the surface of the nanobeads. Thus, the surface charge is positive.

The positive charge of the polyelectrolyte results from the presence of the quaternary ammonium groups of Eudragit which, however, are not amenable to coupling reactions. Therefore, another scheme was pursued in which layers of different charge were superimposed. Specifically, the negatively charged polyelectrolyte Eudragit L100 was adsorbed on the positively charged polyelectrolyte layer (Fig. 4).

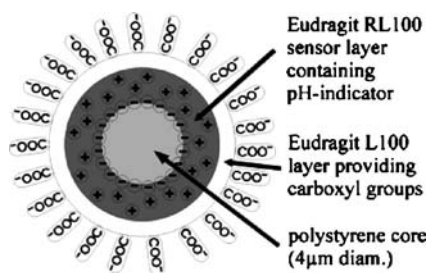


**Fig. 4** Schematic representation of layer-by-layer structure of pH-sensitive microbeads

As in case of the pH-sensitive nanobeads, the ratiometric approach can be used since both the protonated and deprotonated forms of the lipophilic fluorescein are strongly fluorescent. By plotting the ratio of these two signals against pH value, calibration curves were generated (Fig. 5).

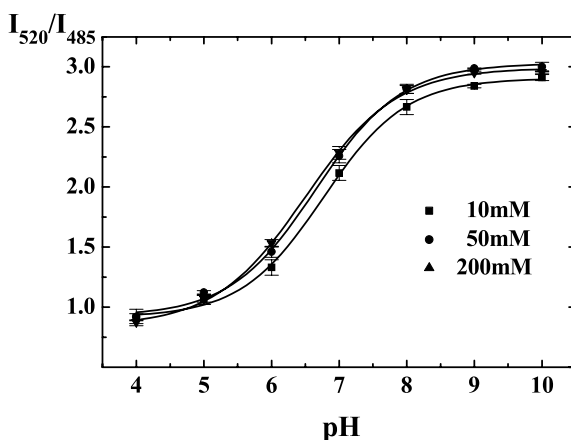


**Fig. 5** Calibration curves of pH-sensitive microbeads at ionic strengths from 10 to 200 mM. Emission was monitored at 590 nm

If there is no need for a selective receptor that could recognize a desired species, the positively charged polyelectrolyte nanobeads can directly adhere

to surfaces of negative charge, for example those of bacteria, fungi, or certain inorganic particles. They form a fluorescent layer around the cells making them visible through a fluorescence microscope (Fig. 1).

Ionic strength is known to affect the activity of  $\text{H}_3\text{O}^+$  ions, thus compromising the accuracy of optical pH sensors. Increasing ionic strength shifts the calibration curves toward smaller pH/ $\text{p}K_a$  values in the case of nanobeads. However, the cross-sensitivity to the ionic strength of the pH-sensitive microbeads is negligible due to the fluorescein derivative used, which is not very sensitive to changes in ionic strength [19].

The sensor beads with the reactive surface can serve as a platform for biologically addressable sensors. Thus, by attaching the sensors to the object of interest, site-specific determination of pH and  $\text{pO}_2$  can be performed. Attachment to bacterial cells is accomplished here via antibodies. The variety of possible indicator dyes and measurement principles enables creation of a wide range of analytically suitable micro- and nanosensors.

### 3

#### Dyed Polymer Microparticles and Their Use in Sensor Layers

Micro- and nanoparticles that are sensitive to a certain analyte (e.g., pH) can also be used as components of optical sensor materials. In contrast to the addressable nanobeads described above, such micro- and nanoparticles should not necessarily possess a functionalized surface for attachment to an object of interest. Particularly, optical pH sensors are an alternative to most commonly used glass electrodes, because they are free of electromagnetic interferences, can be easily miniaturized, and, if combined with fiber-optic technology, enable pH measurement even in remote locations [20]. Moreover, multianalyte sensing becomes possible when several types of beads (e.g., pH-sensitive and oxygen-sensitive) are incorporated into one polymer matrix. It is evident that for the purpose of sensing pH, the polymer matrix should be proton-permeable. Since most pH indicators possess excellent solubility in water, leaching of an indicator into the (usually aqueous) medium can be problematic [21]. An excellent solution to this problem consists in the covalent attachment of a pH indicator to the surface of a microparticle.

CF, one of the most common fluorescent pH indicators, has a  $\text{p}K_a$  of 6.5 in aqueous solution [4] and possesses a free carboxy group (Fig. 6) for covalent immobilization on the surface of polymer microparticles. However, other dyes were used as well. Their chemical structures are given in Fig. 6, and their properties are summarized in Table 3.

Both the protonated and deprotonated forms of the various pH indicators are emissive. The absorption spectrum of the low-energy (i.e., longwave absorbing) form, however, overlaps almost completely with the emission spectrum of the high-energy form. Thus, the inner filter effect is significant when

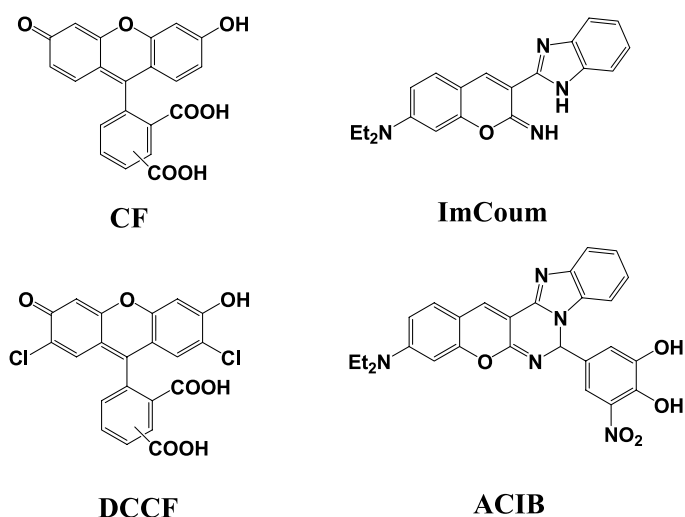


**Fig. 6** Chemical structures of the fluorescent indicators used for the preparation of pH-sensitive microparticles

**Table 3** Maxima (in nm) of the excitation and emission spectra of the pH-sensitive dyed beads, and  $pK_a$  values for bead-immobilized probes

pH-sensitive probe	Excitation <sup>a</sup>	Emission <sup>a</sup>	$pK_a$
CF/AM-pHEMA	470	524	6.81
CF/AmCell	472	525	5.27
CF/AA-Q-N2	473	527	6.58
DCCF/AM-pHEMA	505	545	3.45
ImCoum/AM-pHEMA	488	520	8.40
ImCoum/AmCell	482	522	7.18
ImCoum/AA-Q-N2	487	522	8.19
ACIB/AM-pHEMA	500	536	3.10
ACIB/AmCell	505	538	3.36
ACIB/AA-Q-N2	505	540	3.65

<sup>a</sup> For the low-energy (longwave) form of the probe. In the case of CF and DCCF this is the base form; in the case of ImCoum and AICB this is the acid form

a high-energy form is excited, and excitation of the low-energy form (the deprotonated form in the case of CF and DCCF, but the protonated form of ImCoum and ACIB) is preferred.

In order to enable covalent immobilization of the pH probes, beads were prepared from polymers containing primary amino groups. The polymers included, in particular, aminocellulose (AmCell), amino-modified polyacrylamide (AA-Q-N2), and amino-modified poly(hydroxyethyl methacrylate)

(AM-pHEMA). They were obtained in the form of microparticles 1–3  $\mu\text{m}$  in diameter. In a typical experiment, CF was covalently attached to the surface of the beads using standard peptide coupling procedures [22]. Other dyes were bound to the surface of polymer microparticles via (a) an amide linkage (in the case of DCCF), (b) Mannich reaction (in the case of ACIB), or (c) a triazine spacer link (in the case of ImCoum).

The  $pK_a$  values of the resulting microparticles are in the range from 8.4 to 3.36 (see Table 3) and this make them suitable for a variety of applications. The titration curves for the CF-based pH-sensitive microparticles are presented in Fig. 7. The  $pK_a$  values for the probes significantly depend on the polymer used. This is attributed to the change of microenvironment upon immobilization of the indicator. The combination of choice is therefore CF/AM-pHEMA, where effects of the microenvironment are negligible and the  $pK_a$  value for the probe (6.71) is close to that of the free indicator in aqueous solution.

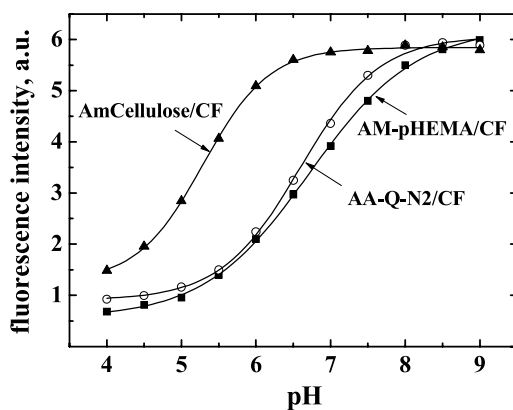


**Fig. 7** Titration curves of the CF-based polymer microparticles dispersed in polyurethane hydrogel

Most pH indicators and probes are cross-sensitive to ionic strength [19, 23] and this can compromise their performance. It is important to note that such pH-sensitive microparticles exhibit very little sensitivity to ionic strength in the physiological range, as can be seen in Fig. 8.

In the experiments described so far, fluorescence intensity was determined as a function of pH which is simple in terms of instrumentation. However, accuracy is often compromised by drifts in the optoelectronic setup and the properties of a probe (e.g., the concentration of the indicator dye and variations of the thickness of a sensor layer, etc.) [24]. The ratiometric approach presented above (Sect. 2) is one of the possible solutions which, however, requires two different optical setups for monitoring emission or excitation at two wavelengths. Measurements of fluorescence decay time (which is in the

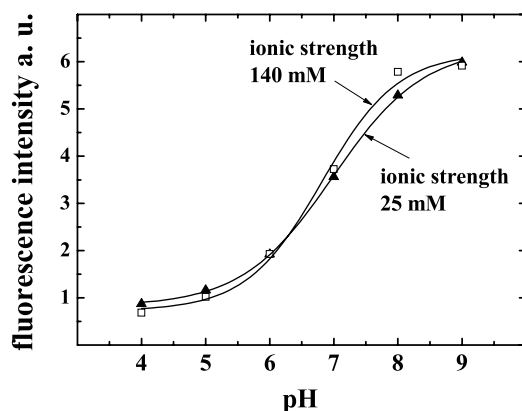


**Fig. 8** Titration curves of the CF-on-pHEMA microparticles dispersed in a 10- $\mu\text{m}$  film of polyurethane hydrogel at different ionic strengths

order of nanoseconds) is very precise, but unfortunately cannot be easily performed by small and low-cost equipment. Measurements of long ( $> 1 \mu\text{s}$ ) decay times is easier, but long-lived phosphorescent pH-sensitive probes are usually less efficient and suffer from severe cross-sensitivities (e.g., to oxygen) [25, 26].

Dual lifetime referencing (DLR) [27, 28] is an elegant solution to this problem. In DLR, fluorescence intensity is converted into a phase shift ( $\Phi$ ). It requires the use of inert (= pH- and oxygen-insensitive) reference particles with long decay time. In our case, phosphorescent reference particles of

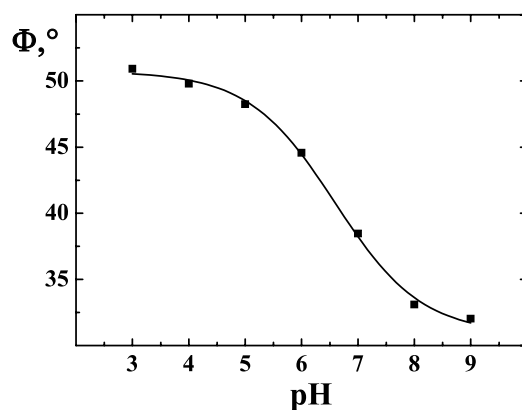


**Fig. 9** Calibration curve for the DLR-based pH sensor. CF/pHEMA microparticles are homogeneously dispersed in a 10- $\mu\text{m}$  hydrogel layer together with reference microparticles. The luminescence of both the indicator (CF) and the reference microparticles (Ru-dpp/PAN) was excited by a 505-nm LED at a modulation frequency of 45 kHz. The line represents fitting via Eq. 1

the ruthenium(II)-tris(4,7-diphenyl-1,10-phenanthroline) complex (Ru-dpp) in PAN were immobilized together with pH-sensitive microparticles into a hydrogel matrix. Both the calibration of, and measurements with, such a sensor are simple and precise (Fig. 9). Calibration plots can be fitted (correlation coefficient  $r^2 > 0.998$ ) with the following equation [29]:

$$\Phi = \frac{\Phi_{\min} - \Phi_{\max}}{1 - e^{(\text{pH}-x_0)/dx}} + \Phi_{\max}, \quad (1)$$

where  $\Phi$  is the phase shift, and  $\Phi_{\min}$ ,  $\Phi_{\max}$ ,  $x_0$ , and  $dx$  are numerical coefficients.

#### 4 Luminescence Lifetime Encoded Microbeads as Carriers for Multiplexed Bioassays

Progress in combinatorial chemistry and genomic and proteomic science, together with advances in high-throughput screening (HTS) techniques, has stimulated the development of multiplexed bioanalytical tools. Various platforms have been developed or are currently in development allowing the parallel quantification of subsets of targets of biochemical or medical relevance. Miniaturization and automation of high-throughput systems offer advantages such as reduced cost, reduction in the amount of sample required, reproducibility of results, and implementation in a benchtop environment.

Multiplexed bead-based assay systems are among the most promising concepts to achieve this goal. In contrast to flat-surface biochips, suspension arrays consist of a multitude of receptor-coated beads dispersed in the analyte solution. In these approaches, beads that bear specific receptors serve to carry a specific code to identify the kinds of assays performed in parallel. Encoded bead families are commonly created by incorporation of one or more fluorophores [30–33] or fluorescent quantum dots [34–36] into polymer beads at selected concentrations and ratios. Bead size typically ranges from 1 to 10  $\mu\text{m}$ . The resulting suspension arrays are then evaluated by, e.g., microfluorimetry [33] or flow cytometry [30, 37]. In the latter the suspended microspheres are passed by a microfluidic system through a detection chamber consisting of one or two lasers as excitation source and a detection unit to acquire the resulting emission of the identification code and labeled analyte. Specialized and automated flow cytometers with a multiplex capability of 100 and a sample throughput of several thousands a day include the *xMap*<sup>TM</sup> platform ([www.luminexcorp.com](http://www.luminexcorp.com)) and the Cytometric Bead Array ([www.bdbiosciences.com](http://www.bdbiosciences.com)).

In this section we report on a method for encoding polymer beads using luminescence lifetime as the information carrier. Recently, the concept of micro-suspension arrays was introduced [38], which consists of a mixture of

magnetic microbeads dispersed in the sample solution and having diameters ranging from 6 to 12  $\mu\text{m}$ . Each bead carries specific capture biomolecules (i.e., capture DNA or antibodies) that are covalently bound to the bead surface and can be identified via a luminescent code. Assays are performed by adding portions of the bead mixture to the analyte solution. Subsequent to binding of the target analytes to capture probes, the microspheres are forced to the bottom of the reaction vessel (e.g., a microtiter plate) by magnetic forces. This leads to in situ formation of a randomly ordered two-dimensional array which can be analyzed by fluorescence microscopy or automated image analysis. The formation of a sedimentation array and the respective readout is illustrated in Fig. 10.

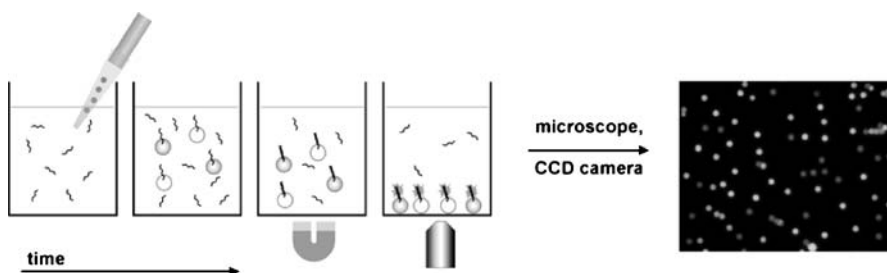


**Fig. 10** Formation of randomly ordered bead arrays by magnetic sedimentation of fluorescently encoded beads in a microplate

In addition to common encoding techniques based on fluorescence intensity, luminescence decay time was introduced as a new parameter for encoding microbeads. Every parameter that can be read out independently multiplies the number of codes that can be created. We have adapted luminescence decay imaging [39] for use in an inverted fluorescence microscope with epi-illumination by integrating ultrabright LEDs into the filter block. This allows switching between the standard mercury arc lamp and the LED as the excitation sources by shifting the filter slider. This has the same effect as changing from one excitation/emission filter combination to another. Images are acquired via a gateable Peltier-cooled CCD camera.

Two routes were pursued to obtain beads showing different luminescence decay time levels. First, nine families of beads were created by staining magnetic polymer beads with different amounts of tris(4,7-diphenyl-1,10-phenanthroline)ruthenium(II) chloride (Ru-dpp) and the dye crystal violet. At ambient conditions, Ru-dpp displays a luminescence lifetime of around 3.7  $\mu\text{s}$ . This value may be decreased to other desired decay times by adding crystal violet, which can act as an acceptor dye in fluorescence resonance energy transfer (FRET), and this reduces the decay time of Ru-dpp.

Nine well-separated bead families were created that consisted of three brightness levels and three decay times (Fig. 11). The coefficient of variation

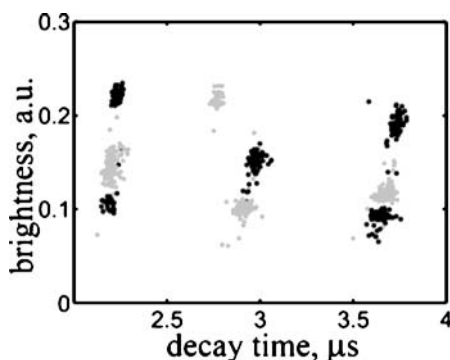


**Fig. 11** Scatter plot of luminescence brightness and decay of nine bead families created by co-staining beads with Ru-dpp and the resonance energy acceptor dye crystal violet

(CV) for the detected luminescence decay within a bead family is 1.3% while the brightness of the beads shows a much wider distribution (9%). Therefore, luminescence decay is less prone to interference, and more single levels of decay time can be adjusted.

Labels used for analyte detection must not spectrally overlap with coding signals. The emission of Ru-dpp enables the use of green labels (fluorescein; emitting between 500 and 530 nm) or red labels (Cy5; excitable at  $>610$  nm). Unfortunately, beads stained with crystal violet also are excited at  $>610$  nm. Hence, an alternative encoding method was sought in order to reduce these interferences. Now, two different ruthenium MLCs were employed. The first is Ru-dpp (used before) and the second is ruthenium(II)-tris(4,4'-diphenyl-2,2'-bipyridyl)chloride (Ru-dbp). The luminescence decay time of Ru-dbp is  $1.2 \mu\text{s}$ . The apparent decay time of a mixture of the two MLCs is a function of the ratio of the dyes (Fig. 12).

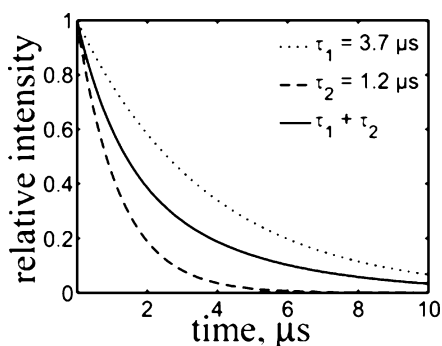


**Fig. 12** Calculated luminescence decay of Ru-dbp ( $\tau = 1.2 \mu\text{s}$ ), Ru-dpp ( $\tau = 3.7 \mu\text{s}$ ), and apparent decay of a mixture of equal emission intensity of both luminophores. Monoexponential decay is assumed for both individual luminophores



By applying this concept to an array, two intensity levels and five levels of decay times are accomplished, this resulting in a total of ten distinguishable bead families (Fig. 13). In fact, this approach toward an array enables three independent kinds of parameters to be employed for encoding microspheres. These include size, luminescence intensity, and luminescence decay time. As a result, this enables the creation of an even larger number of distinguishable codes. It is noted here again that luminescence decay can be adjusted and detected with higher accuracy than luminescence intensity. The possible number of codes calculated from the CV is 140, with further potential given by automated staining procedures.

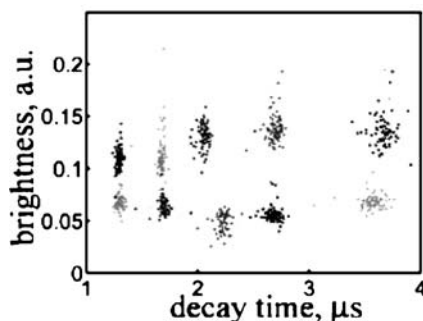


**Fig. 13** Scatter plot of luminescence brightness and decay time of ten discernable bead families created by co-staining beads with Ru-dpp and Ru-dbp

Detection of the analyte can be carried out with red or green fluorescent labels, which are established in array technology. When performing DNA hybridization assays, a detection limit of 2 nM of oligo-DNA in a 50- $\mu$ l sample volume was found using Cy5 as label or SYBR Green as a stain. This limit is likely to be further improved by the use of high-performance labels like quantum dots or fluorescent proteins.

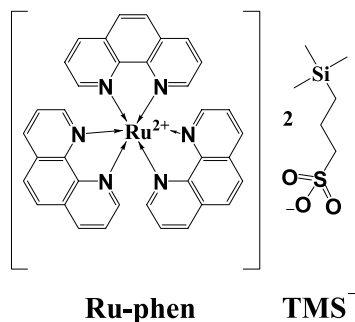
## 5

### **Dyed Polymer Microparticles and Their Use in Pressure-Sensitive and Temperature-Sensitive Paints (PSPs and TSPs)**

PSPs rely on the quenching of an indicator's luminescence by oxygen and provide information about total air pressure [40, 41]. Quenching by oxygen is always temperature dependent, therefore knowing the temperature (which is also a very important parameter itself) is essential for pressure determination. Most paints developed so far respond to a single parameter only. They are applied in the form of sensor foils or spots containing an indicator dissolved in a polymer [42–44].

The situation is much more complicated when simultaneous sensing of two analytes is envisioned. If both indicators are dissolved in a single polymer, undesirable cross-sensitivities are observed. This situation prevents the “simple” combination of two sensor “chemistries”. Two-layer sensors, on the other hand, are more difficult to manufacture, may also display mutual interferences, and often suffer from mechanical instability. Simultaneous sensing of both parameters is an ultimate goal. We believe that a material for simultaneous sensing of oxygen partial pressure and temperature performs best when both indicators are contained in a single polymer matrix in the form of nano- or microparticles. The sensitivity to a given analyte may then be tuned within the sensing microparticles while undesirable cross-sensitivities are avoided. We have identified the probes shown in Fig. 14 as being viable for sensing temperature and oxygen, respectively.

### temperature indicators



### oxygen indicators

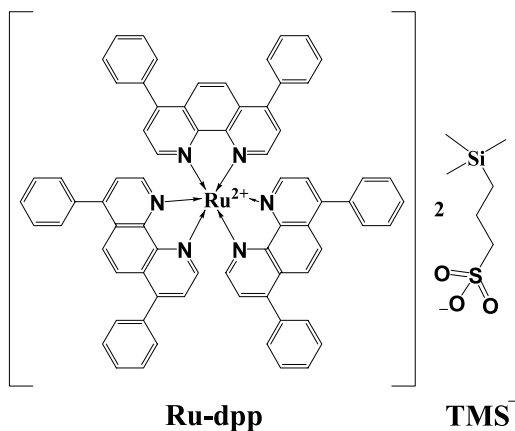
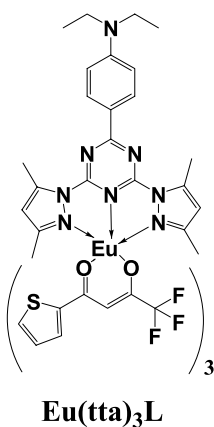
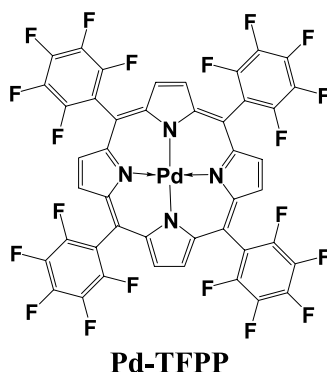


**Fig. 14** Chemical structures of the temperature and oxygen luminescent indicators

## 5.1

### Beads for Use in TSPs

The luminescence of ruthenium(II)-tris(phenanthroline) (Ru-phen; see Fig. 14) is highly temperature-dependent [45], as can be seen from Fig. 15. The decay time of the complex drops with temperature as a result of thermally activated nonradiative decay. In the presence of oxygen, however, dynamic quenching of the excited state occurs as well [46]. This undesirable cross-sensitivity is completely avoided when the indicator is immobilized in PAN microparticles, which are virtually impermeable to oxygen [47]. As can be seen from Fig. 15, quenching by oxygen is negligible at air saturation, and

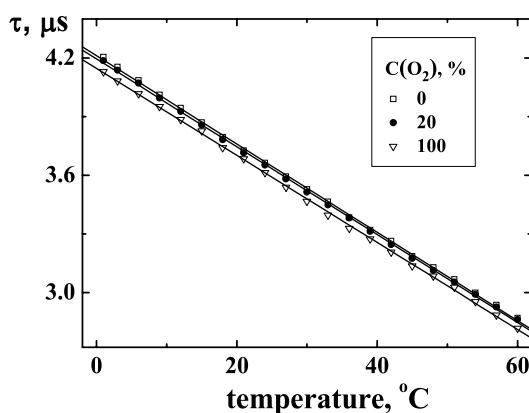


**Fig. 15** Temperature dependence of luminescence decay time for the Ru-phen/PAN probe

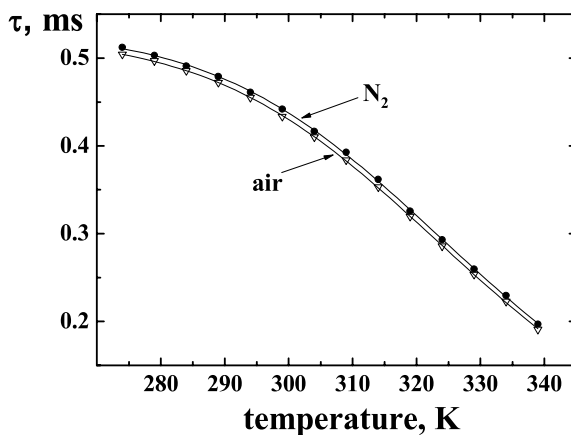


**Fig. 16** Temperature dependence of luminescence decay time for the Eu(tta)<sub>3</sub>L/PVMK probe

still extremely low even at 100% of oxygen. Dyed beads with a size of less than  $1\ \mu\text{m}$  have been obtained [18]. Moreover, the probe can be excited with a blue LED.

Europium(III) complexes usually exhibit highly temperature-dependent luminescence, which is only scarcely affected by molecular oxygen. Their application as probes is, however, compromised by the need for excitation in the UV [48, 49] and/or by low quantum yields [50, 51]. The europium(III)-tris( $\beta$ -diketonate) complex shown in Fig. 14 represents a new and bright ( $\Phi = 0.75$  at  $1\ ^\circ\text{C}$ ) temperature-sensitive probe that is excitable with visible light (with a maximum at 411 nm). If incorporated into poly(vinylmethyl ketone) (PVMK), its cross-sensitivity to oxygen is very low (Fig. 16).

## 5.2

### Beads for Use in PSPs

We use two types of oxygen probes whose luminescence is strongly quenched by molecular oxygen even in polymer solution. In dually sensing materials (PSP/TSP composites), separation of luminescences by decay time is mandatory. When Ru-phen is used as a temperature probe (with a decay time in the order of several microseconds), an oxygen probe having significantly longer lifetime is preferable. Thus, we use palladium(II) porphyrin complex Pd-TFPP (Fig. 14) which has a decay time of about 1 ms in the absence of oxygen. In order to tune oxygen sensitivity, the indicator was embedded in poly(styrene-*co*-acrylonitrile) (PSAN) microparticles. The size of the microparticles varied from 3 to  $6\ \mu\text{m}$ . Figure 17 presents calibration plots for the Pd-TFPP/PSAN oxygen-sensitive probe. The data also illustrate the dependence of the response to oxygen on temperature.

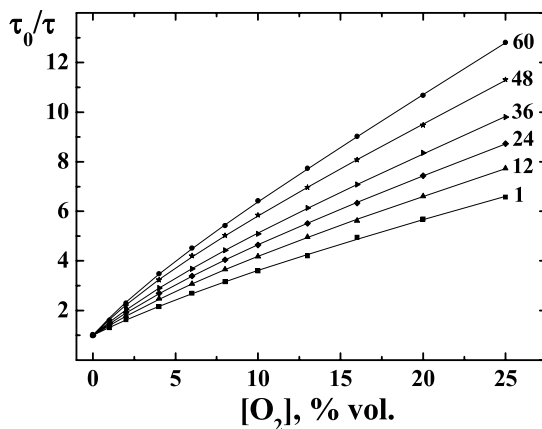


**Fig. 17** Stern–Volmer plots for oxygen sensing via the Pd-TFPP/PSAN probe between 1 and  $60\ ^\circ\text{C}$

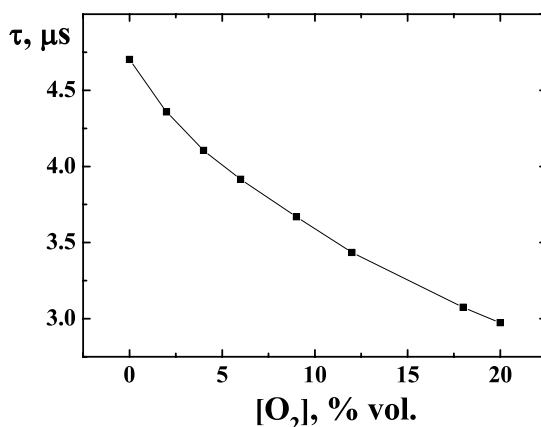


**Fig. 18** Stern–Volmer plots for oxygen sensing via the Ru-dpp/sol-gel microparticles

The situation is opposite if the europium(III) temperature-sensitive probe (with a decay time in the order of hundreds of microseconds) is used. For separation of the luminescences it is now desirable to use an oxygen-sensitive probe having a much shorter decay time. The bright ruthenium(II) polypyridyl complex Ru-dpp (Fig. 14) is the indicator of choice in this case. The complex, having a decay time in the order of several microseconds, can serve as an oxygen probe only if contained in a highly oxygen-permeable polymer. Thus, Ru-dpp was embedded in ethylcellulose microparticles and in a sol-gel. The typical size of the microparticles was about 15  $\mu\text{m}$  (for ethylcellulose) and 1  $\mu\text{m}$  (for the sol-gel). The calibration plot for Ru-dpp/sol-gel (S 5) microparticles is presented in Fig. 18.

### 5.3

#### Use of the Microparticles for Simultaneous Imaging of Oxygen and Temperature

The temperature-sensitive and oxygen-sensitive microparticles were homogeneously dispersed in a polymer matrix (biocompatible polyurethane hydrogel or silicone, respectively) in order to obtain a composite material for simultaneous monitoring of both parameters. The “cocktail” containing both types of microparticles can be coated on a support foil, and also sprayed onto a metal surface (for PSPs). The composite material is excited by a violet LED ( $\lambda_{\text{max}} = 405 \text{ nm}$ ). The luminescences are separated both spectrally (due to different emission maxima of the indicators: 580 nm for Ru-phen; 670 nm for Pd-TFPP) and by decay time. The composite material can thus be employed for simultaneous sensing and imaging of both analytes. Figure 19 represents photographic images (a and c) and lifetime images (b and d) for sensing temperature (a and b) and oxygen (c and d) by the dually sensing material. The

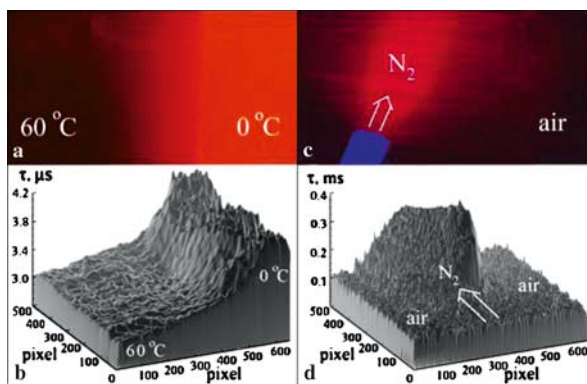


**Fig. 19** Temperature (a and b) and oxygen (c and d) sensing via the dually sensing material. The photographic images (a and c) were recorded through Chroma 580 and Chroma 680 bandpass filters, respectively. The lifetime images (b and d) were acquired with the same optical setup, using the following parameters: 0.25–2.25  $\mu\text{s}$  gate 1 and 2.25–4.25  $\mu\text{s}$  gate 2 (for b), 50–150  $\mu\text{s}$  gate 3 and 150–250  $\mu\text{s}$  gate 4 (for d)

reduction of the quenching efficiency can be clearly seen in the area exposed to a flow of pure nitrogen. On the other hand, the luminescence intensity and decay time of the temperature-sensitive particles are lower at higher temperature.

## 6 Phosphorescent Polymeric Nanospheres as Labels for Homogeneous Protein Assays and Protein Arrays Using Luminescence Lifetime Imaging

Microbeads and nanobeads responsive to small molecules or changes in the environment can serve as probes for (bio)chemical species, as shown in previous sections of this chapter. However, there has also been much interest in the development of fluorescent nanoparticles which are completely inert over a wide range of conditions, and therefore can serve as fluorescent labels in bioanalysis. Luminescent nanospheres can be divided into two categories: those where the nanoparticle itself is responsible for the emission of light, most prominently semiconductor nanocrystals (“quantum dots”) [52], and those where dyes are incorporated into a nonluminescent carrier material, which itself forms tiny (nanometer-sized) beads. Among the latter category, most attention has been paid to silica beads [53] and organic polymer spheres [54].

In order to be useful as a label, the particles need to fulfill several requirements in that they (a) are expected to be bioconjugatable, (b) are capable of incorporating and retaining fluorescent dyes, (c) display water solubility,

(d) are resistant to nonspecific binding, and (e) do not interfere with binding events (of antibodies or polynucleotides) occurring on the surface. Copolymers containing functionalities, such as carboxy, amino, or hydroxy groups, can be prepared by standard protocols for polymer synthesis or even be purchased. Polymers with carboxy groups are most often used because they are easier to activate than hydroxy groups, and also are more stable than particles containing amino groups. Fluorescent doping of the particles requires lipophilic dyes, which will prefer to reside in the polymer matrix even in a mainly aqueous environment.

Most work on organic polymer particles has been performed with PS (“latex”) beads. The starting material is quite affordable and even nanospheres are comparatively easy to prepare in various sizes and stained with various fluorophores. However, they are highly permeable to oxygen, and thus are not well suited for use along with phosphorescent dyes displaying long luminescence lifetimes because of efficient quenching by oxygen. PS is also known for its strong hydrophobic interactions with proteins, this making selective protein binding rather difficult. PAN is a viable alternative because of its low permeability for oxygen. PAN nanoparticles containing various fractions of carboxy groups can be obtained by copolymerization of acrylonitrile with acrylic acid. Such nanobeads can be easily stained with the phosphorescent complex Ru-dpp. The particles were shown to be useful for biomolecular interaction screening [13].

Due to its specific chemical properties, PAN unfortunately is not suitable for some kinds of dyes. In looking for alternatives, we have investigated nanospheres made from the copolymer referred to as PD. It is obtained by copolymerization of methacrylonitrile, divinylbenzene, and acrylic acid. Nanoparticles are formed spontaneously by slowly adding an alkaline aqueous solution to a DMF solution containing the copolymer. In the presence of a lipophilic fluorescent dye, the latter will be incorporated into the polymer as soon as the ratio of organic solvent to water reaches a certain value at which the polymer becomes insoluble in DMF. The size of the particles can be controlled by variation of the organic solvent, the rate of addition of water (smaller particles are obtained at slow rates), and the concentration of the polymer. The lower size limit appears to be at a bead diameter of around 40 nm. To obtain smaller particles, other procedures need to be employed [55]. The results presented here were achieved using PD particles of diameter ca. 50 nm, having a monodispersity of >99% as determined by dynamic light scattering and fluorescence correlation spectroscopy (FCS).

Such particles have been stained with lipophilic metalloporphyrins, preferably with platinum(II) *meso*-tetra(pentafluorophenyl)porphyrin (Pt-TFPP). This luminophore displays a bright emission in the red (650 nm) and a strong absorption in the violet and the green region (see Table 4). Due to the large efficiency of spin-orbit coupling, Pt-TFPP undergoes efficient  $S_1-T_1$  intersystem crossing (ISC), has a comparably large quantum yield (almost 50%), and

**Table 4** Spectral maxima (in nm) and molar absorbance ( $M^{-1} \text{ cm}^{-1}$ ) of the fluorophore Pt-TFPP in different environments

Transition	Excitation	Emission	Molar absorbance
$S_0-S_2$ (Soret band)	396 (toluene), 397 (in PS) <sup>a</sup> , 391 (PD) <sup>b</sup>	650	200 000
$S_0-S_1$ (Q band)	541 (toluene and PS) <sup>a</sup> , 539 (PD) <sup>b</sup>	650	40 000

<sup>a</sup> Polystyrene <sup>b</sup> Poly(methacrylonitrile-*co*-divinylbenzene-*co*-methacrylic acid)

has a phosphorescence lifetime in the range of 80  $\mu\text{s}$ . This allows sensitive and time-resolved (“gated”) detection even in the presence of high levels of biological background whose fluorescence decays within nanoseconds.

Such optical properties would make the Pt-TFPP chromophore the preferred choice for many labeling applications. Unfortunately, porphyrins have a strong tendency to aggregate in polar solvents. In addition, they are efficiently quenched by molecular oxygen. Both of these problems can be overcome by encapsulating the dye in PD nanoparticles. Figure 20a shows the excitation and emission spectra of the dye in toluene solution, and (b) inside PS and PD nanobeads (in aqueous buffer). A small blue shift of around 5 nm in the Soret band can be observed for PD. Nevertheless, the dye can still be efficiently excited using the 405-nm laser diode.

Figure 20b shows that by using the standard preparation and staining methods employed, PD nanoparticles allow more dye to be incorporated and thus are significantly brighter than PS nanospheres. Moreover, and in strong

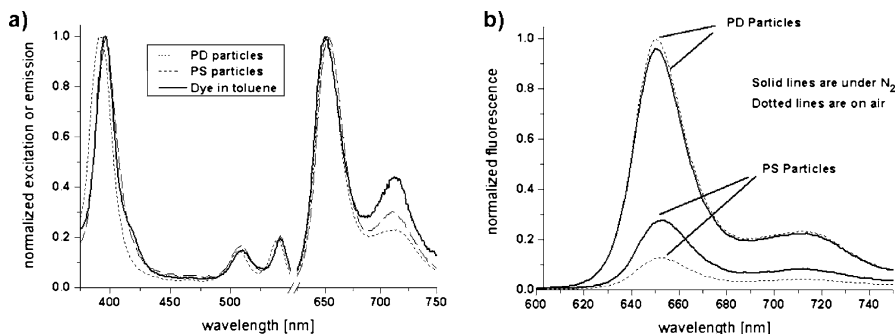


**Fig. 20** **a** Excitation and emission spectra of Pt-TFPP in toluene and in PS and PD particles. **b** PS and PD particles under nitrogen and in air. Particles were suspended at a concentration of 1 ppm (w/v) each in PBS buffer, 150 mM, pH 7.4, 0.05%  $\text{NaN}_3$



contrast to PS nanobeads, the dye remains virtually unquenched by oxygen inside PD particles.

In a first approach, we used the dyed nanoparticles as labels in a homogeneous protein assay based on fluorescence resonance energy transfer (FRET) [56]. FRET is an attractive method to determine distances (in fact it can be employed as a “molecular ruler”) [57], and also to detect the presence of a particular molecular target with high specificity, often without requiring tedious separation steps. In cases where labeling of the analyte is impossible (or should be avoided), detection can also be performed in a competitive manner, with the analyte displacing a labeled counterpart and therefore lowering the extent of FRET. In our case, we have found that Pt-TFPP can serve as a donor in FRET systems along with a variety of cyanine dyes (e.g., well-known Cy5) which absorb in the red to NIR region. The PD particles are small enough to allow efficient energy transfer from dyes inside the polymer to receptor-bound dyes located on the surface of the particles. Figure 21 schematically shows the nanoparticle FRET.

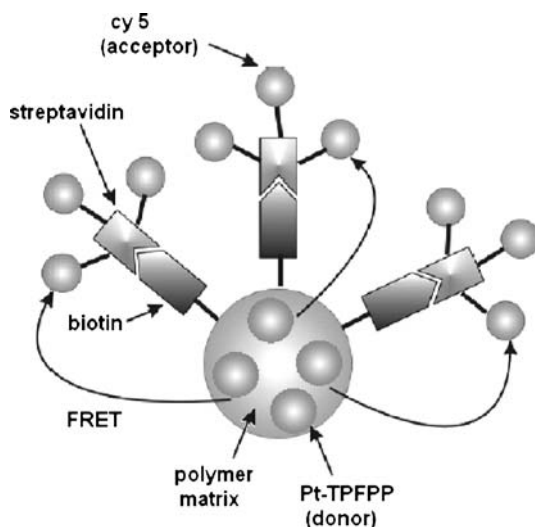


**Fig. 21** Schematic of the energy transfer process from the Pt-TFPP donor dye (inside the PD particles) to the acceptor dye Cy5 via biotin–streptavidin coupling

In order for the PD particles to serve as probes in affinity-based assays, they need to be functionalized with suitable protein-binding receptors, such as antibodies, haptens, or aptamers. We have employed the biotin–streptavidin system. PD nanospheres were first bound to an amino-tris(ethylene glycol) derivative of biotin via EDC/NHS-mediated coupling, and then were purified by size exclusion chromatography. The resulting particles were tested for binding of streptavidin labeled with the acceptor dye Cy5.

Most studies employing FRET on nanoparticles have focussed either on steady-state or on time-resolved detection of fluorescence intensity [58, 59]. By employing a donor and an acceptor, respectively, with largely different fluorescence lifetimes, separation of donor and acceptor fluorescence is accomplished by recording the emission after a certain delay time (after which the emission of the short-lived dye can no longer be observed). In the given case, the luminescence of Pt-TFPP in the PD spheres decays with a lifetime of nearly 80  $\mu$ s, whereas the red-emitting cyanine dyes generally have lifetimes of only a few nanoseconds (2–3 ns in case of Cy5). While gated detection allows for selective recording of a single dye and can efficiently suppress background, the signal is still subject to errors caused by local heterogeneities of the sample and variations of the light source. It is therefore more attractive to exploit fluorescence lifetime, as it is self-referenced and not responsive to certain artifacts.

The optical setup used for luminescence lifetime imaging of microplate-based assays has been described previously [60]. Briefly, an array of 96 violet LEDs (405 nm, 9 mW each) was used to excite all wells of a 96-well microplate simultaneously from the bottom after the light was guided through an appropriate excitation filter (BG 12, Schott). The emission was collected by an array of 96 optical fibers (PMMA) and filtered (RG 665) before being collected by the CCD camera. Rather than recording the whole decay curve (which can be rather time-consuming and results in large sets of data), the phase delay rationing (PDR) and rapid lifetime determination (RLD) schemes, which are both ratiometric, allow for a quick evaluation of changes in lifetime and of mean lifetimes, respectively (Fig. 22, left).

The images (Fig. 22, right) show a strong decrease in the lifetime of Pt-TFPP in biotinylated PD nanoparticles upon addition of Cy5-labeled strep-

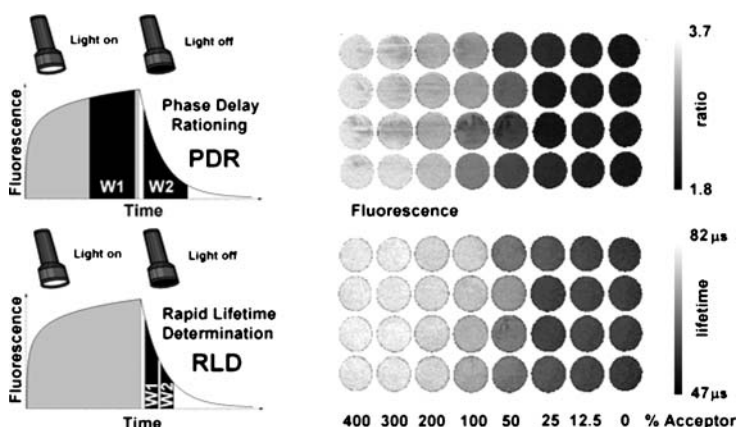


**Fig. 22** *Left*: Schematic of the lifetime schemes employed. *Right*: Lifetime images of microplate wells with decreasing amounts of streptavidin, labeled with FRET acceptor Cy5, from the *left* to the *right*

tavidin. An evaluation of the data (Fig. 23) showed that the dynamic range extends over several orders of magnitude and can be adjusted by the amount of nanospheres added (10 ppm in this case). The binding is specific, as determined with control experiments with plain carboxylated particles and with human serum albumin (HSA) conjugated particles. Both showed only a very small decrease in donor lifetime upon addition of labeled streptavidin. Detection limits in the upper picomolar (pM) range can be achieved. Several other proteins were also shown not to interfere.

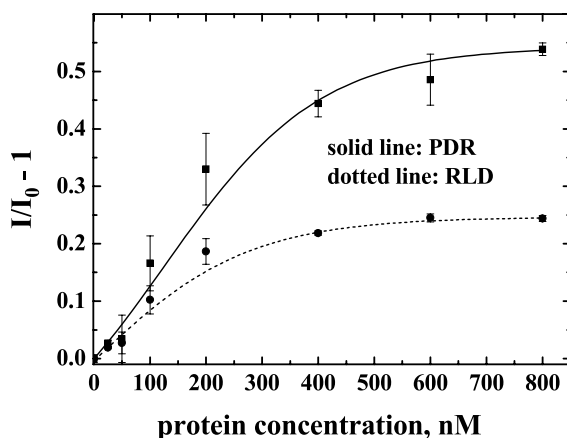


**Fig. 23** Evaluation of the luminescence lifetime-based FRET assay using PD-biotin nanobeads

In the second approach, biofunctionalized PD nanobeads were used as labels for protein arrays. Functional and analytical protein microarrays are a rapidly growing field, allowing quantification of interactions of proteins with other proteins or other kinds of molecules [61, 62]. Interaction analysis can be carried out using minute amounts of protein and to a degree of multiplexing that, in principle, allows even the screening of an entire proteome on a single chip. Fluorescence detection is dominant in the microarray area. However, standard organic dyes like Cy3 and Cy5 are most often used for labeling, although there have been studies using larger labels, such as quantum dots [63], silica [64], and PS [65] nanobeads. The use of such labels results in a much larger signal (compared to organic labels). This lowers the limits of detection and therefore allows quantitative determination of even low-concentration proteins. It simultaneously reduces the complexity of the optical setup (thereby the cost of equipment). Unfortunately, most protocols established for protein arrays are quite sensitive to experimental conditions. Nonmolecular labels, such as Q-dots, have also led to unspecific adsorption on the surface, and this has prevented a more widespread use of such labels to date.

Fluorescence lifetime has been shown recently to be suitable for detecting affinity binding [66] and this may be extended to detection schemes for microarrays [62]. Adding lifetime information can increase the quality of the readout, as it is mostly unaffected by aggregation and possible imprecision in the optical setup because lifetime is a self-referenced parameter. Finally, gated detection with long-lived dyes also tolerates unspecific adsorption to a certain extent and may add an additional dimension for multiplexing [67, 68].

The optical setup used for protein array imaging was a modification of the one described above, with the excitation light from the 96-LED array filtered and guided through optical fibers onto a glass slide with 96 individually addressable cavities delineated by a Teflon mask. The filtered emission was recorded directly by the CCD camera (Fig. 24, left).

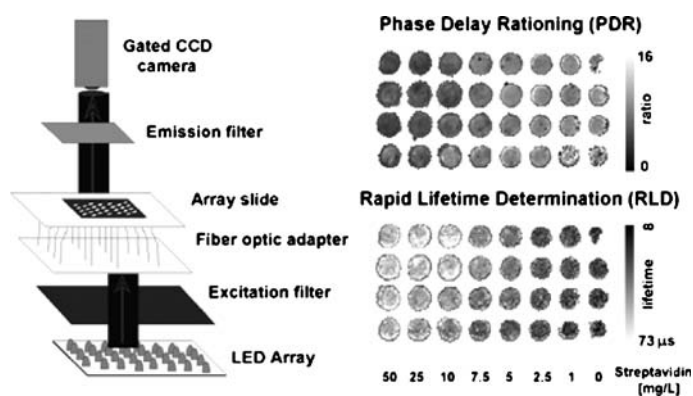


**Fig. 24** *Left:* Optical setup used for protein array imaging. *Right:* Lifetime images of protein arrays with decreasing amount of PD–streptavidin nanos from the *left* to the *right*

The surface of the PD nanobeads was modified with biotin and streptavidin functionalities in order to make them useful as labels in protein microarrays. Shown in Fig. 24 (right) are lifetime images of Pt-TPPP-doped PD nanospheres, surface-modified with streptavidin, immobilized, and bound covalently onto glass slides functionalized with *N*-hydroxysuccinimide (NHS) ester groups. Streptavidin could be selectively quantified in nanomolar concentrations. Adding lifetime contrast leads to an immense improvement in image quality and lowers the detectable concentration substantially.

Other binding interactions (such as of those PD–streptavidin particles with a biotinylated surface or use of PD–biotin particles in a biotin–streptavidin–PD–biotin surface) could also be verified, as they were shown to be detectable with comparable sensitivity using luminescence lifetime imaging. It was also found that the PD particles caused a high background due to unspecific absorption and aggregation, and therefore required careful control of the experimental conditions. The solid-phase array format does not

require proximity to other dyes. Thus, adding a hydrophilic shell around the particles (e.g., of polyethylene glycol) before bioconjugation may also prove advantageous.

In summary, dyed PD nanoparticles can be synthesized that exhibit advantages over PS beads, for example, higher dye loading capacity or lack of oxygen quenching. The long lifetime of the encapsulated Pt-TFPP dye allows time-resolved (“gated”) detection and selective fluorescence lifetime imaging in the presence of shorter-lived dyes, as shown in the FRET approach. The brightness of the dye enables high sensitivity of detection. Biofunctionalized PD nanoparticles can be used for protein analysis in several ways: (a) homogeneous assays can be performed with appropriate ligand–receptor pairs by resonance energy transfer and readout using intensity or lifetime-based detection, and (b) solid-phase protein arrays can be constructed using suitable conjugates with PD nanobeads. Moreover, the nanospheres may be employed as labels for DNA.

## References

1. Kumar CS (ed) (2005) *Biofunctionalization of nanomaterials*. Wiley, Weinheim, p 366
2. Meier W (2000) *Chem Soc Rev* 29:295
3. Buck SM, Koo Y, Park E, Xu H, Philbert M, Brasuel M, Kopelman R (2004) *Curr Opin Chem Biol* 8:540
4. Haugland RP (2002) *Handbook of fluorescent probes and research products*. Molecular Probes, Eugene, OR, p 831
5. Brackmann U (1997) *Lambdachrome laser dyes*. Lambda Physik, Goettingen, p 284
6. Daehne S, Resch-Genger U, Wolfbeis OS (eds) (1998) *Near-infrared dyes for high technology applications*. Kluwer, London
7. Latos-Grazynski L (2000) In: Kadish KM, Smith KM, Guillard R (eds) *The Porphyrin Handbook Vol. 2*. Academic Press, San Diego, p 361–417
8. Klimant I, Wolfbeis OS (1995) *Anal Chem* 67:3160
9. Alford PC, Cook MJ, Lewis AP, McAuliffe GSG, Skarda V, Thomson AJ, Glasper JL, Robbins DJ (1985) *J Chem Soc Perkin Trans II* 5:705
10. Lamansky S, Djurovich P, Murphy D, Abdel-Razzaq F, Lee H, Adachi C, Burrows PE, Forrest SR, Thompson ME (2001) *J Am Chem Soc* 123:4304
11. Kokko L, Sandberg K, Loevgren T, Soukka T (2004) *Anal Chim Acta* 503:155
12. Landfester K (2003) *Top Curr Chem* 227:75
13. Park EJ, Brasuel M, Behrend C, Philbert MA, Kopelman R (2003) *Anal Chem* 75:3784
14. Brasuel MG, Miller TJ, Kopelman R, Philbert MA (2003) *Analyst* 128:1262
15. Brasuel M, Kopelman R, Aylott JW, Clark H, Xu H, Hoyer M, Miller TJ, Tjalkens R, Philbert MA (2002) *Sensor Mater* 14:309
16. Xu H, Aylott JW, Kopelman R (2002) *Analyst* 127:1471
17. Sumner JP, Aylott JW, Monson E, Kopelman R (2002) *Analyst* 127:11
18. Kuerner JM, Klimant I, Krause C, Preu H, Kunz W, Wolfbeis OS (2001) *Bioconjug Chem* 12:883
19. Weidgans BM, Krause C, Klimant I, Wolfbeis OS (2004) *Analyst* 129:645
20. Song A, Parus S, Kopelman R (1997) *Anal Chem* 5:863
21. Butler TM, MacCraith BD, McDonagh C (1998) *J Non-Cryst Solids* 224:249

22. Hermanson GT (1996) *Bioconjugate techniques*. Academic, New York, p 785
23. Opitz N, Luebbers DW (1983) *Sens Actuators B* 4:473
24. Wolfbeis OS, Klimant T, Werner T, Huber C, Kosch U, Krause C, Duerkop A (1998) *Sens Actuators B* 51:17
25. Clarke Y, Xu W, Demas JN, DeGraff BA (2000) *Anal Chem* 72:3468
26. Neurauter G, Klimant I, Wolfbeis OS (1999) *Anal Chim Acta* 382:67
27. Klimant I, Huber Ch, Liebsch G, Neurauter G, Stangelmayer A, Wolfbeis OS (2001) In: *Springer series on fluorescence spectroscopy*, vol 1. Springer, Berlin, p 257
28. Huber Ch, Klimant I, Krause C, Wolfbeis OS (2001) *Anal Chem* 73:2097
29. Liebsch G, Klimant I, Krause C, Wolfbeis OS (2001) *Anal Chem* 73:4354
30. Fulton RJ, McDade RL, Smith PL, Kienker LJ, Kettman JR (1997) *Clin Chem* 43:1749
31. Smith RA, Giorgio TD (2004) *Comb Chem High Throughput Screen* 7:141
32. Ferguson JA, Steemers FJ, Walt DR (2000) *Anal Chem* 72:5618
33. Hakala H, Virta P, Salo H, Lonnberg H (1998) *Nucleic Acids Res* 26:5581
34. Mulvaney SP, Mattoussi HM, Whitman LJ (2004) *BioTechniques* 36:602
35. Xu H, Sha MY, Wong EY, Uphoff J, Xu Y, Treadway JA, Truong A, O'Brien E, Asquith S, Stubbins M, Spurr NK, Lai EH, Mahoney W (2003) *Nucleic Acids Res* 31:e43/1
36. Han M, Gao X, Su JZ, Nie S (2001) *Nat Biotechnol* 19:631
37. Gao X, Nie S (2004) *Anal Chem* 76:2406
38. Moser C, Mayr T, Klimant I (2006) *Anal Chim Acta* 558:102
39. Liebsch G, Klimant I, Frank B, Holst G, Wolfbeis OS (2000) *Appl Spectrosc* 54:548
40. Khalil GE, Costin C, Crafton J, Grenoble S, Gouterman M, Callis JB, Dalton LR (2004) *Sens Actuators B* 97:13
41. Zelelow B, Khalil G, Phelan G, Carlson B, Gouterman M, Callis JB, Dalton LR (2003) *Sens Actuators B* 96:304
42. Mills A, Thomas M (1997) *Analyst* 122:63
43. Mills A, Lepre A (1997) *Anal Chem* 69:4653
44. Apostolidis A, Klimant I, Andrzejewski D, Wolfbeis OS (2004) *J Comb Chem* 6:325
45. Liebsch G, Klimant I, Wolfbeis OS (1999) *Adv Mater* 11:1296
46. Wang Z, McWilliams A, Evans C, Lu X, Chung S, Winnik M, Manners I (2002) *Adv Funct Mater* 12:415
47. Brandrup J, Immergut EH, Grulke EA (eds) (1999) *Polymer handbook*. Wiley, New York
48. Berry MT, May PS, Xu HJ (1996) *Phys Chem* 100:9216
49. Khalil GE, Lau K, Phelan GD, Carlson B, Gouterman M, Callis JB, Dalton LR (2004) *Rev Sci Instrum* 75:192
50. Dadabhoy A, Faulkner S, Sammes PG (2000) *J Chem Soc Perkin Trans II* 2359
51. Van Deun R, Nockemann P, Fias P, Van Hecke K, Van Meervelt L, Binnemans K (2005) *Chem Commun* 590
52. Alivisatos P (2004) *Nat Biotechnol* 22:47
53. Van Blaaderen A, Vrij A (1992) *Langmuir* 8:2921
54. Bangs LB (1987) *Am Biotechnol Lab* 5:10
55. Gilbert R (1995) *Emulsion polymerisation: a mechanistic approach*. Academic, London
56. Förster T (1967) *Compr Biochem* 22:61
57. Valeur B (2002) *Molecular fluorescence: principles and applications*. Wiley, Weinheim, p 387
58. Valanne A, Lindroos H, Lövgren T, Soukka T (2005) *Anal Chim Acta* 539:251
59. Clapp AR, Medintz IL, Mauro JM, Fisher BR, Bawendi MG, Mattoussi H (2004) *J Am Chem Soc* 126:301

60. Schäferling M, Wu M, Enderlein J, Bauer H, Wolfbeis OS (2003) *Appl Spectrosc* 57:1386
61. Zhu H, Snyder M (2003) *Curr Opin Chem Biol* 7:55
62. Nagl S, Schäferling M, Wolfbeis OS (2005) *Microchim Acta* 151:1
63. Gerion D, Chen F, Kannan B, Fu A, Parak WJ, Chen DJ, Majumdar A, Alivisatos AP (2003) *Anal Chem* 75:4766
64. Lian W, Litherland SA, Badrane H, Tan W, Wu D, Baker HV, Gulig PA, Lim DV, Jin S (2004) *Anal Biochem* 334:135
65. Wiese R (2003) *Luminescence* 18:25
66. Hoefelschweiger BK, Pfeifer L, Wolfbeis OS (2005) *J Biomol Screen* 10:685
67. Waddell E, Wang Y, Stryjweski W, McWorther S, Henry AC, Evans D, McCarley RL, Soper SA (2000) *Anal Chem* 72:5907
68. Cubeddu R, Comelli D, Andrea CD, Taroni P, Valentini G (2002) *J Phys D Appl Phys* 35:R61